DIELECTRIC METAMATERIALS

FUNDAMENTALS, DESIGNS, AND APPLICATIONS

Edited by

IGAL BRENER, SHENG LIU, ISABELLE STAUDE, JASON VALENTINE AND CHRISTOPHER HOLLOWAY

ELSEVIER

Dielectric Metamaterials

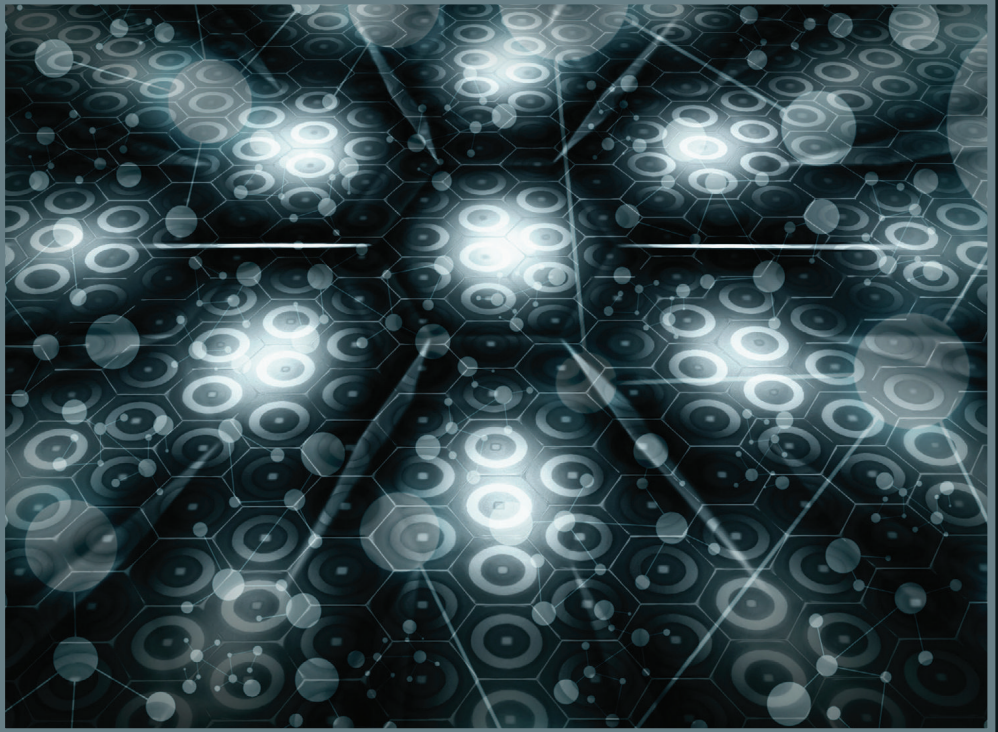This page intentionally left blank

Woodhead Publishing Series in Electronic and Optical Materials

Dielectric Metamaterials

Fundamentals, Designs, and Applications

Edited by

Igal Brener

Sheng Liu

Isabelle Staude

Jason Valentine

Christopher Holloway

Notices

Knowledge and best practice in this field are constantly changing. As new research and experience broaden our understanding, changes in research methods, professional practices, or medical treatment may become necessary.

Practitioners and researchers must always rely on their own experience and knowledge in evaluating and using any information, methods, compounds, or experiments described herein. In using such information or methods they should be mindful of their own safety and the safety of others, including parties for whom they have a professional responsibility.

To the fullest extent of the law, neither the Publisher nor the authors, contributors, or editors, assume any liability for any injury and/or damage to persons or property as a matter of products liability, negligence or otherwise, or from any use or operation of any methods, products, instructions, or ideas contained in the material herein.

For information on all Woodhead Publishing publications
visit our website at https://www.elsevier.com/books-and-journals

Working together
to grow libraries in
developing countries

www.elsevier.com • www.bookaid.org

Contents

This page intentionally left blank

List of contributors

Amir Arbabi

Department of Electrical and Computer Engineering, University of Massachusetts Amherst, Amherst, MA, United States

Ehsan Arbabi

T.J. Watson Laboratory of Applied Physics, California Institute of Technology, Pasadena, CA, United States

Nicolas Bonod

Aix-Marseille Univ, CNRS, Centrale Marseille, Institut Fresnel, Marseille, France

Igal Brener

Sandia National Laboratories, Albuquerque, NM, United Sates

Center for Integrated Nanotechnologies, Sandia National Laboratories, Albuquerque, NM, United States

Andrei Faraon

T.J. Watson Laboratory of Applied Physics, California Institute of Technology, Pasadena, CA, United States

Andrey Fedyanin

Faculty of Physics, Lomonosov Moscow State University, Moscow, Russia

Christopher L. Holloway

National Institute of Standards and Technology, U.S. Department of Commerce, Boulder, CO, United States

Seyedeh Mahsa Kamali

T.J. Watson Laboratory of Applied Physics, California Institute of Technology, Pasadena, CA, United States

Yuri Kivshar

Nonlinear Physics Centre, Australian National University, Canberra ACT, Australia

Sergey Kruk

Nonlinear Physics Centre, Australian National University, Canberra ACT, Australia

Edward F. Kuester

Department of Electrical, Computer, and Energy Engineering, University of Colorado at Boulder, Boulder, CO, United States

Arseniy I. Kuznetsov

Institute of Materials Research and Engineering, A*STAR (Agency for Science, Technology and Research), Singapore, Singapore

Sheng Liu

Sandia National Laboratories, Albuquerque, NM, United Sates

Boris Luk'yanchuk

Division of Physics and Applied Physics, School of Physical and Mathematical Sciences, Nanyang Technological University, Singapore, Singapore

Faculty of Physics, Lomonosov Moscow State University, Moscow, Russia

Arka Majumdar

Department of Electrical Engineering, University of Washington, Seattle, WA, United States

Physics Department, University of Washington, Seattle, WA, United States

Dragomir N. Neshev

Nonlinear Physics Centre, Research School of Physics, The Australian National University, Canberra, ACT, Australia

Manuel Nieto-Vesperinas

Instituto de Ciencia de Materiales de Madrid, C.S.I.C., Madrid, Spain

Ramon Paniagua-Dominguez

Institute of Materials Research and Engineering, A*STAR (Agency for Science, Technology and Research), Singapore, Singapore

Jörg Schilling

Institute of Physics, Martin-Luther-University Halle–Wittenberg, Halle, Germany

Maxim Shcherbakov

School of Applied and Engineering Physics, Cornell University, Ithaca, NY, United States

Faculty of Physics, Lomonosov Moscow State University, Moscow, Russia

Alexander Sprafke

Institute of Physics, Martin-Luther-University Halle–Wittenberg, Halle, Germany

Isabelle Staude

Institute of Applied Physics, Abbe Center of Photonics, Friedrich Schiller University Jena, Germany

Chengjun Zou

Institute of Applied Physics, Abbe Center of Photonics, Friedrich Schiller University Jena, Germany

This page intentionally left blank

Electromagnetic metamaterials and metasurfaces: historical overview, characterization, and the effect of length scales

1

Christopher L. Holloway[a], Edward F. Kuester[b]
[a]National Institute of Standards and Technology, U.S. Department of Commerce, Boulder, CO, United States, [b]Department of Electrical, Computer, and Energy Engineering, University of Colorado at Boulder, Boulder, CO, United States

1.1 Introduction

The study of electromagnetic (EM) interactions with materials has a long and rich history dating back to Fresnel, Maxwell, Rayleigh, and many others [1–4]. Over these nearly 200 years, EM material development and applications have blossomed dramatically, culminating in the recent developments of metamaterials [5–16]. The prefix "meta" is a Greek preposition meaning (among other things) "beyond". Metamaterials are novel, synthetic materials engineered to achieve unique properties not normally found in nature, i.e., materials beyond those occurring naturally. Metamaterials are often realized by arranging a set of small scatterers in a regular array throughout a region of space (Fig. 1.1), thus obtaining some desirable bulk behavior. Artificial dielectrics were early examples of these engineered materials. However, the term metamaterial is a newer designation that includes, but is not limited to, artificial dielectrics. Nor does the term metamaterial refer to classical periodic structures, such as what are now called photonic bandgap (PBG) structures or frequency-selective surfaces (FSSs). The term metamaterial refers to a material or structure with more exotic properties than artificial dielectrics, but which can still be described by bulk material parameters as natural materials can. One particular class of metamaterial that is being studied extensively consists of the so-called "double-negative" (DNG) materials [17–32] (also known as negative-index materials (NIM), backward-wave (BW) media, or left-handed materials (LHM)). Such materials have the property that their effective permittivity and effective permeability are simultaneously negative in a given frequency band. Another property not normally found in nature that can be achieved with metamaterials is that of near-zero refractive index. In this type of material, either the permittivity or permeability is designed to have its real part close to zero. Materials with unique properties such as these have a wide range of potential applications in electromagnetics at frequencies ranging from the low microwaves to optical, including shielding, low-reflection materials, novel substrates, antennas, electronic switches, devices, "perfect lenses," resonators, and of course cloaking, to name only a few.
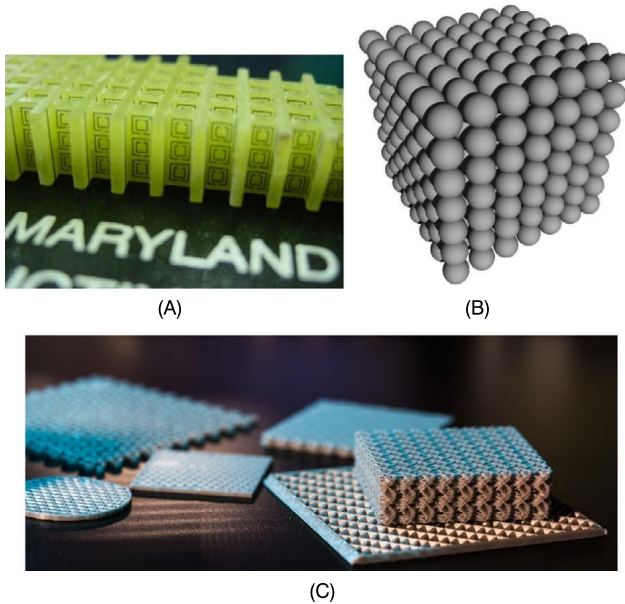
Figure 1.1 Three examples of metamaterials: (A) array of split-rings (Courtesy of Dr. N. Orloff of NIST and Prof. S.M. Anlage of the University of Maryland), (B) array of spherical particles, and (C) array of arbitrarily shaped dielectric inclusions (from Shutterstock, https://www.shutterstock.com/image-photo/example-metamaterials-physics-laboratory-1074505616?src=library).

Initially, the pursuit of cloaking was the "Holy Grail" of these metamaterials and received much attention in the early years of metamaterial research. Cloaking (or the ability to "hide" an object) has appeared throughout the years in popular literature and, depending on your generation, examples include Tolkien's ring, Romulan warships, and Harry Potter's cloak. However, due to physical limitations (no broadband lossless metamaterials are available) cloaking materials have not come to practical fruition. So researchers have turned their attention to other exotic material properties. Properties that are of great interest for a wide range of applications include controllability (that is, a material whose properties can easily be changed over a wide range of frequencies), designs for a very narrow bandwidth, and engineering materials with tailored unnatural permittivities and permeabilities, e.g., materials with near-zero indices.

The concept of metamaterials has been extended to two-dimensional arrays (referred to as metasurfaces) [33,34]; see Figs. 1.1C and 1.2. These types of metastructures have an advantage over three-dimensional metamaterials because they take up less physical space and have the potential for lower losses. Metasurfaces have become a popular alternative to metamaterials. Applications of metasurfaces at frequencies from low microwave to optical have attracted great interest in recent years. These applications in electromagnetics include controllable "smart" surfaces, miniaturized cavity resonators, novel waveguiding structures, angular-independent surfaces, absorbers, biomedical devices, terahertz switches, and fluid-tunable frequency-agile materials, to name only a few.
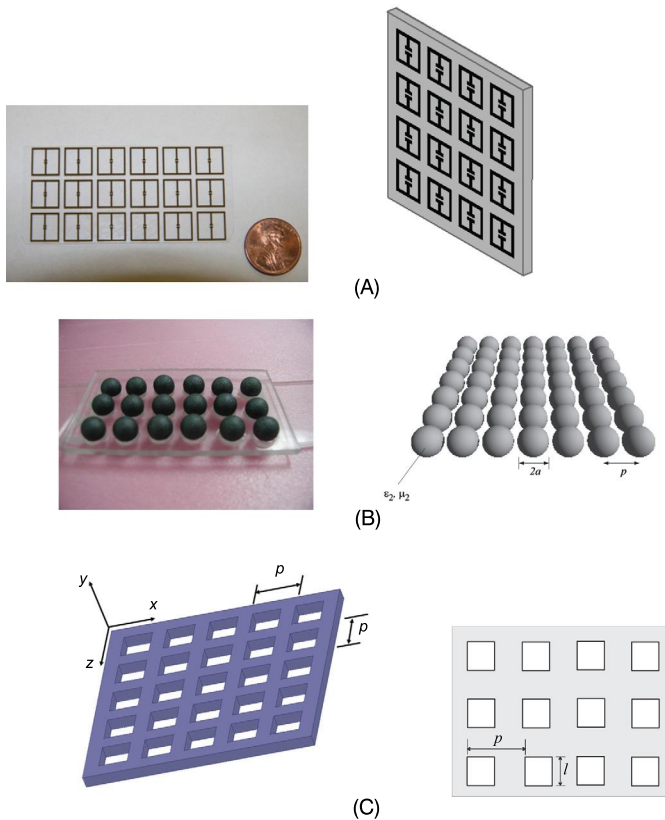
Figure 1.2 Three examples of metasurfaces: (A) array of metallic scatterers (from C.L. Holloway, E.F. Kuester, J.A. Gordon, J. O'Hara, J. Booth, D.R. Smith, An overview of the theory and applications of metasurfaces: the two-dimensional equivalents of metamaterials, IEEE Antennas Propag. Mag. 54 (2) (April 2012) 10–35, © 2012 IEEE), (B) array of magneto-dielectric spherical particles (from C.L. Holloway, E.F. Kuester, J.A. Gordon, J. O'Hara, J. Booth, D.R. Smith, An overview of the theory and applications of metasurfaces: the two-dimensional equivalents of metamaterials, IEEE Antennas Propag. Mag. 54 (2) (April 2012) 10–35, © 2012 IEEE), and (C) array of square apertures (from C.L. Holloway, E.F. Kuester, Generalized sheet transition conditions (GSTCs) for a metascreen, IEEE Trans. Antennas Propag. 66 (5) (2018) 2414–2427, © 2018 IEEE).

The metasurface concept can be extended even further by use of only a linear unit cell, rather than a surface element, as the building block, or even only a single subwavelength resonant element for some desired effect or behavior. In this chapter, we will discuss different aspects of various electromagnetic metastructures. We will provide a historical perspective, a study of the concepts that underlly their behavior, a discussion of the characterization of these metastructures, and a discussion on how these different metastructures behave at different length scales (that is, periodicity and inclusion size relative to the wavelength of interest).

1.2   Electromagnetic behavior of ordinary materials

Before we discuss the behavior of engineered materials and how this behavior changes
at different wavelength scales, we need to first discuss electromagnetic material prop-
erties, in general. We start by revisiting how the permittivity and permeability of a
medium arise. Permittivity is due to the induced electric-dipole response of a large
number of small particles [35, pp. 159–162]. Classically, these particles have been re-
garded as atoms or molecules, but in the past 70 years so-called artificial dielectrics
have been developed whose "atoms" are small metal or dielectric objects, of dimen-
sions large compared to atomic size, but still small compared to the wavelength of
the electromagnetic waves acting in the "host" medium in which these inclusions are
embedded [2,3,36–46]. In either case, the induced dipole moments are related by the
electric polarizabilities of the scatterers to the electric field acting on each one. The
dipole moments are then volume-averaged into a polarization density **P**, and the elec-
tric field is likewise averaged into a macroscopic or effective field **E**. From these, the
electric displacement vector **D** and permittivity ϵ are defined by:

$$\mathbf{D} = \epsilon_0 \mathbf{E} + \mathbf{P} = \epsilon \mathbf{E} ,$$

where ϵ is related to the electric polarizability densities of the scatterers in space.

Permeability originates in an analogous way from the volume density **M** of mag-
netic dipole moments arising from the angular momentum of charge due to particle
spin and orbital movement, and is related to the magnetic polarizabilities of the scat-
terers. The effective fields **H** and **B** are then related to each other by the expression:

$$\mathbf{B} = \mu_0 \left(\mathbf{H} + \mathbf{M} \right) = \mu \mathbf{H} ,$$

where μ is related to the magnetic polarizability densities of the scatterers in space.[1]
We will denote the relative permittivities and permeabilities by a subscript r, and
express ϵ and μ in terms of their real and imaginary parts by: $\epsilon = \epsilon_0(\epsilon_r' - j\epsilon_r'')$ and $\mu =
\mu_0(\mu_r' - j\mu_r'')$ [Note that throughout this chapter the time dependence is $e^{j\omega t}$]. In this
description, details of the field behavior on the scale of scatterer size and separation
are lost, and indeed are often not of practical interest.

The problem of effective-medium theory and modeling the electromagnetic re-
sponse of inclusions embedded in a medium is known as the "classical composite
medium" and has a long history [2,3,36–46]. In recent years, artificial materials
formed from periodic arrays of unusually-shaped conducting scatterers have been de-
signed so as to have negative μ_r' and ϵ_r' (i.e., $\mu_r' < 0$ and $\epsilon_r' < 0$) and were given the
name metamaterials [5–32]. Sufficiently deep within such a material, and if the fre-
quency is low enough for scatterer spacing to be small compared to a wavelength, the
medium appears to the average field as a continuous effective medium with some bulk
effective material property. On the other hand, near the interface of such a material

---

[1] Scatterers of complex geometry can result in an anisotropic medium, for which ϵ and μ are tensors, or
even in a *bianisotropic* medium, for which **D** and **H** are each affected by both **E** and **B**. We limit our
attention in this paper to isotropic, non-bianisotropic composite materials.

with another medium, the fields acting on the scatterers that make up the material are expected to be differnet from deep within the bulk material, and the magnitude of this effect is uncertain [47].

For passive materials, $\mu_r'' \geq 0$ and $\epsilon_r'' \geq 0$. The real parts of the material parameters (i.e., μ_r' and ϵ_r') for many common materials are positive, but there are exceptions. We will see that negative permittivity and permeability are possible in composite/engineered materials. However, negative permittivity and permeability can occur at a more fundamental level. For example, in plasmas the combination of ordinary displacement current density with electron-convection current density can yield a net negative real part of the permittivity for sufficiently low frequencies [35, pp. 309–319]. Indeed, Rotman [42] has shown how an artificial dielectric can reproduce such a negative permittivity and serve as a model for a plasma. A transmission-line equivalent circuit for describing a plasma is discussed in [48]. Negative permittivity also appears near a resonance frequency in Lorentz's theory of dispersion (see [4], for example).

When one (but not both) of ϵ_r' or μ_r' is negative, plane waves decay exponentially, like modes below cutoff in a waveguide. However, when both ϵ_r' and μ_r' are negative, waves can still propagate in such a medium since the product $\mu\epsilon$ remains positive. In this case, we have a "backward wave", for which the phase of the wave moves in the direction opposite from that of the energy flow. For lossless media, this means that the phase velocity and group velocity have opposite signs.

1.3 Metamaterials and periodic composites: length-scale effects

Let us now discuss the global behavior of a periodic composite material. Depending on the wavelength and the periodicity of the inclusions that make up a composite material, the composite may or may not behave as an effective medium. Metamaterials are commonly engineered by designing specifically shaped scatterers/inclusions or other objects, placed throughout a volume to achieve a desirable bulk behavior of the materials. In these types of engineered materials the scatterers can be of various length scales: the dimensions of the scatterers can range from relatively large to nanometer size and even smaller, depending on the frequencies of interest. In some of these situations, the scatterers and the spacing between them can become comparable to the wavelength of the electromagnetic waves [specifically, the wavelength in the "host" medium in which these inclusions (scatterers) are embedded, or the wavelength in the inclusions]. In natural materials, where the inclusions are atoms or molecules, this does not happen until frequencies reach the x-ray region. But with artificial materials, this can happen at much lower frequencies and one has to revisit the notion of electromagnetic material properties. In fact, the electromagnetic field interaction with these types of engineered materials falls into three separate regions of behavior (see Fig. 1.3), with distinctive behaviors in each region. It is important to be aware of this and to understand the behavior in each region when either performing measurements or analyzing metamaterials at different length scales and/or frequencies, as will be described in the following subsections.
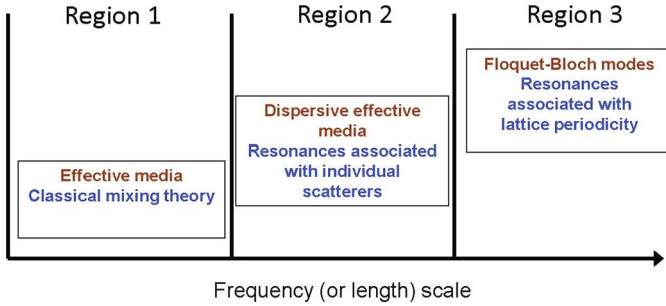
Figure 1.3 Three characteristic regions of composite materials or metamaterials.

1.3.1 Effective media: classical mixing theory

The first region in Fig. 1.3 corresponds to that of quasi-static behavior. This implies low frequencies—or specifically, frequencies where the wavelength is much larger than the lattice constant of the structure, that is, compared to the period of the scatterers that compose the composite medium, as well as the size of the inclusions. These scatterers could correspond to induced or permanent dipole moments, as is the case for atoms or molecules for classical materials, or could be generic in shape and placed in a host matrix to obtain an artificial composite material designed to have some desirable property. Using asymptotic techniques it is possible to show that the electromagnetic field in this low frequency limit sees the composite material as an equivalent effective medium with homogeneous material properties. The effective material properties are obtained from quasi-static field solutions of the periodic structure [49,50]. The basic result is that the effective permittivity is obtained by taking the ratio of some averaged D-field to an averaged E-field (as discussed above). The effective permeability is likewise obtained by taking the ratio of an averaged B-field to an averaged H-field.

The problem of effective-medium theory and modeling of electromagnetic response to an array of inclusions embedded in a host material has a long history going back to Maxwell, Rayleigh, as well as Poisson, Clausius and Mossotti before that. Much work has been done since then to compute the effective properties of homogeneous composite materials. A survey of this work can be found in [36,37,41]. The formulas for the effective properties given throughout the literature take on many forms. These range from simple bounds [41,51–53] to elaborate closed-form approximate formulas [36–38,41,43–45]. Note that these types of mixing formulas are only valid when the period of the structure is small in comparison to the wavelength of the electromagnetic wave. The reason for this is discussed in Section 1.3.2.

Let us look at a composite structure composed of particles embedded in a host matrix (shown in Fig. 1.4 for the case of spherical particles) in order to illustrate the implications of these classical mixing formulas (that is, the static limit). The Hashin–Shtrikman (HS) upper (ϵ_{HS}^U) and lower (ϵ_{HS}^L) bounds [51] are the best obtainable bounds using only the material parameters ϵ_1 (host matrix material), ϵ_2 (the material of the inclusion), and the fill factor g (volume fraction of space occupied by the bulk inclusion ϵ_2). They apply to composites based on inclusions of arbitrary shape. For a
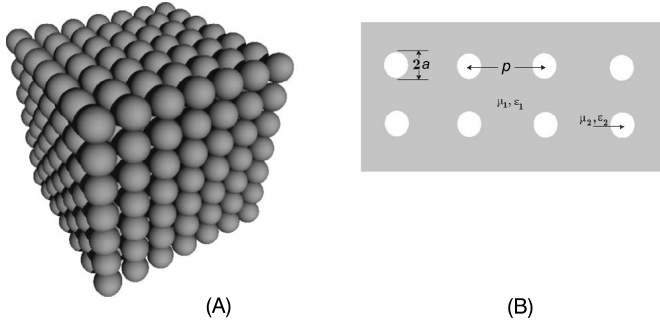
Figure 1.4 Composite structure containing spherical particles: (A) three-dimensional view and (B) cut-away view (from C.L. Holloway, E.F. Kuester, J. Baker-Jarvis, P. Kabos, A double negative (DNG) composite medium composed of magneto-dielectric spherical particles embedded in a matrix, IEEE Trans. Antennas Propag. 51 (10) (2003) 2596–2603, © 2003 IEEE).

three-dimensional composite material in which $\epsilon_2 > \epsilon_1$, the bounds are defined as

$$\epsilon_{\mathrm{HS}}^{L} \equiv \epsilon_1 + \frac{g}{\frac{1}{\epsilon_2-\epsilon_1} + \frac{1-g}{3\epsilon_1}}, \qquad \epsilon_{\mathrm{HS}}^{U} \equiv \epsilon_2 + \frac{1-g}{\frac{1}{\epsilon_1-\epsilon_2} + \frac{g}{3\epsilon_2}}. \tag{1.1}$$

If $\epsilon_2 < \epsilon_1$, the lower bound in Eq. (1.1) becomes an upper bound, and the upper bound becomes the lower bound (see [51] for details). Note that the expressions for these bounds need to be modified for other types of composite materials [41,50]. The variation of the effective permittivity (ϵ_{eff}) based on the expressions given in Eq. (1.1) is shown as a function of g ranging from 0 to 1 in Fig. 1.5 for two different values of the inclusion permittivity. Although results in this figure are shown for g approaching 1, for specific inclusion shapes, the limit $g = 1$ may not be achievable. For example, in the array of spheres, the spheres touch each other when $g = \pi/6$, and larger values of g have no meaning in this case.

For the composite shown in Fig. 1.4, Lewin [38] made a notable study of the effective permittivity and permeability μ_e and ϵ_e, by incorporating the solution of a boundary-value problem for scattering by a sphere into a unit cell, and then assuming that the medium is composed of a large number of these cells. For an array of lossless magneto-dielectric spheres, the relative effective μ'_{re} and ϵ'_{re} were found to be

$$\epsilon'_{\mathrm{re}} = \epsilon_{\mathrm{eff}} = \epsilon_{r1}\left(1 + \frac{3g}{\frac{F(\theta)+2b_e}{F(\theta)-b_e} - g}\right) \tag{1.2}$$

and

$$\mu'_{\mathrm{re}} = \mu_{\mathrm{eff}} = \mu_{r1}\left(1 + \frac{3g}{\frac{F(\theta)+2b_m}{F(\theta)-b_m} - g}\right). \tag{1.3}$$

In these expressions, μ_{r1} and ϵ_{r1} are the relative permeability and permittivity of the matrix (host) medium, μ_{r2} and ϵ_{r2} are the relative permeability and permittivity of the
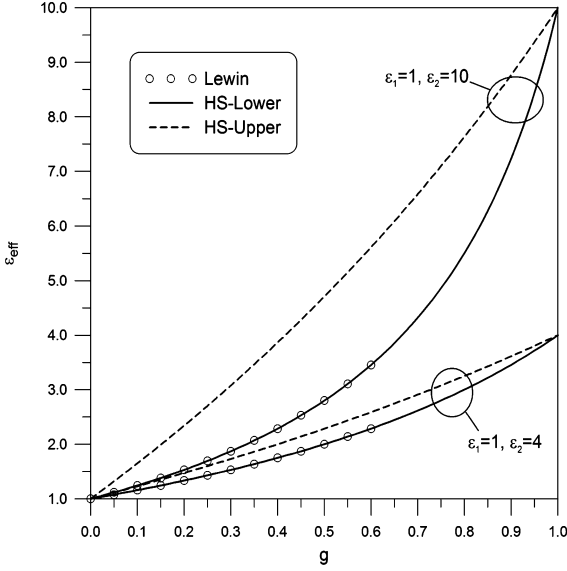
Figure 1.5 Effective properties of a spherical particle composite.

inclusions where

$$b_e = \frac{\epsilon_1}{\epsilon_2}, \qquad b_m = \frac{\mu_1}{\mu_2}. \tag{1.4}$$

The volume fraction g of the spherical inclusions is given by

$$g = \frac{4\pi a^3}{3p^3}, \tag{1.5}$$

where a is the particle radius and p is the particle spacing. The function $F(\theta)$ is

$$F(\theta) = \frac{2(\sin\theta - \theta\cos\theta)}{(\theta^2 - 1)\sin\theta + \theta\cos\theta}, \tag{1.6}$$

where

$$\theta = k_0 a \sqrt{\epsilon'_{r2}\mu'_{r2}} \tag{1.7}$$

and the free-space wavenumber is $k_0 = 2\pi/\lambda$, λ being the free-space wavelength. In the static limit $\theta \to 0$ (which implies no resonances in the inclusions), $F(\theta) \to 1$, and Lewin's formulas reduce to the Hashin–Shtrikman (HS) lower bounds, as can be observed in Fig. 1.5. Note that the results from Lewin's formula are only plotted to $g = \pi/6$, for the reason stated in the previous paragraph.

These results are typical of any mixing formula that one might choose to use for any type of composite material, in that a monotonic change takes place from the bulk

properties of the host towards the bulk properties of inclusion as the filling factor g increases from 0. Keep in mind that some mixing formulas may be more accurate than others depending on the geometry of the composite [36,37,41,49,50], but in general this trend is universal. This will be seen to be quite different from what occurs in the resonant effective material properties region (the second region in Fig. 1.3), which we will discuss in subsection 1.3.3. Notice also that there is no frequency dependence in the mixing formulas that we have discussed so far. The formulas are based on a quasi-static approximation, and the only frequency dependence that could occur would be because the bulk material properties of the matrix or inclusions are frequency-dependent. This is not the case in the second region, where resonant effects of the scatterers are important. This also will be discussed in subsection 1.3.3.

1.3.2 Floquet–Bloch modes: frequency selective surfaces and photonic band gap structures

Before we discuss Region 2 in Fig. 1.3, let us examine Region 3. In this region, the wavelength approaches the period of a periodic structure, and the fields no longer 'see' the composite as an effective medium. At these frequencies, a more complicated field behavior exists and more elaborate full-wave modeling techniques to analyze the EM field interaction with the composite periodic structures must be used. The classical approach that is used to analyze periodic structures is the Floquet–Bloch-mode approach [54–56]. To understand this method, we first review how fields in a homogeneous medium are expressed.

A plane wave is a solution of Maxwell's equations in a uniform, source-free region of space characterized by the material constants μ and ϵ. A typical component of (say) the electric field is given by

$$E = E_0 e^{-j(k_x x + k_y y + k_z z)} , \tag{1.8}$$

where E_0 is a constant amplitude, and the constants k_x, k_y and k_z are components of a wave-vector indicating the direction of propagation of the wave. All of the field components ($\mathbf{E}$ and $\mathbf{H}$) have the same (x, y, z) dependence as in (1.8), but with different amplitudes. If the field is not identically zero, these amplitudes are related to each other by constraints imposed by Maxwell's equations; in addition, at a given frequency ω, the components of the wave-vector must obey

$$k^2 = \omega^2 \mu\epsilon = k_x^2 + k_y^2 + k_z^2 . \tag{1.9}$$

More general fields are representable by a superposition of plane-wave fields, either a sum or an integral over suitable sets of possible values of k_x, k_y, and $k_z = \sqrt{k^2 - k_x^2 - k_y^2}$. Those plane waves for which $k_x^2 + k_y^2 > k^2$ are evanescent in the z-direction and do not contribute significantly in the far field when z is large enough.

For a three-dimensional periodic medium, when μ and ϵ are periodic functions of x, y, and z, with periods p_x, p_y, and p_z, respectively, a Floquet–Bloch mode for a

component of the E-field has the form

$$E = E_p(x, y, z)e^{-j(k_x x + k_y y + k_z z)}, \tag{1.10}$$

where E_p is a function periodic in x, y and z with the same periods as μ and ϵ. As with the plane-wave solution, the constants k_x, k_y, and k_z and the amplitude functions E_p, etc., cannot take on arbitrary values, but are constrained by the requirement that the field is nontrivial and obeys Maxwell's equations. For given values of k_x, k_y, and k_z, this can happen only when the frequency ω is equal to one of a set of *eigenfrequencies* $\omega_r(k_x, k_y, k_z)$. The relation between components of the wave-vector is then the implicit equation $\omega = \omega_r(k_x, k_y, k_z)$, which generalizes (1.9). The periodic function E_p can be represented as a complex exponential Fourier series:

$$E_p(x, y, z) = \sum_{l,m,n=-\infty}^{\infty} C_{lmn} e^{-j\left(\frac{2\pi l x}{p_x} + \frac{2\pi m y}{p_y} + \frac{2\pi n z}{p_z}\right)} \tag{1.11}$$

or

$$E = \sum_{l,m,n=-\infty}^{\infty} C_{lmn} e^{-j(k_{xl} x + k_{ym} y + k_{zn} z)}, \tag{1.12}$$

where

$$k_{xl} = k_x + \frac{2l\pi}{p_x}, \qquad k_{ym} = k_y + \frac{2m\pi}{p_y}, \qquad k_{zn} = k_z + \frac{2n\pi}{p_z}, \tag{1.13}$$

and $p_{x,y,z}$ are the lattice periods in the x, y, and z directions, respectively. The constants $C_{l,n,m}$ and eigenfrequencies $\omega_r(k_x, k_y, k_z)$ are determined by constraining the field to obey Maxwell's equations—this is usually done numerically.

Analogous to the plane-wave case, if $k_{xl}^2 + k_{ym}^2$ is large enough, the field will decay in the z-direction, and such waves will not contribute in the far field. It turns out that, for $k p_x$, $k p_y$, and $k p_z$ smaller than about π (where k is now a suitably-defined representative wavenumber), only the lowest-order Floquet–Bloch mode (the one with the smallest value of $\omega_r = \omega_0$) can propagate without attenuation. Put another way, if the wavelength is large in comparison to the periods, only the lowest-order Floquet–Bloch mode propagates. As the frequency increases, more of the higher-order modes begin to propagate. For small periods and long wavelengths, the lowest-order Floquet–Bloch mode represents (in some sense) the averaged fields propagating through the composite periodic structure. These fields along with the eigenfrequency ω_0 allow us to determine an effective medium in terms of ϵ_e and μ_e.

The situation is quite different once the higher-order modes begin to propagate. No longer do unique values of ϵ_e and μ_e fully determine the non-evanescent field, and complicated interference effects among the Floquet–Bloch modes will arise. Certainly, important practical applications of these effects exist (Bragg scattering perhaps foremost among them), but a simplified effective-medium description is no longer possible. A field propagating through a composite sees the structure as an effective
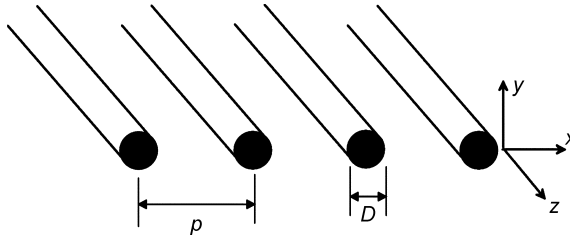
Figure 1.6 Infinitely-long metal wire grating in free space, where p is the period of the grating and D is the wire diameter.

medium as long as the higher-order Floquet–Bloch modes do not propagate into it. For a background medium of free space, the restriction on $k_0 p$ as a function of the plane-wave incidence angle ϕ for this to happen is

$$k_o p < \frac{2\pi}{1 - \sin\phi}.$$

Periodic structures used in such higher-frequency applications have been given various names throughout the literature. In recent years, high-frequency periodic surfaces have been given the name frequency-selective surfaces (FSSs) [57,58] (historically known as periodic gratings) and high-frequency three-dimensional periodic materials have been given the name photonic band gap (PBG) materials [5,59]. FSS and PBG structures have similar characteristics, that is, at certain frequencies the FSS and PBG can block the propagation of an EM wave. The frequency bands where this blocking effect occurs are referred to as stopbands. At other frequencies, the periodic structure allows energy to propagate through the structure; these frequency bands are referred to as passbands.

This can be readily seen by considering the infinitely-long metal wire grating shown in Fig. 1.6. The transverse electric (TE) reflection and transmission coefficients of this two-dimensional wire grating in free space are shown in Fig. 1.7. These results were obtained with a finite-element numerical program. These quantities are a complicated function of the lattice configuration (e.g., the period p and diameter D of the wires). The lattice will severely attenuate the transmitted field at wavelengths that are much larger than the lattice period p. In general, the attenuation of the fields due to the lattice is monotonic and decreases with frequency up to the first resonance (i.e., the peak in the transmitted field). For example, Fig. 1.7A shows results for a lattice in free space, where $p = 7.62$ cm and $D = 1.91$ cm, and Fig. 1.7B shows results for a lattice in free space, where $p = 15.24$ cm and $D = 5.08$ cm.

At low frequencies, the lattice acts inductively and the transmitted field strength increases with frequency to a maximum at the first resonance with the wavelength (i.e., $\lambda \approx p$). It should be noted that the shape of the curves as well as the wavelength at the first resonance are, in general, a function of the wire diameter as well as the period. The first resonance occurs when $\lambda \approx p$ (and not $\lambda/2 \approx p$), because the plane-wave excitation causes currents to flow in the same direction on adjacent parallel conducting elements of the lattice that are aligned with the incident electric field. Since the
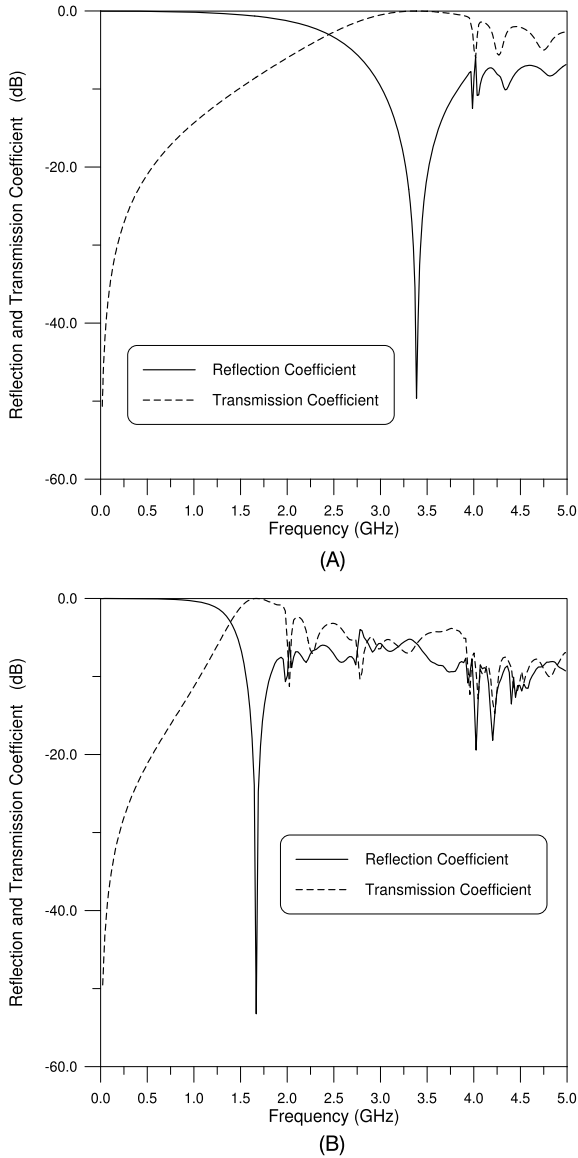
Figure 1.7 TE reflection and transmission characteristics of a two-dimensional array of infinitely-long metal wires: (A) $p = 7.62$ cm and $D = 1.91$ cm, (B) $p = 15.24$ cm and $D = 5.08$ cm. These results are for normal incidence.

currents on two adjacent conductors are equal in magnitude and direction, there is a null in the induced magnetic and electric fields halfway between the conductors which is consistent with this mode. From these results, we see that there is a passband when $\lambda \approx p$. Similar types of results are seen for different types of periodic structures, that

is, stopbands and passbands will develop in the structure (FSS and PBG structures; see [5,57–59]).

These effects of constructive and destructive interference of the various modes as the wave propagates through the composite, are what give rise to the unique characteristics of FSS and PBS structures. It is important to note that such effects cannot be represented or captured by an effective-media theory. These stopband and passband effects of FSS and PBG structures are caused by resonances associated with the periodicity of the structure. In Section 1.3.3 we see that resonances associated with the scatterers themselves can cause interesting and unexpected effects in the effective material properties of a composite.

1.3.3 Effective media: scatterer resonances

Resonant features of the scatterers (or inclusions) that compose an effective medium provide us the power to engineer the medium's permittivity and/or permeability in order to achieve unique and interesting properties. Region 2 in Fig. 1.3 corresponds to a region where the scatterers are designed in such a manner (either via their shape or bulk material properties) such that the scatterers themselves can resonate. When this occurs, so-called metamaterials can be realized.

When the scatterers are non-resonant, the real parts of the material parameters (i.e., μ_r' and ϵ_r') for the engineered materials are usually positive, but there are exceptions, as discussed in Section 1.2. When the scatterers are resonant, negative permittivity and permeability are possible in composite materials. Materials of this type are also called "double" negative (DNG) media, negative-index materials, backward-wave media (BW), or left-handed materials. This kind of material is just one of many types of metamaterials. Early investigators in the fledgling area of metamaterials attributed the first study of such media to Veselago [12] in 1967, but Lamb [60] in 1904, Schuster [61] in 1904, Pocklington [62] in 1905, Mandel'shtam [63,64] in 1945, Malyuzhinets in 1951 [65] and Sivukhin in 1957 [66] had all previously discussed the properties of wave propagation in backward-wave media. Some other historical (or "pre-historical") surveys have been given in [15,67–69]. More recently, many other authors [5–32] have studied the properties and potential applications of DNG materials in detail. Also see [70–76].

Much of the early work on DNG materials concentrated on metallic inclusions [5–32]. An interesting question is: "Can the DNG material effect occur in a pure dielectric or magneto-dielectric composite medium?" To address this question, we refer back to the work of Lewin [38], in which he used Mie's exact solution of the problem of scattering by a material sphere to derive an expression for the effective properties of an array of spherical particles embedded in a background matrix (although many of his results had already been obtained, albeit in a much more cumbersome form, by previous researchers [39,40]). Lewin's work showed that when the size of the spherical scatterers is not small compared to a wavelength *in the material of the scatterers* (but *is* small compared to a wavelength in the matrix material), μ_e and ϵ_e become frequency-dependent. The expressions for the effective permittivity and permeability are presented in Eqs. (1.2) and (1.3). The interesting parameter in these equations is

Figure 1.8 ϵ_{re} and μ_{re} for an array of spheres with $g = 0.5$, $\epsilon'_{r1} = \mu'_{r1} = 1$, $\epsilon'_{r2} = 40$, and $\mu'_{r2} = 200$. The dashed-dot lines represent the asymptotes for ϵ_{re}. From C.L. Holloway, E.F. Kuester, J. Baker-Jarvis, P. Kabos, A double negative (DNG) composite medium composed of magneto-dielectric spherical particles embedded in a matrix, IEEE Trans. Antennas Propag. 51 (10) (2003) 2596–2603, © 2003 IEEE.

the factor $F(\theta)$. In section 1.3.1, the quasi-static of $F(\theta)$ is emphasized. In that static limit $F(\theta) \to 1$. From Eq. (1.6) and plots shown in [29], it is apparent that $F(\theta)$ has a resonant behavior. The possibility of such a composite structure (a pure dielectric or magneto-dielectric composite) having both negative effective permittivity and permeability was first demonstrated in [29], where the conditions that must be met for the effective permittivity and permeability to be negative were given.

In [29] it is shown that these conditions can be met with realistic bulk material properties of the matrix and the spherical inclusions. For example, Fig. 1.8 shows results for $g = 0.5$, $\epsilon'_{r1} = \mu'_{r1} = 1$, $\epsilon'_{r2} = 40$, and $\mu'_{r2} = 200$ as a function of $k_0 a$ (where a is the radius of the spheres and k_0 is the free-space wavenumber). Between $0 \le k_0 a \le 0.1$ there are two regions where both μ'_{re} and ϵ'_{re} become negative, producing a negative-index material [29]. This negative-index behavior also occurs when $\epsilon'_{r1}/\epsilon'_{r2} = \mu'_{r1}/\mu'_{r2}$. Fig. 1.9 shows such a composite that has a bandwidth (bands where permittivity and permeability are simultaneously negative) of 10 %. Fig. 1.10 shows results for the real and imaginary part of ϵ_{re} for an array of lossy spherical particles. The results in this figure are for different values of the dielectric loss tangent of the spherical particles, defined as $\tan\delta = \epsilon''_r/\epsilon'_r$. Notice that, for this example, the real part of the effective permittivity can still be negative for loss tangents as large as 0.04. However, for larger values of $\tan\delta$ the resonance is damped out and the real part of the effective permittivity remains positive. This shows that if the inclusion (i.e., the spherical particle) becomes too lossy, DNG properties cannot be realized. While large values of negative properties can be attained near resonance as shown in Fig. 1.10A, working too near these resonances has an adverse feature. The imaginary part of ϵ_{eff} shown in Fig. 1.10B illustrates an important aspect of using metamaterials too close to

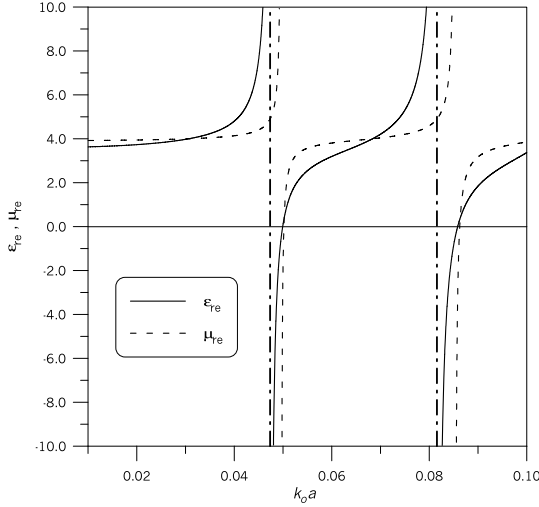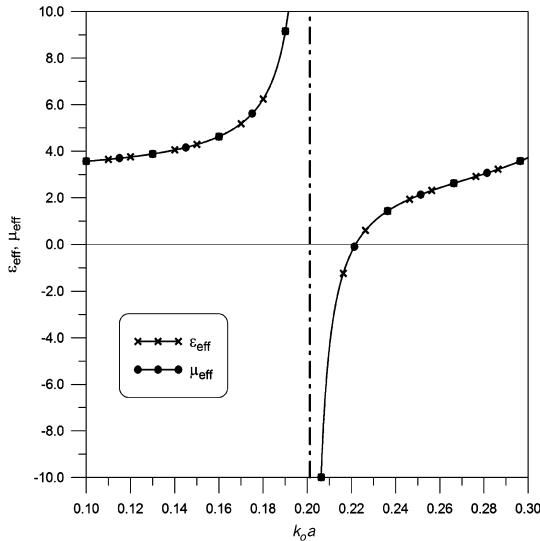**Figure 1.9** ϵ_{re} and μ_{re} for an array of spheres with $g = 0.5$, $\epsilon'_{r1} = \mu'_{r1} = 1$, $\epsilon'_{r2} = 20$, and $\mu'_{r2} = 20$. The dashed-dot line represents the asymptote. Notice that ϵ_{re} and μ_{re} are identical. From C.L. Holloway, E.F. Kuester, J. Baker-Jarvis, P. Kabos, A double negative (DNG) composite medium composed of magneto-dielectric spherical particles embedded in a matrix, IEEE Trans. Antennas Propag. 51 (10) (2003) 2596–2603, © 2003 IEEE.

a resonance, in that losses can be very large near the resonance. As a result, researchers have been investigating and designing metamaterials away from these resonances. Tailoring materials to a desired value and near-zero index materials are two examples of metamaterial applications for frequencies away from resonance.

Once it was demonstrated in [29] that metamaterials composed of dielectric spherical inclusions were possible, other dielectric and magneto-dielectric inclusions started appearing as a means to develop DNG materials and other desirable properties. This includes layered-spherical particles, arrays of different sized spheres, cylindrical and cubic inclusions, as well as other geometries [30,77–94].

The negative material properties are a result of the resonances associated with the scatterers that make up the composite material. Therefore, it should not be a surprise that any scatterer that can resonate can be used to obtain the DNG effect. In fact, the Lewin approach can be readily extended to other geometries and to other types of inclusions. Khizhniak wrote a series of papers [43–45] in which he generalized Lewin's model and presented expressions for the effective material property tensors of an artificial material formed by an array of scatterers with arbitrary geometric shapes. Khizhniak presents expressions for the effective material properties that have the same functional behavior as Lewin's and does indeed suggest that negative material properties can be obtained via arbitrarily shaped inclusions. Recently, several papers have studied the problem of designing engineered artificial materials with negative μ'_r and ϵ'_r formed from periodic arrays of unusually-shaped conducting scatterers, in particular, split metal rings and posts [5–28,31,32,95]. These structures
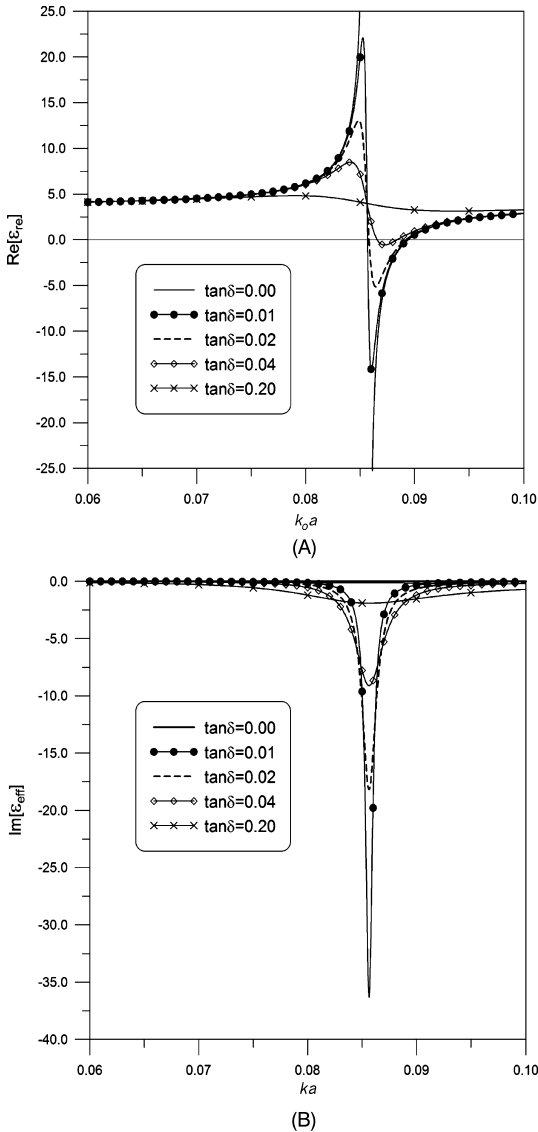
Figure 1.10 Array of lossy spherical particles: ϵ_{re} and μ_{re} for $g = 0.5$, $\epsilon'_{r1} = \mu'_{r1} = 1$, $\epsilon'_{r2} = 50$, and $\mu'_{r2} = 50$: (A) real part for ϵ_{re} (from C.L. Holloway, E.F. Kuester, J. Baker-Jarvis, P. Kabos, A double negative (DNG) composite medium composed of magneto-dielectric spherical particles embedded in a matrix, IEEE Trans. Antennas Propag. 51 (10) (2003) 2596–2603, © 2003 IEEE) and (B) imaginary part for ϵ_{re}.

can be quite complicated to fabricate when compared to composites composed of the magneto-dielectric inclusions.

Since these conducting scatterers are essentially resonant structures, the goal is to design the microfabricated resonant circuits with desired effective properties in a unit

cell. The design of such a structure was described in detail in [18]. The design is based on the averaging of the magnetic field components along the axes of the unit cell. Pendry averages the magnetic field in a cube of side $a(= p_x = p_y = p_z)$. For each magnetic field component

$$< H >_i = \frac{1}{a} \int_{r_i} \mathbf{H} \cdot d\mathbf{r}, \tag{1.14}$$

the induction field is averaged as

$$< B >_i = \frac{1}{a^2} \int_{S_i} \mathbf{B} \cdot d\mathbf{S}, \tag{1.15}$$

where $i = x$, y, or z, r_i is a path from the origin to $p_i \mathbf{a}_i$, $\mathbf{a}_i$ is a unit vector in the direction i, and S_i is a square of side a in the plane $i = 0$. Following these averaging definitions the effective permeability is then defined as

$$\mu_{\mathrm{eff}(i)} = \frac{< B >_i}{\mu_0 < H >_i}. \tag{1.16}$$

The effective permittivity is given by a similar expression

$$\epsilon_{\mathrm{eff}(i)} = \frac{< D >_i}{\epsilon_0 < E >_i}. \tag{1.17}$$

For negative permittivity or permeability, the equivalent circuit of the scatterer circuit has to be resonant, which requires the introduction of capacitance into the inductive system (or vice versa). Pendry introduced the capacitance through gaps in coupled-ring resonators; details are discussed in [18]. Any microstructured microwave resonant device, passive and/or active, can in principle be used to produce a desired effective permeability in a periodic structure designed for double-negative applications [31].

The most convenient (and traditional) method to model metamaterials is with effective-medium theory. It should be emphasized that the averaging (or homogenization, or effective material model presentation) is valid only when the wavelength is large compared to the lattice constant of the period cell. While period cell averaging for the fields is the correct method for defining effective material properties, most researchers in practice use an approach where they obtain the reflection and transmission properties (either through measurements or numerical simulations) of a metamaterial consisting of several layers (sometimes as few as three). The term "layer" means a plane of scatterers with an associated thickness. When referring to the layers of a metamaterial, the thickness is the period of the bulk materials in the direction perpendicular to the plane of scatterers. Once the reflection and transmission properties are obtained, a Nicolson–Ross–Weir (NRW) approach [96,97] is used to obtain the effective material properties of the bulk metamaterials. Note that the standard NRW approach must be modified when negative material properties exist; typically, the choice of the sign of a square-root is made unambiguous by ensuring

positive power flow [98–102]. In general, for a bulk three-dimensional material (with five layers or more) the approach results in unique effective material properties for the metamaterials. However, there are conditions where these modified NRW approaches fail; for details see [47,100,101], and [103]. This failure manifests itself in a dependence of the extracted bulk electromagnetic material parameters on the thickness of the sample used [98,104–106].

If used properly, the effective material approach can be a self-consistent and unique method for characterizing a metamaterial. That is, no matter what thickness of the same metamaterial is modeled (i.e., no matter the number of layers that compose the metamaterial), the same values for the bulk effective material properties should be obtained. By definition, a bulk property should not depend on the size (or shape, for that matter) of the material sample. True bulk properties of a material should be retrievable independent of the thickness of the sample chosen. Let us note here that some models of metasurfaces in terms of "bulk" properties are actually nonlocal–the obtained permittivity and permeability are spatially dispersive, dependent on the wavenumber of the wave propagating through the medium. This approach can address the issues raised here to some extent, but is more complicated to use, in general, than a local model. See, for example, [107].

Applications of DNG materials include, 1) shielding materials, 2) low-reflection materials, 3) substrate materials, 4) antenna applications, 5) electronic switches, 6) resonators, 7) controllable surfaces, 8) cloaking, and 9) the so-called perfect lens. When resonance is used to obtain some desired metamaterial behavior, a structure made from passive materials must exhibit dispersion and therefore loss. This is required by the Kramers–Kronig dispersion relations for the behavior to obey causality. As discussed above, losses are high near resonances, and as such, one typically avoids this region.

We need to emphasize that Region 2 in Fig. 1.3 does not always occur. The scatterers need to be designed so that the scatterers' resonances occur before the next higher-order Floquet–Bloch mode can propagate. For example, in the case of spherical particle inclusions, if the bulk properties and the radius of a spherical particle composite are too small, the scatterer resonances would be pushed toward the Floquet–Bloch-mode region and a DNG material would not be realized. The scatterer resonance region and the Floquet–Bloch-mode region would overlap and an effective-medium model would not capture the behavior of the composite material. Furthermore, if the size and shape of the inclusions (the dielectric structures used in [29,30,77–82] or metallic inclusions in [5–28,31], and [32]) are not chosen properly, then the resonance would be pushed into the Floquet–Bloch-mode region and once again DNG materials would not be realized. Similar effects are also discussed in [122].

In summary, in the first two regions, the electromagnetic field behaves as if the composite material is some type of effective medium. In region 1 (the classical mixing theory region) the effective material properties have no frequency dependence (except for that due to the constituent materials). In region 2 (the scatterer resonant region) the material behaves as an effective medium and has the inherent frequency dependence preserved in the effective material property model. In this region it is possible to achieve DNG materials and other desirable exotic material properties. Finally, for the last region (region 3 in Fig. 1.3), the electromagnetic field interaction with

the periodic structure is more complex. Scattering is the mechanism for the field behavior, and we can no longer think of the composite material simply as an effective medium. When the wavelength approaches the lattice constant, higher-order Floquet–Bloch modes must be considered. FSS and PBG are the predominant applications found in this region.

1.4   Metasurfaces

Metamaterials are engineered by arranging a set of scatterers throughout a three-dimensional region of space in a specific pattern so as to achieve some desirable bulk behavior of the material. This concept can be extended by judiciously placing scatterers in a two-dimensional pattern at a surface or interface. Such a surface version of a metamaterial has been given the name metasurface, and includes metafilms and metascreens (both of these subcategories will be discussed below) as special cases [33, 34,108–110]. Metasurfaces have also been referred to in the literature as single-layer metamaterials.

The simplicity and relative ease of fabrication of metasurfaces make them attractive alternatives to three-dimensional (3D) metamaterials. In many applications, metasurfaces can be used in place of metamaterials. Metasurfaces have the advantage of taking up less physical space than do full 3D metamaterial structures; as a consequence they can also offer the possibility of lower losses. The application of metasurfaces at frequencies from microwave to optical has attracted great interest in recent years [33,34, 115–159]. In addition to the applications mentioned above for metamaterials, metasurfaces allow for controllable "smart" surfaces, miniaturized cavity resonators, novel waveguiding structures, compact and wide-angle absorbers, impedance matching surfaces, biomedical devices, tailoring wave fronts, polarization conversion, antennas, and high speed switching devices, to name only a few.

We will call any periodic two-dimensional structure whose thickness and periodicity are small compared to a wavelength in the surrounding media a metasurface. Within this general designation, we can identify two important subclasses. Metasurfaces that have a "cermet" topology, which refers to an array of isolated (non-touching) scatterers (Fig. 1.11), are called metafilms [33] and [108] (a term coined in [110] for such surfaces). Metasurfaces with a "fishnet" structure (Fig. 1.12) are called metascreens [33,109]. These metascreens are characterized by periodically-spaced apertures in an otherwise relatively impenetrable surface. Other kinds of metasurfaces exist that lie somewhere between these two extremes. For example, a grating of parallel conducting wires (a metagrating) behaves like a metafilm to electric fields perpendicular to the wire axes, but like a metascreen for electric fields parallel to the wire axes [112]. It is important to note that the individual scatterers constituting a metafilm (or apertures constituting a metascreen) are not necessarily of zero thickness (or even small compared to the lattice constants); they may be of arbitrary shape, and their dimensions are required to be small only in comparison to a wavelength in the surrounding medium, which is true *a fortiori* because the lattice constant has been assumed small compared to a wavelength.
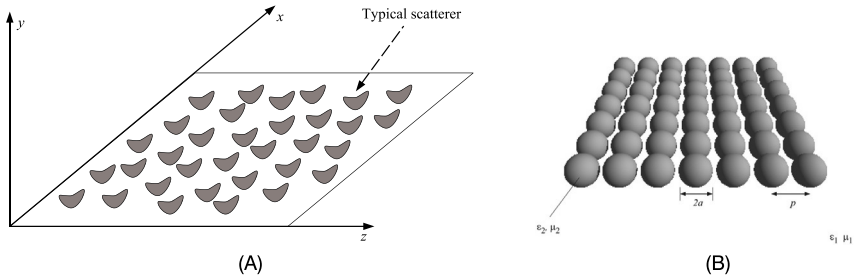
Figure 1.11 Metafilm examples: (A) array of arbitrary shaped scatterers and (B) array of spherical particles. Parts (A) and (B) from C.L. Holloway, E.F. Kuester, J.A. Gordon, J. O'Hara, J. Booth, D.R. Smith, An overview of the theory and applications of metasurfaces: the two-dimensional equivalents of metamaterials, IEEE Antennas Propag. Mag. 54 (2) (April 2012) 10–35, © 2012 IEEE.
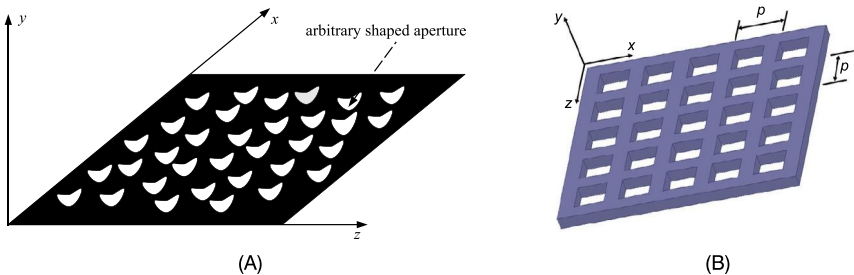
Figure 1.12 Metascreen examples: (A) array of arbitrary shaped apertures and (B) array of square apertures. Parts (A) and (B) from C.L. Holloway, E.F. Kuester, Generalized sheet transition conditions (GSTCs) for a metascreen, IEEE Trans. Antennas Propag. 66 (5) (2018) 2414–2427, © 2018 IEEE.
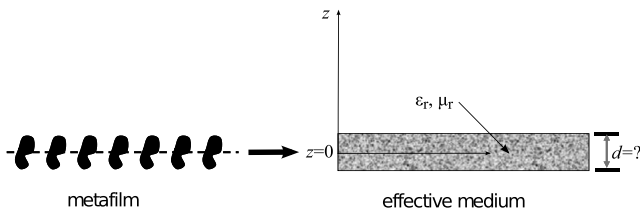
Figure 1.13 Representing a metafilm as an effective medium with thickness d. From C.L. Holloway, E.F. Kuester, A. Dienstfrey, Characterizing metasurfaces/metafilms: the connection between surface susceptibilities and effective material properties, IEEE Antennas Wirel. Propag. Lett. 10 (2011) 1507–1511, © 2011 IEEE.

Similar to metamaterials, depending on the wavelength-to-period spacing, three regions of behavior will occur for EM interactions with a metasurface. For a two-dimensional lattice of scatterers or apertures, region 1 in Fig. 1.3 corresponds to classical thin-film materials, while region 3 in Fig. 1.3 corresponds to resonances associated with the periodicity of the scatterers/apertures. The conventional FSS and PBG [57–59] fall into this third region. On the other hand, when we talk about a metasurface, we are referring to an array of scatterers/apertures that lies in region 2 (or even region 1). Resonances of the surface may be associated with the resonances of

the scatterers/apertures, but not with the periodicity of the array. Ordinary frequency-selective surfaces are sometimes operated in this regime, but the distinction between this type of operation and that of region 3 has not usually been made.

We emphasize that, as for the case of a metamaterial, region 2 in Fig. 1.3 may not always occur for a metasurface. The scatterers/apertures need to be properly designed, such that the scatterers' resonances occur at a frequency well below that where the next higher-order Floquet–Bloch mode can propagate. For example, if the bulk properties and the radius of a spherical-particle composite (see [29]) are too small, or if the sizes or shapes of the scatterers used in the material are not properly chosen, the scatterers' resonances would be pushed toward the Floquet–Bloch-mode region, and in this case an effective-medium model would not adequately describe the behavior of the composite material.

In summary, in regions 1 and 2 of Fig. 1.3 the interaction of an electromagnetic field with a metasurface is described by effective surface parameters of some kind, to be discussed below. In region 1 (analogous to the classical mixing theory region for the case of a metamaterial), the effective surface parameters are not frequency-dependent (except insofar as the constituent bulk properties have a frequency dependence). In region 2 (the scatterers' resonant region), the metasurface still is modeled by effective surface properties, which now may possess an inherent frequency dependence. In this region, it is possible to achieve interesting resonant behaviors. In the last region (region 3 in Fig. 1.3), the electromagnetic field's interaction with the periodic array is very involved. We may no longer think of the surface as behaving like an interface with effective surface parameters. When the wavelength approaches the period, higher-order Floquet–Bloch modes must be considered, and one typically does not refer to these structures as metasurfaces in this region.

1.4.1 Characterizing a metasurface

Like a metamaterial, the behavior of a metafilm is determined by the electric and magnetic polarizabilities of its constituent scatterers (or its constituent apertures for a metascreen). The traditional and most convenient method by which to model metamaterials is with effective-medium theory. Attempts to use a similar bulk-parameter analysis for metasurfaces have been less successful (see [113], [33], and [114] for a detailed discussion on this point). Indeed, some previous metafilm studies have modeled the film as a single-layer metamaterial in which effective bulk material properties of the metasurface are obtained by forcing the introduction of an arbitrary non-zero thickness parameter into the analysis. As we will demonstrate, several problems arise from the physically artificial character of this parameter; the bulk property characterization of a metasurface is incorrect at a fundamental level. To the extent that classical algorithms for bulk-parameter extraction give results that depend on sample size, we would be forced to conclude that some localized effect is occurring near the boundary of the sample [47,100,101,110], analogous to the effect of cutoff modes near the junction between two different waveguides.

An equivalent-bulk layer representation of a metasurface is shown in Fig. 1.13. The problem is that the thickness of a metasurface would not be uniquely defined,

nor would the effective material properties. In [108,109,113,114], it is shown that the effective surface parameters of a metafilm/metascreen are unique properties of a metasurface and thus are the most appropriate way to characterize a metasurface. We will see below that the surface parameters correspond to what we will call effective surface susceptibilities (defined below as χ_{MS} and χ_{ES} for the magnetic and electric surface susceptibilities, respectively) for metafilms [33,108], and in addition so-called surface porosities (defined below as π_{MS} and π_{ES} for the magnetic and electric surface porosities, respectively) for metascreens [33,109]. Techniques for retrieving the surface susceptibilities for a given metasurface based on reflection and transmission measurements (or simulations) are presented in [33,113,114,117].

To illustrate the issue of representing a metasurface as a material with a bulk effective permittivity and permeability, we present in Fig. 1.14A retrieved values of ϵ_r (the effective permittivity) for an array of lossy spherical particles (radius $a = 10$ mm, period $p = 25.59$ mm, $\epsilon_p = 2$, $\mu_p = 900$, and $\tan\delta = 0.04$) for different values of the assumed thickness d. These results were obtained by computing numerical values of the reflection and transmission coefficients for this array of spheres and then using the modified Nicolson–Ross–Weir (NRW) method [98,99,102] for determining ϵ_r of the slab (see [114] for details). As expected, these results show a functional dependence of ϵ_r on d. Fig. 1.14B shows results for $d(\epsilon_r - 1)$ for different values of d. We have also plotted the retrieved values of the surface susceptibility χ_{ES}^{yy} (the first superscript "y" corresponds to the component of the surface susceptibility and the second superscript "y" corresponds to the polarization of the incident field; see [108] for details) for this array that appears in (1.18) below (also obtained from using retrieval algorithms and the numerical values of reflection and transmission coefficients [114]). The retrieved values for χ_{ES}^{yy} are the same as the analytical values given in [113]. The results shown in Fig. 1.14B illustrate that, for sufficiently low frequencies, $d(\epsilon_r - 1)$ is independent of d and identical to χ_{ES}^{yy}. Although the connection between surface susceptibilities and the effective bulk properties of a slab was not discussed explicitly in [27], Smith et al. [27] do allude to the fact that the product of the slab thickness and the effective material properties of the slab should be constant.

Additional examples of the surface susceptibilities for two different metafilm structures are shown in Fig. 1.15. One is an array of lossy spherical particles and the other is an array of thin metallic scatterers (Fig. 1.15D). As we will see below, a metascreen requires both surface susceptibilities and surface porosities to fully characterize the metascreen. Fig. 1.16 shows both surface susceptibilities and surface porosities for a metascreen composed of an array of square apertures.

When all is said and done, we would argue that a model for a metafilm that uses uniquely specified quantities (i.e., χ_{MS} or χ_{ES} as defined below) is more natural than an approach that involves two arbitrary quantities (d and ϵ_r). Likewise, for a metascreen we should use both surface susceptibilities and surface porosities as defined below [33,109]. Even though it has been shown that the electrical and magnetic surface susceptibilities are the most appropriate manner to characterize metafilms, some researchers continue to characterize them in terms of bulk effective material properties. If one insists on characterizing a metasurface as a thin material slab with bulk effective material properties and a thickness d, the only meaningful (and unique)
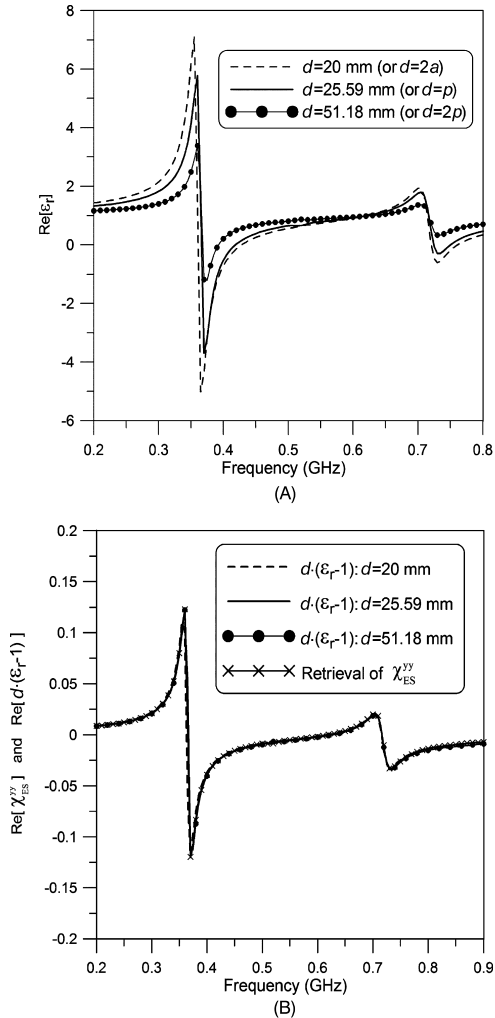
Figure 1.14 Results for an array of lossy spheres: (A) retrieved ϵ_r and (B) $d(\epsilon_r - 1)$ and χ_{ES}^{yy}. From C.L. Holloway, E.F. Kuester, A. Dienstfrey, Characterizing metasurfaces/metafilms: the connection between surface susceptibilities and effective material properties, IEEE Antennas Wirel. Propag. Lett. 10 (2011) 1507–1511, © 2011 IEEE.

parameters will be products such as $d(\epsilon_r - 1)$ and $d(\mu_r - 1)$, if the slab is centered at the plane containing the metafilm. A retrieval approach that gives unique quantities like χ_{MS} and χ_{ES} is more natural than one that merely gives products of otherwise undetermined quantities [33,113,114,117].

In contrast to the effective-medium description used for a metamaterial, boundary conditions incorporating the effective surface parameters (surface susceptibilities and surface porosities) of the metasurface are the best way to characterize it. These boundary conditions are called generalized sheet-transition conditions (GSTCs) [33,
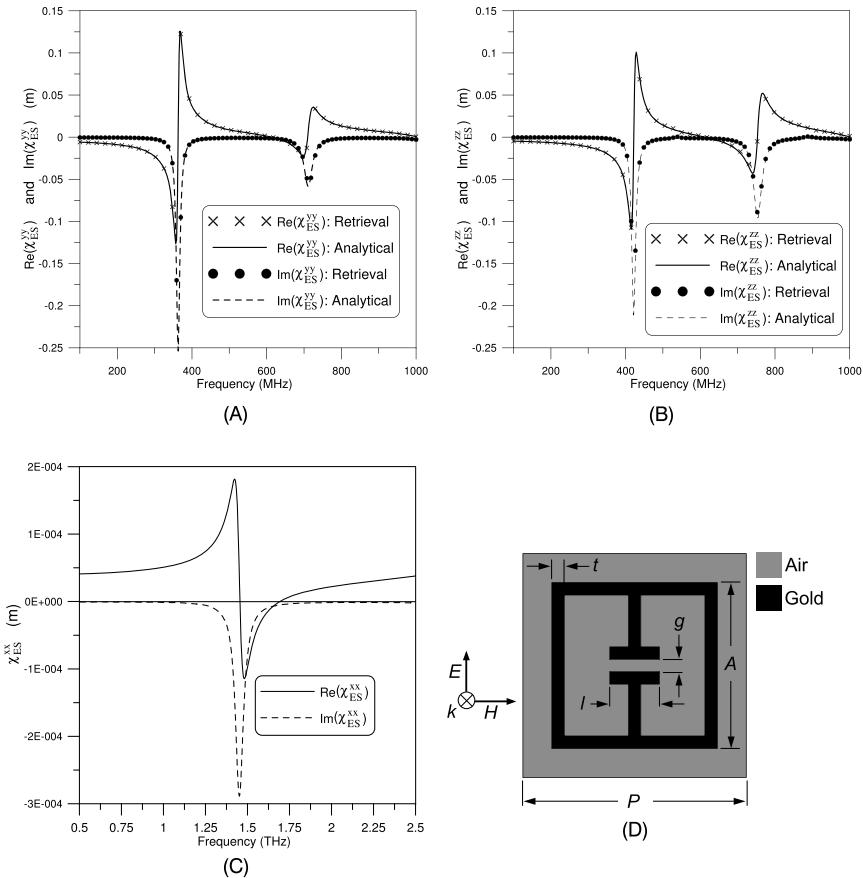
Figure 1.15 Surface susceptibilities for a metafilm composed of (A) χ_{ES}^{yy} for spherical particles ($a = 10$ mm, $p = 25.59$ mm, $\epsilon_r = 2$, $\mu_r = 900$, and $\tan\delta = 0.04$), (B) χ_{ES}^{zz} for the same array as in (A), (C) χ_{ES}^{zz} for an array of thin metallic scatterers shown in (D), and (D) thin metallic scatterer for electrical surface susceptibility ($t = 3$ μm, $A = 40$ μm, $p = 54$ μm, and $l = 12$ μm). Parts (A), (B), (C), (D) from C.L. Holloway, A. Dienstfrey, E.F. Kuester, J.F. O'Hara, A.K. Azad, A.J. Taylor, A discussion on the interpretation and characterization of metafilms-metasurfaces: the two-dimensional equivalent of metamaterials, Metamaterials 3 (2009) 100–112.

108–110]. The coefficients appearing in the GSTCs for any given metasurface are all that are required to model its macroscopic interaction with an electromagnetic field. The GSTCs allow this surface distribution of scatterers to be replaced with a boundary condition that is applied across an infinitely thin equivalent surface (hence the name metasurface, metafilm, or metascreen), as indicated in Fig. 1.17. The size, shape, and spacing of the scatterers are incorporated into this boundary condition through the polarizability densities of the scatterers on the interface. These surface polarizability densities are related to the effective surface susceptibilities and surface porosities.

The GSTCs for a metasurface take on different forms for either a metafilm or a metascreen. For a metafilm the GSTCs apply to jumps in both the tangential compo-
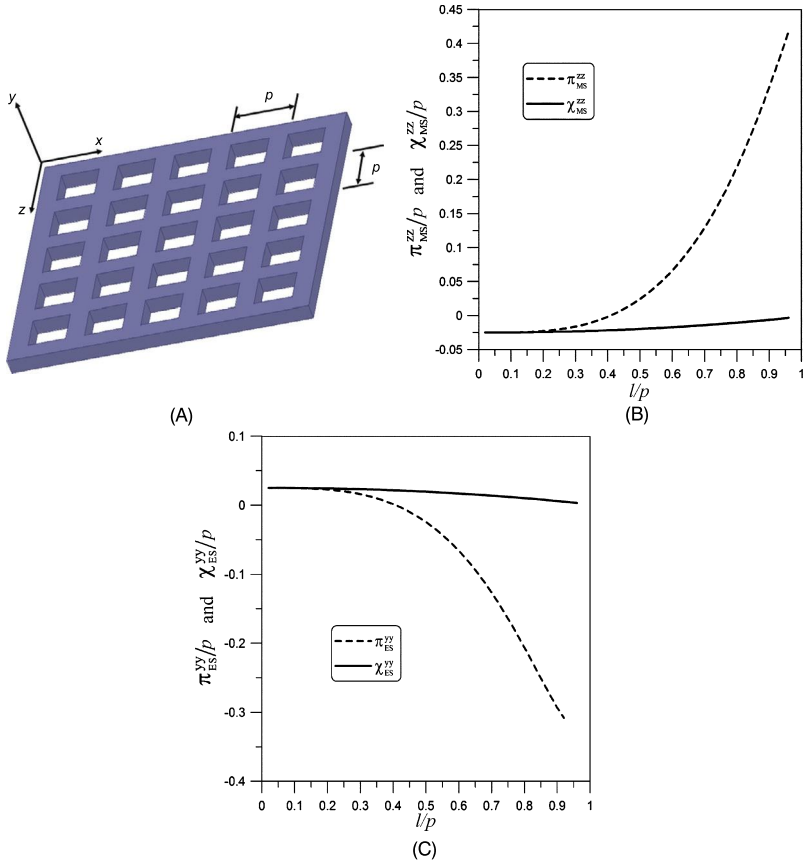
Figure 1.16 Surface susceptibilities and surface porosities for a metascreen composed of an array of square apertures of length l: (A) array of square apertures (from C.L. Holloway, E.F. Kuester, Generalized sheet transition conditions (GSTCs) for a metascreen, IEEE Trans. Antennas Propag. 66 (5) (2018) 2414–2427, © 2018 IEEE), (B) χ_{MS}^{zz} and π_{MS}^{zz} for square apertures ($h = 5$ mm and $p = 100$ mm), and (C) χ_{ES}^{yy} and π_{ES}^{yy} for circular apertures ($h = 5$ mm and $p = 100$ mm).

nents of the electric (E) and magnetic (H) fields across the metafilm [see Figs. 1.17A and 1.17C] and take on the following form [108,110,113]:

$$\mathbf{a}_y \times \left[\mathbf{E}^A - \mathbf{E}^B \right]_{y=0} = -j\omega\mu_0 \left(\overleftrightarrow{\chi}_{MS} \cdot \tilde{\mathbf{H}}_{av} \right)_t - \mathbf{a}_y \times \nabla_t \left(\mathbf{a}_y \cdot \overleftrightarrow{\chi}_{ES} \cdot \tilde{\mathbf{E}}_{av} \right) \quad (1.18)$$

and

$$\mathbf{a}_y \times \left[\mathbf{H}^A - \mathbf{H}^B \right]_{y=0} = j\omega\epsilon_0 \left(\overleftrightarrow{\chi}_{ES} \cdot \tilde{\mathbf{E}}_{av} \right)_t - \mathbf{a}_y \times \nabla_t \left(\mathbf{a}_y \cdot \overleftrightarrow{\chi}_{MS} \cdot \tilde{\mathbf{H}}_{av} \right), \quad (1.19)$$

where the average fields are defined by

$$\mathbf{E}_{av} = \frac{1}{2} \left(\mathbf{E}^A + \mathbf{E}^B \right)_t + \frac{1}{2}\epsilon_0 \, \mathbf{a}_y \left(D_y^A + D_y^B \right), \quad (1.20)$$
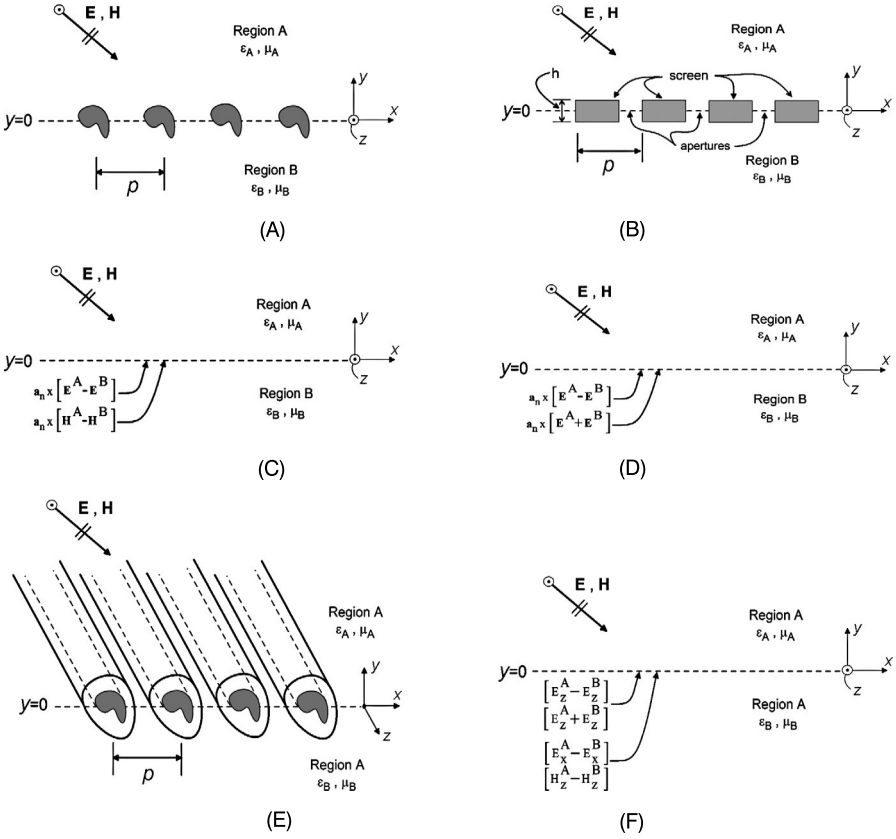
Figure 1.17 Reference plane to allow GSTCs: (A) a metafilm with arbitrarily shaped scatterers, (B) a metascreen with arbitrarily shaped apertures, (C) reference plane for a metafilm at which the GSTCs are applied, (D) reference plane for a metascreen at which the GSTCs are applied, (E) a metagrating with arbitrary shaped coated wire grating, and (F) reference plane for a metagrating at which the GSTCs are applied.

and similarly for $\mathbf{H}_{av}$, $\mathbf{D}_{av}$, and $\mathbf{B}_{av}$. The surface susceptibility dyadics are defined as

$$
\begin{aligned}
\overset{\leftrightarrow}{\chi}_{ES} = {} & \chi_{ES}^{xx}\mathbf{a}_x\mathbf{a}_x + \chi_{ES}^{xy}\mathbf{a}_x\mathbf{a}_y + \chi_{ES}^{xz}\mathbf{a}_x\mathbf{a}_z \\
& + \chi_{ES}^{yx}\mathbf{a}_y\mathbf{a}_x + \chi_{ES}^{yy}\mathbf{a}_y\mathbf{a}_y + \chi_{ES}^{yz}\mathbf{a}_y\mathbf{a}_z \\
& + \chi_{ES}^{zx}\mathbf{a}_x\mathbf{a}_x + \chi_{ES}^{zy}\mathbf{a}_z\mathbf{a}_y + \chi_{ES}^{zz}\mathbf{a}_z\mathbf{a}_z \, ,
\end{aligned}
\tag{1.21}
$$

$$
\begin{aligned}
\overset{\leftrightarrow}{\chi}_{MS} = {} & \chi_{MS}^{xx}\mathbf{a}_x\mathbf{a}_x + \chi_{MS}^{xy}\mathbf{a}_x\mathbf{a}_y + \chi_{MS}^{xz}\mathbf{a}_x\mathbf{a}_z \\
& + \chi_{MS}^{yx}\mathbf{a}_y\mathbf{a}_x + \chi_{MS}^{yy}\mathbf{a}_y\mathbf{a}_y + \chi_{MS}^{yz}\mathbf{a}_y\mathbf{a}_z \\
& + \chi_{MS}^{zx}\mathbf{a}_x\mathbf{a}_x + \chi_{MS}^{zy}\mathbf{a}_z\mathbf{a}_y + \chi_{MS}^{zz}\mathbf{a}_z\mathbf{a}_z \, .
\end{aligned}
\tag{1.22}
$$

The surface susceptibilities have units of length.

For a metascreen, a different set of GSTCs is needed. For a metascreen, a boundary condition for the magnetic field is not usable *a priori*, because it would involve surface currents that are not yet known, much like what occurs for a wire grating [112]. The required GSTCs for a metascreen should constrain only tangential E [see Figs. 1.17B and 1.17D], and can be expressed as conditions on the jump of the tangential E-field and on the sum (twice the average) of the tangential E-fields [33,109]:

$$
\begin{aligned}
\mathbf{a}_y \times \left[\mathbf{E}^A(\mathbf{r}_o) - \mathbf{E}^B(\mathbf{r}_0) \right] = & - \mathbf{a}_x \, j\omega\mu_0 \left[\chi_{MS}^{Axx} H_x^A(\mathbf{r}_o) + \chi_{MS}^{Bxx} H_x^B(\mathbf{r}_o) \right. \\
& \left. + \chi_{MS}^{Axz} H_z^A(\mathbf{r}_o) + \chi_{MS}^{Bxz} H_z^B(\mathbf{r}_o) \right] \\
& - \mathbf{a}_z \, j\omega\mu_0 \left[\chi_{MS}^{Azx} H_x^A(\mathbf{r}_o) + \chi_{MS}^{Bzx} H_x^B(\mathbf{r}_o) \right. \\
& \left. + \chi_{MS}^{Azz} H_z^A(\mathbf{r}_o) + \chi_{MS}^{Bzz} H_z^B(\mathbf{r}_o) \right] \\
& - \mathbf{a}_y \times \left[\chi_{ES}^{Ayy} \nabla_t E_y^A(\mathbf{r}_o) + \chi_{ES}^{Byy} \nabla_t E_y^B(\mathbf{r}_o) \right]
\end{aligned}
\tag{1.23}
$$

and

$$
\begin{aligned}
\mathbf{a}_y \times \left[\mathbf{E}^A(\mathbf{r}_o) + \mathbf{E}^B(\mathbf{r}_0) \right] = & - \mathbf{a}_x \, j\omega\mu_0 \left[\pi_{MS}^{Axx} H_x^A(\mathbf{r}_o) - \pi_{MS}^{Bxx} H_x^B(\mathbf{r}_o) \right. \\
& \left. + \pi_{MS}^{Axz} H_z^A(\mathbf{r}_o) - \pi_{MS}^{Bxz} H_z^B(\mathbf{r}_o) \right] \\
& - \mathbf{a}_z \, j\omega\mu_0 \left[\pi_{MS}^{Azx} H_x^A(\mathbf{r}_o) - \pi_{MS}^{Bzx} H_x^B(\mathbf{r}_o) \right. \\
& \left. + \pi_{MS}^{Azz} H_z^A(\mathbf{r}_o) - \pi_{MS}^{Bzz} H_z^B(\mathbf{r}_o) \right] \\
& - \mathbf{a}_y \times \left[\pi_{ES}^{Ayy} \nabla_t E_y^A(\mathbf{r}_o) - \pi_{ES}^{Byy} \nabla_t E_y^B(\mathbf{r}_o) \right].
\end{aligned}
\tag{1.24}
$$

As before, χ_{ES} and χ_{MS} are interpreted as effective electric and magnetic surface susceptibilities, respectively, while π_{ES} and π_{MS} are interpreted as effective electric and magnetic surface porosities of the metascreen [109]. Like the surface susceptibilities, the surface porosities have units of length.

A metagrating [112] behaves like a metafilm to electric fields perpendicular to the wire axes, but like a metascreen for electric fields parallel to the wire axes [see Figs. 1.17E and 1.17F]. Metagratings require GSTCs that are a combination of those needed for a metafilm and a metascreen, which are given by the following:

$$
\begin{aligned}
\mathbf{a}_y \times \left[\mathbf{E}^A(\mathbf{r}_o) - \mathbf{E}^B(\mathbf{r}_o) \right] = & - j\omega\mu_0 \, \chi_{MS}^{zz} H_{z,av}(\mathbf{r}_o) \, \mathbf{a}_z - j\omega \, \chi_{MS}^{xy} B_{y,av}(\mathbf{r}_o) \, \mathbf{a}_x \\
& - j\omega \left[\chi_{MS}^{Axx} B_x^A(\mathbf{r}_o) + \chi_{MS}^{Bxx} B_x^B(\mathbf{r}_o) \right] \mathbf{a}_x \\
& - \mathbf{a}_y \times \left[\chi_{ES}^{yx} \nabla E_{x,av}(\mathbf{r}_o) \right] \\
& - \mathbf{a}_y \times \left[\chi_{ES}^{Ayy} \nabla E_y^A(\mathbf{r}_o) + \chi_{ES}^{Byy} \nabla E_y^B(\mathbf{r}_o) \right],
\end{aligned}
\tag{1.25}
$$

$$H_z^A(\mathbf{r}_o) - H_z^B(\mathbf{r}_o) = j\omega\epsilon_0\, \chi_{ES}^{xx}\, E_{x,av}(\mathbf{r}_o)$$

$$+ j\omega\epsilon_0 \left[\chi_{ES}^{Axy}\, E_y^A(\mathbf{r}_o) + \chi_{ES}^{Bxy}\, E_y^B(\mathbf{r}_o) \right]$$

$$-\frac{1}{\mu_0}\left[\chi_{MS}^{yy}\,\frac{\partial B_{y,av}(\mathbf{r}_o)}{\partial z} + \chi_{MS}^{Ayx}\,\frac{\partial B_x^A(\mathbf{r}_o))}{\partial z} \right.$$

$$\left. +\chi_{MS}^{Byx}\,\frac{\partial B_x^B(\mathbf{r}_o)}{\partial z} \right], \tag{1.26}$$

and

$$E_z^A(\mathbf{r}_o) + E_z^B(\mathbf{r}_o) = -\, j\omega\pi_{MS}^{xy}\, B_{y,av}(\mathbf{r}_o)$$

$$- j\omega\left[\pi_{MS}^{Axx}\, B_x^A(\mathbf{r}_o) - \pi_{MS}^{Bxx}\, B_x^B(\mathbf{r}_o) \right]$$

$$- \pi_{ES}^{xy}\,\frac{\partial E_{x,av}(\mathbf{r}_o)}{\partial z} - \pi_{ES}^{Ayy}\,\frac{\partial E_y^A(\mathbf{r}_o)}{\partial z}$$

$$- \pi_{ES}^{Byy}\,\frac{\partial E_y^B(\mathbf{r}_o)}{\partial z}\,. \tag{1.27}$$

The coefficients χ_{ES} and χ_{MS} are effective electric and magnetic surface susceptibilities of the metagrating, while π_{ES} and π_{MS} are effective electric and magnetic surface *porosities* of the metagrating; both have units of length.

Calculating the surface susceptibilities and surface porosities can be difficult for generally-shaped inclusions or apertures. However, the GSTCs can be used to retrieve these surface parameters from measured or calculated plane-wave reflection and transmission coefficients, as done in [33,113,114], and [117–119]. These GSTCs, along with the surface parameters, are also convenient to use in the analysis of various applications of the EM interaction of metasurfaces with EM fields [47,111,115–123].

The GSTCs can also be cast in the form of impedance-type boundary conditions [13,160–163]. For plane-wave fields, whose variation parallel to a metafilm is of the form

$$e^{-j\mathbf{k}\cdot\mathbf{r}_t}, \tag{1.28}$$

where

$$\mathbf{k} = k_x\mathbf{a}_x + k_y\mathbf{a}_y \quad \text{and} \quad \mathbf{r}_t = x\mathbf{a}_x + y\mathbf{a}_y, \tag{1.29}$$

we can use Maxwell's equations to write Eqs. (1.18) and (1.19) as

$$\mathbf{a}_y \times \left[\mathbf{E}^A - \mathbf{E}^B \right]_{y=0} = -\overleftrightarrow{\mathbf{Z}}_{MS}\cdot\mathbf{H}_{t,av}, \tag{1.30}$$

$$\mathbf{a}_y \times \left[\mathbf{H}^A - \mathbf{H}^B \right]_{y=0} = \overleftrightarrow{\mathbf{Y}}_{ES}\cdot\mathbf{E}_{t,av}. \tag{1.31}$$

Here, the spatially dispersive (**k**-dependent) surface transfer admittance and transfer impedance are given by

$$\overset{\leftrightarrow}{\mathbf{Y}}_{ES} = j\omega\overset{\leftrightarrow}{\boldsymbol{\chi}}_{ES} + \frac{j\overset{\leftrightarrow}{\boldsymbol{\chi}}_{MS}}{\omega\mu}(\mathbf{a}_z \times \mathbf{k})(\mathbf{a}_z \times \mathbf{k}),\tag{1.32}$$

$$\overset{\leftrightarrow}{\mathbf{Z}}_{MS} = j\omega\overset{\leftrightarrow}{\boldsymbol{\chi}}_{MS} + \frac{j\overset{\leftrightarrow}{\boldsymbol{\chi}}_{ES}}{\omega\epsilon}(\mathbf{a}_z \times \mathbf{k})(\mathbf{a}_z \times \mathbf{k}).\tag{1.33}$$

Boundary conditions of this form can also be interpreted as lumped elements in equivalent transmission-line circuits [161].

1.5   Isolated scatterers and one-dimensional array

So far we have discussed three-dimensional metamaterials and two-dimensional metasurfaces. What about one-dimensional metastructures? The two-dimensional metamaterial (i.e., a metasurface) concept can be extended even further to the concept of using only a linear unit cell rather than a surface cell, that is, using only a single subwavelength resonant structure for some desired effect or behavior. In fact, we have already begun to see a few applications of this concept. One in particular is the use of a unit cell in the design of electrically small antennas. In antenna applications, the unit cell acts like a parasitic element to the radiating element of the antenna and serves as a means to match the electrically small radiating element to both (1) the feeding transmission line and (2) free space. Such designs have been shown to achieve efficient electrically small antennas [164–171]. Nanoparticles have also been used for tuning "so-called" optical nanoantennas [172]. An additional example is the use of a one-dimensional unit cell as a tuning structure for planar transmission lines [173]. Another emerging area of application is the use of one-dimensional chains of nanoparticles as waveguides supporting surface waves, of which examples can be found in [174–180].

1.6   Summary

The recent development of various engineered materials (3-D metamaterials, 2-D metasurfaces, single arrays and single particles) is bringing us closer to realizing the exciting predictions (exotic material behavior) made over one hundred years ago by the work of Lamb, Schuster, and Pocklington [60–62]. As we saw from the many references cited in this chapter, in recent years, many authors have studied the properties and potential applications of these exotic materials. While there is still much work needed in the understanding, analysis, design, and fabrication of these engineered materials, the potential of these materials has forever changed the landscape of RF, microwaves, optics and photonics for the future. This book intends to address some of the potential applications of these engineered materials. Including this chapter, the book contains a total of 9 chapters covering different aspects of dielectric metastruc-

tures (i.e., metamaterials, metasurfaces, isolated scatterers, and one-dimensional linear arrays).

References

[1] A. Fresnel, La loi des modifications que la réflexion imprime à la lumière polarisée, Mem. Acad. R. Sci. Inst. France 11 (1832) 393–433.

[2] J.C. Maxwell, A Treatise on Electricity and Magnetism, Vol. 1, Dover, New York, 1954, sections 306–307.

[3] Lord Rayleigh, On the influence of obstacles arranged in rectangular order on the properties of a medium, Philos. Mag. Ser. 5 34 (1892) 481–502.

[4] M. Born, E. Wolf, Principles of Optics: Electromagnetic Theory of Propagation, Interference and Diffraction of Light, sixth ed., Pergamon Press, Oxford, 1980.

[5] S. Zouhdi, A. Sihvola, M. Arsalane (Eds.), Advances in Electromagnetics of Complex Media and Metamaterials, Kluwer Academic Pub., Boston, 2002.

[6] C. Caloz, T. Itoh, Electromagnetic Metamaterials: Transmission Line Theory and Microwave Applications, Wiley–IEEE Press, 2005.

[7] G.V. Eleftheriades, K.G. Balmain, Negative Refraction Metamaterials: Fundamental Principles and Applications, Wiley, 2005.

[8] N. Engheta, R.W. Ziolkowski, Electromagnetic Metamaterials: Physics and Engineering Explorations, John Wiley & Sons, 2006.

[9] R. Marqués, F. Martín, M. Sorolla, Metamaterials With Negative Parameters: Theory, Design, and Microwave Applications, Wiley–Interscience, Hoboken, NJ, 2008.

[10] F. Capolino (Ed.), Metamaterials Handbook: Theory and Phenomena of Metamaterials, CRC Press, Boca Raton, FL, 2009.

[11] T.J. Cui, D.R. Smith, R. Liu (Eds.), Metamaterials: Theory, Design, and Applications, Springer, New York, 2010.

[12] V.G. Veselago, The electrodynamics of substances with simultaneously negative values of ϵ and μ, Usp. Fiz. Nauk 92 (1967) 517–526 [in Russian], Engl. transl. in Sov. Phys. Usp. 10 (1968) 509–514.

[13] S. Tretyakov, Analytical Modeling in Applied Electromagnetics, Artech House, Boston, 2003.

[14] A. Sihvola, Metamaterials in electromagnetics, Metamaterials 1 (1) (2007) 2–11.

[15] E. Shamonina, L. Solymar, Metamaterials: how the subject started, Metamaterials 1 (1) (2007) 12–18.

[16] M. Lapine, S. Tretyakov, Contemporary notes on metamaterials, IET Microw. Antennas Propag. 1 (1) (2007) 3–11.

[17] J.B. Pendry, A.J. Holden, W.J. Stewart, I. Youngs, Extremely low frequency plasmons in metallic mesostructure, Phys. Rev. Lett. 76 (1996) 4773–4776.

[18] J.B. Pendry, A.J. Holden, D.J. Robbins, W.J. Stewart, Magnetism from conductors and enhanced nonlinear phenomena, IEEE Trans. Microw. Theory Tech. 47 (1999) 2075–2084.

[19] C.A. Kyriazidou, H.F. Contopanagos, W.M. Merrill, N.G. Alexópoulos, Artificial versus natural crystals: effective wave impedance of printed photonic bandgap materials, IEEE Trans. Antennas Propag. 48 (2000) 95–105.

[20] C.A. Kyriazidou, R.E. Daiz, N.G. Alexópoulos, Novel material with narrow-band transparency window in the bulk, IEEE Trans. Antennas Propag. 48 (2000) 107–116.

[21] D.R. Smith, D.C. Vier, N. Kroll, S. Schultz, Direct calculation of permeability and permittivity for a left-handed metamaterial, Appl. Phys. Lett. 77 (2000) 2246–2248.

[22] S.G. Johnson, J.D. Joannopoulos, Three-dimensionally periodic dielectric layered structure with omnidirectional photonic band gap, Appl. Phys. Lett. 77 (2000) 3490–3492.

[23] P. Markos, C.M. Soukoulis, Numerical studies of left-handed materials and arrays of split ring resonators, Phys. Rev. E 65 (2002) 036622-1–036622-8.

[24] N. Engheta, S.R. Nelatury, A. Hoorfar, Omega media as a metamaterial with negative permittivity and permeability, in: Dig. of USNC/URSI Meeting, San Antonio, TX, June 16–21, 2002, p. 47.

[25] J.B. Pendry, A.J. Holden, D.J. Robbins, W.J. Stewart, Extremely low frequency plasmons in thin-wire structures, J. Phys. Condens. Matter 10 (1998) 4785–4809.

[26] D.A. Smith, N. Kroll, Negative refractive index in left-handed materials, Phys. Rev. Lett. 85 (2000) 2933–2936.

[27] D.R. Smith, W.J. Padilla, D.C. Vier, S.C. Nemat-Nasser, S. Schultz, Composite medium with simultaneously negative permeability and permittivity, Phys. Rev. Lett. 84 (2000) 4184–4186.

[28] R. Marques, J. Martel, F. Mesa, F. Medina, A new 2D isotropic left-handed metamaterial design: theory and experiment, Microw. Opt. Technol. Lett. 35 (5) (2002) 405–408.

[29] C.L. Holloway, E.F. Kuester, J. Baker-Jarvis, P. Kabos, A double negative (DNG) composite medium composed of magneto-dielectric spherical particles embedded in a matrix, IEEE Trans. Antennas Propag. 51 (10) (2003) 2596–2603.

[30] E.F. Kuester, N. Memić, S. Shen, A.D. Scher, S. Kim, K. Kumley, H. Loui, A negative refractive index metamaterial based on a cube array of layered nonmagnetic spherical particles, Prog. Electromagn. Res. B 33 (2011) 175–202.

[31] R.W. Ziolkowski, E. Heyman, Wave propagation in media having negative permittivity and permeability, Phys. Rev. E 64 (2001) 056625.

[32] R.A. Shelby, D.R. Smith, S.C. Nemat-Nasser, S. Schultz, Microwave transmission through a two-dimensional, isotropic left-handed material, Appl. Phys. Lett. 78 (2001) 489–491.

[33] C.L. Holloway, E.F. Kuester, J.A. Gordon, J. O'Hara, J. Booth, D.R. Smith, An overview of the theory and applications of metasurfaces: the two-dimensional equivalents of metamaterials, IEEE Antennas Propag. Mag. 54 (2) (April 2012) 10–35.

[34] A.A. Maradudin (Ed.), Structured Surfaces as Optical Metamaterials, Cambridge University Press, Cambridge, UK, 2011.

[35] J.D. Jackson, Classical Electrodynamics, Wiley, New York, 1999.

[36] P.S. Neelakanta, Handbook of Electromagnetic Materials, CRC Press, New York, 1995.

[37] A.H. Sihvola, Electromagnetic Mixing Formulas and Application, The Institution of Electrical Engineers, London, United Kingdom, 1999.

[38] L. Lewin, The electrical constants of a material loaded with spherical particles, Proc. Inst. Elec. Engrs. 94 (part 3) (1947) 65–68.

[39] R. Gans, H. Happel, Zur Optik kolloidaler Metallösungen, Ann. Phys. 29 (1909) 277–300.

[40] J.A. Stratton, The effect of rain and fog on the propagation of very short radio waves, Proc. IRE 18 (1930) 1064–1074.

[41] E.F. Kuester, C.L. Holloway, Comparison of approximations for effective parameters of artificial dielectrics, IEEE Trans. Microw. Theory Tech. 38 (1990) 1752–1755.

[42] W. Rotman, Plasma simulation by artificial dielectrics and parallel-plate media, IRE Trans. Antennas Propag. 10 (1962) 82–95.

[43] N.A. Khizhniak, Artificial anisotropic dielectrics: I, Zh. Tekh. Fiz. 27 (1957) 2006–2013, [in Russian], Engl. transl. in Sov. Phys. Tech. Phys. 2 (1957) 1858–1864.

[44] N.A. Khizhniak, Artificial anisotropic dielectrics: II, Zh. Tekh. Fiz. 27 (1957) 2014–2026 [in Russian], Engl. transl. in Sov. Phys. Tech. Phys. 2 (1957) 1865–1876.

[45] N.A. Khizhniak, Artificial anisotropic dielectrics: III, Zh. Tekh. Fiz. 27 (1957) 2027–2037 [in Russian], Engl. transl. in Sov. Phys. Tech. Phys. 2 (1957) 1877–1886.

[46] R.E. Collin, Field Theory of Guided Waves, IEEE Press, New York, 1991, Chap. 12.

[47] C.L. Holloway, E.F. Kuester, Corrections to the classical continuity conditions at the interface of a composite medium, Photonics Nanostruct. Fundam. Appl. 11 (4) (November 2013) 397–422.

[48] R.N. Bracewell, Analogues of an ionized medium, Wirel. Eng. 31 (1954) 320–326.

[49] E.F. Kuester, C.L. Holloway, A low-frequency model for wedge or pyramid absorber array – I: theory, IEEE Trans. Electromagn. Compat. 36 (4) (1994) 300–306.

[50] M. Johansson, C.L. Holloway, E.F. Kuester, Effective electromagnetic properties of honeycomb composites, and hollow pyramidal and alternating wedge absorbers, IEEE Trans. Antennas Propag. 53 (2) (Feb 2005) 728–736.

[51] Z. Hashin, S. Shtrikman, A variational approach to the theory of the effective magnetic permeability of multiphase materials, J. Appl. Phys. 33 (1962) 3125–3131.

[52] K. Lichtenecker, Über den widerstand gewisser zusammengesetzter körperlicher Leiter, Phys. Z. 19 (1918) 374–382.

[53] K. Lichtenecker, Der elektrische leitungswiderstand künstlicher und natürlicher Aggregate, Phys. Z. 25 (1924) 169–181, 193–204, 225–233.

[54] L. Brillouin, Wave Propagation in Periodic Structures, Dover Pub., New York, 1953, Chapter 7.

[55] A. Ishimaru, Electromagnetic Wave Propagation, Radiation, and Scattering, Prentice Hall, Englewood Cliffs, N.J., 1991, Chapter 7.

[56] J.A. Kong, Electromagnetic Wave Theory, John Wiley & Sons, N.Y., 1986, Chapter 6.

[57] T.K. Wu, Frequency Selective Surface and Grid Array. , John Wiley & Sons, Inc., N.Y., 1995.

[58] B.A. Munk, Frequency Selective Surfaces: Theory and Design, Wiley, Inc., 2000.

[59] C.M. Soukoulis, Photonic Band Gap Materials, Kluwer Academic Publishers, Dordrecht, 1996.

[60] H. Lamb, On group-velocity, Proc. Lond. Math. Soc., Ser. 2 1 (1904) 473–479.

[61] A. Schuster, An Introduction to the Theory of Optics, Edward Arnold, London, 1904, pp. 313–318.

[62] H.C. Pocklington, Growth of a wave-group when the group velocity is negative, Nature 71 (1905) 607–608.

[63] L.I. Mandel'shtam, Lectures on certain problems of oscillation theory: Lecture 4, in: Polnoe Sobraniye Trudov, tom 5, Izdat. Akad. Nauk SSSR, Leningrad, 1950, pp. 461–467 [in Russian], also in his Lektsii po Optike, Teorii Otnositel'nosti i Kvantovoi Mekhanike, Nauka, Moscow, 1972, pp. 431–437.

[64] L.I. Mandel'shtam, Group velocity in crystalline arrays, Zh. Eksp. Teor. Fiz. 15 (1945) 475–478 [in Russian], also in: Polnoe Sobraniye Trudov, tom 2, Izdat. Akad. Nauk SSSR, Leningrad, 1945, pp. 334–338.

[65] G.D. Malyuzhinets, A note on the radiation principle, Zh. Tekh. Fiz. 21 (1951) 940–942 [in Russian].

[66] D.V. Sivukhin, The energy of electromagnetic fields in dispersive media, Opt. Spektrosk. 3 (1957) 308–312 [in Russian].

[67] E. Shamonina, Slow waves in magnetic metamaterials: history, fundamentals and applications, Phys. Status Solidi B 245 (2008) 1471–1482.

[68] R.A. Silin, On the history of backward electromagnetic waves in metamaterials, Meta-materials 6 (2012) 1–7.

[69] S.A. Tretyakov, A personal view on the origins and developments of the metamaterial concept, J. Opt. 19 (2017) 013002.

[70] P. Markoš, C.M. Soukoulis, Transmission studies of left-handed materials, Phys. Rev. B 65 (2001) 033401.

[71] R.M. Walser, A.P. Valanju, P.M. Valanju, Comment on: extremely low frequency plas-mons in metallic mesostructures, Phys. Rev. Lett. 87 (2001) 119701.

[72] I.V. Lindell, S.A. Tretyakov, K.I. Nikoskinen, S. Iivonen, BW media-media with nega-tive parameters, capable of supporting backward waves, Microw. Opt. Technol. Lett. 31 (2001) 129–133.

[73] S.A. Tretyakov, Meta-material with wideband negative permittivity and permeability, Mi-crow. Opt. Technol. Lett. 31 (2001) 163–165.

[74] C. Caloz, C.-C. Chang, T. Itoh, Full-wave verification of the fundamental properties of left-handed materials in waveguide configurations, J. Appl. Phys. 90 (2001) 5483–5486.

[75] R.A. Silin, I.P. Chepurnykh, On media with negative dispersion, Radiotekh. Elektron. 46 (2001) 1212–1217 [in Russian], Engl. transl. in J. Commun. Technol. Electron. 46 (2001) 1121–1125.

[76] P.M. Valanju, R.M. Walser, A.P. Valanju, Wave refraction in negative-index media: al-ways positive and very inhomogeneous, Phys. Rev. Lett. 88 (2002) 187401-1–187401-4.

[77] O.G. Vendik, M.S. Gasinova, Artificial double negative (DNG) media composed by two different dielectric sphere lattices embedded in a dielectric matrix, in: 34th European Microwave Conference, Amsterdam, 2004, pp. 1209–1212.

[78] L. Jylha, I. Kolmakov, S. Maslovski, S. Tretyakov, Modeling of isotropic backward-wave materials composed of resonant spheres, J. Appl. Phys. 99 (2006) 043102.

[79] M.S. Wheeler, J.S. Aitchison, M. Mojahedi, Coated nonmagnetic spheres with a negative index of refraction at infrared frequencies, Phys. Rev. B 73 (2006) 045105.

[80] Q. Zhao, J. Zhou, F. Zhang, D. Lippens, Mie resonance-based dielectric metamaterials, Mater. Today 12 (12) (Dec. 2009) 60–69.

[81] L. Peng, L. Ran, H. Chen, H. Zhang, J. auKong, T.M. Grzegorczyk, Experimental obser-vation of left-handed behavior in an array of standard dielectric resonators, Phys. Rev. Lett. 98 (2007) 157403.

[82] J. Kim, A. Gopinath, Simulation of a metamaterial containing cubic high dielectric res-onators, Phys. Rev. B 76 (2007) 115126.

[83] Q. Zhao, L. Kang, B. Du, H. Zhao, Q. Xie, X. Huang, B. Li, J. Zhou, L. Li, Experi-mental demonstration of isotropic negative permeability in a three-dimensional dielectric composite, Phys. Rev. Lett. 101 (July 2008) 027402.

[84] S. Kim, C.L. Holloway, K.L. Kumley, M.D. Janezic, J. Baker-Jarvis, E.F. Kuester, A frequency-bandgap waveguide controlled with metafilms composed of cubic particles, J. Appl. Phys. 112 (2012) 104904.

[85] P. Moitra, B.A. Slovick, W. Li, I.I. Kravchencko, D.P. Briggs, S. Krishnamurthy, J. Valentine, Large-scale all-dielectric metamaterial perfect reflectors, ACS Photonics 2 (6) (2015) 692–698.

[86] J.C. Ginn, G.A. Ten Eyck, I. Brener, D.W. Peters, M.B. Sinclair, Infrared cubic dielectric resonator metamaterial, in: Photonic Metamaterials and Plasmonics, Tucson, Arizona, June 7–8, 2010.

[87] J.C. Ginn, I. Brener, D.W. Peters, J.R. Wendt, J.O. Stevens, P.F. Hines, L.I. Basilio, Larry K. Warne, Jon F. Ihlefeld, Paul G. Clem, Michael B. Sinclair, Realizing optical magnetism from dielectric metamaterials, Phys. Rev. Lett. 108 (2012) 097402.

[88] I. Staude, A.E. Miroshnichenko, M. Decker, N.T. Fofang, S. Liu, E. Gonzales, J. Dominguez, T. Shan Luk, D.N. Neshev, I. Brener, Y. Kivshar, Tailoring directional scattering through magnetic and electric resonances in subwavelength silicon nanodisks, ACS Nano 7 (9) (2013) 7824–7832.

[89] S. Liu, M.B. Sinclair, S. Saravi, G.A. Keeler, Y. Yang, J. Reno, G.M. Peake, F. Setzpfandt, I. Staude, T. Pertsch, I. Brener, Resonantly enhanced second-harmonic generation using III–V semiconductor all-dielectric metasurfaces, Nano Lett. 16 (9) (2016) 5426–5432.

[90] I. Staude, V.V. Khardikov, N.T. Fofang, S. Liu, M. Decker, D.N. Neshev, T. Shan Luk, I. Brener, Y.S. Kivshar, Shaping photoluminescence spectra with magnetoelectric resonances in all-dielectric nanoparticles, ACS Photonics 2 (2) (2015) 172–177.

[91] S. Liu, G.A. Keeler, J.L. Reno, M.B. Sinclair, I. Brener, III–V semiconductor nanoresonators—a new strategy for passive, active, and nonlinear all-dielectric metamaterials, Adv. Opt. Mater. 4 (10) (2016) 1457.

[92] I. Brener, Optical magnetism from dielectric resonator metamaterials, in: META 2014 Conference, Singapore, May 20–23, 2014.

[93] L.K. Warne, L.I. Basilio, W.L. Langston, W.A. Johnson, M.B. Sinclair, Perturbation theory in the design of degenerate rectangular dielectric resonators, PIER B 44 (2012) 1–29.

[94] L.K. Warne, L.I. Basilio, W.L. Langston, W.A. Johnson, M.B. Sinclair, Perturbation theory in the design of degenerate spherical dielectric resonators, IEEE Trans. Antennas Propag. 61 (2013) 2130–2141.

[95] L.K. Warne, W.A. Johnson, L.I. Basilio, W.L. Langston, M.B. Sinclair, Subcell method for modeling metallic resonators in metamaterials, PIER B 38 (2012) 135–164.

[96] A.M. Nicolson, G. Ross, Measurement of the intrinsic properties of materials by time domain techniques, IEEE Trans. Instrum. Meas. 19 (1970) 377–382.

[97] W.B. Weir, Automatic measurements of complex dielectric constant and permeability at microwave frequencies, Proc. IEEE 62 (1974) 33–36.

[98] D.R. Smith, S. Schultz, P. Markos, C.M. Soukoulis, Determination of effective permittivity and permeability of metamaterials from reflection and transmission coefficients, Phys. Rev. B 65 (2002) 195104.

[99] R.W. Ziolkowski, Designs, fabrication, and testing of double negative metamaterials, IEEE Trans. Antennas Propag. 51 (2003) 1516–1529.

[100] S. Kim, E.F. Kuester, C.L. Holloway, A.D. Scher, J. Baker-Jarvis, Boundary effects on the determination of the effective parameters of a metamaterials from normal incidence reflection and transmissions, IEEE Trans. Antennas Propag. 59 (6) (2011).

[101] S. Kim, E.F. Kuester, C.L. Holloway, A.D. Scher, J. Baker-Jarvis, Effective material property extraction of a metamaterial by taking boundary effects into account at TE/TM polarized incidence, Prog. Electromag. Res. B 36 (2011) 1–33.

[102] X. Chen, T.M. Grezegorczyk, B.-I. Wu, J. Pacheco, J.A. Kong, Robust method to retrieve the constitutive effective parameters of metamaterials, Phys. Rev. E 70 (2004) 016608.

[103] A.D. Scher, E.F. Kuester, Extracting the bulk effective parameters of a metamaterial via the scattering parameters for a single planar array of particles, Metamaterials 3 (2009) 44–55.

[104] J. Zhou, T. Koschny, M. Kafesaki, C.M. Soukoulis, Size dependence and convergence of the retrieval parameters of metamaterials, Photonics Nanostruct. Fundam. Appl. 6 (2008) 96–101.

[105] C. Rockstuhl, T. Paul, F. Lederer, T. Pertsch, T. Zentgraf, T.P. Meyrath, H. Giessen, Transition from thin-film to bulk properties of metamaterials, Phys. Rev. B 77 (2008) 035126.

[106] C. Rockstuhl, C. Menzel, T. Paul, C. Helgert, E. Pshenay-Severin, J. Petschulat, A. Chipouline, T. Pertsch, F. Lederer, Bulk properties of metamaterials, Proc. SPIE 6987 (2008) 698710.

[107] M.G. Silveirinha, C.A. Fernandes, Homogenization of metamaterial surfaces and slabs: the crossed wire mesh canonical problem, IEEE Trans. Antennas Propag. 53 (2005) 59–69.

[108] C.L. Holloway, E.F. Kuester, A homogenization technique for obtaining generalized sheet transition conditions (GSTCs) for a metafilm embedded in a magneto-dielectric interface, IEEE Trans. Antennas Propag. 64 (11) (2016) 4671–4686.

[109] C.L. Holloway, E.F. Kuester, Generalized sheet transition conditions (GSTCs) for a metascreen, IEEE Trans. Antennas Propag. 66 (5) (2018) 2414–2427.

[110] E.F. Kuester, M.A. Mohamed, M. Piket-May, C.L. Holloway, Averaged transition conditions for electromagnetic fields at a metafilm, in: Special Issue on Metamaterials, IEEE Trans. Antennas Propag. 51 (10) (Oct. 2003) 2641–2651.

[111] C.L. Holloway, D.C. Love, E.F. Kuester, J.A. Gordon, D.A. Hill, Use of generalized sheet transition conditions to model guided waves on metasurfaces/metafilms, IEEE Trans. Antennas Propag. 60 (2012) 5173–5186.

[112] C.L. Holloway, E.F. Kuester, A homogenization technique for obtaining generalized sheet transition conditions for an arbitrarily shaped coated wire grating, Radio Sci. 49 (10) (2014) 813–850.

[113] C.L. Holloway, A. Dienstfrey, E.F. Kuester, J.F. O'Hara, A.K. Azad, A.J. Taylor, A discussion on the interpretation and characterization of metafilms–metasurfaces: the two-dimensional equivalent of metamaterials, Metamaterials 3 (2009) 100–112.

[114] C.L. Holloway, E.F. Kuester, A. Dienstfrey, Characterizing metasurfaces/metafilms: the connection between surface susceptibilities and effective material properties, IEEE Antennas Wirel. Propag. Lett. 10 (2011) 1507–1511.

[115] C.L. Holloway, M.A. Mohamed, E.F. Kuester, Reflection and transmission properties of a metafilm: with an application to a controllable surface composed of resonant particles, IEEE Trans. Electromagn. Compat. 47 (4) (Nov. 2005) 853–865.

[116] C.L. Holloway, D.C. Love, E.F. Kuester, A. Salandrino, N. Engheta, Sub-wavelength resonators: on the use of metafilms to overcome the $\lambda/2$ size limit, IET Microw. Antennas Propag. 2 (2) (March 2008) 120–129.

[117] C.L. Holloway, E.F. Kuester, Retrieval approach for determining surface susceptibilities and surface porosities of a symmetric metascreen from reflection and transmission coefficients, arXiv:1902.08703, 2019.

[118] C.L. Holloway, E.F. Kuester, A.H. Haddab, Using reflection and transmission coefficients to retrieve surface parameters for an anisotropic metascreen: with a discussion on conversion between TE and TM polarizations, J. Appl. Phys. 125 (2019) 095102.

[119] F. Yang, Y. Rahmat-Samii (Eds.), Surface Electromagnetics: With Applications in Antenna, Microwave, and Optical Engineering, Cambridge University Press, July 2019, Chapter 3: Using generalized sheet transition conditions (GSTCs) in the analysis of metasurfaces.

[120] C.L. Holloway, E.F. Kuester, D. Novotny, Waveguides composed of metafilms–metasurfaces: the two-dimensional equivalent of metamaterials, IEEE Antennas Wirel. Propag. Lett. 8 (2009) 525–529.

[121] C.L. Holloway, P. Kabos, M.A. Mohamed, E.F. Kuester, J. Gordon, M.D. Janezic, J. Baker-Jarvis, Realization of a controllable metafilm/metasurface composed of resonant magnetodielectric particles: measurements and theory, in: Special Issue on Microwave Metamaterials, IET Microw. Antennas Propag. 4 (8) (August 2010) 1111–1122.

[122] M.V. Rybin, D.S. Filonov, K.B. Samusev, P.A. Belov, Y.S. Kivshar, M.F. Limonov, Phase diagram for the transition from photonic crystals to dielectric metamaterials, Nat. Commun. 6 (1) (2015) 10102.

[123] J. Gordon, C.L. Holloway, J. Booth, Fluid interactions with metafilms/metasurfaces for tuning, sensing, and microwave-assisted chemical processes, Phys. Rev. B 83 (2011) 205130.

[124] S.A. Tretyakov, S.I. Maslovski, Thin absorbing structure for all incident angles based on the use of a high-impedance surface, Microw. Opt. Technol. Lett. 38 (3) (2003) 175–178.

[125] Y. Kotsuka, K. Murano, M. Amano, S. Sugiyama, Novel right-handed metamaterial based on the concept of 'autonomous control system of living cells,' and its absorber applications, IEEE Trans. Electromagn. Compat. 52 (3) (2010) 556–565.

[126] Hu Tao, C.M. Bingham, A.C. Strikwerda, D. Pilon, C. Shrekenhamer, N.I. Landy, K. Fan, X. Zhang, W.J. Padilla, R.D. Averitt, Highly flexible wide angle of incidence terahertz metamaterial absorber: design, fabrication, and characterization, Phys. Rev. B 78 (2008) 241103.

[127] N.I. Landy, S. Sajuyigbe, J.J. Mock, D.R. Smith, W.J. Padilla, Perfect metamaterial absorber, Phys. Rev. Lett. 100 (2008) 207402.

[128] O. Luukkonen, F. Costa, C.R. Simovski, A. Monorchio, S.A. Tretyakov, A thin electromagnetic absorber for wide incidence angles and both polarizations, IEEE Trans. Antennas Propag. 57 (10) (2009) 3119–3125.

[129] F. Bilotti, A. Toscano, K.B. Alici, E. Ozbay, L. Vegni, Design of miniaturized narrowband absorber based on resonant-magnetic inclusions, IEEE Trans. Electromagn. Compat. 53 (1) (2011) 63–72.

[130] S. Sajuyigbe, M. Ross, P. Geren, S.A. Cummer, M.H. Tanielian, D.R. Smith, Wide angle impedance matching metamaterials for waveguide-fed phased-array antenna, IET Microw. Antennas Propag. 4 (8) (2010) 1063–1072.

[131] H.-T. Chen, W.J. Padilla, J.M.O. Zide, S.R. Bank, A.C. Gossard, A.J. Taylor, R.D. Averitt, Ultrafast optical switching of terahertz metamaterials fabricated on ErAs/GaAs nanoisland superlattices, Opt. Lett. 32 (12) (2007) 1620–1622.

[132] H.-T. Chen, W.J. Padilla, J.M.O. Zide, A.C. Gossard, A.J. Taylor, R.D. Averitt, Active terahertz metamaterial devices, Nature 444 (2006) 597–600.

[133] H.-T. Chen, W.J. Padilla, M.J. Cich, A.K. Azad, R.D. Averitt, A.J. Taylor, A metamaterial solid-state terahertz phase modulator, Nat. Photonics 3 (2009) 148–151.

[134] H.-T. Chen, J.F. O'Hara, A.K. Azad, A.J. Taylor, R.D. Averitt, D.B. Shrekenhamer, W.J. Padilla, Experimental demonstration of frequency-agile terahertz metamaterials, Nat. Photonics 2 (2008) 295–298.

[135] W.L. Chan, H.-T. Chen, A.J. Taylor, I. Brener, M.J. Cich, D.M. Mittleman, A spatial light modulator for terahertz beams, Appl. Phys. Lett. 94 (2009) 213511.

[136] X.G. Peralta, I. Brener, W.J. Padilla, E.W. Young, A.J. Hoffman, M.J. Cich, R.D. Averitt, M.C. Wanke, J.B. Wright, H.-T. Chen, J.F. O'Hara, A.J. Taylor, J. Waldman, W.D. Goodhue, J. Li, J. Reno, External modulators for terahertz quantum-cascade lasers based on electrically-driven active metamaterials, Metamaterials 4 (2) (2010) 83–88.

[137] H. Tao, A.C. Strikwerda, K. Fan, W.J. Padilla, X. Zhang, R.D. Averitt, Reconfigurable terahertz metamaterials, Phys. Rev. Lett. 103 (2009) 147401.

[138] J. Han, A. Lakhtakia, Semiconductor split-ring resonators for thermally tunable terahertz metamaterials, J. Mod. Opt. 56 (2009) 554–557.

[139] T. Driscoll, S. Palit, M.M. Qazilbash, M. Brehm, F. Keilmann, B.-G. Chae, S.-J. Yun, H.-T. Kim, S.Y. Cho, N.M. Jokerst, D.R. Smith, D.N. Basov, Dynamic tuning of an

infrared hybrid-metamaterial resonance using vanadium dioxide, Appl. Phys. Lett. 93 (2008) 024101.

[140] T. Driscoll, H.-T. Kim, B.-G. Chae, B.-J. Kim, Y.-W. Lee, N.M. Jokerst, S. Palit, D.R. Smith, M. Di Ventra, D.N. Basov, Memory metamaterials, Science 325 (2009) 1518–1521.

[141] T. Driscoll, G.O. Andreev, D.N. Basov, S. Palit, S.Y. Cho, N.M. Jokerst, D.R. Smith, Tuned permeability in terahertz split-ring resonators for devices and sensors, Appl. Phys. Lett. 91 (2007) 062511.

[142] T.A. Klar, A.V. Kildishev, V.P. Drachev, V.M. Shalaev, Negative-index metamaterials: going optical, IEEE J. Sel. Top. Quantum Electron. 12 (6) (2006) 1106–1115.

[143] A.V. Kildishev, W. Cai, K. Chettiar, H. Yuan, A.K. Sarychev, V.P. Drachev, V.M. Shalaev, Negative refractive index in optics of metal-dielectric composites, J. Opt. Soc. Am. B 23 (3) (2006) 423–433.

[144] J.B. Pendry, Negative refraction makes a perfect lens, Phys. Rev. Lett. 85 (2000) 3966–3969.

[145] A. Alù, A. Salandrino, N. Engheta, Negative effective permeability and left-handed materials at optical frequencies, Opt. Express 14 (4) (2006) 1557–1567.

[146] G. Dolling, C. Enkrick, M. Wegener, C.M. Soukoulis, S. Linden, Low-loss negative-index metamaterials at telecommunication wavelengths, Opt. Lett. 31 (12) (2006) 1800–1802.

[147] T.J. Yen, W.J. Padilla, N. Fang, D.C. Vier, D.R. Smith, J.B. Pendry, D.N. Basov, X. Zhang, Terahertz magnetic response from artificial materials, Science 303 (2004) 1494–1496.

[148] J.A. Gordon, R.W. Ziolkowski, The design and simulated performance of a coated nanoparticle laser, Opt. Express 15 (5) (2007) 2622–2653.

[149] M.I. Stockman, Spasers explained, Nat. Photonics 2 (2008) 327–329.

[150] V.M. Shalaev, Optical negative-index metamaterials, Nat. Photonics 1 (2007) 41–48.

[151] A. Alu, N. Engheta, Theory of linear chains of metamaterials/plasmonic particles as sub-diffraction optical nanotransmission lines, Phys. Rev. B 74 (2006) 205436.

[152] C. Pfeiffer, A. Grbic, Metamaterial Huygens' surfaces: tailoring wave fronts with reflectionless sheets, Phys. Rev. Lett. 110 (2013) 197401.

[153] C. Pfeiffer, A. Grbic, Cascaded metasurfaces for complete phase and polarization control, Appl. Phys. Lett. 102 (23) (2013) 231116.

[154] N.M. Estakhri, A. Alu, Wave-front transformation with gradient metasurfaces, Phys. Rev. X 6 (2016) 041008.

[155] A. Epstein, G.V. Eleftheriades, Arbitrary power-conserving field transformations with passive lossless omega-type bianisotropic metasurfaces, IEEE Trans. Antennas Propag. 64 (9) (2017).

[156] A.T. Pereda, F. Caminita, E. Martini, I. Ederra, J.C. Iriarte, R. Gonzalo, S. Maci, Dual circularly polarized broadside beam metasurface antenna, IEEE Trans. Antennas Propag. 64 (7) (2016) 2944–2953.

[157] S.B. Glybovski, S.A. Tretyakov, P.A. Belov, Y.S. Kivshar, C.R. Simovski, Metasurfaces: from microwaves to visible, Phys. Rep. 634 (2016) 1–72.

[158] D. Morits, M. Morits, V. Ovchinnikov, M. Omelyanovich, A. Tamminen, S. Tretyakov, C. Simovski, Multifunctional stretchable metasurface for the THz range, J. Opt. 16 (3) (2014) 032001.

[159] A. Alu, N. Engheta, Three-dimensional nanotransmission lines at optical frequencies: a recipe for broadband negative-refraction optical metamaterials, Phys. Rev. B 75 (2007) 024304.

[160] T.B.A. Senior, J.L. Volakis, Approximate Boundary Conditions in Electromagnetics, Stevenage, UK, IEE, 1995.

[161] M.I. Oksanen, S.A. Tretyakov, I.V. Lindell, Vector circuit theory for isotropic and chiral slabs, J. Electromagn. Waves Appl. 4 (1990) 613–643.

[162] S.A. Tretyakov, A.J. Viitanen, S.I. Maslovki, I.E. Saarela, Impedance boundary conditions for regular dense arrays of dipole scatterers, IEEE Trans. Antennas Propag. 51 (8) (2003) 2073–2078.

[163] O. Luukkonen, C. Simovski, G. Granet, G. Goussetis, D. Lioubtchenko, A.V. Räisänen, S.A. Tretyakov, Simple and accurate analytical model of planar grids and high-impedance surfaces comprising metal strips or patches, IEEE Trans. Antennas Propag. 56 (6) (2008) 1624–1632, correction in: IEEE Trans. Antennas Propag. 58 (2010) 2162.

[164] R.W. Ziolkowski, P. Jin, C.-C. Lin, Metamaterial-inspired engineering of antennas, Proc. IEEE 99 (10) (2011) 1720–1731.

[165] P. Jin, R.W. Ziolkowski, Metamaterial-inspired, electrically small, Huygens sources, IEEE Antennas Wirel. Propag. Lett. 9 (2010) 501–505.

[166] P. Jin, R.W. Ziolkowski, Multiband extensions of the electrically small metamaterial-engineered Z antenna, IET Microw. Antennas Propag. 4 (8) (2010) 1016–1025.

[167] C.-C. Lin, R.W. Ziolkowski, Dual-band 3D magnetic EZ antenna, Microw. Opt. Technol. Lett. 52 (4) (2010) 971–975.

[168] P. Jin, R.W. Ziolkowski, Broadband, efficient, electrically small metamaterial-inspired antennas facilitated by active near-field resonant parasitic elements, IEEE Trans. Antennas Propag. 58 (2) (2010) 318–327.

[169] P. Jin, R.W. Ziolkowski, Low Q, electrically small, efficient near field resonant parasitic antennas, IEEE Trans. Antennas Propag. 57 (9) (2009) 2548–2563.

[170] A. Erentok, R.W. Ziolkowski, Metamaterial-inspired efficient electrically-small antennas, IEEE Trans. Antennas Propag. 56 (3) (2008) 691–707.

[171] R.W. Ziolkowski, A. Erentok, Metamaterial-based efficient electrically small antennas, IEEE Trans. Antennas Propag. 54 (7) (2006) 2113–2130.

[172] A. Alu, N. Engheta, Tuning the scattering response of optical nanoantennas with nanocircuit loads, Nat. Photonics 2 (May 2008) 307–310.

[173] I.A. Ibrahheem, M. Koch, Coplanar waveguide metamaterials: the role of bandwidth modifying slots, Appl. Phys. Lett. 91 (2007) 113517.

[174] M. Quinten, A. Leitner, J.R. Krenn, F.R. Aussenegg, Electromagnetic energy transport via linear chains of silver nanoparticles, Opt. Lett. 23 (17) (1998) 1331–1333.

[175] S.A. Tretyakov, A.J. Viitanen, Line of periodically arranged passive dipole scatterers, Electr. Eng. 82 (6) (2000) 353–361.

[176] M.L. Brongersma, J.W. Hartman, H.A. Atwater, Electromagnetic energy transfer and switching in nanoparticle chain arrays below the diffraction limit, Phys. Rev. B 62 (2000) 16356–16359.

[177] W.H. Weber, G.W. Ford, Propagation of optical excitations by dipolar interactions in metal nanoparticle chains, Phys. Rev. B 70 (2004) 125429.

[178] R.A. Shore, A.D. Yaghjian, Traveling electromagnetic waves on linear periodic arrays of lossless spheres, Electron. Lett. 41 (10) (2005) 578–580.

[179] R.A. Shore, A.D. Yaghjian, Traveling electromagnetic waves on linear periodic arrays of lossless penetrable spheres, IEICE Trans. Commun. E 88-B (6) (2005) 2346–2352.

[180] M. Guasoni, C. De Angelis, Analytical approximations of the dispersion relation of a linear chain of nanoparticles, Opt. Commun. 284 (7) (2011) 1822–1827.

Fundamentals of Mie scattering

<div style="float:right">**2**</div>

Manuel Nieto-Vesperinas
Instituto de Ciencia de Materiales de Madrid, C.S.I.C., Madrid, Spain

2.1 Introduction

Gustav Mie's paper [1], establishing a series expansion solution to the scattering and absorption of light and other electromagnetic waves by a sphere, is over 110 years old. Due to the lack of computers at the time, this work had little impact during the following 50 years [2]. However, it later experienced a strong upsurge, becoming of widespread use in a large variety of areas spanning from astronomy, atmospheric physics and meteorology to colloids and aerosols; domains in which it was further extended to other particles, like coated and anisotropic spheres and rods. Subsequently, surface science advances have made extensive use of Mie's method, expanding it to the presence of substrates. In the last years, this theory has acquired an extraordinary relevance in the emergent branch of nano-optics and the effects of morphological resonances in plasmonics [3,4], and in dielectric nanostructures based on the optics of high refractive index dielectric nanoparticles [5,6]. Sections 2.2–2.7 contain an overview of the standard theory of scattering by spheres and infinitely long circular cylinders. We outline it following the methodology and notation of [7]. Section 2.8 is devoted to morphology dependent resonances (MDRs), introducing the concepts of *localized surface plasmons* (LSPs) and *whispering gallery modes* (WGMs). Then the dipolar approximation is dealt with in Section 2.9; the Rayleigh limit being presented in Section 2.10. Finally, Section 2.11 deals with *magnetoelectric effects*, introducing the concepts of Fano resonances and Kerker conditions, both of importance in directional scattering.

Although this chapter is self-contained, the interested reader may find further details on the contents of Sections 2.2–2.7 of Mie's theory in the classical texts [7–11].

2.2 Uniform sphere: internal and scattered fields

Let a monochromatic, time harmonic, arbitrarily polarized plane wave of wavevector $\mathbf{k}_i$ impinges on a sphere of radius a and refractive index $n_p = \sqrt{\epsilon_p \mu_p}$, with permittivity ϵ_p and permeability μ_p, immersed in an optically homogeneous, non-absorbing, and isotropic medium of index $n = \sqrt{\epsilon \mu}$, then the incident electric and magnetic vectors obeying Maxwell's equations at a generic point $\mathbf{r}$ of space are

$$\mathbf{E}_i = \mathbf{E}_0 e^{i(\mathbf{k}_i \cdot \mathbf{r} - \omega t)}, \quad \mathbf{B}_i = \mathbf{B}_0 e^{i(\mathbf{k}_i \cdot \mathbf{r} - \omega t)}, \quad \mathbf{B}_0 = (n\mathbf{k}_i/k) \times \mathbf{E}_0. \tag{2.1}$$

Here $|\mathbf{k}_i| = k = n\omega/c = 2\pi/\lambda$. ω being the circular frequency; c and λ representing the speed of light in vacuum and the wavelength in the medium.
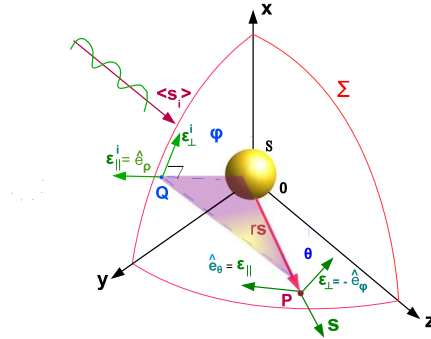
Figure 2.1 A plane wave, with time-averaged power flow $< \mathbf{s}_i >$ incident along OZ on a polarizable spherical particle of radius a and center at the origin $\mathbf{0}$ of coordinates X, Y, Z. The scattered field is evaluated at the observation point $\mathbf{P}$ of coordinates (r, θ, ϕ) and position vector $\mathbf{r} = r\mathbf{s}$, which belongs to a sphere Σ of radius r, and center $\mathbf{0}$. The point $\mathbf{Q}$ is the projection of $\mathbf{P}$ on the XY-plane; the *scattering plane* being OPQ. We show the three orthonormal vectors that form the local basis in P: $\mathbf{s}$ (normal to Σ), $\epsilon_\parallel$ (in the plane OPQ and in the sense of rotation of θ), and $\epsilon_\perp$ (normal to OPQ).

The fields inside and outside the particle are denoted by the pairs $\mathbf{E}_1, \mathbf{B}_1$ and $\mathbf{E}_2, \mathbf{B}_2$, respectively. Moreover, we write

$$\mathbf{E}_2 = \mathbf{E}_i + \mathbf{E}_s, \quad \mathbf{B}_2 = \mathbf{B}_i + \mathbf{B}_s. \tag{2.2}$$

The subindex s standing for the scattered field. We employ Gaussian units.

These fields fulfill the *saltus* conditions on the boundary S of the scattering sphere:

$$(\mathbf{E}_2 - \mathbf{E}_1) \times \mathbf{n} = \mathbf{0}; \quad (\mathbf{B_2} - \mathbf{B_1}) \times \mathbf{n} = \mathbf{0}. \tag{2.3}$$

$\mathbf{n}$ being the outward local normal to S.

As Fig. 2.1 shows, we build at the observation point P of the *scattering plane* OPQ the local basis $\{\hat{\mathbf{e}}_r, \hat{\mathbf{e}}_\theta, \hat{\mathbf{e}}_\phi\}$ from the three unit vectors $\epsilon_\perp$, $\epsilon_\parallel$, and $\mathbf{s}$ along the directions of the spherical coordinates (r, θ, ϕ). With $\hat{\mathbf{e}}_r = \mathbf{s}$, $\hat{\mathbf{e}}_\theta = \epsilon_\parallel$, and $\hat{\mathbf{e}}_\phi = -\epsilon_\perp$. In terms of these vectors the scattered field is written as

$$\mathbf{E}_s = E_{s\,\parallel}\,\epsilon_\parallel + E_{s\,\perp}\,\epsilon_\perp. \tag{2.4}$$

Also, choosing $\mathbf{k}_i$ along OZ, the incident field, which will vibrate in the OXY-plane, may be expressed in terms of the perpendicular and parallel component to the scattering plane by means of the unit vectors $\{\hat{\mathbf{e}}_\rho, \hat{\mathbf{e}}_\phi, \hat{\mathbf{z}}\}$ of the cylindrical coordinates of point Q: $\epsilon_\parallel^i = \hat{\mathbf{e}}_\rho$ and $\epsilon_\perp^i = -\hat{\mathbf{e}}_\phi$. Thus its electric vector reads

$$\mathbf{E}_i = (E_{0\,\parallel}\,\epsilon_\parallel^i + E_{0\,\perp}\,\epsilon_\perp^i)e^{i(kz - \omega t)}. \tag{2.5}$$

Then the solution is obtained by expanding the fields in a series of vector spherical harmonics [7]:

$$\mathbf{M}_{emn}^{(1)} = -\frac{m}{\sin\theta}\sin m\phi\, P_n^m(\cos\theta)\, j_n(\rho)\hat{\mathbf{e}}_\theta - \cos m\phi\frac{d P_n^m(\cos\theta)}{d\theta}\, j_n(\rho)\hat{\mathbf{e}}_\phi. \tag{2.6}$$

$$\mathbf{M}_{omn}^{(1)} = \frac{m}{\sin\theta}\cos m\phi\, P_n^m(\cos\theta)\, j_n(\rho)\hat{\mathbf{e}}_\theta - \sin m\phi\frac{d P_n^m(\cos\theta)}{d\theta}\, j_n(\rho)\hat{\mathbf{e}}_\phi. \tag{2.7}$$

$$\mathbf{N}_{emn}^{(1)} = n(n+1)\cos m\phi\, P_n^m(\cos\theta)\frac{j_n(\rho)}{\rho}\hat{\mathbf{e}}_r$$
$$+ \cos m\phi\frac{d P_n^m(\cos\theta)}{d\theta}\frac{1}{\rho}\frac{d}{\rho}[\rho j_n(\rho)]\hat{\mathbf{e}}_\theta$$
$$- m\sin m\phi\frac{P_n^m(\cos\theta)}{\sin\theta}\frac{1}{\rho}\frac{d}{\rho}[\rho j_n(\rho)]\hat{\mathbf{e}}_\phi. \tag{2.8}$$

$$\mathbf{N}_{omn}^{(1)} = n(n+1)\sin m\phi\, P_n^m(\cos\theta)\frac{j_n(\rho)}{\rho}\hat{\mathbf{e}}_r$$
$$+ \sin m\phi\frac{d P_n^m(\cos\theta)}{d\theta}\frac{1}{\rho}\frac{d}{\rho}[\rho j_n(\rho)]\hat{\mathbf{e}}_\theta$$
$$+ m\cos m\phi\frac{P_n^m(\cos\theta)}{\sin\theta}\frac{1}{\rho}\frac{d}{\rho}[\rho j_n(\rho)]\hat{\mathbf{e}}_\phi. \tag{2.9}$$

The subindices o and e denote odd and even dependence on the azimuthal angle ϕ of the generating functions of these spherical harmonics [7,10], as they contain either the factor $\sin(m\phi)$ and $\cos(m\phi)$, respectively. $P_n^m(\cos\theta)$ are the associated Legendre functions of the first kind with degree n and order m. The superindex (1) means that in (2.6)–(2.9) the radial dependence $\rho = kr$ is given in terms of the first kind spherical Bessel function $j_n(\rho) = \sqrt{\pi/2\rho}\, J_{n+1/2}(\rho)$. $J_n(\rho)$ being the Bessel function of the first kind [12].

The incident plane wave is then expressed as

$$\mathbf{E}_i = E_0 \sum_{n=1}^{\infty} i^n \frac{2n+1}{n(n+1)}[\mathbf{M}_{o1n}^{(1)} - i\mathbf{N}_{e1n}^{(1)}], \tag{2.10}$$

$$\mathbf{B}_i = -\frac{k}{\omega}E_0 \sum_{n=1}^{\infty} i^n \frac{2n+1}{n(n+1)}[\mathbf{M}_{e1n}^{(1)} + i\mathbf{N}_{o1n}^{(1)}]. \tag{2.11}$$

The internal and scattered fields read

$$\mathbf{E}_1 = E_0 \sum_{n=1}^{\infty} i^n \frac{2n+1}{n(n+1)}[c_n\mathbf{M}_{o1n}^{(1)} - i d_n\mathbf{N}_{e1n}^{(1)}], \tag{2.12}$$

$$\mathbf{B}_1 = -\frac{k_p}{\omega}E_0 \sum_{n=1}^{\infty} i^n \frac{2n+1}{n(n+1)}[d_n\mathbf{M}_{e1n}^{(1)} + i c_n\mathbf{N}_{o1n}^{(1)}], \tag{2.13}$$

and

$$\mathbf{E}_s = E_0 \sum_{n=1}^{\infty} i^n \frac{2n+1}{n(n+1)} [i a_n \mathbf{N}_{e1n}^{(3)} - b_n \mathbf{M}_{o1n}^{(3)}], \tag{2.14}$$

$$\mathbf{B}_s = -\frac{k}{\omega} E_0 \sum_{n=1}^{\infty} i^n \frac{2n+1}{n(n+1)} [i b_n \mathbf{N}_{o1n}^{(3)} + a_n \mathbf{M}_{e1n}^{(3)}]. \tag{2.15}$$

In (2.12) and (2.13) $\rho = kmr$, where $m = n_p/n$ is the relative refractive index. On the other hand, in (2.14) and (2.15) the superindex (3) means that in Eqs. (2.6)–(2.9) the radial dependence $\rho = kr$ is given by the spherical Hankel function of the first kind: $h_n^{(1)}(\rho) = j_n(\rho) + i y_n(\rho)$ rather than by $j_n(\rho)$. The spherical Bessel function of the second kind is $y_n(\rho) = \sqrt{\pi/2\rho} Y_{n+1/2}(\rho)$. $Y_n(\rho)$ being the Bessel function of the second kind [12].

The radial dependence of the vector spherical harmonics in the incident and interior fields, makes them proportional to wavefunctions with both incoming and outgoing components; in addition the incident fields are source-free [11,13]. On the other hand, one observes from the radial dependence of the scattered fields an asymptotic behavior as outgoing spherical waves.

On defining the *size parameter* $x = ka$, the Mie coefficients of the interior and scattered fields are obtained from the saltus conditions (2.3). They are

$$a_n = \frac{\mu m^2 j_n(mx)[x j_n(x)]' - \mu_p j_n(x)[mx j_n(mx)]'}{\mu m^2 j_n(mx)[x h_n^{(1)}(x)]' - \mu_p h_n^{(1)}(x)[mx j_n(mx)]'}. \tag{2.16}$$

$$b_n = \frac{\mu_p j_n(mx)[x j_n(x)]' - \mu j_n(x)[mx j_n(mx)]'}{\mu_p j_n(mx)[x h_n^{(1)}(x)]' - \mu h_n^{(1)}(x)[mx j_n(mx)]'}. \tag{2.17}$$

Those of the interior fields read

$$c_n = \frac{\mu_p j_n(x)[x h_n^{(1)}(x)]' - \mu_p h_n^{(1)}(x)[x j_n(x)]'}{\mu_p j_n(mx)[x h_n^{(1)}(x)]' - \mu h_n^{(1)}(x)[mx j_n(mx)]'}. \tag{2.18}$$

$$d_n = \frac{\mu_p m j_n(mx)[x h_n^{(1)}(x)]' - \mu_p m h_n^{(1)}(x)[x j_n(x)]'}{\mu m^2 j_n(mx)[x h_n^{(1)}(x)]' - \mu_p h_n^{(1)}(x)[mx j_n(mx)]'}. \tag{2.19}$$

Therefore, the interior and scattered fields appear expanded into a series of partial waves, or modes, each of which has a weight given by its corresponding Mie coefficient. a_n and b_n in the scattered field are associated to two distinct types of partial waves: Considering a generic sphere S of arbitrary radius, concentric with the particle, one class, the *electric partial waves*, generated by $\mathbf{N}_{e1n}^{(3)}$, correspond to the a_n-coefficients, and are transversal magnetic (TM modes, often denoted as TM_{nl}) because the magnetic field has no component along any radial direction of the S-sphere. The $\mathbf{E}$-field lines of force on S are those characteristic of either an electric dipole ($n = 1$), or electric multipoles ($n > 1$), induced by the illuminating field in the particle. The $\mathbf{B}$-field lines of force form closed loops so that the sectional planes of S

that contain the **E** and **B**-lines are perpendicular to each other. (These field lines are shown in Figs. 3–10 of Mie's original paper [1], and have been reproduced in several well-known texts (see e.g. [7,10,11]), to which we refer the reader).

The other class, generated by $\mathbf{N}_{o1n}^{(3)}$, correspond to the b_n-coefficients and are transversal electric (TE, expressed as TE_{nl}). The **E**- and **B**-field lines of force are similar to those of the **B**- and **E**-field of the former case, respectively; and represent the nth *magnetic partial wave* which characterizes an induced magnetic dipole ($n = 1$), or multipoles ($n > 1$).

Thus, as seen from Eqs. (2.14) and (2.15) each nth normal mode is generally composed of one electric and one magnetic nth partial wave. Commonly, at optical frequencies, $b_n << a_n$; however, recently, strong magnetic coefficients b_n have been discovered in high refractive index particles; this constitutes a novel research line of optics, which will be addressed in Sections 2.9 and 2.11 as it is at the heart of the design of resonant dielectric metamaterials and metasurfaces (which are the subject of the present book), as well as of micro- and nanoantennas.

2.3 Extinction and scattering of energy. Cross-sections

The time-averaged density of energy flow $< \mathbf{S} >$ traversing a sphere Σ (cf. Fig. 2.1), whose radius r eventually becomes large so that $kr \rightarrow \infty$ is, taking the decomposition (2.2) into account, given by the Poynting vector time-average (denoted by $< . >$),

$$< \mathbf{S}> = <\mathbf{S_i} > + < \mathbf{S_s} > + < \mathbf{S_{ext}} >, \tag{2.20}$$

where the density of energy flow incident, scattered and extinguished by the spherical particle is

$$< \mathbf{S}_i > = \frac{c}{8\pi\mu}\Re\{\mathbf{E}_i \times \mathbf{B}_i^*\}, \tag{2.21}$$

$$< \mathbf{S}_s > = \frac{c}{8\pi\mu}\Re\{\mathbf{E}_s \times \mathbf{B}_s^*\}, \tag{2.22}$$

$$< \mathbf{S}_{ext} > = \frac{c}{8\pi\mu}\Re\{\mathbf{E}_i \times \mathbf{B}s^* + \mathbf{E}_s \times \mathbf{B}_i^*\}, \tag{2.23}$$

respectively.

Let $\mathcal{W}^{(a)}$ be the rate of energy absorbed by the sphere; on integrating the density flow $< \mathbf{S} >$ across the sphere Σ one has

$$-\mathcal{W}^{(a)} = \mathcal{W}^{(i)} + \mathcal{W}^{(s)} - \mathcal{W}^{(ext)}. \tag{2.24}$$

Here $\mathcal{W}^{(i)} = \int_\Sigma < \mathbf{S}_i > \cdot\mathbf{s}d\Sigma = 0$ represents the total flow across Σ of the incident field, which is, of course, zero, $\mathcal{W}^{(s)} = \int_\Sigma < \mathbf{S}_s > \cdot\mathbf{s}d\Sigma$ stands for the total flow across Σ of the scattered field, and $\mathcal{W}^{(ext)} = -\int_\Sigma < \mathbf{S}_{ext} > \cdot\mathbf{s}d\Sigma$ is the extinction flow given by the interference of the incident and scattered fields. Notice that rearranging terms in (2.24), $\mathcal{W}^{(ext)}$ constitutes the total flow across Σ extinguished from that of the incident field by scattering and absorption.

Namely, Eq. (2.24) becomes

$$\mathcal{W}^{(ext)} = \mathcal{W}^{(s)} + \mathcal{W}^{(a)}. \tag{2.25}$$

Taking into account the asymptotic values for $\rho = kr \to \infty$:

$$h_n^{(1)}(\rho) \sim (-i)^{n+1}\frac{e^{i\rho}}{\rho}; \quad \frac{d}{d\rho}h_n^{(1)}(\rho) \sim (-i)^n\frac{e^{i\rho}}{\rho}. \tag{2.26}$$

One may express the scattered fields in the far zone, $kr \to \infty$, by

$$\mathbf{E}_s(\mathbf{r}) \sim \mathbf{E}_s^{(0)}(\mathbf{s})\frac{e^{ikr}}{r}; \quad \mathbf{B}_s(\mathbf{r}) \sim \mathbf{B}_s^{(0)}(\mathbf{s})\frac{e^{ikr}}{r}; \quad \mathbf{B}_s^{(0)} = n\mathbf{s} \times \mathbf{E}_s^{(0)}, \tag{2.27}$$

which have the spherical wave envelope $\exp(ikr)/r$ with the scattering amplitudes $\mathbf{E}_s^{(0)}(\mathbf{s})$ and $\mathbf{B}_s^{(0)}(\mathbf{s})$.

Operating and using the principle of the stationary phase [11], (2.25) leads to

$$\mathcal{W}^{(ext)} = \mathcal{W}^{(s)} + \mathcal{W}^{(a)} = \frac{c}{2k}\Im\{\mathbf{E}_i \cdot \mathbf{E}_s^{(0)}(\mathbf{k}_i/k)\}. \tag{2.28}$$

$\Im$ denotes imaginary part. This equation expresses the extinction of energy $\mathcal{W}^{(ext)}$ as the sum of the total energies, scattered and absorbed by the particle. The right side of (2.28) shows that the energy extinguished from that illuminating the particle is given by the interference of the incident and scattered fields in the forward direction $\mathbf{k}_i/k$. Eq. (2.28) constitutes the *optical theorem* for energies [11,13].

On dividing $\mathcal{W}^{(ext)}$, $\mathcal{W}^{(s)}$ and $\mathcal{W}^{(a)}$ by the rate at which the energy is incident on a unit cross-sectional area of the obstacle: $| < \mathbf{S}_i > | = cE_i^2/8\pi$ one obtains the extinction $Q^{(ext)}$, scattering $Q^{(s)}$, and absorption $Q^{(a)}$ cross-sections of the particle, respectively. Then (2.28) reads

$$Q^{(ext)} = Q^{(s)} + Q^{(a)} = \frac{4\pi}{k}\Im\{\frac{\mathbf{E}_i \cdot \mathbf{E}_s^{(0)}(\mathbf{k}_i/k)}{E_i^2}\}. \tag{2.29}$$

In Section 2.11.2 we shall address the important form that this optical theorem adopts in the special case of dipolar particles.

From Eqs. (2.26)–(2.27) and the scattered field expansions, one obtains after some calculation [7,9] the cross-sections in terms of the Mie coefficients

$$Q^{(s)} = \frac{2\pi}{k^2}\sum_{n=1}^{\infty}(2n+1)(|a_n|^2 + |b_n|^2) \tag{2.30}$$

and

$$Q^{(ext)} = \frac{2\pi}{k^2}\sum_{n=1}^{\infty}(2n+1)\Re\{a_n + b_n\}. \tag{2.31}$$

Where $\Re$ means real part.

2.4 The scattering matrix

Using (2.4) and (2.5), and the asymptotic expressions (2.26) and (2.27) we may write the field longitudinal and transversal scattered components as a spherical wave in terms of the corresponding components of the incident field through the scattering **S**-matrix as

$$
\begin{pmatrix} E_{s\,\parallel} \\ E_{s\,\perp} \end{pmatrix} = \frac{ie^{ik(r-z)}}{kr} \begin{pmatrix} S_2(\theta,\phi) \ S_3(\theta,\phi) \\ S_4(\theta,\phi) \ S_1(\theta,\phi) \end{pmatrix} \begin{pmatrix} E_{i\,\parallel} \\ E_{i\,\perp} \end{pmatrix}.
\tag{2.32}
$$

Now taking into account (2.4), (2.5), (2.6)–(2.9), (2.10), (2.14), (2.26), and (2.27), and defining

$$
\pi_n(\cos\theta) = \frac{P_n^1(\cos\theta)}{\sin\theta}, \quad \tau_n(\cos\theta) = \frac{d P_n^1(\cos\theta)}{d\theta},
\tag{2.33}
$$

one obtains $S_3(\theta,\phi) = S_4(\theta,\phi) = 0$ while S_1 and S_2 are functions of $\cos\theta$ only

$$
S_1(\cos\theta) = \sum_{n=1}^{\infty} \frac{2n+1}{n(n+1)} [a_n \pi_n(\cos\theta) + b_n \tau_n(\cos\theta)].
\tag{2.34}
$$

$$
S_2(\cos\theta) = \sum_{n=1}^{\infty} \frac{2n+1}{n(n+1)} [a_n \tau_n(\cos\theta) + b_n \pi_n(\cos\theta)].
\tag{2.35}
$$

Since $\pi_n(1) = \tau_n(1) = n(n+1)/2$, one sees that in the forward direction $\theta = 0°$: $S_1(0°) = S_2(0°) = (1/2)\sum_{n=1}^{\infty}(2n+1)(a_n + b_n)$. Hence (2.31) becomes

$$
Q^{(ext)} = \frac{4\pi}{k^2} \Re\{S(0°)\}.
\tag{2.36}
$$

Furthermore, the polarization state of the scattered field with respect to that of the incident wave is described by its *Stokes parameters*:

$$
\mathcal{S}_s^{(1)} = \ <E_{s\,\parallel} E_{s\,\parallel}^* + E_{s\,\perp} E_{s\,\perp}^*>,
\tag{2.37}
$$

$$
\mathcal{S}_s^{(2)} = \ <E_{s\,\parallel} E_{s\,\parallel}^* - E_{s\,\perp} E_{s\,\perp}^*>,
\tag{2.38}
$$

$$
\mathcal{S}_s^{(3)} = \ <E_{s\,\parallel} E_{s\,\perp}^* + E_{s\,\perp} E_{s\,\parallel}^*>,
\tag{2.39}
$$

$$
\mathcal{S}_s^{(4)} = i \ <E_{s\,\parallel} E_{s\,\perp}^* - E_{s\,\perp} E_{s\,\parallel}^*>.
\tag{2.40}
$$

These are linked to those of the incident field $\mathcal{S}_0^{(i)}$ ($i = 1, 2, 3, 4$) through the combination of the **S**-matrix elements:

$$
\begin{pmatrix} \mathcal{S}_s^{(1)} \\ \mathcal{S}_s^{(2)} \\ \mathcal{S}_s^{(3)} \\ \mathcal{S}_s^{(4)} \end{pmatrix} = \frac{1}{k^2 r^2} \begin{pmatrix} S_{11} & S_{12} & 0 & 0 \\ S_{12} & S_{11} & 0 & 0 \\ 0 & 0 & S_{33} & S_{34} \\ 0 & 0 & -S_{34} & S_{33} \end{pmatrix} \begin{pmatrix} \mathcal{S}_0^{(1)} \\ \mathcal{S}_0^{(2)} \\ \mathcal{S}_0^{(3)} \\ \mathcal{S}_0^{(4)} \end{pmatrix}.
\tag{2.41}
$$

The 4×4 matrix with elements S_{ij} is the *Mueller matrix* for the scattering by a sphere.

$$S_{11} = \frac{1}{2}(|S_1|^2 + |S_2|^2), \quad S_{12} = \frac{1}{2}(|S_2|^2 + |S_1|^2), \tag{2.42}$$

$$S_{33} = \frac{1}{2}(S_2^* S_1 + S_2 S_1^*), \quad S_{34} = \frac{1}{2}(S_1^* S_2 - S_2 S_1^*), \tag{2.43}$$

and $S_{11}^2 = S_{12}^2 + S_{33}^2 + S_{34}^2$.

If the incident light is polarized parallel to a scattering plane, the Stokes parameters of the scattered light are $\mathcal{S}_s^{(1)} = I_s = (S_{11} + S_{12})I_i$, $\mathcal{S}_s^{(2)} = Q_s = I_s$, $\mathcal{S}_s^{(3)} = \mathcal{S}_s^{(4)} = 0$; and let $i_\parallel$ be the intensity scattered per unit of intensity of incident light linearly polarized parallel to the scattering plane, then $i_\parallel = S_{11} + S_{12} = |S_2|^2$. On the other hand, if the incident wave is perpendicular to the scattering plane, the Stokes parameters of the scattered light are $\mathcal{S}_s^{(1)} = I_s = (S_{11} - S_{12})I_i$, $\mathcal{S}_s^{(2)} = Q_s = -I_s$, $\mathcal{S}_s^{(3)} = \mathcal{S}_s^{(4)} = 0$ then the intensity $i_\perp$ scattered by unit of intensity of incident light linearly polarized perpendicular to the scattering plane is $i_\perp = S_{11} - S_{12} = |S_1|^2$.

Depending on whether the ratio [7]

$$P = \frac{i_\perp - i_\parallel}{i_\perp + i_\parallel} = \frac{S_{12}}{S_{11}}, \tag{2.44}$$

which defines the *degree of polarization* $|P|$ ($|P| \leq 1$), is positive or negative, the scattered light is partially polarized perpendicular or parallel to the scattering plane, respectively. Also, $P(0°) = P(180°) = 0$.

Of special interest are the scattering cross-sections in the forward and backward directions. The former, $Q_{forw} = d Q^{(s)}(0°)/d\Omega$, is readily obtained from $S_1(0°)$ and $S_2(0°)$, given below Eq. (2.35), while the latter is from (2.34) and (2.35)

$$Q_{back}^{(s)} = \frac{d Q^{(s)}(180°)}{d\Omega} = \frac{1}{(ka)^2}|\sum_{n=1}^{\infty}(2n+1)(-1)^n(a_n - b_n)|^2. \tag{2.45}$$

2.5 Scattering from a coated sphere

The design of coated spheres and rods consisting of appropriate materials plays an important role in engineering the angular distribution of scattered intensity. This takes place through the interplay of electric and magnetic Mie coefficients [14–16], so that either highly directional scattering may be obtained from such objects, or even exotic effective refractive indices may result when these bodies are packed in arrays as metamaterial elements. Therefore, we shall address here the scattering solution in such spheres.

The plane wave, Eqs. (2.10) and (2.11), is incident on a sphere consisting of a core, denoted as region 1, whose radius and size parameter are a and $x = ka$, and whose refractive index relative to that n of the surrounding medium is m_1, and a shell, region 2, of radius b, size parameter $y = kb$, and relative refractive index m_2; (see
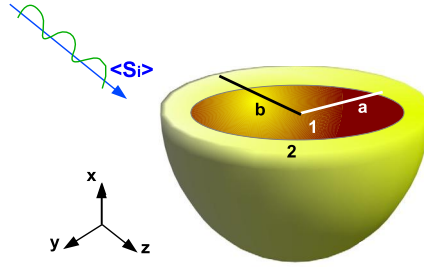
Figure 2.2 Details of a coated sphere. The scattering geometry is the same as in Fig. 2.1.

Fig. 2.2). We assume the permeabilities of these three media 1, 2 and exterior to be the same. The fields $\mathbf{E}_1$ and $\mathbf{B}_1$ in the region $0 \le r \le a$ are given by Eqs. (2.12) and (2.13). The scattered fields $\mathbf{E}_s$ and $\mathbf{B}_s$ are those of Eqs. (2.14) and (2.15). On the other hand, in the region $a \le r \le b$ both spherical Bessel functions j_n and y_n are bounded, and the fields $\mathbf{E}_2$ and $\mathbf{B}_2$ in this region are expanded as [7]

$$\mathbf{E}_2 = \sum_{n=1}^{\infty} i^n E_0 \frac{2n+1}{n(n+1)} [f_n \mathbf{M}_{o1n}^{(1)} - i g_n \mathbf{N}_{e1n}^{(1)} + v_n \mathbf{M}_{o1n}^{(2)} - i w_n \mathbf{N}_{e1n}^{(2)}], \qquad (2.46)$$

$$\mathbf{B}_2 = -\frac{k_2}{\omega} \sum_{n=1}^{\infty} i^n E_0 \frac{2n+1}{n(n+1)} [g_n \mathbf{M}_{e1n}^{(1)} + i f_n \mathbf{N}_{o1n}^{(1)} + w_n \mathbf{M}_{e1n}^{(2)} + i v_n \mathbf{N}_{o1n}^{(2)}].$$

$$(2.47)$$

The superindex (2) in (2.46) and (2.47) means that in the spherical harmonics of Eqs. (2.6)–(2.9) the radial dependence is given by $y_n(\rho)$ rather than by $j_n(\rho)$. Introducing the Ricatti–Bessel functions $\psi(\rho) = \rho j_n(\rho)$, $\xi(\rho) = \rho h_n^{(1)}(\rho)$ and $\chi(\rho) = -\rho y_n(\rho)$, the saltus conditions (2.3) at $r = a$ and $r = b$ yield for the coefficients of the scattered fields [7]:

$$a_n = \frac{\psi_n(y)[\psi_n'(m_2 y) - A_n \chi_n'(m_2 y)] - m_2 \psi_n'(y)[\psi_n(m_2 y) - A_n \chi_n(m_2 y)]}{\xi_n(y)[\psi_n'(m_2 y) - A_n \chi_n'(m_2 y)] - m_2 \xi_n'(y)[\psi_n(m_2 y) - A_n \chi_n(m_2 y)]},$$

$$(2.48)$$

$$b_n = \frac{m_2 \psi_n(y)[\psi_n'(m_2 y) - B_n \chi_n'(m_2 y)] - \psi_n'(y)[\psi_n(m_2 y) - B_n \chi_n(m_2 y)]}{m_2 \xi_n(y)[\psi_n'(m_2 y) - B_n \chi_n'(m_2 y)] - \xi_n'(y)[\psi_n(m_2 y) - B_n \chi_n(m_2 y)]},$$

$$(2.49)$$

$$A_n = \frac{m_2 \psi_n(m_2 x) \psi_n'(m_1 x) - m_1 \psi_n'(m_2 x) \psi_n(m_1 x)}{m_2 \chi_n(m_2 x) \psi_n'(m_1 x) - m_1 \chi_n'(m_2 x) \psi_n(m_1 x)}, \qquad (2.50)$$

$$B_n = \frac{m_2 \psi_n(m_1 x) \psi_n'(m_2 x) - m_1 \psi_n(m_2 x) \psi_n'(m_1 x)}{m_2 \chi_n'(m_2 x) \psi_n(m_1 x) - m_1 \chi_n(m_2 x) \psi_n'(m_1 x)}. \qquad (2.51)$$

2.6   Optically active sphere

The physics of optically active particles, like e.g. those being bi-isotropic [17] or chiral, constitutes one of the research forefronts of nanophotonics, involving the spin and orbital angular momenta of light, in which the wave helicity, which is a conserved electromagnetic quantity, plays an informational role analogous to that of energy in the present context [18,20–25]. This has recently extended the concept of circular dichroism beyond the standard difference between absorption from left and right circularly polarized illumination [26] to the difference of scattered, absorbed and converted helicity between both CPL polarizations [22–25,27–29]. Although this important subject lies beyond the scope of this chapter, we address, nevertheless, the essentials of the scattering problem by this kind of spheres.

Harmonic plane waves propagate in the material of an optically active object without change in their polarization if they are circularly polarized (CPL), either left circularly (LCP) or right circularly (RCP). In terms of the fields $\mathbf{E}_\parallel$ and $\mathbf{E}_\perp$ of the incident, interior, or scattered fields, Eqs. (2.5) and (2.4), such CPL waves are expressed as $\mathbf{E}_L = (E_\parallel \, \epsilon_\parallel + i E_\perp \, \epsilon_\perp) \exp(i\mathbf{k}_L \cdot \mathbf{r} - \omega t)$ for LCP, and $\mathbf{E}_R = (E_\parallel \, \epsilon_\parallel - i E_\perp \, \epsilon_\perp) \exp(i\mathbf{k}_R \cdot \mathbf{r} - \omega t)$ for RCP.

The (generally complex) refractive indices n_L and n_R for these two handedness are different, i.e. their wavenumbers are $k_L = 2\pi n_L/\lambda$ for LCP plane waves, and $k_R = 2\pi n_R/\lambda$ for RCP plane waves. The constitutive relations are

$$\mathbf{D} = \epsilon \mathbf{E} + i\omega\beta\epsilon\mathbf{B}, \quad \mathbf{B} = \mu\mathbf{H} + \beta\mu(\mathbf{J} - i\omega\mathbf{D}). \tag{2.52}$$

We have $\beta = (1/2)(1/k_R - 1/k_L), n\omega = 2/(1/k_R + 1/k_L)$ [7]. Media with Eq. (2.52) holding are *bi-isotropic*. For an incident plane wave represented by Eqs. (2.10) and (2.11), the scattered fields are given by the expansions [7,19]

$$\mathbf{E}_s = \sum_{n=1}^{\infty} i^n E_0 \frac{2n+1}{n(n+1)} [i a_n \mathbf{N}_{e1n}^{(3)} - b_n \mathbf{M}_{o1n}^{(3)} + c_n \mathbf{M}_{e1n}^{(3)} - i d_n \mathbf{N}_{o1n}^{(3)}], \tag{2.53}$$

$$\mathbf{B}_s = \frac{k}{\omega} \sum_{n=1}^{\infty} i^n E_0 \frac{2n+1}{n(n+1)} [a_n \mathbf{M}_{e1n}^{(3)} + i b_n \mathbf{N}_{o1n}^{(3)} - i c_n \mathbf{N}_{e1n}^{(3)} - d_n \mathbf{M}_{o1n}^{(3)}]. \tag{2.54}$$

There are now two Mie coefficients because inside the sphere only CPL waves can propagate and, hence, the interior fields are expanded into combinations of vector spherical harmonics of the form $\mathbf{M}_{o1n}^{(1)}(k_L) + \mathbf{N}_{o1n}^{(1)}(k_L)$, $\mathbf{M}_{e1n}^{(1)}(k_L) + \mathbf{N}_{e1n}^{(1)}(k_L)$; $\mathbf{M}_{o1n}^{(1)}(k_R) - \mathbf{N}_{o1n}^{(1)}(k_R)$, $\mathbf{M}_{e1n}^{(1)}(k_R) - \mathbf{N}_{e1n}^{(1)}(k_R)$, where the argument k_L or k_R applies to the radial dependence generated by $j_n(\rho)$, ρ being either $k_L r$ or $k_R r$. Hence the boundary condition (2.3) at the sphere surface conveys four Mie coefficients for the scattered field.

Introducing the index Ξ which refers to L or R depending on whether the incident wave is LCP or RCP, respectively; and writing the refractive indices relative to that of the isotropic surrounding medium $n = \sqrt{\epsilon\mu}$, as $m_L = n_l/n$ and $m_R = n_R/n$, respectively, we define the mean refractive index m by $1/m = (\mu_p/\mu)(1/m_R + 1/m_L) \simeq$

$2/(m_R + m_L)$ for the usually small difference $m_L - m_R$. Then the Mie coefficients are [7,19]

$$a_n = \frac{V_n(R)A_n(L) + V_n(L)A_n(R)}{W_n(L)V_n(R) + V_n(L)W_n(R)}, \quad b_n = \frac{W_n(L)B_n(R) + W_n(R)B_n(L)}{W_n(L)V_n(R) + V_n(L)W_n(R)},$$

(2.55)

$$c_n = \frac{W_n(R)A_n(L) + W_n(L)A_n(R)}{W_n(L)V_n(R) + V_n(L)W_n(R)} = -d_n.$$

(2.56)

Here

$$W_n(\Xi) = m\psi_n(m_\Xi x)\xi_n'(x) - \psi_n'(m_\Xi x)\xi_n(x),$$ (2.57)

$$V_n(\Xi) = \psi_n(m_\Xi x)\xi_n'(x) - m\psi_n'(m_\Xi x)\xi_n(x),$$ (2.58)

$$A_n(\Xi) = m\psi_n(m_\Xi x)\psi_n'(x) - \psi_n'(m_\Xi x)\psi_n(x),$$ (2.59)

$$B_n(\Xi) = \psi_n(m_\Xi x)\psi_n'(x) - m\psi_n'(m_\Xi x)\psi_n(x).$$ (2.60)

Of course, if the sphere is not optically active, $m_L = m_R$, then $c_n = 0$, and a_n and b_n reduce to those of Eqs. (2.16) and (2.17), respectively.

Spheres fulfilling (2.56) are *chiral*. Then it is usual to introduce a *chirality parameter* κ such that $m_{L,R} = \sqrt{(\epsilon_p \mu_p)/(\epsilon\mu)} \pm \kappa$, and $2\kappa = m_L - m_R$. $|\kappa| \leq 1$; and often $|\kappa| \leq 0.1$.

For the scattering matrix, now in addition to S_1 and S_2 of (2.34) and (2.35), we have

$$S_3(\cos\theta) = \sum_{n=1}^{\infty} \frac{2n+1}{n(n+1)} c_n[\pi_n(\cos\theta) + \tau_n(\cos\theta)] = -S_4(\cos\theta).$$

(2.61)

And CPL scattered and incident fields are related by

$$\begin{pmatrix} E_{sL} \\ E_{sR} \end{pmatrix} = \frac{ie^{ik(r-z)}}{kr} \begin{pmatrix} S_{2c}(\theta,\phi) & S_{3c}(\theta,\phi) \\ S_{3c}(\theta,\phi) & S_{1c}(\theta,\phi) \end{pmatrix} \begin{pmatrix} E_{i\parallel} \\ E_{i\perp} \end{pmatrix}$$

(2.62)

with

$$S_{1c} = \frac{1}{2}(S_1 + S_2 + 2iS_3); \quad S_{2c} = \frac{1}{2}(S_1 + S_2 - 2iS_3);$$

$$S_{3c} = \frac{1}{2}(S_2 - S_1) = S_{4c}.$$

(2.63)

Meanwhile the Mueller matrix elements fulfill

$$S_{31} = -S_{13}, \quad S_{32} = -S_{23}, \quad S_{43} = -S_{34},$$
$$S_{41} = S_{14}, \quad S_{42} = -S_{24}, \quad S_{21} = -S_{12}.$$

(2.64)

The cross-sections for LCP and RCP incident plane waves are [7]

$$Q_L^{(s)} = \frac{2\pi}{k^2} \sum_{n=1}^{\infty} (2n+1)[|a_n|^2 + |b_n|^2 + 2|c_n|^2 - 2\Im\{(a_n + b_n)c_n^*\}].$$
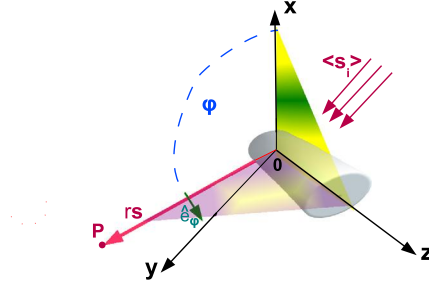
(2.65)

Figure 2.3 Scattering geometry for an infinite circular cylinder of radius a. The incident plane wave has $\mathbf{k}_i$ and time-averaged Poynting vector $< \mathbf{S}_i >$ along $\hat{\mathbf{y}}$. The scattering plane OPZ is determined by the position vector $r\mathbf{s}$ of the observation point P of the scattered field and the OZ-axis. For this incidence P is in the XY-plane.

$$Q_R^{(s)} = \frac{2\pi}{k^2} \sum_{n=1}^{\infty} (2n+1)[|a_n|^2 + |b_n|^2 + 2|c_n|^2 + 2\Im\{(a_n + b_n)c_n^*\}], \qquad (2.66)$$

and

$$Q_L^{(ext)} = \frac{4\pi}{k^2} \Re\{S_{2\,c}(0°)\} = \frac{2\pi}{k^2} \sum_{n=1}^{\infty} (2n+1)\Re\{a_n + b_n - 2ic_n\}, \qquad (2.67)$$

$$Q_R^{(ext)} = \frac{4\pi}{k^2} \Re\{S_{1\,c}(0°)\} = \frac{2\pi}{k^2} \sum_{n=1}^{\infty} (2n+1)\Re\{a_n + b_n + 2ic_n\}. \qquad (2.68)$$

2.7   Scattering from an infinite circular cylinder

In the last years, the scattering from cylinders has acquired a renewed interest due to their use as elements of photonic components [5,30–32] either in plasmonics or metamaterial research, therefore we present the essentials of the scattering formulation from these objects. This will be further discussed in Sections 2.8 and 2.9.

Let the incident field $\mathbf{E}_i$, propagating in the surrounding medium of index n, be given by Eq.(2.1). We shall consider the case in which the incident wavevector is normal to the cylinder axis OZ (cf. Fig. 2.3), thus $\mathbf{k}_i = k\hat{\mathbf{y}}$. More details for other incidences and cylinders of finite length can be found in [7–9].

2.7.1   I. *s-polarization (TE): incident electric field linearly polarized along the cylinder axis*

Now the generating functions of the fields include Bessel functions of integer order: $J_n(mkr)$ and $Y_n(mkr)$. At a point P the incident field with wavevector $\mathbf{k}_i = k\hat{\mathbf{y}}$ and

electric vector $\mathbf{E}_i = E_0\hat{\mathbf{z}}\exp[i(kr\cos(\pi/2 - \phi) - \omega t)]$ admits the expansion

$$\mathbf{E}_i = \sum_{n=-\infty}^{\infty} \frac{(-i)^n}{k} E_0 \mathbf{N}_n^{(1)}, \quad \mathbf{B}_i = \sum_{n=-\infty}^{\infty} \frac{(-i)^{n+1}}{\omega} E_0 \mathbf{M}_n^{(1)}; \tag{2.69}$$

$\rho = kr$, $\hat{\mathbf{e}}_r = \mathbf{s}$. The vector cylindrical harmonics are

$$\mathbf{M}_n^{(1)} = k[n\,i\,\frac{J_n(\rho)}{\rho}\hat{\mathbf{e}}_r - J_n'(\rho)\hat{\mathbf{e}}_\phi]e^{in\phi}, \tag{2.70}$$

$$\mathbf{N}_n^{(1)} = k J_n(\rho)\hat{\mathbf{z}}\,e^{in\phi}. \tag{2.71}$$

The internal fields are

$$\mathbf{E}_1^I = \sum_{n=-\infty}^{\infty} \frac{(-i)^n}{k} E_0\, c_n \mathbf{N}_n^{(1)}, \quad \mathbf{B}_1^I = \sum_{n=-\infty}^{\infty} \frac{(-i)^{n+1}}{\omega} E_0\, c_n \mathbf{N}_n^{(1)}. \tag{2.72}$$

The superindex I denotes both internal and external fields for this polarization. The argument ρ of the internal fields in (2.72) is $\rho = mkr$, where $m = n_p/n$. n_p being the cylinder refractive index. The scattered fields read

$$\mathbf{E}_s^I = -\sum_{n=-\infty}^{\infty} \frac{(-i)^n}{k} E_0\, b_n \mathbf{N}_n^{(3)}, \quad \mathbf{B}_s^I = \sum_{n=-\infty}^{\infty} \frac{(-i)^{n-1}}{\omega} E_0\, b_n \mathbf{N}_n^{(3)}. \tag{2.73}$$

Here the superindex (3) in $\mathbf{M}_n$ and $\mathbf{N}_n$ means that in (2.70) and (2.71) the Bessel function $J_n(\rho)$ is replaced by the Hankel function $H_n^{(1)}(\rho) = J_n(\rho) + i Y_n(\rho)$. Also, recalling the size parameter $x = ka$, where a is the cylinder radius, and operating with the saltus conditions (2.3), the Mie coefficients are

$$b_n = \frac{J_n(mx)J_n'(x) - m J_n'(mx)J_n(x)}{J_n(mx)H_n^{(1)'}(x) - m J_n'(mx)H_n^{(1)}(x)} \tag{2.74}$$

and

$$c_n = \frac{1}{J_n(mx)}[J_n(x) - b_n H_n^{(1)}(x)]. \tag{2.75}$$

2.7.2 II *p*-polarization (TM): incident magnetic field linearly polarized along the cylinder axis

The incident magnetic vector now reads $\mathbf{B_i} = B_0\hat{\mathbf{z}}\exp[i(kr\cos(\pi/2 - \phi) - \omega t)]$. The electric vector of the incident field is obtained from the curl of $\mathbf{B_i}$ and can be expanded as

$$\mathbf{E}_i = \sum_{n=-\infty}^{\infty} \frac{(-i)^{n+1}}{k} E_0 \mathbf{M}_n^{(1)}. \tag{2.76}$$

The internal fields are

$$\mathbf{E}_1^{II} = \sum_{n=-\infty}^{\infty} \frac{(-i)^{n+1}}{k} E_0 \, d_n \mathbf{N}_n^{(1)}, \quad \mathbf{B}_1^{II} = \sum_{n=-\infty}^{\infty} \frac{(-i)^n}{\omega} E_0 \, d_n \mathbf{N}_n^{(1)}. \tag{2.77}$$

The scattered fields read

$$\mathbf{E}_s^{II} = \sum_{n=-\infty}^{\infty} \frac{(-i)^{n-1}}{k} E_0 \, a_n \mathbf{M}_n^{(3)}, \quad \mathbf{B}_s^{II} = \sum_{n=-\infty}^{\infty} \frac{(-i)^n}{\omega} E_0 \, a_n \mathbf{N}_n^{(3)}. \tag{2.78}$$

Here the superindex II has been employed to denote both internal and external fields for this p-polarization.

The Mie coefficients are

$$a_n = \frac{m \, J_n(mx) J_n'(x) - J_n'(mx) J_n(x)}{m \, J_n(mx) H_n^{(1)\,\prime}(x) - J_n'(mx) H_n^{(1)}(x)} \tag{2.79}$$

and

$$d_n = \frac{1}{J_n(mx)}[J_n(x) - a_n H_n^{(1)}(x)]. \tag{2.80}$$

2.7.3 Scattering matrix

With reference to Fig. 2.3, for normal incidence to the cylinder axis OZ the spatial part of the time harmonic incident field may be expressed in terms of a parallel and a perpendicular component to the plane OXZ:

$$\mathbf{E}_i = (E_{i\,\|}\hat{\mathbf{z}} - E_{i\,\perp}\hat{\mathbf{x}})e^{ik\cos(\pi/2-\phi)r}. \tag{2.81}$$

Likewise, the scattered field is expressed by a parallel and a perpendicular component to the scattering plane OPZ:

$$\mathbf{E}_s = (E_{s\,\|}\hat{\mathbf{z}} + E_{s\,\perp}\hat{\mathbf{e}}_\phi)e^{ik\cos(\pi/2-\phi)r}. \tag{2.82}$$

Taking into account the form for $kr \to \infty$ acquired by the vector cylindrical harmonics which are expressed by means of the asymptotic values of the Hankel function, we write in terms of the **S**-matrix

$$\begin{pmatrix} E_{s\,\|} \\ E_{s\,\perp} \end{pmatrix} = e^{i3\pi/4}\sqrt{\frac{2}{\pi kr}}\,e^{ikr}\begin{pmatrix} T_1(\Phi) & T_4(\Phi) \\ T_3(\Phi) & T_2(\Phi) \end{pmatrix}\begin{pmatrix} E_{i\,\|} \\ E_{i\,\perp} \end{pmatrix} \tag{2.83}$$

where $\Phi = \pi - \phi$ and

$$T_1(\Phi) = \sum_{n=-\infty}^{\infty} b_n e^{-in\Phi}, \tag{2.84}$$

$$T_2(\Phi) = \sum_{n=-\infty}^{\infty} a_n e^{-in\Phi}, \tag{2.85}$$

$$T_3(\Phi) = T_4(\Phi) = 0. \tag{2.86}$$

2.7.4 Cross-sections

In a manner similar to that employed in Section 2.3, we obtain from the flow of energy across a cylinder of large radius, concentric with the scattering cylinder, the expressions for the scattering and extinction cross-sections:

$$Q_I^{(s)} = \frac{2}{x}[|b_0|^2 + 2\sum_{n=1}^{\infty} |b_n|^2], \quad Q_I^{(ext)} = \frac{2}{x}\Re\{b_0 + 2\sum_{n=1}^{\infty} b_n\}, \tag{2.87}$$

$$Q_{II}^{(s)} = \frac{2}{x}[|a_0|^2 + 2\sum_{n=1}^{\infty} |a_n|^2], \quad Q_{II}^{(ext)} = \frac{2}{x}\Re\{a_0 + 2\sum_{n=1}^{\infty} a_n\}. \tag{2.88}$$

And the optical theorem for each of these polarizations reads

$$Q_I^{(ext)} = \frac{2}{x}\Re\{T_1(\Phi = 0)\}, \quad Q_{II}^{(ext)} = \frac{2}{x}\Re\{T_2(\Phi = 0)\}. \tag{2.89}$$

2.8 Mie resonances and natural modes

Returning to the Mie coefficients (2.16)–(2.19), (2.74), (2.75), (2.79), and (2.80), we notice that for the sphere the denominators a_n and d_n coincide, as well as those of b_n and c_n. In the case of cylinders, the same happens with the denominators b_n and c_n, as well as of a_n and d_n. When either denominator of the Mie coefficients is zero, or near zero, the corresponding nth normal mode will dominate in the series expansion of the interior and scattered fields. This characterizes a *morphology dependent resonance* (MDR) of the sphere or cylinder, and the size parameters or the complex frequencies at which it takes place define the so-called *natural* frequencies of the particle. The real parts of these frequencies are close to the real resonance frequencies ω_r, while the imaginary parts determine their resonance linewidths Γ. The corresponding nth mode is then a *natural* mode [10].

The particle behaves as a resonator for the incident wave that circumnavigates it after either penetrating inside, remaining confined by total internal reflection (TIR), or propagates as a wave attached to its outer surface and being evanescent away from it. In both cases the MDR field is described by surface waves interfering with themselves
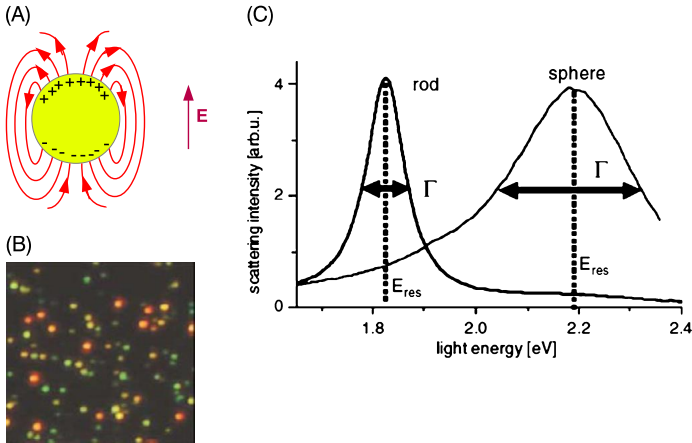
Figure 2.4 (A) Field lines and charge distribution in a sphere or in a circular cylinder illuminated by a light wave with electric vector **E** pointing upwards. (B) Color photograph in dark-field illumination of a sample of gold nanorods (red) of diameters 15–25 nm, and lengths of up to 100 nm, and nanospheres (green) with diameter of 60 nm. Here the **E**-vector is polarized along the rod longer axis. (C) Light-scattering spectra from a gold nanorod and a nanosphere, measured under identical conditions as (B). The resonant energy peaks are $W_{res} = 1.82$ eV, i.e. at $\lambda = 681$ nm, for the rods, and $W_{res} = 2.19$ eV, i.e. at $\lambda = 566$ nm for the spheres. (1 eV is equivalent to a wavelength of 1239.84 nm.) The linewidths Γ are also shown. (B) and (C) are reproduced from [35].

after traveling around the particle perimeter a number of cycles, thus returning to their starting position in phase. This results in large scattering cross-sections, as well as strong localized near fields, at these resonant size parameters, or frequencies, due to the enhancement of this nth natural mode in the Mie series [7–9,33].

The MDR modes are radiative for any real frequency, thus they are virtual modes, and thus the energy dissipation by this radiation, as well as by possible absorption in the particle, make the MDR lineshapes to have a non-zero linewidth Γ. The fraction: $2\pi \times energy\ stored\ in\ the\ particle\ /\ dissipated\ energy\ per\ cycle$ defines the *quality factor* $Q = -\omega_r W / dW / dt = \omega_r / \Gamma$ [34,35].

2.8.1 Localized surface plasmons

Mie resonances in noble metals may be envisaged as due to charge oscillations in the free-electron cloud, induced by the incident electric vector [see Fig. 2.4A], thus emitting an electromagnetic field which, like a surface plasmon–polariton (SPP) of a planar metal interface [36], is evanescent away from the particle surface, i.e. it is a surface mode. Observed colors are due to the strong absorption at the plasmon resonant optical frequencies, and they are manifestations of the nanometric scale of the particle [cf. Fig. 2.4B]. The resonance peak Q-factor increases as the linewidth, and hence energy dissipation on scattering, decreases [Fig. 2.4C] [35]. The effects underlying these strong localized surface plasmons (LSP) give rise to new photonic devices [37] ranging from those with superresolving power and molecular fluorescence to biomedical sensors and markers.
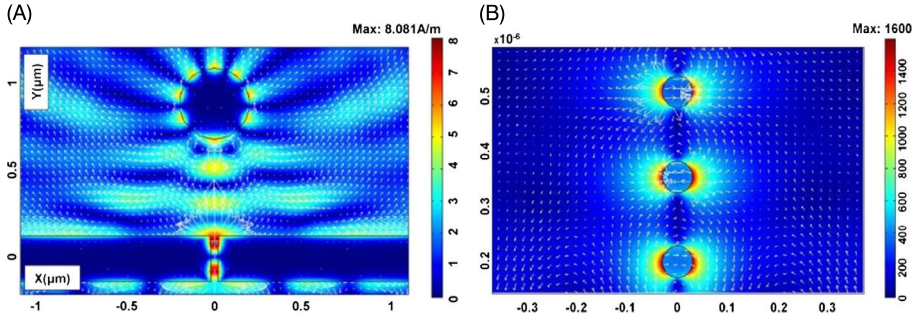
Figure 2.5 (A): Magnetic field magnitude H_z (colors in Ampères per meter) and time-averaged energy flow $< S(r) >$ (arrows in Joules per squared meters per second), maximum arrow length $\simeq$ 80.02 KeV/(nm$^2 \times$ s), minimum arrow length $\simeq 0$ eV/(nm^{2}s), localized on the surface of an Ag cylinder (radius: 200 nm, refractive index: $0.186 + i1.61$) in front of a slit of width: 55 nm in a tungsten (W) slab of width: 2610 nm, thickness: 237.55 nm, and refractive index: $3.39 + i2.41$. The incident radiation, at $\lambda = 364.7$ nm, is *p*-polarized. The distance between the cylinder surface and the exit plane of the slit is $3\lambda/2 = 549$ nm. The intensity spikes around the cylinder correspond to the TM_{51} LSP mode. (B) Detail of the electric field **E** in the first three Ag cylinders of a linear chain of six with surface interdistance: 100 nm, radius: 30 nm and refractive index: $0.173 + i1.95$, illuminated through a slit in a W slab (slit width: 39.59 nm, slab width: 2610 nm, slab thickness: 237.55 nm, refractive index: $3.39 + i2.41$) at $\lambda = 400$ nm in *p*-polarization. The distance between the bottom surface of the first cylinder and the exit plane of the slit is $\lambda_r/8$, $\lambda_r = 349.3$ nm being the resonant wavelength of the LSP TM_{11} mode of one of those cylinders when being isolated. Both its magnitude in *volts per meter* and directions (arrows) are shown. After [38].

Figs. 2.5A and 2.5B show an example of coupling the linear momentum of an incident light wave with that of a LSPs, in either an Ag cylinder in air, or propagating through a linear chain of them. The mechanism shown in the aperture is the phenomenon of extraordinary transmission [39] by a subwavelength slit. In both figures one should notice that, as is well known, the presence of the slab slightly redshifts the LSP line peaks with respect to those of the isolated cylinder. Also, in the region between the particle and the slit, one sees stationary waves as well as saddle points and vortices in the mean energy flow pattern. The spatial field distributions of the LSP TM_{nl} mode show $2n = 10$ [Fig. 2.6A] and $2n = 2$ [Fig. 2.6B] lobes of the mode along the azimuthal angle, as well as $l = 1$ radial maxima.

2.8.2 Whispering gallery modes (WGM)

Dielectric particles act as resonators for MDRs. The field enhanced inside tends to be confined closer to the particle surface the higher its nth order is; thus they are well described as surface waves, from which the term WGM comes [34]. Their mathematical structure makes them to have analogies with atomic orbitals [41], so that grouping particles close to each other produce *bonding* and *antibonding* states, depending on whether the MDR maxima and minima of neighbor particles are, or are not, in front of each other [42]. This grouping and the mode formation have given rise to the concept of *photonic molecule* pairs, or groups, with the associated splitting of resonance wavelengths like in atomic orbitals [41]. It is interesting that this bonding or antibonding
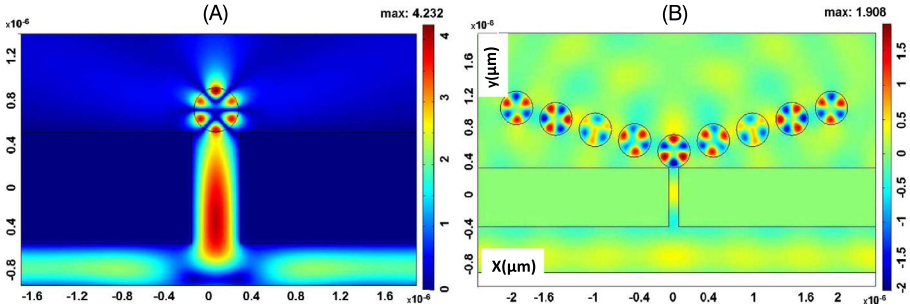
Figure 2.6 (A) Spatial distribution of |**E**| (V/m) from a slit of width: 117, 5 nm in a metallic slab (refractive index: $0.135 + i10.275$, slab width: 6807.41 nm, slab thickness: 1000 nm, slit width: 440 nm) and s-wave illumination ($\lambda = 919$ nm) showing the TE_{31} WGM in a dielectric cylinder (refractive index: $3.670 + i0.005$, radius: 200 nm) close to the slit exit. (B) B_z (A/m) in a bifurcated chain of dielectric cylinders like that in (A), placed in front of a slit of width 117, 5 nm in a metallic slab (refractive index: $0, 135 + i10, 275$, width: 7000 nm, thickness: 705 nm) illuminated at $\lambda = 754$ nm, which is very close to the slit extraordinary transmission wavelength, and p-polarized light. One sees the transmission through the chain arms of the TM_{31} WGM with bonding states of light between pairs of adjacent particles, since lobe maxima and minima in the B_z- spatial distribution of their respective MDRs are in front of each other. Actually, the optical force between these pairs of cylinders is attractive. After [40].

character of the WGMs in pairs of neighbor particles also holds for the photonic force created between the pair, which may be attractive or repulsive [42,43]. Such optical microcavities may have multiple use in atomic physics, or as optical components such as photonic crystals, metamaterials, or nanoantennas.

Fig. 2.6A illustrates the formation of a TE_{31} WGM in a cylinder in air over a slit in a slab, excited by extraordinary transmission. The linear momentum of the light emerging from the slit is coupled to that of the WGM. On the other hand, Fig. 2.6B shows the propagation of this WGM through a bifurcated chain of similar cylinders placed at the slit exit.

2.9   Small particles: dipolar approximation

Although plasmonics has been considered of potential for micro and nano optical devices, there are metal losses at optical frequencies. In recent years there has been a growing interest on the excitation of the electric and magnetic dipoles and quadrupoles of high refractive index particles with very low absorption losses, like those of semi-conductors dealt with in this section. Notwithstanding they were initially aimed as elements of metamaterials, high scattering losses at resonance have to be circumvented for their use in composites acting as effective media [44]; however, they are currently being studied as building blocks of 2D metasurfaces [45], or as nanosources, either primary (i.e. emitters) or secondary (scatterers), in a variety of applications [5,6].
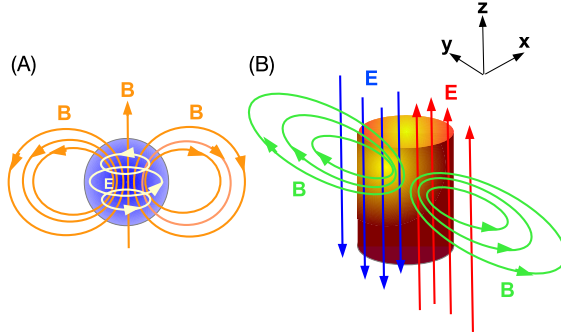
Figure 2.7 (A) Illustration of the electric and magnetic fields, described by the b_1 Mie coefficient in a high refractive index dielectric sphere. The **E**-field loops form a magnetic dipole giving rise to strong **B** lines. (B) The same in an infinitely long circular cylinder under s-incidence described by the b_1 coefficient. Now there are two counterpropagating electric fields and large displacement currents along the cylinder axis which form a magnetic dipole. Following Ampère's law, strong magnetic field loops are generated.

2.9.1   Isotropic sphere

For spheres and cylinders whose diameter is smaller than the incident wavelength, the Mie series (2.14), (2.15), (2.53), (2.54), (2.73), and (2.78) may converge fast enough to make the first electric and magnetic terms sufficient to fully describe their scattering.

The scattered fields acquire the form

$$\mathbf{E}_s = k^2[\frac{1}{\epsilon}(\mathbf{n} \times \mathbf{p}) \times \mathbf{n} - \sqrt{\frac{\mu}{\epsilon}}(\mathbf{n} \times \mathbf{m})]\frac{e^{ikr}}{r}$$

$$+ \frac{1}{\epsilon}(3\mathbf{n}(\mathbf{n} \cdot \mathbf{p} - \mathbf{p})(\frac{1}{r^3} - \frac{ik}{r^2})e^{ikr} + \sqrt{\frac{\mu}{\epsilon}}k^2(\mathbf{n} \times \mathbf{m})\frac{e^{ikr}}{ikr^2}, \qquad (2.90)$$

$$\mathbf{B}_s = k^2[\mu(\mathbf{n} \times \mathbf{m}) \times \mathbf{n} + \sqrt{\frac{\mu}{\epsilon}}(\mathbf{n} \times \mathbf{p})]\frac{e^{ikr}}{r}$$

$$+ \epsilon(3\mathbf{n}(\mathbf{n} \cdot \mathbf{m} - \mathbf{m})(\frac{1}{r^3} - \frac{ik}{r^2})e^{ikr} - \sqrt{\frac{\mu}{\epsilon}}k^2(\mathbf{n} \times \mathbf{p})\frac{e^{ikr}}{ikr^2}. \qquad (2.91)$$

Eqs. (2.90) and (2.91) are identical to those of the fields emitted by an electric and a magnetic dipole of moments **p** and **m**, respectively [10]. In the case of the sphere, with center being the origin of coordinates (cf. Fig. 2.1), their link with the Mie expressions (2.14) and (2.15) appears through the polarizabilities α_e and α_m that connect the dipole moments with the incident field (2.1) at $\mathbf{r} = 0$ [see Fig. 2.7A]. The case of a dipolar cylinder, Fig. 2.7B, is detailed in Sections 2.9.3 and 2.9.4:

$$\mathbf{p} = \alpha_e \mathbf{E}_i(\mathbf{r} = \mathbf{0}), \quad \mathbf{m} = \alpha_m \mathbf{B}_i(\mathbf{r} = \mathbf{0}). \qquad (2.92)$$

With $\mathbf{E}_i(\mathbf{r} = \mathbf{0}) = \mathbf{E}_0$, $\mathbf{B}_i(\mathbf{r} = \mathbf{0}) = \mathbf{B}_0$ [cf. Eq. (2.1)], and

$$\alpha_e = i\frac{3\epsilon}{2k^3}a_1, \quad \alpha_m = i\frac{3}{2\mu k^3}b_1; \qquad (2.93)$$
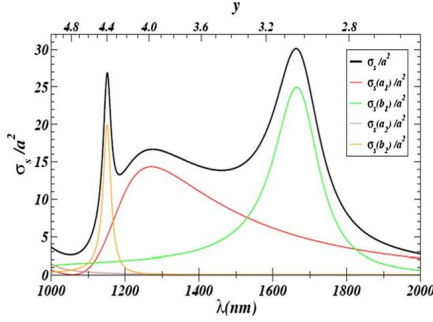
Figure 2.8 Scattering cross-section versus λ for a Si sphere (radius: 230 nm, relative refractive index: $m = 3.5$ constant, and real in the studied wavelength range). The contribution of the nth partial wave in the Mie expansion is plotted. The green line corresponds to the contribution of the b_1-resonance of the induced magnetic dipole. After [49].

which may be written as

$$\alpha_e = \alpha_e^{(0)} \left(1 - i \frac{2}{3\epsilon} k^3 \alpha_e^{(0)} \right)^{-1}, \quad \alpha_m = \alpha_m^{(0)} \left(1 - i \frac{2}{3} \mu k^3 \alpha_m^{(0)} \right)^{-1}, \tag{2.94}$$

a_1 and b_1 being the first electric and magnetic Mie coefficients, Eqs. (2.16) and (2.17), respectively; and $\alpha_e^{(0)}$ and $\alpha_m^{(0)}$ standing for the static polarizabilities:

$$\alpha_e^{(0)} = \frac{3\epsilon}{2k^3} \frac{\mu n_p^2 j_1(n_p x) \left[x j_1(x) \right]' - \mu_p j_1(x) \left[n_p x j_1(n_p x) \right]'}{\mu n_p^2 j_1(n_p x) \left[x y_1(x) \right]' - \mu_p y_1(x) \left[n_p x j_1(n_p x) \right]'}, \tag{2.95}$$

$$\alpha_m^{(0)} = \frac{3}{2\mu k^3} \frac{\mu_p j_1(n_p x) \left[x j_1(x) \right]' - \mu j_1(x) \left[n_p x j_1(n_p x) \right]'}{\mu_p j_1(n_p x) \left[x y_1(x) \right]' - \mu y_1(x) \left[n_p x j_1(n_p x) \right]'}. \tag{2.96}$$

Thus using (2.92)–(2.96) in Eqs. (2.90) and (2.91), one obtains the scattered fields in terms of the first dipolar partial waves of their Mie expansion under plane wave illumination.

It is important to emphasize [46] that, since the dipolar approximation connects the polarizabilities and first Mie coefficients through Eqs. (2.93), and thus involves the complex spherical Hankel functions $h_1^{(1)}$ in the denominators of a_1 and b_1, the polarizabilities are correctly expressed by (2.94)–(2.96). Otherwise, if, as commonly done, one directly employs in (2.92) the static polarizabilities, Eqs. (2.95) and (2.96), one obtains a result inconsistent with the optical theorem and hence with the con-servation of energy. This has been recurrently noticed in the literature [47,48] in the very small particle limit, or Rayleigh approximation, where both $x = ka << 1$ and $y = kma << 1$.

Fig. 2.8 shows the variation versus λ of the contribution to the scattering cross-section of the first electric and magnetic partial waves in a Si sphere of radius $a = 230$ nm in air. As shown by the green line, the b_1-magnetic dipole resonance appears strongly excited in such a high refractive index dielectric particle, being dom-
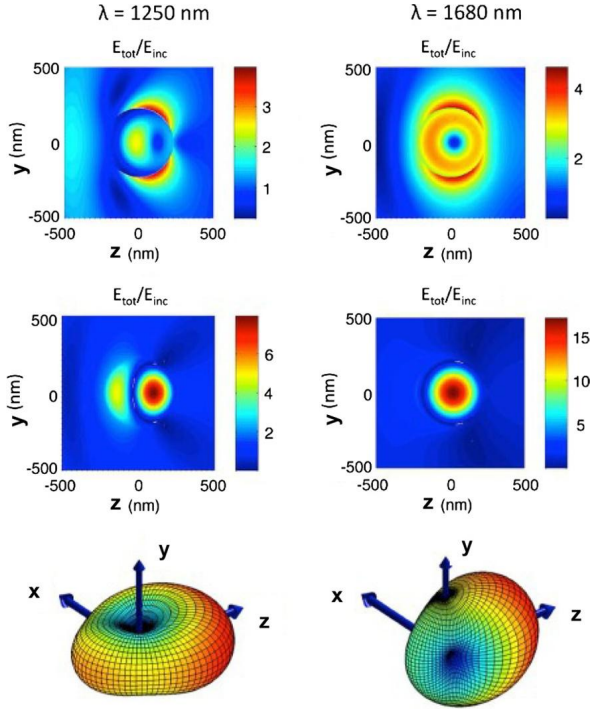
Figure 2.9 Maps for the modulus of the total electric a magnetic field vectors normalized to the incident electric and magnetic field, respectively (E_{tot}/E_{inc} and H_{tot}/H_{inc}), for a Si nanoparticle of radius $a = 230$ nm under plane wave illumination (cf. Fig. 2.1). YZ planes crossing $X = 0$ are depicted. The incident $\mathbf{k}_i$-vector is along OZ, the incident $\mathbf{E}_i$-vector is linearly polarized along OY and the $\mathbf{H}_i$-vector is along $-OX$. The left and right panels correspond to $\lambda = 1250$ nm and $\lambda = 1680$ nm, of the electric and magnetic resonance peaks, respectively, of Fig. 2.4. The corresponding far-zone scattering patterns for the two wavelengths are shown in the bottom row. After [49].

inant with respect to that of the a_1-electric dipole. Also the magnetic quadrupole resonance, which occurs at a lower wavelength, has a higher Q-factor. The existence of a strong magnetic dipole response to the magnetic field vector of the incident wave following Eq. (2.92), allows an interplay with that of the electric dipole and magnetic quadrupole (see also [50,51]), endowing the sphere with the property of being magnetodielectric, even though its magnetic permeability is $\mu = 1$. This is the source of a wide variety of phenomena leading to optical devices capable of controlling light emission and propagation [5,6].

With reference to the scattering geometry of Fig. 2.1, the spatial field amplitude distributions $|\mathbf{E}|$ and $|\mathbf{H}| = \mu^{-1}|\mathbf{B}|$ re-emitted by the electric and magnetic dipoles of Fig. 2.8, are shown in Fig. 2.9. Different field patterns, and associated currents, are observed depending on the projection plane of those 3-D distributions, manifesting the characteristic landscapes of electric and magnetic dipole radiation.

For dielectric particles with $m \gtrsim 2.45$ the approximate values of $y = kma$ at which there is a peak in either the electric or magnetic dipole resonance, are constant ver-
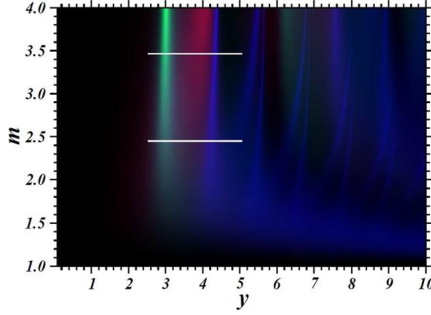
Figure 2.10 Scaling property of high refractive index spheres: Scattering cross-section map of a non-absorbing dielectric sphere as a function of the relative refractive index m and the y-parameter, $y = mx$, $x = ka$ being the particle size parameter. The green areas correspond to ranges where the magnetic dipole contribution dominates the total scattering cross-section, while the red areas represent regions where the electric dipole contribution is dominating. The remaining blue-saturated areas are dominated by higher-order multipoles. Brightness in the color-map is proportional to the total cross-section. The white horizontal lines represent the y-range covered by the case in which $m = 3.5$ (Si sphere, cf. Fig. 2.9) and by a sphere with $m = 2.45$ (TiO$_2$). After [49].

sus m, their quality factor growing as m increases. This is seen in Fig. 2.10, and physically constitutes an important *scaling* property of these high index particles which allows one to play with combinations of m, a and λ exciting the electric or the magnetic dipole. Namely, one may equally induce the particle p and m-dipoles at a given refractive index m by either decreasing/increasing the particle size, in whose case these MDRs will appear at lower/higher wavelengths. Conversely, one may increase/decrease m above the critical value $m = 2.45$, in which case an adequate choice of size a and illuminating frequency will keep the position and widths of the α_p- and α_m-lineshapes.

2.9.2 Bi-isotropic sphere

We address the most frequent case of bi-isotropy of the dipolar spherical particle which, in addition to the electric and magnetic polarizabilities, it exhibits cross electric-magnetic polarizabilities, α_{em}^{ch} and α_{me}^{ch}, immersed in an isotropic surrounding medium of refractive index n. This is when the particle is *chiral*, $\alpha_{em}^{ch} = -\alpha_{me}^{ch}$. We recall the *chirality parameter* κ, which pertains to CPL illumination and, as seen in Section 2.6, accounts for the difference of refractive indices: m_L and m_R for LCP and RCP light, respectively: $m_l - m_R = 2\kappa$. Then the dipoles induced by the incident field are

$$\mathbf{p} = \alpha_e^{ch} \mathbf{E}_i(\mathbf{0}) - \alpha_{me}^{ch} \mathbf{B}_i(\mathbf{0}), \quad \mathbf{m} = \alpha_{me}^{ch} \mathbf{E}_i(\mathbf{0}) + \alpha_m^{ch} \mathbf{B}_i(\mathbf{0}), \tag{2.97}$$

with

$$\alpha_e^{ch} = i\frac{3\epsilon}{2k^3}a_1, \quad \alpha_m^{ch} = i\frac{3}{2\mu k^3}b_1, \quad \alpha_{me}^{ch} = -\alpha_{em}^{ch} = i\frac{3\sqrt{\epsilon\mu}}{2k^3}c_1 = -i\frac{3\sqrt{\epsilon\mu}}{2k^3}d_1. \tag{2.98}$$

The Mie coefficients a_1, b_1, c_1, and d_1 of (2.98) are given by Eqs. (2.55) and (2.56) with $n = 1$.

2.9.3 Circular cylinder. s-polarization: E along the cylinder axis. (Case I)

Eqs. (2.92) hold with [52]

$$\alpha_e^{(I)} = i\frac{4\epsilon}{k^2}b_0, \qquad \alpha_m^{(I)} = i\frac{8}{\mu k^2}b_1. \tag{2.99}$$

This may be expressed as

$$\alpha_e^{(I)} = \alpha_e^{(0)\,I}\left(1 - \frac{i}{4\epsilon}k^2\alpha_e^{(0)\,I}\right)^{-1}, \qquad \alpha_m^{(I)} = \alpha_m^{(0)\,I}\left(1 - \frac{i}{8}\mu k^2\alpha_m^{(0)\,I}\right)^{-1}, \tag{2.100}$$

where the static polarizabilities $\alpha_e^{(0)\,I}$ and $\alpha_m^{(0)\,I}$ are

$$\alpha_e^{(0)\,I} = \frac{4\epsilon}{k^2}\frac{J_0(n_p x)J_0'(x) - n_p J_0'(n_p x)J_0(x)}{J_0(n_p x)Y_0'(x) - n_p J_0'(n_p x)Y_0(x)}, \tag{2.101}$$

$$\alpha_m^{(0)\,I} = \frac{8}{\mu k^2}\frac{J_1(n_p x)J_1'(x) - n_p J_1'(n_p x)J_1(x)}{J_1(n_p x)Y_1'(x) - n_p J_1'(n_p x)Y_1(x)}. \tag{2.102}$$

The b_0 and b_1 coefficients correspond to an electric and a magnetic dipole, respectively. Fig. 2.11A shows the electric currents flowing upwards and backwards in the magnetic dipole induced by the incident wave in the cylinder, manifested by the dipolar landscape of the electric vector amplitude E_z. The magnetic field created by these currents is depicted in Fig. 2.11B. Notice that these spatial distributions are identical to those of the scheme of Fig. 2.7B. The complex moduli of $|b_0|$, $|b_1|$, and $|b_2|$ for cylinders with $\epsilon = 600$ are displayed in Fig. 2.11C. As shown, in the region of the normalized frequency $a/\lambda \simeq 0.1$ the electric and magnetic dipole resonances dominate over the higher multipole $|b_2|$, thus conferring magnetodielectric optical properties to such cylinders of high real permittivity (its imaginary part being very small), and magnetic permeability $\mu = 1$.

2.9.4 Circular cylinder. p-polarization. B along the cylinder axis. (Case II)

In this case the polarizabilities are [52]

$$\alpha_e^{(II)} = i\frac{8\epsilon}{k^2}a_1, \qquad \alpha_m^{(II)} = i\frac{4}{\mu k^2}a_0. \tag{2.103}$$

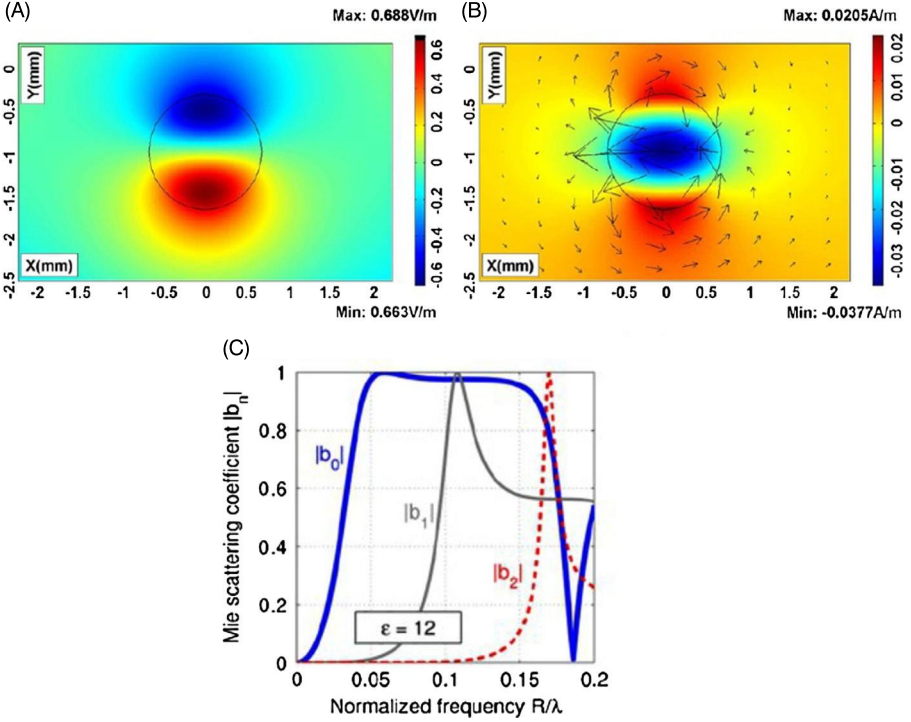**Figure 2.11** (A) Electric field E_z in a cylinder of BST ceramic with $\epsilon = 600$ and radius $R = 0.68$ mm. (B) Magnetic field **B** (arrows) and its x-component (colors). An s-polarized Gaussian beam of unit amplitude and halfwidth $\sigma = 12$ mm at $\lambda = 41.638$ mm is launched upwards (i.e. along the y-axis), from below the cylinder section. Both (A) and (B) are characteristics patterns of the magnetic dipole $TM_{1,1}$. From [44]. (C) Coefficient moduli $|b_0|$, $|b_1|$, and $|b_2|$. R is the cylinder radius. After [30].

This may be expressed as

$$\alpha_e^{(II)} = \alpha_e^{(0)\,II} \left(1 - \frac{i}{8\epsilon} k^2 \alpha_e^{(0)\,II}\right)^{-1}, \qquad \alpha_m^{(II)} = \alpha_m^{(0)\,II} \left(1 - \frac{i}{4}\mu k^2 \alpha_m^{(0)\,II}\right)^{-1}.$$

$$(2.104)$$

Here the static polarizabilities $\alpha_e^{(0)\,II}$ and $\alpha_m^{(0)\,II}$ are

$$\alpha_e^{(0)\,II} = \frac{8\epsilon}{k^2} \frac{J_1'(n_p x) J_1(x) - n_p J_1(n_p x) J_1'(x)}{J_1'(n_p x) Y_1(x) - n_p J_1(n_p x) Y_1'(x)},$$

$$(2.105)$$

$$\alpha_m^{(0)\,II} = \frac{4}{\mu k^2} \frac{J_0'(n_p x) J_0(x) - n_p J_0(n_p x) J_0'(x)}{J_0'(n_p x) Y_0(x) - n_p J_0(n_p x) Y_0'(x)}.$$

$$(2.106)$$

Like for the magnetodielectric dipolar sphere, there are maps of the position of the electric and magnetic dipoles and multipoles induced in high refractive index dielectric cylinders, under either s or p-polarized illumination, similar to that shown

in Fig. 2.10 [53]. Similarly to spheres, the position $y = kma$ of the cylinder electric and magnetic dipole lineshapes is constant as m varies above $m \gtrsim 2.5$; hence these magnetodielectric cylinders also possess the *scaling property* noted above for spheres.

Electric and magnetic resonance peaks may be made to approximately coincide at the same wavelength by using coated spheres and cylinders (see e.g. [54] and references therein). This is of interest in building photonic crystal nanostructures capable of steering light beams.

2.10 Very small particles: the Rayleigh approximation

For very small size parameters, $x << 1$, $y << 1$, $x_L << 1$, and $x_R << 1$, the various Bessel functions in the a_1, b_1 and c_1 coefficients are expanded in powers of the small argument x, y, x_L, or x_R as: $j_n(x) = x/3 - x^3/30$; $h_n^{(1)}(x) = -i/x^2 - i/2 + x/3$; $J_{n+1/2}(x) = \sqrt{2x/\pi}(x/3 - x^3/30)$; $H_{n+1/2}^{(1)}(x) = \sqrt{2x/\pi}(-i/x^2 - i/2 + x/3)$. After retaining only the first few terms, one obtains an additional limit within the dipole approximation. For the isotropic sphere embedded in the surrounding medium with permittivity ϵ and permeability μ, the electric and magnetic polarizabilities which fulfill the optical theorem [cf. Eq. (2.29)], are given by Eqs. (2.94) with the static polarizabilities [cf. Eqs. (2.95) and (2.96)]:

$$\alpha_e^{(0)} = \epsilon a^3 \frac{\epsilon_p - \epsilon}{\epsilon_p + 2\epsilon}, \qquad \alpha_m^{(0)} = \mu^{-1}a^3 \frac{\mu_p - \mu}{\mu_p + 2\mu}, \tag{2.107}$$

leading to the following relationship between the polarizabilities:

$$Q^{(ext)} = Q^{(s)} + Q^{(a)} = 4\pi k \Im\{\epsilon^{-1}\alpha_e + \mu\,\alpha_m\}, \tag{2.108}$$

the scattering cross-section being

$$Q^{(s)} = \frac{8\pi}{3}k^4(\epsilon^{-1}|\alpha_e|^2 + \mu^2|\alpha_m|^2\}. \tag{2.109}$$

As for the chiral sphere [cf. Eq. (2.97)], for the electric and magnetic polarizabilities hold Eqs. (2.94): $\alpha_e = \alpha_e^{(0)}\left(1 - i\frac{2}{3\epsilon}k^3\alpha_e^{(0)}\right)^{-1}$, $\alpha_m = \alpha_m^{(0)}\left(1 - i\frac{2}{3}\mu k^3\alpha_m^{(0)}\right)^{-1}$. With the static values [55–57]

$$\alpha_e^{(0)\,ch} = a^3\epsilon \frac{(\epsilon_p - \epsilon)(\mu_p + 2\mu) - \kappa^2\epsilon\mu}{(\epsilon_p + 2\epsilon)(\mu_p + 2\mu) - \kappa^2\epsilon\mu},$$

$$\alpha_m^{(0)\,ch} = a^3\mu \frac{(\mu_p - \mu)(\epsilon_p + 2\epsilon) - \kappa^2\epsilon\mu}{(\mu_p + 2\mu)(\epsilon_p + 2\epsilon) - \kappa^2\epsilon\mu}. \tag{2.110}$$

Meanwhile the mixed electric-magnetic polarizability reads

$$\alpha_{me}^{ch} = -a^3\sqrt{\epsilon\mu} \frac{i3\kappa\epsilon\mu}{(\epsilon_p + 2\epsilon)(\mu_p + 2\mu) - \kappa^2\epsilon\mu}. \tag{2.111}$$

This expression has useful applications in the analysis and manipulation of chiral nanostructures and molecules with chiral light [20,22,57,58].

On the other hand, concerning circular cylinders, one obtains, assuming $\epsilon = \mu = 1$:

$$\alpha_e^{(0)\,I} = \pi a^2 (\epsilon_p - 1), \qquad \alpha_m^{(0)\,I} = 2\pi a^2 \frac{\mu_p - 1}{\mu_p + 1}, \tag{2.112}$$

$$\alpha_e^{(0)\,II} = 2\pi a^2 \frac{\epsilon_p - 1}{\epsilon_p + 1}, \qquad \alpha_m^{(0)\,II} = \pi a^2 (\mu_p - 1). \tag{2.113}$$

It is worth stressing that even in the Rayleigh limit of the dipolar approximation, the electric and magnetic polarizabilities that comply with the optical theorem are those of (2.94). Only in limiting situations of extremely small particles versus the wavelength, where the scattered intensity is drastically small, the expansion of the full polarizabilities (2.94) in powers of $k^3 a^3$ make them practically coincide with their static vales.

2.11   Effects due to interference between Mie resonances. Directional scattering

Interference between dipolar and/or quadrupolar electric and magnetic resonances produce changes in the normalized *asymmetry factor g*, given by the averaged polar angle (cf. Fig. 2.1):

$$g = \;< \cos\theta > \; = \frac{\int \frac{dQ^{(s)}(\theta)}{d\Omega} \cos\theta \, d\Omega}{Q^{(s)}}, \tag{2.114}$$

which manifest effects in the directionality of the scattering [59], which, among other phenomena, gives rise to an unusual diffusive transport of light in suspensions of these particles. For example, due to these interference effects, g can take negative values and, hence, the transport mean free path l^* may go down to values below those of the scattering mean free path l_s ($l^* = l_s/(1 - g)$) [60].

2.11.1   Fano resonances

Resonance models fit asymmetric spectra, coined as *Fano resonances* [61], due to interference of broad and narrow resonances of the same physical system. In optics, they are ubiquitous and appear in, for example, Wood anomalies of diffraction gratings, frustrated TIR, as well as in Bragg resonances of photonic crystals. Of special interest here is their appearance in Mie scattering due to the interference between a narrow electric (or magnetic) quadrupole peak and a broader electric (or magnetic) dipole lineshape, which contributes to the total and differential scattering cross-sections with their respective coefficients a_2 (or b_2) and a_1 (or b_1) through Eqs. (2.30), (2.34), and (2.35).
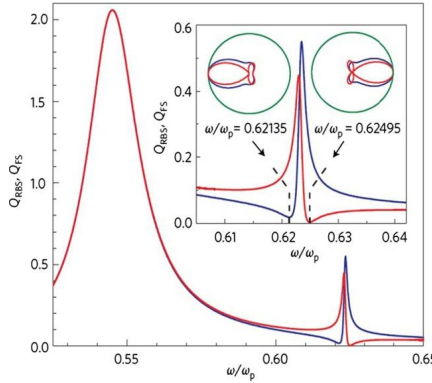
Figure 2.12 Radar backscattering (RBS; red) and forward scattering (FS; blue) cross-sections versus normalized frequency ω/ω_p of a plasmonic sphere. The dielectric permittivity ϵ is described by the Drude formula: $\gamma/\omega_p = 10^{-3}$, ω_p and γ being the plasma and collision frequencies, respectively. $q = \omega_p a/c = 0.7$. The calculations use Eqs. (2.34) and (2.35) to which only a_1 and a_2 contribute. Inset: Polar scattering diagrams in the XZ-plane (azimuthal angle $\phi = 0$, see Fig. 2.1) near the quadrupole resonance of a plasmonic particle. Red lines shows linear polarization; blue lines pertain to non-polarized light. After [62].

Fig. 2.12 illustrates $Q_{forw}^{(ext)} = dQ^{(ext)}(0°)/d\Omega = (1/q^2)|a_1 + 5a_2/3|^2$ and $Q_{back}^{(ext)} = dQ^{(ext)}(180°)/d\Omega = (1/q^2)|a_1 - 5a_2/3|^2$ ($q = \omega_p a/c$, ω_p being the electron plasma frequency), for a plasmonic sphere near a Fano resonance [62]. Both scattering cross-sections were addressed in Section 2.4 [cf. Eqs (2.34)–(2.35) and paragraph below them, as well as Eq. (2.45)]. One observes a symmetric electric dipole resonant peak and an asymmetric Fano lineshape due to the electric dipole–quadrupole interference. As expected, its Q-factor increases as both the sphere radius a and the bandwidth Γ decreases. The interference of both MDRs gives rise to enhancement or suppression of either $Q_{forw}^{(ext)}$ or $Q_{back}^{(ext)}$. Namely, the angular distribution of scattered intensity at wavelengths near a Fano resonance frequency exhibits strong variations between forward and backward scattering, as shown in the inset of Fig. 2.12.

2.11.2 Kerker conditions

Due to ohmic losses, the observation of Fano scattering phenomena may become difficult in plasmonic particles. However, dipolar magnetodielectric spheres and cylinders like those dielectric of high refractive index (e.g. semiconductor or ceramic), addressed in Section 2.9, may produce easily observable directional scattering due to the interference between their induced electric and magnetic dipoles.

The following theory starts from a study by Kerker et al. [63] of 1983, where it was theoretically established that hypothetical magnetic spheres with permittivity ϵ_p and permeability μ_p, such that $\epsilon_p = \mu_p$, and hence $a_n = b_n$, would produce a zero scattered intensity in the backscattering direction. Also, since if $\epsilon_p = \mu_p$ one has, according to (2.34) and (2.35), $S_1(\cos\theta) = S_2(\cos\theta)$, linearly polarized incident light would give rise to a scattered angular distribution of waves with the same polarization

for any θ. In addition, in the Rayleigh limit, considering the quasistatic approximation: $\alpha_e \simeq \alpha_e^{(0)}$ and $\alpha_m \simeq \alpha_m^{(0)}$ [cf. Eq. (2.107)], for $\epsilon = (4 - \mu)/(2\mu + 1)$, it follows: $a_1 = -b_1$, and since then $S_1(\cos 0° = 1) = S_2(\cos 0° = 1) = 0$, the intensity in the forward direction would be zero; and the scattered light would have the same polarization as the incident one.

However, when we address real particles capable of producing such effects, we first draw attention to those dipolar magnetodielectric of Section 2.9, in which the contribution of their induced electric and magnetic dipoles to the differential scattering cross-section, after averaging over the two states of polarization: $\parallel$ and $\perp$, is

$$\frac{dQ^{(s)}(\theta)}{d\Omega} = \frac{k^4}{2} \left(\left| \epsilon^{-1}\alpha_e \right|^2 + |\mu\alpha_m|^2 \right) (1 + \cos^2\theta) + 2k^4 \frac{\mu}{\epsilon} \Re(\alpha_e \alpha_m^*) \cos\theta.$$
(2.115)

Which is mainly distributed in the forward or backward region according to whether $\Re(\alpha_e \alpha_m^*)$ is positive or negative, respectively. Specifically, in the forward ($\theta = 0°$; or "+") and backward ($\theta = 180°$; or "−") directions, the angular distribution of intensity is

$$\frac{dQ^{(s)}}{d\Omega}(\pm) = k^4 \left| \epsilon^{-1}\alpha_e \pm \mu\alpha_m \right|^2.$$
(2.116)

Therefore, this asymmetry arises from the interference between the electric and magnetic dipolar fields, and leads to the following effects:

i) The intensity in the backscattering direction is exactly zero: $\frac{dQ^{(s)}}{d\Omega}(180°) = 0$ when

$$\epsilon^{-1}\alpha_e = \mu\alpha_m.$$
(2.117)

For the backscattered intensity this coincides with the first statement of the above quoted Reference [63], formulated when $\epsilon_p = \mu_p$. Notice, however, that (2.116) and (2.117) do not impose any condition on ϵ_p and μ_p, but only on the polarizabilities. It was coined after [64] the *first Kerker condition* (K1).

ii) Taking into account the theory of Section 2.9, the conservation of energy and the consequent optical theorem (2.29) adopts the form [46,64]

$$\mathcal{W}^{(a)} + \frac{c}{n}\frac{k^4}{3}\{\epsilon^{-1}|\mathbf{p}|^2 + \mu|\mathbf{m}|^2\} = \frac{\omega}{2}\Im\{\mathbf{p} \cdot \mathbf{E}_i^*(\mathbf{r_0})\} - \frac{\omega}{2}\Im\{\mathbf{m} \cdot \mathbf{B}_i^*(\mathbf{r_0})\}. \quad (2.118)$$

The second term of the left side is the scattering cross-section $Q^{(s)}$. Thus the right side of (2.118) represents the extinction of incident energy on scattering and absorption by the particle whose center is at $\mathbf{r}_0$.

According to (2.29) and (2.118), the scattered intensity cannot be exactly zero in the forward direction, in contrast with the above quoted prediction by Kerker for a quasistatic Rayleigh particle. In fact, it was pointed out in Section 2.9.1 that the quasistatic polarizabilities lead to results that are inconsistent with energy conservation.
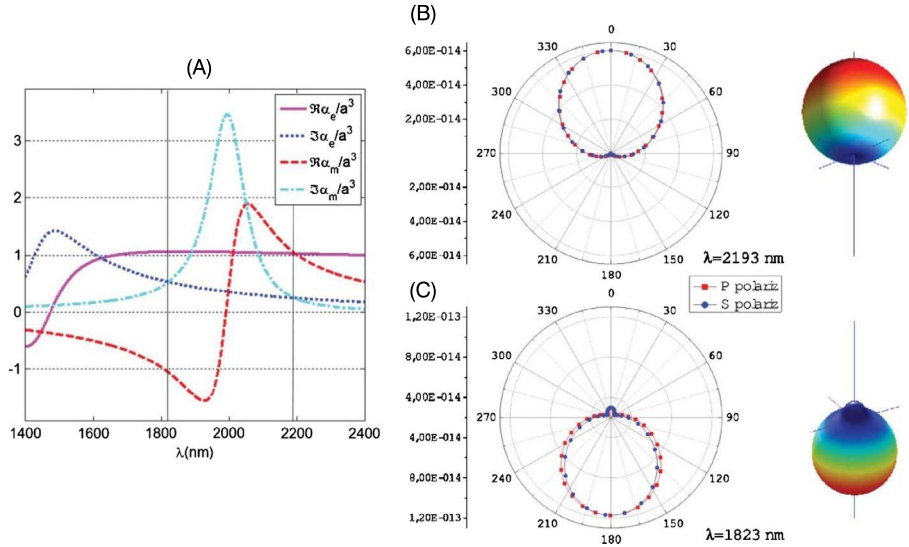
Figure 2.13 (A) Normalized real and imaginary parts of the electric and magnetic polarizabilities of a Ge sphere of radius $a = 240$ nm, $\epsilon_p = 16$ and $\mu = 1$ in vacuum. The right and left vertical lines mark the wavelengths: $\lambda = 2193$ nm and $\lambda = 1823$ nm, at which K1 and K2 hold, respectively. From [65]. (B) Polar 2-D and 3-D scattering diagrams from this particle at the two polarizations: s and p corresponding to the incident electric vector perpendicular and parallel to the scattering plane, respectively, at $\lambda = 2193$ nm (K1). (C) Same as (B) at $\lambda = 1823$ nm (K2). After [65].

Also, causality and absence of gains impose $\Im\{\alpha_e\} > 0$, $\Im\{\alpha_m\} > 0$. Hence the forward intensity presents a minimum at

$$\Re\{\epsilon^{-1}\alpha_e\} = -\Re\{\mu\alpha_m\}, \quad \Im\{\epsilon^{-1}\alpha_e\} = \Im\{\mu\alpha_m\}, \tag{2.119}$$

with

$$\frac{dQ^{(s)}}{d\Omega}(0°) = k^4\left|2\Im\{\epsilon^{-1}\alpha_e\}\right|^2 = \frac{16}{9}k^{10}\left|\epsilon^{-1}\alpha_e\right|^4\left|\frac{2}{3}k^3\epsilon^{-1}\alpha_e\right|^2\frac{dQ^{(s)}}{d\Omega}(180°). \tag{2.120}$$

Eq. (2.119), which thus leads to $\frac{dQ^{(s)}}{d\Omega}(0°) \sim (ka)^{10}$, generalizes the above quoted condition formulated in [63] for zero forward intensity. Once again in contrast with [63], it does not impose any constraint on ϵ_p and μ_p, but only on the polarizabilities. It was coined after [64] the *generalized second Kerker condition* (K2) as it goes beyond the quasistatic Rayleigh approximation and, like K1, it does not require the particle to be magnetic ($\mu_p \neq 0$), but to behave as magnetodielectric, namely, to produce scattered fields fully stemming from the emission of the electric and magnetic induced dipoles, respectively characterized by the first electric and magnetic Mie coefficients: a_1 and b_1, as discussed in Section 2.9.

Hence, we conclude that the two Kerker conditions K1 (2.117), and K2 (2.119), and their respective associated zero backward and minimum forward differential scattering
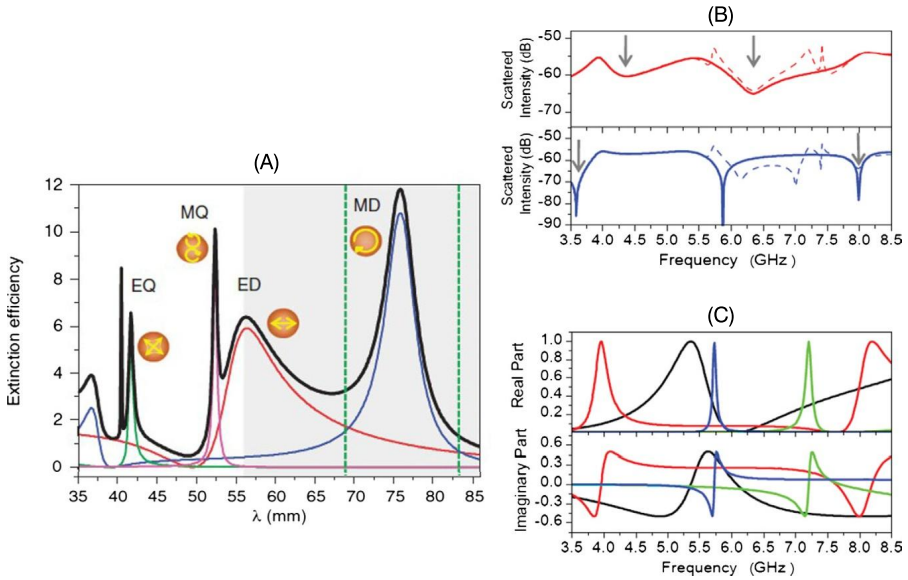
Figure 2.14 (A) Mie calculations of the extinction efficiency $Q^{(ext)}$ as a function of the incident wavelength λ (in mm) of a dielectric subwavelength sphere ($a = 9$ mm, $\epsilon = 16.5$). The total $Q^{(ext)}$ (black solid line), and their first four multipolar contributions: electric dipolar (red), magnetic dipolar (blue), electric quadrupolar (green), and magnetic quadrupolar (pink) are included. The grey area corresponds to the spectral range where dipolar terms dominate. In this region, $Q^{(ext)}$ presents two main peaks due to the excitation of either an electric dipolar (ED at $\lambda = 57$ mm) or a magnetic dipolar (MD at $\lambda = 76$ mm) resonance. Higher-order resonances are also observed (EQ: electric quadrupolar, MQ: magnetic quadrupolar). These resonant modes are consequence of the distribution of the electric field inside the particle (see orange-yellow insets which symbolically represent this **E**-distribution). (B) Simulated forward (upper part in red), and backward (lower part in blue), scattered intensities versus incident frequency (GHz), considering either a full Mie computation (dashed line), or an approximate calculation with only the first two Mie terms (dipolar electric/magnetic) (continuous line), for the same particle as in (A). *Kerker* frequencies are marked with vertical arrows (i.e. interference between the induced electric and magnetic dipole contributions at 4.3 GHz and 6.3 GHz in forward and 3.6 GHz and 8 GHz in backward). Two dips in the backscattered intensity also appear at 6.2 GHz and 7 GHz whose main contribution is due to magnetic and electric *Fano* resonances from the interference of the Mie terms $b_1–b_2$ and $a_1–a_2$, respectively. (Notice that the dip at 5.8 GHz of the approximate calculation is an artifact as it has no correspondence with any dip of the full Mie computation.) (C) Spectra of both real (top) and imaginary (bottom) parts of the first four Mie coefficients corresponding to dipolar electric, a_1 (black), and magnetic, b_1 (red), and quadrupolar electric, a_2 (green), and magnetic, b_2 (blue), contributions. After [66].

cross-sections, apply to, and are observable in, dipolar purely dielectric particles with the above quoted magnetodielectric nature.

Fig. 2.13A illustrates the polarizabilities (2.94)–(2.96) of a Ge sphere in the infrared, showing the K1 and K2 wavelengths. The corresponding angular distributions of scattered intensity on illumination at these values of λ are shown in Figs. 2.13B and C [65].

Fig. 2.14A shows the Mie solution for the spectral distribution of the extinction efficiency Q_{ext} as a function of the incident wavelength λ (in mm) from a dielec-
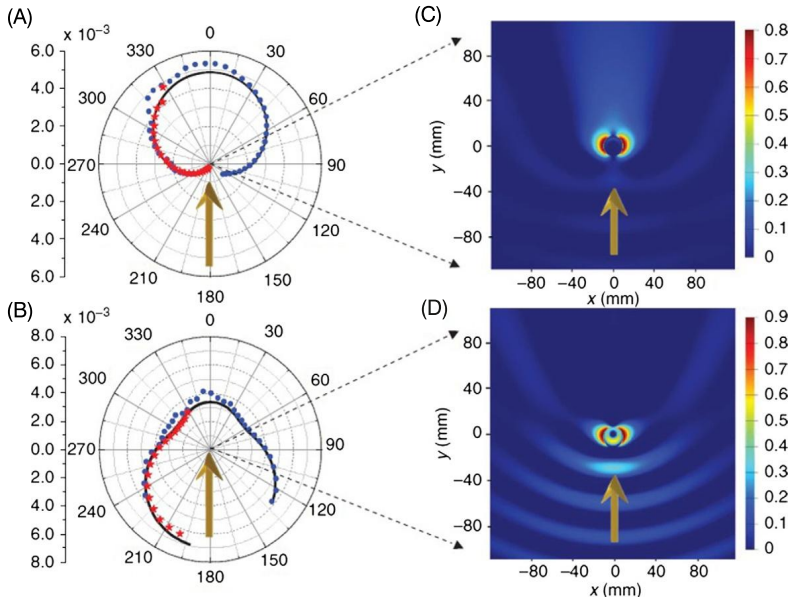
Figure 2.15 (A) and (B) Experimental values (full circles/stars) of the scattered intensity from the sphere of radius $a = 9$ mm and $\epsilon = 16.5$, addressed in Fig. 2.14, on illumination from below (yellow arrows) by a *p*-polarized plane wave, which satisfies either $K1$ (at $\lambda = 84$ mm). (A), or $K2$ ($\lambda = 69$ mm). (B) Detection of the angular distribution of scattered intensity for *s*-polarization (**E** normal to the plane of incidence and measurement, cf. blue full circles), and for *p*-polarization (**E** into the plane of incidence and measurement, see red stars). Theoretical results (black line) are also included for comparison purposes. (C) and (D) Calculated distribution of the total near-field intensity around the particle (in logarithmic scale) for the same cases considered in (A) and (B), that is, when the incident wavelength satisfies either $K1$ (C), or $K2$ (D), respectively. After [66].

tric subwavelength sphere ($a = 9$ mm, $\epsilon = 16.5$). This calculation is a model for a magnetodielectric sphere whose material is ECCOSTOCK-HIK from Emerson and Cuming (http://www.eccosorb.com/), having a permittivity and permeability like those of semiconductor materials (Si, Ge); with almost no dispersion in the frequency range of interest, and very low losses (the dissipation factor is given to be less than 0.002 in the 1 to $10GHz$ range of microwaves). The electric and magnetic dipoles and quadrupoles are shown. The crossing points at certain wavelengths of the lineshapes of these excitations, are responsible for interference phenomena that can be categorized as either Fano or Kerker effects. Accordingly, one can see in Fig. 2.14B the computation of $\frac{dQ^{(s)}}{d\Omega}(0°)$ and $\frac{dQ^{(s)}}{d\Omega}(180°)$ versus illuminating frequency, in the microwave range, corresponding to the existence of Fano dips along with those predicted $K1$ and $K2$ phenomena. The latter correspond to the first experimental demonstration [66] of both zero backward and almost zero forward scattered intensity, exhibited by Figs. 2.15A–D. Further observations at shorter and visible wavelengths have subsequently been made [67,68].

These special properties of magnetodielectric particles may find applications in metamaterials and nanocomposites, optical switching or sensing, as well as in emis-

sion devices like Huygens metasurfaces [69,70] and nanoantennas with high directionality [71].

Acknowledgments

References

[1] G. Mie, Ann. Phys. 25 (1908) 377.

[2] H. Horvath, J. Quant. Spectrosc. Radiat. Transf. 110 (2009) 787.

[3] L. Novotny, B. Hecht, Principles of Nano-Optics, 2nd ed., Cambridge University Press, Cambridge, 2012.

[4] S.A. Maier, Plasmonics: Fundamentals and Applications, Springer, Berlin, New York, 2007.

[5] M. Decker, I. Staude, J. Opt. 18 (2016) 103001.

[6] A.I. Kuznetsov, A.E. Miroshnichenko, M.L. Brongersma, Y.S. Kivshar, B. Luk'yanchuk, Science 354 (2016) 2472.

[7] C.F. Bohren, D.R. Huffman, Absorption and Scattering of Light by Small Particles, Wiley, New York, 1983.

[8] M. Kerker, The Scattering of Light and Other Electromagnetic Radiation, Academic Press, New York, 1969.

[9] C. Van de Hulst, Light Scattering by Small Particles, Dover, New York, 1981.

[10] J.A. Stratton, Electromagnetic Theory, McGraw–Hill, New York, 1941.

[11] M. Born, E. Wolf, Principles of Optics, Cambridge University Press, Cambridge, 1995.

[12] M. Abramowitz, I.M. Stegun, Handbook of Mathematical Functions, National Bureau of Standards Applied Mathematical Series, vol. 25, 1972, 3rd Printing, Washington, DC.

[13] M. Nieto-Vesperinas, Scattering and Diffraction in Physical Optics, 2nd ed., World Scientific, Singapore, 2006.

[14] W. Liu, A.E. Miroshnichenko, D.N. Neshev, Y.S. Kivshar, ACS Nano 6 (2012) 5489.

[15] R. Paniagua-Domínguez, D.R. Abujetas, J.A. Sánchez-Gil, Sci. Rep. 3 (2013) 1507.

[16] W. Liu, J. Zhang, B. Lei, H. Ma, W. Xie, H. Hu, Opt. Express 22 (2014) 16178.

[17] J.A. Kong, Proc. IEEE 60 (1972) 1036.

[18] R.P. Cameron, S.M. Barnett, A.M. Yao, New J. Phys. 14 (2012) 053050.

[19] C.F. Bohren, Chem. Phys. Lett. 29 (1974) 458.

[20] D.L. Andrews, M. Babiker (Eds.), The Angular Momentum of Light, Cambridge University Press, Cambridge, 2013.

[21] K.Y. Bliokh, J. Dressel, F. Nori, New J. Phys. 16 (2014) 093037.

[22] M. Nieto-Vesperinas, Phys. Rev. A 92 (2015) 023813.

[23] B. Hopkins, A.N. Poddubny, A.E. Miroshnichenko, Y.S. Kivshar, Laser Photonics Rev. 10 (2016) 137.

[24] P. Gutsche, L.V. Poulikakos, M. Hammerschmidt, S. Burger, F. Schmidt, Proc. SPIE 9756 (2016) 97560X.

[25] M. Nieto-Vesperinas, Philos. Trans. R. Soc. A 375 (2017) 20160314.

[26] J.A. Schellman, Chem. Rev. 75 (1975) 323.

[27] P. Gutsche, M. Nieto-Vesperinas, Sci. Rep. 8 (2018) 9416.

[28] S. Nechayev, J.S. Eismann, G. Leuchs, P. Banzer, Phys. Rev. B 99 (2019) 075155.

[29] S. Nechayev, P. Banzer, Phys. Rev. B 99 (2019) 241101(R).

[30] K. Vynck, D. Felbacq, E. Centeno, A.I. Cabuz, D. Cassagne, B. Guizal, Phys. Rev. Lett. 102 (2009) 133901.

[31] R. Paniagua-Domínguez, D.R. Abujetas, J.A. Sanchez-Gil, Sci. Rep. 3 (2013) 1507.

[32] W. Liu, A.E. Miroshnichenko, R.F. Oulton, D.N. Neshev, O. Hess, Y.S. Kivshar, Opt. Lett. 38 (2013) 2621.

[33] P.W. Barber, J.F. Owen, R.K. Chang, IEEE Trans. Antennas Propag. 30 (1982) 168.

[34] S.C. Hill, R.E. Benner, Morphology-dependent resonances, in: P.W. Barber, R.K. Chang (Eds.), Optical Effects Associated With Small Particles, World Scientific, Singapore, 1988, Chapter 1.

[35] C. Sönnichsen, T. Franzl, T. Wilk, G. von Plessen, J. Feldmann, O. Wilson, P. Mulvaney, Phys. Rev. Lett. 88 (2002) 077402.

[36] H. Raether, Surface Plasmons, Springer Verlag, Berlin, 1988.

[37] M.I. Stockman, Opt. Express 19 (2011) 22029.

[38] F.J. Valdivia-Valero, M. Nieto-Vesperinas, J. Nanophotonics 5 (2011) 053520.

[39] T.W. Ebbesen, H.J. Lezec, H.F. Ghaemi, T. Thio, P.A. Wolff, Nature 391 (1998) 667.

[40] F.J. Valdivia-Valero, M. Nieto-Vesperinas, Opt. Express 18 (2010) 6740.

[41] S.V. Boriskina, Photonic molecules and spectral engineering, in: O. Schwelb, I. Chremmos, N. Uzunoglu (Eds.), Photonic Microresonator Research and Applications, Springer Science and Business Media, LLC, 2010.

[42] M.L. Povinelli, S.G. Johnson, M. Loncar, M. Ibanescu, E.J. Smythe, F. Capasso, J.D. Joannopoulos, Opt. Express 1 (2005) 8286.

[43] J.M. Auñon, F.J. Valdivia-Valero, M. Nieto-Vesperinas, J. Opt. Soc. Am. A 31 (2014) 206.

[44] F.J. Valdivia-Valero, M. Nieto-Vesperinas, Photonics Nanostruct. Fundam. Appl. 10 (2012) 423.

[45] S. Jahani, Z. Jacob, Nat. Nanotechnol. 11 (2016) 23.

[46] M. Nieto-Vesperinas, J.J. Sáenz, R. Gómez-Medina, L. Chantada, Opt. Express 18 (2010) 11428.

[47] P. Chylek, R.G. Pinnick, Appl. Opt. 18 (1979) 1123.

[48] B.T. Draine, Ap. J. 333 (1988) 848.

[49] A. Garcia-Etxarri, R. Gomez-Medina, L.S. Froufe-Perez, C. Lopez, L. Chantada, F. Scheffold, J. Aizpurua, M. Nieto-Vesperinas, J.J. Saenz, arXiv:1005.5446v1, 29 May 2010, Opt. Express 19 (2011) 4816.

[50] A. Evlyukhin, C. Reinhardt, A. Seidel, B. Luk'yanchuk, B. Chichkov, Phys. Rev. B 82 (2010) 045404.

[51] A.I. Kuznetsov, A.E. Miroshnichenko, Y.H. Fu, J. Zhang, B. Luk'yanchuk, Sci. Rep. 2 (2012) 492.

[52] J.M. Auñon, M. Nieto-Vesperinas, J. Opt. Soc. Am. A 31 (2014) 1984.

[53] J.M. Auñon, Interaction Between Randomly Fluctuating Light and Small Particles, Ph.D. thesis, Universidad Complutense, 2014.

[54] D.R. Abujetas, R. Paniagua-Dominguez, M. Nieto-Vesperinas, J.A. Sánchez-Gil, J. Opt. 17 (2015) 125104.

[55] A.H. Sihvola, I.V. Lindell, Electron. Lett. 26 (1990) 118.

[56] Z.S. Wu, Q.C. Shang, Z.J. Li, Appl. Opt. 51 (2012) 6661.

[57] A. Canaguier-Durand, C. Genet, Phys. Rev. A 92 (2015) 043823.

[58] Y. Tang, A.E. Cohen, Science 332 (2011) 333.

[59] D. Tzarouchis, A. Sihvola, Light scattering by a dielectric sphere: perspectives on the Mie resonances, Appl. Sci. 8 (2018) 184, https://doi.org/10.3390/app8020184.

[60] R. Gomez-Medina, L.S. Froufe-Perez, M. Yepez, F. Scheffold, M. Nieto-Vesperinas, J.J. Saenz, Phys. Rev. A 85 (2012) 035802.

[61] U. Fano, Phys. Rev. 124 (1961) 1866.

[62] B. Luk'yanchuk, N.I. Zheludev, S.A. Maier, N.J. Halas, P. Nordlander, H. Giessen, C.T. Chong, Nat. Mater. 9 (2010) 707.

[63] M. Kerker, D.S. Wang, C.L. Giles, J. Opt. Soc. Am. 73 (1983) 765.

[64] M. Nieto-Vesperinas, R. Gomez-Medina, J.J. Saenz, J. Opt. Soc. Am. A 28 (2011) 54.

[65] R. Gomez-Medina, B. Garcia-Camara, I. Suarez-Lacalle, F. Gonzalez, F. Moreno, M. Nieto-Vesperinas, J.J. Saenz, J. Nanophotonics 5 (2011) 053512.

[66] J.M. Geffrin, B. Garcıia-Camara, R. Gomez-Medina, P. Albella, L.S. Froufe-Perez, C. Eyraud, A. Litman, R. Vaillon, F. Gonzalez, M. Nieto-Vesperinas, J.J. Saenz, F. Moreno, Nat. Commun. 3 (2012) 1171.

[67] S. Person, M. Jain, Z. Lapin, J.J. Saenz, G. Wicks, L. Novotny, Nano Lett. 13 (2013) 1806.

[68] Y.H. Fu, A.I. Kuznetsov, A.E. Miroshnichenko, Y.F. Yu, B. Luk'yanchuk, Nat. Commun. 4 (2013) 1527.

[69] C. Pfeiffer, A. Grbic, Phys. Rev. Lett. 110 (2013) 197401.

[70] M. Decker, I. Staude, M. Falkner, J. Dominguez, D.N. Neshev, I. Brener, T. Pertsch, Y.S. Kivshar, Adv. Opt. Mater. 3 (2015) 2015813.

[71] M.F. Picardi, A.V. Zayats, F.J. Rodrııguez-Fortuño, Phys. Rev. Lett. 120 (2018) 117402.

Control of scattering by isolated dielectric nanoantennas

3

Ramon Paniagua-Dominguez[a], Boris Luk'yanchuk[b,c], Arseniy I. Kuznetsov[a]
[a]Institute of Materials Research and Engineering, A*STAR (Agency for Science, Technology and Research), Singapore, Singapore, [b]Division of Physics and Applied Physics, School of Physical and Mathematical Sciences, Nanyang Technological University, Singapore, Singapore, [c]Faculty of Physics, Lomonosov Moscow State University, Moscow, Russia

3.1 Introduction

Resonant nanoparticles made of high-refractive index dielectric and semiconductor materials constitute the main building blocks for dielectric nanoantennas, metamaterials and metasurfaces. Light scattering by these nanoparticles is controlled by their Mie multipolar resonances and resonant interference effects. Understanding of the light scattering, including its efficiency and directivity, is important for future applications of these nanostructures as fundamental building blocks for resonant metadevices.

In conventional resonant plasmonics, which has been studied extensively over the last few decades, nanoparticle resonances are mainly limited to electric multipole series. Interference of these electric resonances of different types, e.g. between electric dipoles and quadrupoles of the same particles or electric dipoles or multipoles of different particles, leads to the so-called Fano resonance phenomena, which provide additional means to control scattering strength and directivity. In contrast to plasmonics, in dielectric nanostructures it is possible to efficiently excite both electric and magnetic multipolar modes. In this case, in addition to conventional Fano interference, there is a broad range of new resonant effects associated with interference between electric and magnetic multipoles. These phenomena, often referred to as Kerker or generalized Kerker effects, form the basis for a number of new resonance properties exhibited by dielectric nanoantennas and metasurfaces. Thorough control of resonant multipole excitation inside dielectric particles and their interference is key to design resonant dielectric metadevices.

In this chapter, we will review the major resonant phenomena associated with single high-index dielectric nanoparticles and nanoparticle structures and draw a perspective on application of these properties to design dielectric nanoantennas, metasurfaces and other resonant metadevices.

3.2   Resonant light scattering by single dielectric nanoparticles

Light scattering by a spherical particle in a medium, both isotropic and homogeneous, is a classical problem having an analytical solution published by Gustav Mie in the beginning of twentieth century, nowadays referred to as Mie theory [1,2].

By applying the Mie theory, it is possible to compute the scattering efficiency, Q_{sca}, defined as the ratio between the scattering and geometrical cross-sections of a particle through the simple formula (see a previous chapter of this book):

$$Q_{sca} = \frac{2}{q_m^2} \sum_{l=1}^{\infty} (2l+1)(|a_l|^2 + |b_l|^2), \tag{3.1}$$

where l is the index numbering of the orbital modes: dipolar ($l = 1$), quadrupolar ($l = 2$), octupolar ($l = 3$), etc. The electric, a_l, and magnetic, b_l, scattering amplitudes are given by

$$a_l = \frac{\mathfrak{R}_l^{(a)}}{\mathfrak{R}_l^{(a)} + i\mathfrak{I}_l^{(a)}}; \quad b_l = \frac{\mathfrak{R}_l^{(b)}}{\mathfrak{R}_l^{(b)} + i\mathfrak{I}_l^{(b)}}, \tag{3.2}$$

where, for non-magnetic media,

$$\begin{aligned}
\mathfrak{R}_l^{(a)} &= n_p \psi_l(q_p)\, \psi_l'(q_m) - n_m \psi_l(q_m)\, \psi_l'(q_p), \\
\mathfrak{I}_l^{(a)} &= n_p \chi_l'(q_m)\, \psi_l(q_p) - n_m \chi_l(q_m)\, \psi_l'(q_p), \\
\mathfrak{R}_l^{(b)} &= n_p \psi_l(q_m)\, \psi_l'(q_p) - n_m \psi_l(q_p)\, \psi_l'(q_m), \\
\mathfrak{I}_l^{(b)} &= n_p \chi_l(q_m)\, \psi_l'(q_p) - n_m \chi_l'(q_m)\, \psi_l(q_p).
\end{aligned} \tag{3.3}$$

Here the functions $\psi_l(z) = \sqrt{\frac{\pi z}{2}} J_{l+\frac{1}{2}}(z)$ and $\chi_l(z) = \sqrt{\frac{\pi z}{2}} N_{l+\frac{1}{2}}(z)$ are expressed through the Bessel and Neumann functions [2]. We use the subscripts m and p to denote the values referring to the external medium and the particle, with refractive indices n_m and n_p, respectively. In the expressions above, $q_m = q n_m$ and $q_p = q n_p$. The symbol q represents the so-called size parameter, defined as $q = \omega R/c = 2\pi R/\lambda$, with ω and λ being the angular frequency and the wavelength in vacuum of the incoming wave, respectively, and R the radius of the particle.

Eq. (3.1) can also be expressed as

$$Q_{sca} = \sum_{l=1}^{\infty} (Q_l^{(e)} + Q_l^{(m)}), \tag{3.4}$$

where $Q_l^{(e)} = 2(2l+1)|a_l|^2/q_m^2$ and $Q_l^{(m)} = 2(2l+1)|b_l|^2/q_m^2$ are the partial electric and magnetic scattering efficiencies associated with the multipolar moment of lth order. A similar analytical solution can also be found for an infinite cylinder (see Chapter 8, Section 8.4 in [2]).
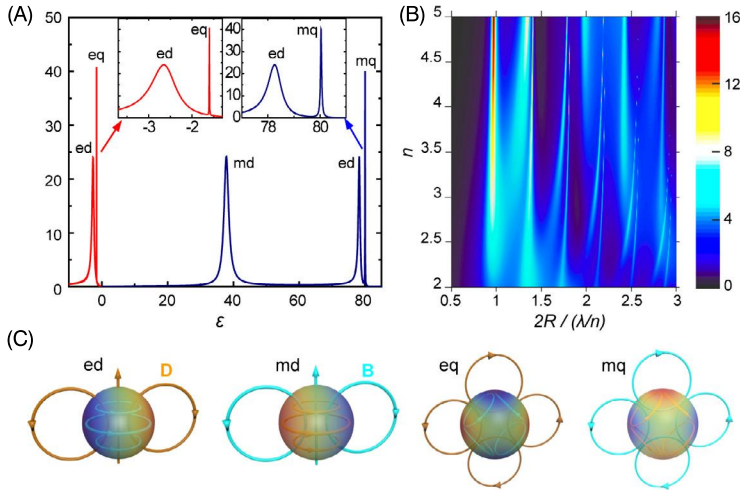
Figure 3.1 Mie resonances of a spherical particle. (A) Scattering efficiency vs. dielectric permittivity ε (lossless particle, size parameter $q = 2\pi R/\lambda = 0.5$, where R is the particle radius and λ is the wavelength of light) for plasmonic ($\varepsilon < 0$) and dielectric ($\varepsilon > 0$) materials: ed is for electric dipole, corresponding to $Q_1^{(e)}$, eq for electric quadrupole, corresponding to $Q_2^{(e)}$, md for magnetic dipole, corresponding to $Q_1^{(m)}$, and mq for magnetic quadrupole, corresponding to $Q_2^{(m)}$, resonances. Higher-order multipole modes are not shown for the sake of simplicity. (B) Scattering efficiency of a lossless dielectric particle as a function of refractive index and size parameter. (C) Illustration of the structure of the electric and magnetic fields for different electric and magnetic resonances supported by a spherical dielectric particle [3].

The solution of this problem reveals, under certain circumstances, a resonant behavior of light scattering, whose characteristics, namely its spectral position and amplitude, depend on the particle material, size and environment. For particles made of metals with the real part of the dielectric permittivity function close to -2 the so-called plasmonic resonances start to appear with the first fundamental mode being electric dipole, associated with the $Q_1^{(e)}$ term in Eq. (3.4), followed by electric quadrupole, octupole and high-order electric multipolar modes (Fig. 3.1A) [3]. The magnetic multipole response, associated with the $Q_l^{(m)}$ terms, is negligible for metallic spheres with a size smaller compared to the wavelength of light. To create a magnetic resonance with metallic elements, one should change the particle geometry. For example, magnetic response can be generated using a *split-ring resonator* configuration [4]. This structure behaves as an effective *LC* circuit exhibiting, at resonance, a strong enhancement of the magnetic field in the center of the ring. The magnetic response of split rings, however, saturates at high frequencies, for which the system also presents large dissipative losses [5]. For dielectric spheres with small refractive index (<2) lower-order modes are not strongly pronounced while higher, whispery gallery-type, modes may have sharp resonances opening many application opportunities in sensing, nanoscale light focusing and nanoscopy [6]. However, the size of such low-index resonant particles is typically of the order or above the free-space resonant wavelength making them irrelevant for the field of nanoantennas, particularly those used in meta-

surfaces and metamaterials, for which their constituents should have sub-wavelength sizes. In contrast, for dielectric materials with refractive index larger than 2 the first fundamental resonance mode is a strongly pronounced magnetic dipole followed by electric dipole, magnetic and electric quadrupoles and other higher-order multipolar modes [7,3], as shown in Figs. 3.1A, B, and C. The diameter of a resonant high-index dielectric sphere at the magnetic dipole resonance is approximately equal to the wavelength of light inside the high-index dielectric material, λ/n_p, which is significantly smaller than the free-space resonant wavelength, λ, for high values of refractive index, n_p [8]. The fact that dielectric particles present both an electric and a magnetic resonant response with low associated losses has attracted significant attention to this field from researches in metamaterial community. There, having optical magnetism with low absorption is critical to achieve novel optical properties not existing in nature.

The resonant behavior of small spherical metallic and dielectric spheres (with a size parameter $q = 2\pi R/\lambda = 0.5$) is compared in Fig. 3.1A, where the scattering cross-section, computed using Eqs. (3.1)–(3.4), of both types of particles is depicted for different values of dielectric permittivity function, $\varepsilon = n_p^2$. Only electric-type resonances are observed for negative values of ε, the case of plasmonic resonances in metallic nanoparticles, while both magnetic and electric resonances are seen at relatively high positive ε values, the case of Mie resonances in high-index dielectrics. For refractive index value above 2, Mie resonances in dielectric particles are well defined and their spectral position scales proportionally to the particle size and refractive index, as shown in Fig. 3.1B. This makes it possible to scale these resonances all the way from optical frequencies to microwaves and obtain similar resonant scattering properties for particles made of different materials with similar refractive index. Electric and magnetic field distribution at the first four Mie resonances of high-index dielectric nanoparticles is schematically illustrated in Fig. 3.1C. The field profile at electric and magnetic resonances looks the same with only the difference that D- and B-field vectors are exchanged. It is important to note that similar resonances can be obtained not just in spheres but also in spheroids [9,10], rods [11], disks [12,13], rings [14], cuboids [15] and other different types of particle shapes [16]. Specific position and order of the resonances might change depending on the particle shape adding an additional important degree of freedom for engineering the resonance position and interference. A typical example of such shape-dependent resonance positioning is the mutual electric and magnetic resonance crossing at specific spheroid and disk particle aspect ratios leading to realization of the so-called *first Kerker condition* discussed later in this chapter [10,12].

First experimental studies of Mie resonances in high-index dielectric particles have been conducted at microwave frequencies and so-called dielectric resonator antennas made of high-index dielectric ceramics are considered as a viable alternative to conventional metallic antennas [17]. The main advantages, which dielectric resonator antennas bring to microwave technologies, are compactness, design simplicity and high radiation directionality. With the emergence of the field of metamaterials, ideas of using 3D structures consisting of resonant dielectric particles to obtain negative refraction have been extensively discussed and first examples of such structures working at microwave frequencies have been demonstrated. A detailed overview of dielectric
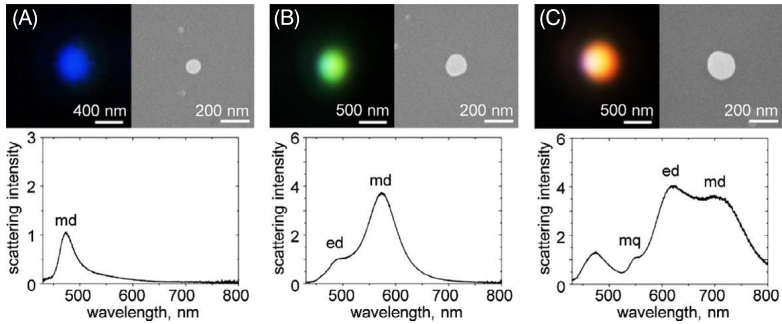
Figure 3.2 (A)–(C) Dark-field optical microscope (top left) and SEM (top right) images of spherical silicon nanoparticles fabricated on a silicon wafer by ablating it with a femtosecond laser. Particle diameter can be measured in the SEM images and is about 100 nm in (A), 140 nm in (B) and 180 nm in (C). (Bottom) are dark-field scattering spectra of the nanoparticles obtained using a single nanoparticle spectroscopy setup. md, ed and mq denote magnetic dipole, electric dipole and magnetic quadrupole, respectively. Adapted from [8]. The original work is licensed under a Creative Commons Attribution-NonCommercial-ShareALike 3.0 Unported License. To view a copy of this license, visit http://creativecommons.org/licenses/by-nc-sa/3.0/.

metamaterials design and experimental realization at microwave frequencies can be found in some review papers [18,19].

At visible and near-infrared frequencies silicon became the first material of choice to observe strong electric and magnetic dipole and higher-order Mie resonances [7, 20]. While having a high-refractive index (>3.5) through the whole visible and near-IR spectral range its losses are relatively low in the visible for wavelengths above 550 nm (with an absorption coefficient, $k_{Si} < 0.5$) and are negligible in the whole near-IR spectrum for wavelengths above 800 nm ($k_{Si} < 0.01$). A first experimental observation of such resonances has been reported for spherical silicon nanoparticles produced by femtosecond laser ablation [8,21]. This method allows generating multiple particles with almost perfect spherical shapes and randomly varied sizes. Later research has shown that similar resonant properties can be obtained not only for spherical particles but also for lithographically fabricated disks, cylinders and prism structures (see examples above). Fig. 3.2 shows dark-field optical and SEM images together with dark-field scattering spectra of silicon nanoparticles fabricated by femtosecond laser ablation of a silicon wafer. In the dark-field microscope images one can see bright visible colors, which are dependent on the nanoparticle size, and changing from blue for particles with about 100 nm diameter to green for particles with 140 nm diameter and red for particles with 180 nm diameter. Dark-field scattering spectra of these nanoparticles reveal that the color is mainly coming from the fundamental magnetic dipole resonance and electric dipole resonance at higher frequencies. Identification of the electric or magnetic nature of the observed resonances can be done through theoretical analysis [22] or by direct measurements of far-field [23,24] or near-field [25] scattering patterns of the nanoparticles. At larger particle sizes electric and magnetic quadrupoles, octupoles and higher-order multipole modes can be detected [26].
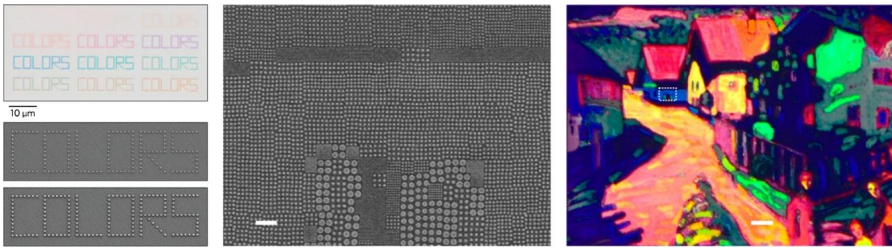
Figure 3.3 Visible colors from silicon nanodisks observed in reflection through a bright-field optical microscope. (Left top) Individual silicon disks on a quartz substrate with sizes ranging from 40 nm to 150 nm with a step of 10 nm and forming word "colors" for each particle size. (Left bottom) SEM images for 70 nm and 150 nm diameter disks. Adapted with permission from [28]. © 2017 American Chemical Society. (Right) Arrays of silicon nanodisks on a silicon wafer with an anti-reflection coating on top, reproducing "Murnau Street with Women" painting by Vasily Kandinsky. The scale bar in the optical image is 20 μm. (Center) SEM image of the selected region in (right) highlighted by the white-dotted rectangle. The scale bar in the SEM image is 1 μm. Adapted with permission from [29]. © 2017 American Chemical Society.

One of the applications of bright visible colors in scattering by silicon nanoparticles is nanoscale color printing [27]. It was recently shown that by controlling nanoparticle interaction with a substrate it is possible to reach vibrant colors with a gamut (i.e. a color range) that goes beyond the standard RGB range. Importantly, this was obtained with a pixel size as small as a single silicon nanoparticle [28,29]. Fig. 3.3 demonstrates several examples of color reproduction using individual silicon nanodisks and arrays of those fabricated by e-beam lithography. The colors are observed in reflection under bright-field optical microscope and can be used to inscribe hidden information at nanoscale beyond eye resolution. It is worth mentioning that arrays of silicon nanoparticles having fundamental resonances and pronounced visible colors have been studied several years earlier for color display applications [30]. However, their resonances at that time were not clearly analyzed and the magnetic nature of the fundamental resonance and associated resonant phenomena were not revealed.

Another direction of research on Mie resonances is related to scattering and absorption properties of dielectric and semiconductor nanorods. These were first experimentally studied with silicon carbide nanorod structures [11]. Their magnetic dipole response was demonstrated and its possible applications to metamaterials were discussed. It is important to mention that in contrast to guided modes in "standing" nanorods/nanowires [31], which can be excited by light propagating along the nanowire axis, Mie resonant modes are excited in "laying" nanorods/nanowires by light propagating perpendicular to the nanorod/nanowire axis [32]. When light impinges obliquely to the nanorod axis a subtle interplay between these two kinds of modes emerges, giving an additional degree of freedom in design [33,34]. In the case of "laying" nanorods, the modes supported have somewhat similar field profiles to Mie modes in a sphere. Fig. 3.4 shows an example of Mie resonances measured through resonantly enhanced photocurrent in a germanium nanowire photodetector [32]. This resonantly enhanced absorption was used to increase the detector sensitivity in the spectral region where the material absorption is low. Later on, different types of Mie resonances in silicon, germanium, gallium arsenide and other types of semiconduc-
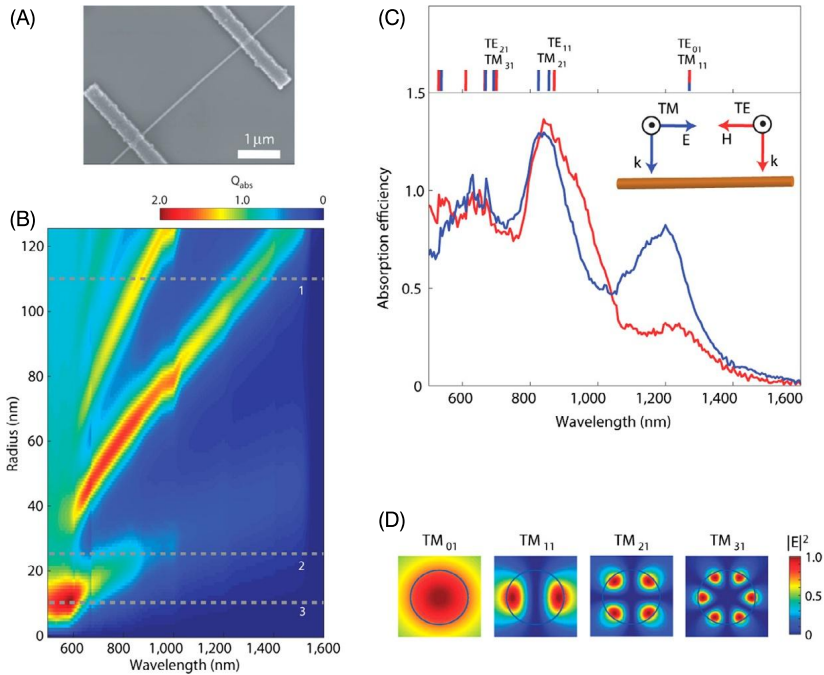
Figure 3.4 (A) SEM image of a 25-nm-radius germanium (Ge) nanowire photodetector device. The nanowire is connected to two metallic (Ti/Al) electrodes for photocurrent readout under supercontinuum light illumination. (B) Two-dimensional plot of calculated absorption efficiency of a Ge nanowire as a function of wavelength and radius of the nanowire. (C) Experimental absorption efficiency spectra of a 110-nm-radius germanium nanowire obtained from photocurrent measurements using linearly polarized transverse-electric (TE; red) or transverse-magnetic (TM; blue) light. The red and blue lines on top of the plot indicate the spectral positions of all nanowire Mie modes in this spectral region. (D) The configuration of the electric field intensity for typical transverse-magnetic leaky modes. The blue circle refers to the nanowire/air interface. Adapted by permission from Springer Nature: [32] (2009).

tor nanorods have been studied at visible and near-IR frequencies for enhancement of light absorption for photovoltaics [35], enhanced thermal emission [36] and color display applications [37].

3.3 Multipolar interference effects and directional scattering

One of the most intriguing properties of dielectric nanoparticles is that, even when they are shaped in simple forms such as cylinders or spheres, they support multiple Mie modes that may spectrally overlap. When this happens, the far-field scattering pattern from these particles can become rather complex, presenting several maxima and minima and strongly deviating from that of a simple Rayleigh scatterer. This complex-

ity arises from the directional constructive and destructive interference of the different multipolar modes excited in the particles and the precise shape depends on the relative amplitudes and phases of the induced multipolar moments. Note that, while total radiation interference between different cylindrical/spherical multipoles is forbidden due to their orthogonality (cf. [2], Chapter 4, Section 4.2), directional interference effects may still arise.

These interference effects can be readily seen even in the simplest case of a monochromatic plane wave scattering from a single, dielectric, spherical particle. Of particular importance in this context are the so-called *Kerker conditions*, which will be presented in the detail in this section. In brief, these conditions refer to particular situations in which the particle presents zero backward scattering, and thus scatters light almost entirely forward, or quasi-zero forward scattering, thus scattering light almost entirely backwards. These two situations highlight the fact that dielectric nanoantennas, even in very simple shapes, can act as very directional antennas for light. Let us, however, derive these conditions from a general perspective. As has been shown before (cf. Fig. 3.1, panel B), when the particle has a refractive index $n_p > 2$, the hierarchy of the optical resonances supported is such that the two lowest-energy ones correspond to the resonant excitation of magnetic dipole and electric dipole modes (in order of increasing energy). In the frequency range in which only these two modes coexist, thus, the incident wave generates a pair of induced electric and magnetic dipoles given, respectively, by the expressions

$$\mathbf{p} = \alpha_E \epsilon_0 \mathbf{E}_0 \tag{3.5}$$
$$\mathbf{m} = \alpha_M \mathbf{H}_0, \tag{3.6}$$

with $\mathbf{E}_0$ and $\mathbf{H}_0 = \mathbf{E}_0/Z$ being the complex amplitudes of the electric and magnetic fields of the incident wave, Z the impedance of the external medium and α_E and α_M the electric and magnetic polarizabilities of the particle, respectively. For a sphere, these polarizabilities can be connected with the first two Mie coefficients through the expressions:

$$\alpha_E = i \frac{6\pi}{k^3} a_1, \tag{3.7}$$

$$\alpha_M = i \frac{6\pi}{k^3} b_1, \tag{3.8}$$

where k is the wavenumber of the incident wave. This connection can be established by direct comparison of the far-field generated by a point electric (magnetic) dipole and the far-field associated with the a_1 (b_1) coefficient in the Mie expansion. The interested reader may refer, e.g., to reference [38] to find, explicitly, such a connection.

Let us, without loss of generality, assume the sphere of radius R to be located in the center of the coordinate system and the incoming monochromatic plane wave to be traveling in vacuum along the positive z-axis with the electric field polarized along the x-axis. In that case, the electric far-field generated by the induced electric dipole $\mathbf{p} = p_i \hat{\mathbf{x}} = \alpha_E \epsilon_0 E_0 \hat{\mathbf{x}}$ and the induced magnetic dipole $\mathbf{m} = m_i \hat{\mathbf{y}} = \alpha_M H_0 \hat{\mathbf{y}}$, which

generally reads

$$\mathbf{E}_{ff} = \mathbf{E}_{ff}^p + \mathbf{E}_{ff}^m = \frac{k^2}{4\pi\epsilon_0}\left[\hat{\mathbf{r}} \times (\mathbf{p} \times \hat{\mathbf{r}}) + \frac{1}{c}\mathbf{m} \times \hat{\mathbf{r}}\right] \tag{3.9}$$

ϵ_0 being the permittivity of vacuum and $\hat{\mathbf{r}}$ a unitary vector in the direction of observation, reduces, in spherical coordinates, to

$$\mathbf{E}_{ff}(\theta, \phi) = \frac{k^2}{4\pi\epsilon_0}\left[\left(\frac{m_i}{c} + p_i\cos\theta\right)\cos\phi\hat{\boldsymbol{\theta}} - \left(p_i + \frac{m_i}{c}\cos\theta\right)\sin\phi\hat{\boldsymbol{\phi}}\right]. \tag{3.10}$$

This last expression can be recast in terms of the polarizabilities and, ultimately, in terms of the first two Mie coefficients as

$$\mathbf{E}_{ff}(\theta, \phi) = \frac{3i}{2k}E_0\left[(b_1 + a_1\cos\theta)\cos\phi\hat{\boldsymbol{\theta}} - (a_1 + b_1\cos\theta)\sin\phi\hat{\boldsymbol{\phi}}\right]. \tag{3.11}$$

From Eqs. (3.10) and (3.11) can be readily seen that, in general, the scattering pattern of a particle supporting both electric and magnetic dipole modes will strongly deviate from that of a Rayleigh scatter. Two cases of particular relevance are that of the plane containing the induced electric dipole ($\phi = 0, \pi$) and that of the plane containing the magnetic dipole ($\phi = \pi/2, 3\pi/2$), for which the azimuthal and polar components of the electric far-field, respectively, vanish. In either of these situations, it is possible to find certain polar angle for which the field completely vanishes due to the destructive interference of the radiation from these modes. In particular, as follows from Eq. (3.11), for the plane containing the electric dipole, the electric far-field completely vanishes when the following relation is fulfilled:

$$b_1 + a_1\cos\theta = 0, \tag{3.12}$$

while in the plane containing the magnetic dipole the condition for vanishing field reads

$$a_1 + b_1\cos\theta = 0. \tag{3.13}$$

Therefore, the scattered far-field from a dielectric sphere may vanish at any polar angle in either of the planes of oscillation of the induced dipoles, provided the appropriate relations (3.12) or (3.13) hold. It should be noted that the scattering coefficients a_1 and b_1 are complex and, thus, the relations impose conditions to both the relative amplitudes and phases of the induced dipoles. In order to obtain a vanishing field in the plane of oscillation of the electric dipole, this dipole should be dominant; in other words, have larger amplitude than the magnetic one. Conversely, in order to obtain a vanishing field in the plane of oscillation of the magnetic dipole, it should dominate over the electric one. From this, it follows that both conditions cannot be simultaneously met and, therefore, scattering from a dielectric sphere cannot vanish for the same polar angle in both planes, with the only exception of the degenerate cases of the forward and backward directions, given, respectively, by $\theta = 0$ and $\theta = \pi$. The latter

corresponds to the so-called *first Kerker condition*, which happens when $a_1 = b_1$ and implies zero backscattering from the particle. This condition was first derived in the context of electromagnetic scattering from spheres with magnetic response [39] and then identified for semiconductor particles at optical frequencies [7,40]. The former is the so-called *second Kerker condition*, which is met when $a_1 = -b_1$ and implies vanishing forward scattering. In reality, this condition can only be approximately met. The reason behind the impossibility to fully satisfy Eq. (3.13) lies in the optical theorem, relating the total extinction from a particle with the electric field scattered in the forward direction. From it, a totally vanishing electric field in the forward direction would necessarily imply a vanishing extinction and, therefore, zero total scattering. The interested reader can find a discussion on this topic in reference [41].

The implications on the phases of the induced dipole moments can be clearly seen if the scattering coefficients are expressed as

$$a_1 = |a_1| e^{i\phi_{a_1}} \tag{3.14}$$

$$b_1 = |b_1| e^{i\phi_{b_1}}. \tag{3.15}$$

Then the differential scattering efficiency, $dQ(\theta, \phi)$, defined as the scattered intensity in a particular direction divided by the intensity of the incoming plane wave and the geometrical cross-section of the sphere, in this dipolar approximation, reads

$$dQ(\theta, \phi) = \frac{9}{4\pi q^2} \left[\Theta \cos^2 \phi + \Phi \sin^2 \phi \right], \tag{3.16}$$

where q is the size parameter introduced before and

$$\Theta = |b_1|^2 + |a_1|^2 \cos^2 \theta + 2 |a_1| |b_1| \cos \theta \cos \Delta_\phi \tag{3.17}$$

$$\Phi = |a_1|^2 + |b_1|^2 \cos^2 \theta + 2 |a_1| |b_1| \cos \theta \cos \Delta_\phi \tag{3.18}$$

associated, respectively, with the polar and azimuthal components of the scattered field. In these expressions

$$\Delta_\phi = |\phi_{a_1} - \phi_{b_1}| \tag{3.19}$$

is the phase different between the induced dipoles. Eq. (3.16) can be directly obtained in the context of Mie theory from the total scattered electric far-field (cf. Section 4.4.4 in [2]) by retaining only the first ($l = 1$) terms in the multipolar expansion.

From Eqs. (3.17) and (3.18) it becomes apparent that, in order to obtain vanishing scattering at a polar angle in the range $\theta \in (\pi/2, \pi)$, corresponding to the backward semi-sphere, the dipoles should be oscillating in phase. Conversely, to obtain vanishing scattering at a polar angle in the range $\theta \in (0, \pi/2)$, corresponding to the forward semi-sphere, the dipoles should be oscillating in anti-phase.

To illustrate the emergence of angle-suppressed scattering patterns predicted by Eq. (3.16) let us consider the case of a spherical particle with a very large, frequency-independent index of refraction $n_p = 8$, and the case of a crystalline silicon sphere at optical frequencies. Fig. 3.5A shows the total scattering efficiency of the sphere with
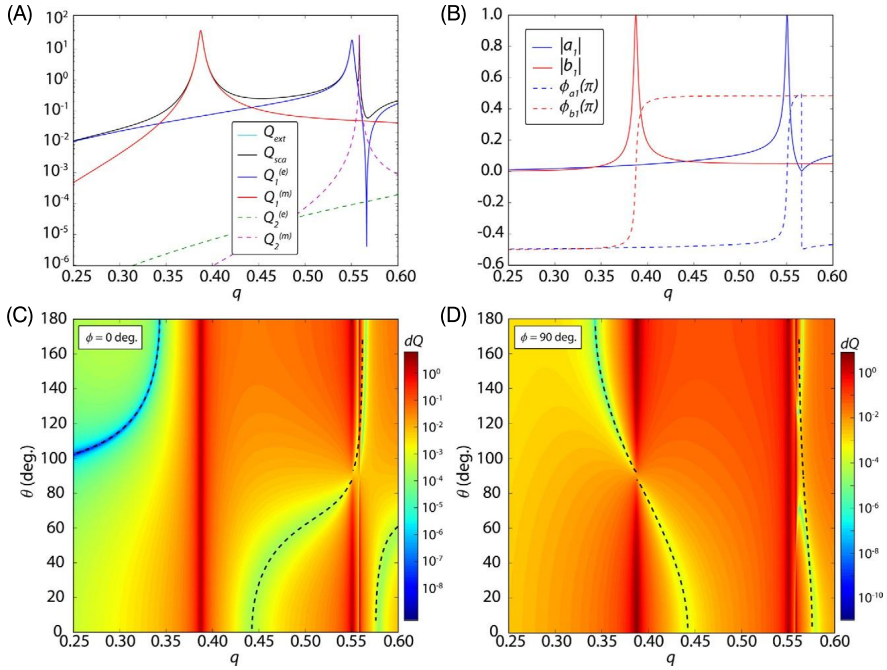
Figure 3.5 (A) Scattering efficiency and multipolar contributions (up to quadrupoles) of a dielectric sphere with refractive index $n_p = 8$ as a function of the size parameter q. The extinction efficiency, represented by the cyan curve, is not seen as it exactly matches the scattering one (black curve) for a lossless particle, such as the one considered here. (B) Amplitude (solid lines) and phase (dashed lines) of the a_1 (blue) and b_1 (red) coefficients. (C)–(D) Differential scattering efficiency dQ as a function of the size parameter q and the scattering angle θ in the $\phi = 0$ (C) and the $\phi = \pi/2$ (D) planes, corresponding to the oscillation planes of the induced electric and magnetic dipoles, respectively. The angle $\theta = 0°$ corresponds to the forward direction and the angle $\theta = 180°$ to the backward direction.

$n_p = 8$ in the range of size parameter in which the lowest-order resonances are excited. As can be seen, in this range the sphere supports an electric dipole resonance, associated with the $Q_1^{(e)}$ term, a magnetic dipole resonance, associated with $Q_1^{(m)}$, and a magnetic quadrupole resonance, with $Q_2^{(m)}$. Leaving aside the narrow spectral range in which the quadrupolar mode is excited, the scattering pattern from this particle should be mainly defined by its electric and magnetic dipolar response and, thus, it should be governed by Eq. (3.16), which in turn depends on (3.17) and (3.18). Fig. 3.5B shows the amplitude and the phase of the a_1 and b_1 coefficients. In this plot, one can identify several size parameter ranges. In the ranges $0.343 < q < 0.443$ and $0.561 < q < 0.576$ the b_1 coefficient (associated with the magnetic dipole term, $Q_1^{(m)}$) has a larger amplitude and, thus, it is possible to satisfy the condition $\Phi = 0$ for vanishing scattered field at a certain polar angle in the $\phi = \pi/2$ plane (plane of oscillation of the magnetic dipole). In the ranges $q < 0.343$, $0.443 < q < 0.561$ and $q > 0.576$ the a_1 coefficient (associated with the electric dipole, $Q_1^{(e)}$, term) dominates, which allows fulfilling the condition $\Theta = 0$ for vanishing scattered field at a certain polar

angle in the $\phi = 0$ plane (plane of oscillation of the electric dipole). By looking at the phases it is possible to identify the ranges of the size parameter for which vanishing scattering occurs in the forward or backward hemi-spheres of the pattern. As mentioned before, for scattering cancellation at an angle in the forward hemi-sphere $(0 < \theta < \pi/2)$ the dipoles should oscillate in anti-phase $(\Delta_\phi = \pi)$, which corresponds to the ranges $0.388 < q < 0.551$ and $q > 0.566$ in the plot. To obtain zero scattering at angles within the forward hemi-sphere $(\pi/2 < \theta < \pi)$ the dipoles must oscillate in phase $(\Delta_\phi = 0)$, which corresponds to the ranges $q < 0.388$ and $0.551 < q < 0.566$ in the plot. With this information it is easy to understand the maps shown in Figs. 3.5C and D, representing the differential scattering efficiency dQ, computed using Mie theory with 50 terms in the sum (cf. [2], Chapter 8, Section 4.4.4), as a function of the size parameter q and the scattering angle θ in the planes containing the induced electric dipole $(\phi = 0)$ and the induced magnetic dipole $(\phi = \pi/2)$, respectively. As predicted, in the plane of oscillation of the electric dipole the vanishing dQ occurs in the size parameter regions in which a_1 dominates. Conversely, vanishing dQ in the plane of oscillation of the magnetic dipole occurs in the regions in which the amplitude of the magnetic dipole is larger. Within these regions, the vanishing happens at polar angles in the forward hemi-sphere when the dipoles oscillate in anti-phase and in the backward one when they do so in phase. By taking into account the precise ratio between the a_1 and b_1 amplitudes and assuming purely in-phase or anti-phase oscillation of the induced dipoles, it is possible to predict, for each size parameter, the scattering angle at which dQ vanishes by the simple relations

$$\cos\theta = \pm |b_1| / |a_1| \quad \text{for } \phi = 0(|a_1| > |b_1|) \tag{3.20}$$

$$\cos\theta = \pm |a_1| / |b_1| \quad \text{for } \phi = \frac{\pi}{2}(|b_1| > |a_1|), \tag{3.21}$$

in which the positive sign corresponds to dipoles oscillating in anti-phase and the negative one to dipoles oscillating in phase. In Figs. 3.5C and D, the predicted (q, θ) trajectories for vanishing differential scattering computed using this simplified dipolar approximation are plotted as black-dashed lines. As can be seen, they closely follow the full Mie results except in the narrow region in which the quadrupolar contribution, $Q_2^{(m)}$, becomes non-negligible. The polar plots of some representative scattering patterns for different size parameters are shown in Fig. 3.6. The selected cases include those of vanishing backward scattering (first Kerker condition) and forward scattering (second Kerker condition) and those leading to vanishing scattering at polar angles $\theta = 60°$ and $\theta = 120°$ in both the plane of oscillation of the electric dipole ($\phi = 0$, xz-plane) and that of the magnetic dipole ($\phi = \pi/2$, yz-plane). These examples illustrate how dielectric particles, even when shaped in simple forms such as a sphere, can show strongly directional scattering, making them excellent candidates for building nanoantennas.

Let us now consider the case of a spherical nanoparticle made of crystalline silicon with a radius $R = 100$ nm. As shown before, silicon nanoparticles with diameters in the range of 100–200 nm support the lowest-order resonances in the visible-near-IR region of the spectrum (see Fig. 3.2). Fig. 3.7A shows the calculated scattering efficiency spectrum and main multipolar contributions of this particle, while Fig. 3.7B
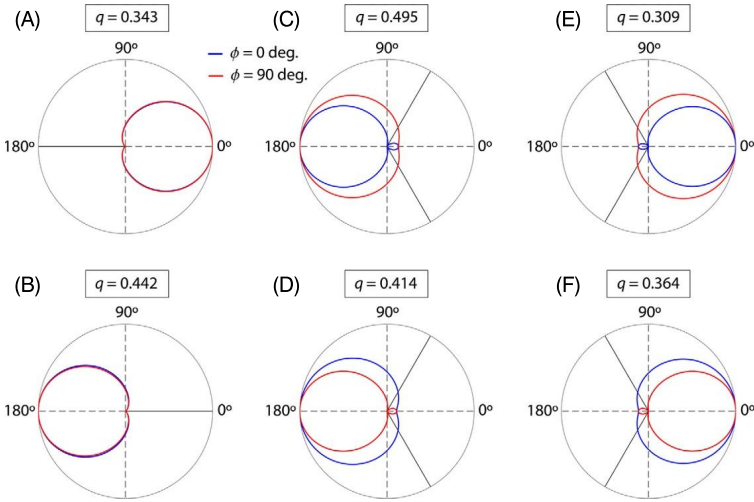
Figure 3.6 Polar plot of the differential scattering efficiency as a function of the scattering angle (scattering pattern) for several size parameter values in the $\phi = 0$ (blue) and the $\phi = \pi/2$ (red) planes, corresponding to the oscillation planes of the induced electric and magnetic dipoles, respectively. (A) Situation in which the backward scattering vanishes (*first Kerker condition*). (B) Situation in which the forward scattering is minimized (*second Kerker condition*). (C)–(D) Situation in which the scattering vanishes at an angle $\theta = 60°$ both in the $\phi = 0$ plane (C) and the $\phi = \pi/2$ plane (D). These situations happen, respectively, when $|a_1|/|b_1| = 2$ and $|b_1|/|a_1| = 2$, and the dipoles oscillate in anti-phase. (E)–(F) Situation in which the scattering vanishes at an angle $\theta = 120°$ both in the $\phi = 0$ plane (E) and the $\phi = \pi/2$ plane (F). The same amplitude relations hold here, but the dipoles oscillate in phase.

shows the amplitude and phase of the a_1 and b_1 coefficients. As can be seen, due to the lower refractive index of silicon, the resonances, which get broader, happen at a larger size parameter. Another important difference is found when looking at the calculated phases of the coefficients. For silicon spheres, the phase variation around the resonance peak is less steep. As a consequence, the oscillation of the induced dipoles is no longer well described by simply assuming that they oscillate either in phase or anti-phase, the latter being particularly the case. This implies that, in general, Eqs. (3.12) and (3.13) are not exactly satisfied and, thus, that the observed minima in the angular scattering are less pronounced. This is clearly seen in Figs. 3.7B and C, showing the angular differential scattering efficiency for the silicon sphere. In the plot, it is clearly seen that some of the observed regions of vanishing dQ in the case of the sphere with $n_p = 8$ are transformed into shallow minima in the case of the silicon sphere. Moreover, in this case, the predicted (q, θ) trajectories for vanishing dQ computed using the assumption of purely in-phase or anti-phase dipoles does not follow the full results so closely. The first Kerker condition is, however, still accurately met in this case (for a size parameter $q = 0.745$, corresponding to a wavelength $\lambda = 842$ nm), implying strong inhibition of backward scattering.

Experimental observations of the angle-suppressed scattering patterns from dielectric particles were performed in the microwave frequency range [42], using a dielectric sphere made of a ceramic material ($n_p \sim 4$) with radius $R = 9$ mm. The measured
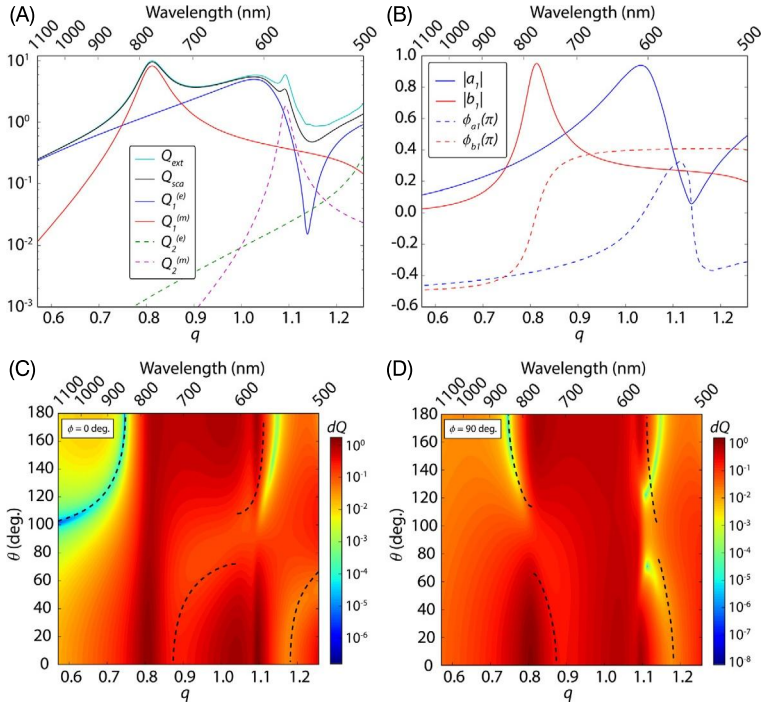
Figure 3.7 (A) Scattering efficiency and multipolar contributions (up to quadrupoles) of a crystalline silicon sphere with radius $R = 100$ nm as a function of the size parameter q. The corresponding wavelengths are also shown. (B) Amplitude (solid lines) and phase (dashed lines) of the a_1 (blue) and b_1 (red) coefficients. (C)–(D) Differential scattering efficiency dQ as a function of the size parameter q and the scattering angle θ in the $\phi = 0$ (C) and the $\phi = \pi/2$ (D) planes, corresponding to the oscillation planes of the induced electric and magnetic dipoles, respectively. The angle $\theta = 0°$ corresponds to the forward direction and the angle $\theta = 180°$ to the backward direction. The corresponding wavelengths are also shown.

scattered intensity as a function of the frequency of the incident light and the scattering angle are shown in Fig. 3.8A. The maps shown closely resemble those of Fig. 3.7A and B, in a restricted size parameter range, due to close value of the refractive index of the dielectric material used to that of silicon. Figs. 3.8B and C show the measured scattering patterns at the first and second Kerker conditions, respectively. Subsequently, directional scattering from dielectric nanoparticles in the visible range was measured in silicon nanospheres [9] and gallium arsenide nanodisks [43] fabricated, respectively, by femtosecond laser ablation and lithographically using a top-down approach. Figs. 3.8D and E show, respectively, the calculated and experimentally measured forward and backward scattering from a single silicon nanosphere, together with the forward-to-backward ratio. It can be seen that at the first Kerker condition realized at around 660 nm the experimental forward-to-backward scattering ratio reaches the values above 6 due to a suppression of backward scattering and non-zero forward scattering. The second Kerker condition is realized around 550 nm, resulting in the
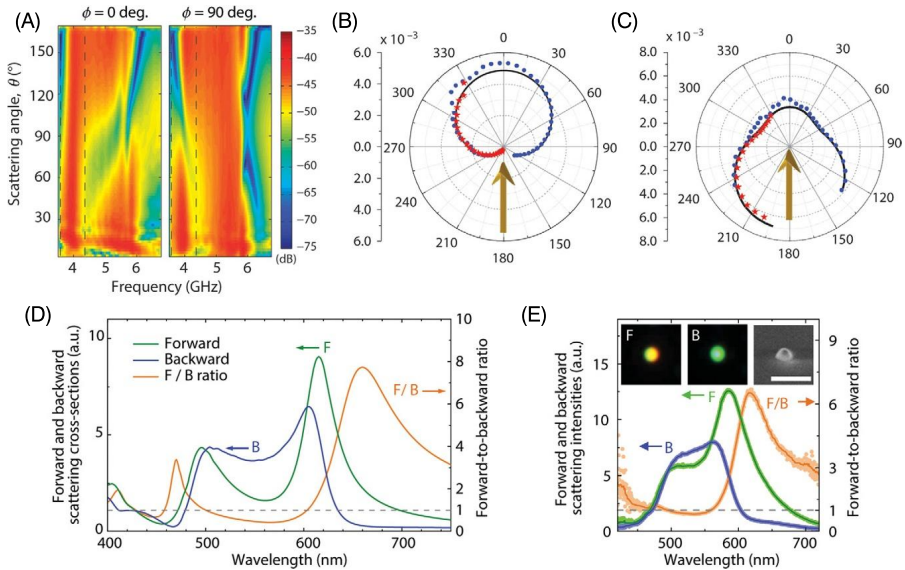
Figure 3.8 (A) Experimentally measured scattering intensity as a function of frequency and scattering angle θ in the $\phi = 0$ (left) and the $\phi = \pi/2$ (right) planes, corresponding to the oscillation planes of the induced electric and magnetic dipoles, respectively, for a dielectric sphere with index $n_p \sim 4$ and radius $R = 9$ mm. (B)–(C) Experimentally measured (symbols) and theoretically calculated (solid line) scattering patterns from the dielectric sphere in (A), at frequencies corresponding to Kerker's first (B) and second (C) conditions, indicated in (A) by vertical dashed lines. Adapted by permission from Springer Nature: [42] (2012). (D)–(E) Theoretical calculation (D) and experimentally measured (E) forwards scattering, backward scattering, and forward-to-backward ratio from a crystalline silicon sphere with radius $R = 75$ nm. The insets in panel (E) show the optical images of the particle in the forward (left, F) and backward (center, B) directions and the SEM image (right), with a scale bar corresponding to 500 nm. Adapted by permission from Springer Nature: [9] (2013).

minimum in the forward-to-backward scattering ratio. These experiments represent the first realizations of simple, directional, dielectric optical nanoantennas.

Interestingly, the angle-suppressed scattering patterns from dielectric spheres, in particular Figs. 3.7A and B and Fig. 3.8A, can be connected with the observed angular reflectivity from sub-diffractive arrays of such particles, often called metasurfaces [44]. These systems have the intriguing property of having a Brewster angle for both p- and s-polarization, in some ways similar to what is observed for media having a non-unity magnetic permeability. In the case of metasurfaces, this phenomenon arises not due to a real magnetic response, but rather due to the angle-suppressed scattering patterns from the particles forming the array, as described here. It is also worth mentioning that, although not described here, similar directionality effects can be found in the scattering from long dielectric nanowires supporting spectrally overlapping resonances [45].

So far, we have shown that even a simple dielectric sphere in the dipolar approximation may be a strongly directional nanoantenna, with a pronounced forward-to-backward asymmetry, via the realization of the Kerker conditions. Unfortunately,
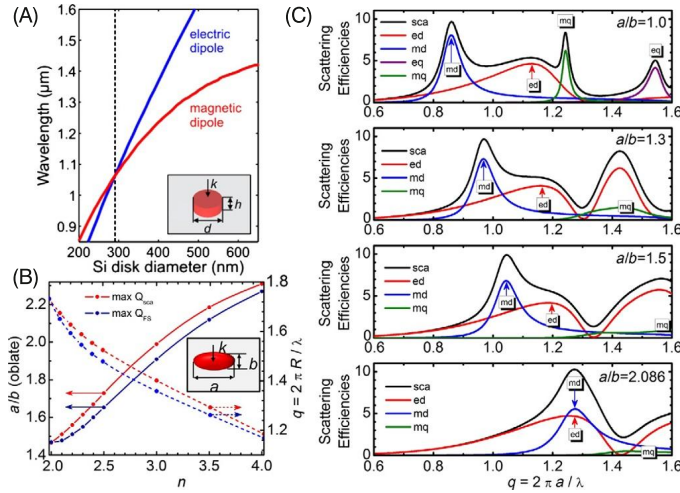
Figure 3.9 (A) Numerically calculated spectral position of the electric dipole and magnetic dipole resonance peak for a silicon disk with height $h = 220$ nm embedded in a medium with refractive index $n_m = 1.5$. Adapted with permission from [12]. © (2013) American Chemical Society. (B) Optimum shape a/b (solid lines) and size parameter q (dashed lines) maximizing total scattering (red) and forward scattering (blue) with minimized backward scattering for oblate spheroidal particles in air as a function of the value of the refractive index of the particle n. (C) Scattering efficiency (black) and multipolar contributions (up to quadrupoles, notations are the same as in Fig. 3.1) from oblate spheroidal particles with refractive index $n_p = 3.5$, as a function of the size parameter q, for several aspect ratios a/b. Panels (B) and (C) adapted with permission from [10]. © (2015) American Chemical Society.

when this system behaves as a *directional* antenna it does not behave as an *efficient* antenna, i.e., when Kerker's conditions are met the total scattering efficiency is low. In particular, for the *first* one the low efficiency is just due to the fact that, for spheres with index $n_p > 2$, the induced electric and magnetic dipoles only have the same amplitudes and phases far away from the spectral position of the resonance peaks, at the tail of the resonances. One possible strategy to overcome this issue is changing the shape of the particle, in particular its aspect ratio. By doing so, it is possible to induce a different spectral shift to the electric dipole mode and the magnetic dipole one, as to make their amplitudes and phases coincide at resonance, therefore simultaneously maximizing the total scattering efficiency as well as the forward-to-backward ratio [10,12]. Fig. 3.9A shows the numerically calculated spectral shift of the peak of the electric and magnetic dipole resonances for different aspect ratios between the height, h, and the diameter, d, of a silicon nanodisk. As can be seen, for an approximate aspect ratio $d/h \sim 1.35$ the peaks of the resonances spectrally overlap. Interestingly, using the quasi-analytical solution of plane wave scattering from spheroidal particles [46] it is possible to systematically study the problem of simultaneous maximization of total scattering and minimization of backward scattering and to show that, for any refractive index of the particle $n_p > 2$ it is possible to find a particular aspect ratio for which these two conditions are simultaneously satisfied. Fig. 3.9B shows the necessary aspect ratio and size parameter that maximized the total scattering effi-

ciency and the forward scattering efficiency for different refractive indices in the range $2 < n_p < 4$ at the condition of backward scattering minimized. For the case of a particle with refractive index $n_p = 3.5$, approximately corresponding to that of silicon in the visible-to-near-IR spectral range, Fig. 3.9C shows the evolution of the total scattering efficiency and the multipolar contributions (up to quadrupoles) when the shape of the particle changes from spherical to spheroidal with optimized aspect ratio, showing the overlapping of electric and magnetic dipole resonances.

3.4   Resonant scattering by dielectric nanoantennas

As shown above, even a single, simple shaped, dielectric particle may act as an efficient and directional optical antenna. Its directionality stems from interference effects, mainly, between electric and magnetic dipolar modes. If one would like, however, to obtain higher directivity or more complex response, three main strategies can be adopted. An immediate one is to increase the number of elements, or particles, forming the antenna. In this approach, each element can be kept within the so-called dipolar approximation (i.e. its response being governed by electric and magnetic dipoles only) and, therefore, have a small physical size. An alternative to increasing the number of particles is complexifying the elements forming the antenna. This can be achieved, e.g., by increasing their size, as to induce a higher-order multipolar response, or by changing their shape to more complex ones. Finally, one can also increase the complexity of the surrounding medium, a good example being the introduction of a reflective element such as a mirror. Let us, in the following, describe in some detail each of these approaches, with practical examples leading to efficient, directional antennas.

3.4.1   Multi-particle configurations

When one considers a system consisting of several dielectric particles interference effects become even more important and provide more opportunities to control the light scattering. In the case in which each element forming the antenna is electrically small, a good way to describe this kind of systems is through the so-called *Coupled Electric and Magnetic Dipole Method* (CEMD) in which each particle is simply described by a pair of electric and magnetic dipoles [47]. Within this approximation, the electric and magnetic fields at any position $\mathbf{r}$ in space can be expressed as

$$\mathbf{E}_{tot}(\mathbf{r}) = \mathbf{E}_0(\mathbf{r}) + \mathbf{E}_{sca}(\mathbf{r})$$

$$= \mathbf{E}_0(\mathbf{r}) + \sum_j \left\{ \frac{k^2}{\epsilon_0 \epsilon_m} \overleftrightarrow{\mathbf{G}}_E(\mathbf{r} - \mathbf{r}_j)\,\mathbf{p}_j + i Z k^2 \overleftrightarrow{\mathbf{G}}_M(\mathbf{r} - \mathbf{r}_j)\,\mathbf{m}_j \right\} \quad (3.22)$$

$$\mathbf{H}_{tot}(\mathbf{r}) = \mathbf{H}_0(\mathbf{r}) + \mathbf{H}_{sca}(\mathbf{r})$$

$$= \mathbf{H}_0(\mathbf{r}) + \sum_j \left\{ -i\frac{k^2}{Z}\epsilon_0 \epsilon_m \overleftrightarrow{\mathbf{G}}_M(\mathbf{r} - \mathbf{r}_j)\,\mathbf{p}_j + k^2 \overleftrightarrow{\mathbf{G}}_E(\mathbf{r} - \mathbf{r}_j)\,\mathbf{m}_j \right\}$$

$$(3.23)$$

where the second term represents the scattered field, the summation extends to all particles in the system with positions $\mathbf{r}_j$, and $\overset{\leftrightarrow}{\mathbf{G}}_E$ and $\overset{\leftrightarrow}{\mathbf{G}}_M$ are, respectively, the free-space electric and magnetic dyadic Green's functions. Their explicit form acting on the electric dipole reads

$$\overset{\leftrightarrow}{\mathbf{G}}_E (\mathbf{r}) \, \mathbf{p} = \frac{e^{ikr}}{4\pi r} \left\{ \left(1 + \frac{i}{kr} - \frac{1}{(kr)^2} \right) \mathbf{p} + \left(-1 - \frac{3i}{kr} + \frac{3}{(kr)^2} \right) (\hat{\mathbf{r}} \cdot \mathbf{p}) \hat{\mathbf{r}} \right\}$$
(3.24)

$$\overset{\leftrightarrow}{\mathbf{G}}_M (\mathbf{r}) \, \mathbf{p} = \frac{e^{ikr}}{4\pi r} \left(i - \frac{1}{kr} \right) (\hat{\mathbf{r}} \times \mathbf{p})$$
(3.25)

This problem can be solved self-consistently by expressing the dipole moments in the jth particle as

$$\mathbf{p}_j = \epsilon_0 \epsilon_m \alpha_E \left[\mathbf{E}_0 (\mathbf{r}_j) + \sum_{l \neq j} \left\{ \frac{k^2}{\epsilon_0 \epsilon_m} \overset{\leftrightarrow}{\mathbf{G}}_E (\mathbf{r}_j - \mathbf{r}_l) \, \mathbf{p}_l + i Z k^2 \overset{\leftrightarrow}{\mathbf{G}}_M (\mathbf{r}_j - \mathbf{r}_l) \, \mathbf{m}_l \right\} \right]$$
(3.26)

$$\mathbf{m}_j = \alpha_M \left[\mathbf{H}_0 (\mathbf{r}_j) + \sum_{l \neq j} \left\{ -i \frac{k^2}{Z} \epsilon_0 \epsilon_m \overset{\leftrightarrow}{\mathbf{G}}_M (\mathbf{r}_j - \mathbf{r}_l) \, \mathbf{p}_l + k^2 \overset{\leftrightarrow}{\mathbf{G}}_E (\mathbf{r}_j - \mathbf{r}_l) \, \mathbf{m}_l \right\} \right]$$
(3.27)

where the summation accounts for the field generated by the rest of the dipoles. While this simplified model fails to predict the near-fields generated around the particles, especially when they are in close proximity, it still gives reasonably accurate results for the far-field characteristics of the system. Its great advantages over full-wave numerical methods are being faster, less computationally demanding and providing physical insight into the different mode interactions occurring in the system.

3.4.1.1 Dielectric dimers

The simplest multi-particle system that can be studied is that of a dimer consisting of two dielectric spheres. Contrary to plasmonic dimers, in which the electromagnetic response is mainly determined by the interplay between the electric dipole modes induced in the metallic particles (forming so-called bonding and anti-bonding modes), in dielectric dimers the situation is more complex, and one needs to consider several types of dipole-dipole interaction. Namely, for a dielectric dimer consisting of particles supporting both electric and magnetic dipole modes, such as spheres made of silicon, it is possible to identify electric-electric, magnetic-magnetic and crossed electric-magnetic dipole interactions [48]. This gives rise to a complex hybridization scheme between the modes, as depicted in Fig. 3.10, which critically depends on the polarization of the incident field by either aligning the electric or the magnetic dipole moments of the particles [49]. As a result, complex dimer modes can be observed for both main polarizations, namely, with the electric field or the magnetic field being parallel to the axis of the dimer, as shown in Fig. 3.10A and 3.10B, respectively. With the
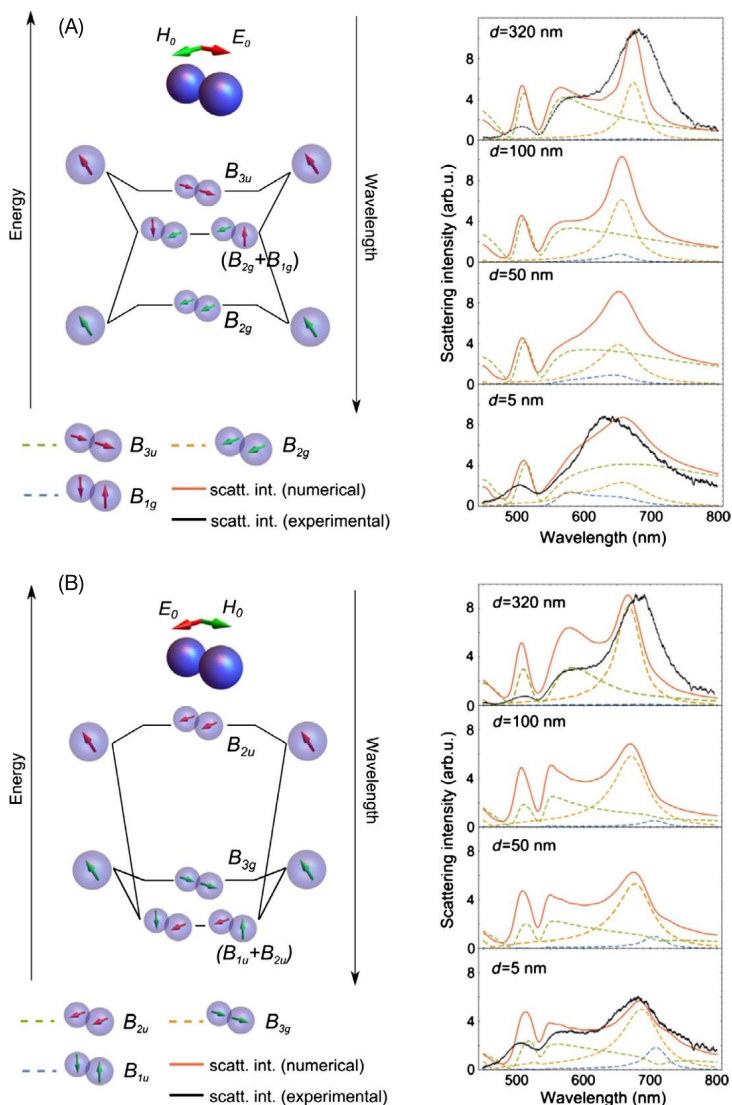
Figure 3.10 (Left) Energy-level diagram describing the hybridization of electric (red arrows) and magnetic (green arrows) dipolar resonances of single particles in the dimer. (Right) Numerically calculated (color lines) and experimentally measured (black lines) scattering spectra for different inter-particle gap d. The calculated spectra are decomposed according to the hybridization scheme shown. Each single scatterer is an oblate ellipsoidal core(silicon)–shell(silica) structure with major and minor external radii of 95 and 78 nm, respectively, and a 4 nm shell layer. (A) When the incident electric field is parallel to the axis of the dimer. (B) When the incident magnetic field is parallel to the axis of the dimer. Adapted with permission from [49]. © (2015) American Chemical Society.
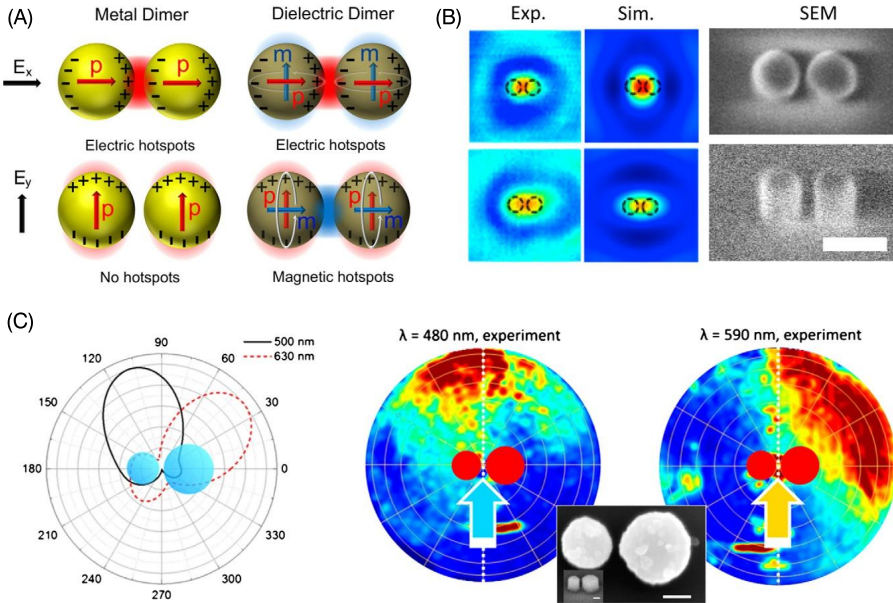
Figure 3.11 (A) Schematics depicted the mechanism behind generation of electric and magnetic hotspots in dielectric dimers, as compared to metallic ones. (B) Experimentally measured (left) and numerically calculated (center) NSOM signal from a silicon dimer. Top (bottom) row corresponds to the case of incident electric (magnetic) field parallel to the axis of the dimer. Low-intensity regions are represented by blue color and high-intensity ones by red color. (Right) SEM images of the measured dimer. The scale bar corresponds to 200 nm. Adapted with permission from [52]. © (2015) American Chemical Society. (C) Theoretically calculated (left) [55] and experimentally measured (center and right) [56] scattering patterns of an asymmetric silicon dimer. For the calculated case, the dimer consists of two silicon spheres with radii 75 nm and 115 nm, separated by a gap of 8 nm. Two different wavelengths are considered. Adapted from [55] under Creative Commons License. In the measured sample the dimer consists of two silicon cylinders with height 170 nm and radii 90 nm and 125 nm, separated by a gap of 40 nm. The SEM image shows the measured sample. The scale bars correspond to 100 nm. Adapted with permission from [56]. © (2017) American Chemical Society.

aid of numerical simulations and mode analysis, different dipole-dipole interactions can be identified, giving rise to the different resonance peaks observed in the measured dark-field scattering spectra. As a consequence of this complex dipole-dipole interaction, for dielectric dimers it is possible to observe generation of both *electric and magnetic hotspots* in the gap between the particles depending on the incidence polarization, a phenomenon that can be used to enhance light emission from quantum emitters with either electric dipole or magnetic dipole electronic transitions [50,51, 48]. This is in contrast to plasmonic dimers for which complex modes, with associated electric hotspots only, are exclusively excited when the electric field is parallel to the axis of the dimer. The schematic comparison of these two situations is depicted in Fig. 3.11A. The experimental observation of electric and magnetic hotspots in silicon dimers using an aperture-type near-field scanning optical microscope is shown in Fig. 3.11B [52]. A high-intensity spot in the gap between the particles is observed in

the NSOM signal both when the electric field is parallel to the dimer axis and when the magnetic field is parallel to the dimer axis. In the experiment, the dimer consisted of two identical cylindrical particles lithographically fabricated, as shown in the SEM image in the figure. Interestingly, large enhancements of the magnetic field can also be found in simplest configurations, such as a single sphere, provided a higher-order mode is supported [6,53]. These modes, however, are very sensitive to fabrication imperfections and, thus, difficult to observe. Although the CEMD described above fails to quantitatively predict the near-field enhancement in the case of a dimer, it can still be used to accurately predict the observed, far-field scattering characteristics from dielectric dimers. Interestingly, this simple model holds up to inter-particle gaps on the order of 10 nm, where the particles are strongly coupled [48]. Using this model, it is possible to design dimers such that the forward scattering is enhanced by adjusting the positions and the sizes of the individual particles forming the dimer [54]. It is also possible to obtain other directionality effects such as the ones shown in Fig. 3.11C, in which asymmetry in the radiation pattern in the plane of oscillation of the electric field is obtained. This effect was theoretically predicted first for a dimer consisting of two silicon spheres [55] and later observed experimentally with lithographically fabricated cylindrical particles [56]. Interestingly, the asymmetry may abruptly change with the wavelength of the incident light, which might find applications in wavelength multiplexing and routing. Additionally, this kind of asymmetry can be used in the design of periodic arrays of nanoantennas to obtain so-called metagratings, in which the energy distribution among the supported diffraction orders can be controlled at will by careful design of the nanoantenna radiation pattern [57–59].

3.4.1.2 Complex, multi-particle antennas

Let us now focus on nanoantennas involving more than two elements. Increasing the number of particles naturally provides additional degrees of freedom as to boost the directivity and efficiency of antennas. A canonical design based on this approach is the so-called *Yagi–Uda* nanoantenna, inherited from the radiofrequency community where it is widely used as a directive emitter and receiver. The design consists of an emitting element, the so-called *feed* of the antenna, one or several elements called *reflectors*, placed at one side of the feed, and several elements called *directors*, at the other side of it. The elements, in the shape of long rods, are designed to behave as dipolar scatterers. The length of these rods, and their mutual spacing, are designed in such a way that the scattered field interferes destructively with the emitted one in the direction of the reflectors and constructively in that of the directors. At optical frequencies, it has been implemented using plasmonic metals and replacing the usual current driven feed by a localized quantum emitter [60]. The schematic of such an optical Yagi–Uda antenna, based on gold nanorods, is shown in Fig. 3.12A. While this nanoantenna shows good directivity, its optical performance is somewhat hindered by the large Ohmic losses associated with metals at optical frequencies. Resonant dielectrics offer an alternative platform to design Yagi–Uda nanoantennas, with two main advantages. The first, obvious one is the mitigations of losses. The second, which may be more attractive, is the possibility to use not only the electric dipole response of the particles, as in
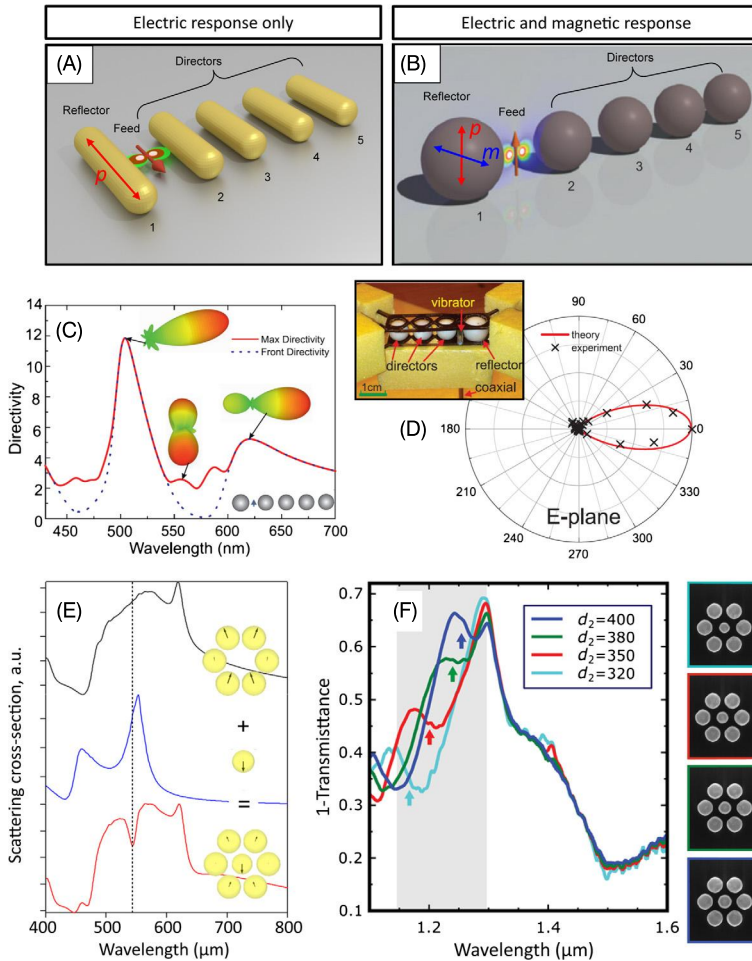
Figure 3.12 (A)–(B) Schematics of plasmonic (A) and dielectric (B) Yagi–Uda antennas. (C) Numerically calculated maximum directivity and forward directivity of a silicon Yagi–Uda nanoantenna consisting of one reflector with radius 75 nm and four directors with radii 70 nm. All particles are spaced by 70 nm. The system is fed with an electric dipole placed in between the reflector and the first director. Panels (B) and (C) adapted with permission from [61]. © (2012) Optical Society of America. (D) Experimentally measured scattering pattern of a dielectric Yagi–Uda antenna (shown in the inset) at a frequency of 10.7 GHz. The antenna consists of a reflector with radius 5 mm and three directors with radii 4 mm made of MgO–TiO$_2$ ceramic (with $n_p \sim 4$). Reprinted from [63], with the permission of AIP Publishing. (E) Numerically calculated scattering cross-section from a silicon hexamer forming a ring (black curve), a single silicon particle (blue curve) and silicon heptamer combining the two, showing the emergence of the Fano resonance (red curve). All particles are spherical. The outer particles have a diameter of 150 nm and the inner one of 130 nm. The gap between the outer particles is of 10 nm. Adapted with permission from [69]. © (2012) American Chemical Society. (F) Experimentally measured extinction spectra from four oligomers made of silicon nanocylinders showing Fano interference. The different curves correspond to different diameters of the central cylinder (as indicated in the legend and shown in the SEM images). The diameter of the cylinders forming the outer ring is 460 nm. The height of the cylinders is 260 nm and the radius of the hexamer ring is 568 nm. Adapted with permission from [70]. © (2014) John Wiley & Sons, Inc.

conventional Yagi–Uda designs, but also the magnetic dipoles induced in the particles, as schematically shown in Fig. 3.12B. This provides the antenna designer with additional degrees of freedom that may be used to further boost the directivity or to reduce the footprint by reducing the number of elements in the antenna. Fig. 3.12C shows the calculated directivity from a dielectric Yagi–Uda nanoantenna consisting of five silicon spheres. One of the particles is slightly bigger, acting as a reflector, while the other four have the same, smaller size. The system is fed by an electric dipole source located between the reflector and the first director. The high (forward) directivity of the antenna nearly coincides, spectrally, with the realization of the first Kerker condition in the directors [61]. Interestingly, this kind of system can be analytically studied with the CEMD, yielding identical results to the full-wave simulations shown here [62], saving time and computational resources to the designer. So far, the concept of dielectric Yagi–Uda antennas has been experimentally demonstrated in the microwave range only [63]; its verification at optical frequencies is still missing. Fig. 3.12D shows the measured scattering pattern of a dielectric Yagi–Uda antenna consisting of a reflector and three directors made of a ceramic material, with refractive index close to that of silicon at optical frequencies. The antenna is fed by a vibrator, as shown in the inset. The measured directivity agrees well with the theoretical prediction, confirming the feasibility of the design as a directional antenna. Interestingly, as the number of particles increases, approaching an infinite chain, guided modes emerge in the system, and light transmission with negligible losses becomes possible. This kind of chains supports different modes depending on the type of dipole-dipole interaction. In the fundamental one, the energy is transported via transverse-magnetic-dipole coupling [64]. This concept has been realized experimentally at optical frequencies using silicon nanoparticles fabricated lithographically, showing very low propagation losses comparable to standard silicon photonics waveguides [65].

Still within the dipolar approximation, but increasing the complexity of the nanoantenna, it is possible to observe interference effects between the modes of the different elements forming the antenna not only in the differential scattering but also in the total scattering from the system. In the case in which this interference occurs between a resonant mode and a non-resonant one the phenomenon is usually referred to as *Fano interference*. The name points to the analogy between the asymmetric spectral line-shapes observed in these systems and those observed in the inelastic scattering of electrons from helium, named after Ugo Fano, who provided the first theoretical explanation of their origin [66]. In the case of isolated nanoantennas, Fano resonances were first observed in plasmonic systems (the interested reader can refer to some of the review articles in this topic [67,68]). In these systems, Fano resonances usually arise as the interference between a *bright* mode, which strongly couples to incident radiation, and a *dark* mode, not easily accessible by external illumination. In this case one usually needs to disturb the symmetry of the system to ensure the coupling between the two modes. Due to their narrow line-widths, systems presenting Fano resonances have been considered for sensing applications. In dielectrics, due to their richer variety of optical modes, Fano resonances with different characteristics can be observed. A canonical system to observe such phenomena are particle oligomers, such as those shown in Fig. 3.12E and F. Among the wealth of Fano modes that can be observed in

these systems, one of the most interesting ones is that with a magnetic-like origin. The mechanism of emergence of one of these modes is shown in Fig. 3.12E. There, the emergence of the Fano resonance observed at the wavelength indicated by the vertical dashed line in the scattering cross-section from the dielectric heptamer (spectrum given by the red curve) stems from the interference between the resonant mode of the central particle (spectrum corresponding to the blue curve) and the broad, non-resonant mode of the hexamer forming the outer ring (spectrum given by the black curve) [69]. For frequencies around the resonance, the dipole moment in the central particle changes its oscillation from in phase to out of phase with respect to the incident field, while the particles in the outer ring remain in phase. This causes either constructive or destructive interference, which gives rise to the asymmetric line-shape. As shown in the insets, at resonance, the magnetic dipole moments induced in the central particle and the particles in the outer ring oscillate out-of-phase with respect to each other. Fig. 3.12F shows the experimentally measured extinction cross-section of a silicon oligomer, demonstrating this effect [70]. In the experiment, the size of the central particle in the heptamer is varied from sample to sample. The increase in size induces a redshift of the resonant frequency of this particle and, as a consequence, a redshift in the Fano dip in the oligomer spectra. This corroborates the origin of the Fano dip as the interference between the resonant mode of the central particle and the non-resonant mode of the outer ring. For the interested reader in this topic, other examples of Fano interference in all-dielectric configurations can be found in the references [71–74].

3.4.2   Complex nanoantenna shapes

As mentioned earlier, a second possible strategy to achieve larger directivity or more complex scattering patterns from a nanoantenna without introducing additional particles is to complexify the elements as to support higher-order multipolar modes. In the simplest case, all that one needs to consider is a dielectric sphere with a larger overall size. In its most general form, the differential scattering cross-section from the spherical particle becomes (cf. [2], Chapter 4, Section 4.4.4):

$$dS = \frac{1}{(kr)^2}(\sin^2\phi\,|S_1(\cos\theta)|^2 + \cos^2\phi\,|S_2(\cos\theta)|^2) \tag{3.28}$$

with

$$S_1(\cos\theta) = \sum_l \frac{2l+1}{l(l+1)}(a_l\pi_l + b_l\tau_l) \tag{3.29}$$

$$S_2(\cos\theta) = \sum_l \frac{2l+1}{l(l+1)}(a_l\tau_l + b_l\pi_l) \tag{3.30}$$

and the angle-dependent functions π_l and τ_l being

$$\pi_l(\cos\theta) = \frac{P_l^1(\cos\theta)}{\sin\theta} \tag{3.31}$$

$$\tau_l \left(\cos\theta\right) = \frac{\mathrm{d}P_l^1 \left(\cos\theta\right)}{\mathrm{d}\theta} \tag{3.32}$$

where $P_l^1 \left(\cos\theta\right)$ is the associated Legendre function of the first kind and order l. Taking into account that the functions π_l and τ_l have alternating even and odd parity on $\cos\theta$ depending on their order it is possible to show, after some algebraic manipulation, that the forward scattering reduces to

$$dS(\theta = 0°) = \frac{1}{(kr)^2} \sum_l \frac{2l+1}{2} |a_l + b_l|^2 \tag{3.33}$$

and also that in the backward direction $\theta = 180°$ [75]

$$\pi_l \left(-1\right) + \tau_l \left(-1\right) = 0. \tag{3.34}$$

This simple relation implies that, whenever the electric and magnetic multipoles of a certain order have the same amplitude and phase, they destructively interfere in the backward direction. In other words, if a pair of electric and magnetic multipoles of a certain order l fulfill the relation $a_l = b_l$, they do not contribute to the backward scattering. Obviously, particles for which all multipoles are individually compensated will have zero backward scattering. Individual compensation of the different electric and magnetic multipolar modes is, however, not the only mechanism from which a vanishing backward scattering can be obtained. If one considers, for example, a single family of multipoles, either electric or magnetic, it is also possible to obtain vanishing backwards scattering provided the scattering coefficients have amplitudes and phases such that they compensate for the difference in value of the angle-dependent functions of different orders. Both situations described above can be considered a sort of *generalized version of the first Kerker condition*. As an example of the latter, for a particle supporting only dipole and quadrupole modes from a certain family (either electric or magnetic and with all other multipoles from the same family and all multipoles from the other family being zero), zero backward scattering is achieved when

$$3a_1 - 5a_2 = 0 \quad \text{or} \quad 3b_1 - 5b_2 = 0. \tag{3.35}$$

The first expression holds for a particle supporting electric dipole [67] and quadrupole modes only and the second one for a particle supporting magnetic dipole and quadrupole modes only. A schematic of the different situations leading to directional scattering from a particle supporting dipole and quadrupole modes, adapted from reference [75] (see also [76]), is shown in Fig. 3.13A. The highest directionality is achieved when all four modes are excited and compensate each other. The higher is the number of modes, the higher is the directionality of the antenna. This is shown in Fig. 3.13B, adapted from reference [77], in which the scattering pattern from a hypothetical spherical particle supporting different sets of modes is shown. The first panel (top) correspond the previously presented case of realization of the first Kerker condition, $a_1 = b_1$. The second panel (center) shows the scattering pattern from a particle supporting compensated electric and magnetic quadrupole modes only ($a_2 = b_2 \neq 0$
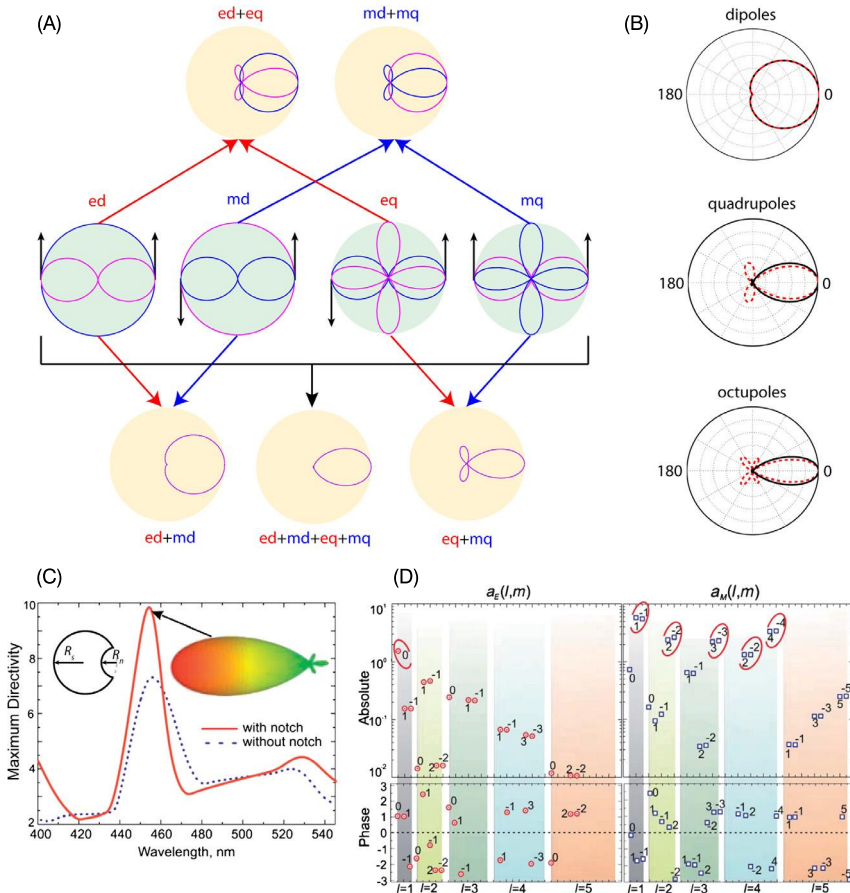
Figure 3.13 (A) Schematic showing directional interference effects from different multipole combinations up to quadrupoles. The central row depicts the modes considered and the black arrows represent whether the scattered field oscillates in phase (downwards arrow) or out of phase (upwards arrow) with the incident one (assumed to propagate from left with the electric field contained in-plane). The resulting patterns arising from different mode combinations are calculated assuming matching phases and amplitudes of the modes. Only the in-plane (purple curves) and out-of-plane (blue curves) scattering patterns are shown for clarity. Adapted from [75]. (B) Scattering patterns corresponding to the situations in which: (top) $a_1 = b_1 \neq 0$ and $a_l = b_l = 0$ for $l > 1$; (center) $a_1 = b_1 = a_2 = b_2 \neq 0$ and $a_l = b_l = 0$ for $l > 2$ (black, solid line) and $a_2 = b_2 \neq 0$ and $a_l = b_l = 0$ for $l \neq 2$ (red, dashed line); (bottom) $a_m = a_n = b_m = b_n \neq 0$ for $m, n < 3$ and $a_l = b_l = 0$ for $l > 3$ (black, solid line) and $a_3 = b_3 \neq 0$ and $a_l = b_l = 0$ for $l \neq 3$ (red, dashed line). Adapted with permission from [77]. © (2014) Optical Society of America. (C) Calculated maximum directivity of a super-directive silicon nanoantenna as a function of wavelength. The antenna consists of a sphere with radius $R_s = 90$ nm and a small hemispherical notch with radius $R_n = 40$ nm. The system is excited by an electric dipole perpendicular to the radius at a distance of around 70 nm from the sphere center. (D) Absolute value and phase of the different electric, $a_E(l, m)$, and magnetic, $a_M(l, m)$, multipolar modes excited in the system at the resonant maximum directivity. Panels (C) and (D) adapted from [78] with permission of The Royal Society of Chemistry. (E) Simulated (left) and measured (center) radiation patterns from the experimental realization of the super-directive antenna (shown in the right) at microwave frequencies. The antenna is made of MgO–TiO$_2$ ceramic (with $n_p \sim 4$) and fed by a small electrical dipole source. Adapted from [79], with permission of AIP Publishing.
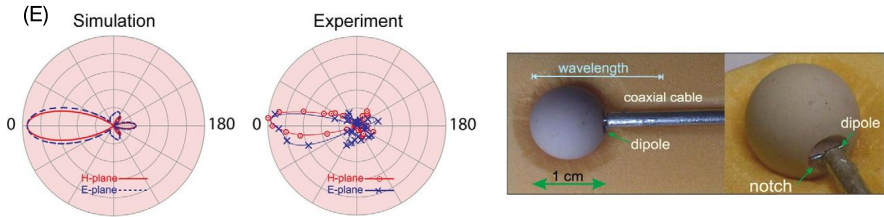
Figure 3.13 (*continued*)

and $a_l = b_l = 0$ for $l \neq 2$) as well as the case in which the particle supports compensated electric and magnetic quadrupole and dipole modes ($a_1 = a_2 = b_1 = b_2 \neq 0$ and $a_l = b_l = 0$, for $l > 2$). Clearly, the latter shows a better directivity. Finally, the third panel (bottom) shows the scattering from a particle supporting compensated electric and magnetic octupole modes only (quadrupoles and dipoles being zero), as well as the case in which all electric and magnetic multipoles up to the octupole are supported and compensated. Of all those cases, the last one provides the largest directivity.

From the theoretical analysis it becomes clear that the larger the number of compensated multipoles, the better directivity can be achieved. The only problem, as usual, is finding an appropriate antenna design to exploit this feature. So far, the most successful proposal is the one depicted in the left inset of Fig. 3.13C. This so-called super-directive dielectric antenna [78] consists of a dielectric spherical particle (made of silicon in this case, with radius $R_s = 90$ nm) and a small notch (considered hemispherical with radius $R_n = 40$ nm). The presence of the notch breaks the symmetry of the system and allows the efficient excitation of higher-order multipoles. While the excitation of these modes is possible using external illumination by plane waves, a more efficient excitation is achieved using a point source, such as a dipole emitter, in the proximity of the antenna. This increase in the excitation efficiency is due to the spatial non-uniformity of the fields created by this kind of source. Fig. 3.13C depicts the simulated maximum directivity of the combined antenna-source system as a function of the excitation wavelength, showing a resonant behavior at around 455 nm, for which a maximum directivity of 10 is achieved. The right inset of this plot represents the radiation pattern of the system. The origin of the large directivity becomes apparent when analyzing the multipolar contributions to the radiation, as plotted in Fig. 3.13D. The calculated amplitudes and phases of the different multipolar modes, as well as the calculated radiation patterns shown below, manifest the origin of the observed directivity as a result of the interference between an electric dipole and a set of magnetic modes consisting of dipoles, quadrupoles, octupoles and even hexadecapoles. This concept of super-directive dielectric antenna has been experimentally demonstrated at microwave frequencies, using a ceramic material and a dipolar feed to excite the antenna [79]. Fig. 3.13E shows the simulated and experimentally measured directivity patterns at the resonant maximum of the directivity of the system. The measured system is shown in the right panel of the graph. The measurements agree well with the numerical calculations demonstrating the feasibility of this design as a compact and directional dielectric nanoantenna. A demonstration at optical frequencies is, however, still to be achieved. For the interested reader in this topic, a plethora of dielectric nanoantennas

of increasingly complex shapes (including rings, cups, v-shaped antennas, etc.) has been studied in the last few years to achieve similarly complex functionalities, such as wavelength-dependent routing, bianisotropy-induced incidence-dependent scattering and many more. Some of this work can be found in the references of this chapter [14,57,80–82].

3.4.3   Substrate and environment influence

Let us now focus on the last strategy to design the multipolar response, and thus the directivity, of an isolated dielectric nanoantenna. As mentioned earlier, it consists of placing the antenna in a complex environment. In this regards, even the presence of a simple substrate, for which an analytical solution exists in the case of spherical particles [83], can significantly alter the scattering properties of the antenna (see, e.g., Chapter 3 in [84]). In the case of a dielectric substrate, the impact of its presence on the modes excited in a nanoantenna depends on its refractive index. As the index increases, the impact becomes more pronounced. The main consequence of the presence of the substrate is the emergence of bi-anisotropy in the system, which follows from magneto-electric coupling effects, affecting only those components that are parallel to the substrate and being strongly enhanced when resonances of the antenna are excited [22]. While the effect of the substrate on the spectral position and amplitude of the modes is only noticeable when its refractive index is moderately high, the impact on the scattering pattern of the antenna, and in particular on its forward-to-backward ratio, can be significant even for low values, being measurable even in the case of a glass substrate [85]. The physical origin of the impact of the substrate can be readily understood on the grounds of dipole emission near interfaces [86] and the affected dipole-dipole interactions. As an example of these effects, Fig. 3.14A shows a comparison of the extinction cross-section and corresponding multipolar contributions from a silicon sphere in air, on top of a glass substrate and on top a silicon one. The magneto-electric coupling becomes apparent in the emergence of an additional electric dipole resonance at the spectral position of the magnetic dipole one, becoming increasingly important as the index of the substrate increases. In the case of a metallic substrate the impact on the modes of the antenna becomes even more important. Due to the presence of free electrons and the associated screening effect optical modes excited in the antenna experience the effect of their mirror images, thus making its scattering characteristic increasingly complex [22,87]. Let us study a particular case to exemplify the kind of effects that arise in this situation. Consider the case of a silicon sphere illuminated by an s-polarized, oblique plane wave. Fig. 3.14B shows the comparison between the calculated extinction cross-section when the particle is placed on top of a glass substrate and when the particle is placed on top of a gold film. The corresponding measured spectra from a silicon particle fabricated by laser ablation are shown in Fig. 3.14C, in which both the co-polarized and cross-polarized scattering intensities are individually plotted. In the case of the gold substrate the higher-energy electric dipole peak presents a broadening with respect to the case of glass (also with respect to the free-standing one) while the lower-energy magnetic one experiences a clear narrowing, increasing its quality factor. It is possible to qualitatively explain this behavior
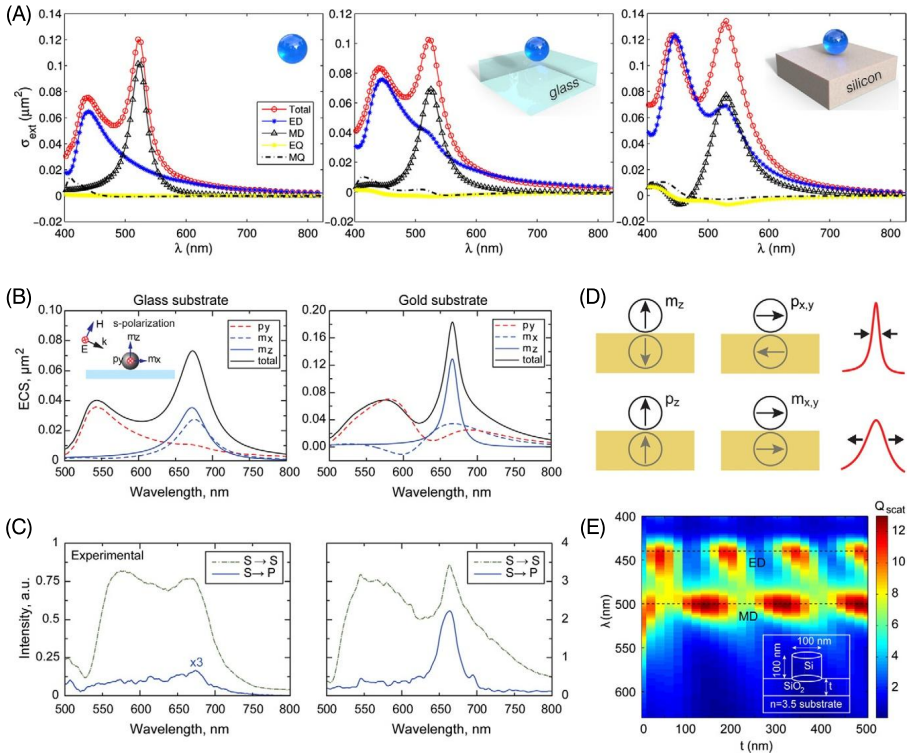
Figure 3.14 (A) Comparison of the extinction cross-section and corresponding multipolar contribution between a silicon sphere (radius $R = 65$ nm) suspended in air (left), deposited on a glass substrate (center) and deposited on a silicon substrate (right). Adapted with permission from [22]. © (2015) American Chemical Society. (B)–(C) Comparison of the (B) calculated extinction cross-section and corresponding multipolar contribution and (C) experimentally measured co- and cross-polarized scattered intensity from a silicon sphere (radius $R = 85$ nm) deposited on a glass substrate (left) and a gold substrate (right) under s-polarized oblique incidence (angle of incidence 65°). In the experiment, the gold substrate is a 40 nm film deposited on a glass substrate. (D) Scheme of the interactions between different dipoles and their mirror images, and corresponding impact on the quality factor of the resonances. Adapted with permission from [87]. © (2016) John Wiley & Sons, Inc. (E) Calculated scattering efficiency from a silicon disk with height and diameter 100 nm deposited on top of a silicon substrate covered with an intermediate silica spacer (as shown in the inset), as a function of the spacer thickness, t. The horizontal dashed lines represent the resonance wavelength of the electric dipole and magnetic dipole modes. Adapted with permission from [88]. © (2013) Optical Society of America.

in simple terms by just studying the interaction of these dipoles with their mirror images. The different cases are schematically summarized in Fig. 3.14D. In the case of vertical (normal to the substrate) magnetic dipoles and horizontal (parallel to the substrate) electric ones their mirror images oscillate out-of-phase, thus reducing the radiative losses and increasing the quality factor of the mode. An opposite situation holds for horizontal magnetic dipoles and vertical electric ones, for which the mirror images oscillate in phase, thus increasing the total dipole moment and the radiative losses, causing the broadening of the associated resonances. In addition to the impact

on the mode characteristics, substrates may also cause the selective excitation of a certain type of mode as a function of the distance between the antenna and the interface [88]. The origin of this selective excitation stems from the standing wave formed between the incident field and the reflected one, which presents alternating nodes and anti-nodes of the electric (magnetic) field as a function of the distance to the interface. Electric (magnetic) modes can only be excited provided the antenna is not placed at a node of the electric (magnetic) field. In the case of dielectric nanoantennas supporting both electric and magnetic modes, specific resonances can be alternatively excited as a function of the distance to the interface. Obviously, this effect is increasingly pronounced as the index of the substrate increases, and even more in the case of a metallic one. Fig. 3.14E illustrates this effect by plotting the simulated scattering cross-section of a silicon nanoantenna deposited on top of a silicon substrate with an intermediate low-index silica spacer as a function of the spacer thickness. The plot clearly reveals the alternating excitation of electric and magnetic dipole resonances in the antenna at different thickness values. Recently, this effect has been used to control the scattering from a single semiconductor nanowire antenna mounted on a microelectromechanical system (MEMS) and placed in front of a metallic mirror [89]. When a voltage is applied to the MEMS the distance between the nanowire and the mirror changes. Consequently, the measured scattering spectra under TM polarization changes according to the selective excitation of the magnetic or the electric resonance in the nanowire. Although just an example, this gives a hint of how even a simple modification of the environment of the antenna can help tailoring its scattering properties.

3.4.4   *Scattering suppression in dielectric nanoantennas*

While most of this chapter has been focused on maximizing the scattering efficiency of dielectric nanoantennas, as well as tailoring their scattering diagram, they may also show interesting properties when it comes to minimizing their scattering. One of the cases in which the scattering from a dielectric nanoantenna is minimized has been already shown in the chapter, though it may have passed unnoticed for the reader unfamiliar with this topic. In Figs. 3.5A and 3.7A we showed the scattering efficiency of dielectric spheres with different refractive indices. In those plots, it can be seen a spectral region in which the scattering associated with the electric dipole is strongly suppressed. This is better seen in Figs. 3.5B and 3.7B, in which the absolute value of the a_1 coefficient is shown, exhibiting a clear minimum reaching near zero. Interestingly, at this spectral position the internal coefficient associated to this mode is non-zero, implying non-zero energy and, thus, a non-vanishing displacement current distribution. This ultimately implies that, at this spectral position, the incident field excites in the sphere a particular oscillating current distribution configured in such a way that does not re-radiate. This nonradiating current configuration, called *anapole*, has its physical origin in the scattering cancellation between the induced Cartesian electric dipole and the dipolar term of a family of Cartesian multipoles referred to as toroidal moments [90]. While the first observation of anapole modes in nanophotonics was done in systems of complex geometries [91] it was soon realized that they could also be observed in the much simpler case of a single dielectric particle [92]. Since

then their study has been extensive and much work can be found now in the literature, including their extension to magnetic modes and higher orders [93], to other geometries [94] as well as their application to inhibition of total scattering (below even the Rayleigh limit [95]), to sub-wavelength lasers designs [96] or to enhanced nonlinear harmonic generation [97], to mention some.

3.5 Conclusions and outlook

As one can see from this chapter, dielectric nanoparticles and nanoantennas represent an excellent playground for controlling and engineering multipolar interference effects. In contrast to conventional plasmonic, which can typically only explore electric multipoles, each dielectric nanoparticle, even of a simple shape, offers a rich set of electric and magnetic multipolar resonances whose phases and amplitudes can be tailored by changing nanoparticle size, shape or environment. This brings excellent opportunities to engineer amplitude, phase and directivity of the light scattered by such particles and nanoantennas. Depending on the application one can enhance or suppress light scattering in certain specific directions and/or narrow down scattering diagrams using multipolar interference. The number and the character of the excited multipoles can be controlled by nanoparticle size, number and geometry. These basic scattering properties build the foundation for applications of dielectric nanoantennas for efficient control of light phase and amplitude with dielectric metasurfaces and metamaterials, enhancement of spontaneous emission, promoting nonlinear effects, and other important application, which will further be discussed in this book.

References

[1] G. Mie, Beiträge zur Optik trüber Medien, speziell kolloidaler Metallösungen, Ann. Phys. 330 (1908) 377–445.

[2] C.F. Bohren, D.R. Huffmann, Absorption and Scattering of Light by Small Particles, Wiley–Interscience, New York, 2004.

[3] A.I. Kuznetsov, A.E. Miroshnichenko, M.L. Brongersma, Y.S. Kivshar, B. Luk'yanchuk, Optically resonant dielectric nanostructures, Science 354 (2016) aag2472.

[4] J.B. Pendry, A.J. Holden, D.J. Robbins, W.J. Stewart, Magnetism from conductors and enhanced nonlinear phenomena, IEEE Trans. Microw. Theory Tech. 47 (1999) 2075–2085.

[5] J. Zhou, T. Koschny, M. Kafesaki, E.N. Economou, J.B. Pendry, C.M. Soukoulis, Saturation of the magnetic response of split-ring resonators at optical frequencies, Phys. Rev. Lett. 96 (2005) 223902.

[6] B.S. Luk'yanchuk, R. Paniagua-Domínguez, I. Minin, O. Minin, Z. Wang, Refractive index less than two: photonic nanojets yesterday, today and tomorrow, Opt. Mater. Express 7 (2017) 1820–1847.

[7] A.B. Evlyukhin, C. Reinhardt, A. Seidel, B.S. Luk'yanchuk, B.N. Chichkov, Optical response features of Si-nanoparticle arrays, Phys. Rev. B 82 (2010) 045404.

[8] A.I. Kuznetsov, A.E. Miroshnichenko, Y.H. Fu, J.B. Zhang, B. Luk'yanchuk, Magnetic light, Sci. Rep. 2 (2012) 492.

[9] Y.H. Fu, A.I. Kuznetsov, A.E. Miroshnichenko, Y.F. Yu, B. Luk'yanchuk, Directional visible light scattering by silicon nanoparticles, Nat. Commun. 4 (2013) 1527.

[10] B.S. Luk'yanchuk, N.V. Voshchinnikov, R. Paniagua-Dominguez, A.I. Kuznetsov, Optimum forward light scattering by spherical and spheroidal dielectric nanoparticles with high refractive index, ACS Photonics 2 (2015) 993–999.

[11] J.A. Schuller, R. Zia, T. Taubner, M.L. Brongersma, Dielectric metamaterials based on electric and magnetic resonances of silicon carbide particles, Phys. Rev. Lett. 99 (2007) 107401.

[12] I. Staude, A.E. Miroshnichenko, M. Decker, N.T. Fofang, S. Liu, E. Gonzales, J. Dominguez, T.S. Luk, D.N. Neshev, I. Brener, Y. Kivshar, Tailoring directional scattering through magnetic and electric resonances in subwavelength silicon nanodisks, ACS Nano 7 (2013) 7824–7832.

[13] A.B. Evlyukhin, R.L. Eriksen, W. Cheng, J. Beermann, C. Reinhardt, A. Petrov, S. Prorok, M. Eich, B.N. Chichkov, S.I. Bozhevolnyi, Optical spectroscopy of single Si nanocylinders with magnetic and electric resonances, Sci. Rep. 4 (2014) 4126.

[14] M.A. Van de Haar, J. Van de Groep, B.J.M. Brenny, A. Polman, Controlling magnetic and electric dipole modes in hollow silicon nanocylinders, Opt. Express 24 (2016) 2047–2064.

[15] S. Liu, M.B. Sinclair, T.S. Mahony, Y.C. Jun, S. Campione, J. Ginn, D.A. Bender, J.R. Wendt, J.F. Ihlefeld, P.G. Clem, J.B. Wright, I. Brener, Optical magnetic mirrors without metals, Optica 1 (2014) 250–256.

[16] A.B. Evlyukhin, C. Reinhardt, B.N. Chichkov, Multipole light scattering by nonspherical nanoparticles in the discrete dipole approximation, Phys. Rev. B 84 (2011) 235429.

[17] R.K. Mongia, P. Bhartia, Dielectric resonator antennas – a review and general design relations for resonant frequency and bandwidth, Int. J. Microwave Mill. 4 (1994) 230.

[18] Q. Zhao, J. Zhou, F. Zhang, D. Lippens, Mie resonance-based dielectric metamaterials, Mater. Today 12 (2009) 60–69.

[19] S. Jahani, Z. Jacob, All-dielectric metamaterials, Nat. Nanotechnol. 11 (2016) 23–36.

[20] A. Garcia-Etxarri, R. Gomez-Medina, L.S. Froufe-Perez, C. Lopez, L. Chantada, F. Scheffold, J. Aizpurua, M. Nieto-Vesperinas, J.J. Sáenz, Strong magnetic response of submicron silicon particles in the infrared, Opt. Express 19 (2011) 4815–4826.

[21] A.B. Evlyukhin, S.M. Novikov, U. Zywietz, R.L. Eriksen, C. Reinhardt, S.I. Bozhevolnyi, B.N. Chichkov, Demonstration of magnetic dipole resonances of dielectric nanospheres in the visible region, Nano Lett. 12 (2012) 3749–3755.

[22] A.E. Miroshnichenko, A.B. Evlyukhin, Y.S. Kivshar, B.N. Chichkov, Substrate-induced resonant magnetoelectric effects for dielectric nanoparticles, ACS Photonics 2 (2015) 1423–1428.

[23] P. Woźniak, P. Banzer, G. Leuchs, Selective switching of individual multipole resonances in single dielectric nanoparticles, Laser Photonics Rev. 9 (2015) 231–240.

[24] V. Valuckas, R. Paniagua-Domínguez, Y.H. Fu, B. Luk'yanchuk, A.I. Kuznetsov, Direct observation of resonance scattering patterns in single silicon nanoparticles, Appl. Phys. Lett. 110 (2017) 091108.

[25] D. Permyakov, I. Sinev, D. Markovich, P. Ginzburg, A. Samusev, P. Belov, V. Valuckas, A.I. Kuznetsov, B.S. Luk'yanchuk, A.E. Miroshnichenko, D.N. Neshev, Y.S. Kivshar, Probing magnetic and electric optical responses of silicon nanoparticles, Appl. Phys. Lett. 106 (2015) 171110.

[26] R. Fenollosa, F. Meseguer, M. Tymczenko, Silicon colloids: from microcavities to photonic sponges, Adv. Mater. 20 (2008) 95–98.

[27] J. Proust, F. Bedu, B. Gallas, I. Ozerov, N. Bonod, All-dielectric colored metasurfaces with silicon Mie resonators, ACS Nano 10 (2016) 7761–7767.

[28] V. Flauraud, M. Reyes, R. Paniagua-Domínguez, A.I. Kuznetsov, J. Brugger, Silicon nanostructures for bright field full color prints, ACS Photonics 4 (2017) 1913–1919.

[29] Z. Dong, J. Ho, Y.F. Yu, Y.H. Fu, R. Paniagua-Dominguez, S. Wang, A.I. Kuznetsov, J.K.W. Yang, Printing beyond sRGB color gamut by mimicking silicon nanostructures in free-space, Nano Lett. 17 (2017) 7620–7628.

[30] E.-H. Cho, H.-S. Kim, B.-H. Cheong, O. Prudnikov, W. Xianyua, J.-S. Sohn, D.-J. Ma, H.-Y. Choi, N.-C. Park, Y.-P. Park, Two-dimensional photonic crystal color filter development, Opt. Express 17 (2009) 8621–8629.

[31] K. Seo, M. Wober, P. Steinvurzel, E. Schonbrun, Y. Dan, T. Ellenbogen, K.B. Crozier, Multicolored vertical silicon nanowires, Nano Lett. 11 (2011) 1851–1856.

[32] L. Cao, J.S. White, J.S. Park, J.A. Schuller, B.M. Clemens, M.L. Brongersma, Engineering light absorption in semiconductor nanowire devices, Nat. Mater. 8 (2009) 643–647.

[33] G. Grzela, R. Paniagua-Dominguez, T. Barten, D. van Dam, J.A. Sanchez-Gil, J. Gómez-Rivas, Nanowire antenna absorption probed with Time-Reversed Fourier Microscopy, Nano Lett. 14 (2014) 3227–3234.

[34] D.R. Abujetas, R. Paniagua-Dominguez, J.A. Sanchez-Gil, Unraveling the Janus role of Mie resonances and leaky/guided modes in semiconductor nanowire absorption for enhanced light harvesting, ACS Photonics 2 (2015) 921–929.

[35] L. Cao, P. Fan, A.P. Vasudev, J.S. White, Z. Yu, W. Cai, J.A. Schuller, S. Fan, M.L. Brongersma, Semiconductor nanowire optical antenna solar absorbers, Nano Lett. 10 (2010) 439–445.

[36] J.A. Schuller, T. Taubner, M.L. Brongersma, Optical antenna thermal emitters, Nat. Photonics 3 (2009) 658–661.

[37] L. Cao, P. Fan, E.S. Barnard, A.M. Brown, M.L. Brongersma, Tuning the color of silicon nanostructures, Nano Lett. 10 (2010) 2649–2654.

[38] M.S. Wheeler, J.S. Aitchison, M. Mojahedi, Three-dimensional array of dielectric spheres with an isotropic negative permeability at infrared frequencies, Phys. Rev. B 72 (2005) 193103.

[39] M. Kerker, D.-S. Wang, C.L. Giles, Electromagnetic scattering by magnetic spheres, J. Opt. Soc. Am. 73 (1983) 765.

[40] M. Nieto-Vesperinas, R. Gomez-Medina, J.J. Saenz, Angle-suppressed scattering and optical forces on submicrometer dielectric particles, J. Opt. Soc. Am. A 28 (2011) 54–60.

[41] A. Alù, N. Engheta, How does zero forward-scattering in magnetodielectric nanoparticles comply with the optical theorem?, J. Nanophotonics 4 (2010) 041590.

[42] J.-M. Geffrin, B. García-Cámara, R. Gómez-Medina, P. Albella, L.S. Froufe-Pérez, C. Eyraud, A. Litman, R. Vaillon, F. González, M. Nieto-Vesperinas, J.J. Sáenz, F. Moreno, Magnetic and electric coherence in forward- and back-scattered electromagnetic waves by a single dielectric subwavelength sphere, Nat. Commun. 3 (2012) 1171.

[43] S. Person, M. Jain, Z. Lapin, J.J. Saenz, G. Wicks, L. Novotny, Demonstration of zero optical backscattering from single nanoparticles, Nano Lett. 13 (2013) 1806–1809.

[44] R. Paniagua-Dominguez, Y.F. Yu, A.E. Miroshnichenko, L.A. Krivitsky, Y.H. Fu, V. Valuckas, L. Gonzaga, Y.T. Toh, A.Y.S. Kay, B. Luk'yanchuk, A.I. Kuznetsov, Generalized Brewster effect in dielectric metasurfaces, Nat. Commun. 7 (2016) 10362.

[45] P.R. Wiecha, A. Cuche, A. Arbouet, C. Girard, G. Colas des Francs, A. Lecestre, G. Larrieu, F. Fournel, V. Larrey, T. Baron, V. Paillard, Strongly directional scattering from dielectric nanowires, ACS Photonics 4 (2017) 2036–2046.

[46] N.V. Voshchinnikov, V.G. Farafonov, Light scattering by dielectric spheroids. I, Opt. Spectrosc. 58 (1985) 81–85.

[47] G.W. Mulholland, C.F. Bohren, K.A. Fuller, Light scattering by agglomerates: coupled electric and magnetic dipole method, Langmuir 10 (1994) 2533–2546.

[48] P. Albella, M.A. Poyli, M.K. Schmidt, S.A. Maier, F. Moreno, J.J. Sáenz, J. Aizpurua, Low-loss electric and magnetic field-enhanced spectroscopy with subwavelength silicon dimers, J. Phys. Chem. C 117 (2013) 13573–13584.

[49] U. Zywietz, M.K. Schmidt, A.B. Evlyukhin, C. Reinhardt, J. Aizpurua, B.N. Chichkov, Electromagnetic resonances of silicon nanoparticle dimers in the visible, ACS Photonics 2 (2015) 913–920.

[50] B. Rolly, B. Bebey, S. Bidault, B. Stout, N. Bonod, Promoting magnetic dipolar transition in trivalent lanthanide ions with lossless Mie resonances, Phys. Rev. B 85 (2012) 245432.

[51] M.K. Schmidt, R. Esteban, J.J. Sáenz, I. Suárez-Lacalle, S. Mackowski, J. Aizpurua, Dielectric antennas – a suitable platform for controlling magnetic dipolar emission, Opt. Express 20 (2012) 13636–13650.

[52] R.M. Bakker, D. Permyakov, Y.F. Yu, D. Markovich, R. Paniagua-Dominguez, L. Gonzaga, A. Samusev, Y.S. Kivshar, B. Luk'yanchuk, A.I. Kuznetsov, Magnetic and electric hotspots with silicon nanodimers, Nano Lett. 15 (2015) 2137–2142.

[53] M.I. Tribelsky, A.E. Miroshnichenko, Giant in-particle field concentration and Fano resonances at light scattering by high-refractive-index particles, Phys. Rev. A 93 (2016) 053837.

[54] T. Shibanuma, P. Albella, S.A. Maier, Unidirectional light scattering with high efficiency at optical frequencies based on low-loss dielectric nanoantennas, Nanoscale 8 (2016) 14184.

[55] P. Albella, T. Shibanuma, S.A. Maier, Switchable directional scattering of electromagnetic radiation with subwavelength asymmetric silicon dimers, Sci. Rep. 5 (2015) 18322.

[56] T. Shibanuma, T. Matsui, T. Roschuk, J. Wojcik, P. Mascher, P. Albella, S.A. Maier, Experimental demonstration of tunable directional scattering of visible light from all-dielectric asymmetric dimers, ACS Photonics 4 (2017) 489–494.

[57] E. Khaidarov, H. Hao, R. Paniagua-Domínguez, Y.F. Yu, Y.H. Fu, V. Valuckas, S.L.K. Yap, Y.T. Toh, J.S.K. Ng, A.I. Kuznetsov, Asymmetric nanoantennas for ultrahigh angle broadband visible light bending, Nano Lett. 17 (2015) 6267–6272.

[58] R. Paniagua-Dominguez, Y.F. Yu, E. Khaidarov, S. Choi, V. Leong, R.M. Bakker, X. Liang, Y.H. Fu, V. Valuckas, L.A. Krivitsky, A.I. Kuznetsov, A metalens with a near-unity numerical aperture, Nano Lett. 18 (2018) 2124–2132.

[59] Y. Ra'di, D.L. Sounas, A. Alù, Metagratings: beyond the limits of graded metasurfaces for wave front control, Phys. Rev. Lett. 119 (2017) 067404.

[60] I.S. Maksymov, I. Staude, A.E. Miroshnichenko, Y.S. Kivshar, Optical Yagi–Uda nanoantennas, Nanophotonics 1 (2012) 65–81.

[61] A.E. Krasnok, A.E. Miroshnichenko, P.A. Belov, Y.S. Kivshar, All-dielectric optical nanoantennas, Opt. Express 20 (2012) 20599–20604.

[62] A.E. Krasnok, A.E. Miroshnichenko, P.A. Belov, Y.S. Kivshar, Huygens optical elements and Yagi–Uda nanoantennas based on dielectric nanoparticles, JETP Lett. 94 (2011) 593–598.

[63] D.S. Filonov, A.E. Krasnok, A.P. Slobozhanyuk, P.V. Kapitanova, E.A. Nenasheva, Y.S. Kivshar, P.A. Belov, Experimental verification of the concept of all-dielectric nanoantennas, Appl. Phys. Lett. 100 (2012) 201113.

[64] R.S. Savelev, A.P. Slobozhanyuk, A.E. Miroshnichenko, Y.S. Kivshar, P.A. Belov, Subwavelength waveguides composed of dielectric nanoparticles, Phys. Rev. B 89 (2014) 035435.

[65] R.M. Bakker, Y.F. Yu, R. Paniagua-Domínguez, B. Luk'yanchuk, A.I. Kuznetsov, Resonant light guiding along a chain of silicon nanoparticles, Nano Lett. 17 (2017) 3458–3464.

[66] U. Fano, Effects of configuration interaction on intensities and phase shifts, Phys. Rev. 124 (1961) 1866.

[67] B. Luk'yanchuk, N.I. Zheludev, S.A. Maier, N.J. Halas, P. Nordlander, H. Giessen, C.T. Chong, The Fano resonance in plasmonic nanostructures and metamaterials, Nat. Mater. 9 (2010) 707–715.

[68] A.E. Miroshnichenko, S. Flach, Y.S. Kivshar, Fano resonances in nanoscale structures, Rev. Mod. Phys. 82 (2010) 2257–2298.

[69] A.E. Miroshnichenko, Y.S. Kivshar, Fano resonances in all-dielectric oligomers, Nano Lett. 12 (2012) 6459–6463.

[70] K.E. Chong, B. Hopkins, I. Staude, A.E. Miroshnichenko, J. Dominguez, M. Decker, D.N. Neshev, I. Brener, Y.S. Kivshar, Observation of Fano resonances in all-dielectric nanoparticle oligomers, Small 10 (2014) 1985–1990.

[71] B. Hopkins, A.N. Poddubny, A.E. Miroshnichenko, Y.S. Kivshar, Revisiting the physics of Fano resonances for nanoparticle oligomers, Phys. Rev. A 88 (2013) 053819.

[72] B. Hopkins, D.S. Filonov, A.E. Miroshnichenko, F. Monticone, A. Alù, Y.S. Kivshar, Interplay of magnetic responses in all-dielectric oligomers to realize magnetic Fano resonances, ACS Photonics 2 (2015) 724–729.

[73] J.H. Yan, P. Liu, Z.Y. Lin, H. Wang, H.J. Chen, C.X. Wang, G.W. Yang, Magnetically induced forward scattering at visible wavelengths in silicon nanosphere oligomers, Nat. Commun. 6 (2015) 7042.

[74] S. Campione, S. Liu, L.I. Basilio, L.K. Warne, W.L. Langston, T.S. Luk, J.R. Wendt, J.L. Reno, G.A. Keeler, I. Brener, M.B. Sinclair, Broken symmetry dielectric resonators for high quality factor Fano metasurfaces, ACS Photonics 3 (2016) 2362–2367.

[75] W. Liu, Y.S. Kivshar, Generalized Kerker effects in nanophotonics and meta-optics, arXiv: 1801.00092v1, 2017.

[76] B.S. Luk'yanchuk, M.I. Tribelsky, Z.B. Wang, Y. Zhou, M.H. Hong, L.P. Shi, T.C. Chong, Extraordinary scattering diagram for nanoparticles near plasmon resonance frequencies, Appl. Phys. A 89 (2007) 259–264.

[77] W. Liu, J. Chang, B. Lei, H. Ma, W. Xie, H. Hu, Ultra-directional forward scattering by individual core-shell nanoparticles, Opt. Express 22 (2014) 16178–16187.

[78] A.E. Krasnok, C.R. Simovski, P.A. Belov, Y.S. Kivshar, Superdirective dielectric nanoantennas, Nanoscale 6 (2014) 7354.

[79] A.E. Krasnok, D.S. Filonov, C.R. Simovski, Y.S. Kivshar, P.A. Belov, Experimental demonstration of superdirective dielectric antenna, Appl. Phys. Lett. 104 (2014) 133502.

[80] R. Alaee, M. Albooyeh, A. Rahimzadegan, M.S. Mirmoosa, Y.S. Kivshar, C. Rockstuhl, All-dielectric reciprocal bianisotropic nanoparticles, Phys. Rev. B 92 (2015) 245130.

[81] J. Li, N. Verellen, D. Vercruysse, T. Bearda, L. Lagae, P. Van Dorpe, All-dielectric antenna wavelength router with bidirectional scattering of visible light, Nano Lett. 16 (2016) 4396–4403.

[82] A. Forouzmand, H. Mosallaei, All-dielectric C-shaped nanoantennas for light manipulation: tailoring both magnetic and electric resonances to the desire, Adv. Opt. Mater. 5 (2017) 1700147.

[83] P.A. Bobbert, J. Vlieger, Light scattering by a sphere on a substrate, Physica A: Stat. Mech. Appl. 137 (1986) 209–242.

[84] B.S. Luk'yanchuk (Ed.), Laser Cleaning, World Scientific, 2002.

[85] A. Pors, S.K.H. Andersen, A.I. Bozhevolniy, Unidirectional scattering by nanoparticles near substrates: generalized Kerker conditions, Opt. Express 23 (2015) 28808–28828.

[86] R.R. Chance, A. Prock, R. Silbey, Molecular fluorescence and energy transfer near interfaces, Adv. Chem. Phys. 37 (1978) 65.

[87] I. Sinev, I. Iorsh, A. Bogdanov, D. Permyakov, F. Komissarenko, I. Mukhin, A. Samusev, V. Valuckas, A.I. Kuznetsov, B.S. Luk'yanchuk, A.E. Miroshnichenko, Y.S. Kivshar, Polarization control over electric and magnetic dipole resonances of dielectric nanoparticles on metallic films, Laser Photonics Rev. 10 (2016) 799–806.

[88] J. van de Groep, A. Polman, Designing dielectric resonators on substrates: combining magnetic and electric resonances, Opt. Express 21 (2013) 26285–26302.

[89] A.L. Holsteen, S. Raza, P. Fan, P.G. Kik, M.L. Brongersma, Purcell effect for active tuning of light scattering from semiconductor optical antennas, Science 358 (2017) 1407–1410.

[90] E.E. Radescu, G. Vaman, Exact calculation of the angular momentum loss, recoil force, and radiation intensity for an arbitrary source in terms of the electric, magnetic, and toroid multipoles, Phys. Rev. E 65 (2002) 046609.

[91] V.A. Fedotov, V. Rogacheva, V. Savinov, D. Tsai, N.I. Zheludev, Resonant transparency and non-trivial non-radiating excitations in toroidal metamaterials, Sci. Rep. 3 (2013) 2967.

[92] A.E. Miroshnichenko, A.B. Evlyukhin, Y.F. Yu, R.M. Bakker, A. Chipouline, A.I. Kuznetsov, B. Luk'yanchuk, B.N. Chichkov, Y.S. Kivshar, Nonradiating anapole modes in dielectric nanoparticles, Nat. Commun. 6 (2015) 8069.

[93] B.S. Luk'yanchuk, R. Paniagua-Domínguez, A.I. Kuznetsov, A.E. Miroshnichenko, Y.S. Kivshar, Hybrid anapole modes of high-index dielectric nanoparticles, Phys. Rev. A 95 (2017) 063820.

[94] A.C. Tasolamprou, O. Tsilipakos, M. Kafesaki, C.M. Soukoulis, E.N. Economou, Toroidal eigenmodes in all-dielectric metamolecules, Phys. Rev. B 94 (2016) 205433.

[95] B.S. Luk'yanchuk, R. Paniagua-Domínguez, A.I. Kuznetsov, A.E. Miroshnichenko, Y.S. Kivshar, Suppression of scattering for small dielectric particles: anapole mode and invisibility, Philos. Trans. R. Soc. A 375 (2017) 20160069.

[96] J.S. Totero Gongora, A.E. Miroshnichenko, Y.S. Kivshar, A. Fratalocchi, Anapole nanolasers for mode-locking and ultrafast pulse generation, Nat. Commun. 8 (2017) 15535.

[97] G. Grinblat, Y. Li, M.P. Nielsen, R.F. Oulton, S.A. Maier, Enhanced third harmonic generation in single germanium nanodisks excited at the anapole mode, Nano Lett. 16 (2016) 4635–4640.

Controlling spontaneous emission with dielectric optical antennas

4

Nicolas Bonod
Aix-Marseille Univ, CNRS, Centrale Marseille, Institut Fresnel, Marseille, France

4.1 Introduction

In this chapter, we describe the concept of all-dielectric nanoantennas and the ability of dielectric nanostructures to tailor the spontaneous photon emission of quantum emitters. Optical antennas aim at tailoring the photon emission process of quantum emitters by increasing or decreasing the Purcell factor and by shaping the emission pattern to collect photons in an efficient way. In this chapter, we first address the basics of both quantum and classical electrodynamics theory, and in particular Fermi's golden rule and the local density of states. Second, we derive analytical expressions that describe the properties of the emission directivity and highlight the interest of a coherent excitation of electric and magnetic modes on the directivity. We describe the main advances that have been reported in the field of all-dielectric and hybrid metal-dielectric directive antennas. Third, we introduce the concepts and basics of fluorescence enhancement, in particular the count rate *per* molecule, excitation rate and collection efficiency. Finally, we present the theory and latest advances of chiral light emission, inhibition of spontaneous emission and magnetic spontaneous emission before providing some perspectives in the conclusion.

4.2 Theory of spontaneous emission

4.2.1 Dipole emission

The theory of spontaneous emission can be well described with the Green's functions. Green's functions were developed by George Green in the 19th century to solve inhomogeneous linear differential equations. Let us consider the inhomogeneous linear differential equation:

$$\mathscr{D}\varphi(\mathbf{r}) = \mathbf{j}(\mathbf{r}) \tag{4.1}$$

defined in a volume V, with known boundary conditions. In the following, $\mathbf{r}$ will be outside the source volume V. The general solution of an inhomogeneous differential equation is the sum of a homogeneous solution $\varphi_{hom}(\mathbf{r})$ and a particular solution

$\varphi_{part}(\mathbf{r})$. $\varphi_{hom}(\mathbf{r})$ is the solution of the homogeneous equation:

$$\mathscr{D}\varphi_{hom}(\mathbf{r}) = 0 \tag{4.2}$$

Green's functions are solutions of the linear differential operator $\mathscr{D}$ when the source term is a Dirac distribution $\delta(\mathbf{r} - \mathbf{r}')$ [1,2]:

$$\mathscr{D}\mathbf{G}(\mathbf{r}, \mathbf{r}') = \delta(\mathbf{r} - \mathbf{r}'). \tag{4.3}$$

Green's functions provide a special solution of the inhomogeneous equation for any inhomogeneity $\mathbf{j}(\mathbf{r})$. The special solution $\varphi_{sp}(\mathbf{r})$ is obtained by the convolution of the Green's function with the source term:

$$\varphi_{sp}(\mathbf{r}) = \int_{V'} \mathbf{G}(\mathbf{r}, \mathbf{r}')\mathbf{j}(\mathbf{r}')dV'. \tag{4.4}$$

In electromagnetism, Green's functions are widely used to solve the Helmholtz equation in the presence of a current source $\mathbf{j}(\mathbf{r})$:

$$\nabla \times \nabla \times \mathbf{E}(\mathbf{r}) - k^2\mathbf{E}(\mathbf{r}) = i\omega\mu_0\mu\mathbf{j}(\mathbf{r}), \tag{4.5}$$

where $k = 2\pi/\lambda = 2\pi n/\lambda_0$ is the wavenumber, λ_0 the wavelength in vacuum, λ the wavelength in the medium of refractive index n. The particularity with the Helmholtz equation is that a current in a given direction x, y or z provides an electric field vector with three components. It turns out that the Green's function must be a tensor. In that case, it is called the dyadic Green's function and is denoted $\overset{\leftrightarrow}{\mathbf{G}}(\mathbf{r}, \mathbf{r}')$.

First, we need to find a solution with Green's functions for all spatial components of the current distribution:

$$\begin{aligned}
\nabla \times \nabla \times \mathbf{G}_x(\mathbf{r}, \mathbf{r}') - k^2\mathbf{G}_x(\mathbf{r}, \mathbf{r}') &= \delta(\mathbf{r} - \mathbf{r}')\mathbf{n_x}, \\
\nabla \times \nabla \times \mathbf{G}_y(\mathbf{r}, \mathbf{r}') - k^2\mathbf{G}_y(\mathbf{r}, \mathbf{r}') &= \delta(\mathbf{r} - \mathbf{r}')\mathbf{n_y}, \\
\nabla \times \nabla \times \mathbf{G}_z(\mathbf{r}, \mathbf{r}') - k^2\mathbf{G}_z(\mathbf{r}, \mathbf{r}') &= \delta(\mathbf{r} - \mathbf{r}')\mathbf{n_z}.
\end{aligned} \tag{4.6}$$

The dyadic Green's function allows for a compact notation of the former equation. The first, second and third column of this tensor are composed of the three $\mathbf{G}_x(\mathbf{r}, \mathbf{r}')$, $\mathbf{G}_y(\mathbf{r}, \mathbf{r}')$ and $\mathbf{G}_z(\mathbf{r}, \mathbf{r}')$ vectorial Green functions. Thanks to the dyadic Green's function, Eq. (4.6) can be cast in a compact form:

$$\nabla \times \nabla \times \overset{\leftrightarrow}{\mathbf{G}}(\mathbf{r}, \mathbf{r}') - k^2\overset{\leftrightarrow}{\mathbf{G}}(\mathbf{r}, \mathbf{r}') = \delta(\mathbf{r} - \mathbf{r}')\overset{\leftrightarrow}{\mathbf{I}}, \tag{4.7}$$

where $\overset{\leftrightarrow}{\mathbf{I}}$ is the unit tensor, also called unit dyad. It can easily be shown that the solution is [2]:

$$\overset{\leftrightarrow}{\mathbf{G}}(\mathbf{r}, \mathbf{r}') = \left(\overset{\leftrightarrow}{\mathbf{I}} - \frac{1}{k^2}\nabla\nabla\right)G(\mathbf{r}, \mathbf{r}') \tag{4.8}$$

with $G(\mathbf{r}, \mathbf{r}') = \frac{\exp(ik|\mathbf{r}-\mathbf{r_0}|)}{4\pi|\mathbf{r}-\mathbf{r_0}|}$.

The solution of the inhomogeneous Helmholtz equation with a source term (Eq. (4.5)) is obtained by adding the solution of the homogeneous differential equation (i.e. Helmholtz equation without source term) $\mathbf{E_h}(\mathbf{r})$, and the special solution φ_{sp} obtained with the convolution defined in Eq. (4.4) when considering the source term $i\omega\mu_0\mu\mathbf{j}(\mathbf{r})$ [2]:

$$\mathbf{E}(\mathbf{r}) = \mathbf{E_h}(\mathbf{r}) + i\omega\mu_0\mu \int_V \overset{\leftrightarrow}{\mathbf{G}}(\mathbf{r}, \mathbf{r}')\mathbf{j}(\mathbf{r}')dV'. \tag{4.9}$$

The question is now to know how to calculate the current source $\mathbf{j}(\mathbf{r})$. A special case of interest for this chapter is the case of an electric harmonic dipole $\mathbf{p}$ located at $\mathbf{r}'$:

$$\mathbf{j}(\mathbf{r}) = -i\omega\mathbf{p}\delta(\mathbf{r} - \mathbf{r}'). \tag{4.10}$$

When plugging Eq. (4.10) in Eq. (4.9), and by assuming $\mathbf{E_h}(0)$, one obtains the field emitted by an electric dipole:

$$\mathbf{E}(\mathbf{r}) = \omega^2\mu_0\mu\overset{\leftrightarrow}{\mathbf{G}}(\mathbf{r}, \mathbf{r}')\mathbf{p}. \tag{4.11}$$

The Poynting theorem states that in the harmonic domain, the radiated power P dissipated by a current density $\mathbf{j}(\mathbf{r})$ (current density that generates the field $\mathbf{E}$) defined in a volume V is $P = -\frac{1}{2}\int_V \text{Re}(\mathbf{j}^*.\mathbf{E})dV$ and is equal to the energy dissipation in the volume V. In the case of an electric dipole $\mathbf{p} = p\mathbf{n_p}$ located at $\mathbf{r}'$, the radiated power is

$$P = \frac{\omega}{2}\text{Im}(\mathbf{p}^*.\mathbf{E}(\mathbf{r}')). \tag{4.12}$$

In a homogeneous environment of dielectric permittivity ϵ, this radiated power simplifies to [3,2]:

$$P_{0,p} = \frac{|\mathbf{p}|^2}{12\pi}\frac{\omega}{\epsilon}k^3. \tag{4.13}$$

When studying spontaneous emission of quantum emitters coupled with dielectric nanostructures, a case of particular interest is the case of an electric or a magnetic dipole radiating electromagnetic energy in an inhomogeneous medium. In the case of homogeneous media, the total field at the location of the dipole $\mathbf{r}'$ is simply equal to the field emitted by the dipole $\mathbf{E_0}(\mathbf{r}')$. On the other hand, in the case of inhomogeneous media, we must consider the self-consistent field that is the sum between the field emitted by the dipole $\mathbf{E_0}(\mathbf{r}')$ and the backscattered field, i.e. the field scattered back to the emitter by the inhomogeneous environment $\mathbf{E_s}(\mathbf{r}')$. In this case, the power radiated by the dipole in the structured environment, normalized with the power radiated in the homogeneous environment $P_{0,p}$, becomes

$$\frac{P}{P_{0,p}} = \frac{\omega}{2P_{0,p}}\text{Im}(\mathbf{p}^*.(\mathbf{E_0}(\mathbf{r}') + \mathbf{E_s}(\mathbf{r}')))$$

$$= 1 + \frac{6\pi\epsilon}{|\mathbf{p}|^2}\frac{1}{k^3}\text{Im}(\mathbf{p}^*.\mathbf{E_s}(\mathbf{r}')). \tag{4.14}$$

A very similar result can be obtained when considering a magnetic dipole oscillating in a structured environment. The important result is that the power radiated by a dipole depends on its electromagnetic environment. By suitably designing the environment of the emitters, it is possible to tailor the radiated power which is exactly the objective of antennas. While this concept can be straightforwardly applied to classical antennas operating at radiofrequencies, it must be adapted when dealing with optical antennas aiming at controlling the spontaneous emission of quantum emitters, which is the aim of the next section.

4.2.2 Spontaneous decay rates

Spontaneous emission refers to the spontaneous decay of a quantum emitter initially in an excited state resulting in the emission of a photon. As we just illustrated, the spontaneous emission process is not an intrinsic property of the emitter and depends on the environment [4]. This fundamental property was discovered relatively recently due to the fast emission process and to the complexity of measuring the emission lifetimes in the visible and near infrared spectrum. The first work unveiling the role of the environment was carried out by Purcell in 1946 who was studying the relaxation time of a nuclear magnetic transition at radiofrequencies coupled with a resonant electrical circuit hosting a single mode characterized by a quality factor Q. In his seminal paper entitled "Spontaneous Emission Probabilities at Radio Frequencies" [5], he defined the factor F_p providing the decrease of the relaxation time τ compared to the relaxation time in the homogeneous environment τ_0 as $\tau = \tau_0/F_p$ with:

$$F_p = \frac{3}{4\pi^2}\lambda^3 \frac{Q}{V_\alpha},\tag{4.15}$$

where λ is the emission wavelength in the cavity, Q is the quality factor of the cavity and V_α its volume. This factor, now called the Purcell factor, shows that the cavity greatly affects the relaxation time thanks to the excitation of a mode, and that the decrease of relaxation time linearly depends on the quality factor of the cavity Q. While the volume V_α was originally defined in [5] as the geometric volume of the cavity, V_α is actually the volume of the mode α. It was highlighted in 2010 that the conventional definition of the mode volume that depends on the product $\epsilon|E|^2$ cannot be applied in plasmonics and more generally in nano-optics [6]. The exact definition of the mode volume has been at the core of intense efforts over the last years in the context of resonant states, also called quasi-normal modes (QNM) [7–9]. It turns out that the effective volume is a complex volume and must be defined as $V_\alpha = \frac{1}{(\mathbf{n_p}.\mathbf{E}_\alpha(\mathbf{r}))^2}$ where $\mathbf{E}_\alpha(\mathbf{r})$ is the complex QNM field taken at position $\mathbf{r}$ associated with the complex eigenfrequencies.

Drexhage confirmed the crucial role of the environment on the spontaneous emission of quantum emitters in 1970 by measuring the fluorescence decay time of monomolecular layers of an europium dibenzoylmethane complex at varying distances from an interface [10]. This study opened the way to a huge field of research

with a wide range of nano/microstructures such as photonic crystals [11] or more recently optical antennas [10,12,13].

The spontaneous decay rates defined as the inverse of the lifetimes $\gamma_t = 1/\tau$ for a two-level quantum system are predicted by Fermi's golden rule [2]. This rule predicts the probability of transition between an initial state $|i>$ with energy E_i and final states $|f>$ that all have energy E_f. We consider the initial state of the emitter to be the excited state $|e>$ and the final state to be the ground state $|g>$, and a transition frequency ω_0 between energies $E_i \equiv \hbar\omega_i$ and $E_f \equiv \hbar\omega_f = \hbar\omega_k$, $E_f - E_i = \hbar\omega_0$. The initial state of the electromagnetic field is the vacuum state (no photon) $|0>$ and the final state corresponds to one photon characterized by a frequency ω and mode $\mathbf{k}$, $|1_{\omega_k}>$. We consider the states of the system "emitter + field". The initial and final states of this combined system are, respectively, $|i>=|e>|0>$ and $|f>=|g>|1_{\omega_k}>$.

The interaction Hamiltonian of the system is $\hat{H} = -\hat{\mathbf{p}}.\hat{\mathbf{E}}$ in the electric dipolar approximation. $\hat{\mathbf{p}} = \tilde{\mathbf{p}}(|e><g| + |g><e|)$ is the electric dipole moment operator, $\tilde{\mathbf{p}}$ is the electric dipolar transition moment, defined by $\tilde{\mathbf{p}} = <g|\hat{\mathbf{p}}|e>$ and assumed to be real. $\mathbf{E}$ is the electric field operator and is obtained with the annihilation and creation operators $\hat{a}_\mathbf{k}(t) = \hat{a}_\mathbf{k}(0)e^{-i\omega_k t}$ and $\hat{a}_\mathbf{k}^\dagger(t) = \hat{a}_\mathbf{k}^\dagger(0)e^{i\omega_k t}$ by summation over all the modes $\mathbf{k}$:

$$\mathbf{E} = \sum_\mathbf{k} \sqrt{\frac{\hbar\omega_k}{2\epsilon_0}} \left[\mathbf{u}_\mathbf{k}(\mathbf{r}, \omega_k)\hat{a}_\mathbf{k}(0)e^{-i\omega_k t} + \mathbf{u}_\mathbf{k}^*(\mathbf{r}, \omega_k)\hat{a}_\mathbf{k}^\dagger(0)e^{i\omega_k t} \right] \tag{4.16}$$

where $\mathbf{u}_\mathbf{k}(\mathbf{r}, \omega_k)$ are the normal modes that satisfy the wave equation:

$$\nabla \times \nabla \times \mathbf{u}_\mathbf{k}(\mathbf{r}, \omega_k) - k^2 \mathbf{u}_\mathbf{k}(\mathbf{r}, \omega_k) = 0 \tag{4.17}$$

and the orthogonality relation:

$$\int_\infty \mathbf{u}_\mathbf{k}(\mathbf{r}, \omega_k).\mathbf{u}_{\mathbf{k}'}^*(\mathbf{r}, \omega_{k'})d^3\mathbf{r} = \delta_{\mathbf{k}\mathbf{k}'}. \tag{4.18}$$

In the weak-coupling regime, the decay rates can be calculated by the Fermi's golden rule [2]:

$$\gamma_t = \frac{2\pi}{\hbar^2} \sum_f |<f|\hat{H}|i>|^2 \delta(\omega_i - \omega_f). \tag{4.19}$$

When plugging the expression of the field operator Eq. (4.16) in the Fermi's golden rule, one obtains

$$\gamma_t = \frac{\omega}{3\hbar\epsilon_0} |\tilde{\mathbf{p}}|^2 \rho_{\tilde{p}}(\mathbf{r}', \omega_0), \tag{4.20}$$

with $\rho_{\tilde{p}}(\mathbf{r}', \omega_0) = 3 \sum_\mathbf{k} \left[\mathbf{n}_{\tilde{p}}.(\mathbf{u}_\mathbf{k}\mathbf{u}_\mathbf{k}^*).\mathbf{n}_{\tilde{p}} \right]$ (with $\tilde{\mathbf{p}} = \tilde{p}\mathbf{n}_{\tilde{p}}$). $\rho_{\tilde{p}}(\mathbf{r}', \omega_0)$ is the so-called partial local density of states. Let us recall that $\tilde{\mathbf{p}}$ is assumed to be real. Expression

in Eq. (4.20) shows that the spontaneous decay rate depends on the local density of states, i.e. the number of available states **k** associated with the ground states. Note also that this quantity depends on the orientation of the emitter, which is why we call it "partial". The important conclusion is that a modification of the local density of states modifies the spontaneous decay rates γ_t.

The Green's tensor is very convenient in writing the expression of the decay rates. For that purpose, one writes the Green's function with respect to the summation of all the modes [2]:

$$\mathrm{Im}(\overleftrightarrow{\mathbf{G}}(\mathbf{r}, \mathbf{r})) = \frac{\pi c^2}{2\omega} \sum_{\mathbf{k}} \left[\mathbf{u}_{\mathbf{k}}^*(\mathbf{r}, \omega_{\mathbf{k}}) \mathbf{u}_{\mathbf{k}}(\mathbf{r}, \omega_{\mathbf{k}}) \right] \delta(\omega - \omega_{\mathbf{k}}). \tag{4.21}$$

The partial local density of states at the frequency ω_0 and location $\mathbf{r}'$ can be simply cast in the form

$$\rho_{\tilde{p}}(\mathbf{r}', \omega_0) = \frac{2\omega_0}{\pi c^2} \left[\mathbf{n}_{\tilde{p}}.(\mathrm{Im}(\overleftrightarrow{\mathbf{G}}(\mathbf{r}', \mathbf{r}'))).\mathbf{n}_{\tilde{p}} \right]. \tag{4.22}$$

When the orientation is unknown and has to be averaged over the three fundamental orientations, $\rho_{\tilde{p}}(\mathbf{r}', \omega_0)$ describes the total local density of states and has to be calculated through the trace of the dyadic Green tensor:

$$\rho_{\tilde{p}}(\mathbf{r}', \omega_0) = \frac{2\omega_0}{\pi c^2} \mathrm{Im} \left(Tr(\overleftrightarrow{\mathbf{G}}(\mathbf{r}', \mathbf{r}'))) \right). \tag{4.23}$$

From Eq. (4.20), the normalized decay rate of a quantum emitter in a structured environment is

$$\frac{\gamma_t}{\gamma_0} = 1 + \eta \frac{6\pi \epsilon}{|\tilde{\mathbf{p}}|^2} \frac{1}{k^3} \mathrm{Im}(\tilde{\mathbf{p}}^*.E_s(\mathbf{r}')) \tag{4.24}$$

where we added η the intrinsic quantum yield of the quantum emitter , and γ_0 is the decay rate in the homogeneous background. For an ideal two-level quantum emitter, $\eta = 1$, this expression which involves the dipolar transition moment, $\tilde{\mathbf{p}} = <g|\hat{\mathbf{p}}|e>$ is identical to the expression of the normalized emitted power by a classical dipole in Eq. (4.14), which involves the dipolar moment **p**:

$$\frac{\gamma_t}{\gamma_0} = \frac{P}{P_0}. \tag{4.25}$$

The important conclusion of this section is that the normalized decay rates derived in the framework of quantum electrodynamics with Fermi's golden rule under a weak coupling regime can be predicted with the classical Maxwell equations. Let us stress that a structured environment does not only affect the decay rate of a quantum emitter but does also affect its emission frequency. This frequency shift is usually called the Lamb shift. While the decay rate is described by the imaginary part of the Green's tensor, the Lamb shift is described by the real part of the Green's tensor [2,14,15].
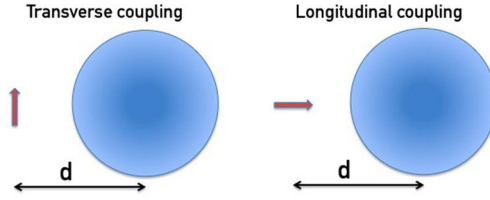
Figure 4.1 Dipole orientation compared with the particle. Left: transverse coupling. Right: longitudinal coupling.

It is important to note that the interaction Hamiltonian between the emitter and the electromagnetic field involves only the electric transition dipole $\tilde{\mathbf{p}}$ that appears in Eq. (4.24). However, in a more general case, the Hamiltonian involves the magnetic dipole transition (which couples to the magnetic component of light) and the electric quadrupole that is involved when the gradient of the electric field at the position of the emitter cannot be neglected. For a homogeneous environment, a dipolar approximation is reasonable since the size of the quantum emitter is much smaller than the wavelength. The curl and the gradient of the electric field are therefore negligible at the scale of the emitter leading to negligible magnetic dipole and electric quadrupole components in the interaction Hamiltonian. This approximation is not valid however for emitters whose electric dipole transition is symmetry forbidden (such as with rare-earth cations) leading to electric dipole and magnetic dipole transitions of similar amplitude [16]. Furthermore, in the vicinity of optical resonators, the curl and gradient of the electric field can be non-negligible, making the dipole approximation no longer valid. This case was discussed theoretically in the literature [17,18] but never observed experimentally. In the case of the magnetic transition dipole, a similar derivation can be performed using Fermi's golden rule.

We consider the fundamental case of an electric or magnetic dipole emitter coupled with an optically resonant particle. At this stage, we provide a general formalism to derive analytical expressions of the normalized decay rates, and we do not need to specify the composition of the optical resonator (metal or dielectrics). We just need to consider a polarizable particle behaving as induced electric and magnetic dipole or quadrupole. We need to distinguish two orientations of the dipole source with respect to the particle: (1) the longitudinal orientation (L) for which the dipole is oriented in the radial direction, (2) the transverse orientation (T) for which the dipole is normal to the radial direction (see Fig. 4.1). The normalized decay rate is [19,20]

$$
\tilde{\gamma}_{tot}^{L,(u)} = 1 + \mathrm{Re}[-9\frac{e^{2ikd}}{(kd)^6}(1-ikd)^2 u_1
$$

$$
+ 45\frac{e^{2ikd}}{(kd)^8}(ik^2d^2 - 3kd - 3i)^2 u_2], \tag{4.26}
$$

$$
\tilde{\gamma}_{tot}^{T,(u)} = 1 + \mathrm{Re}[-\frac{9e^{2ikd}}{4(kd)^6}(1-ikd-k^2d^2)^2 u_1
$$

$$
+ 15\frac{e^{2ikd}}{(4kd)^8}(-k^3d^3 - 3ik^2d^2 + 6kd + 6i)^2 u_2
$$

$$+ \frac{9e^{2ikd}}{4(kd)^4}(kd+i)^2 v_1$$

$$+ 15\frac{e^{2ikd}}{(kd)^6}(-k^2d^2 - 3ikd + 3)^2 v_2], \tag{4.27}$$

where d is the distance separating the emitting dipole from the center of the particle, u and v denoting either the electric e or magnetic h, and u_n and v_n denoting either the electric a_n or magnetic b_n scattering Mie coefficients. If $u = e$, $u_n = a_n$, $v_n = b_n$ and *vice versa*, if $u = h$, $u_n = b_n$, $v_n = a_n$. This equation is also valid for plasmonic particles but in this case, the magnetic coefficients are negligible [21]. When comparing the two expressions in Eq. (4.26) for the transverse case and in Eq. (4.26) for the longitudinal case, we can see that the transverse case has two extra crossed terms, meaning that the electric (magnetic) response of a scatterer affects the decay rates of a magnetic (electric) emitter. This is not the case in the longitudinal coupling where the decay rates of an electric (magnetic) dipole can be modified only by the electric (magnetic) responses of the scatterer. All these expressions tend to 1 when the emitter-to-particle distance d increases since the coupling becomes negligible. The longitudinal coupling provides the strongest response and is well indicated to maximize the decay rates. This requires a specific control of the orientation of the emitter with respect to the optical cavity. It is also important to note that the electric or magnetic decay rates can also be calculated when the emitter is coupled with more complex nanostructures, in particular clusters of spheres [19] or arbitrary geometries [22] (Fig. 4.2).

4.3 Controlling the emission directivity

4.3.1 Introduction

The directivity of emitters in the far field is classically weak since the far-field radiation of all multipolar orders feature symmetric patterns. It means that half of the energy is emitted in a half plane, the other half being emitted in the opposite half plane. The most common example is generally given by the electric dipole which features two out-of-plane lobes. One of the objectives of optical antennas is to modify the electromagnetic coupling to quantum emitters in order to improve the collection of emitted photons for a given optical set-up with limited numerical aperture. The gain in directivity D_{dBi} is defined by the ratio between the radiated intensity in the direction of interest I and the total radiated power of the antenna P_{rad}: $D_{\text{dBi}} = 10\log(4\pi I/P_{\text{rad}})$. Optical elements are therefore coupled with the emitter in order to maximize the radiant intensity in the direction of the collective element such as a microscope objective or an optical waveguide. Different strategies can be followed to achieve this goal.

The high potential of dielectric particles to collect light emission can be intuitively understood by the fact that in optical waveguides, light is guided in high refractive index materials. The ability of dielectrics to collect light emission by electric dipoles was first studied in the context of a harmonic electric dipole in air above a dielectric substrate in 1977 [23,24]. In particular, it was shown that most of the energy was
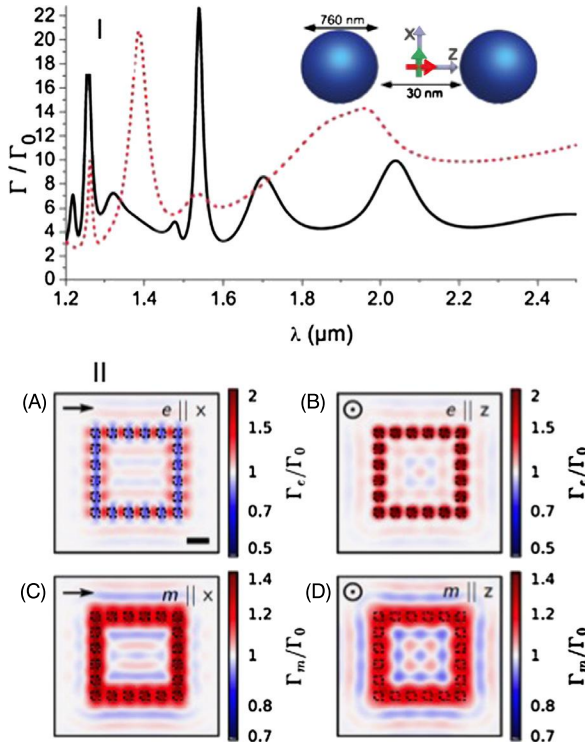
Figure 4.2 I. Normalized decay rates of an electric or magnetic emitting dipole coupled with a dimer of silicon particles 720 nm in diameter (emitter-to-particle surface distance of 15 nm, embedding medium of refractive index 1.45). Taken from [20]. II. Calculation of the normalized electric and magnetic decay rates of electric (ED) (A, B) and magnetic dipoles (MD) (C, D) 30 nm above a square assembly of 20 dielectric nanocubes made of Si at the wavelength $\lambda_0 = 500$ nm. Taken from [22].

emitted toward the high refractive index medium. The motivation of such studies was to collect the emission of fluorescent emitters for applications in microscopy. It was shown that the collection of light by a planar interface is optimized when the emitter is close to the interface. In particular, in the case of a glass-water interface, up to 72% of the power emitted by an orientationally averaged electric dipole can be collected by a glass substrate with refractive index 1.5. More recently, dielectric microspheres were used to enhance the excitation and to collect the fluorescence signal [25]. Different materials can be considered with refractive index slightly larger than the refractive index of water such as glass, latex, or polystyrene (with refractive index ≈ 1.6). By acting on both excitation and collection, dielectric microspheres made of cost effective and lossless dielectrics are good candidates to design optical antennas [26–28]. The need for compactness and integrated devices motivated the development of smaller scatterers. Scatterers with sizes typically smaller than the wavelength can be considered for that purpose if they resonantly interact with light. Two classes of materials can therefore be considered: metals for exciting localized surface plasmon resonances and high (or moderate) refractive index materials for exciting Mie resonances [29].

Plasmonic antennas attracted attention first in the 2000s before the rise of dielectric antennas in the 2010s [30].

Plasmonic nanoantennas have benefited from intense efforts in terms of design and nanofabrication and several geometries had been proposed first to enhance the near-field intensities and second to tailor the emission patterns [31,32]. In particular, dimers of plasmonic particles provide intense near-field intensities in the nanogap separating the neighboring particles [33,34]. Also, they allow for an efficient tuning of the resonance frequency by simply modifying the nanogap length [35–37]. A hybridization model, inspired from chemical bonds, allows a simple intuitive explanation for the frequency redshift when decreasing the nanogap length, and the concept of bright and dark modes [38,39]. Regarding the emission directivity, the concept of Yagi–Uda antennas, very well known in telecommunications, was downscaled to the nanometer scale with plasmonic particles [40,41]. Yagi–Uda antennas are composed of a reflector, a feed element and several collectors [40]. The reflector is typically the largest element of this directive antenna, the feed element is made of a particle of intermediate size whose plasmon resonance matches the emission spectrum while the collector is composed of several self similar smaller particles. The reflector or collector behavior of particles depends on their shape and location with respect to the emitter [42]. The first experimental report involving a Yagi–Uda antenna composed of 5 elements (1 reflector, 1 feed and 3 collectors) was published in 2010. Gains in directivity as high as 6 dB were reported by coupling colloidal quantum dots with a Yagi–Uda antenna [43]. A promising alternative consists in replacing the feed by III–V nanowires, opening the route towards electrically driven optical Yagi–Uda antenna emitters [44].

Let us now address an important question related to optical antennas: how can optical resonant scatterers strongly affect the emission pattern of quantum emitters? In order to answer this question, it is enlightening to study first the reflector or collector behavior of a single particle behaving as an induced electric dipole coupled with an emitting electric dipole. In a second step, we will extend this model to the case of an electric dipole coupled with an optically resonant dielectric scatterer hosting an induced electric dipole *plus* an induced magnetic dipole.

4.3.2   Theory of directional light emission

Let us consider an electric dipole oriented along the z-axis (see Fig. 4.3). The excitation field emitted by the electric dipole $\mathbf{p}_{em}$ at the position of the scatterer (at its center) is composed of three terms: the near field which decays as $\frac{1}{r^3}$, the intermediate field which decays as $\frac{1}{r^2}$ with a π phase shift compared with the near and far fields, and the far field which decays as $\frac{1}{r}$ [2]

$$
\begin{aligned}
\mathbf{E}_{\text{exc}}(d) = \mathbf{E}_{\text{inc}}(d) &= \frac{e^{ikd}}{4\pi\epsilon_m\epsilon_0 d^3}\big[k^2 d^2(\hat{\mathbf{z}}\times\mathbf{p}_e m)\times\hat{\mathbf{x}} \\
&\quad + (1-ikd)(3(\hat{\mathbf{x}}\cdot\mathbf{p}_{em})\hat{\mathbf{x}} - \mathbf{p}_{em})\big] \\
&= -\frac{e^{ikd}}{4\pi\epsilon_m d^3}(1-ikd-k^2 d^2)\hat{\mathbf{z}} \quad\quad (4.28)
\end{aligned}
$$
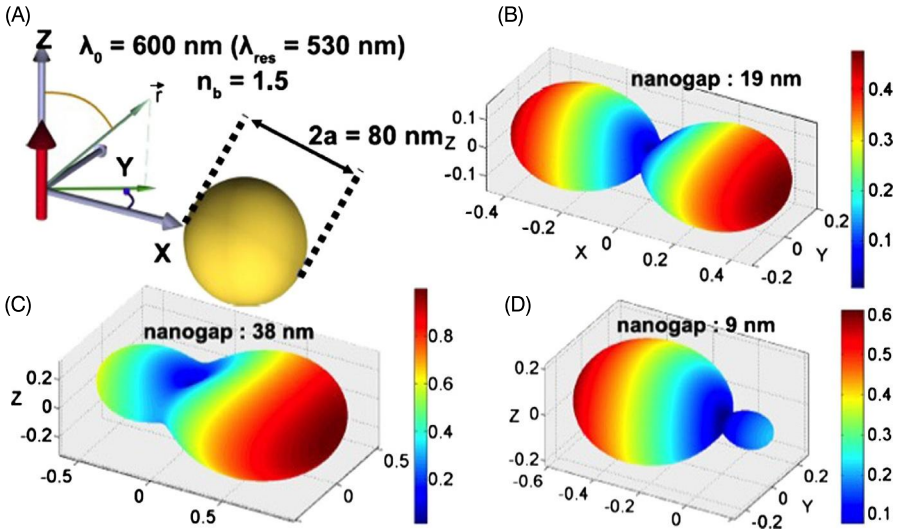
Figure 4.3 Emission directivity. (A) Sketch of the model under study: an electric dipolar emitter oriented along the Oz axis is coupled with a plasmonic nanoparticle of diameter $2a$, whose center is located at a distance d from the emitter along the Ox axis. The embedding medium has a refractive index of 1.5. The emission wavelength is 600 nm in vacuum and 530 nm in the embedding medium. (B–D) 3D emission patterns calculated for three different emitter-to-particle distances d: (A) 19 nm, (B) 38 nm, (C) 9 nm. Reprinted with permission from Brice Rolly, Brian Stout, Sebastien Bidault, Nicolas Bonod, Crucial role of the emitter–particle distance on the directivity of optical antennas, Optics Letters 36 (2011) 3368–3370, Optical Society of America.

where k is the wavenumber. It turns out that the induced dipolar moment $\mathbf{p}_{in}$ in the sphere is

$$\mathbf{p}_{in} = -\alpha \frac{e^{ikd}}{4\pi d^3}(1 - ikd - k^2 d^2)\hat{\mathbf{z}}. \tag{4.29}$$

The electric dipole polarizability α can be simply calculated with the electric Mie coefficient a_1. It is important to stress that the dipole induced in the sphere is coherent with respect to the source dipole. The emission directivity in the far field can be predicted by calculating the Poynting vector that results from the interference between the two electric fields and the two magnetic fields. More precisely, we wrote for $\cos \phi > 0$ and $r \gg d$ the Poynting vector $\mathbf{P}$ of the field emitted by the two dipoles ($\mathbf{p}_{in}$ and $\mathbf{p}_{em}$) and then added the Poynting vector symmetric with respect to the origin $\mathbf{P}(r, \pi - \theta, \pi + \varphi)$ [45]:

$$\Delta\mathbf{P}(r, \theta, \varphi) = \mathbf{P}(r, \theta, \varphi) + \mathbf{P}(r, \pi - \theta, \pi + \varphi)$$
$$= \frac{\omega^3 k |p_1||p_2|}{8\pi^2 \epsilon_0 c^2 r^2} \{\sin \phi \sin[kd \sin \theta \cos \varphi]\} \sin^2 \theta \, \mathbf{e_r}$$

where $\phi = \arg(p_{em}/p_{in})$ is the relative phase of the two dipoles. This expression confirms that, for small parameters kd, the directivity is directly linked to the sign of

$\sin(\phi)$, i.e. to the capacitive or inductive behavior of the dipolar metallic particle [40]. When considering an emission along the x-axis, $\sin\theta = \cos\varphi = 1$, the last expression simplifies to

$$\Delta\mathbf{P}(x, d) = \frac{\omega^3 k |p_1||p_2|}{8\pi^2\epsilon_0 c^2 x^2}\sin\phi\sin(kd)\widehat{\mathbf{x}}. \tag{4.30}$$

In this case, the direction of emission can be predicted by the difference of phase between the dipolar emitter ($\mathbf{p_{em}} \cdot \widehat{\mathbf{z}}$) and the induced electric dipole in the particle ($\mathbf{p_{in}} \cdot \widehat{\mathbf{z}} = -\alpha\frac{e^{ikd}}{4\pi d^3}(1 - ikd - k^2 d^2)$) [42]. The phase ϕ is a nonlinear function of kd:

$$\phi(kd) = \mathrm{Arg}\,\frac{\mathbf{p_{in}} \cdot \widehat{\mathbf{z}}}{\mathbf{p_{em}} \cdot \widehat{\mathbf{z}}} = \mathrm{Arg}\left(-\alpha e^{ikd}(1 - ikd - k^2 d^2)\right). \tag{4.31}$$

This phase term is very interesting to study since it contains most of the information on the directivity. It contains two terms: $\phi(kd) = \phi_\alpha(kd) + \phi_d(kd)$ with

$$\phi_\alpha(kd) = \mathrm{Arg}(\alpha), \tag{4.32}$$

$$\phi_d(kd) = \mathrm{Arg}\left(-e^{ikd}(1 - ikd - k^2 d^2)\right). \tag{4.33}$$

Two terms contribute to $\phi_d(kd)$: the first term e^{ikd} describes the far-field propagation while the second term $1 - ikd - k^2 d^2$ describes the near-field coupling between the two dipoles. When $kd \to 0$, $\phi_d \to \pi$ and $\sin(\phi) \to -\sin[\arg(\alpha)] < 0$ since $\arg(\alpha) \in [0, \pi]$. When plugging $\sin(\phi) < 0$ in Eq. (4.30), one obtains $\Delta\mathbf{P} < 0$, meaning that most of the energy goes in the $-0x$ direction: the particle behaves like a reflector. This property does not depend on the size and composition of the particle. When the emitter is close to the particle, $kd \to 0$, the particle reflects the light emitted by the dipole. When kd increases, ϕ decreases and achieves its minimum of $\phi \approx \frac{3\pi}{4}$ when $kd = \sqrt{2}$. Under this condition, $kd = \sqrt{2}$, and the particle collects light, $\Delta\mathbf{P} > 0$ if $\phi_\alpha < \pi/4$ [42]. Let us stress that the phase due to the polarization ϕ_α shifts from π for the shortest wavelengths to 0 for the largest wavelengths with a maximum of phase variation around the resonance. This means that the condition $\phi_\alpha < \pi/4$ (condition corresponding to a collector behavior) is observed for wavelengths larger than the resonance wavelength. Hence, at the emission wavelength, we understand why large particles are used to reflect light while smaller particles are used to collect light. We also understand why, for small particles, the directivity is very sensitive to the emitter-to-particle distance.

Let us now go further by considering a dielectric resonator hosting in addition to an electric dipolar resonance, a magnetic dipolar resonance. Subwavelength sized dielectric Mie scatterers have benefited from intense efforts in radiofrequencies [46] and more recently in visible and near infrared frequencies [47]. Sub-micron titania particles were numerically investigated in 2010 to tailor the direction of light emission of quantum emitters and to enhance the near electric field intensity [48]. The idea was to combine the advantages of metallic antennas to enhance the decay rates

and of Mie resonators to achieve high directivity. In 2011, the problem of an emitter coupled with a single Si particle was considered. Very interestingly, it was shown that a single Si particle behaves like an effective Huygens source and can switch the directivity of emission in the forward or backward scattering by simply tuning the emission frequency [49]. The concept of all-dielectric Yagi–Uda optical antennas was also introduced in the same study by coupling an emitter to three silicon particles, one forming the reflector, two forming the collector. It was also suggested to further increase the directivity by coupling additional particles in the collector element. This was done in 2012 by the same group by considering four self-similar particles in the collector [50] (Fig. 4.4). Besides the control of directivity, the authors also studied the enhancement of the Purcell factor and made a comparison with plasmonic particles.

The extension of this dipolar model to particles hosting electric and magnetic dipolar resonances is equivalent to extending the so-called Kerker conditions to the near field. Let us briefly summarize that the Kerker conditions were originally established in the case of a magnetic scatterer illuminated from the far field [51] and were extended to the case of purely dielectric particles in 2011 [52,53]. The first Kerker condition corresponds to a maximum of forward scattering associated with a vanishing backward scattering while the second Kerker condition corresponds to a minimum of forward scattering. The observation of Kerker conditions in nonmagnetic particles is allowed by the excitation of electric and magnetic induced dipoles. While the conventional Kerker conditions are established when exciting a scatterer from the far-field region, typically with a plane wave or a collimated beam, this concept can be extended to the near field by exciting a single high refractive index particle with an electric dipolar emitter. The key difference between the two configurations is the crucial role of the difference of phase between the exciting electric dipole and the two dipoles induced in the scatterer. The method is the same as before when we considered electric dipole resonances. The difference is that the emitting electric dipole now also induces a magnetic dipole through its magnetic field emission:

$$\mathbf{H}_{\mathrm{p}}(r\hat{\mathbf{r}}) = \frac{e^{ikr}}{4\pi\varepsilon_m\epsilon_0\mu_0\omega r}k^3(1+\frac{i}{kr})\hat{\mathbf{r}}\times\mathbf{p} \tag{4.34}$$

due to the resonant magnetic response of the dielectric scatterer. The Poynting vector results now from the interference between the electric and magnetic fields emitted by two electric dipoles and one magnetic dipole [54] (Fig. 4.4). By introducing the coupling parameters $\gamma_e = -e^{ikd}\frac{a^3}{d^3}(1-ikd-k^2d^2)$ and $\gamma_m = e^{ikd}\frac{a^3}{d^3}(ikd+k^2d^2)$, and the polarizabilities $\tilde{\alpha} = i\frac{3}{2k^3a^3}a_1; \tilde{\beta} = i\frac{3}{2k^3a^3}b_1$, the time-averaged Poynting vector can be cast in the form

$$\mathbf{P}(x, y, z) = \frac{\omega k^3}{32\pi^2 r^2\epsilon_0\epsilon_m} \times \tag{4.35}$$

$$\left\{(1-x^2)|1+\gamma_e\tilde{\alpha}e^{-ikdz}|^2 + (1-y^2)|\gamma_m\tilde{\beta}|^2 \right. \tag{4.36}$$

$$\left. + 2z\Re[\gamma_m^*\tilde{\beta}^*e^{ikdz}(1+\gamma_e\tilde{\alpha}e^{-ikdz})]\right\}\hat{\mathbf{r}}.$$

Let us first optimize the collecting behavior, a situation that corresponds to the first Kerker condition for the near-field excitation. This condition is satisfied when the Poynting vector along the $-z$ direction, $\mathbf{P}(0, 0, -z)$, is minimized:

$$\mathbf{P}(0, 0, -r) \cong \frac{\omega}{32\pi^2\epsilon_m\epsilon_0 r^2}k^3(|\gamma_m\tilde{\beta}|^2 + |1 + \gamma_e\tilde{\alpha}e^{ikd}|^2$$
$$- 2|\gamma_m\tilde{\beta}||1 + \gamma_e\tilde{\alpha}e^{ikd}|)\hat{\mathbf{r}}.$$

This condition can be satisfied if

$$e^{-ikd} + \gamma_e\tilde{\alpha} = \gamma_m\tilde{\beta} \rightarrow \mathbf{P}(0, 0, -r) = 0. \tag{4.37}$$

The extension of the second Kerker condition to a near-field excitation corresponds to the condition

$$e^{ikd} + \gamma_e\tilde{\alpha} \cong -\gamma_m\tilde{\beta}. \tag{4.38}$$

As we can see, the excitation of a magnetic dipole in the dielectric particle offers additional pathways to tailor the emission such as switching the directivity, or increasing the gain in directivity. This method can also be used in plasmonics but at the price of more complex shapes such as U-shapes in order to excite induced magnetic dipoles in the plasmonic scatterers [55–57] or nanorings to couple electric dipoles and quadrupoles [58] or by coupling different electric dipolar metallic scatterers [59]. The coupling of quantum or classical emitters to additional multipolar orders (electric quadrupole and magnetic dipole) allows for a more directive emission.

4.3.3 All-dielectric directive antennas

Highly directive dielectric antennas with dielectric permittivity close to that of silicon in the visible spectrum were first characterized in hyperfrequencies [61–63,60]. This range of frequencies offers materials with a wide range of dielectric permittivities. Moderate dielectric permittivities (≈ 7) are interesting to tune the emission frequency since they feature resonances wider than high dielectric permittivity resonators. Wider Mie resonances allow a spectral overlap between resonances from different multipolar orders. The high number of modes involved in the emission pattern allows for a fine tuning of the directivity. In particular, it is possible to switch the directivity from the forward direction to the backward direction by simply modifying the emission frequency. The coupling between the emission dipole and higher order modes of the dielectric scatterer can be achieved by considering a notch in the dielectric antenna. Placing the emitter inside the notch offers highly directive antennas (Fig. 4.4).

An experimental realization and characterization of an all-dielectric directive antenna in the visible spectrum was reported in 2017 [64]. The antenna was composed of a reflector and a collector made of hafnium dioxide and the light source was pro-
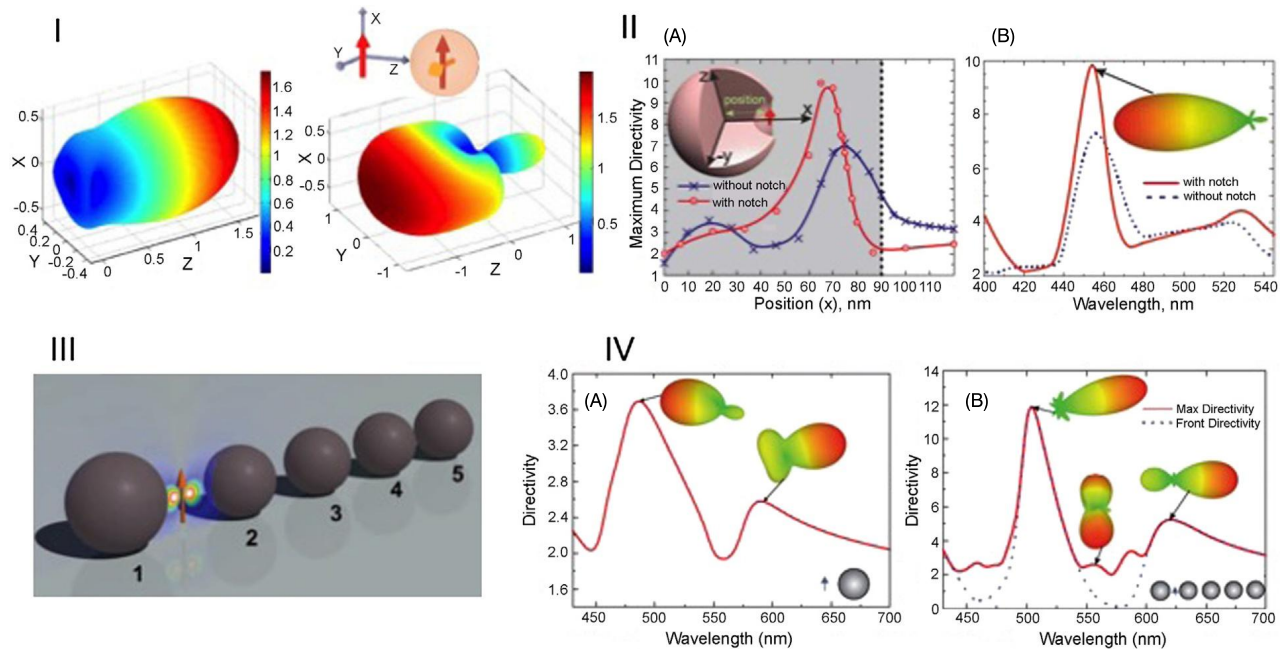
Figure 4.4 Highly directive all-dielectric antennas. I: Forward and backward light emission of an electric dipole emitter coupled with a 85 nm in radius GaP nanosphere and emitting at $\lambda = 550$ nm. The surrounding medium is made of glass. Distance between the emitter and the surface of the particle: 10 nm (A, left) and 100 nm (right, B). Reprinted with permission from Brice Rolly, Brian Stout, Nicolas Bonod, Boosting the directivity of optical antennas with magnetic and electric dipolar resonant particles, Optics Express 20 (2012) 20376–20386, Optical Society of America. II: notch antenna. The electric dipolar emitter is placed in a notch etched in the dielectric particle. (A) Maximum directivity obtained when the emitter $\lambda = 455$ nm is displaced along the Ox axis with and without a notch. (B) Directivity plotted with respect to the wavelength with and without notch. Inset: 3D emission pattern. Taken from [60]. Bottom: all-dielectric Yagi–Uda antenna. III: Sketch of the Yagi–Uda antenna. The radius of the reflector element is $Rr = 75$ nm, and the radius of the 2–5 smaller director elements is $Rd = 70$ nm. IV: directivity with respect to the wavelength when the distance between the elements is 70 nm; (A) monomer, (B) Yagi–Uda antenna. Parts III, IV reprinted with permission from Alexander E. Krasnok, Andrey E. Miroshnichenko, Pavel A. Belov, Yuri S. Kivshar, All-dielectric optical nanoantennas, Optics Express 20 (2012) 20599–20604, Optical Society of America.
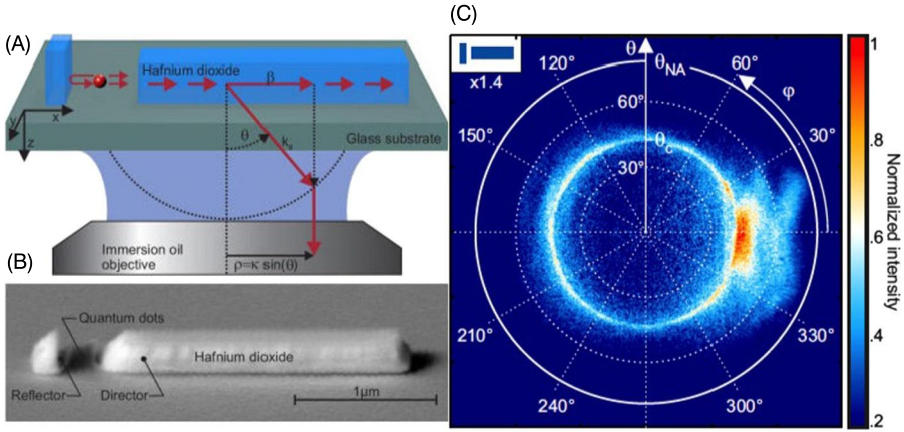
Figure 4.5 (A) Sketch of the experiment: The intensity distribution in the back-focal plane of the collecting objective is obtained from the angular distribution of light emission. (B) SEM image of the fabricated dielectric antenna. (C) Angular intensity distribution of dielectric antennas. Taken from [64].

vided by quantum dots deposited into the feed gap between director and reflector (see Fig. 4.5).

2D transition metal dichalcogenide materials (WS_2, MoS_2, WSe_2, and $MoSe_2$) are very promising for developing integrated photon sources as they are cost effective, atomically thin, and their shape makes them easy to integrate into planar photonic devices [66]. The coupling with optical antennas is particularly interesting since it will redirect the emission to a direction normal to the surface [67]. We now know that the distance between the emitter and the antenna is crucial for both decay rates and directionality (see Eqs. (4.27), (4.30)). The coupling between excitons in 2D semiconductors and semiconductor-based antennas is therefore well mastered, i.e. the emitter-to-antenna distance is very well controlled and repeatable. In this context, 2D semiconductors coupled with high refractive index antennas have a high potential in terms of fabrication and implementation to develop integrated, efficient and compact directive sources of photons. By coupling a silicon nanowire to a MoS_2 atomically thin layer, a forward-to-backward ratio of 20 was demonstrated in 2018 at the emission wavelength of 680 nm [65]. This study nicely combines the photoluminescence properties of 2D materials with the scattering properties of silicon nanorods [68] to redirect the fluorescence emission in a direction normal to the plane (Fig. 4.6).

Let us also stress that plasmonic and Mie resonators can judiciously be combined in hybrid metal-dielectric antennas [48,71–73] (see Fig. 4.7). Mie resonators feature high extinction cross-sections when excited from the far field and reciprocally, they can provide high directivity when excited from the near field [74,75,69,70].
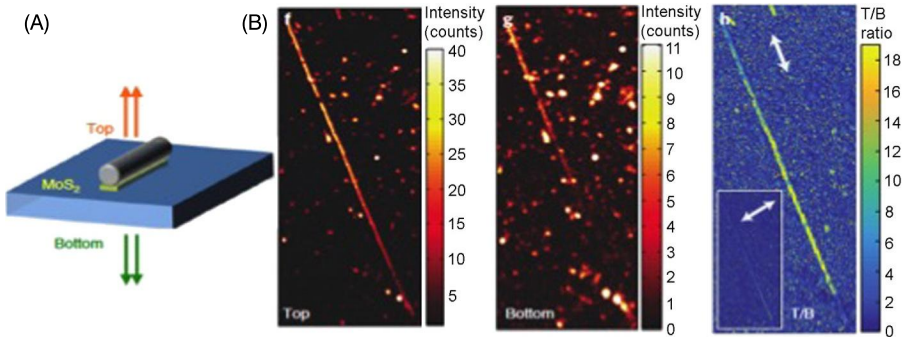
Figure 4.6 Top: highly directional fluorescence emission. (A) Sketch of the experiment: a MoS$_2$ monolayer is grown on a transparent sapphire substrate and a silicon nanorod is drop cast on top and the MoS$_2$ layer is etched around the nanorod. (B) Fluorescence images for transverse magnetic polarization: Top (T), bottom (B), and top over bottom (T/B) ratio. Inset: (T/B) ratio in transverse electric polarization. Taken from [65].
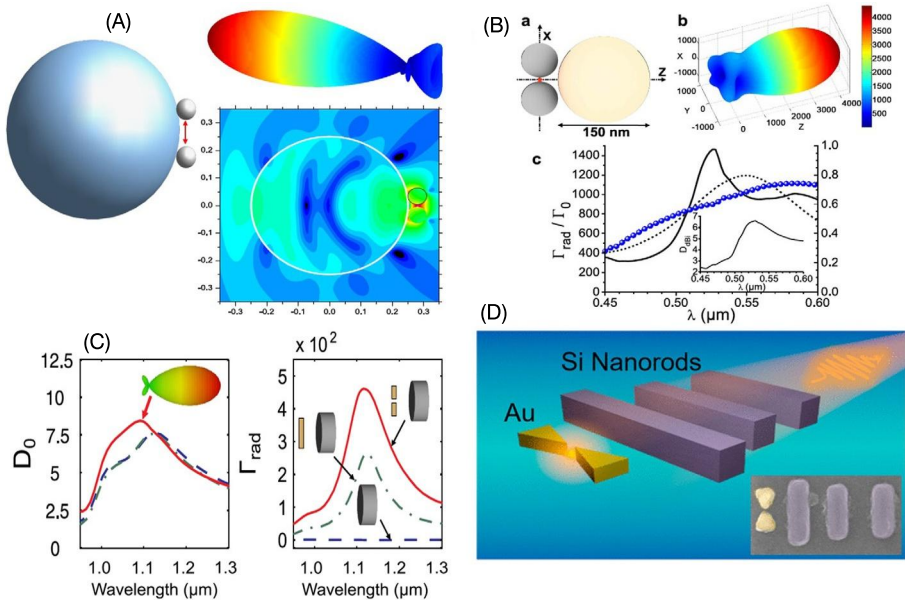
Figure 4.7 (A) Hybrid Ag-TiO$_2$ antenna: sketch of the hybrid antenna; 3D emission pattern when excited by an electric dipole emitter located in the gap of the Ag dimer; near electric field intensity distribution when excited by a polarized plane wave. Taken from [48]. (B) Hybrid Ag-GaP antenna: sketch; 3D emission pattern; normalized decay rate of the emitter located in the gap of the Ag dimer alone (dotted line, left scale) or coupled with the GaP particle (full line, left scale), antenna efficiency (blue dotted line, right scale). Reprinted with permission from Brice Rolly, Brian Stout, Nicolas Bonod, Boosting the directivity of optical antennas with magnetic and electric dipolar resonant particles, Optics Express 20 (2012) 20376–20386, Optical Society of America. (C) Comparison between three different antennas: pure dielectric antenna (blue dotted line), metallic monomer (green dotted line) and metallic dimer (red full line) coupled with the dielectric antenna. Left: directivity in the forward direction; right: radiative decay rate. Taken from [69]. (D) Experimental fabrication and characterization of a hybrid antenna: a gold bow-tie antenna is coupled with 3 Si nanorods. The emission is provided the photoluminescence of gold. Taken from [70].

4.4 Fluorescence enhancement of electric and magnetic emitters

4.4.1 Fluorescence enhancement

When coupling quantum emitters with optical antennas, the number of photons collected by the optical set-up can be drastically enhanced [76,77]. The fluorescence enhancement depends on different parameters: (i) the excitation strength, (ii) the quantum efficiency, and (iii) the collection efficiency. Quantum emitters are classically described by a two-level energy system. The excitation strength describes the excitation by the incoming light from the ground state to the excited state. It is equal to the product σI_e between the extinction cross-section σ of the quantum emitter and the light intensity I_e at the location of the quantum emitter. Excited emitters can release their energy through radiative (emission of photons) decay γ_r or through non-radiative decay γ_{nr}. The total decay rate γ_t is the sum of these two decay channels $\gamma_t = \gamma_r + \gamma_{nr}$. The quantum yield of the emitter $\eta = \gamma_{rad}/\gamma_t$ describes the ratio between these two decay channels. A saturation intensity defined by $I_s = \frac{\gamma_t}{\sigma}$ describes the capacity of the emitter to release its energy compared with its capacity to be excited by photons σ. Therefore, the excitation strength is defined as $\frac{\sigma I_e}{1+I_e/I_s}$. When $I_e \ll I_s$, it is linearly proportional to I_e. However, for larger excitation intensities $I_e \gg I_s$, it reaches a threshold and tends towards σI_s. The brightness of the fluorescence signal measured in a given optical set-up is generally given by the Count Rate *per* Molecule (CRM). This quantity is defined by the product between three terms, the collection efficiency κ, the quantum yield η and the excitation strength [76,77]:

$$CRM = \kappa\eta\frac{\sigma I_e}{1+I_e/I_s}. \tag{4.39}$$

We retrieve the two conditions of excitation, namely the weak excitation regime $I_e \ll I_s$ and the saturation excitation regime $I_e \gg I_s$. Under the weak excitation regime, the CRM is linearly proportional to I_e, $CRM = \kappa\eta\sigma I_e$ and depends on the three parameters, collection efficiency, quantum yield and excitation rate. Under the strong excitation regime, the CRM saturates, $CRM = \kappa\eta\sigma I_s = \kappa\eta\gamma_t = \kappa\gamma_r$, and simply reduces to the product $CRM = \kappa\gamma_r$ [76,77]. These expressions show the crucial role of the collection efficiency κ in the count rate *per* molecule. In the weak excitation regime, the excitation rate also plays a fundamental role. When designing optical antennas, one has to take into account these constraints and antennas must satisfy the following rules: in both regimes (weak and saturation regimes), a high directivity is required to maximize the collection efficiency and the radiative decay rate has to be optimized. In the weak excitation regime, the excitation rate must also be optimized while the radiative decay rate must maximize the quantum yield. While metallic antennas are well suited to maximize the excitation rate with huge field enhancements, dielectric antennas are very good candidates to satisfy all these parameters simultaneously and to combine high excitation rate with high collection efficiency and quantum yield. The weak losses of dielectrics compared with metals allow the design of high

quantum yield antennas that can overcome the weaker excitation rates. Besides the interest of weak losses, dielectric antennas can outperform metallic antennas in the design of highly directive antennas thanks to the coherent excitation of multipolar electric and magnetic modes.

4.4.2   Excitation rate

Dimers of silicon Mie resonators were proposed to enhance the near-field intensities in the gap separating the two resonators. The idea was first proposed by Sigalas et al., with thin silicon cylinders hosting electric dipolar modes [78]. The electric field distribution shows a strong electric field intensity enhancement in the nanogap separating the two Si disks. The light intensity distribution becomes completely different when considering thicker disks: (i) electric and (ii) magnetic fields are maximized inside the high refractive index material. The electric and magnetic near fields in the nanogap of silicon dimers can be probed with near-field scanning probes [79]. The nanogaps separating dielectric particles provide a good platform to perform fluorescence based molecular spectroscopy. First, they decrease the detection volume which is limited in an unstructured environment by the Rayleigh criterion. Decreasing the detection volume is of high interest since it allows the decrease of the number of molecules diffusing in the excitation spot [80,81]. There is therefore a trade-off between decreasing the nanogap size to reduce the detection volume and to enhance the excitation rate, and increasing the gap to decrease the quenching between the fluorophores and the lossy material used to fabricate the nanoantenna (Fig. 4.8).

The material used to fabricate the nanogap antenna plays an important role [84]. Attention was first paid to silicon [85,82]. Cambiasso et al. studied GaP for an efficient platform to enhance both second harmonic generation (SHG) and fluorescence emission [86]. Dimers of silicon particles were also investigated with fluorescence correlation spectroscopy which provides an efficient means to probe the number of molecules and the fluorescence enhancement of freely diffusing molecules in solution. Dimers of silicon particles can be fabricated with conventional electron beam lithography (EBL) followed by reactive ion etching (RIE). Basically, a water solution of fluorescence molecule is dropped on the sample of silicon nanogap antennas. The sample is illuminated by a CW laser beam focused by a high numerical aperture objective. The fluorescence signal can be collected with the same objective and transferred to avalanche photodiodes. The number of detected photons is plotted with respect to time from which can be calculated the autocorrelation function. The analysis of the autocorrelation function provides the number of detected molecules, the detection volume and the fluorescence signal *per* molecule. When comparing the results for two sets of samples, the set with nanogaps of 20 nm, and the second set with nanogaps of 30 nm, the difference in fluorescence enhancement is striking: smaller nanogaps (20 nm) provide much better results. First, a 3600-fold reduction of the detection volume is observed compared with the case without the antenna, i.e. compared with the diffraction limited confocal volume. This strong decrease of the detection volume results in a large decrease in the number of detected molecules since on average, the number of observed molecules can be smaller than one. This result proves the ability
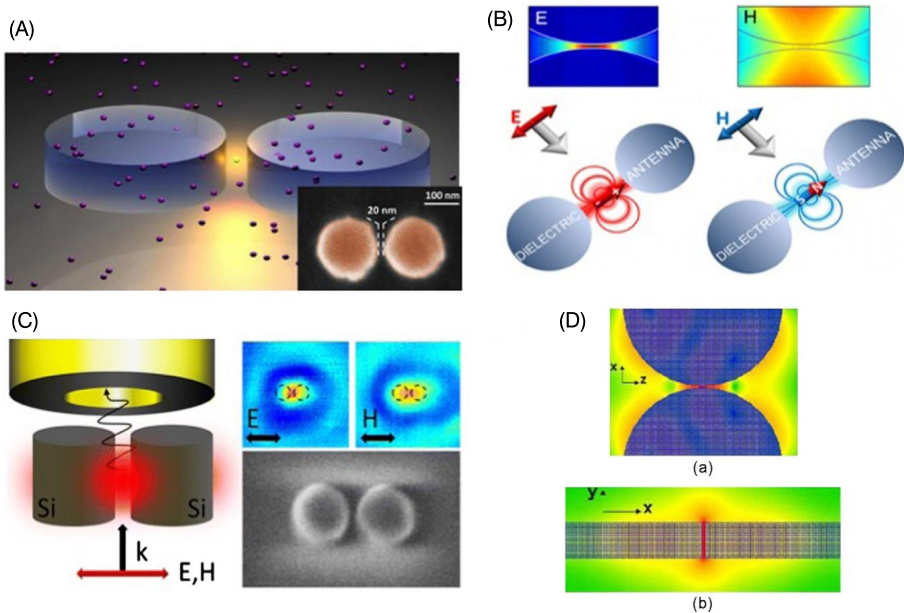
Figure 4.8 (A) Silicon nanogap antenna used to detect fluorescent molecule freely diffusing in water. Inset: SEM image of a fabricated Si dimer antenna with 20 nm gap. Taken from [82]. (B) Dielectric nanogap antennas enhance either the electric or the magnetic field intensity. Taken from [83]. (C) Electric and magnetic hot spots in silicon nanogap antennas can be imaged thanks to a near-field scanning optical microscopy technique. Taken from [79]. (D) Electric field distribution in the vicinity of two Si disks of 2 μm diameter and 200 nm thick separated by a 20 nm gap illuminated by a plane wave at normal incidence with $\lambda = 2.437$ μm polarized along the dimer axis (longest wavelength resonance). Reprinted with permission from M.M. Sigalas, D.A. Fattal, R.S. Williams, S.Y. Wang, R.G. Beausoleil, Electric field enhancement between two Si microdisks, Optics Express 15 (2007) 14711–14716, Optical Society of America.

of all-dielectric antennas to detect molecules in physiological conditions, in particular at micromolar concentration, with a sensitivity down to the single molecule level. Silicon Mie resonators possess all the properties required to design highly efficient platforms for biosensing [87,47].

An alternative strategy to nanogap antennas in order to achieve strong excitation strength is to embed light sources directly inside the Mie resonator, where the excitation strength and the Purcell factor are maximum [9,88]. Ge(Si) quantum dots were embedded in silicon nanodisks to optimize the spatial overlap between the modes of the dielectric nanodisks and the light source (see Fig. 4.9). Importantly, the concept of mode hybridization and Mie nanodisk coupling that was used in nanogap antennas can be also applied with quantum dots doped Si resonators. A linear trimer of Si nanodisks leads to a 10-fold enhancement of the photoluminescence signal when anti-symmetric electric and magnetic dipolar modes are excited. Spontaneous emission can also be tailored with metasurfaces [89–92,91,93]. Metasurfaces are very well indicated to tailor the spontaneous emission and the emission directivity (see Fig. 4.9). The solid-state emitters can also be embedded directly in the resonant Mie metasurface [92]. The spa-
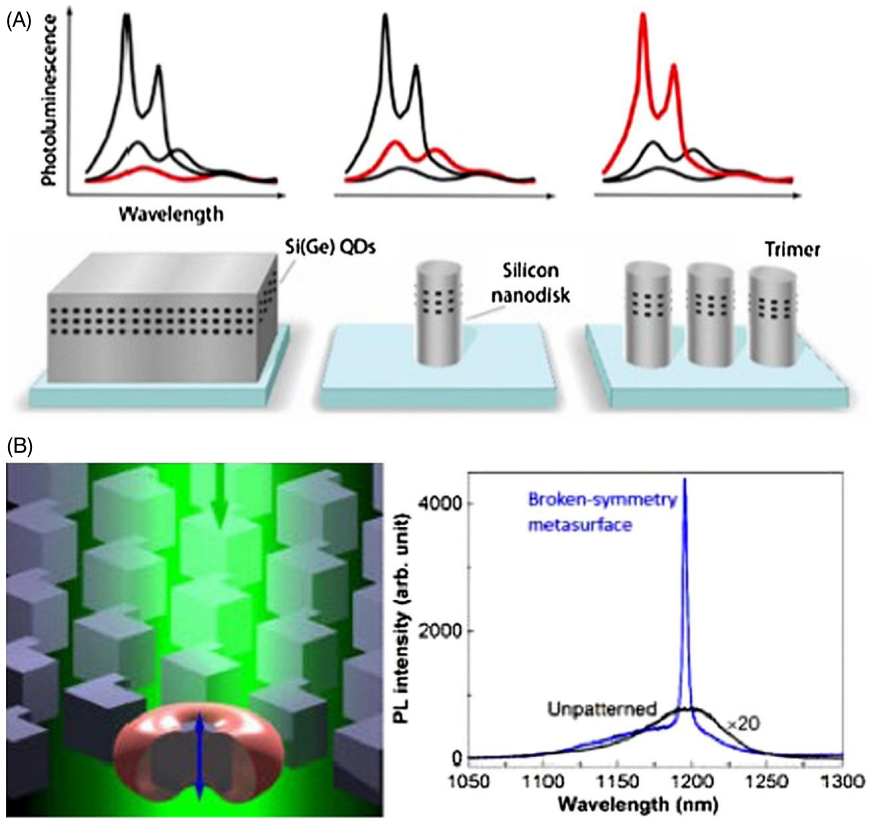
Figure 4.9 Solid-state emitters embedded in dielectric Mie nanostructures. (A) The photoluminescence of quantum dots embedded in silicon Mie resonators is studied for different configurations: Si bulk (left), monomers (center) and linear trimers (right). Taken from [88]. (B). Solid-state emitters embedded in III–V metasurfaces. Photoluminescence spectra measured at room temperature is studied for different geometries of meta-atoms. Taken from [92].

tial overlap between the emitters and the spatial profile of the modes is maximized by tuning the geometry of the meta-atoms. It is found that maximizing the spatial overlap by breaking the symmetry of meta-atoms leads to an increase of 2 orders of magnitude of the photoluminescence signal and a beaming of the photoluminescence signal (see Fig. 4.9B).

4.4.3 Chirality of light emission

An interesting feature of high refractive index antennas is that the excitation of both electric and magnetic induced dipoles in the particle offers an efficient means to control the chirality of light emission by chiral light sources [94]. Chiral emitters are characterized by the existence of both electric and magnetic emitting dipolar moments, with **p** being of real amplitude and **m** of complex amplitude [95,96]. The chirality
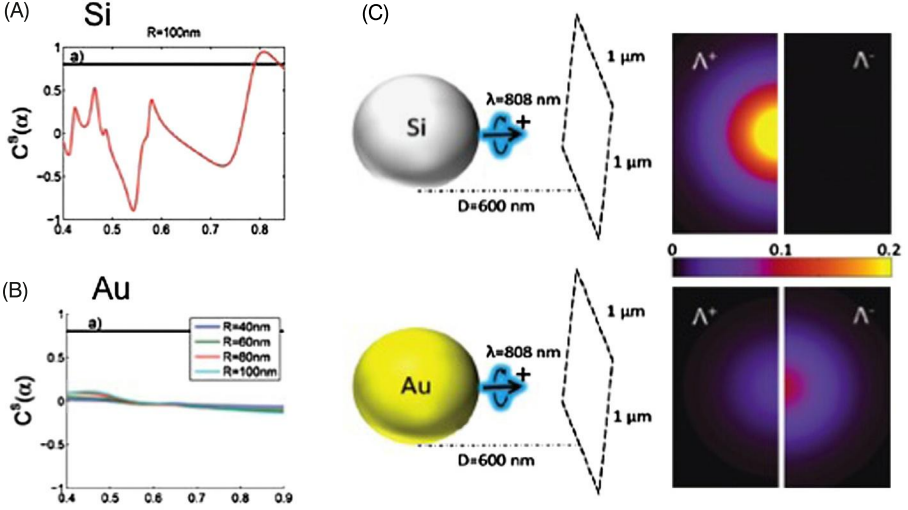
Figure 4.10 (A–B) Scattered far-field chirality signal. Chirality of the light scattered by a silicon (A) or a gold (B) antenna with respect to the wavelength in micrometers. The black straight line represents $\alpha = \sqrt{0.9}$. The colored lines in (B) represent the 4 different radii $R = 40, 60, 80, 100$ nm. The radius of the silicon particle is 100 nm. (C) Scattered field projected on the XY plane at 600 nm of the center of the resonator and projected on the ± 1 helicity basis. Chiral emitter ($\alpha = \sqrt{0.9}$, $\lambda = 808$ nm) located at 10 nm from the surface of the particle and oriented along the 0z axis. Top: silicon antenna, bottom: gold antenna. Taken from [94].

of light emission is quantified in the helicity basis A^+_{j,m_z}, A^-_{j,m_z} with the multipolar field components $A^{(e)}_{j,m_z}$ and $A^{(h)}_{j,m_z}$: $A^+_{j,m_z} = \frac{A^{(e)}_{j,m_z} + iA^{(h)}_{j,m_z}}{\sqrt{2}}$, $A^-_{j,m_z} = \frac{A^{(e)}_{j,m_z} - iA^{(h)}_{j,m_z}}{\sqrt{2}}$. j and m_z are the multipolar components, $j = 1$ for dipolar emitter, and m_z describes the orientation of the emitter. By denoting $|\alpha|^2$ the probability that the emitter radiates light with helicity $+1$, the electric field emitted by the chiral emitter is $\mathbf{E} = \alpha A^+_{j,m_z} + \sqrt{1 - |\alpha|^2} A^-_{j,m_z}$. It is therefore enlightening to study the scattered light obtained with the system "chiral emitter+spherical antenna". The scattered field Q_s is the sum of the field scattered in the $+1$ and -1 helicity basis, $Q_s = Q_s^+ + Q_s^-$. The chirality of the light emitter and of the scattered light far from the antenna can be defined, respectively, by the factors $C(\alpha)$ and $C^s(\alpha)$ that range between $[-1; +1]$:

$$C(\alpha) = \frac{|\alpha|^2 - (1 - |\alpha|^2)}{|\alpha|^2 + (1 + |\alpha|^2)}, \tag{4.40}$$

$$C^s(\alpha) = \frac{Q_s^+ - Q_s^-}{Q_s^+ + Q_s^-}. \tag{4.41}$$

Let us first consider the case of a chiral dipolar emitter characterized by $\alpha^2 = 0.9$ coupled with a plasmonic (gold) resonator. We calculate $C^s(\alpha)$ and the scattered field for different radii of the gold particle in the visible spectrum (see Fig. 4.10). When comparing the two spectra, it is clear that the electric dipolar resonances hosted by

the spherical gold nanoparticle entirely inhibit the chirality of light emission since $C^s(\alpha) = 0$ at the electric dipolar resonance. If we now consider the same chiral emitter coupled with a silicon particle of diameter 200 nm, the $C^s(\alpha)$ spectrum is very different. It is evident that if an almost pure electric dipolar resonance kills the chirality of light emission, Mie resonators that host electric and magnetic multipolar resonances strongly tune the chirality of the scattered light since $C^s(\alpha)$ spans in the visible spectrum all the possible values in the range $[-1; +1]$. We see in Fig. 4.10 that the silicon particle can increase the chirality of light emission ($C^s(\alpha) > C(\alpha)$) in a given range of frequencies. It can also reduce the initial chirality of the emitter, especially at a given electric or magnetic multipolar resonance. It can be observed that $C^s(\alpha)$ is almost zero when Q_s is maximum [94]. This comes from the fact that electric/magnetic modes split 50%–50% into modes of helicities $+1$ and -1. As the maxima of Q_s occur at a given electric or magnetic mode, both Q_s^+ and Q_s^- contribute equally to this maximum. Interestingly, the helicity is preserved when the condition $C^s(\alpha) = C(\alpha)$ is satisfied. It is preserved at two frequencies, one frequency corresponding to the dual condition. Let us stress that dual scatterers preserve the helicity of light [97]. These results show the high potential of all dielectric nanostructures to manipulate the helicity of the spontaneous emission of chiral emitters [98,99].

4.4.4   Inhibition of spontaneous emission

Dielectrics with weak losses offer new paths to manipulate decay rates. If photonic nanostructures can modify the local density of optical states, they can *a priori* either enhance or decrease the decay rates. Increasing the decay rates has attracted most of the attention in nanophotonics for accelerating the light emission process and to increase the number of photons emitter *per* second. However, it should be pointed out that photonic crystals were initially developed to inhibit spontaneous emission [11] before being used to produce high quality factor cavities [100].

The question is now to know whether dielectric optical antennas can also achieve inhibition. It is important to stress that, in the case of photonic crystals or other dielectric microcavities, the interaction with quantum emitters generally only involves a modification of the local density of radiative optical states as these resonators feature negligible ohmic losses. This is certainly not the case in plasmonic resonators that can quench fluorescence when the gain in local density of states is dominated by non-radiative modes. In practice, an inhibition of spontaneous emission can only be performed through an engineering of radiative modes while maintaining non-radiative modes as weak as possible. Such a case cannot be observed with plasmonic antennas: even if the radiative local density of states can be lowered by a plasmonic resonator, in particular when its induced dipolar mode is out-of-phase with the emitting dipole in a transverse geometry [101], the non-radiative local density of states will always be strongly increased leading to an overall reduction of the luminescence lifetime. This is why it is interesting to consider whether dielectric antennas with low ohmic losses can provide, at the same time, a reduced local density of radiative states and negligible non-radiative modes. All-dielectric nanostructures are *a priori* well indicated since they feature low losses that should avoid significant quenching.
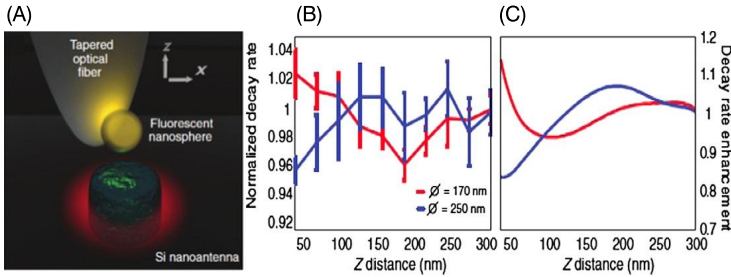
Figure 4.11 (A) Sketch of the experiment. (B) Experimental and (C) theoretical emission decay rates with respect to the axial distance between the fluorescent nanosphere and the 170-nm-diameter (red data points and solid line) or 250-nm-diameter (blue data points and solid line) Si resonators. Taken from [102].

This property of dielectric antennas can be verified by measuring the emission lifetime of quantum emitters coupled with a silicon antenna [102]. A straightforward method to monitor the LDOS in the vicinity of a silicon antenna is to graft a nanoparticle doped with fluorophores at the tip of a near-field probe and to measure the emission lifetime of the fluorophores when scanning the antenna. The challenge is that the LDOS is highly dependent on the distance between the fluorophores and the antenna. This scanning probe technique is well suited to address this challenge since it allows for a precise positioning of the emitter, in the three dimensions, with respect to the antenna.

Experiments were carried out by scanning a 100 nm fluorescent nanosphere over silicon monomer antennas of diameters ranging between 170 nm and 250 nm. Measurements of emission lifetime showed increased and decreased total spontaneous decay rates by up to 15%. In practice, tuning the size of the resonator modifies the resonance wavelength of its dipolar electric mode. For a 170 nm Si disk, the resonance matches exactly the emission wavelength of the fluorescent molecules while, for a 250-nm-diameter resonator, there is a frequency mismatch. As discussed in paragraph 3.2, this frequency mismatch modifies the phase ϕ_α of the polarizability of the resonator. As shown in Fig. 4.11, this leads to the emitting dipoles from the molecule and the induced dipole in the particle to be in-phase for the 170 nm particle but out-of phase with the 250 nm antenna when the distance between the fluorescent particle and the resonator is minimum. In-phase dipoles provide stronger radiated power when considering classical dipoles and, therefore, larger radiative decay rates for quantum dipoles. Inversely, an out-of-phase condition will reduce the radiative decay rate. Since non-radiative decay rates are weak with low-ohmic-losses antennas like Si nanodisks, this process leads overall to an inhibited spontaneous emission with the out-of-resonance particle (250 nm diameter) but an increased decay rate for the resonant case (170 nm disk). When the distance between the antenna and the fluorescent particle is increased, this modifies the phase term ϕ_d related to the propagation of the electric field emitted by fluorescent molecules. This propagative phase term can bring the resonant antenna out-of-phase with the emitting molecules and, similarly, the out-of-resonance antenna in-phase. This phenomenon explains the damped oscillations of decay rates observed both theoretically and experimentally in Fig. 4.11. The damping

arises from the reduced interaction between fluorescent emitters and antenna as the distance increases. However, one can note that the measured spontaneous decay rate modulations observed in Fig. 4.11 remain weak. This is due both to the weak modulation of the local density of states offered by a single Si nanodisk and to the size of the fluorescent particle (100 nm diameter over which the modulation of the density of states is averaged). It was theoretically estimated that a dimer of silicon disks, which features much stronger modulations of the local density of optical states, should allow an inhibition of spontaneous emission by more than one order of magnitude for transverse emitters [83].

4.4.5 Magnetic emission

An interesting aspect of Mie resonators is that they can host electric and magnetic resonances. Therefore, by resonantly exciting electric or magnetic multipoles in the antenna, it is possible to enhance either the electric or magnetic near-field intensities. Dielectric antennas have attracted a special interest for enhancing the magnetic LDOS through the excitation of magnetic Mie resonances. The strong magnetic response of silicon spherical particles in the visible and near infrared was stressed as early as 2011 [103]. In parallel, there were very inspiring studies on the enhancement of magnetic dipole transitions of trivalent lanthanide ions by simply modifying their electromagnetic environment. Lanthanide ions are particularly interesting since their intra-$4f^n$ optical transitions feature strong magnetic dipolar contribution [104,16]. Among the wide variety of emitters and transitions that can offer magnetic dipolar transitions, europium and erbium ions have been particularly studied and have a long history in optical spectroscopy. The $^5D_0 \rightarrow {}^7F_1$ magnetic dipolar (MD) transition of Eu^{3+} near 588 nm was used in the seminal experiments devoted to modified spontaneous emission carried out by Drexhage [105] or Kunz et al. [106] while the $^4I_{13/2} \rightarrow {}^4I_{15/2}$ MD transition of Er^{3+} near 1550 nm is used for signal amplifiers in optical fibers. Lanthanide ions are also suitable emitters to probe the electric and magnetic local density of optical states [107–111].

Magnetic dipolar transitions were first considered in nanophotonics to probe the artificial magnetism created in optical metamaterials [112–114]. Photonic nanostructures modify both the electric and the magnetic local density of states. Therefore, they can modify the competition between electric and magnetic transitions. An experiment close to the initial Drexhage reported a four-fold enhancement of the far-field emission from the $^5D_0 \rightarrow {}^7F_1$ MD and $^5D_0 \rightarrow {}^7F_2$ electric dipolar (ED) transition when varying the distance between europium ions and a gold mirror [115]. As the excited state $^5D_0$ is common for these two transitions, and as the relaxed states feature different energy levels, tailoring the electric or magnetic LDOS offers an additional degree of freedom to tune the emission frequency [116].

All of these great advances highlight the interest of coupling lanthanide ions with dielectric Mie resonators supporting electric and magnetic multipolar resonances. The analytical expressions in Eq. (4.27) show that the magnetic decay rates can be promoted when coupling the dipolar emitter with a dipolar or quadrupolar resonance. It was shown in [20] that the quadrupolar magnetic resonance, classically described in
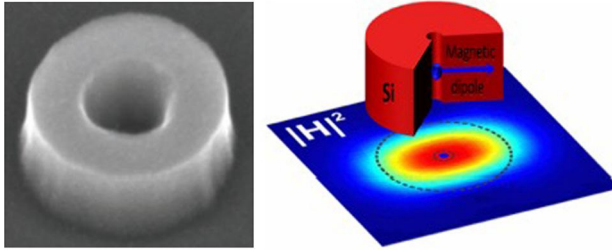
Figure 4.12 (A) SEM image of a hollow silicon resonator designed to feature a strong magnetic resonance around $\lambda = 600$ nm. Reprinted with permission from Marie Anne van de Haar, Jorik van de Groep, Benjamin J.M. Brenny, Albert Polman, Controlling magnetic and electric dipole modes in hollow silicon nanocylinders, Optics Express 24 (2016) 2047–2064, Optical Society of America. (B) Hollow dielectric resonators optimized to enhance specifically the radiative decay rates of magnetic dipolar emitters located at the center of the resonator. Taken from [121].

the multipolar Mie theory by the coefficient b_2, is particularly interesting to enhance the magnetic decay rate. The longitudinal coupling offers much stronger decay rate enhancements, and they also forbid transverse electric-magnetic coupling (i.e. electric resonances cannot influence magnetic decay rates, and *vive-versa*). This forbidden coupling is highly suitable to promote magnetic decay rates. When the orientation of the emitter is not controlled, enhancement of electric decay rates by magnetic resonances in transverse coupling cannot be avoided. However, when averaging the decay rates over all the possible orientations, the magnetic decay rates can be significantly enhanced by magnetic resonances. It turns out that silicon and more generally high refractive index particles are suitable platforms to enhance magnetic decay rates [117]. Dimers of dielectric Mie resonators [118] can also be considered to further enhance the electric or magnetic decay rates [20,83,111] and also enhance the electric or magnetic near-field intensities [83,119,79].

When comparing electric and magnetic near-field distributions in the gap of dimer antennas, one can observe that the magnetic field intensity remains confined in the high refractive index material. This means that the highest magnetic field intensity and LDOS remains inaccessible to lanthanide ions. Alternative designs have been proposed to circumvent this issue. Hollow silicon cylinders and coaxial silicon cylinders provide very interesting solutions to yield strong magnetic near-field intensities outside silicon [120,123,124,121] (Fig. 4.12). The coupling with lanthanide ions remains challenging since the distance between the emitters and the engineered antenna has to be very well controlled at a deep subwavelength scale. This issue can be solved by etching a silicon hollow cylinder antenna at the tip of a near-field optical scanning tip [122]. The engineered tip is scanned over 50–70-nm-diameter colloidal europium-doped particles. The europium ions are excited at 465 nm and the photoluminescence is collected by a high numerical aperture microscope. The $^5D_0 \rightarrow {}^7F_1$ MD (590 nm) and $^5D_0 \rightarrow {}^7F_2$ ED (610 nm) transitions can be channeled in two paths by a dichroic mirror and a set of spectral filters. The photoluminescence signals recorded by the two channels can be plotted separately with respect to the position of the scanning tip compared with the luminescent particle (see Fig. 4.13). The results show that the electric
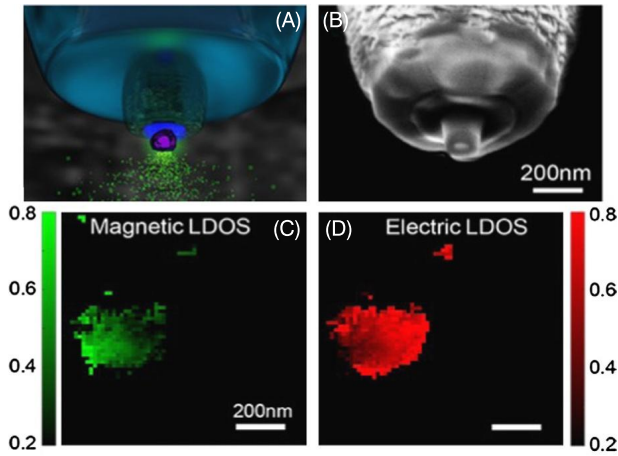
Figure 4.13 (A) Sketch and principle of the experiment. (B) Image obtained by Scanning Electron Microscopy of the silicon coaxial antenna etched at the extremity of a near-field fiber probe. (C, D) Magnetic (C) and electric (D) relative radiative LDOS surrounding the silicon coaxial antenna. Taken from [122].

and magnetic LDOS can both be separately enhanced depending on the position of the scanning tip. A MD transition can be enhanced when the scanning tip is centered above the particle, while the ED transition is enhanced when the center of the scanning tip is shifted with respect to the particle. In order to assess the ability of hollow silicon antennas to promote a MD transition, the experiment is reproduced with a metallic monopole antenna etched at the tip of the scanning probe. This antenna hosts electric dipolar resonances only and cannot promote magnetic decay rates [122]. In that case, the photoluminescence spectra recorded on the two distinct channels reveal that only the 610 nm channel collects photons. This experiment illustrates very well how properly designed antennas can tailor specifically the electric and magnetic LDOS.

4.5   Conclusion and perspectives

The resonant interaction between light and high refractive index nanostructures allows for an efficient control of spontaneous emission through the design of all-dielectric antennas. The major interests of all-dielectric optical antennas are that (i) they can excite electric and magnetic low order Mie resonances, (ii) they exhibit weak losses. The first advantage, linked to the excitation of both electric and magnetic modes has impact on the spontaneous emission that can be applied to the enhancements of both electric and magnetic decay rates. In other words, dielectric antennas can boost the fluorescence enhancement of quantum dots, fluorescent molecules among other fluorophores that feature electric dipolar transitions only. But their magnetic modes can also be optimized in order to boost the luminescence of lanthanide ions that feature magnetic dipole transitions, opening novel routes to manipulate spontaneous emission. The interplay between electric and magnetic modes offers also novel possibilities to

tailor the emission directivity. Controlling the directivity of spontaneous emission is of crucial importance to enhance the efficiency of optical antennas. The richness of the modal decomposition of dielectric nanostructures with electric and magnetic multipolar orders leads to high gains in directivity. The second property associated with weak losses has also a strong impact on the antenna efficiencies by reducing the non-radiative decay rates and by allowing an inhibition of spontaneous emission.

Regarding the perspectives, optical antennas will benefit from the latest advances in numerical optimization such as evolutionary algorithms and deep learning. This will boost the near-field excitation and allow for better control over the strength and the location of electric or magnetic hot spots in all-dielectric nanostructures. Electric and magnetic radiative decay rates will also benefit from optimization procedures. Dielectric nanostructures are also expected to provide significant advances in strong coupling. Dielectric antennas will also benefit from efforts in material technology and while attention was first paid to group IV semiconductors, III–V semiconductors have more recently shown huge potential to tailor spontaneous emission. Oxide materials and chalcogenides are also of interest. The coupling between all-dielectric antennas and 2D materials is expected to provide highly efficient integrated photon sources. The combined efforts in design and technology should lead to the development of compact, integrated and highly efficient optical antennas in terms of decay rates and directivity. One of the major technological challenges will be the successful combination of optimized antenna designs offering high emission count rates with an electrical excitation of the emitters. The external tunability of antenna properties such as emission directivity will play a central role in the upcoming development of all-dielectric antennas.

Acknowledgments

References

[1] Philip M. Morse, Herman Feshbach, Methods of theoretical physics, American Journal of Physics 22 (6) (1954) 410–413.
[2] L. Novotny, B. Hecht, Principles of Nano-Optics, Cambridge University Press, 2006.
[3] John David Jackson, Classical Electrodynamics, third ed., John Wiley & Sons, New York, 1999.
[4] Dorian Bouchet, Rémi Carminati, Quantum dipole emitters in structured environments: a scattering approach: tutorial, Journal of the Optical Society of America A 36 (2) (2019) 186–195.
[5] Edward Mills Purcell, Spontaneous emission probabilities at radio frequencies, in: Confined Electrons and Photons, Springer, 1995, p. 839.

[6] A.F. Koenderink, On the use of Purcell factors for plasmon antennas, Optics Letters 35 (24) (December 2010) 4208–4210.

[7] Christophe Sauvan, Jean-Paul Hugonin, I.S. Maksymov, Philippe Lalanne, Theory of the spontaneous optical emission of nanosize photonic and plasmon resonators, Physical Review Letters 110 (23) (2013) 237401.

[8] E.A. Muljarov, W. Langbein, Exact mode volume and Purcell factor of open optical systems, Physical Review B 94 (23) (2016) 235438.

[9] Xavier Zambrana-Puyalto, Nicolas Bonod, Purcell factor of spherical Mie resonators, Physical Review B 91 (19) (2015) 195422.

[10] K.H. Drexhage, Influence of a dielectric interface on fluorescence decay time, Journal of Luminescence 1 (1970) 693–701.

[11] Eli Yablonovitch, Inhibited spontaneous emission in solid-state physics and electronics, Physical Review Letters 58 (20) (1987) 2059.

[12] Mickael P. Busson, Brice Rolly, Brian Stout, Nicolas Bonod, Sébastien Bidault, Accelerated single photon emission from dye molecule-driven nanoantennas assembled on DNA, Nature Communications 3 (2012) 962.

[13] G.P. Acuna, F.M. Möller, P. Holzmeister, S. Beater, B. Lalkens, P. Tinnefeld, Fluorescence enhancement at docking sites of DNA-directed self-assembled nanoantennas, Science 338 (6106) (2012) 506–510.

[14] Emmanuel Lassalle, Alexis Devilez, Nicolas Bonod, Thomas Durt, Brian Stout, Lamb shift multipolar analysis, Journal of the Optical Society of America B 34 (7) (2017) 1348–1355.

[15] Emmanuel Lassalle, Nicolas Bonod, Thomas Durt, Brian Stout, Interplay between spontaneous decay rates and lamb shifts in open photonic systems, Optics Letters 43 (9) (2018) 1950–1953.

[16] Christopher M. Dodson, Jonathan A. Kurvits, Dongfang Li, Mingming Jiang, Rashid Zia, Magnetic dipole emission of $Dy^{3+}:Y_2O_3$ and $Tm^{3+}:Y_2O_3$ at near-infrared wavelengths, Optical Materials Express 4 (11) (2014) 2441–2450.

[17] Jorge R. Zurita-Sánchez, Lukas Novotny, Multipolar interband absorption in a semiconductor quantum dot. I. Electric quadrupole enhancement, Journal of the Optical Society of America B 19 (6) (2002) 1355–1362.

[18] Jorge R. Zurita-Sánchez, Lukas Novotny, Multipolar interband absorption in a semiconductor quantum dot. II. Magnetic dipole enhancement, Journal of the Optical Society of America B 19 (11) (2002) 2722–2726.

[19] B. Stout, A. Devilez, B. Rolly, N. Bonod, Multipole methods for nanoantennas design: applications to Yagi–Uda configurations, Journal of the Optical Society of America B 28 (5) (May 2011) 1213–1223.

[20] Brice Rolly, Betina Bebey, Sebastien Bidault, Brian Stout, Nicolas Bonod, Promoting magnetic dipolar transition in trivalent lanthanide ions with lossless Mie resonances, Physical Review B, Condensed Matter and Materials Physics 85 (Jun. 2012) 245432.

[21] R. Carminati, J.J. Greffet, C. Henkel, J.M. Vigoureux, Radiative and non-radiative decay of a single molecule close to a metallic nanoparticle, Optics Communications 261 (2) (May 2006) 368–375.

[22] Peter R. Wiecha, Arnaud Arbouet, Aurélien Cuche, Vincent Paillard, Christian Girard, Decay rate of magnetic dipoles near nonmagnetic nanostructures, Physical Review B 97 (8) (2018) 085411.

[23] W. Lukosz, R.E. Kunz, Light emission by magnetic and electric dipoles close to a plane interface. I. Total radiated power, Journal of the Optical Society of America 67 (12) (1977) 1607–1615.

[24] W. Lukosz, R.E. Kunz, Light emission by magnetic and electric dipoles close to a plane dielectric interface. II. Radiation patterns of perpendicular oriented dipoles, Journal of the Optical Society of America 67 (12) (1977) 1615–1619.

[25] Davy Gérard, Alexis Devilez, Heykel Aouani, Brian Stout, Nicolas Bonod, Jérôme Wenger, Evgeny Popov, Hervé Rigneault, Efficient excitation and collection of single-molecule fluorescence close to a dielectric microsphere, Journal of the Optical Society of America B, Optical Physics 26 (7) (Jul 2009) 1473–1478.

[26] Heykel Aouani, Frédérique Deiss, Jérôme Wenger, Patrick Ferrand, Neso Sojic, Hervé Rigneault, Optical-fiber-microsphere for remote fluorescence correlation spectroscopy, Optics Express 17 (21) (2009) 19085–19092.

[27] Petru Ghenuche, Juan de Torres, Patrick Ferrand, Jérôme Wenger, Multi-focus parallel detection of fluorescent molecules at picomolar concentration with photonic nanojets arrays, Applied Physics Letters 105 (13) (2014) 131102.

[28] Yinzhou Yan, Yong Zeng, Yan Wu, Yan Zhao, Lingfei Ji, Yijian Jiang, Lin Li, Ten-fold enhancement of zno thin film ultraviolet-luminescence by dielectric microsphere arrays, Optics Express 22 (19) (2014) 23552–23564.

[29] Alexis Devilez, Xavier Zambrana-Puyalto, Brian Stout, Nicolas Bonod, Mimicking localized surface plasmons with dielectric particles, Physical Review B 92 (24) (2015) 241412.

[30] Arseniy I. Kuznetsov, Andrey E. Miroshnichenko, Mark L. Brongersma, Yuri S. Kivshar, Boris Luk'yanchuk, Optically resonant dielectric nanostructures, Science 354 (6314) (2016) aag2472.

[31] Peter Muehlschlegel, H-J. Eisler, Olivier J.F. Martin, B. Hecht, D.W. Pohl, Resonant optical antennas, Science 308 (5728) (2005) 1607–1609.

[32] Lukas Novotny, Niek van Hulst, Antennas for light, Nature Photonics 5 (2) (2011) 83–90.

[33] Javier Aizpurua, Garnett W. Bryant, Lee J. Richter, F.J. García De Abajo, Brian K. Kelley, T. Mallouk, Optical properties of coupled metallic nanorods for field-enhanced spectroscopy, Physical Review B 71 (23) (2005) 235420.

[34] Anika Kinkhabwala, Zongfu Yu, Shanhui Fan, Yuri Avlasevich, Klaus Mullen, W.E. Moerner, Large single-molecule fluorescence enhancements produced by a bowtie nanoantenna, Nature Photonics 3 (11) (2009) 654–657.

[35] Björn M. Reinhard, Merek Siu, Harish Agarwal, A. Paul Alivisatos, Jan Liphardt, Calibration of dynamic molecular rulers based on plasmon coupling between gold nanoparticles, Nano Letters 5 (11) (2005) 2246–2252.

[36] Jennifer I.L. Chen, Yeechi Chen, David S. Ginger, Plasmonic nanoparticle dimers for optical sensing of DNA in complex media, Journal of the American Chemical Society 132 (28) (2010) 9600–9601.

[37] Mickael P. Busson, Brice Rolly, Brian Stout, Nicolas Bonod, Eric Larquet, Albert Polman, Sébastien Bidault, Optical and topological characterization of gold nanoparticle dimers linked by a single DNA double strand, Nano Letters 11 (11) (2011) 5060–5065.

[38] E. Prodan, C. Radloff, N.J. Halas, P. Nordlander, A hybridization model for the plasmon response of complex nanostructures, Science 302 (5644) (Oct. 17 2003) 419–422.

[39] P. Nordlander, C. Oubre, E. Prodan, K. Li, M.I. Stockman, Plasmon hybridizaton in nanoparticle dimers, Nano Letters 4 (5) (May 2004) 899–903.

[40] Jingjing Li, Alessandro Salandrino, Nader Engheta, Shaping light beams in the nanometer scale: a Yagi–Uda nanoantenna in the optical domain, Physical Review B, Condensed Matter and Materials Physics 76 (Dec 2007) 245403.

[41] Tim H. Taminiau, Fernando D. Stefani, Niek F. van Hulst, Enhanced directional excitation and emission of single emitters by a nano-optical Yagi–Uda antenna, Optics Express 16 (14) (2008) 10858–10866.

[42] Brice Rolly, Brian Stout, Sebastien Bidault, Nicolas Bonod, Crucial role of the emitter–particle distance on the directivity of optical antennas, Optics Letters 36 (17) (Sep. 2011) 3368–3370.

[43] Alberto G. Curto, Giorgio Volpe, Tim H. Taminiau, Mark P. Kreuzer, Romain Quidant, Niek F. van Hulst, Unidirectional emission of a quantum dot coupled to a nanoantenna, Science 329 (5994) (Aug. 20 2010) 930–933.

[44] Mohammad Ramezani, Alberto Casadei, Grzegorz Grzela, Federico Matteini, Gozde Tutuncuoglu, Daniel Ruffer, Anna Fontcuberta i Morral, Jaime Gomez Rivas, Hybrid semiconductor nanowire–metallic Yagi–Uda antennas, Nano Letters 15 (8) (2015) 4889–4895.

[45] Nicolas Bonod, Alexis Devilez, Brice Rolly, Sebastien Bidault, Brian Stout, Ultracompact and unidirectional metallic antennas, Physical Review B, Condensed Matter and Materials Physics 82 (11) (Sep. 16 2010) 115429.

[46] Rajesh K. Mongia, Prakash Bhartia, Dielectric resonator antennas – a review and general design relations for resonant frequency and bandwidth, International Journal of Microwave and Millimeter-Wave Computer-Aided Engineering 4 (3) (1994) 230.

[47] Alex Krasnok, Martín Caldarola, Nicolas Bonod, Andrea Alú, Spectroscopy and biosensing with optically resonant dielectric nanostructures, Advanced Optical Materials 6 (5) (2018) 1701094.

[48] Alexis Devilez, Brian Stout, Nicolas Bonod, Compact metallo-dielectric optical antenna for ultra directional and enhanced radiative emission, ACS Nano 4 (6) (Jun. 2010) 3390–3396.

[49] A. Krasnok, A. Miroshnichenko, P. Belov, Yu. Kivshar, Huygens optical elements and Yagi–Uda nanoantennas based on dielectric nanoparticles, JETP Letters 94 (2011) 593–598.

[50] Alexander E. Krasnok, Andrey E. Miroshnichenko, Pavel A. Belov, Yuri S. Kivshar, All-dielectric optical nanoantennas, Optics Express 20 (18) (2012) 20599–20604.

[51] M. Kerker, D.-S. Wang, C.L. Giles, Electromagnetic scattering by magnetic spheres, Journal of the Optical Society of America 73 (6) (Jun. 1983) 765–767.

[52] Raquel Gomez-Medina, Braulio Garcia-Camara, Irene Suarez-Lacalle, Francisco Gonzalez, Fernando Moreno, Manuel Nieto-Vesperinas, Juan Jose Saenz, Electric and magnetic dipolar response of germanium nanospheres: interference effects, scattering anisotropy, and optical forces, Journal of Nanophotonics 5 (2011) 053512.

[53] M. Nieto-Vesperinas, R. Gomez-Medina, J.J. Saenz, Angle-suppressed scattering and optical forces on submicrometer dielectric particles, Journal of the Optical Society of America A: Optics, Image Science, and Vision 28 (1) (Jan. 2011) 54–60.

[54] Brice Rolly, Brian Stout, Nicolas Bonod, Boosting the directivity of optical antennas with magnetic and electric dipolar resonant particles, Optics Express 20 (18) (2012) 20376–20386.

[55] Ion M. Hancu, Alberto G. Curto, Marta Castro-López, Martin Kuttge, Niek F. van Hulst, Multipolar interference for directed light emission, Nano Letters 14 (1) (2013) 166–171.

[56] Toon Coenen, Felipe Bernal Arango, A. Femius Koenderink, Albert Polman, Directional emission from a single plasmonic scatterer, Nature Communications 5 (2014) 3250.

[57] Julien Proust, Nicolas Bonod, Johan Grand, Bruno Gallas, Optical monitoring of the magnetoelectric coupling in individual plasmonic scatterers, ACS Photonics 3 (9) (2016) 1581–1588.

[58] R. Alaee, R. Filter, D. Lehr, F. Lederer, C. Rockstuhl, A generalized Kerker condition for highly directive nanoantennas, Optics Letters 40 (11) (2015) 2645–2648.

[59] Marc Dubois, Lisa Leroi, Zo Raolison, Redha Abdeddaim, Tryfon Antonakakis, Julien de Rosny, Alexandre Vignaud, Pierre Sabouroux, Elodie Georget, Benoit Larrat, et al.,

Kerker effect in ultrahigh-field magnetic resonance imaging, Physical Review X 8 (3) (2018) 031083.

[60] Alexander E. Krasnok, Constantin R. Simovski, Pavel A. Belov, Yuri S. Kivshar, Superdirective dielectric nanoantennas, Nanoscale (2014).

[61] Dmitry S. Filonov, Alexander E. Krasnok, Alexey P. Slobozhanyuk, Polina V. Kapitanova, Elizaveta A. Nenasheva, Yuri S. Kivshar, Pavel A. Belov, Experimental verification of the concept of all-dielectric nanoantennas, Applied Physics Letters 100 (20) (2012) 201113.

[62] Brice Rolly, Jean-Michel Geffrin, Redha Abdeddaim, Brian Stout, Nicolas Bonod, Controllable emission of a dipolar source coupled with a magneto-dielectric resonant subwavelength scatterer, Scientific Reports 3 (2013).

[63] Alexander E. Krasnok, Dmitry S. Filonov, Constantin R. Simovski, Yuri S. Kivshar, Pavel A. Belov, Experimental demonstration of superdirective dielectric antenna, Applied Physics Letters 104 (13) (2014).

[64] Manuel Peter, Andre Hildebrandt, Christian Schlickriede, Kimia Gharib, Thomas Zentgraf, Jens Forstner, Stefan Linden, Directional emission from dielectric leaky-wave nanoantennas, Nano Letters 17 (7) (2017) 4178–4183.

[65] Ahmet Fatih Cihan, Alberto G. Curto, Søren Raza, Pieter G. Kik, Mark L. Brongersma, Silicon Mie resonators for highly directional light emission from monolayer mos 2, Nature Photonics 12 (5) (2018) 284.

[66] Alex Krasnok, Sergey Lepeshov, Andrea Alú, Nanophotonics with 2d transition metal dichalcogenides, Optics Express 26 (12) (2018) 15972–15994.

[67] Sergey Lepeshov, Alex Krasnok, Andrea Alu, Enhanced excitation and emission from 2d transition metal dichalcogenides with all-dielectric nanoantennas, arXiv preprint, arXiv: 1810.06417, 2018.

[68] Peter R. Wiecha, Aurélien Cuche, Arnaud Arbouet, Christian Girard, Gérard Colas des Francs, Aurélie Lecestre, Guilhem Larrieu, Frank Fournel, Vincent Larrey, Thierry Baron, et al., Strongly directional scattering from dielectric nanowires, ACS Photonics 4 (8) (2017) 2036–2046.

[69] Evgenia Rusak, Isabelle Staude, Manuel Decker, Jürgen Sautter, Andrey E. Miroshnichenko, David A. Powell, Dragomir N. Neshev, Yuri S. Kivshar, Hybrid nanoantennas for directional emission enhancement, Applied Physics Letters 105 (22) (2014) 221109.

[70] Jinfa Ho, Yuan Hsing Fu, Zhaogang Dong, Ramón Paniagua-Dominguez, Eleen H.H. Koay, Ye Feng Yu, Vytautas Valuckas, Arseniy I. Kuznetsov, Joel K.W. Yang, Highly directive hybrid metal–dielectric Yagi–Uda nanoantennas, ACS Nano 12 (8) (2018) 8616–8624.

[71] Xianghao Zeng, Wenhai Yu, Peiju Yao, Zheng Xi, Yonghua Lu, Pei Wang, Metallo-dielectric hybrid antenna for high Purcell factor and radiation efficiency, Optics Express 22 (12) (2014) 14517–14523.

[72] M. Decker, T. Pertsch, I. Staude, Strong coupling in hybrid metal–dielectric nanoresonators, Philosophical Transactions. Series A, Mathematical, Physical, and Engineering Sciences 375 (2090) (2017).

[73] Song Sun, Mo Li, Qingguo Du, Ching Eng Png, Ping Bai, Metal–dielectric hybrid dimer nanoantenna: coupling between surface plasmons and dielectric resonances for fluorescence enhancement, The Journal of Physical Chemistry C 121 (23) (2017) 12871–12884.

[74] Alireza Bonakdar, Hooman Mohseni, Hybrid optical antenna with high directivity gain, Optics Letters 38 (15) (2013) 2726–2728.

[75] Florian Bigourdan, François Marquier, J-P. Hugonin, J-J. Greffet, Design of highly efficient metallo-dielectric patch antennas for single-photon emission, Optics Express 22 (3) (2014) 2337–2347.

[76] Jérôme Wenger, Davy Gérard, José Dintinger, Oussama Mahboub, Nicolas Bonod, Evgeny Popov, Thomas W. Ebbesen, Hervé Rigneault, Emission and excitation contributions to enhanced single molecule fluorescence by gold nanometric apertures, Optics Express 16 (5) (2008) 3008–3020.

[77] Jérôme Wenger, Fluorescence enhancement factors on optical antennas: enlarging the experimental values without changing the antenna design, International Journal of Optics (2012) 2012.

[78] M.M. Sigalas, D.A. Fattal, R.S. Williams, S.Y. Wang, R.G. Beausoleil, Electric field enhancement between two Si microdisks, Optics Express 15 (22) (2007) 14711–14716.

[79] Reuben M. Bakker, Dmitry Permyakov, Ye Feng Yu, Dmitry Markovich, Ramón Paniagua-Domínguez, Leonard Gonzaga, Anton Samusev, Yuri Kivshar, Boris Luk'yanchuk, Arseniy I. Kuznetsov, Magnetic and electric hotspots with silicon nanodimers, Nano Letters 15 (3) (2015) 2137–2142.

[80] Heykel Aouani, Oussama Mahboub, Nicolas Bonod, Eloise Devaux, Evgeny Popov, Hervé Rigneault, Thomas W. Ebbesen, Jérôme Wenger, Bright unidirectional fluorescence emission of molecules in a nanoaperture with plasmonic corrugations, Nano Letters 11 (2) (2011) 637–644.

[81] Deep Punj, Mathieu Mivelle, Satish Babu Moparthi, Thomas S. Van Zanten, Hervé Rigneault, Niek F. Van Hulst, María F. García-Parajó, Jérôme Wenger, A plasmonic antenna-in-box platform for enhanced single-molecule analysis at micromolar concentrations, Nature Nanotechnology 8 (7) (2013) 512.

[82] Raju Regmi, Johann Berthelot, Pamina M. Winkler, Mathieu Mivelle, Julien Proust, Frédéric Bedu, Igor Ozerov, Thomas Begou, Julien Lumeau, Hervé Rigneault, et al., All-dielectric silicon nanogap antennas to enhance the fluorescence of single molecules, Nano Letters 16 (8) (2016) 5143–5151.

[83] Pablo Albella, M. Ameen Poyli, Mikolaj K. Schmidt, Stefan A. Maier, Fernando Moreno, Juan José Sáenz, Javier Aizpurua, Low-loss electric and magnetic field-enhanced spectroscopy with subwavelength silicon dimers, The Journal of Physical Chemistry C 117 (26) (2013) 13573–13584.

[84] Denis G. Baranov, Dmitry A. Zuev, Sergey I. Lepeshov, Oleg V. Kotov, Alexander E. Krasnok, Andrey B. Evlyukhin, Boris N. Chichkov, All-dielectric nanophotonics: the quest for better materials and fabrication techniques, Optica 4 (7) (2017) 814–825.

[85] Martín Caldarola, Pablo Albella, Emiliano Cortés, Mohsen Rahmani, Tyler Roschuk, Gustavo Grinblat, Rupert F. Oulton, Andrea V. Bragas, Stefan A. Maier, Non-plasmonic nanoantennas for surface enhanced spectroscopies with ultra-low heat conversion, Nature Communications 6 (2015) 7915.

[86] Javier Cambiasso, Gustavo Grinblat, Yi Li, Aliaksandra Rakovich, Emiliano Cortés, Stefan A. Maier, Bridging the gap between dielectric nanophotonics and the visible regime with effectively lossless gallium phosphide antennas, Nano Letters 17 (2) (2017) 1219–1225.

[87] Ozlem Yavas, Mikael Svedendahl, Paulina Dobosz, Vanesa Sanz, Romain Quidant, On-a-chip biosensing based on all-dielectric nanoresonators, Nano Letters 17 (7) (2017) 4421–4426.

[88] Viktoriia Rutckaia, Frank Heyroth, Alexey Novikov, Mikhail Shaleev, Mihail Petrov, Joerg Schilling, Quantum dot emission driven by Mie resonances in silicon nanostructures, Nano Letters 17 (11) (2017) 6886–6892.

[89] Isabelle Staude, Vyacheslav V. Khardikov, Nche T. Fofang, Sheng Liu, Manuel Decker, Dragomir N. Neshev, Ting Shan Luk, Igal Brener, Yuri S. Kivshar, Shaping photolu-

minescence spectra with magnetoelectric resonances in all-dielectric nanoparticles, ACS Photonics 2 (2) (2015) 172–177.

[90] Aleksandr Vaskin, Justus Bohn, Katie E. Chong, Tobias Bucher, Matthias Zilk, Duk-Yong Choi, Dragomir N. Neshev, Yuri S. Kivshar, Thomas Pertsch, Isabelle Staude, Directional and spectral shaping of light emission with Mie-resonant silicon nanoantenna arrays, ACS Photonics 5 (4) (2018) 1359–1364.

[91] Justus Bohn, Tobias Bucher, Katie E. Chong, Andrei Komar, Duk-Yong Choi, Dragomir N. Neshev, Yuri S. Kivshar, Thomas Pertsch, Isabelle Staude, Active tuning of spontaneous emission by Mie-resonant dielectric metasurfaces, Nano Letters 18 (6) (2018) 3461–3465.

[92] Sheng Liu, Aleksandr Vaskin, Sadhvikas Addamane, Benjamin Leung, Miao-Chan Tsai, Yuanmu Yang, Polina Vabishchevich, Gordon A. Keeler, George T. Wang, Xiaowei He, et al., Light emitting metasurfaces: simultaneous control of spontaneous emission and far-field radiation, Nano Letters (2018).

[93] Masanobu Iwanaga, Recent progress in emittance-controlled optical metasurfaces, Journal of Physics: Conference Series 1092 (2018) 012053, IOP Publishing.

[94] Xavier Zambrana-Puyalto, Nicolas Bonod, Tailoring the chirality of light emission with spherical Si-based antennas, Nanoscale 8 (19) (2016) 10441–10452.

[95] Nozomu Suzuki, Yichun Wang, Paolo Elvati, Zhi-Bei Qu, Kyoungwon Kim, Shuang Jiang, Elizabeth Baumeister, Jaewook Lee, Bongjun Yeom, Joong Hwan Bahng, et al., Chiral graphene quantum dots, ACS Nano 10 (2) (2016) 1744–1755.

[96] Alexander I. Shlykov, Anvar S. Baimuratov, Alexander V. Baranov, Anatoly V. Fedorov, Ivan D. Rukhlenko, Optically active quantum-dot molecules, Optics Express 25 (4) (2017) 3811–3825.

[97] Xavier Zambrana-Puyalto, I. Fernandez-Corbaton, M.L. Juan, Xavier Vidal, Gabriel Molina-Terriza, Duality symmetry and Kerker conditions, Optics Letters 38 (11) (2013) 1857–1859.

[98] Weixuan Zhang, Tong Wu, Rongyao Wang, Xiangdong Zhang, Amplification of the molecular chiroptical effect by low-loss dielectric nanoantennas, Nanoscale 9 (17) (2017) 5701–5707.

[99] Florian Graf, Carsten Rockstuhl, Ivan Fernandez-Corbaton, Helicity preserving and resonant structures for enhanced chiral molecule detection, arXiv preprint, arXiv:1810.08385, 2018.

[100] Susumu Noda, Masayuki Fujita, Takashi Asano, Spontaneous-emission control by photonic crystals and nanocavities, Nature Photonics 1 (8) (2007) 449.

[101] H. Mertens, A.F. Koenderink, A. Polman, Plasmon-enhanced luminescence near noble-metal nanospheres: comparison of exact theory and an improved Gersten and Nitzan model, Physical Review B, Condensed Matter and Materials Physics 76 (Sep. 2007) 115123.

[102] Dorian Bouchet, Mathieu Mivelle, Julien Proust, Bruno Gallas, Igor Ozerov, Maria F. Garcia-Parajo, Angelo Gulinatti, Ivan Rech, Yannick De Wilde, Nicolas Bonod, et al., Enhancement and inhibition of spontaneous photon emission by resonant silicon nanoantennas, Physical Review Applied 6 (6) (2016) 064016.

[103] A. García-Etxarri, R. Gómez-Medina, L.S. Froufe-Pérez, C. López, L. Chantada, F. Scheffold, J. Aizpurua, M. Nieto-Vesperinas, J.J. Sáenz, Strong magnetic response of submicron silicon particles in the infrared, Optics Express 19 (6) (Mar. 2011) 4815–4826.

[104] Christopher M. Dodson, Rashid Zia, Magnetic dipole and electric quadrupole transitions in the trivalent lanthanide series: calculated emission rates and oscillator strengths, Physical Review B 86 (Sep. 2012) 125102.

[105] Karl H. Drexhage, IV interaction of light with monomolecular Dye layers, in: Progress in Optics, vol. 12, Elsevier, 1974, pp. 163–232.

[106] R.E. Kunz, W. Lukosz, Changes in fluorescence lifetimes induced by variable optical environments, Physical Review B 21 (10) (1980) 4814.

[107] L. Aigouy, A. Cazé, P. Gredin, M. Mortier, R. Carminati, Mapping and quantifying electric and magnetic dipole luminescence at the nanoscale, Physical Review Letters 113 (7) (2014) 076101.

[108] Rabia Hussain, Sergey S. Kruk, Carl E. Bonner, Mikhail A. Noginov, Isabelle Staude, Yuri S. Kivshar, Natalia Noginova, Dragomir N. Neshev, Enhancing Eu 3+ magnetic dipole emission by resonant plasmonic nanostructures, Optics Letters 40 (8) (2015) 1659–1662.

[109] Freddy T. Rabouw, P. Tim Prins, David J. Norris, Europium-doped NaYF4 nanocrystals as probes for the electric and magnetic local density of optical states throughout the visible spectral range, Nano Letters 16 (11) (2016) 7254–7260.

[110] Dongfang Li, Sinan Karaveli, Sébastien Cueff, Wenhao Li, Rashid Zia, Probing the combined electromagnetic local density of optical states with quantum emitters supporting strong electric and magnetic transitions, Physical Review Letters 121 (22) (2018) 227403.

[111] Peter R. Wiecha, Clément Majorel, Christian Girard, Arnaud Arbouet, Bruno Masenelli, Olivier Boisron, Aurélie Lecestre, Guilhem Larrieu, Vincent Paillard, Aurélien Cuche, Enhancement of electric and magnetic dipole transition of rare-earth-doped thin films tailored by high-index dielectric nanostructures, Applied Optics 58 (7) (2019) 1682–1690.

[112] N. Noginova, G. Zhu, M. Mavy, M.A. Noginov, Magnetic dipole based systems for probing optical magnetism, Journal of Applied Physics 103 (7) (2008) 07E901.

[113] N. Noginova, Yu. Barnakov, H. Li, M.A. Noginov, Effect of metallic surface on electric dipole and magnetic dipole emission transitions in Eu3+ doped polymeric film, Optics Express 17 (13) (Jun 2009) 10767–10772.

[114] Xingjie Ni, Gururaj V. Naik, Alexander V. Kildishev, Yu Barnakov, Alexandra Boltasseva, Vladimir M. Shalaev, Effect of metallic and hyperbolic metamaterial surfaces on electric and magnetic dipole emission transitions, Applied Physics B 103 (3) (2011) 553–558.

[115] Sinan Karaveli, Rashid Zia, Strong enhancement of magnetic dipole emission in a multi-level electronic system, Optics Letters 35 (20) (Oct. 2010) 3318–3320.

[116] Sinan Karaveli, Rashid Zia, Spectral tuning by selective enhancement of electric and magnetic dipole emission, Physical Review Letters 106 (May 2011) 193004.

[117] Mikolaj K. Schmidt, Ruben Esteban, JJl Sáenz, I. Suárez-Lacalle, S. Mackowski, Javier Aizpurua, Dielectric antennas-a suitable platform for controlling magnetic dipolar emission, Optics Express 20 (13) (2012) 13636–13650.

[118] Urs Zywietz, Mikolaj K. Schmidt, Andrey B. Evlyukhin Carsten Reinhardt, Javier Aizpurua, Boris N. Chichkov, Electromagnetic resonances of silicon nanoparticle dimers in the visible, ACS Photonics 2 (7) (2015) 913–920.

[119] Guillaume Boudarham, Redha Abdeddaim, Nicolas Bonod, Enhancing the magnetic field intensity with a dielectric gap antenna, Applied Physics Letters 104 (2) (2014) 021117.

[120] Marie Anne van de Haar, Jorik van de Groep, Benjamin JM Brenny, Albert Polman, Controlling magnetic and electric dipole modes in hollow silicon nanocylinders, Optics Express 24 (3) (2016) 2047–2064.

[121] Jiaqi Li, Niels Verellen, Pol Van Dorpe, Enhancing magnetic dipole emission by a nano-doughnut-shaped silicon disk, ACS Photonics 4 (8) (2017) 1893–1898.

[122] Maria Sanz-Paz, Cyrine Ernandes, Juan Uriel Esparza, Geoffrey W. Burr, Niek F. van Hulst, Agnès Maitre, Lionel Aigouy, Thierry Gacoin, Nicolas Bonod, Maria F. Garcia-

Parajo, et al., Enhancing magnetic light emission with all-dielectric optical nanoantennas, Nano Letters 18 (6) (2018) 3481–3487.

[123] Tianhua Feng, Yi Xu, Zixian Liang, Wei Zhang, All-dielectric hollow nanodisk for tailoring magnetic dipole emission, Optics Letters 41 (21) (2016) 5011–5014.

[124] Kseniia V. Baryshnikova, Andrey Novitsky, Andrey B. Evlyukhin, Alexander S. Shalin, Magnetic field concentration with coaxial silicon nanocylinders in the optical spectral range, Journal of the Optical Society of America B 34 (7) (2017) D36–D41.

Tailoring transmission and reflection with metasurfaces

5

Sergey Kruk, Yuri Kivshar
Nonlinear Physics Centre, Australian National University, Canberra ACT, Australia

5.1 Introduction

Mie-resonant dielectric nanoparticles provide a full control over the light scattering. When arranged into two-dimensional structures to form metasurfaces, they bring a new paradigm to optics allowing one to engineer both transmission and reflection of light in a nearly arbitrary way [1–7].

Conventional optical elements based on refraction, diffraction or material birefringence require light propagation through optically thick media. In striking contrast to that, the concept of metasurfaces allows one to enhance light-matter interactions via resonant response. Despite their ultrathin design, metasurfaces allow one to gain full control over the electromagnetic space. This includes the control over amplitude, phase and polarization of light. Importantly, metasurfaces can provide *spatially varying* wave control over a thin interface. This allows one to steer and reshape the light waves in an arbitrary complex way. Importantly, as the metasurfaces diminish our dependence on the propagation effects, they can introduce abrupt changes to amplitude, phase, and polarization structure of light.

For functional metasurfaces components and devices, control over transmission and reflection amplitudes is of primal importance as it defines the overall efficiency of the device. We have seen a remarkable progress in metasurface performance over the recent years. Specifically, all-dielectric metasurfaces optimized to work in reflection have reached the efficiencies of over 99% [8–11]. To put this into perspective, metasurfaces are better in reflecting light than metal mirrors, and are comparable in their efficiency to dielectric layered mirrors based on interference effects. Transmissive metasurfaces have surpassed 90% transparency [12,13]. This essentially makes them as transparent as glass slides. Fig. 5.1 shows some examples of efficiencies of recently demonstrated functional metasurfaces. In addition, all-dielectric metasurface absorbers have recently reached near-unity efficiencies [14]. Overall, metasurfaces based on dielectric nanostructures with both electric and magnetic Mie-type resonances have resulted in the best efficiency to date for functional flat metasurface-based optical components. In the recent years we have seen demonstrations of flat metadevices which match or outperform conventional optical elements while offering much thinner elements.

In this chapter, we discuss general approaches for the control of transmission, reflection, and absorption of light in metasurfaces via the interplay of Mie resonances.
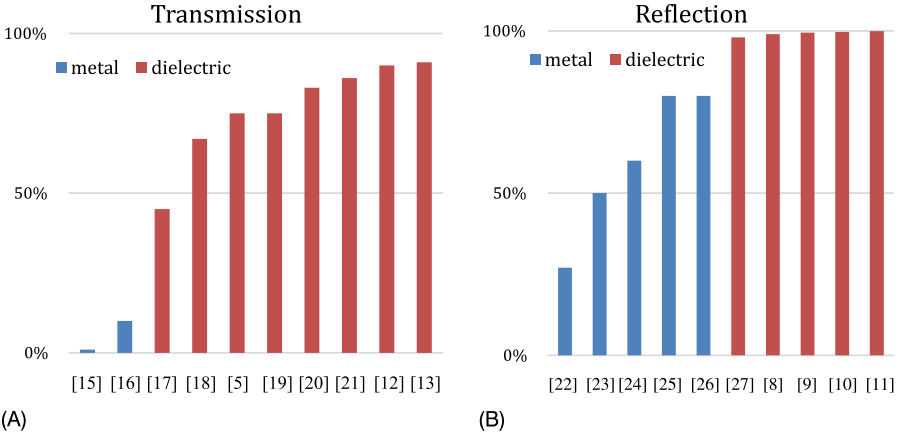
Figure 5.1 Comparison of the efficiencies of plasmonic and dielectric metasurfaces operating in both (A) transmission [5,12,13,15–21] and (B) reflection regimes [8–11,22–27].

5.2 Reflection

Electric and magnetic metasurface mirrors. We start from considering a sub-wavelength array of particles supporting a single Mie resonance: either electric dipole or a magnetic dipole. When illuminated with a plane wave, such array can behave as a perfect mirror.

The electric farfield scattered by an electric and a magnetic dipole can be written as

$$\mathbf{E}^{ED}(\mathbf{r}) = \left[\mathbf{n} \times [\mathbf{p} \times \mathbf{n}]\right] e^{i(\omega_{ED}t - \mathbf{k}_{ED}\mathbf{r} + \varphi_{ED})}$$
$$\mathbf{E}^{MD}(\mathbf{r}) = [\mathbf{m} \times \mathbf{n}] e^{i(\omega_{MD}t - \mathbf{k}_{MD}\mathbf{r} + \varphi_{MD})}$$

(5.1)

where $\mathbf{p}$ is the electric dipole amplitude with $|\mathbf{p}| = p = \frac{k_0^2}{4\pi\varepsilon_0 r} p$ with p denoting the electric dipole moment; and $\mathbf{m}$ represents the magnetic dipole amplitude with $|\mathbf{m}| = m = \sqrt{\frac{\mu_0}{\varepsilon_0}} \frac{k_0^2}{4\pi r} m$, with m denoting the magnetic dipole moment; $\mathbf{k}_{ED,MD}$ is the wavevector of electric/magnetic dipole; and $\mathbf{n} = \mathbf{k}/|\mathbf{k}|$ is the unit vector in the direction of scattering; $\omega_{ED,MD}$ is the resonant frequency of electric/magnetic dipole; $\mathbf{r}$ is the coordinate vector, and $r = |\mathbf{r}|$; the $\varphi_{ED,MD}$ are the phases of electric/magnetic dipoles. We consider a two-dimensional subwavelength array of such scatterers in $x-y$ plane at $z = 0$ illuminated by a plane wave propagating in z-direction. The only two directions allowed for scattering are forward $(+z)$ and backward $(-z)$.

For this case the scattering equations reduce to its scalar projection:

$$E^{ED}(z) = E_p e^{i\pi} e^{i(\omega_{ED}t\frac{z}{|z|} - k_{ED}z)}$$
$$E^{MD}(z) = E_m e^{i\pi\theta[z]} e^{i(\omega_{MD}t\frac{z}{|z|} - k_{MD}z)}$$

(5.2)
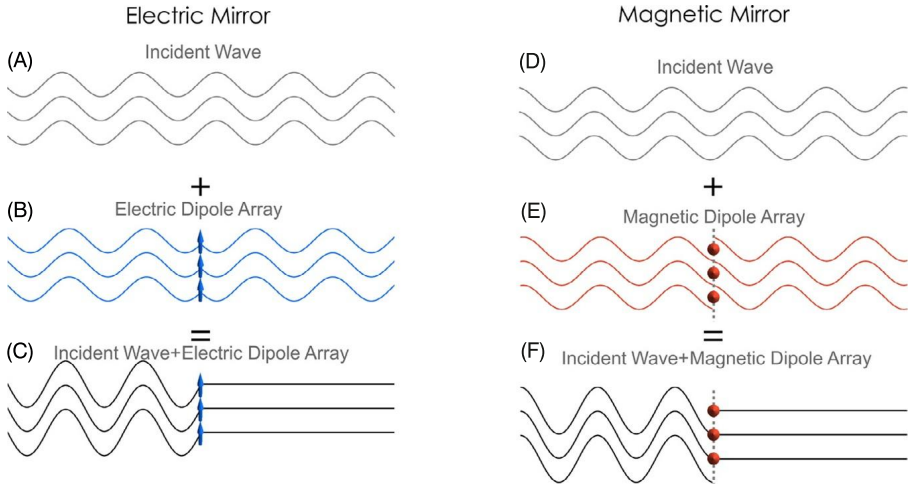
Figure 5.2 Concepts of electric and magnetic mirrors. Light scattering by arrays of (A–C) electric and (B–D) magnetic dipoles. Interferences between the incident scattered fields result in fully-destructive interference in forward direction, and in a standing wave in backward direction. At the surface of the electric mirror an anti-node of the standing wave is formed. In contrast, at the surface of the magnetic mirror, a node is formed.

where $E_{p,m}$ are amplitudes of the field scattered by the electric and the magnetic dipoles; $e^{i\pi}$ phase factor that accounts for out-of-phase excitation of the dipoles at resonance, $\theta[z]$ is a Heaviside function accounting for the antisymmetric nature of the magnetic dipole resonance (e.g. $\theta[z] = 0$ for $z < 0$, and $\theta[z] = 1$ for $z > 0$ accounting for $E^{MD}(-z) = -E^{MD}(z)$).

The incident field E_0 interferes with the scattered field E_p for the electric dipole or E_m for the magnetic dipole. And if $E_0 = E_{p,m}$, this results in a destructive interference in forward direction and a formation of a standing wave in backward direction [see Fig. 5.2 in which Eq. (5.2) are plotted for these conditions]. Notably, a standing wave formed by electric dipoles has a node at the mirror surface. This is equivalent to reflection from perfect electric conductor (PEC), therefore we refer to such metasurface an *electric mirror*. In contrast, an anti-node is formed at a surface of a mirror formed by magnetic dipoles. Therefore, we call a metasurface formed by magnetic dipoles a *magnetic mirror*.

To describe the spectral response of the electric and magnetic mirrors at around their resonant frequency, we approximate the electric dipole and magnetic dipole resonances with Lorentz oscillators [28] with reflectivity written as

$$r^{ED}(\omega) = \frac{2i\gamma_{ED}\omega}{\omega_0^2 - \omega^2 - 2i\gamma_{ED}\omega},$$

$$r^{MD}(\omega) = -\frac{2i\gamma_{MD}\omega}{\omega_0^2 - \omega^2 - 2i\gamma_{MD}\omega},$$

(5.3)
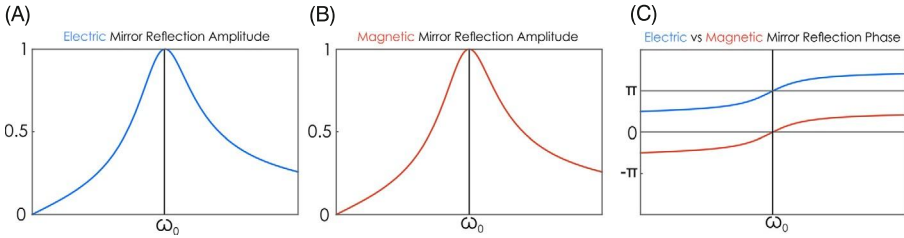
Figure 5.3 Spectral characteristics of the electric and the magnetic mirrors. (A–B) Reflection amplitude of the electric field reaching unity at (A) ED resonant frequency ω; and (B) MD resonance frequency ω. (C) Reflection phase of the electric field featuring π phase difference for the electric and magnetic mirrors.

where γ_{ED} and γ_{MD} are radiation losses of the electric and the magnetic dipole resonances correspondingly.

In Fig. 5.3 we plot amplitudes and phases of reflectivity of electric and magnetic mirrors as per Eq. (5.3) at around their resonant frequency. We observe amplitude of reflection reaching unity in both cases. The difference between the two mirrors is revealed in their reflection phase: light reflected from an array of electric dipoles experiences a π phase shift at resonance. In contrast, no phase shift occurs after reflection from magnetic dipole array.

Generalized metasurface mirrors. Our discussions of electric and magnetic mirrors can be readily extended to higher-order multipoles, such as electric and magnetic quadrupoles, octupoles, hexadecapoles etc. [29].

An array of electric dipole scatters acts as an electric mirror because $E^{ED}(z)$ is an *even* function, i.e. $E^{ED}(z) = E^{ED}(-z)$ [see Fig. 5.4]. Exemplarily, the **E**-field from an array of magnetic quadrupoles is an even function as well, and correspondingly a magnetic quadrupole metasurface acts as an electric mirror as well. Analogously, a magnetic dipole array acts as a magnetic mirror because $E^{MD}(z)$ is an *odd* function, i.e. $E^{MD}(z) = -E^{MD}(-z)$. And the next higher-order multipole of the same symmetry is an electric quadrupole, thus an array of electric quadrupoles would create a magnetic mirror. Fig. 5.4 demonstrates numerical results of field reflected by an array of dielectric rods of different diameters supporting various multipolar excitations. It shows electric mirror behavior at ED and MQ resonance, and magnetic mirror behavior at MD and EQ resonance. This analysis further extends to higher-order multipoles with even or odd **E**-fields [29].

Experimental demonstrations. Nearly-perfect reflection from dielectric metasurfaces supporting Mie resonances was demonstrated in the past using Tellurium (Te) cube resonators acting as electric or magnetic dipole scatterers at two different wavelengths [30] in the mid-infrared spectral range. Time-domain spectroscopy of the metasurface reflection [31] revealed the magnetic mirror behavior at the magnetic dipole resonance [see Fig. 5.5A]. In the near-infrared spectral range the metasurface mirrors were demonstrated using silicon nanodisks as scatterers [8]. A low-cost and scalable approach to fabricating dielectric metasurface mirrors was demonstrated in reference [10] [see Fig. 5.5B].
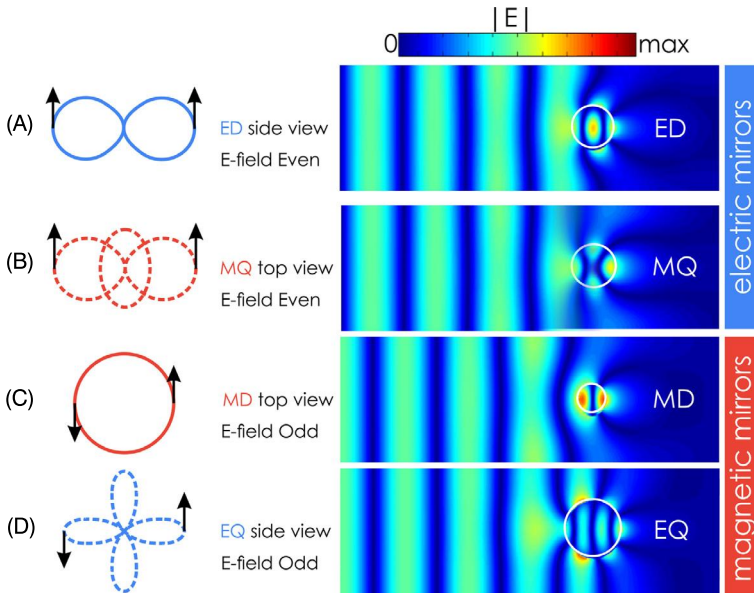
Figure 5.4 Generalized electric and magnetic mirrors. (A) An electric dipole array creates a *symmetric* distribution of the electric field in forward and backward directions and therefore acts as an electric mirror. (B) The same symmetry of magnetic quadrupole array leads to an electric mirror-type response as well. (C) A magnetic dipole array creates an *antisymmetric* field distribution in forward and backward directions, which is the origin of a magnetic mirror effect. (D) An electric quadrupole array features the same antisymmetric field distribution, and therefore it acts as a magnetic mirror as well. Adapted from [29].

5.3 Transparency

Huygens' metasurfaces. Interference between the electric and magnetic dipole modes of comparable strength can lead to the enhancement of forward scattering and suppression of backward scattering [32,33]. This resembles an object described back to 1690: a Huygens source [34] – a building block of a wavefront shaping interface or surface. The well-known Huygens principle states that each point on a wavefront acts as a secondary source of outgoing waves. The principle implies that sources do not radiate backward; however, in its original formulation this principle does not specify the structure of the sources that would satisfy this requirement. More recently, it was suggested that a Huygens source can be realized as electrically small antenna that is a superposition of crossed electric and magnetic dipoles [35,36]. Thus, a dielectric nanoparticle that supports both electric and magnetic dipole modes does fulfill these requirements. An array of such nanoparticles creates a Huygens metasurface [28].

When an x-polarized plane wave propagating in z-direction hits the Huygens' source, it excites electric dipoles in x-direction, and magnetic dipoles in y-direction. An array of electric dipoles produces a *symmetric* electric field distribution in propagating in $+z$- and $-z$-directions [as shown in Fig. 5.6A]. An array of magnetic dipoles, in its turn, produces an *antisymmetric* electric field distribution in $+z$- and
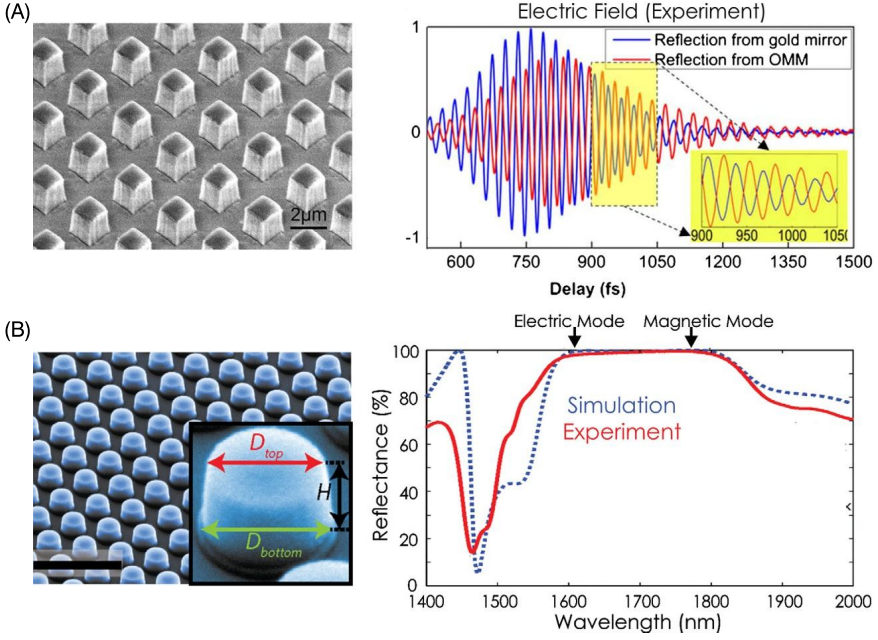
Figure 5.5 Experimental demonstrations of magnetic and electric all-dielectric metasurface mirrors. (A) Scanning electron micrograph of a fabricated metasurface consisting of Tellurium (Te) cube resonators acting as electric or magnetic dipole scatterers at two different wavelengths [30]. The time-domain spectroscopy of the metasurface reflection at the magnetic resonance features out-of-phase reflection when compared to ordinary metal mirror. [31] Reprinted figure with permission from [30]. © (2017) by the American Physical Society. (B) Scanning electron micrograph (left) and reflection spectrum (right) of a broadband dielectric metasurface mirror made of Si cylinders. Adapted with permission from [10]. © (2015) American Chemical Society.

$-z$-directions [see Fig. 5.6B]. A result of interference of superimposed electric dipole and magnetic dipole scatterers is written as $E^{\mathrm{ED}}(z) + E^{\mathrm{MD}}(z)$ as per Eq. (5.2). We assume the two dipoles have same resonant frequencies, amplitudes and resonance width. This leads to a destructive interference of the electric fields scattered by the two dipoles in backward direction [see Fig. 5.6C]. Thus, the field is scattered in forward direction only, making Huygens' metasurfaces fully transparent.

To understand spectral performance of Huygens' metasurfaces, we again employ the approximation of the dipoles as Lorentzian oscillators. The frequency-dependent transmittance in $+z$-direction, and the reflectance in $-z$-direction are

$$
\begin{aligned}
t &= 1 + \frac{2i\gamma_{\mathrm{ED}}\omega}{\omega_{\mathrm{ED}}^2 - \omega^2 - 2i\gamma_{\mathrm{ED}}\omega} + \frac{2i\gamma_{\mathrm{MD}}\omega}{\omega_{\mathrm{MD}}^2 - \omega^2 - 2i\gamma_{\mathrm{MD}}\omega} \\
r &= \frac{2i\delta_{\mathrm{ED}}\omega}{\omega_{\mathrm{ED}}^2 - \omega^2 - 2i\gamma_{\mathrm{ED}}\omega} - \frac{2i\delta_{\mathrm{MD}}\omega}{\omega_{\mathrm{MD}}^2 - \omega^2 - 2i\gamma_{\mathrm{MD}}\omega}
\end{aligned}
\tag{5.4}
$$

The condition of full transparency requires $\omega_{\mathrm{ED}} = \omega_{\mathrm{MD}}$, amplitudes $A_{\mathrm{ED}} = A_{\mathrm{MD}}$, and damping parameters $\gamma_{\mathrm{ED}} = \gamma_{\mathrm{MD}}$.
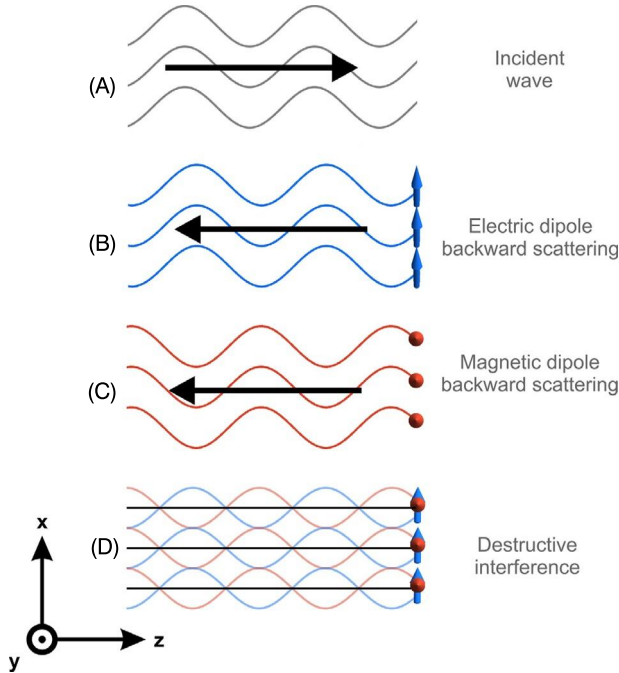
Figure 5.6 Zero backward scattering by Huygens' metasurfaces. Electric field of an incident plane wave (A) scattered backwards by an array of electric dipoles (B) superimposed with the scattering of an array of magnetic dipoles (C) resulting in destructive interference of backward scattering (D).

In Fig. 5.7A–C we plot *amplitude* of transmittance of an array of (A) electric dipoles, (B) magnetic dipoles, and (C) superimposed electric and magnetic dipoles.

Besides full transparency, Huygens' metasurfaces pack one more important feature. That is the *phase* of transmittance. In Figs. 5.7 D–F we see that while individual ED and MD resonances allow for a maximum of π phase accumulation, when added-up together, they provide a complete phase coverage of the entire range $0-2\pi$. This allows for wavefront control of light by a subwavelength planar device.

We note that complete transparency requires exact balance of all the parameters of the two dipoles that is their resonant frequencies, amplitudes and damping levels (or quality factors) must be the same. A deviation in any of these parameters reduces the transmission of light near the resonant frequencies.

The concept of Huygens' metasurfaces shares similarities with the Kerker condition [37] for zero backward scattering, derived by Kerker et al. for a hypothetical magnetic particle having similar electric and magnetic properties and published in 1983. We note, however, that the Kerker condition paves the way towards a forward scattering at a single wavelength only, and it can be satisfied for less strict requirements, e.g. partially overlapping resonances. The concept of Huygens' metasurfaces in contrast allows for a spectrally-wide forward scattering.
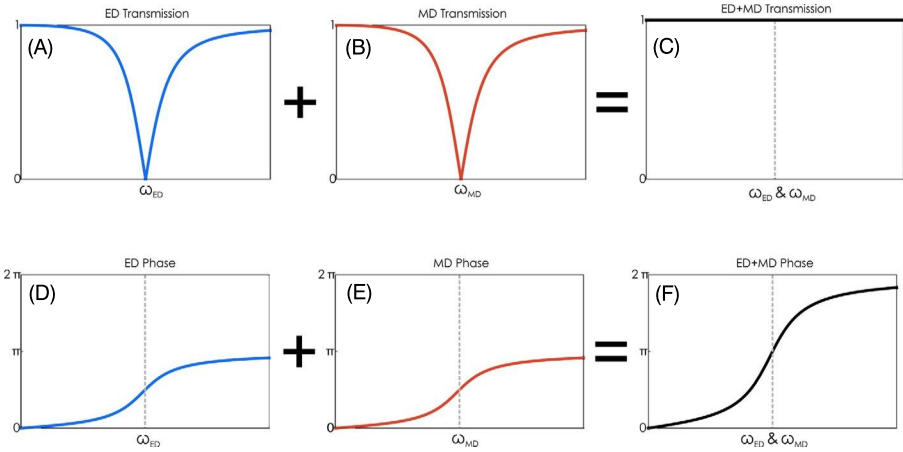
Figure 5.7 Spectral responses of metasurfaces operating at magnetic and electric dipole resonances. While transmission spectra of individual arrays of ED (A) and MD (B) exhibit minima at the resonant frequency, the transmission spectrum of an array of superimposed ED and MD (Huygens' metasurface) exhibits unity transmission over a broad spectral bandwidth. The phase accumulation in the vicinity of individual ED (D) and MD (E) resonances reaches a maximum of π, the phase accumulation of the Huygens' metasurface covers the entire 2π range (F).

Generalized Huygens' metasurfaces. Interference of electric and magnetic dipole modes offers only one example of a larger class of multipolar interference effects achievable with dielectric metasurfaces. The concept of Huygens' metasurfaces extends further to higher orders as well as higher number of multipoles. The regime of unidirectional scattering, the key ingredient of transparent metasurfaces, is not uniquely limited to dipolar resonances. Exemplarily, an array of superimposed magnetic and electric quadrupoles would interfere similarly to an array of electric and magnetic dipoles. More generally, a unidirectional scattering can be achieved by overlapping several multipoles of both *even* and *odd* symmetries that can interfere destructively in backward direction and constructively in forward direction [12]. Fig. 5.8A shows several examples of interferences of even and odd multipoles all resulting in a unidirectional forward scattering.

In a generalized case of higher number as well as higher order of multipoles, the transmittance and reflectance of a normally incident plane wave propagating in the z-direction, can be written as

$$t = 1 + \sum_{even} E(z) + \sum_{odd} E(z)$$
$$r = \sum_{even} E(z) - \sum_{odd} E(z)$$

(5.5)

An example of a unity-transmission spectrum as a result of interference of three multipoles is shown in Fig. 5.8B, C. Here we bring into consideration ED having even symmetry, as well as MD and electric quadrupole (EQ) both having odd symmetry.
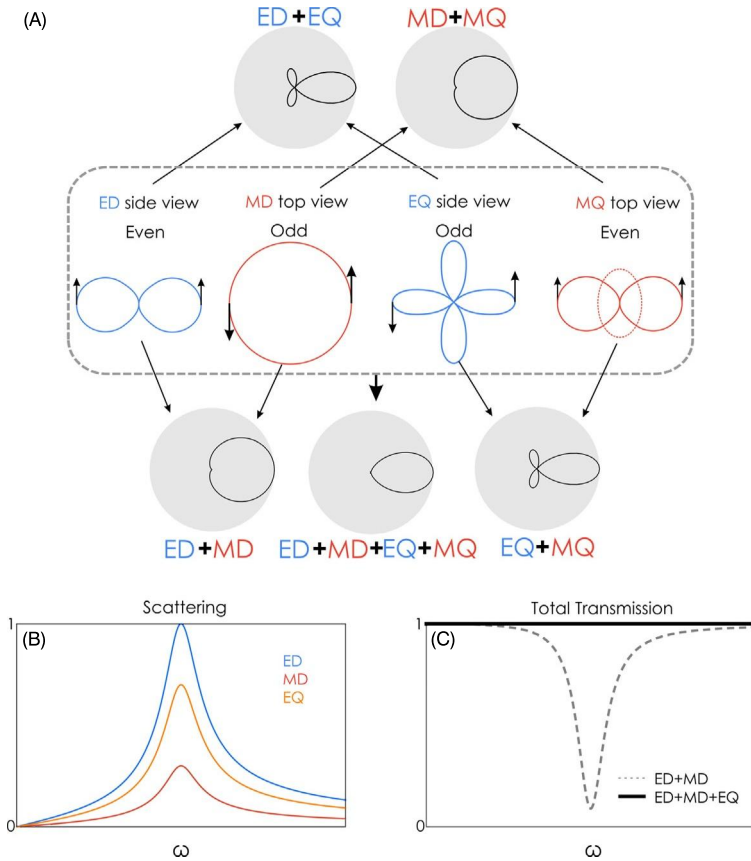
Figure 5.8 Generalized Huygens' metasurface realized by a superposition of several multipoles of both even and odd symmetry. (A) Different scenarios of interferences of first four multipoles all resulting in unidirectional forward scattering (generalized Kerker condition) and thus readily applicable for generalized Huygens' metasurfaces. Image adapted from [38]. (B) Exemplarily spectra of three multipoles: ED, MD, and EQ all having different amplitudes and damping levels. (C) The interference of the three multipoles results in unity transmission across the spectrum. Part (A) adapted with permission from W. Liu, Y.S. Kivshar, Generalized Kerker effects in nanophotonics and meta-optics, Opt. Exp. 26 (10) (2018) 13085–13105, © The Optical Society.

All three mutlipoles generally have different amplitudes and damping levels. While in this case ED and MD cannot satisfy Huygens' condition [see dashed gray line in Fig. 5.8C], the interference of all three multipoles leads to unity transmittance.

Importantly, the generalized Eqs. (5.5) can be satisfied over a broadband spectral range when $\sum_{even} E(z)$ and $\sum_{odd} E(z)$ each a linear combination of many multipoles. Then near-unity transmittance is achieved by a balance between multipoles, and it does not require resonances of equal amplitude, spectral width, and most notably, frequency. This makes multipolar structures inherently suited for realizing resonant broadband transmittance. We can thereby achieve a broadband response as a result of multi-wave interference between the scattering waves produced by several multipoles
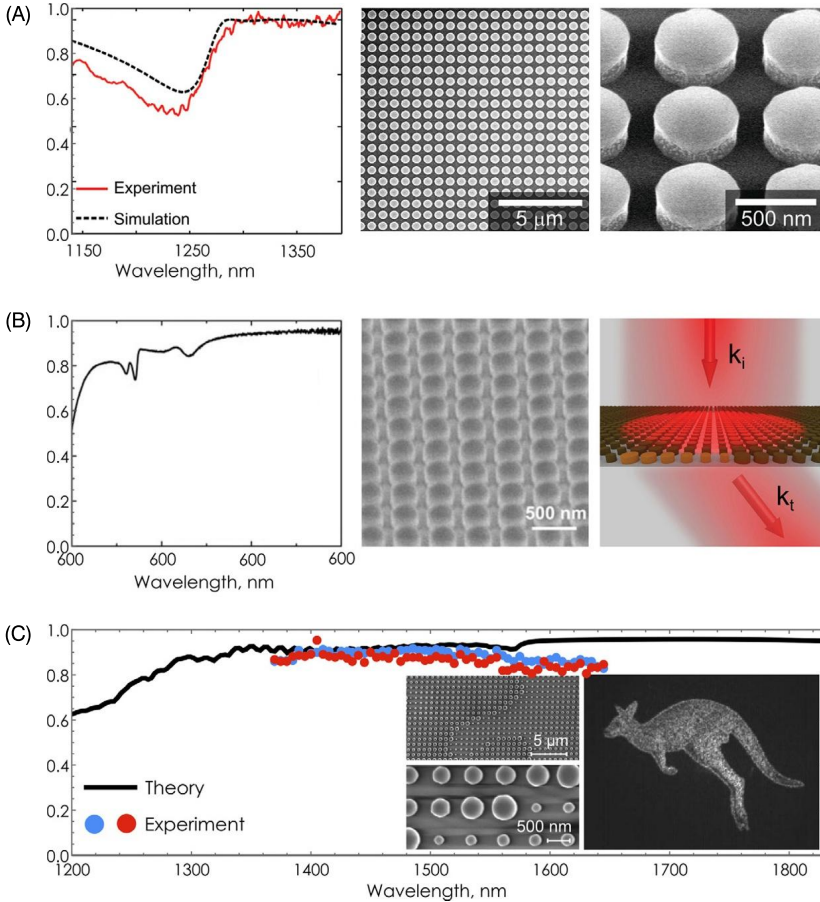
Figure 5.9 Experimental demonstrations of all-dielectric Huygens' metasurfaces. (A, B) Metasurfaces composed of silicon disks supporting overlapped ED and MD resonances that closely satisfies Huygens regime [28,42]. Transmission spectra are shown on the left, and scanning micrographs are featured on the right. (B) features a concept image of a 2π phase control revealed by the metasurface with linear phase gradient and functionality of a blazed diffraction grating [42]. (C) Generalized Huygens' metasurface made of silicon nanopillars supporting several multipoles of both even and odd symmetries [13]. The metasurface features a broadband spectrum of high transmission and showcases complex phase front control by transforming incident beam into holographic images. Part (C) reprinted with permission from L. Wang et al., Grayscale transparent metasurface holograms, Optica 3 (12) (2016) 1504–1505, © The Optical Society.

of opposite parity. Such multipolar forward scattering is referred to as the *generalized Huygens condition*.

The generalized Huygens condition also incorporates to a certain extent the forward scattering from two higher-order multipoles called generalized Kerker condition [39–41], which is fulfilled in this case over a broad spectral range.

Experimental demonstrations. In Fig. 5.9 we demonstrate transmission spectra of several fabricated Huygens' and generalized Huygens' metasurfaces. By now, over

90% transmission efficiencies have been achieved. Effectively, it makes Huygens' metasurfaces as transparent as glass within their operation range.

5.4   Phase and polarization control

Polarization control with the form-birefringent metasurfaces. Traditionally, polarization of light is controlled using birefringent optical materials with anisotropic crystalline lattices (such as that of calcite) [43]. With metasurfaces, however, the birefringence can be introduced at the level of individual meta-atom. A nanoparticle made of an isotropic material can alter polarization of light due to its anisotropic form as its multipolar scattering spectrum becomes polarization-dependent. This effect is known as form birefringence, and in metasurfaces it can originate from their geometry, not the properties of their constituent materials (schematically visualized in Fig. 5.10). Meta-atoms of different shapes with different levels of form birefringence can be used to create high-resolution subwavelength polarization gradients, which is difficult to achieve with conventional anisotropic crystals or even with liquid-crystal light modulators.

Concept of geometric phase. The ability to change polarization of incident light opens an opportunity for the wavefront control via the geometric phase approach [5,44]. The geometric phase concept can be introduced by referring to the Poincaré sphere, that is, a hypothetical sphere representing a variety of the polarization states of light.

We demonstrate the acquisition of the geometric phase with the following example of a hypothetical experiment: we start with right-circularly polarized light [north pole of the Poincaré sphere; see point A in Fig. 5.10B]. We then change the polarization from right to left-circular by a half-wave plate oriented at θ angle. This brings us to the south pole of the Poincaré sphere, i.e. point B in Fig. 5.10B. After that we change the polarization back to right-circular polarized by a half-waveplate oriented at 0 degree. Thus, we make a closed circuit on the sphere shown with arrows enclosing the solid angle of 4θ. We next describe this procedure with Jones calculus [45]. The transformation of the polarization can be written as

$$E_{\text{output}} = T \cdot R(-\theta) \cdot T \cdot R(\theta) \cdot E_{\text{RCP}} \tag{5.6}$$

where the half-waveplate matrix is

$$T = \begin{pmatrix} 1 & 0 \\ 0 & -1 \end{pmatrix} \tag{5.7}$$

the rotation matrix is

$$R = \begin{pmatrix} \cos\theta & \sin\theta \\ -\sin\theta & \cos\theta \end{pmatrix} \tag{5.8}$$
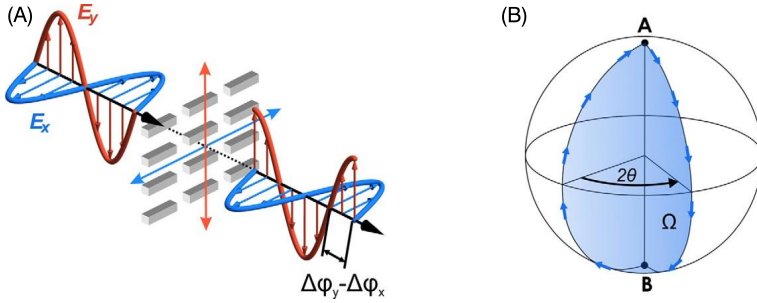
Figure 5.10 (A) Form birefringence of an anisotropic metasurface leads to a phase delay between two principal polarizations. (B) Geometric phase accumulation on the Poincaré sphere.

and the right-circular polarization vector is

$$E_{\mathrm{RCP}} = \frac{1}{\sqrt{2}} \begin{pmatrix} 1 \\ -i \end{pmatrix} \tag{5.9}$$

The resulting output is

$$E_{\mathrm{output}} = e^{i(-2\theta)} E_{\mathrm{RCP}}$$

Thus, the light acquired an extra phase equal in magnitude to 2θ, or half the solid angle Ω enclosed by the trajectory on a Poincaré sphere. As the total solid angle of the Poincaré sphere is 4π, the geometric phase approach allows one to vary the phase on an incident light within the full 2π region.

The sign of the acquired phase depends on clockwise or counterclockwise motion along the closed trajectory. If light does not make a full circuit on a Poincaré sphere, the geometric phase accumulation is found by connecting the starting and the final points with the shortest geodesic line [46].

Phase control with Huygens metasurfaces. Huygens metasurfaces and described in the previous section allow for phase accumulation between 0 and 2π. Indeed, a single resonance, an electric dipole or a magnetic dipole, gives up to π phase accumulation depending on spectral position of the resonance. When the two resonances are overlapped, the total phase accumulation reaches 2π. A Huygens metasurface can be assembled from different elements tuned to different resonant frequency such that it creates subwavelength phase gradients in the region $0 - 2\pi$.

Experimental demonstrations. In Fig. 5.11 we show several demonstrations of metasurfaces for phase and polarization control based on birefringence, the geometric phase, and Huygens' concept.
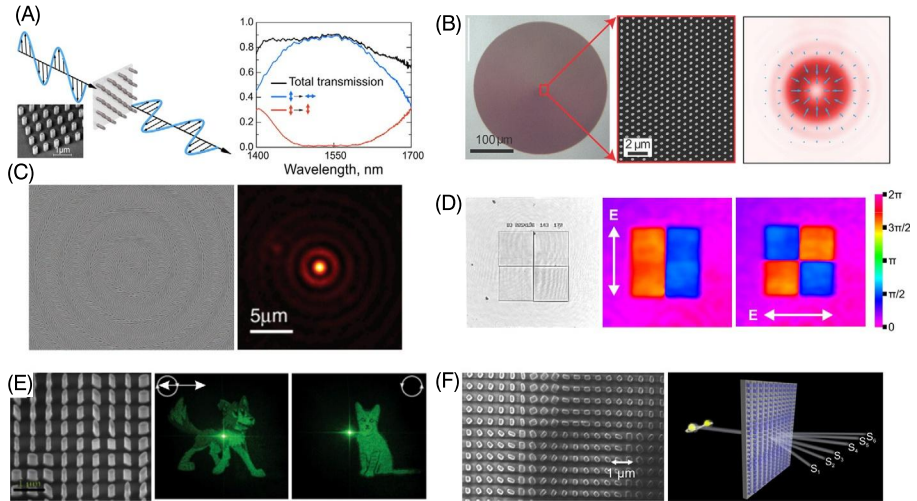
Figure 5.11 Phase and polarization control with dielectric metasurfaces. (A) A metasurface working as a half-waveplate over an extended spectral range covering three major communication bands of an optical fiber [12]. (B) A metasurface creating polarization gradients forming cylindrical vector beams [47]. (C) Metasurface flat lens based on geometric phase [5]. (D) A metasurface with independent control of phase for two orthogonal polarizations of light based on the combination of form birefringence and generalized Huygens' principle [48]. (E) A metasurface producing two independent holographic images for two orthogonal polarizations of light. (F) A metasurface splitting a beam of light into 6 channels with 6 different polarizations based on a combination of geometric phase and generalized Huygens' approaches [49].

5.5 Absorption

Coherent perfect absorption. Dielectric metasurfaces with electric and magnetic Mie resonances allow one to achieve 100% absorption of light. Here, by absorption we mean any process by which the energy of an electromagnetic wave is transferred to a medium and hence converted to another form. This is allowed by a process of coherent perfect absorption. Perfect absorption can be achieved with lossy Mie-resonant metasurfaces in the regime when the cavities act as critically coupled resonators. It relies on the destructive interference between the incident waves and waves scattered on resonant Mie-modes. The phenomenon of coherent perfect absorption can be generalized to arbitrary incoming waveforms that can consist of two or more waves, and to metasurfaces supporting several Mie resonances.

The simplest yet most illustrative example of a coherent perfect absorber is a two-port linear system. This may be represented by a metasurface coherently illuminated from both sides. Each input beam is partially reflected, partially transmitted, and partially absorbed inside the metasurface. The total outgoing wave on each side, therefore, is a superposition of a reflected wave and of a wave transmitted from the opposite side. This picture can be described rigorously using the scattering-matrix formalism

[50–52]:

$$\begin{pmatrix} b_1 \\ b_2 \end{pmatrix} = \begin{pmatrix} r_{11} & t_{12} \\ t_{21} & r_{22} \end{pmatrix} \begin{pmatrix} a_1 \\ a_2 \end{pmatrix} \tag{5.10}$$

where the complex scalars a_i and b_i denote the input and output wave amplitudes in the ith channel (or port), respectively; r_{ij} are the reflection coefficients and t_{ij} are the transmission coefficients of the scattering matrix $\hat{S}$. This formalism can be extended to describe more scattering channels and to include polarization degrees of freedom.

Coherent perfect absorption occurs when $\hat{S}\mathbf{a} = 0$ while $\mathbf{a} \neq 0$. This means that at least one eigenvalue of $\hat{S}$ is zero. The solution of this equation provides the parameters for critical perfect absorption regime. We further note that we are interested only in the solutions where the frequency of light is a real number, i.e. $\text{Im}[\omega] = 0$. This filters out unphysical solutions, such as input waves that grow exponentially with time.

Interestingly, the coherent perfect absorption condition can be interpreted as the time-reverse of the lasing threshold [53,54]. The complex conjugate of a coherent perfect absorption solution, for real ω, is a wave that is purely outgoing rather than incoming.

Absorption of Mie-resonant metasurfaces. To describe absorption in resonant metasurface we again employ Lorentz oscillator model with the only difference that absorption losses δ_{ED} and δ_{MD} are now included along with the radiation losses γ_{ED} and γ_{MD} [55]. Eqs. (5.3) for reflection now take the form

$$r^{ED}(\omega) = \frac{2i\gamma_{ED}\omega}{\omega_{ED}^2 - \omega^2 - 2i(\gamma_{ED} + \delta_{ED})\omega}$$

$$r^{MD}(\omega) = -\frac{2i\gamma_{MD}\omega}{\omega_{MD}^2 - \omega^2 - 2i(\gamma_{MD} + \delta_{MD})\omega} \tag{5.11}$$

The transmission correspondingly reads

$$t^{ED}(\omega) = 1 + \frac{2i\gamma_{ED}\omega}{\omega_{ED}^2 - \omega^2 - 2i(\gamma_{ED} + \delta_{ED})\omega}$$

$$t^{MD}(\omega) = 1 + \frac{2i\gamma_{MD}\omega}{\omega_{MD}^2 - \omega^2 - 2i(\gamma_{MD} + \delta_{MD})\omega} \tag{5.12}$$

The absorption can then be found to be

$$a = 1 - |r|^2 - |t|^2 \tag{5.13}$$

We first consider light absorption by a metasurface supporting a single Mie resonance (electric or magnetic) which is illuminated from one side. In this case, as per Eqs. (5.11)–(5.13) the maximum absorption can reach 50% [see Fig. 5.12A–C]. This requires balance between radiative and absorption losses: $\gamma = \delta$. In this regime transmission and reflection $|t|^2 = |r|^2 = 25\%$.

We note, however, that if the same metasurface is coherently illuminated from both sides, the absorption may vary between 0% and 100%. The absorption reaches 0% if
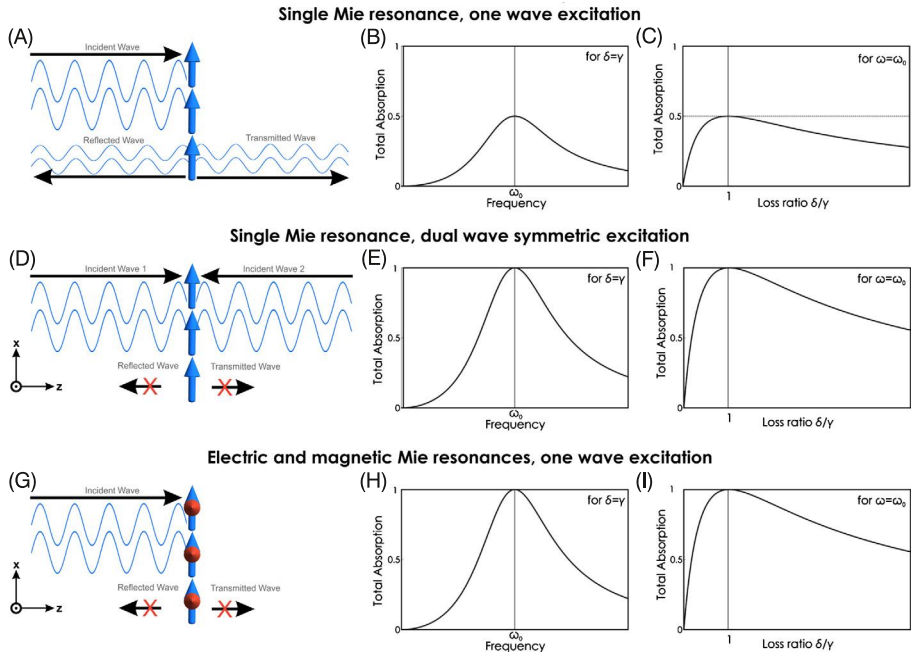
Figure 5.12 Light absorption by a dielectric metasurface composed of lossy Mie resonators. (A) Concept image of a single-resonant metasurface absorbing up to 50% of light when illuminated from one side. (B) Absorption spectra at around the resonant frequency for the case of optimal balance between radiative and absorption loss of Mie resonators. (C) Absorption as a function of the ratio of absorptive and radiative losses at the resonant frequency. (D) A scenario of a single-resonant metasurface coherently illuminated from both sides absorbing up to 100% of light. (E, F) corresponding dependencies of absorption on frequency detuning (E) and balance of losses (F). (G) A scenario of a metasurface supporting overlapped ED and MD resonances with absorption losses. The metasurface reaches 100% absorption even for one-side illumination. (H, I) corresponding dependencies of absorption on frequency detuning (H) and balance of losses (I).

a node of standing wave is formed at the metasurface, and 100% absorption may be achieved when an anti-node is formed at the metasurface. To achieve 100% absorption, a second incident beam can also be replaced with a reflective ground plane. This resembles a classic example of interference-assisted absorption, the Salisbury screen [56], and it requires a balance of amplitudes and phases or reflected waves to achieve fully destructive interference in reflection, and thus perfect absorption.

When the metasurface supports two Mie resonances, an electric dipole and a magnetic dipole, the absorption can reach 100% even for a single-side illumination [see Fig. 5.12G–I]. This requires $\omega_{ED} = \omega_{MD}$; $\gamma_{ED} = \delta_{ED}$; and $\gamma_{MD} = \delta_{MD}$.

To summarize, coherent perfect absorption in all-dielectric Mie-resonant metasurfaces can be achieved if at least three wave sources are involved: either two incident waves and one scattered wave on a single Mie multipole (e.g. electric dipole or magnetic dipole), or one incident wave and two waves scattered on a pair of Mie multipoles. The phenomenon of coherent perfect absorption can be readily extended
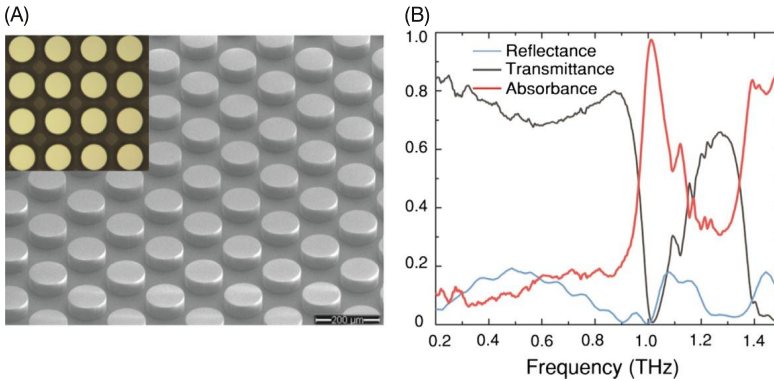
Figure 5.13 Experimental demonstration of a perfect absorber based on a dielectric metasurface. (A) Metasurface made of doped silicon disks that support electric dipole and magnetic dipole Mie resonances at around 1 THz frequency. A certain doping level of silicon is chosen to introduce absorption loss equal to resonant radiation loss. (B) Experimental transmission, reflection and absorption spectra. The metasurface is illuminated with one incident wave from the top. The spectrum features virtually perfect absorption of an incident wave at around 1 THz frequency. Reprinted with permission from X. Liu, K. Fan, I.V. Shadrivov, W.J. Padilla, Experimental realization of a terahertz all-dielectric metasurface absorber, Opt. Express 25 (1) (2017) 191, © The Optical Society.

to higher number of incident waves, and higher number as well as higher order of multipoles.

Experimental demonstrations. Perfect absorption in all-dielectric metasurfaces has been demonstrated in THz frequency range. In Refs. [14,55,57] the research demonstrated coherent perfect absorption at around 1 THz frequency in a metasurface made of doped silicon [see Fig. 5.13]. The researched demonstrated experimentally virtually 100% absorption of an incident wave when the electric dipole and magnetic dipole resonances are brought into overlap, and when absorption loss equals radiation loss.

5.6   Transmission and reflection at the oblique illumination

It is well known since the 19th century that when light encounters a boundary between two media at a specific angle, known as Brewster angle, the p-polarized component of light is perfectly transmitted, thus the reflected light is perfectly s-polarized. The common microscopic interpretation of this effect is illustrated in Fig. 5.14A. In response to the driving electromagnetic wave, electric dipoles are induced within the material. These dipoles oscillate along the direction of the electric field, that is, perpendicular to the propagation direction. As the far-field power radiated by a dipole vanishes along its oscillation axis, whenever the dipoles and the reflection direction are parallel, no radiation is emitted into that direction and reflection is inhibited. In all other directions apart from that of refraction, radiation is compensated by the rest of the dipoles within
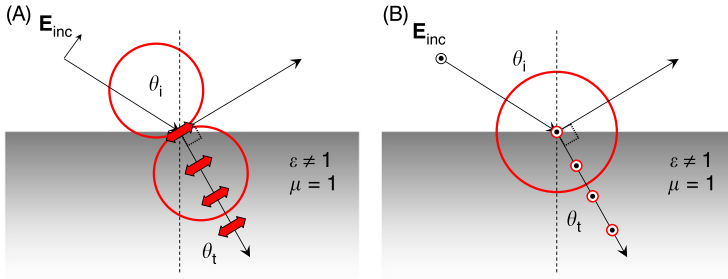
Figure 5.14 Concept image of a microscopic interpretation of classical Brewster effect. Adapted from [58].

the medium. If polarization is switched, as shown in Fig. 5.14B, due to the non-zero radiation in the plane perpendicular to the dipole, such effect cannot be achieved.

In this section, we extend the Brewster effect to the case of metasurfaces supporting magnetic dipole excitations along with electric dipole excitations [58].

We start from the Eq. (5.1) for the electric and magnetic fields, and we assume that $\omega_{ED} = \omega_{MD} = \omega_0$, and $\mathbf{k}_{ED} = \mathbf{k}_{MD} = \mathbf{k}_0$. We consider a plane wave illuminating the metasurface at an incident angle θ_i in $x-z$ plane. Here we consider a sub-diffraction metasurface consisting of identical scatterers, for which the only direction allowed for non-zero reflection is at an angle $\theta_r = -\theta_i$ as in all other directions the scattering from different resonators in the metasurface interfere destructively and cancel out. We further consider separately the two cases of p-polarized and s-polarized waves.

Generalized Brewster effect for the p-polarized waves. The p-vector induced along the $\mathbf{E}$ field is pointing at an angle $\theta_i - \pi/2$. The $\mathbf{p}$, $\mathbf{m}$, and $\mathbf{n}$ vectors correspondingly take the form

$$\mathbf{p} = p \begin{pmatrix} \sin[\theta_i - \pi/2] \\ 0 \\ \cos[\theta_i - \pi/2] \end{pmatrix}; \quad \mathbf{m} = m \begin{pmatrix} 0 \\ 1 \\ 0 \end{pmatrix}; \quad \mathbf{n} = \begin{pmatrix} \sin[-\theta_i] \\ 0 \\ \cos[-\theta_i] \end{pmatrix} \tag{5.14}$$

The total electric field in the $\mathbf{n}$ direction then reads

$$\mathbf{E}^{ED} + \mathbf{E}^{MD} = \begin{pmatrix} \cos\theta_i \left[m\, e^{i\varphi_{MD}} - p\, e^{i\varphi_{ED}} \cos 2\theta_i \right] \\ 0 \\ \sin\theta_i \left[m\, e^{i\varphi_{MD}} - p\, e^{i\varphi_{ED}} \cos 2\theta_i \right] \end{pmatrix} e^{i(\omega_0 t - \mathbf{k}_0 \mathbf{r})} \tag{5.15}$$

For $m = 0$, and $p \neq 0$ i.e. a metasurface with pure electric dipole response, zero reflection happens at an angle $\theta_i = 45°$. For a pure magnetic metasurface with $m \neq 0$, and $p = 0$ zero reflection is not possible for p-polarized incident field. When both electric and magnetic components are present, reflection drops to zero at an angle

$$\cos 2\theta_i = \frac{m}{p} e^{i(\varphi_{MD} - \varphi_{ED})} \tag{5.16}$$

Note that, as the angle θ_i is a real number, the phase difference between the electric dipole and the magnetic dipole $\varphi_{MD} - \varphi_{ED}$ must be either 0 or π for the effect to occur.

In addition to that, zero reflection occurs only for the case of $m \leq p$. Note that when $m = p$, $\theta_i = 90°$, e.g. zero reflection occurs at normal incidence, which corresponds to a condition of Huygens' metasurface described in Section 5.3.

Generalized Brewster effect for the s-polarized waves. In this case, the **m**-vector induced along the **H** field is pointing at an angle $\theta_i - \pi/2$. The **p**, **m**, and **n** vectors correspondingly take form:

$$\mathbf{p} = p \begin{pmatrix} 0 \\ 1 \\ 0 \end{pmatrix}; \quad \mathbf{m} = m \begin{pmatrix} \sin[\theta_i - \pi/2] \\ 0 \\ \cos[\theta_i - \pi/2] \end{pmatrix}; \quad \mathbf{n} = \begin{pmatrix} \sin[-\theta_i] \\ 0 \\ \cos[-\theta_i] \end{pmatrix} \tag{5.17}$$

The total electric field in the **n** direction then reads

$$\mathbf{E}^{\mathrm{ED}} + \mathbf{E}^{\mathrm{MD}} = \begin{pmatrix} \cos\theta_i \left[p\, e^{i\varphi_{\mathrm{ED}}} - m\, e^{i\varphi_{\mathrm{ED}}} \cos 2\theta_i \right] \\ 0 \\ \sin\theta_i \left[p\, e^{i\varphi_{\mathrm{ED}}} - m\, e^{i\varphi_{\mathrm{ED}}} \cos 2\theta_i \right] \end{pmatrix} e^{i(\omega_0 t - \mathbf{k}_0 \mathbf{r})} \tag{5.18}$$

For a pure magnetic metasurface with $m \neq 0$, and $p = 0$ zero reflection occurs at an angle $\theta_i = 45°$. For $m = 0$, and $p \neq 0$ i.e. a metasurface with pure electric dipole response, zero reflection is not possible for s-polarized incident field. When both electric and magnetic components are present, reflection drops to zero at an angle

$$\cos 2\theta_i = \frac{p}{m} e^{i(\varphi_{\mathrm{ED}} - \varphi_{\mathrm{MD}})} \tag{5.19}$$

Similarly, the phase difference between the electric dipole and the magnetic dipole has to be either 0 or π, and $p \leq m$ for the effect to occur.

Experimental demonstrations. Generalized Brewster effects were demonstrated experimentally in visible spectral range in metasurfaces made of silicon nanodisks supporting both electric and magnetic dipole Mie resonances [see Fig. 5.15].

5.7   Transmission and reflection polarization phenomena

Low-symmetry metasurfaces. Here we focus on the effects arising in metasurfaces with low symmetry. We consider three main sources of symmetry reduction here:

- Low symmetry of constituting resonators – meta-atoms. Such as rotation symmetry lower than 3-fold, or absence of mirror symmetry planes.
- Low symmetry of metasurface lattice (lattice rotation symmetry lower than 3-fold) that leads to asymmetric coupling between meta-atoms. Alteration of the lattice symmetry of a metasurface changes the coupling between meta-atoms and therefore changes the optical response.
- Oblique illumination under which the directions of **k**, **E**, and **H** fields break the symmetry of the system. In this case, the effective symmetry must be considered for the combined system of a metasurface and an incident wave [59].
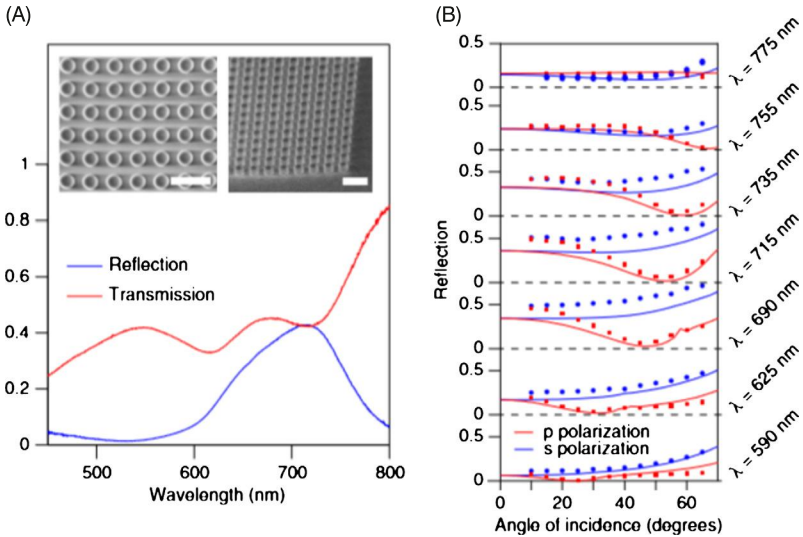
Figure 5.15 Angular reflection of light from arrays of silicon nanodisks. (A) Experimentally measured reflection (blue solid curve) and transmission (red solid curve) under normal incidence of a square lattice of silicon disks with diameter $D = 180$ nm, height $H = 150$ nm and pitch $P = 300$ nm placed on a glass substrate. The insets show the top (left) and tilted (right) SEM images of the measured sample. The scale bar is 500 nm. (B) Reflection versus angle of incidence measured for different wavelengths under p-polarized (red circles) and s-polarized (blue circles) illumination. The numerical results, obtained for $D = 170$ nm and $H = 160$ nm with the same pitch, are shown as solid curves. [58].

Such systems exhibit a wide range of polarization phenomena that can be described qualitatively based on Jones matrix formalism [60,54]. This analysis can be used for any symmetries and any arrangement of meta-atoms with long-range positional order, and therefore it can be applied for both periodic and quasicrystalline structures [61, 62]. Random layouts of meta-atoms can be described within this framework as having ∞-fold rotation symmetry [63].

Here we consider a sub-diffraction metasurface illuminated by a plane wave. The components of the transmitted wave t can be related to those of the incident wave i via the Jones matrix:

$$\begin{pmatrix} E_{t1} \\ E_{t2} \end{pmatrix} = \begin{pmatrix} J_{11} & J_{12} \\ J_{21} & J_{22} \end{pmatrix} \begin{pmatrix} E_{i1} \\ E_{i2} \end{pmatrix} \tag{5.20}$$

Similarly, incident and reflected waves can be related. The matrix may be expressed in linear [TE,TM] or circular [+, −] polarization basis, and conversion between these forms is well known [60]. The Jones matrix immediately shows which polarization phenomena the media may exhibit. Below we provide some relations between polarization phenomena and Jones matrix components valid for both transmission and reflection.

- Circular dichroism: $CD \propto |J_{++}|^2 - |J_{--}|^2$
- Linear dichroism: $LD \propto |J_{TE,\,TE}|^2 - |J_{TM,\,TM}|^2$

- Asymmetric transmission in both bases: $AT \propto |J_{12}|^2 - |J_{21}|^2$
- Linear birefringence: $LB \propto \arg\left[J_{TE,TE}/J_{TM,TM}\right]$
- Circular birefringence and optical activity: $CB \propto \arg\left[J_{++}/J_{--}\right]$

The relations between the Jones matrix components J_{ij} depend on the following point symmetry elements:

$C_N^{(k)}$ – Rotational axis parallel to the incident wave vector $\mathbf{k}$, where $2\pi/N$ is the angle of the rotational symmetry; note that the axis should correspond to both the point symmetry of individual meta-atom and the symmetry of the lattice.

$\sigma_v^{(k)}$ – Mirror plane (of both the meta-atom and the lattice), parallel to $\{\mathbf{k}, \mathbf{E}\}$, or $\{\mathbf{k}, \mathbf{H}\}$ plane;

i – Center of inversion symmetry.

Note that mirror planes and rotational axes which are neither parallel nor perpendicular to $\{\mathbf{k}, \mathbf{E}\}$, or $\{\mathbf{k}, \mathbf{H}\}$ planes have no effect on the Jones matrix. We consider four different scenarios summarized in Table 5.1. The symmetry elements which dictate the symmetry of the optical response are shown in each case. We calculate the general form of the Jones matrices in both linear and circular bases, following the procedure described in Ref. [60]. From these symmetry rules, we determine permitted polarization phenomena for each case.

Case (a) is a normal illumination of lattices with rotational symmetry $N > 2$. Jones matrix is diagonal with equal elements in both linear and circular bases. Accordingly, no polarization phenomena are expected.

Case (b) is normal illumination of chiral metasurface. The metasurface has a rotation symmetry with $N > 2$, but no mirror symmetry planes. Such a medium gives different phase accumulation to two orthogonal circular polarizations, and thus it exhibits optical activity.
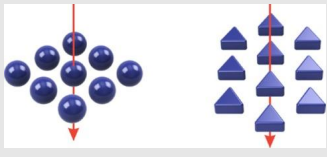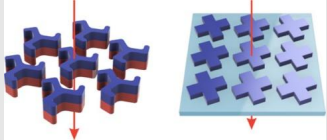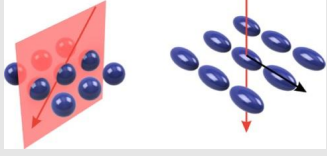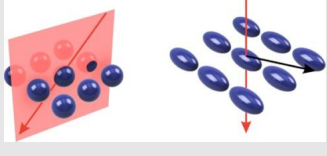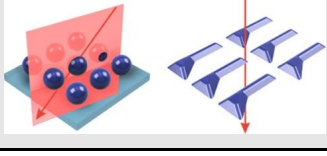
Case (c) may correspond to one of the following: oblique illumination of a high-symmetry structure such that $\mathbf{k}$ is parallel to the symmetry plane; normal illumination of a rectangular lattice of meta-atoms (or meta-atoms with $N = 2$) such that $\mathbf{E}$ field is parallel to the meta-atom symmetry plane. Trivial effects of linear dichroism and linear birefringence can be observable.

Case (d) applies to arbitrary oblique illumination of highly-symmetric metasurface; or normal illumination of a rectangular lattice of meta-atoms (or meta-atoms with $N = 2$) such that $\mathbf{E}$ field is neither parallel nor perpendicular to the meta-atom symmetry plane. In this case general polarization conversion may be observable.

Case (e) is the most general form of metasurface symmetry and its excitation. One example is arbitrary oblique illumination of a structure on a substrate. In comparison to Case (d), the substrate removes the inversion symmetry. The other example are meta-atoms with no point symmetry. For this case dichroism, asymmetric transmission, and birefringence can be observed.

The optical phenomena in transmission and reflection originating from the low symmetry are mostly analogous, with the exception: difference in reflection phase from a bianisotropic metasurfaces (or a metasurface that lacks the center of inversion $\{i\}$) [64].

Table 5.1 Symmetry-driven optical effects with metasurfaces.

Case	Symmetry group and operations	Examples of possible realizations	Jones matrix	Polarization phenomena
a	D_{Nh}, $\{C_N, \sigma_v, i\}$ $N>2$		$\begin{pmatrix} A & 0 \\ 0 & A \end{pmatrix}$	• None
b	C_N, $\{C_N\}$ $N>2$		$\begin{pmatrix} A & B \\ -B & A \end{pmatrix}$	• Optical activity • Polarization rotation
c	D_{2h} $\{C_2, \sigma_v, i\}$		$\begin{pmatrix} A & 0 \\ 0 & D \end{pmatrix}$	• Linear dichroism • Linear birefringence
d	C_i $\{i\}$		$\begin{pmatrix} A & B \\ B & D \end{pmatrix}$	• Linear dichroism • Linear birefringence • Polarization conversion
e	C_1 $\{\}$		$\begin{pmatrix} A & B \\ C & D \end{pmatrix}$	• Dichroism • Asymmetric transmission • Polarization conversion

Experimental demonstrations. Fig. 5.16 summarizes some of the previous demonstrations of low-symmetry phenomena in dielectric metasurfaces. Figs. 5.16A, B show a form-birefringent metasurface [Case (c) in Table 5.1] providing polarization conversion in reflection and transmission correspondingly. Fig. 5.16C is a chiral metasurface [Case (b) in Table 5.1] demonstrating different response for left- and right-circularly polarized light. And Fig. 5.16D is a bianisotropic metasurface with no inversion symmetry showing a difference in phase in reflection for the opposite top and bottom direction of excitation.

(A)

(B)

(C)

(D)
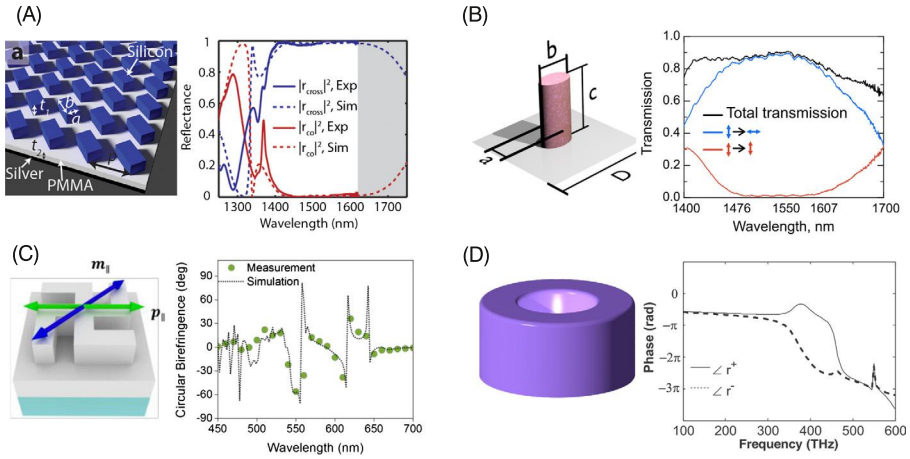
Figure 5.16 Examples of optical phenomena in low-symmetry metasurfaces. (A) Polarization rotation metasurface working in reflection [27]. (B) Half-wave plate (linear polarization rotator) metasurfaces working in transmission [12]. (C) Chiral metasurface with high circular dichroism and optical activity [65]. (D) A metasurface consisting of bianisotropic dielectric elements showing difference in phase in reflection for the opposite top and bottom direction of excitation [64].

5.8 Fano resonances

Fano resonances were introduced by Ugo Fano in 1961 as a special type of resonances that occur when a discrete quantum state interferes with a continuum band of states [66]. Interestingly, the original results for an important limiting case appeared back in 1935 [67]. The resonance manifests itself in the absorption spectrum, $\sigma(E)$, with the shape described by the Fano equation:

$$\sigma(E) = D^2 \frac{(q + \Omega)^2}{1 + \Omega^2} \tag{5.21}$$

where E is the energy, $q = \cot \delta$ is the Fano parameter, δ is the phase shift of the continuum, $\Omega = 2(E - E_0)/\Gamma$, where Γ and E_0 are the resonance width and energy, respectively, and $D^2 = 4 \sin^2 \delta$ [68].

The Fano equation has found broad applications in physics, and in particular it has been widely used in optics in order to describe not only absorption, but also transmission and scattering of light in various systems including dielectric metasurfaces. The wide applicability of this equation arises from the fact that almost any resonant state can be considered as quasi-discrete with a complex frequency thus resembling the conditions described by Fano. Metasurfaces supporting Fano resonances found an important role in nanophotonics as they exhibit high-Q resonances leading to sharp transmission–reflection spectral curves. Optical response of Fano metasurfaces changes from high transmission to high reflection within a narrow spectral range.

Fig. 5.17 shows an example of a dielectric nanoresonator exhibiting characteristic spectral response of Fano resonance. It has two critical points: when the scattering
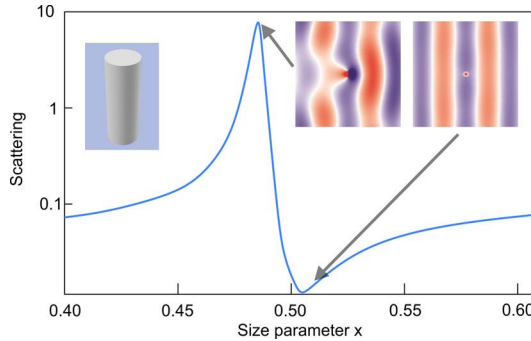
Figure 5.17 Scattering efficiency around a Fano-shape resonance in a dielectric ($\varepsilon = 60$) embedded in air ($\varepsilon = 1$). Insets on the left show the transverse magnetic field component for the two critical points Here $x = r\omega/c$, and r is the rod radius and c the speed of light.

efficiency vanishes and when it takes the maximum value close to unity. This leads to a rapid spectral switch of Fano metasurfaces from total reflection to total transmission.

In metasurfaces, the characteristic spectra of transmission or absorption with sharp resonances can also be observed in different regimes, such as the regimes of the Borrmann effect [69] or by the optical analog of electromagnetically induced transparency (EIT) [70]. The interested reader can find an in-depth analysis of Fano resonances in photonics in Reference [33].

Experimental demonstrations. Fig. 5.18 summarizes some of the demonstrations of metasurfaces featuring sharp Fano resonances.

5.9 Bound states in the continuum

Bound states in the continuum (BIC) were originally introduced in 1929 by von Neuman and Wigner as peculiar solutions of the Schrödinger equation in quantum mechanics [74], and the physics and origin of such exotic states is depicted in Fig. 5.19A. The spectrum of a conventional quantum well consists of two families of modes, which are clearly separated in energies: delocalized states existing within the continuum of propagating solutions and bound states which form a discrete set of modes. Exotic bound in the continuum states, which are spatially localized despite their energies lie in the continuous part of spectrum, can be achieved by the specific modulation of the potential with unbound oscillations.

Due to the universal nature of the Schrödinger equation, BICs represent an ubiquitous phenomenon pertaining to all domains of wave physics including optics of dielectric metasurfaces, where the effect originates from strong coupling between the resonant optical modes of metasurfaces. Importantly, a true bound state in the continuum is *a mathematical object* with an infinite value of the quality factor (Q factor) and vanishing resonance width, and it can exist only in ideal lossless infinite structures or for extreme values of parameters [76]. In practice, a quasi-BIC mode can be real-
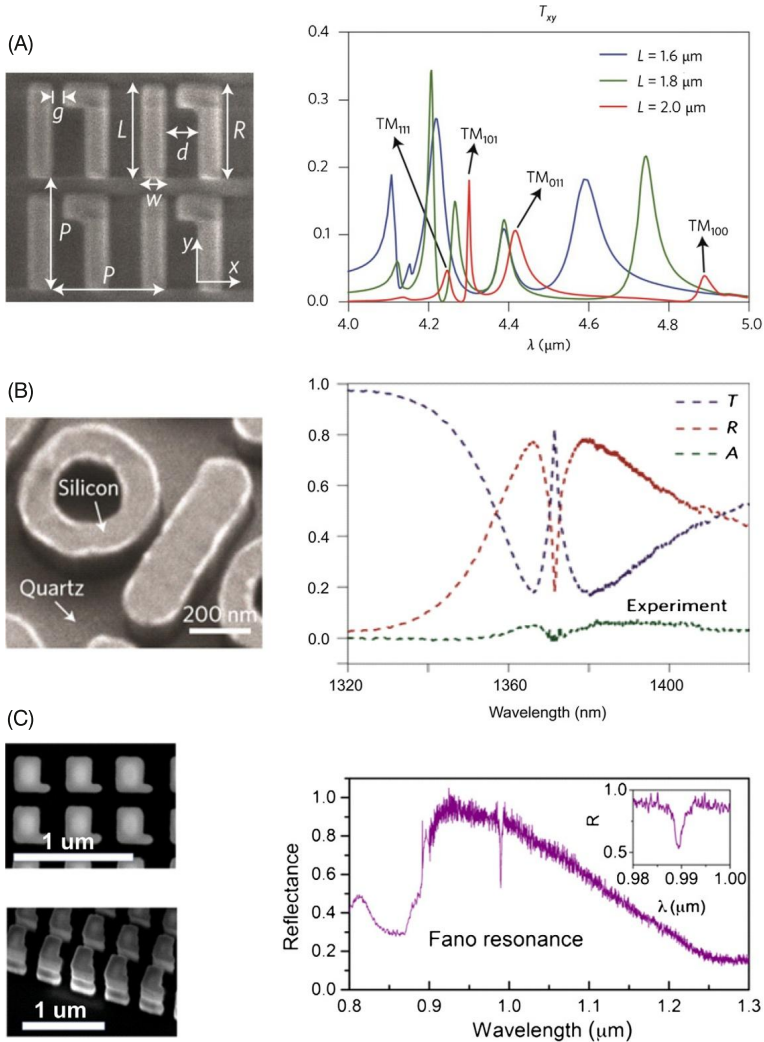
Figure 5.18 Fano-resonant metasurfaces (A) Fano-resonant silicon metasurface, left: electron microscope image of silicon metasurface; and right: its cross-polarized transmission spectra for different nanorod lengths L [71]. (B) Fano-resonant silicon metasurface; SEM image of a unit cell on the left, and its transmittance (T), reflectance (R) and absorption (A) spectra on the right [72]. (C) Symmetry broken GaAs metasurface exhibiting a Fano resonance employed for the enhancement of second harmonic generation [73].

ized, also known as *a supercavity mode* [77], when both the Q factor and resonance width remain finite and approach the mathematical BIC condition asymptotically. The BIC-inspired localizations of light made it possible to realize high-Q modes in metasurfaces that feature sharp spectral resonances in transmission or reflection spectra.
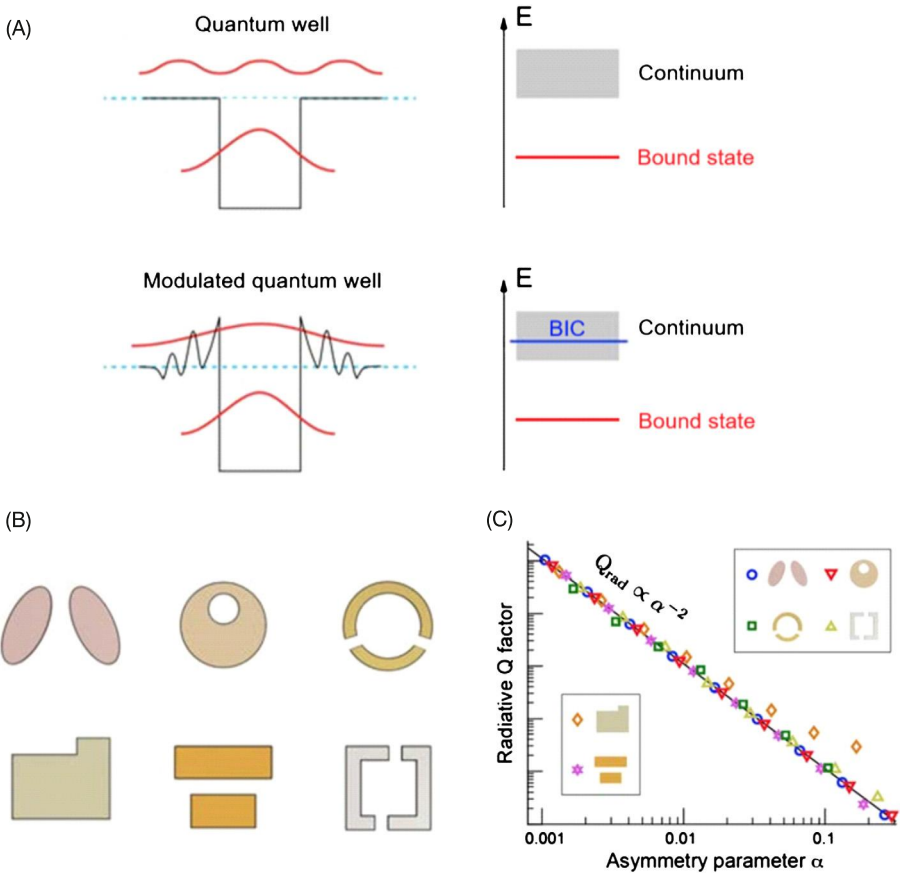
Figure 5.19 Metasurfaces hosting the bound states in the continuum (A) A sketch of a conventional energy potential in quantum mechanics supporting a discrete bound state (top) and an exotic potential supporting a bound state localized within the radiation continuum (bottom), with the energy levels shown schematically at the right [75]. (B) Unit cells of metasurfaces with a broken symmetry supporting sharp resonances [75]. (C) Design-independent Q factor vs. asymmetry parameter α for the shown meta-atoms with broken symmetry [75].

Such metasurfaces consist of arrays of dissimilar meta-atoms with a broken in-plane symmetry, with some examples shown in Fig. 5.19B, C.

The behavior of accidental BICs can be theoretically explained within the temporal coupled mode theory applied to a simple system of two resonances, where the amplitudes $a = [a_1(t), a_2(t)]^T$ of the modes evolve in time as $d\mathbf{a}/dt = \mathcal{H}\mathbf{a}$ with the following Hamiltonian:

$$\mathcal{H} = \begin{bmatrix} \omega_1 & \kappa \\ \kappa & \omega_2 \end{bmatrix} - i \begin{bmatrix} \gamma_1 & \sqrt{\gamma_1\gamma_2}e^{i\psi} \\ \sqrt{\gamma_1\gamma_2}e^{i\psi} & \gamma_2 \end{bmatrix} \tag{5.22}$$
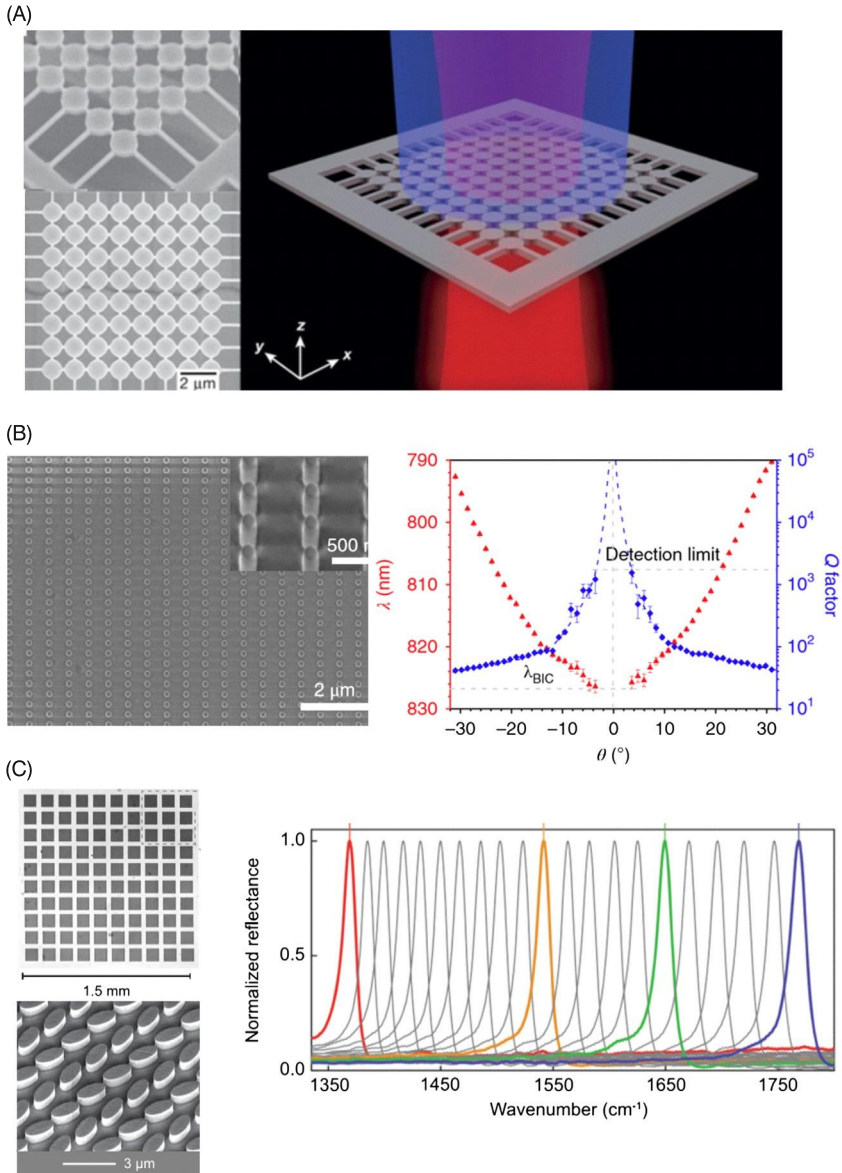
Figure 5.20 Metasurfaces with sharp resonances associated with bound states in the continuum. (A) Fano-resonant silicon metasurface, left: electron microscope image of silicon metasurface; and right: its cross-polarized transmission spectra for different nanorod lengths *L* [71]. (B) Fano-resonant silicon metasurface; SEM image of a unit cell on the left, and its transmittance (T), reflectance (R) and absorption (A) spectra on the right [72]. (C) Nanopatterned membrane fabricated of InGaAsP multiple quantum wells and suspended in air. The membrane support BIC resonance facilitating lasing at room temperature [79]. (D) GaAs BIC metasurface facilitating lasing [80]. (E) Symmetry broken GaAs metasurface exhibiting a Fano resonance employed for the enhancement of second harmonic generation [73]. (F) Silicon BIC metasurface employed for biosensing [81].

Here, ω_i, γ_i are the resonant frequencies and the damping rates of the modes $i = 1, 2$, respectively, ψ is the phase shift between the modes and κ is the coupling factor. One of the eigenvalues becomes purely real with no decay, turning into a BIC, when the following conditions are attained:

$$(\omega_1 - \omega_2)\kappa = e^{i\psi}\sqrt{\gamma_1\gamma_2}\,(\gamma_1 - \gamma_2), \tag{5.23}$$

$$\psi = \pi m, \tag{5.24}$$

where m is an integer number. This condition can be fulfilled through the tuning of the parameters of two coupled resonances (this case is known as a Friedrich–Wingten BIC), or when the two resonances are the identical $\omega_1 = \omega_2$, $\gamma_1 = \gamma_2$ (Fabry–Pérot BIC).

BIC concept describes optical response of a large class of metasurfaces exhibiting high-Q resonances with broken-symmetry meta-atoms, including a number of designs of metasurfaces previously described within the formalism of Fano resonances [78].

Experimental demonstrations. Fig. 5.20 summarizes some of the previous demonstrations of metasurfaces featuring sharp resonances closely related to physics of bound states in the continuum that facilitate various optical phenomena including lasing, nonlinear frequency conversion, and sensing.

References

[1] N.I. Zheludev, Y.S. Kivshar, From metamaterials to metadevices, Nat. Mater. 11 (11) (2012) 917–924.

[2] A.I. Kuznetsov, A.E. Miroshnichenko, M.L. Brongersma, Y.S. Kivshar, B. Luk'yanchuk, Optically resonant dielectric nanostructures, Science 354 (6314) (2016) aag2472.

[3] I. Staude, J. Schilling, Metamaterial-inspired silicon nanophotonics, Nat. Photonics 11 (5) (Apr. 2017) 274–284.

[4] D.G. Baranov, et al., All-dielectric nanophotonics: the quest for better materials and fabrication techniques, Optica 4 (7) (Jul. 2017) 814.

[5] D. Lin, P. Fan, E. Hasman, M.L. Brongersma, Dielectric gradient metasurface optical elements, Science 345 (6194) (2014) 298–302.

[6] S.S. Kruk, Y.S. Kivshar, Functional meta-optics and nanophotonics govern by Mie resonances, ACS Photonics (2017).

[7] H.-T. Chen, A.J. Taylor, N. Yu, A review of metasurfaces: physics and applications, Rep. Prog. Phys. 79 (7) (Jul. 2016) 076401.

[8] P. Moitra, B.A. Slovick, Z.G. Yu, S. Krishnamurthy, J. Valentine, Experimental demonstration of a broadband all-dielectric metamaterial perfect reflector, Appl. Phys. Lett. 104 (17) (2014) 171102.

[9] D.A. Baranov, et al., Broadband antireflective coatings based on two-dimensional arrays of subwavelength nanopores, Appl. Phys. Lett. 106 (17) (2015) 171913.

[10] P. Moitra, et al., Large-scale all-dielectric metamaterial perfect reflectors, ACS Photonics 2 (6) (2015) 692–698.

[11] P. Spinelli, M.A. Verschuuren, A. Polman, Broadband omnidirectional antireflection coating based on subwavelength surface Mie resonators, Nat. Commun. 3 (2012) 692.

[12] S. Kruk, B. Hopkins, I.I. Kravchenko, A. Miroshnichenko, D.N. Neshev, Y.S. Kivshar, Broadband highly efficient dielectric metadevices for polarization control, APL Photonics 1 (3) (2016) 30801.

[13] L. Wang, et al., Grayscale transparent metasurface holograms, Optica 3 (12) (2016) 1504–1505.

[14] X. Liu, K. Fan, I.V. Shadrivov, W.J. Padilla, Experimental realization of a terahertz all-dielectric metasurface absorber, Opt. Express 25 (1) (2017) 191.

[15] F. Aieta, et al., Aberration-free ultrathin flat lenses and axicons at telecom wavelengths based on plasmonic metasurfaces, Nano Lett. 12 (9) (2012) 4932–4936.

[16] X. Ni, S. Ishii, A.V. Kildishev, V.M. Shalaev, Ultra-thin, planar, Babinet-inverted plasmonic metalenses, Light Sci. Appl. 2 (4) (2013) e72.

[17] M.I. Shalaev, J. Sun, A. Tsukernik, A. Pandey, K. Nikolskiy, N.M. Litchinitser, High-efficiency all-dielectric metasurfaces for ultracompact beam manipulation in transmission mode, Nano Lett. 15 (9) (2015) 6261–6266.

[18] Z. Zhou, et al., Efficient silicon metasurfaces for visible light, ACS Photonics 4 (3) (2017) 544–551.

[19] D. Sell, J. Yang, S. Doshay, R. Yang, J.A. Fan, Large-angle, multifunctional metagratings based on freeform multimode geometries, Nano Lett. 17 (6) (2017) 3752–3757.

[20] A. Arbabi, Y. Horie, M. Bagheri, A. Faraon, Dielectric metasurfaces for complete control of phase and polarization with subwavelength spatial resolution and high transmission, Nat. Nanotechnol. 10 (11) (2015) 937–943.

[21] M. Khorasaninejad, W.T. Chen, R.C. Devlin, J. Oh, A.Y. Zhu, F. Capasso, Metalenses at visible wavelengths: diffraction-limited focusing and subwavelength resolution imaging, Science 352 (6290) (2016) 1190–1194.

[22] A. Pors, M.G. Nielsen, R.L. Eriksen, S.I. Bozhevolnyi, Broadband focusing flat mirrors based on plasmonic gradient metasurfaces, Nano Lett. 13 (2) (2013) 829–834.

[23] L. Zou, et al., Spectral and angular characteristics of dielectric resonator metasurface at optical frequencies, Appl. Phys. Lett. 105 (19) (2014) 191109.

[24] A. Pors, O. Albrektsen, I.P. Radko, S.I. Bozhevolnyi, Gap plasmon-based metasurfaces for total control of reflected light, Sci. Rep. 3 (2013).

[25] S. Sun, et al., High-efficiency broadband anomalous reflection by gradient meta-surfaces, Nano Lett. 12 (12) (2012) 6223–6229.

[26] G. Zheng, H. Mühlenbernd, M. Kenney, G. Li, T. Zentgraf, S. Zhang, Metasurface holograms reaching 80% efficiency, Nat. Nanotechnol. 10 (4) (2015) 308–312.

[27] Y. Yang, W. Wang, P. Moitra, I.I. Kravchenko, D.P. Briggs, J. Valentine, Dielectric meta-reflectarray for broadband linear polarization conversion and optical vortex generation, Nano Lett. 14 (3) (2014) 1394–1399.

[28] M. Decker, et al., High-efficiency dielectric Huygens' surfaces, Adv. Opt. Mater. 3 (6) (2015) 813–820.

[29] W. Liu, Generalized magnetic mirrors, Phys. Rev. Lett. 119 (12) (Sep. 2017) 123902.

[30] J.C. Ginn, et al., Realizing optical magnetism from dielectric metamaterials, Phys. Rev. Lett. 108 (9) (2012) 97402.

[31] S. Liu, et al., Optical magnetic mirrors without metals, Optica 1 (4) (2014) 250–256.

[32] Y.H. Fu, A.I. Kuznetsov, A.E. Miroshnichenko, Y.F. Yu, B. Luk'yanchuk, Directional visible light scattering by silicon nanoparticles, Nat. Commun. 4 (Feb. 2013) 1527.

[33] M.F. Limonov, M.V. Rybin, A.N. Poddubny, Y.S. Kivshar, Fano resonances in photonics, Nat. Photonics 11 (9) (Sep. 2017) 543–554.

[34] C. Huygens, Treatise on Light, Pieter van der Aa, Leiden, 1690.

[35] A.E. Krasnok, A.E. Miroshnichenko, P.A. Belov, Y.S. Kivshar, Huygens optical elements and Yagi—Uda nanoantennas based on dielectric nanoparticles, JETP Lett. 94 (8) (Dec. 2011) 593–598.

[36] J.-M. Geffrin, et al., Magnetic and electric coherence in forward- and back-scattered electromagnetic waves by a single dielectric subwavelength sphere, Nat. Commun. 3 (2012) 1171.

[37] M. Kerker, D.-S. Wang, C.L. Giles, Electromagnetic scattering by magnetic spheres, J. Opt. Soc. Am. 73 (6) (Jun. 1983) 765.

[38] W. Liu, Y.S. Kivshar, Generalized Kerker effects in nanophotonics and meta-optics, Opt. Express 26 (10) (2018) 13085–13105.

[39] W. Liu, J. Zhang, B. Lei, H. Ma, W. Xie, H. Hu, Ultra-directional forward scattering by individual core-shell nanoparticles, Opt. Express 22 (13) (2014).

[40] R. Alaee, R. Filter, D. Lehr, F. Lederer, C. Rockstuhl, A generalized Kerker condition for highly directive nanoantennas, Opt. Lett. 40 (11) (Jun. 2015) 2645.

[41] H.K. Shamkhi, et al., Transverse scattering with the generalised Kerker effect in high-index nanoparticles, arXiv:1808.10708, Aug. 2018.

[42] Y.F. Yu, A.Y. Zhu, R. Paniagua-Dominguez, Y.H. Fu, B. Luk'yanchuk, A.I. Kuznetsov, High-transmission dielectric metasurface with 2π phase control at visible wavelengths, Laser Photonics Rev. 9 (4) (2015) 412–418.

[43] A.E.H. Love, The integration of the equations of propagation of electric waves, Proc. R. Soc. London 68 (442–450) (1901) 19–21.

[44] Z. Bomzon, G. Biener, V. Kleiner, E. Hasman, Space-variant Pancharatnam–Berry phase optical elements with computer-generated subwavelength gratings, Opt. Lett. 27 (13) (2002) 1141–1143.

[45] R.C. Jones, A new calculus for the treatment of optical systems I. Description and discussion of the calculus, J. Opt. Soc. Am. 31 (7) (1941) 488–493.

[46] K. Wang, Y. Shi, A.S. Solntsev, S. Fan, A.A. Sukhorukov, D.N. Neshev, Non-reciprocal geometric phase in nonlinear frequency conversion, Opt. Lett. 42 (10) (2017) 1990–1993.

[47] S.M. Kamali, E. Arbabi, A. Arbabi, A. Faraon, A review of dialectric optical metasurfaces for wavefront control, Nanophotonics 7 (2018) 1041–1068.

[48] S. Kruk, et al., Transparent dielectric metasurfaces for spatial mode multiplexing, Laser Photon. Rev. 12 (8) (Aug. 2018) 1800031.

[49] K. Wang, et al., Quantum metasurface for multiphoton interference and state reconstruction, Science 361 (6407) (Sep. 2018) 1104–1108.

[50] B.E.A. Saleh, M.C. Teich, Fundamentals of Photonics, John Wiley & Sons, Inc., New York, USA, 1991.

[51] H.A. Haus, Waves and Fields in Optoelectronics, Prentice Hall, 1984.

[52] D.G. Baranov, A. Krasnok, T. Shegai, A. Alù, Y. Chong, Coherent perfect absorbers: linear control of light with light, Nat. Rev. Mater. 2 (Oct. 2017) 17064.

[53] Y.D. Chong, L. Ge, H. Cao, A.D. Stone, Coherent perfect absorbers: time-reversed lasers, Phys. Rev. Lett. 105 (5) (Jul. 2010) 053901.

[54] H. Haken, Light: Laser Dynamics, Vol. 2, Holl. Elsevier, Amsterdam, 1985.

[55] X. Ming, X. Liu, L. Sun, W.J. Padilla, Degenerate critical coupling in all-dielectric metasurface absorbers, Opt. Express 25 (20) (2017) 24658.

[56] W.W. Salisbury, Absorbent body for electromagnetic waves, US2599944A Patents, 1952.

[57] K. Fan, J.Y. Suen, X. Liu, W.J. Padilla, All-dielectric metasurface absorbers for uncooled terahertz imaging, Optica 4 (6) (2017) 601.

[58] R. Paniagua-Domínguez, et al., Generalized Brewster effect in dielectric metasurfaces, Nat. Commun. 7 (Jan. 2016) 10362.

[59] E. Plum, X.-X. Liu, V.A. Fedotov, Y. Chen, D.P. Tsai, N.I. Zheludev, Metamaterials: optical activity without chirality, Phys. Rev. Lett. 102 (11) (Mar. 2009) 113902.

[60] C. Menzel, C. Rockstuhl, F. Lederer, Advanced Jones calculus for the classification of periodic metamaterials, Phys. Rev. A 82 (5) (Nov. 2010) 053811.

[61] S.S. Kruk, et al., Optical metamaterials with quasicrystalline symmetry: symmetry-induced optical isotropy, Phys. Rev. B, Condens. Matter Mater. Phys. 88 (20) (2013).

[62] S.S. Kruk, et al., Polarization properties of optical metasurfaces of different symmetries, Phys. Rev. B, Condens. Matter Mater. Phys. 91 (19) (2015).

[63] M. Albooyeh, et al., Resonant metasurfaces at oblique incidence: interplay of order and disorder, Sci. Rep. 4 (2014).

[64] R. Alaee, M. Albooyeh, A. Rahimzadegan, M.S. Mirmoosa, Y.S. Kivshar, C. Rockstuhl, All-dielectric reciprocal bianisotropic nanoparticles, Phys. Rev. B 92 (2015) 245130.

[65] A.Y. Zhu, et al., Giant higher-order multipoles enable strong intrinsic chirality in planar nanostructures, in: Frontiers in Optics 2017, 2017, p. JW3A.92.

[66] U. Fano, Effects of configuration interaction on intensities and phase shifts, Phys. Rev. 124 (6) (Dec. 1961) 1866–1878.

[67] U. Fano, Sullo spettro di assorbimento dei gas nobili presso il limite dello spettro darco, Il Nuovo Cimento 12 (1935) 154–161.

[68] J.-P. Connerade, A.M. Lane, Interacting resonances in atomic spectroscopy, Rep. Prog. Phys. 51 (11) (Nov. 1988) 1439–1478.

[69] G. Borrmann, Die Absorption von Rontgenstrahlen im Fall der Interferenz, Z. Phys. 127 (4) (Aug. 1950) 297–323.

[70] B. Peng, Ş.K. Özdemir, W. Chen, F. Nori, L. Yang, What is and what is not electromagnetically induced transparency in whispering-gallery microcavities, Nat. Commun. 5 (1) (Dec. 2014) 5082.

[71] C. Wu, et al., Spectrally selective chiral silicon metasurfaces based on infrared Fano resonances, Nat. Commun. 5 (1) (Dec. 2014) 3892.

[72] Y. Yang, I.I. Kravchenko, D.P. Briggs, J. Valentine, All-dielectric metasurface analogue of electromagnetically induced transparency, Nat. Commun. 5 (2014).

[73] P.P. Vabishchevich, S. Liu, M.B. Sinclair, G.A. Keeler, G.M. Peake, I. Brener, Enhanced second-harmonic generation using broken symmetry III–V semiconductor Fano metasurfaces, ACS Photonics 5 (5) (May 2018) 1685–1690.

[74] J. von Neuman, E. Wigner, Uber merkwürdige diskrete Eigenwerte. Uber das Verhalten von Eigenwerten bei adiabatischen Prozessen, Phys. Z. 30 (1929) 467–470.

[75] K. Koshelev, G. Favraud, A. Bogdanov, Y. Kivshar, A. Fratalocchi, Nonradiating photonics with resonant dielectric nanostructures, arXiv:1903.04756, Mar. 2019.

[76] S.A. Maier, Plasmonics: Fundamentals and Applications, Springer, 2007.

[77] Y. Kivshar, All-dielectric meta-optics and non-linear nanophotonics, Natl. Sci. Rev. 5 (2) (Mar. 2018) 144–158.

[78] K. Koshelev, S. Lepeshov, M. Liu, A. Bogdanov, Y. Kivshar, Asymmetric Metasurfaces with High-Q Resonances Governed by Bound States in the Continuum, Phys. Rev. Lett. 121 (19) (Nov. 2018) 193903.

[79] A. Kodigala, T. Lepetit, Q. Gu, B. Bahari, Y. Fainman, B. Kanté, Lasing action from photonic bound states in continuum, Nature 541 (7636) (Jan. 2017) 196–199.

[80] S.T. Ha, et al., Directional lasing in resonant semiconductor nanoantenna arrays, Nat. Nanotechnol. 13 (11) (Nov. 2018) 1042–1047.

[81] A. Tittl, et al., Imaging-based molecular barcoding with pixelated dielectric metasurfaces, Science 360 (6393) (Jun. 2018) 1105–1109.

Applications of wavefront control using nano-post based dielectric metasurfaces

6

Andrei Faraon[a], Amir Arbabi[b], Seyedeh Mahsa Kamali[a], Ehsan Arbabi[a], Arka Majumdar[c,d]

[a]T.J. Watson Laboratory of Applied Physics, California Institute of Technology, Pasadena, CA, United States, [b]Department of Electrical and Computer Engineering, University of Massachusetts Amherst, Amherst, MA, United States, [c]Department of Electrical Engineering, University of Washington, Seattle, WA, United States, [d]Physics Department, University of Washington, Seattle, WA, United States

6.1 Introduction

In this chapter, we outline applications of dielectric metasurfaces for wavefront control. We will focus on metasurfaces composed of nano-posts, previously introduced in Chapter 5, with thicknesses comparable to the free-space wavelength [1]. These metasurfaces can be fabricated using conventional nano-fabrication techniques like lithography, thin film deposition and etching. These techniques are suitable for wafer-scale mass-production of devices, which is very important for the future penetration of this technology into various products. Several groups reported fabrication of large-area metasurfaces using conventional stepper lithography [2,3]. Going beyond traditional semiconductor manufacturing, the ultra-thin and flat nature of metasurfaces also allows for printable photonic technologies for large-volume and low-cost manufacturing. In the last few years, the optical metasurfaces have created an exploding research field, and it is impossible to cover every aspect in one single chapter. In this chapter, we primarily focus the discussion on research performed by the authors and lay out its relation to other work in the field.

6.2 Capabilities for phase and polarization control enabled by dielectric metasurfaces

In this section, we review the properties of dielectric metasurfaces that enable the applications discussed in the following sections. Metasurfaces composed of high index nano-posts placed on a sub-wavelength periodic lattice were introduced in the late 1990s [4–6] and later investigated by other research groups [7–10]. These metasurfaces (Fig. 6.1) are appealing because they can provide complete control of both the polarization and the phase of the transmitted/reflected light while using nano-posts
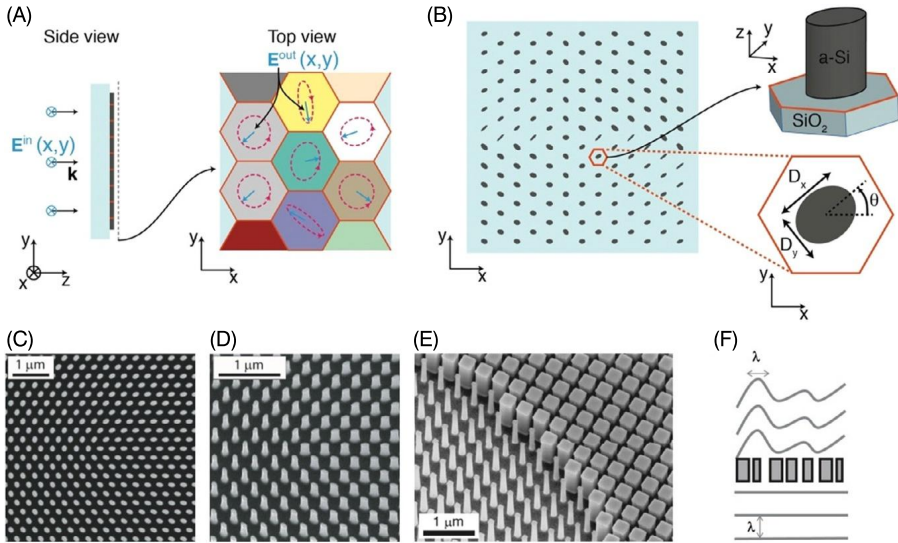
Figure 6.1 (A) Schematic of a dielectric metasurface composed of sub-wavelength hexagonal pixels. Left panel shows light polarized along the x direction incident on the metasurface. Right panel shows that light propagating through each pixel acquires a different phase delay and polarization ellipse. (B) Complete control of the polarization and phase at each pixel can be achieved by placing a high index nano-post, made from amorphous Si (a-Si) in this case, resting on a silicon dioxide (SiO_2) substrate. The control is achieved by modifying the diameters of the ellipse and the orientation of its axes. (C–D) Scanning electron microscope images of dielectric metasurfaces fabricated from amorphous silicon nano-posts on a hexagonal lattice. (E) Scanning electron microscope image of a dielectric metasurface fabricated from amorphous silicon nano-posts on a square lattice. (F) Schematic showing how nano-posts can modify a plane wave to a wave with arbitrary shape. The spatial control in shaping the wavefront is on the order of the wavelength. (Panels (A) and (B) are adapted from [11], (C) and (D) from [16], (E) from [17].)

with aspect ratios smaller than ~10:1, which are relatively straightforward to fabricate [11]. The nano-posts are most often made of high index materials like silicon for operation in red and near infrared and titanium dioxide for operation at the shorter wavelength range of the visible spectrum [4,12]. Lower index materials like silicon nitride can also be used in some cases [13–15], although the light bending capability and subsequently the numerical aperture of metasurface lenses are limited at lower index. The medium surrounding the nano-posts needs to have a lower refractive index and it usually consists of either silicon dioxide, polymers, or air.

One of the most intuitive ways to think about the operating principle for these metasurfaces based on nano-posts is to consider each nano-posts as a short waveguide. Depending on the cross-section of the nano-post, light can experience different phase delays. Also, if the cross-section of the nano-post is not symmetric under a 90° rotation around its axis, the nano-post can exhibit structural birefringence which leads to a polarization transformation as light propagates through it. Using nano-posts with elliptical or rectangular cross-sections, it is possible to achieve designs where arbitrary phase delays and polarization rotations can be realized by controlling the dimensions and the orientation of the ellipse or rectangle (Fig. 6.1A, B). To create a metasurface,

the nano-posts are usually placed on a sub-wavelength periodic lattice. This way, the light is primarily scattered with high efficiency only into the zeroth order. In order to achieve spatial wavefront control with resolution comparable to the lattice period (Fig. 6.1F) it is important to use nano-posts with high refractive index. This ensures that the nano-posts have a high scattering cross-section for the incident wave, and at the same time the coupling between nano-posts is highly reduced.

The metasurfaces we discuss in this chapter are arranged either in square or hexagonal lattice geometry, and some examples of fabricated devices are shown in Fig. 6.1C, D, E. The polarization and phase of the wavefront can be sampled at each pixel by placing a nano-post that provides the desired phase delay and polarization transformation. For example, using amorphous silicon nano-posts with a height of $0.6\lambda_{air}$ placed on a hexagonal lattice with a lattice constant of $0.5\lambda_{air}$, it is possible to control the phase of light transmitted through the nano-posts from 0 to 2π by changing the post diameters from $\lambda_{air}/8$ to $\lambda_{air}/3$ [9], where λ_{air} is the design wavelength in air. Full polarization and phase control can be achieved using elliptical amorphous silicon nano-posts with a height of $\sim 0.8\lambda_{air}$, placed on a hexagonal lattice with a lattice constant of $\sim 0.7\lambda_{air}$ by changing the ellipse diameters between $\sim 0.07\lambda_{air}$ and $\sim 0.5\lambda_{air}$ and also changing the orientation of the major axis of the ellipse. The transmission efficiency of these structures is $> 85\%$, while the total device efficiency depends on the actual device function [11]. Similar performance can be achieved for devices operating in the reflection mode as well [18].

Controlling only the phase is suitable for applications such as lenses used for imaging, focusing and other mode converters. Controlling both the polarization and the phase enables devices where the wavefronts corresponding to two orthogonal polarizations are controlled independently. For example, two polarization states can be focused at different points, or deflected at different angles. These are examples of multi-functional devices that can simultaneously do polarization splitting and imaging [11,19].

Most dielectric metasurfaces are designed to operate at a single wavelength. Structures that operate simultaneously at multiple wavelengths can be achieved in multiple ways, albeit generally at the cost of reduced efficiency [20–25]. For example, elliptical or rectangular nano-posts can be engineered to independently control a different wavelength for each of the two orthogonal polarization states [22]. Spatial multiplexing of nano-posts designed to operate at two different wavelengths and the same polarization can also be used [21]. Also, a localized set of nano-posts (meta-molecule) can be collectively engineered to simultaneously operate at multiple wavelengths [20]. When the polarization states of two wavelengths that are independently controlled are not orthogonal, the wavelengths need to be spaced quite far apart. This is because the scattering responses of low-quality factor meta-atoms are correlated at wavelengths that are close to each other.

Dispersion engineering can be used to control the response of dielectric structures over a continuous wavelength interval [26–30]. Being short truncated waveguides, the nano-posts exhibit resonances, so the phase delay of the light scattered by the nano-posts depends on the exact wavelength. The absolute phase delay (ϕ) and phase dispersion ($d\phi/d\lambda$) can be controlled by changing the dimensions of the nano-posts.

These effects can be used to further control the dispersion properties of the final devices (lenses, gratings, etc.) created using dielectric metasurfaces, leading to diffraction gratings with interesting angular dispersion profiles and lenses with chromatic dispersions that are different from conventional diffractive devices. Dispersion control can be applied for both transmissive and reflective devices. However, larger absolute phase delays can be achieved primarily for reflective devices, as conceptually light propagates for a longer path back and forth through these structures. Having large absolute phase delays is important especially when designing broadband devices for wavefront control that cover a large area.

So far, the dielectric metasurfaces that we discussed can control degrees of freedom like phase and polarization at different wavelengths. Another degree of freedom for optical waves is their propagation direction, or momentum. An interesting question is whether dielectric metasurfaces can be used to independently control the phase of two or more emerging optical wavefronts that propagate along different directions. To implement this functionality, one needs to consider the nano-posts forming the metasurface as multi-mode resonators. Depending on the direction of the light incident on the nano-posts, different sets of modes can be excited, which can have very different scattering coefficients. Using nano-posts with a more complex cross-section (U-shaped for example), it is possible to independently control the phase of the scattered light between zero and 2π for two different angles of incidence (0 and $\pi/6$). This allows for the creation of angle-multiplexed gratings and holograms [31].

6.3 Widefield imaging

Imaging using refractive lenses is one of the most widespread applications of optics, including almost all areas of engineering, science and healthcare. Replacing refractive lenses with thin, flat, lithographically patterned optical components is one of the most desired applications for dielectric metasurfaces. When discussing imaging it is very important to note that there is a very wide range of specifications for various imaging applications. In this section, we discuss the suitability of metasurface imaging systems for different applications.

The most basic imaging system can be created using a single metasurface lens [10, 9,12]. A single metasurface lens can be formed with a phase mask that transforms a plane wave to a spherical one as shown in Fig. 6.2A, B. Often, the required phase delay is larger than 2π and in this case an operating wavelength needs to be chosen and the phase needs to be wrapped every multiple of 2π as shown in Fig. 6.2C, D. To create the lens, the phase profile is sampled on a subwavelength lattice, and a nano-post imposing the necessary phase delay is placed on each lattice point as shown in Fig. 6.2E. The simulated electromagnetic field for a plane wave passing through a metasurface lens is shown in Fig. 6.2F. Examples of lenses fabricated in amorphous silicon for operation at telecommunications wavelengths, and from titanium dioxide for visible wavelengths are shown in Fig. 6.3A, B. These components can be used to focus light to a point, and perform some basic imaging. However, similar to refractive systems,
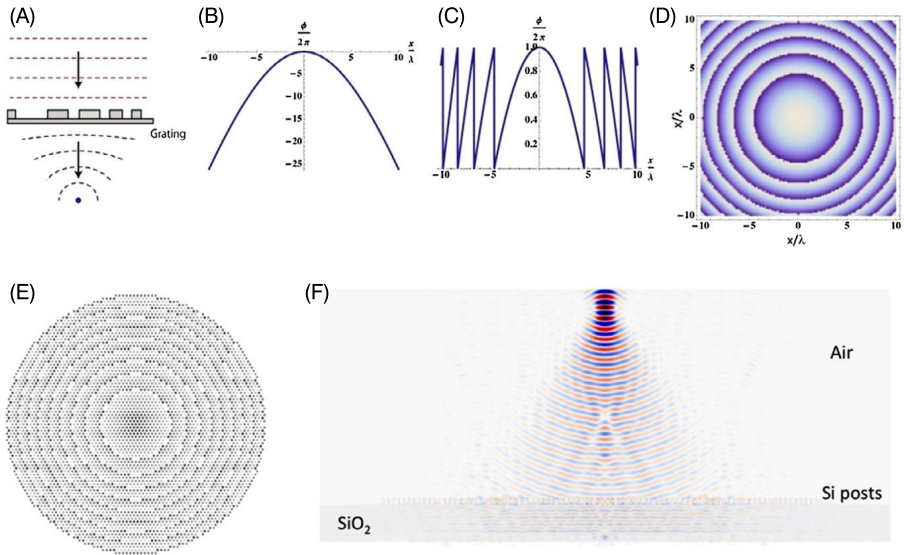
Figure 6.2 (A) Schematic of a plane wave being focused to a point using a metasurface lens. (B) Diametral cross-section of the phase profile that needs to be imposed by a circular metasurface such that it acts as a focusing lens. (C) Diametral cross-section of the phase profile of a circular metasurface focusing lens where the phase is wrapped every 2π. (D) Two-dimensional phase profile of a metasurface focusing lens, where the phase is wrapped every 2π. (White is 2π phase and dark blue is 0 phase.) (E) Drawing showing a metasurface lens composed of circular nano-posts. (F) Simulation (diametral cross-section) showing focusing of a plane wave using a metasurface lens.

a single metasurface lens exhibits multiple optical aberrations and is not well suited for imaging an extended scene. Systems of at least two lenses are generally required to image a wider field of view. Towards this end, metasurface lens doublets were developed to create imaging systems that can capture a wide angular range as shown in Fig. 6.3C [32]. The two metasurfaces, with diameters of 1600 µm and 800 µm were made from amorphous silicon for an operation wavelength of 850 nm and were separated by a 1-mm-thick glass substrate. The system was optimized for a focal length of 717 µm, an f-number of 0.9 and had an efficiency of ∼70% for light at normal incidence. Because of the freedom in designing the phase profiles, the doublet reached a nearly diffraction-limited performance for light incident at angles up to 25°, a large improvement compared to a single lens of a similar f-number and focal length that exhibits significant aberrations even for incident angles of a few degrees. A similar device, designed to operate at green wavelength, but with a smaller field of view and operating only with one circular polarization was also developed [33].

As with most imaging systems based on diffractive elements, the main drawback of using metasurface lenses for optical imaging is the chromatic dispersion. While these lenses can perform well at the design wavelength, their performance degrades away from it. The chromatic dispersion is partially caused by the dispersive nature of the nano-posts' scattering response, but even more importantly from the construction of metasurface lenses that are composed on Fresnel zones whose locations, with some
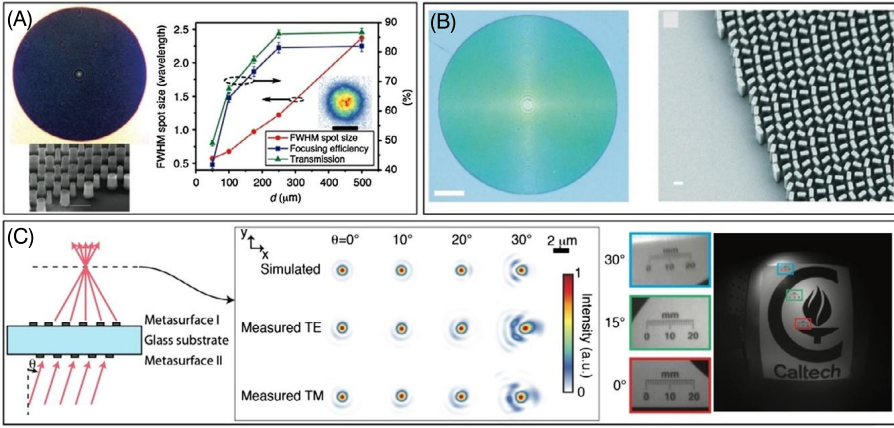
Figure 6.3 (A) Metasurface lens fabricated in amorphous silicon for operation at telecom wavelengths (1550 nm). The lens has a diameter of 400 μm, and the distance between two nano-posts is 800 nm. The right panel shows the size of the focal spot and the focusing efficiency. (B) Metasurface lens fabricated in titanium dioxide for operation at visible wavelengths. Scale bar for the left panel is 40 μm, and 300 nm for the right panel. (C) Schematic, focusing performance, and imaging performance of a metasurface lens doublet operating at 850 nm. (Panel (A) is adapted from [9], (B) from [12], and (C) from [32]).

exceptions [27], are fixed by the design wavelength. For achromatic operation, the locations of these Fresnel zones need to change as a function of wavelength, which is generally not possible once the device is fabricated.

A pedagogical example that illustrates the problem of achromatic imaging using metasurface lenses is to consider focusing of coherent broadband light, like an ultra-short light pulse, using a circular lens with radius R, focal length f, and numerical aperture $NA = R/\sqrt{R^2 + f^2}$ in vacuum (Fig. 6.4). To make use of the entire numerical aperture of the lens, the beam would need to fill it entirely. Thus, we will have parts of the light traveling through the center of the lens and parts of it traveling close to its circumference. For broadband focusing, parts of the pulse traveling along rays going through the middle of the lens need to arrive at the focal point at the same time and with the same phase as parts of the pulse traveling along rays going through the lens circumference. This cannot be achieved unless light going through the center of the lens experiences a real delay of $\tau = \frac{\sqrt{f^2+R^2}-f}{c} = \frac{f}{c}\left(\frac{1}{\sqrt{1-NA^2}} - 1\right)$. This delay becomes larger for increasing focal lengths and increasing numerical aperture (or lens radius). A focusing refractive lens applies this real time delay by being significantly thicker at its center than at its circumference. In contrast, metasurface lenses are thin and operate using low-quality factor resonances, which means that they cannot apply very large time delays and thus cannot be achromatic over a wide range.

Time delays corresponding to a few wavelengths can be achieved using dielectric metasurfaces, and efforts in this direction resulted in lenses and focusing mirrors with an achromatic behavior over an extended range compared to initial demonstrations [27,29,30]. However, this comes at the cost of reduced efficiency, and most importantly the demonstrated devices have a small size, up to only a few hundred microns
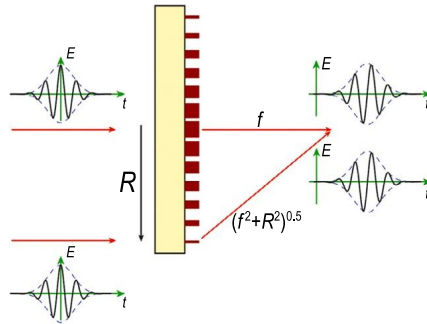
Figure 6.4 Schematic showing a metasurface lens with radius R and focal length f that focuses broadband light, in the form of short pulses. For broadband operation, the part of the pulse traveling along a ray going through the center of the lens needs to arrive at the focal point at the same time and with the same phase profile as the part of the pulse traveling along a ray passing close to the circumference of the lens and defected to the focal point. Reprinted with permission from Ehsan Arbabi, Amir Arbabi, Seyedeh Mahsa Kamali, Yu Horie, Andrei Faraon, Controlling the sign of chromatic dispersion in diffractive optics with dielectric metasurfaces, Optica 4 (6) (2017) 625–632, Optical Society of America.

in diameter at telecommunications wavelengths. The achromatic operation for devices with a larger size would require larger time delays, which are difficult to achieve in thin diffractive devices. One possibility would be to use nano-resonators with multiple resonances, each one with a much higher quality factor, so a larger time delay could be realized over a broader bandwidth, but suitable designs of this kind have not been proposed so far.

6.4 Computational imaging

Besides the conventional approach where a system of lenses creates a good quality image directly on the image sensor, another useful approach is to use a metasurface device to impose a specific transformation for the optical wavefront and then use algorithms to recover a higher quality image. This technique was used to engineer broadband imaging systems.

As explained earlier, ordinary metalenses (Fig. 6.5A) suffer from strong chromatic aberrations. Depending on the wavelength of the incident light, the metalens focuses light at different depth along the optical axis. This results in vastly different modulation transfer functions (MTF) of the lens for different wavelengths at the plane of the sensor. Fig. 6.5B shows the MTF of a metalens measured for three different colors (red, green, and blue). The sensor is placed in the focal plane of the metalens under green illumination: while a large distribution of spatial frequency is captured for green light, for blue and red only a small distribution of spatial frequencies reaches the sensor. This results in images with strong chromatic aberrations (Fig. 6.5C). One way to circumvent this problem is to employ wavefront shaping to extend the depth of the focus (EDOF) [34]. EDOF lenses can be demonstrated using a separate cubic phase mask in conjunction with a refractive lens. The sub-wavelength periodicity
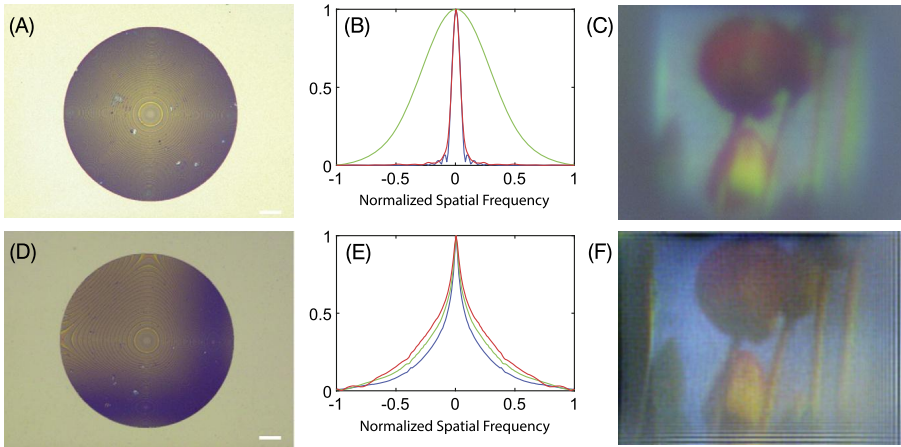
Figure 6.5 Full-color imaging using wavefront shaping metasurface and computational imaging: (A–C) optical microscope image of a metalens, measured modulation transfer function for red, green and blue and captured color image. (D–F): the addition of a cubic phase mask results in rotational asymmetry, and a non-zero MTF for the whole visible frequency range. This results in better color information in the captured image. (Adapted from [35].)

allows for combining the cubic phase-function and the lens in a single metasurface [35]. Adding the cubic function breaks the rotational asymmetry as can be seen in Fig. 6.5D. A direct result of the EDOF is a non-zero MTF over a large distribution of the spatial frequencies over the whole visible spectrum (red, green and blue are shown in Fig. 6.5E), although the large spatial frequencies are more attenuated compared to a well-focused lens. Some of the image quality can be recovered using a computational deconvolution, as shown in the captured full-color image in Fig. 6.5F.

Another computational approach is to use a random metasurface phase mask with a known scattering matrix. When the object is illuminated with a coherent light source, it produces a speckle pattern on the image sensor. By measuring the speckle pattern and knowing the scattering matrix of the object, it is possible to recover both the amplitude and the phase of the object using the speckle-correlation scattering matrix method [38].

6.5 Focus scanning fluorescence imaging

Focus scanning imaging techniques are widely used in biological samples containing fluorescent labels. In these techniques, fluorescence is emitted mainly at the focal spot where the excitation light has the highest intensity. The excitation can be realized via a one-photon or two-photon process. In both cases, the excitation wavelength is relatively narrow-band and the emitted fluorescence is collected, but not directly imaged. These conditions are well suited for metasurface devices operating in a narrower band.
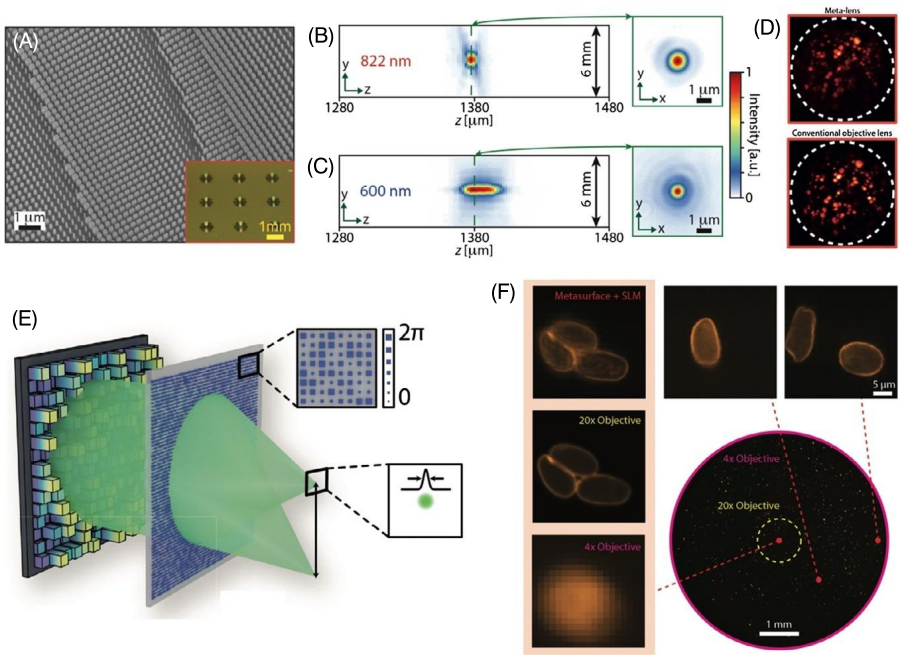
Figure 6.6 (A) Scanning electron microscope of a double-wavelength metasurface lens fabricated from birefringent amorphous silicon nano-posts on glass. (B, C) Focal spot of the metasurface lens at the target excitation wavelength of 822 nm and collection wavelength of 600 nm. (D) Two photon images acquired using the metasurface lens and a conventional microscope objective. (E) Principle of focus scanning using a random metasurface phase mask and a spatial light modulator. (F) Fluorescence imaging of single cells acquired using the disorder-engineered metasurface and comparison with a microscope objective. (Panels (A–D) adapted from [36], panels (E–F) adapted from [37].)

Both one-photon and two-photon microscopy can be implemented using double-wavelength metasurface lenses. For the two-photon case, this was already implemented using a lens with a diameter of 1.6 mm, a numerical aperture of 0.5 and a focal distance f ∼ 1.386 mm at the wavelengths of 820 nm and 605 nm (Fig. 6.6A, B, C), corresponding to the two-photon excitation and emission wavelength of the fluorophore [36]. The focusing efficiencies were measured to be 61% and 45% at ∼820 nm and ∼600 nm, respectively. This lens was used as a direct replacement for the objective lens in a two-photon microscope setup, where fluorescent beads were imaged with good quality (Fig. 6.6D). The excitation and collection with the metasurface lens were not as efficient when compared to a corrected microscope objective with similar focal length and numerical aperture. This is again related to the chromatic dispersion that results in diminished peak intensity for the focused pulsed laser and smaller collection efficiency for the broadband fluorescence. While double-wavelength metasurface lenses are unlikely to replace objective lenses in a versatile table-top two-photon microscope setup, they may find use in more specialized applications where they are designed specifically for a fluorophore and are incorporated in highly compact lightweight setups like a scientific endoscope.

An interesting method for focus scanning, which was used for one-photon imaging, is based on random metasurfaces; see Fig. 6.6E, F [37]. It is based on the well-known principle that it is possible to focus light with a high peak to background ratio using a spatial light modulator that imposes a specific phase profile on a scattering medium. Then the position of the focal point can be scanned to arbitrary locations after the scattering medium by properly changing the phase profile applied by the spatial light modulator as shown in Fig. 6.6E. However, to know what phase profile should be applied, the scattering properties of the medium need to be carefully characterized. Using dielectric metasurfaces it is possible to fabricate random scattering media with a scattering matrix that is known a priori, with a large angular correlation range, and with an engineered angular profile for the scattered field. This elegant approach, which eliminates the need for careful characterization of the scattering medium, was implemented using a metasurface device fabricated from silicon nitride nano-posts operating for green light [37]. The method enabled focusing of light to small spots corresponding to a high numerical aperture (NA > 0.5), and fluorescence imaging with an estimated $\sim 2.2 \times 10^8$ addressable points in a wide ~ 8 mm field of view as shown in Fig. 6.6F.

6.6   Mechanically tunable devices

In this section we will discuss metasurfaces that dynamically tune wavefronts. A more general discussion of tunable dielectric metamaterials can be found in Chapter 7. One of the great advantages of optical metasurfaces is that they can be integrated in various complex systems including micro-electro-mechanical structures (MEMSs). These systems are uniquely positioned to exploit the minute thickness and ultra-low weight of optical metasurfaces. Being thin, metasurfaces can be brought into very close proximity of each other, something that cannot easily be done with curved refractive lenses. At the same time, they can be actuated at fast speeds using electrostatic forces. A system that makes use of these unique advantages for metasurfaces is a scanning lens doublet where one of the lenses is patterned on a rigid flat substrate and the other lens is patterned on a membrane that can be moved with respect to the flat substrate (Fig. 6.7A). The actuation is done electrostatically using electrodes patterned both on the glass substrate and the membrane. The freedom provided by the metasurface lens design allows for large changes in the focal distance of the entire system only by small changes in the distance between the two lenses. This idea was realized in practice [39] with a system composed of two lenses with 300 μm diameter and designed spacing of 10 μm at zero voltage. Images of the device are shown in Fig. 6.7B. The focal distances of the two lenses were 120 μm and −130 μm, respectively. A small change of only 1 μm in the distance between the lenses allows for tuning of the total focal length of the system from 781 μm to 817 μm. The focal length tuning was verified experimentally both by measuring it directly (Fig. 6.7C, D) and by showing that an image can be brought in and out of focus (Fig. 6.7E). In the experiment the focal length was slightly different from the design. The actuation speed was ~230 Hz, limited by air friction. In vacuum, the system can operate at speeds approaching 4 kHz. This type
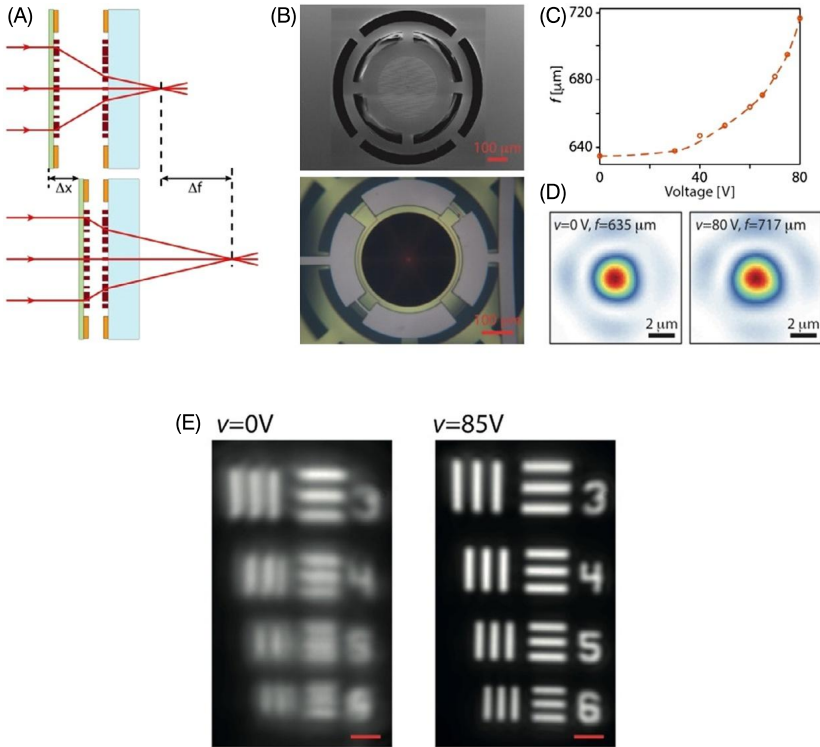
Figure 6.7 (A) Concept of tuning of the focal length of a metasurface lens doublet by changing the distance between the lenses using micro-electro-mechanical structures. (B) Scanning electron microscope (top) and optical (bottom) image of the fabricated system of lenses. (C) Change in the focal length of the system with applied voltage. (D) Image of the focal spot for two applied voltages. (E) Bringing an image in and out of focus by changing the voltage actuating the distance between the lenses. (Adapted from [39].)

of optical system is well suited for applications where fast focus tuning is needed in a small package like a miniaturized microscope.

Mechanical actuation can also be used to tune the focal length of a system of metasurfaces by displacing them laterally. This was realized using a set of two Alvarez lenses [40,2]. In an Alvarez lens system, two cubic phase masks work in tandem to produce a lens-like behavior. One of the masks has a phase profile of the form

$$\varphi_{alv}(x, y) = \mathrm{mod}\left(\frac{2\pi}{\lambda} A\left(\frac{1}{3}x^3 + xy^2\right), 2\pi\right)$$

and the other mask satisfies the condition $\varphi_{alv}(x, y) + \varphi_{inv}(x, y) = 0$. This enables a combined phase of a lens with focal length of $f = \frac{1}{4Ad}$, when the two plates are displaced by a distance d (Fig. 6.8A). Fig. 6.8B shows one of the fabricated Alvarez lenses. Under lateral displacement, the focal length changes as indicated in Fig. 6.8C. While the initial experiments were performed using metasurfaces fabricated using electron-beam lithography, large-area Alvarez lenses were recently reported us-
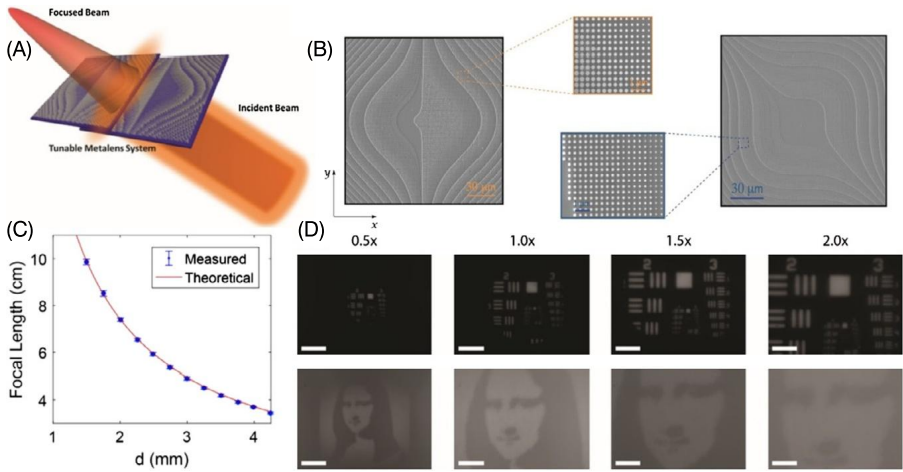
Figure 6.8 Tunable Alvarez lens: (A) two cubic phase masks together behave like a lens, whose focal length is tuned as the metasurfaces are laterally displaced, (B) SEM of the fabricated Alvarez lens; (C) measured focal length as a function of the displacement; (D) varifocal zoom imaging using large-area Alvarez metalens. Parts (A), (C), (D) reprinted with permission from Shane Colburn, Alan Zhan, Arka Majumdar, Varifocal zoom imaging with large area focal length adjustable metalenses, Optica 5 (7) (2018) 825-831, Optical Society of America. Part (B) from A. Zhan, S. Colburn, C.M. Dodson, A. Majumdar, Metasurface freeform nanophotonics, Sci. Rep. 7 (2017) 1673.
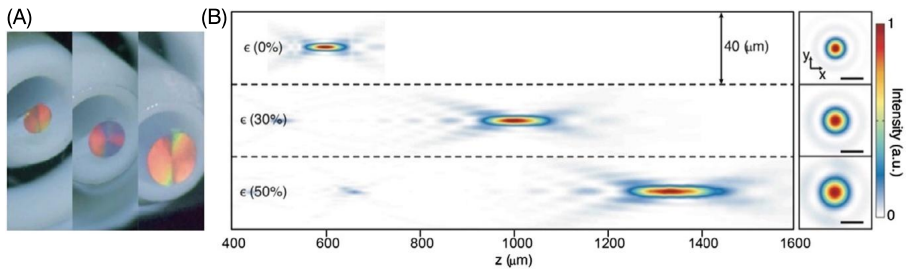
Figure 6.9 (A) Stretchable dielectric metasurface lens while being expanded. (B) Change in the focal distance as the lens is expanded. Scale bars 5 μm. (Adapted from [17].)

ing stepper photolithography [2]. Using these metasurface Alvarez lenses, varifocal zoom imaging was demonstrated as shown in Fig. 6.8D. In all these experiments, the Alvarez lenses were manually displaced using kinematic stages. Micro-electro-mechanical systems can be readily used to actuate small area Alvarez lenses, while large-area lenses can be actuated via stepper motors.

Another type of mechanical actuation that can be used to tune metasurface lenses is stretching of the substrate where the lens is located [41]. For uniform stretching of the substrate by a ratio $1 + \epsilon$, the focal length of the lens changes by a factor of $(1 + \epsilon)^2$. This has been realized by embedding a metasurface lens with diameter of 200 μm, composed of amorphous silicon nano-posts, in a flexible and deformable polymer [17] as shown in Fig. 6.9. A focal length change from 600 μm to 1400 μm at an operation
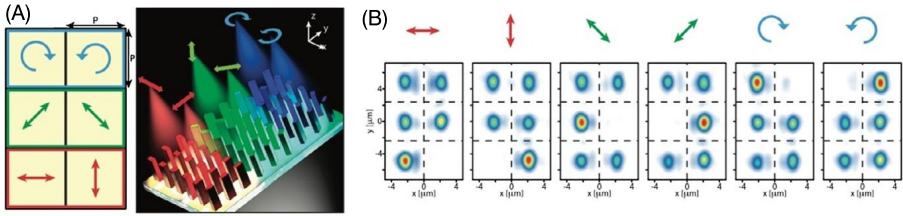
Figure 6.10 (A) Schematic of a superpixel for polarization imaging using metasurfaces. It is composed of six pixels, measuring the light in three polarization bases chosen such that the full Stokes parameters can be reconstructed. (B) Response of the intensity recorded on the superpixel under illumination with different polarization states indicated by the arrows above. (Adapted from [43].)

wavelength of 915 nm was demonstrated (Fig. 6.9B). Stretchable metasurfaces with electrical control can also be used to tune the focal length and correct aberrations [42].

6.7 Devices based on simultaneous polarization and phase control

One property of dielectric metasurfaces that makes them powerful for optical engineering is that the polarization and phase of optical wavefronts can be controlled completely and independently. This enables diffractive devices that are difficult to implement using other techniques, like lenses that focus two states of polarization at two different focal points [11]. More complex polarization imaging can be realized by projecting the image onto three different bases which allows for the full determination of the Stokes parameters of the incident light. Using metasurfaces, this type of projection can be performed directly in the focal plane to image an entire scene [43]. The image sensor can be divided into superpixels each consisting of six pixels. Metasurfaces placed on the top of the superpixel are used to split the light into three different bases: linear horizontal/vertical, linear plus/minus 45°, and right/left hand circular (Fig. 6.10A). This allows for full measurement of the Stokes parameters of the light incident on the superpixel. The implementation was done at a center wavelength of 850 nm for pixel sizes ranging from 2.4 µm to 7.2 µm. The response of the superpixel under various polarizations is shown in Fig. 6.10B. Other polarimetry schemes using metasurfaces have also been implemented [44,45].

Optical elements imposing complex transformations of polarization and phase are also utilized in more specialized microscopy techniques. For example, elements that transform linear polarization to azimuthal/radial polarization were used for microscopy applications where the unknown orientation of the optical dipole moment of molecules leads to localization error [16]. A molecule generally emits light in a dipolar pattern. If the dipole is aligned either in the focal plane or along the microscope axis, the location of the molecule can be well determined by measuring its fluorescence and fitting it. When the dipole makes an arbitrary angle with the microscope axis, it emits light primarily at an angle which makes it difficult to determine its location.

The dipole can be decomposed in a component oscillating along the microscope axis which emits radially polarized light, and a component oscillating in the focal plane which emits light polarized along its direction. The radially polarized light can be completely removed using a device that converts radial to linear polarization followed by a linear polarizer. Thus, the remaining light is emitted only by the in-plane dipole whose location can be well determined. This technique can be used to measure the distance between two molecules that have dipoles with unknown orientations. It was implemented using a metasurface phase mask, operating around 685 nm, that converts linear to radial/azimuthal polarizations [16].

6.8   Devices exploiting spectral control

While the spectral dispersion of diffractive optical elements is generally a disadvantage for broadband imaging devices, it is successfully exploited in spectrometry applications. Spectrometers based on metasurfaces can be realized in various ways, starting from the trivial implementation of diffraction gratings using metasurface phase masks in combination with conventional collimating and focusing optical elements. The focusing dispersive elements can also be combined into a single flat optical metasurface element designed to focus off-axis [46]. However, in this configuration, the image sensor needs to be placed at an angle with respect to the lens axis, which is not convenient for some applications. An appealing configuration for metasurface spectrometers is based on folded optics [18]. The idea is to use a transparent substrate coated with reflective metasurfaces and mirrors on both sides as shown in Fig. 6.11A. Light is inserted in the device via an aperture in the mirror. It is then dispersed, reflected and focused through another aperture in the device using metasurface and plain reflective components. One example, shown in Fig. 6.11B, C is a folded spectrometer composed of three metasurfaces fabricated using a single lithography step, where light is reflected inside the transparent substrate 10 times. The device is designed to operate between 760 nm and 860 nm with a resolution of ~ 1.25 nm and an efficiency of $\sim$25% as shown in Fig. 6.11D. Such a device, with dimensions of 7 mm $\times$ 1 mm $\times$ 1 mm is promising for applications where very compact spectrometers are required.

Beside spectrometers, metasurfaces can be used to implement other types of dispersion engineering. For example, all diffractive devices exhibit negative dispersion, which means that, for the same diffraction order, gratings deflect red light at larger angles than blue light. Using dispersion-engineered metasurfaces, it is possible to change this behavior to some degree and create devices with positive and zero dispersion within a band as shown schematically in Fig. 6.12 and demonstrated in Reference [27]. This leads to gratings with interesting dispersive regimes that can have applications in optical engineering where optical pulses need to be dispersed in a particular way. The same concepts can be used to develop lenses and focusing mirrors with flat dispersion within some bandwidth, which can be useful in various imaging applications [27,29,30].
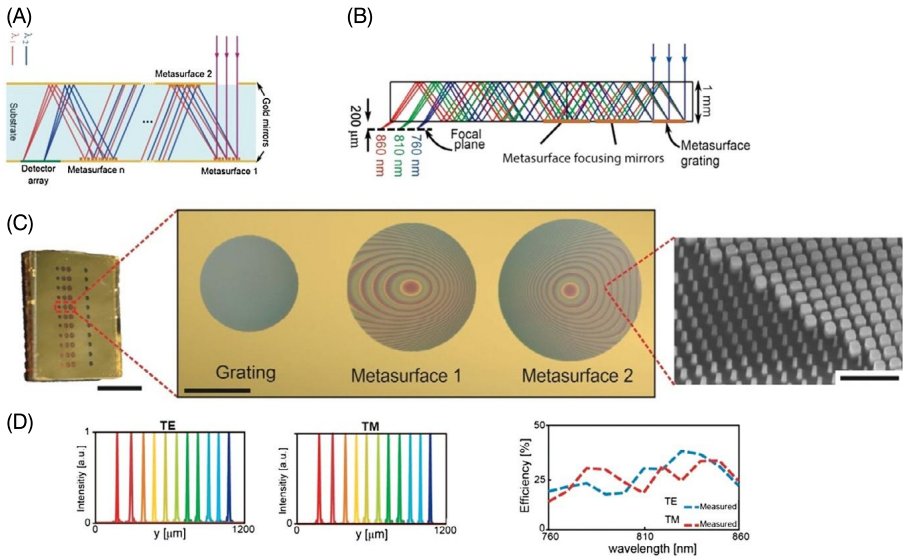
Figure 6.11 (A) Concept of folded optics design, where light enters inside a slab via an aperture, and then it is manipulated via metasurfaces while being confined in the slab via mirrors. (B) Ray diagram showing a folded spectrometer composed of a slab coated with mirrors, a reflective metasurface grating, and two metasurface focusing mirrors. Light enters the slab via an aperture, it is dispersed by the grating, and then it is reflected inside the slab 9 times while being focused using two metasurface focusing mirrors outside the slab via an aperture. (C) Images of the spectrometer. An array of 11 spectrometers is shown on the left. Optical images of the metasurfaces are shown in the center. A scanning electron microscope image of the metasurface is shown on the right. (D) Spectra for the TE and TM polarizations collected with the spectrometer for laser light tuned between 760 nm and 860 nm. The plot on the right shows the total measured efficiency. (Adapted from [18].)
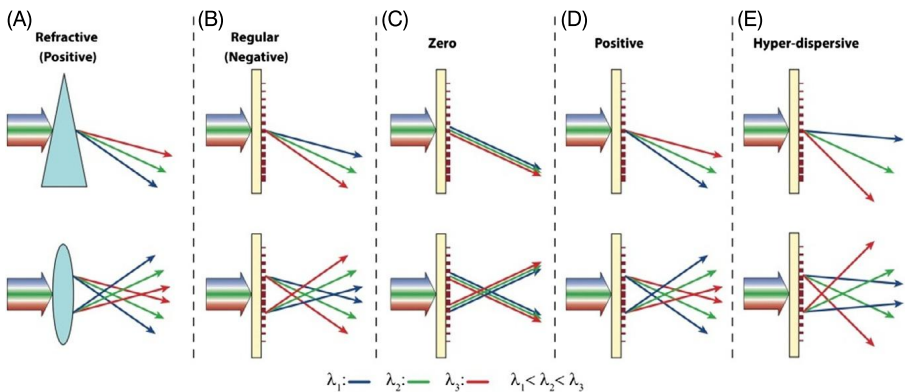
Figure 6.12 Dispersion regimes in refractive and diffractive optics. (A) Positive dispersion in refractive optics where shorter wavelengths are deflected more than longer wavelengths by a prism. Focal length of normal refractive lenses is larger for longer wavelengths than for shorter wavelengths. (B) Negative dispersion regime for diffractive gratings and diffractive lenses. (C–E) Diffractive devices with zero, positive, and enhanced negative dispersion. Reprinted with permission from Ehsan Arbabi, Amir Arbabi, Seyedeh Mahsa Kamali, Yu Horie, Andrei Faraon, Controlling the sign of chromatic dispersion in diffractive optics with dielectric metasurfaces, Optica 4 (6) (2017) 625–632, Optical Society of America.
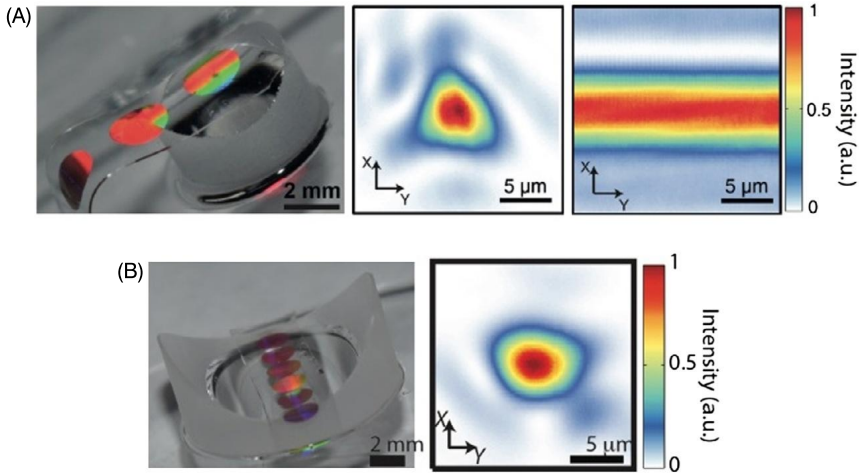
Figure 6.13 (A) Convex cylinder coated with a metasurface (left) which causes the light to be focused to a point (center). Without the metasurface, light is focused to a line (right). (B) Concave cylinder coated with a metasurface (left) that focuses light to a point (right). (Adapted from [47].)

6.9 Conformal optics

The applications discussed so far are based on flat planar metasurfaces. However, metasurface devices do not necessarily need to be flat and there are applications where metasurfaces taking various shapes are required. For example, in some applications, it may be necessary to integrate an optical lens into a package that cannot accommodate the shape of a lens, but could fit a device with a different shape. A metasurface can be used to coat the object with the required shape and make it act as a lens by providing the necessary phase compensation. Such a demonstration was done using concave or convex glass cylinders coated with metasurfaces, as shown in Fig. 6.13A, B [47]. Without the metasurface coating, a concave cylinder behaves like a diverging cylindrical lens, but with the properly designed metasurface it had the optical response of a converging optical lens that focuses light to a point as shown in Fig. 6.13B. This work was done using metasurfaces made from amorphous silicon nano-posts embedded in a flexible polymer. Transferring metasurfaces initially fabricated on a flat substrate to other surfaces that can be projected to a plane using isometric transformations is relatively straightforward. When the transformation is not isometric, like when coating the surface of a sphere with a planar metasurface, one needs to consider in the design the local deformations of the substrate containing the metasurface.

6.10 Other applications

The landscape of optical components is very broad, and optical metasurfaces have the potential to impact a large part of it. Besides the applications discussed above,

metasurfaces have also been used to create phase masks that project various images [11]. Systems of two metasurfaces stacked on top of each other have been used to demonstrate miniaturized retroreflectors that can be used in applications for remote detection and communications [48]. Metasurface phase masks for generating optical angular momentum beams were used to demonstrate optical communications systems for high-capacity underwater optical communication systems [49,50]. In medical devices, metasurface lenses were integrated into systems for optical coherence tomography [51]. Metasurfaces also can be used for applications related to mixed reality [52, 53].

6.11 Outlook

In the past few years, dielectric metasurfaces have progressed from a basic understanding of their principles of operation to demonstrations of devices with practical applications. Given the state of the art, the most likely application for metasurface lenses will be in components operating in a narrower bandwidth range. This way the overall efficiency of the system is not significantly degraded and the chromatic aberration effects are minimized. Examples of these systems include shaping of laser beams, specialized microscopy techniques and communication systems. In conjunction with some computational algorithms for image retrieval, they may also be employed in more broadband imaging systems where system size is more important than the best image resolution. Other metasurface devices that do not involve changing the direction of the optical wavefront, like various waveplates and polarizers, can already be made broadband and could be utilized in various applications that require them. Metasurface spectrometer devices already feature good performance and could be adopted in spectrum analysis applications that need highly miniaturized components. The adoption by the industry of the dielectric metasurface technology now relies on making them low cost, as many of these devices, especially in the visible range, still require electron-beam lithography which is expensive. At longer wavelengths metasurfaces can already be fabricated with photolithography, which is a more cost-effective technique well suited for mass production, so we may see metasurface devices incorporated in various optical systems in the near future.

References

[1] S.M. Kamali, E. Arbabi, A. Arbabi, A. Faraon, A review of dielectric optical metasurfaces for wavefront control, Nanophotonics 7 (2018) 1041–1068.

[2] S. Colburn, A. Zhan, A. Majumdar, Varifocal zoom imaging with large area focal length adjustable metalenses, Optica 5 (2018) 825–831.

[3] A. She, S. Zhang, S. Shian, D.R. Clarke, F. Capasso, Large area metalenses: design, characterization, and mass manufacturing, Opt. Express 26 (2018) 1573–1585.

[4] P. Lalanne, S. Astilean, P. Chavel, E. Cambril, H. Launois, Blazed binary subwavelength gratings with efficiencies larger than those of conventional échelette gratings, Opt. Lett. 23 (1998) 1081–1083.

[5] P. Lalanne, P. Chavel, Metalenses at visible wavelengths: past, present, perspectives, Laser Photonics Rev. 11 (2017) 1600295.

[6] S. Astilean, P. Lalanne, P. Chavel, E. Cambril, H. Launois, High-efficiency subwavelength diffractive element patterned in a high-refractive-index material for 633 nm, Opt. Lett. 23 (1998) 552–554.

[7] D. Fattal, J. Li, Z. Peng, M. Fiorentino, R.G. Beausoleil, A silicon lens for integrated free-space optics, Optical Society of America, 2011, ITuD2-ITuD2, Toronto.

[8] S. Vo, D. Fattal, W.V. Sorin, P. Zhen, T. Tho, M. Fiorentino, R.G. Beausoleil, Subwavelength grating lenses with a twist, IEEE Photonics Technol. Lett. 26 (2014) 1375–1378.

[9] A. Arbabi, Y. Horie, A.J. Ball, M. Bagheri, A. Faraon, Subwavelength-thick lenses with high numerical apertures and large efficiency based on high-contrast transmitarrays, Nat. Commun. 6 (2015) 7069.

[10] P.R. West, J.L. Stewart, A.V. Kildishev, V.M. Shalaev, V.V. Shkunov, F. Strohkendl, Y.A. Zakharenkov, R.K. Dodds, R. Byren, All-dielectric subwavelength metasurface focusing lens, Opt. Express 22 (2014) 26212–26221.

[11] A. Arbabi, Y. Horie, M. Bagheri, A. Faraon, Dielectric metasurfaces for complete control of phase and polarization with subwavelength spatial resolution and high transmission, Nat. Nanotechnol. 10 (2015) 937–943.

[12] M. Khorasaninejad, W.T. Chen, R.C. Devlin, J. Oh, A.Y. Zhu, F. Capasso, Metalenses at visible wavelengths: diffraction-limited focusing and subwavelength resolution imaging, Science 352 (2016) 1190–1194.

[13] E. Bayati, A. Zhan, S. Colburn, M.V. Zhelyeznyakov, A. Majumdar, Appl. Opt. 58 (6) (2019) 1460–1466.

[14] A. Zhan, S. Colburn, R. Trivedi, T.K. Fryett, C.M. Dodson, A. Majumdar, Low-contrast dielectric metasurface optics, ACS Photonics 3 (2016) 209–214.

[15] J. Yang, J.A. Fan, Analysis of material selection on dielectric metasurface performance, Opt. Express 25 (2017) 23899–23909.

[16] M.P. Backlund, A. Arbabi, P.N. Petrov, E. Arbabi, S. Saurabh, A. Faraon, W.E. Moerner, Removing orientation-induced localization biases in single-molecule microscopy using a broadband metasurface mask, Nat. Photonics 10 (2016) 459–462.

[17] S.M. Kamali, E. Arbabi, A. Arbabi, Y. Horie, A. Faraon, Highly tunable elastic dielectric metasurface lenses, Laser Photonics Rev. 10 (2016) 1062.

[18] M. Faraji-Dana, E. Arbabi, A. Arbabi, S.M. Kamali, H. Kwon, A. Faraon, Compact folded metasurface spectrometer, arXiv preprint, arXiv:1807.10985, 2018.

[19] M. Khorasaninejad, W.T. Chen, A.Y. Zhu, J. Oh, R.C. Devlin, D. Rousso, F. Capasso, Multispectral chiral imaging with a metalens, Nano Lett. 16 (2016) 4595–4600.

[20] E. Arbabi, A. Arbabi, S.M. Kamali, Y. Horie, A. Faraon, Multiwavelength polarization-insensitive lenses based on dielectric metasurfaces with meta-molecules, Optica 3 (2016) 628–633.

[21] E. Arbabi, A. Arbabi, S.M. Kamali, Y. Horie, A. Faraon, Multiwavelength metasurfaces through spatial multiplexing, Sci. Rep. 6 (2016) 32803.

[22] E. Arbabi, A. Arbabi, S.M. Kamali, Y. Horie, A. Faraon, High efficiency double-wavelength dielectric metasurface lenses with dichroic birefringent meta-atoms, Opt. Express 24 (2016) 18468–18477.

[23] B. Wang, F. Dong, Q.-T. Li, D. Yang, C. Sun, J. Chen, Z. Song, L. Xu, W. Chu, Y.-F. Xiao, Q. Gong, Y. Li, Visible-frequency dielectric metasurfaces for multiwavelength achromatic and highly dispersive holograms, Nano Lett. 16 (2016) 5235–5240.

[24] W. Zhao, B. Liu, H. Jiang, J. Song, Y. Pei, Y. Jiang, Full-color hologram using spatial multiplexing of dielectric metasurface, Opt. Lett. 41 (2016) 147–150.

[25] B.H. Chen, P.C. Wu, V.-C. Su, Y.-C. Lai, C.H. Chu, I.C. Lee, J.-W. Chen, Y.H. Chen, Y.-C. Lan, C.-H. Kuan, D.P. Tsai, GaN metalens for pixel-level full-color routing at visible light, Nano Lett. 17 (2017) 6345–6352.

[26] E. Arbabi, A. Arbabi, S.M. Kamali, Y. Horie, A. Faraon, Dispersionless metasurfaces using dispersive meta-atoms, in: Conference on Lasers and Electro-Optics, Optical Society of America, San Jose, California, 2016, 2016/06/05, FM2D.4.

[27] E. Arbabi, A. Arbabi, S.M. Kamali, Y. Horie, A. Faraon, Controlling the sign of chromatic dispersion in diffractive optics with dielectric metasurfaces, Optica 4 (2017) 625–632.

[28] M. Khorasaninejad, Z. Shi, A.Y. Zhu, V. Sanjeev, A. Zaidi, F. Capasso, Achromatic metalens over 60 nm bandwidth in the visible and metalens with reverse chromatic dispersion, Nano Lett. 17 (2017) 1819–1824.

[29] W.T. Chen, A.Y. Zhu, V. Sanjeev, M. Khorasaninejad, Z. Shi, E. Lee, F. Capasso, A broadband achromatic metalens for focusing and imaging in the visible, Nat Nanotechnol 13 (2018) 220–226.

[30] S. Wang, P.C. Wu, V.-C. Su, Y.-C. Lai, M.-K. Chen, H.Y. Kuo, B.H. Chen, Y.H. Chen, T.-T. Huang, J.-H. Wang, R.-M. Lin, C.-H. Kuan, T. Li, Z. Wang, S. Zhu, D.P. Tsai, A broadband achromatic metalens in the visible, Nat. Nanotechnol. 13 (2018) 227–232.

[31] S.M. Kamali, E. Arbabi, A. Arbabi, Y. Horie, M. Faraji-Dana, A. Faraon, Angle-multiplexed metasurfaces: encoding independent wavefronts in a single metasurface under different illumination angles, Phys. Rev. X 7 (2017) 41056.

[32] A. Arbabi, E. Arbabi, S.M. Kamali, Y. Horie, S. Han, A. Faraon, Miniature optical planar camera based on a wide-angle metasurface doublet corrected for monochromatic aberrations, Nat. Commun. 7 (2016) 13682.

[33] B. Groever, W.T. Chen, F. Capasso, Meta-lens doublet in the visible region, Nano Lett. 17 (2017) 4902–4907.

[34] E.R. Dowski, W.T. Cathey, Extended depth of field through wave-front coding, Appl. Opt. 34 (1995) 1859–1866.

[35] S. Colburn, A. Zhan, A. Majumdar, Metasurface optics for full-color computational imaging, Sci. Adv. 4 (2018) eaar2114.

[36] E. Arbabi, J. Li, R.J. Hutchins, S.M. Kamali, A. Arbabi, Y. Horie, P. Van Dorpe, V. Gradinaru, D.A. Wagenaar, A. Faraon, Two-photon microscopy with a double-wavelength metasurface objective lens, Nano Lett. 18 (2018) 4943–4948.

[37] M. Jang, Y. Horie, A. Shibukawa, J. Brake, Y. Liu, S.M. Kamali, A. Arbabi, H. Ruan, A. Faraon, C. Yang, Wavefront shaping with disorder-engineered metasurfaces, Nat. Photonics 12 (2018) 84–90.

[38] H. Kwon, E. Arbabi, S.M. Kamali, M. Faraji-Dana, A. Faraon, Computational complex optical field imaging using a designed metasurface diffuser, Optica 5 (2018) 924–931.

[39] E. Arbabi, A. Arbabi, S.M. Kamali, Y. Horie, M. Faraji-Dana, A. Faraon, MEMS-tunable dielectric metasurface lens, Nat. Commun. 9 (2018) 812.

[40] A. Zhan, S. Colburn, C.M. Dodson, A. Majumdar, Metasurface freeform nanophotonics, Sci. Rep. 7 (2017) 1673.

[41] H.-S. Ee, R. Agarwal, Tunable metasurface and flat optical zoom lens on a stretchable substrate, Nano Lett. 16 (2016) 2818–2823.

[42] A. She, S. Zhang, S. Shian, D.R. Clarke, F. Capasso, Adaptive metalenses with simultaneous electrical control of focal length, astigmatism, and shift, Sci. Adv. 4 (2018) eaap9957.

[43] E. Arbabi, S.M. Kamali, A. Arbabi, A. Faraon, Full-Stokes imaging polarimetry using dielectric metasurfaces, ACS Photonics 5 (2018) 3132–3140.

[44] J.P.Balthasar Mueller, K. Leosson, F. Capasso, Ultracompact metasurface in-line polarimeter, Optica 3 (2016) 42–47.

[45] N.A. Rubin, A. Zaidi, M. Juhl, R.P. Li, J.P.B. Mueller, R.C. Devlin, K. Leósson, F. Capasso, Polarization state generation and measurement with a single metasurface, Opt. Express 26 (2018) 21455–21478.

[46] A.Y. Zhu, W.-T. Chen, M. Khorasaninejad, J. Oh, A. Zaidi, I. Mishra, R.C. Devlin, F. Capasso, Ultra-compact visible chiral spectrometer with meta-lenses, APL Photonics 2 (2017) 036103.

[47] S.M. Kamali, A. Arbabi, E. Arbabi, Y. Horie, A. Faraon, Decoupling optical function and geometrical form using conformal flexible dielectric metasurfaces, Nat. Commun. 7 (2016) 11618.

[48] A. Arbabi, E. Arbabi, Y. Horie, S.M. Kamali, A. Faraon, Planar metasurface retroreflector, Nat. Photonics 11 (2017) 415–420.

[49] Y. Ren, L. Li, Z. Wang, S.M. Kamali, E. Arbabi, A. Arbabi, Z. Zhao, G. Xie, Y. Cao, N. Ahmed, Y. Yan, C. Liu, A.J. Willner, S. Ashrafi, M. Tur, A. Faraon, A.E. Willner, Orbital angular momentum-based space division multiplexing for high-capacity underwater optical communications, Sci. Rep. 6 (2016) 33306.

[50] Z. Wang, Y. Yan, A. Arbabi, G. Xie, C. Liu, Z. Zhao, Y. Ren, L. Li, N. Ahmed, A.J. Willner, E. Arbabi, A. Faraon, R. Bock, S. Ashrafi, M. Tur, A.E. Willner, Orbital angular momentum beams generated by passive dielectric phase masks and their performance in a communication link, Opt. Lett. 42 (2017) 2746–2749.

[51] H. Pahlevaninezhad, M. Khorasaninejad, Y.-W. Huang, Z. Shi, L.P. Hariri, D.C. Adams, V. Ding, A. Zhu, C.-W. Qiu, F. Capasso, M.J. Suter, Nano-optic endoscope for high-resolution optical coherence tomography in vivo, Nat. Photonics (2018).

[52] C. Hong, S. Colburn, A. Majumdar, Flat metaform near-eye visor, Appl. Opt. 56 (2017) 8822–8827.

[53] D. Lin, M. Melli, E. Poliakov, P.S. Hilaire, S. Dhuey, C. Peroz, S. Cabrini, M. Brongersma, M. Klug, Optical metasurfaces for high angle steering at visible wavelengths, Sci. Rep. 7 (2017) 2286.

Tunable metasurfaces and metadevices

7

Chengjun Zou[a], Isabelle Staude[a], Dragomir N. Neshev[b]
[a]Institute of Applied Physics, Abbe Center of Photonics, Friedrich Schiller University Jena, Germany, [b]Nonlinear Physics Centre, Research School of Physics, The Australian National University, Canberra, ACT, Australia

7.1   Motivation and introduction

Dielectric metasurfaces consisting of designed dielectric nanoresonators arranged in a planar fashion have emerged as a successful concept for implementing a multitude of optical functionalities [1–5]. Most prominently, they have been established as a platform for efficient wavefront shaping achieved by imprinting position dependent phase onto an incident light field. The advances in the design and fabrication of wavefront shaping dielectric metasurfaces have led to the development of ultra-thin and lightweight optical metadevices, including flat lenses [6–9], beam converters [10–12], deflectors [11,13–16] and holograms [17–19]. Apart from wavefront shaping, dielectric and semiconductor metasurfaces have been shown to allow for polarization and dispersion control [20,17], nonlinear frequency generation [21–24] and for the manipulation of spontaneous emission [25,26]. Furthermore, it is possible to combine several of the above-mentioned functionalities into a single metasurface, opening the door to novel multifunctional photonic devices.

Importantly, dielectric metasurfaces can exhibit very low absorption losses in the infrared and the visible spectral ranges, enabling highly efficient devices with resonance quality factors largely exceeding those of plasmonic metasurfaces [27,28]. Furthermore, the dielectric nanoparticles composing the metasurfaces can exhibit Mie-type resonances. These can be classified by two independent families of resonant modes – electric and magnetic [1,4,5]. The far-field interference of these two types of resonant modes leads to fundamentally new effects, such as unidirectional scattering [29–31], unconventional reflection behavior associated with the generalized Brewster effect [32] and near-unity transmission with 2π phase response in the Huygens regime of spectrally overlapping electric and magnetic dipole resonances [20,31,33,11,12,19]. Based on these properties, Huygens metasurfaces are the key to the realization of optically resonant functional dielectric metasurfaces with potentially near-unity transmission efficiency.

While all these aspects were already discussed in detail in the previous chapters, so far, mainly static metasurfaces have been discussed, whose optical functionalities were encoded permanently in the design during fabrication. However, the scope and technology potential of dielectric metasurfaces would be greatly expanded if the metasurface optical response could be modified in time in a controlled, reversible, and

reproducible fashion after fabrication, thus enabling *dynamic tunability* of metasurface devices. Adaptive or tunable optical components are required in many optical systems, ranging from imaging systems and camera lenses to beam scanners, light-field displays and projectors. For example the focal distance of a camera lens needs to be changed when taking pictures of objects at different distances and the ranging beam in driverless vehicles needs to continuously scan different directions.

Dielectric metasurfaces hold an exceptional potential for the next generation tunable optical systems. The opportunities and perspectives offered are essentially twofold:

On the one hand, they could provide much more compact, lightweight and energy efficient solutions than possible with conventional tunable optics, which are typically based on solid glass or plastic lenses that are moved back and forth to achieve focusing or zooming. Another common solution basically copies the working principle of the human eye by using an elastic lens material, which is reshaped for focusing. These solutions are in general bulky, expensive, and energy-hungry since macroscopic parts have to be moved or deformed. In metasurfaces, on the contrary, in order to obtain dramatic changes of their optical properties, it is sufficient to only induce changes of optical properties or geometry in subwavelength-scale volumes. This not only reduces the energy threshold for tuning or switching, but could furthermore allow for a drastic reduction in the response times.

On the other hand, active control could further be extended to optical functionalities for which no solutions are currently available, such as multidimensional control (for instance, simultaneous active control of the wavefront and its polarization) via tunable multifunctional metasurfaces, on-demand synthesis of harmonics by tunable nonlinear metasurfaces, or active tuning of spontaneous emission by agile light-emitting metasurfaces.

Choosing dielectric materials instead of metals for metasurfaces not only takes their advantages of lower losses, multipolar response, option of CMOS compatibility, and easy integration of emitters, gain, or nonlinearities, but also offers tuning mechanisms that are not available for plasmonic metasurfaces. Most importantly, it offers the possibility to fabricate the metasurface building blocks directly from the functional materials, such as semiconductors or phase-change materials. On the other hand, certain challenges also originated from dielectric metasurfaces, such as large mode volumes and highly concentrated fields inside the resonators, which make the tuning more difficult. This chapter aims at providing an overview of the current research on tunable dielectric metasurfaces and metadevices, and highlighting the current challenges.

7.2   Mechanisms for tuning dielectric metasurfaces

Tunable dielectric metasurfaces are metasurfaces whose properties can be changed by external influence, e.g. by control voltage, temperature, magnetic field, pressure, or strain. Overall we can distinguish three distinct mechanisms for changing the metasurface's optical response.

- Tuning by changing the structure geometry: Achieved by altering the arrangement of nanoresonators in a metasurface, which affects the overall properties due to the alteration of mutual couplings among the elements, e.g. by elastic deformation of the substrate or of an embedding matrix surrounding the nanoresonators. Deforming the shape of the individual dielectric nanoresonators themselves is another option, but difficult to realize in a reproducible fashion at the nanoscale.
- Tuning by changing the nanoresonator surrounding environment: Achieved by immersing the metasurface in an environment, whose properties change as a function of external control parameters such as temperature or an applied voltage. Typical examples include immersing metasurfaces in functional polymers or liquids or placing metasurfaces on active substrates.
- Tuning by changing of the resonator material: Achieved by changing the optical properties of the materials composing the dielectric resonators by an external stimulus. For example, by optically injecting free electrons in semiconductor nanoresonators, their conductivity and thus their refractive index can be modified. Another example is to fabricate the nanoresonators from phase-changing materials.

While the tuning response of a specific metasurface will typically be dominated by one of these mechanisms, two or more can also occur simultaneously. For example, heating of a metasurface can change the optical properties of both the nanoresonator material and their surrounding environment, but at the same time, for instance, lead to a thermal expansion resulting in a change of geometry.

Each of the above tuning mechanisms can be realized in different ways, which are also specific to the frequency range where the respective metasurface operates in. Table 7.1 provides a summary of representative recent demonstrations of different types of tunable dielectric metasurfaces. Clearly, dielectric metasurfaces offer many feasible opportunities for tuning, with significant portions of their optical near-fields concentrated both inside and outside of the nanoresonators. For dielectric metasurfaces highly confining their resonant near-fields, the possibility to engineer the field characteristics by the structure design means their optical properties are highly susceptible to the resonator material. While for the less-confined cases, the same approach are expected to result in strong sensitivity to the variation of the surrounding environment, and the mutual coupling between neighboring elements.

All of the above-mentioned mechanisms can in turn result in one or a combination of the following effects in resonant dielectric metasurfaces: a spectral shift of the metasurface resonances, a change in resonance strength, or a change of the entire mode structure of the metasurface, i.e. vanishing or emergence of resonances. Spectral tuning is the most commonly considered case. Key performance parameters for spectral tuning are the spectral shift $\Delta\lambda$, the tuning range λ/λ_0, and the change in transmittance or reflectance amplitude ($\Delta T = T(x) - T_0$, $\Delta R = R(x_0) - R_0$), also known as the modulation depth, and phase ($\Delta\phi = \phi(x) - \phi_0$) observed at a given wavelength. Here, λ_0 is the resonance wavelength and x stands for the control parameter. The subscript "0" denotes the response of the metasurface at its reference state. The parameters $\Delta\lambda$ and ΔT are connected, since a significant modulation in the phase or amplitude responses usually requires that the achieved spectral shift should

be comparable to the spectral bandwidth of the resonance. Note that the strong spectral dispersion of Mie-resonant dielectric metasurfaces makes them ideal candidates for tuning and switching, since small spectral shifts of resonances sufficiently result in strong changes of the optical response for a specific frequency range.

Another performance parameter commonly used in the literature is the switching or tuning contrast. Different definitions of the contrast are used, such as for example $\Delta T / T_0$ or $T(x)/T_0$, for the case of transmittance. However, contrasts can assume very large values even for moderate tuning performance, especially in resonant systems. For example, the transmittance contrast becomes automatically large when the denominator is close to zero at resonance. Therefore, in this chapter absolute transmittance/reflectance changes are provided where possible.

For tunable wavefront control, apart from the dynamic control of *spatially variant* transmitted or reflected phase and/or amplitude responses, it is furthermore required to induce the desired changes of the optical response as a function of in-plane position with the required spatial resolution. There are two general strategies to achieve this goal:

- Starting from a spatially variant metasurfaces, one can use one of the above tuning mechanisms to dynamically adjust its functionality. This strategy is suitable e.g. for metalenses with tunable focal length, for dynamic beam deflectors, or for sweeping the operation wavelength of a given metadevice.
- Starting from a spatially homogeneous metasurface and inducing local changes of its optical response. For instance, by appropriately segmented or pixellated supercells. In principle, this strategy is suitable for implementing generic devices, which can take any desired wavefront shaping functionalities on demand, e.g. for dynamic holography or for a new generation of spatial light modulators capable of controlling multiple properties of light fields simultaneously.

Hybrid forms of the above strategies, such as spatially variant metasurfaces in combination with coarsely segmented electrodes, are another option.

7.2.1   Tuning by changing of geometry

Optical resonances are sensitive to geometrical changes of the resonant structures, where deformations can be introduced to the resonator shape, orientation [44], and the periodicities of resonator arrays. In general, a change in the resonator shape predominantly affects the local resonance mode and thus the resonance frequency of a resonator; while a change in the mutual nanoresonator orientations and the periodicity of an array alters the inter-element couplings [45], which result in mode hybridizations [46,47]. Changes in the periodicity of the array also affect the lattice resonances of the metasurface [48]. In this section, we discuss several implementations of tunable dielectric metasurfaces based on geometrical deformations. Before dielectric metasurfaces became a research focus, reconfigurable metallic metamaterials employing geometrical changes were extensively studied with demonstrations ranging from microwave to optical frequencies. This work has served as a source of inspiration and many of the suggested tuning concepts and ideas have been adapted to dielectric

Table 7.1 Summary of demonstrated tunable dielectric metasurfaces. Data marked by "*" are relative tuning contrasts since absolute values are not available.

Designs	Mechanism	Materials	Operation wavelength	ΔT; ΔR	Tuning range (%)	Pros & Cons
[34]	phase-changing of LCs	LCs (E7), silicon	near-infrared	84%	2.42	flexible but slow and limited tuning range
[35]	nonlinear effect; free-carrier generation	silicon	visible-near-infrared	60*%	3.33	ultrafast switching; not convenient for implementation
[36]	mechanical stretching	TiO$_2$, PDMS	visible	27%	5.08	durable; large tuning range; inconvenient for integration
[37]	nonlinear effect	silicon	visible	36*%	0.57	small variation leads to large tuning; low efficiency
[38]	optical force	silicon	near-infrared	0.2%	no shift	fast, but very limited tuning and modulation range
[39]	phase-changing material	GST	near-infrared	~40%	10	large modulation and shift; inconvenient operation; operation wavelength limited by the material
[40]	refractive indices tensor rotation of LCs	LCs (E7), silicon	near-infrared	75%	3.55	fast tuning
[41]	NEMS	silicon	visible	10* dB	21.64	large tuning range
[42]	free-carrier generation	GaAs	near-infrared	~35%	3	ultrafast tuning
[43]	Carrier injection	ITO & silicon	near-infrared	~30%	not applicable	fast tuning; low-power modulation

metasurfaces. Therefore, before discussing tuning of dielectric metasurfaces by geometrical changes in detail, we briefly summarize previous work on their metallic counterparts. At optical and terahertz frequencies, metallic structures, such as split ring resonators have been patterned on or embedded inside elastomer substrate such as Polydimethylsiloxane (PDMS) [49–51]. This method exhibits a large tuning range in transmission spectra and allows for a durable device with consistent performance. Another method for creating subwavelength deformations is based on thermal stimulus. In both the optical [52] and the terahertz [53] range, deformations resulting from
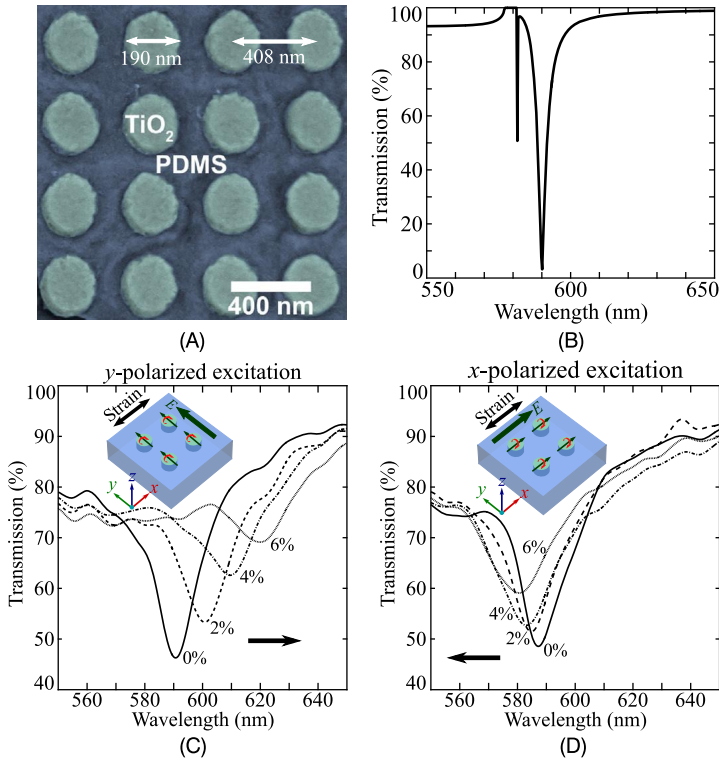
Figure 7.1 Mechanically tunable dielectric metasurface [36]. (A) False-color scanning electron microscopy image of the fabricated sample. The resonators have a height of 95 nm. (B) Simulated transmission spectrum of the unstretched array. (C–D) Measured transmission spectra under (C) x- and (D) y-polarized normal incidence when the sample array is gradually deformed starting from the unstretched case (0%) up to a stretch of 6% along the x-direction. Figure reproduced with copyright permission from the American Chemistry Society (ACS) Publications.

temperature changes were demonstrated to lead to large resonances shifts. At terahertz frequencies, due to the microscale resonator size, microelectromechanical (MEMS) switches can be used for controlling accurate inter-element displacements, and were demonstrated as a tuning method for reconfigurable metamaterials [54,55]. At microwave frequencies, an interesting design was implemented by partly embedding water in an array of ellipsoid containers. By rotating the array vertically, the shape of the water resonators changes leading to tunable transmission [56]. Significant research efforts have also been made in the field of reconfigurable microwave dielectric resonator antennas [57,58].

As a representative example of a tunable optical dielectric metasurface based on geometrical deformations, we consider an array of TiO_2 nanoresonators embedded in polydimethylsiloxane (PDMS) elastomer [36]. As shown in Fig. 7.1A, by applying an external strain to the PDMS matrix, the embedding material is deformed and thus the inter-element distances between the TiO_2 resonators are changed. The deformation of

the soft PDMS does not affect the shape of the hard TiO_2 resonators. Therefore, the change of the metasurface optical response observed upon deformation of the matrix results solely from the changes of the field interactions among TiO_2 resonators.

Fig. 7.1B shows simulated transmission spectra for an exemplary structure with dimensions given in Fig. 7.1A. For the unstretched array, under excitation with a normally incident plane wave polarized along the x-direction, an electric dipole resonance at 591 nm is excited. The other sharp peak observed at 582 nm wavelength corresponds to the first-order diffraction. The simulations further predict that by applying an external strain along the x-direction that deforms the PDMS elastomer by up to 6%, a pronounced change is induced in the optical response of the resonator array.

Fig. 7.1C, D summarize measured transmission spectra as a function of the external strain for y- and x-polarized normally incident excitation, respectively. For y-polarized Gaussian beam excitation, the resonance peak occurs at 591 nm for non-deformed array, and significantly redshifts to 620 nm for only a 6% deformation. However, for excitation with an x-polarized Gaussian beam and the identical deformation conditions, the electric dipole resonance peak blueshifts from 587 nm for the non-deformed array, to 581 nm for a 6% PDMS deformation. The slightly different resonance frequencies for the unstretched array under x- and y-polarized excitations are likely due to sample imperfections. An absolute modulation depth of up to $\sim$30% is achieved for the y-polarized case in experiments.

The different directions of the resonance shifts for the two orthogonal polarizations originate from the polarization dependence of the interactions among the TiO_2 resonators in the array. For the incident polarization (x-polarization) aligned along with the external strain direction, the main effect is a weakening of the (attractive) longitudinal coupling between electric dipoles, and the results shows blueshift of the resonance peak. However, for the incident polarization (y-polarization) aligned perpendicularly to the external strain direction, the main effect is a weakening of the (repulsive) transverse coupling between electric dipoles, and consequently the redshift of the resonance peak is observed. The inter-element coupling and thus the resonance shifts can be analyzed with a Lagrangian model [59] that takes both electric and magnetic dipole interactions into account. From this model, the resonance angular frequency is calculated as

$$\omega_s = \omega_0 \sqrt{\frac{1 + \kappa_{ET} - \kappa_{EL}}{1 + \kappa_{HL} - \kappa_{HT}}}, \tag{7.1}$$

where ω_0 is the decoupled resonance frequency of a single TiO_2 resonator, and κ denotes the coupling coefficients, where the subscripts E and H stand for the electric and magnetic components, while T and L denote the transverse and longitudinal couplings. From the model, Gutruf et al. [36] conclude that the transverse electric coupling dominates the resonance shifts. This design demonstrates a durable tuning platform that can support various nanoresonators for applications such as integrated optics and telecommunications.

As a different approach, optical forces inducing nanoscale deformations have also been utilized for achieving tunable dielectric metasurfaces. In general, electromag-

netic radiation can create radiation and gradient forces on objects. The time-averaged optical force acting on an object can be expressed as [60]

$$\langle F_i \rangle = \oint_S \langle T_{ij} \rangle n_j dS, \tag{7.2}$$

where S is the bounding surface around the object and n_j are the unit vector components pointing out of the surface. Here, $\langle T_{ij} \rangle$ is the time-averaged Maxwell stress tensor defined as [61]

$$\langle T_{ij} \rangle = \frac{1}{2} \text{Re} \left[\epsilon \epsilon_0 \left(E_i E_j^* - \frac{1}{2} \delta_{ij} |E|^2 \right) + \mu \mu_0 \left(H_i H_j^* - \delta_{ij} |H|^2 \right) \right]. \tag{7.3}$$

At resonance, the electric and magnetic fields within a nanoresonator are significantly enhanced, leading to resonantly enhanced optical forces. Optical forces in this scenario can be comparable or even stronger than elastic forces from mechanical deformation within the nanoresonator system. Zhang et al. have theoretically studied that resonantly enhanced optical forces for both dielectric and plasmonic nanostructures [60]. For example, an array of asymmetric bar pairs oriented along x-direction as shown in Fig. 7.2A, can support a resonant mode with a magnetic field in the z-direction. The oscillating currents in the bars in turn respond to this out-of-plane magnetic field, resulting in in-plane optical forces (y-direction) on the asymmetric bars in the opposite directions. Meanwhile, the oscillating currents on the bars responding to the in-plane magnetic field of the incident light field result in out-of-plane optical forces (z-direction) on the asymmetric bars. These forces can be asymmetric too due to the asymmetrically induced currents. While this concept can in principle be implemented either with plasmonic or with dielectric bar pairs, the study by Zhang et al. clearly shows that the optical forces can be several magnitudes stronger in dielectric structures than those in equivalent plasmonic structures. This is mainly because currents in plasmonic structures are largely confined to the metal surface and suffer from high Ohmic loss [60], leading to resonances of lower quality factors. Based on this study, Zhang et al. also theoretically proposed a tunable dielectric metamaterial based on optical forces [62]. Their design consists of silicon bricks sitting on silicon nitride strips, where the latter can be distorted by the optical forces. Theoretical results indicate that such systems can provide transmission tunability and bistability.

Along similar lines, Karvounis et al. have experimentally demonstrated a tunable optical dielectric metamaterial based on an optical force induced structure deformation [38]. They suggested and experimentally confirmed by a dedicated pump-probe experiment that modulation of the incident light at the mechanical eigenfrequency of the nanostructure can dramatically increase the optical modulation strength. Fig. 7.2B illustrates the design of the metamaterial, which consists of an array of nanocantilevers defined by perforating a silicon membrane. The unit cell consists of a complementary bar resonator and a complementary split ring resonator. Excited by normally incident plane-wave, both an electric dipole mode and a mode with an out-of-plane magnetic dipole can be excited in this structure at 1550 nm and 1310 nm, respectively (see Fig. 7.2C). Due to the strong displacement current at the nanocantilever tip for excitation at a wavelength of 1550 nm, this resonance offers the best conditions for
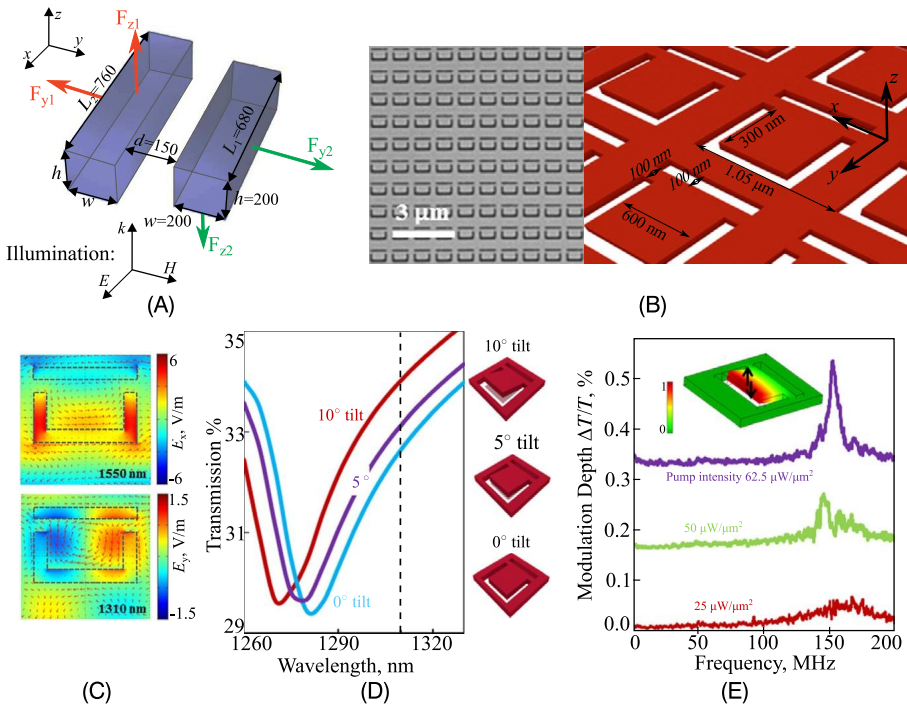
Figure 7.2 Tunable dielectric metamaterials based on optical force induced deformation. (A) Theoretical illustration of optical forces induced in an asymmetric bar pair [60]. (B) SEM and schematic concept of a nanooptomechanical dielectric metamaterial consisting of an array of nanocantilevers [38]. (C) Simulated electric field distributions of a unit cell at probe wavelength (1310 nm) and pump wavelength (1550 nm) for nanocantilever tilt angle of 0° [38]. (D) Simulated transmission spectra for different tilt angles of the nanocantilevers. The dashed vertical line indicates the probe wavelength (1310 nm). (E) Optical transmission contrast spectra at different pump intensities [38]. Figure (A) reprinted with permission from J. Zhang, K.F. MacDonald, N.I. Zheludev, Giant optical forces in planar dielectric photonic metamaterials, Opt. Lett. 39 (16) (2014) 4883–4886, Optical Society of America; (B–E) are reproduced with copyright permission from AIP Publishing.

optical force induced structure deformations. Thus, 1550 nm was chosen as the pump wavelength. On the other hand, the mode at 1310 nm was very sensitive to geometrical changes, as can be seen from the simulated transmission spectra for different nanocantilever tilt angles shown in Fig. 7.2D. Therefore, 1330 nm is chosen as the probe wavelength. However, even at the pump wavelength, the tilt angle change observed in the experiment was only 2 arcseconds with an illumination power of 60 μW/μm². To increase the modulation depth, the pump wavelength was modulated at the frequency of the fundamental mechanical eigenmode of the nanocantilever to excite the mechanical resonance. Fig. 7.2E shows the measured transmission modulation depth as a function of the modulation frequency of the pump excitation. It is seen that, at a modulation frequency of 152 MHz, the optical modulation depth is significantly increased for different pump intensities. Using numerical calculations, Karvounis et al. determined that the nanocantilever tile angle increased to 10 arcminutes for a modulated
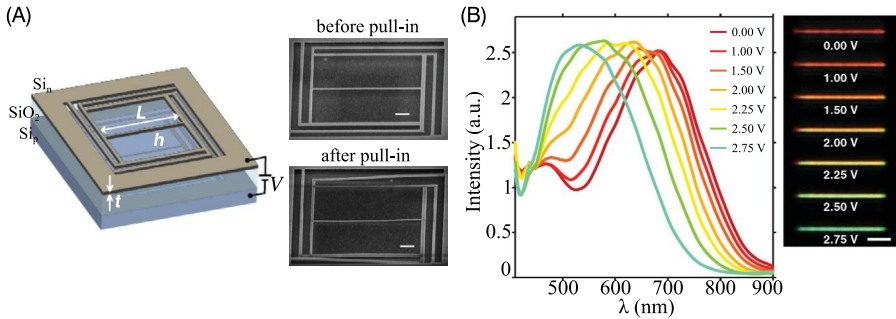
Figure 7.3 Active tuning of light scattering from silicon NWs based on NEMS [41]. (A) Structure illustration is shown on the left, and the SEM images of the structure before and after pull-in are shown on the right. The scale bars in the right images are 1 μm. (B) Measured dark-field scattering spectra (left) and dark-field microscopy images (right) at different bias voltage for the case $t = 35$ nm. The scale bar in the right graph is 2 μm. Figure reproduced with copyright permission from the American Association for the Advancement of Science (AAAS).

pump beam. However, even under these conditions, a maximum modulation depth of only about 0.2% is achieved. Nevertheless, high tuning speeds that can be achieved by this method make it interesting for applications in high-speed optoelectronic systems.

Tunable dielectric nanostructures based on geometrical deformations have also been demonstrated by using a nanoelectromechanical system (NEMS) platforms. Recently, Holsteen et al. reported on active tuning of light scattering from silicon nanowires (NWs) [41], which could be employed as building blocks of resonant dielectric metasurfaces. In their work, silicon NWs have been placed above a reflective surface. Under plane-wave excitation, the scattered light from the NWs and the corresponding reflection from the mirror form standing waves, which can selectively enhance the electric or magnetic Mie resonances in the NWs by changing the distances between the NWs and the mirror. Such a light scattering enhancement is similar to the Purcell effect experienced by quantum emitters enhanced by a resonant cavity [63].

To demonstrate tuning of the light scattering strength, a NW together with a mechanical deformable structure is fabricated based on a silicon-on-insulator platform, as shown in Fig. 7.3A. The high reflectivity of the silicon surface allows for the formation of standing waves between the NW and the silicon substrate. By applying voltages between the top NW pattern and the substrate, deformations can be induced to the suspended structured layer, thereby changing the distance between the NW and the silicon substrate. The SEM images in Fig. 7.3 present the induced deformation. With this tuning platform, the scattering spectra of the enhanced light scattering from the silicon NW were measured with a dark-field microscopy. The spectra and the corresponding dark-field images are presented in Fig. 7.3B. Even for only small applied voltages the scattering spectra undergo a significant blueshift, making NEMS-based tunable metasurfaces interesting candidates for active integrated optoelectronic devices. The polarization-dependent selective enhancement and suppression of NW resonances has also been studied using grating mirrors with different grating depths [64].

7.2.2   *Tuning through modulation of the surrounding materials*

While the metasurface tuning approach based on geometrical deformations offers certain unique advantages as detailed in the last section, their implementation often requires sophisticated fabrication techniques or the use of elastic materials. The tuning performance based on the manipulation of the coupling strength between neighboring resonators is inherently sensitive to the incident angle. However, in many cases, the structure architecture has to be as simple as possible, and accessible by standard fabrication techniques. A remaining option for post-fabrication tuning of such metasurfaces is to change the optical properties of the surrounding environment. Since the optical modes of dielectric particles can extend largely into the surrounding environment, they offer excellent opportunities for tuning of their resonance frequency with this strategy. This property also makes dielectric metasurfaces attractive for refractive index and biophotonic sensing devices, as any change of the environment will result in a change of the metasurface resonance strength or spectral position, similar to the well explored localized surface plasmon resonance (LSPR) sensors [65]. Several groups have explored these properties of the dielectric metasurfaces to design and demonstrate high-sensitivity refractive index and bio-sensors [28,66–69].

As a simple way to explore the change of the metasurface optical properties as a function of the background refractive index, liquids with different refractive indices can be easily applied on top of the dielectric metasurfaces [67]. One efficient and flexible tuning approach is the embedding of a metasurface into a (usually nematic) liquid crystal (LC) cell, such that the nanoresonators composing the metasurface are surrounded by the LC material. LCs are routinely used in several mature technologies, the most important of which are LC displays for monitors and television sets. The LCs consist of mixtures of highly elongated molecules with strong electric dipole moment. Due to the dipole–dipole interactions among the LC molecules, they can align in a crystal-like fashion [70]. In this regular orientation of the elongated LC molecules, the LCs can exhibit high optical anisotropy reaching values of $\Delta n \sim 0.3$ and even higher. The direction of alignment can be controlled by externally applied electric and magnetic fields, as well as by the optical field itself. Above its critical temperature, the LC can turn into its isotropic phase, where the molecules are randomly oriented. Therefore, by controlling the temperature or applied voltages and thus the phase of the LC or the orientation of the LC molecules in the region of the optical near-fields of the nanoresonators, one can tune the optical response of the metasurface. This tuning mechanism provides unique opportunities for the use of LCs in tunable optical metasurfaces, being previously used with various plasmonic elements [71,72]. However, due to the strong anchoring of the LC molecules to the metal surfaces of the plasmonic structure [70,72], the overall spectral shift in the plasmonic resonances is negligible [72].

Unlike plasmonic nanostructures, dielectric metasurfaces are, in essence, strongly immune to strong LC surface anchoring. This is because the near-fields of the Mie-resonance modes can extend over hundreds of nanometers into the surrounding environment, which is well beyond the thickness of the typical anchoring layer in the LCs, typically about 10 nm above the surface. Note that, for the case of silicon dielectric
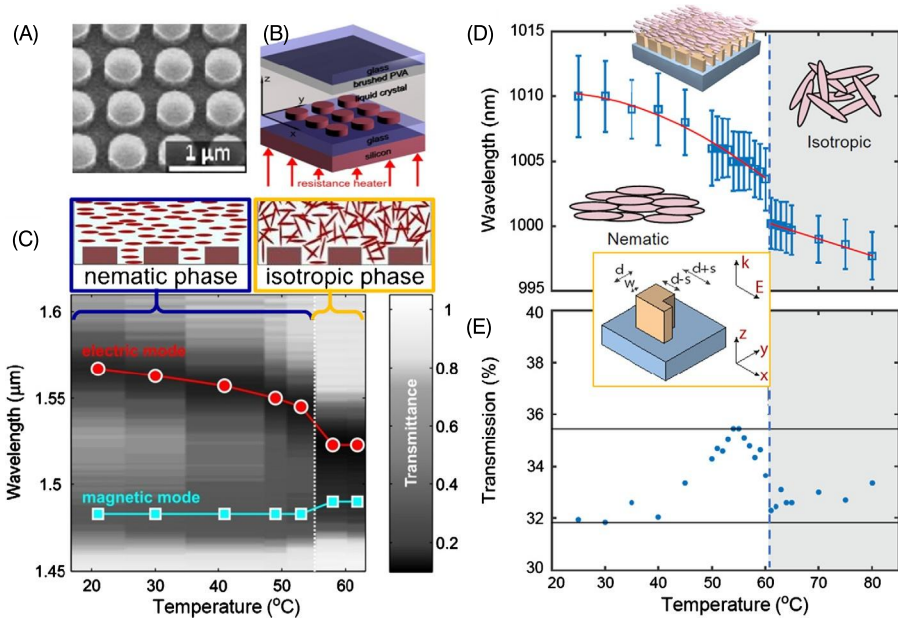
Figure 7.4 (A) Scanning electron micrograph of a fabricated silicon nanodisk metasurface. (B) Sketch of a silicon nanodisk metasurface integrated into an LC cell. (C) Measured transmittance spectra versus LC temperature, demonstrating the tuning of both electric and magnetic dipolar resonances of the metasurface. The regions of nematic and isotropic LC phases are indicated by the schematics at the top, and the phase transition at a temperature of 56° is depicted with a dashed line [34]. (D, E) Fano-resonant LC tunable metasurface: (D) Spectral shift of the Fano resonance with temperature. The vertical bars mark the full width at half maximum of the resonance for different temperatures. The red line is the best fit with a second order polynomial in the nematic state and a linear fit in the isotropic state. (E) The minimum transmission of the resonance as a function of the temperature. The insets in (D, E) show the geometry of the meta-atoms and the orientation of the LC molecules in the nematic and isotropic phase [73]. (A–C) are reproduced with copyright permission from ACS Publications. (D–E) are reproduced with copyright permission from AIP Publishing.

metasurfaces, the native oxide offers the possibility for similar surface functionalization as in many LC on silicon (LCoS) technologies. Indeed LC tuning of dielectric metasurfaces has attracted significant research interest. In the following, we describe some of the examples in this research direction.

7.2.2.1 Temperature tuning of LC infiltrated dielectric metasurfaces

Temperature tuning of dielectric metasurfaces by integration into an LC cell was first experimentally demonstrated by Sautter et al. [34]. A metasurface composed of silicon nanodisks (Fig. 7.4A) was infiltrated with the nematic LC E7. A cover slip (Fig. 7.4B) that was coated with a LC alignment layer to define a linear initial orientation of the LCs at room temperature (Fig. 7.4C-*left*) was used as the upper window of the LC cell. By heating the cell to near 60 °C, the LCs transitioned into their isotropic phase (Fig. 7.4C-*right*). Resulting from this phase transition, the resonance frequencies of

both the electric (red curve in Fig. 7.4C-*bottom*) and the magnetic (blue curve) dipolar resonances of the metasurface shifted significantly, to shorter and longer wavelengths, respectively. The maximum shift of about 40 nm was observed for the electric resonance of the metasurface. The spectral shift of the resonances also resulted in a strong phase and intensity modulation in transmission. For wavelengths of around 1.5 μm an absolute change in the transmittance through the metasurface of about 45% is achieved. Even higher absolute transmission modulation of 84% could be achieved for a variation of the metasurface design [34].

This concept was further extended by using Fano-resonant metasurfaces [73], which possess high-quality factor resonances ($Q = 270$). The metasurface was composed of a broken symmetry dielectric resonators [74], as shown in the inset of Fig. 7.4D, E. The asymmetry in the resonators was introduced so that x-polarized light can indirectly (through the excitation of a transverse electric dipole) couple to the longitudinal magnetic dipole m_z, which radiates dominantly in-plane of the metasurface. As such, for an infinite array of resonators, the energy stored into the excitation of the longitudinal magnetic dipoles is damped only by the near-field coupling with the transverse electric dipole p_x [74]. Such a low damping scheme results in the formation of a narrow transmission dip. Due to the change of the refractive index of the surrounding LC with temperature, the wavelength of this resonance blueshifts with the increase of the temperature, as seen in Fig. 7.4D. The vertical blue bars depict the full width at half maximum (FWHM) of the resonance. Specifically, the narrowband Fano transmission dip of FWHM $= 3.7 \pm 0.3$ nm has shifted to shorter wavelengths by more than 3.3 times its width. Importantly, the transmission level at the minimum remains approximately constant over the entire tuning range at $34\% \pm 2\%$. This property makes such devices attractive for potential use as narrowband spectral filters.

An important practical application of the temperature tuning of LC infiltrated dielectric metasurfaces is their use to actively controlling the wavelength of the enhanced spontaneous emission from the metasurface substrate [75]. The shift of the resonance of the metasurface was demonstrated to lead to a two-fold increase of the emission enhancement at a wavelength of 900 nm.

7.2.2.2   Voltage-tunable dielectric metasurfaces infiltrated with LCs

While the above experiments demonstrate the feasibility of the temperature tunable LC-based dielectric metasurfaces, the tuning speed remains relatively low, as the entire volume of the LC needs to be heated up. For practical applications, however, techniques using fast electrical control of the properties of the metasurface are more desirable.

Electrical tuning of the spectral response of a Mie-resonant dielectric metasurface consisting of silicon nanodisks embedded into LCs was studied in Reference [40]. It relied on the reorientation of nematic LCs in a moderate applied electric field to alter the uniaxial permittivity tensor of the LC material surrounding the metasurface. By switching a control voltage "on" and "off" (Fig. 7.5A, B, respectively) a large spectral shift of the metasurface resonances was induced, resulting in an absolute transmission modulation of up to 75% at the positions of the magnetic dipole resonances, as seen in Fig. 7.5C.
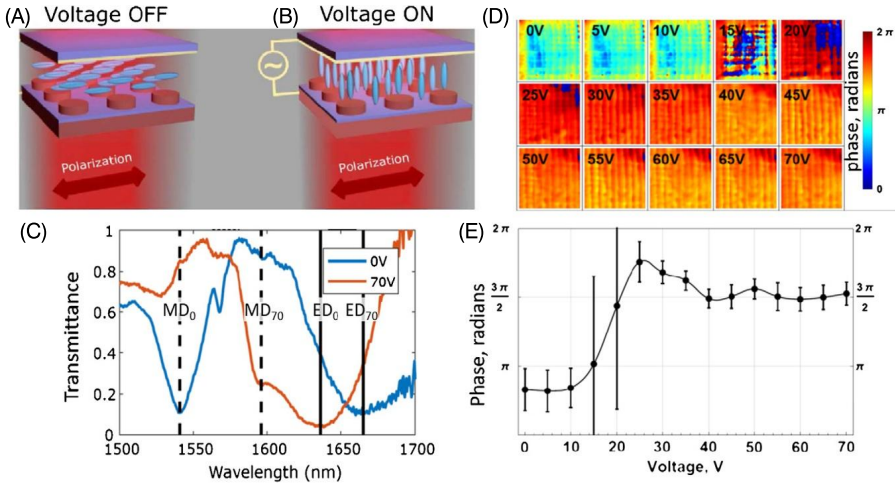
Figure 7.5 Schematic of the LC alignment for (A) no applied voltage ("off" case) and (B) for the case when a moderate voltage is applied between the two electrodes of the LC cell ("on" case). The red arrow indicates the polarization of the incident light. (C, D) Measured transmission phase across the array of the LC metasurface for different biasing voltages at $\lambda = 1550$ nm. (E) Phase accumulated by the light transmitted through the metasurface. The error bars indicate the spatial phase variation observed over the extent of the metasurface [40]. Figures are reproduced with copyright permission from AIP Publishing.

The authors also directly measured the phase change introduced by the metasurface for different applied voltages at the telecommunication wavelength of $\lambda = 1550$ nm. Using an imaging Mach–Zehnder interferometer and a four-frame-interferogram phase retrieval method [12], they imaged the phase imprinted onto the beam upon transmission through the metasurface for a variation of the applied voltage from 0 V to 70 V, as shown in Fig. 7.5D. For complete detuning of a single resonance away from the laser wavelength, a phase change with a magnitude of up to π was observed, as shown in the plot of Fig. 7.5E. The strongest switching dynamics was observed between 10 V and 30 V corresponding to the reorientation of the LC molecules. Note that for a single resonance the observed phase change is connected to a change in transmission intensity. The concept of silicon Huygens metasurfaces employing overlapping electric and magnetic dipole resonances [20] promises to open a way for achieving a pure phase modulation without changing the transmission intensity. This experimental demonstration of voltage control of dielectric metasurfaces paves the way for new types of electrically tunable metadevices, including dynamic displays and holograms.

7.2.3 Tuning by change of resonator material

Dielectric optical materials are usually characterized by their complex dielectric permittivity exhibiting a positive real part and a small imaginary part. More specifically, multipolar Mie-type resonances are favored for dielectric materials having a high real part and a vanishing imaginary part. Within this regime, the spectral position of the
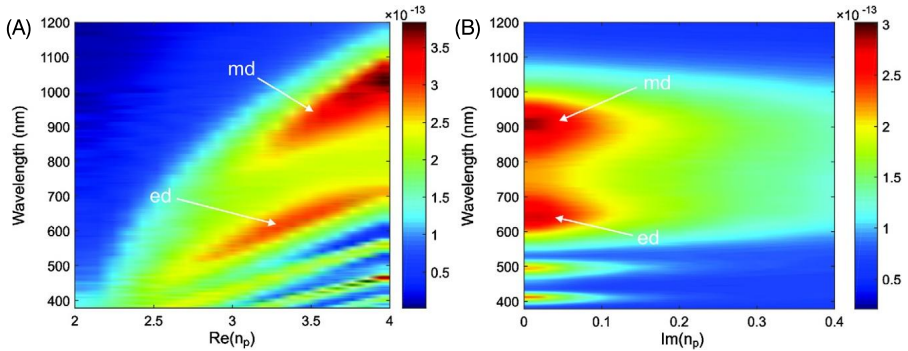
Figure 7.6 (A) Numerically calculated scattering cross section (in units of m^2) of an individual lossless nanocylinder (height $h = 220$ nm, diameter $d = 220$ nm, incident wave vector oriented along the rotational symmetry axis of the nanocylinder) embedded in a dielectric material with a refractive index of 1.5 for a systematic variation of (A) the real part and (B) the imaginary part of its refractive index. Figure is adopted from [76] with permission from Institute of Physics (IOP) Publishing.

resonant modes depends sensitively on the real part of the permittivity, while for a given metasurface design, their quality factor is highly affected by its imaginary part.

This typical connection is illustrated in Fig. 7.6, showing the scattering cross section of a single dielectric nanocylinder as a function of the real and imaginary part of its refractive index. Note that an increase of the real part of the nanoresonator's refractive index leads to a red shift of its resonances, while an increase of the imaginary part results in broader and weaker resonances. These changes in the scattering response of the individual nanoresonators are translated to the response of a metasurface composed of dielectric nanoresonators. As such, tuning of dielectric metasurfaces via changes in the resonator material are expected to be very effective. In the following, we describe such possibilities.

7.2.3.1 Tuning based on phase-change materials

Phase-change materials such as germanium antimony telluride (Ge$_2$Sb$_2$Te$_5$ or GST) are currently one of the most promising classes of materials for fully solid state implementations of switchable metasurfaces, owing to the dramatic difference in optical and electrical properties between their crystalline and amorphous state [77]. This phase transition can be controlled thermally, all-optically, or electrically. The crystalline-to-amorphous transition is a melt-quenching process caused by a short, intense excitation that momentarily raises the local temperature above the melting point. The amorphous-to-crystalline transition is triggered by a lower intensity excitation to hold the material above its glass transition temperature but below its melting point for a slightly longer time. For GST, the respective phase states are non-volatile, i.e. the states are preserved also after the external stimulus is removed. This is in contrast to materials like vanadium oxide, whose phase states depend on the momentary condition such as temperature. Reversible switching between the states of a phase-change material is possible. Phase-change materials are widely used in commercial rewritable optical disks and as media for storage cells in electronic phase-change memories.
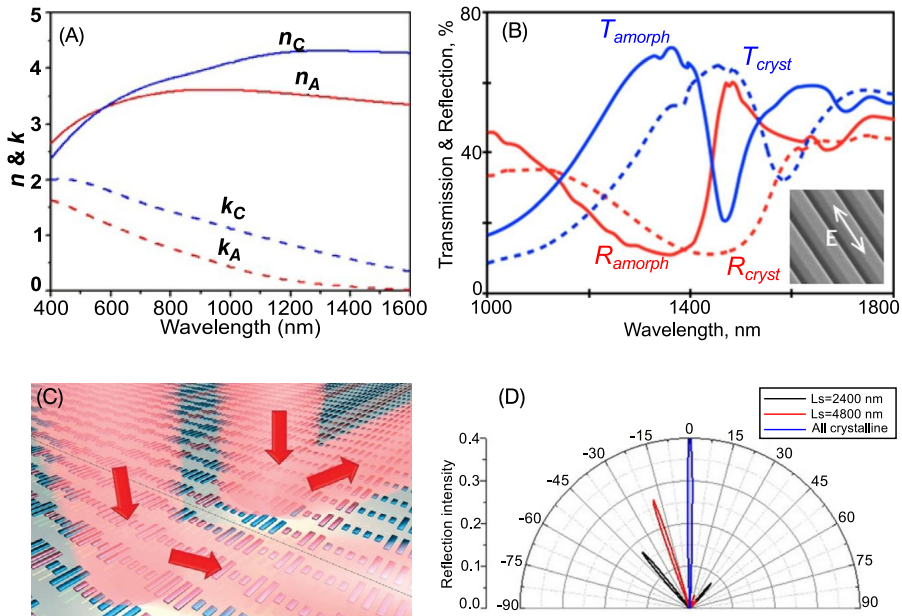
Figure 7.7 (A) Refractive index n and extinction coefficient κ of GST in its amorphous (n_A, k_A) and crystalline (n_C, k_C) states. (B) Microspectrophotometrically measured TE-mode reflectivity and transmission spectra for the as-deposited amorphous and laser-annealed [partially] crystalline phases of a 300 nm thick GST nanograting metamaterial. The inset shows a scanning electron micrograph of the fabricated structure with a period of 850 nm. (C) An artist's impression of a tunable gradient metasurfaces with a variable supercell period consisting of different patterns of the GST rods. (D) Anomalous reflection (calculated scattered electric field intensity pattern) from a tunable gradient metasurfaces for three different superlattice periods ($Ls = \infty$, 2400 nm, 4800 nm) and normally incident light at 1550 nm. Figure (A) original from B. Gholipour, J. Zhang, K.F. MacDonald, D.W. Hewak, N.I. Zheludev, An all-optical, non-volatile, bidirectional, phase-change meta-switch, Adv. Mater. 25 (2013) 3050–3054. Figures (C), (D) are taken from [78] with copyright permission from John Wiley and Sons. Figure (B) is taken from [39] with copyright permission from AIP Publishing.

Previously, for plasmonic metasurfaces phase-change materials were employed as a substrate or surrounding medium of its metallic building blocks, where the refractive index change associated with the phase transition resulted in tuning of the plasmonic resonance. For dielectric metasurfaces one has the additional option of directly fabricating the resonators out of the phase-change materials, thereby enhancing the overlap of the optical modes with the active material and thus the tunable response. Tuning the spectral resonance positions of a GST nanograting metasurfaces was experimentally demonstrated in [39], showing up to about 50% modulation of reflection (slightly less in transmission) when the as-deposited amorphous GST forming the resonators was laser-annealed to transit into its (partially) crystalline phase (see Fig. 7.7A). Phase transitions between the amorphous and crystalline states of GST as well as its partial crystallization were furthermore theoretically suggested for the construction of tunable Fano-resonant dielectric metasurfaces, and of dielectric gradient metasurfaces for dynamically controlling the angle of anomalous reflection (see Fig. 7.7B, C) [78].

7.2.3.2   Thermal tuning

Another important way to tune the resonator material is by heating or cooling the metasurface itself, taking advantage of the thermo-optic effect. For example the thermo-optic effect in silicon is routinely used to construct phase shifters and tune resonant cavities [80]. In a recent publication [79], Rahmani et al. demonstrated that the thermo-optic effect can be used to tune nanoscale resonators arranged in a two-dimensional array to form a metasurfaces. The authors use a silicon metasurface composed of nanodisks which exhibits sharp resonances due to the excitation of magnetic dipole and electric quadrupole modes. The heating and cooling of the metasurface (see Fig. 7.8) can cause drastic but reciprocal changes in the position of the resonances in a spectral window of 75 nm. This change can result in a dramatic change of the transmission and reflection from the metasurface at specific wavelengths.

In their experiments, the authors heated the silicon metasurfaces from 20 °C to 300 °C and measured the transmittance and reflectance for different metasurfaces in both the visible and the near-infrared spectral ranges. Fig. 7.8 shows the transmittance and reflectance spectra for three different metasurfaces with nanodisks having diameters of 170 nm, 470 nm, and 770 nm, respectively. The black curves show the spectra before heating, while the red curves represent the spectra at 300 °C. The green curves show the spectra after cooling, demonstrating the reversibility of the tuning mechanism. As can be seen from both experiments and simulations, all resonances experience a similar redshift of about 30 nm, for all diameters. The agreement between theory and experiments is good, being in line with the thermo-optic behavior of bulk silicon, where between room temperature and 300 °C, a nearly linear variation for refractive index is expected. This type of the reversible tuning can play a significant role in novel flat optical devices including metalenses and metaholograms.

Thermal tuning of semiconductor metasurfaces based on PbTe nanocrystals operating at mid-infrared wavelengths has also been explored [81]. Taking advantage of the extremely large thermo-optic coefficient and the high refractive index of PbTe, the authors have demonstrated tuning of their Mie resonances by several times of the resonance linewidths with temperature modulations as small as 10 K. This work shows the versatility of the thermo-optic tuning of the Mie resonances in dielectric metasurfaces and opens avenues to novel applications of tunable meta-optics.

7.2.3.3   Ultrafast tuning by carrier injection

While all tuning mechanisms discussed so far are operating at low or moderate tuning speeds up to MHz frequencies, ultrafast dynamic effects in Mie-resonant semiconductor metasurfaces have been a major milestone. In this respect, electrical carrier injection using a combination of dielectric resonators with an epsilon-near-zero thin films [43], hetero-junction resonators [82] and permittivity tuning of metal-oxides [83] has been explored. This work has shown promise for future applications; however, still with a limited speed.

The fastest switching times, so far, has been realized by the nonlinear induction of charge carriers in semiconductors metasurfaces, utilizing the intensity dependent complex refractive index of the semiconductor materials through third-order nonlinear
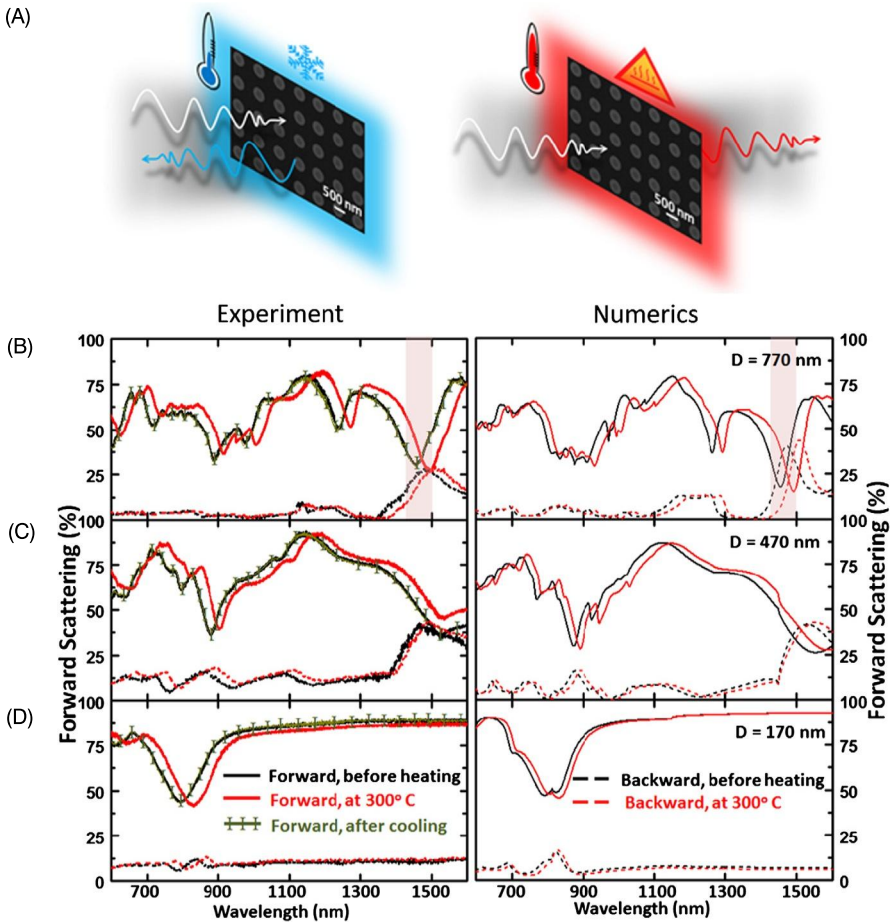
Figure 7.8 (A) Illustration of the temperature effect on the transmission and reflection properties of meta-surfaces. The metasurface can operate in either reflection (*left*) or transmission regime (*right*). (B–D) Experimentally measured (left) and numerically simulated (right) forward and backward scattering spectra of metasurfaces composed of the nanodisks with diameters of 770 nm, 470 nm, and 170 nm, at room temperature or at 300°C, respectively. Solid lines – transmission in forward direction; dashed lines – reflection in backward directions (only zeroth order) [79]. Figures reproduced with copyright permission from John Wiley and Sons.

effects, free-carrier generation and lattice heating [35,37,84,42]. First implementations of this concept used silicon as a constituent material of the nanoresonators [35,37,85]. In a first demonstration, ultrafast all-optical switching of the transmittance of hydrogenated amorphous silicon nanocylinders metasurfaces exhibiting localized magnetic Mie resonances was realized [35]. A strong self-modulation of femtosecond pulses with a relative modulation depth of 60% at picojoule-per-disk pump energies was observed. Furthermore, pump–probe measurements revealed that by proper spectral positioning of the magnetic resonance, free-carrier effects can be suppressed and the

switching process can become governed by two-photon absorption, and thus be extremely fast. In the experiment, switching times of 65 fs were demonstrated, which was limited by the pulse duration of the employed laser source. However, although the switching amplitude was enhanced by a factor of 80 with respect to the unstructured silicon film, the transient change in transmission $\Delta T/T$ was small, less than 1% at a pump fluence of 30 mJ/cm^2. Note that if picosecond switching times are sufficient, free-carrier effects can be employed to obtain much higher switching amplitudes.

A route to enhance the switching contrast is by designing the metasurface resonances to feature high-quality-factor Fano resonances, such that small resonance shifts translate to larger variations in the optical response in a narrow frequency range. Absolute ultrafast transmittance modulations ΔT of up to 0.2% at a pump fluence of 60 mJ/cm^2 were achieved in silicon metasurfaces along these lines [37].

Further, the transient optical response from anisotropic nanobrick amorphous silicon particles, exhibiting Mie-type resonances was studied in [84]. The authors derived a quantitative model to identify and disentangle the three physical processes that govern the ultrafast changes of the nanobrick optical properties, namely two-photon absorption, free-carrier relaxation, and lattice heating. The authors found a set of operating windows where ultrafast all-optical modulation of transmission is achieved with full return to zero in 20 ps. This is possible because the different and competing nonlinear processes exhibit different dispersive features with opposite strengths. Because of the anisotropic shape of the nanoresonators, the observed ultrafast switching behavior can be independently engineered for both orthogonal polarizations thus allowing ultrafast anisotropy control. This dynamic anisotropy control opens the possibility for constructing ultrafast polarization rotators. Tuning of silicon Huygens metasurfaces in the THz spectral range was also recently demonstrated based on photoexcitation of free carriers [86].

Beyond silicon, direct bandgap semiconductors offer the advantage of more efficient all-optical free-carrier generation and thus stronger switching amplitudes at lower pump fluences. This was demonstrated using an ultrafast tunable metasurface consisting of subwavelength gallium arsenide nanoparticles supporting Mie-type resonances in the near infrared [42]. The metasurface was pumped by a 800 nm femtosecond laser at fluences of less than 400 μJ/cm^{-2} to excite free carriers inside the nanoresonators. A near-infrared supercontinuum was used as a probe, revealing a picosecond scale absolute reflectance modulation of up to 0.35 at the magnetic dipole resonance wavelength. Remarkably, recovery times of only about 6 ps were observed, which are reduced compared to bulk GaAs wafers mainly due to surface-mediated recombination processes. The observed reflectance modulation originates from an ultrafast blueshift of the spectral position of the magnetic dipole resonance by 30 nm due to a reduction of the real part of the nanoresonator refractive index as a consequence of the plasma contribution, as well as from a resonance broadening and weakening due to an increase of the imaginary part of the nanoresonator refractive index. Apart from the tuning of transmission and reflection phase and amplitude, ultrafast tuning of directional scattering [85] could offer additional interesting opportunities, e.g. for ultrafast beam scanners.

More generally, ultrafast all-optical tuning holds the potential for ultrafast wavefront control. Theoretically it has already been demonstrated that Huygens metasurfaces with spectrally overlapping electric and magnetic dipole resonances can be designed to provide a continuously tunable transmission phase between 0 and 2π with less than 3 dB loss in intensity by introducing free charge carriers into these metasurfaces [87].

For more details on the nonlinear processes in semiconductor nanostructures enabling ultrafast tuning, please refer to the chapter by Shcherbakov & Fedyanin dedicated to nonlinear semiconductor metasurfaces.

7.3   Tunable functional metadevices

While huge progress on tunable dielectric metasurfaces has been reported over the last few years, the realization of active wavefront shaping metadevices requires more than just a tunable resonant response. Wavefront shaping with metasurfaces relies on controlling the phase of an incident light field as a function of the in-plane position. Therefore, dynamic wavefront control in its most general form will require spatially resolved tuning of optical responses.

This poses the challenge of locally addressing and tuning segments or pixels of the metasurface, where the spatial resolution of the reconfigurable phase masks will be directly related to the number and size of the segments or pixels. Only a few of the above-discussed tuning approaches appear compatible with a sufficiently large number of pixels to implement complex arbitrary phase masks. For example, for temperature tuning and elastic stretching, spatially selective control may be difficult to implement with high spatial resolution. Approaches based on the direct application of a voltage, in contrast, where spatially selective control can be accomplished by segmented or pixelated electrodes, appear being better suited for this task. This approach was adopted in some recent work [88,43]. A general technical challenge of this approach is the development of suitable electronics for addressing a large number of pixels while providing sufficiently high voltages to achieve sufficient tuning with the demonstrated mechanisms. An alternative route would be to improve the structure designs such that they can operate at lower voltages.

To the best of our knowledge, up to now there have been no experimental demonstrations of freely reconfigurable resonant dielectric/semiconductor metasurface devices. These would require a high-resolution two-dimensional pixelation of the control electrodes to modify the metasurface response actively as a function of in-plane position. In contrast, the few tunable wavefront shaping devices based on dielectric metasurfaces, which have been realized so far rely on a different concept. Instead of implementing spatially resolved tuning of an initially homogeneous metasurface, one can design a spatially inhomogeneous wavefront shaping metasurface, which is then tuned globally, within coarse macroscopic regions or within specialized patterns, using one of the above mechanisms. For example, mechanical tuning or liquid crystal tuning allow one to change the steepness of a linear or radial monotonous phase gradient,

which is fully sufficient for a range of dynamic wavefront shaping devices, including lenses with a tunable focal length or beam scanners. Importantly, while being less general in the sense that the metasurface functionality cannot be freely reconfigured by the controls but only adjusted in its parameters, this concept is technically easier to implement. In the following, we will discuss two prototypical examples of such devices, namely mechanically tunable dielectric metasurface lenses enabled and a dynamic beam deflector using liquid crystal-based temperature control.

7.3.1 Mechanically tunable metalenses

With the increasing research efforts made in tunable dielectric metasurfaces, several tunable metalenses employing elastic encapsulations [89] have been reported recently [90,88,91]. Tunable dielectric metalenses have the advantages of high numerical aperture, thin-profile, and low loss, thus enabling convenient integration with integrated photonic systems. A representative example has been demonstrated by Kamali et al. at near-infrared frequencies [90]. In their design, the metalens consists of a two-dimensional nonuniform array of silicon nanoresonators, whose phase responses follow a hyperbolic phase distribution, embedded inside PDMS. By applying an external strain that deforms the PDMS from 0 to 53% in the radial direction, the focal length is tuned from 600 μm to 1400 μm, corresponding to a tunability of more than 130%. However, since the PDMS deformation has to be done manually, the convenience, accuracy, and speed of the tuning is limited. As a step to solve these issues, tuning by external strain exerted from dielectric elastomer actuators (DEAs) [88] and MEMS [91] has been proposed and experimentally demonstrated. She et al. demonstrated the integration of DEAs with highly elastic near-infrared metalenses [88]. As shown in Fig. 7.9A, B, several electrodes for controlling strains from DEAs are patterned symmetrically around a dielectric metalens. By electrically tuning the DEAs individually or collectively, functionalities such as focusing and defocussing, focus shifts, and astigmatisms can be realized. Such an integration enables robust tuning performances and significantly improves the tuning accuracy and speed. In another way, Arbabi et al. successfully applied a MEMS platform for achieving a tunable metalens system [91], as illustrated in Fig. 7.9C. The MEMS is used to control the distance between two dielectric metalenses as a tunable two-lens system operating at 915 nm. In this way, a remarkable 35 μm tuning range of the focal length has been achieved by with only 1 μm displacement between the two metalenses. Fig. 7.9D clearly demonstrates the measured clear and blur imagings at different voltages and imaging distance, visually showing the function of tunable focusing.

7.3.2 Tunable beam deflector

Dynamic steering of laser beams by ultra-thin optical metasurfaces is another significant example for tunable dielectric metasurfaces, having possible applications in remote ranging and sensing. A unique platform for such important functionalities is offered by dielectric Huygens metasurfaces infiltrated with LCs. Based on this plat-
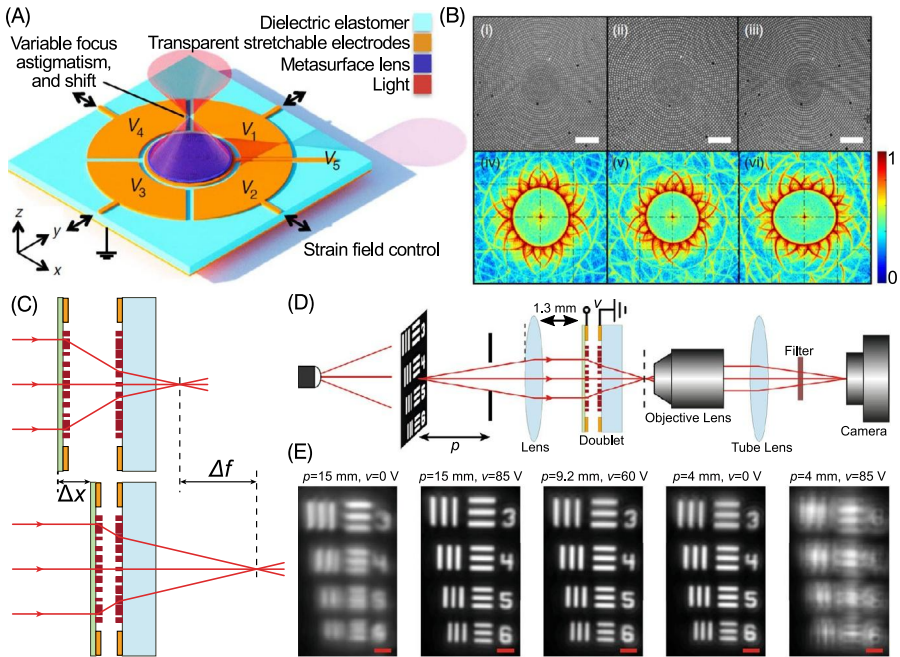
Figure 7.9 Mechanically tunable metalenses and systems. (A) Illustration of stretchable lenses realized with dielectric elastomer actuators [88]. (B) Optical microscope images (i–iii) and the corresponding Fourier transforms (iv–vi) for the device at (i) no voltage, (ii) with 2.5 kV applied to V_5 in (A), and (iii) with 2.75 kV applied to V_1 and V_3 in (A), respectively. The scale bar is 20 μm. (C) Conceptual illustration of a two-metalens MEMS system [91]. (D) Sketch of the optical setup employed for the tunable doublet. (E) Imaging results for applied voltage of 0 V, 60 V, and 85 V and imaging distance p ranging from 4 to 15 mm. The scale bar is 10 μm. (A–B) are reproduced with permission supported by the Creative Commons Attribution-NonCommercial license. (C–E) are reproduced with permission from Creative Commons Attribution 4.0 International License.

form, Komar et al. [92] demonstrated the dynamic switching of the beam position by all-dielectric metasurfaces composed of silicon nanodisks using the temperature-controlled phase transition of LCs from nematic to isotropic (Fig. 7.10A). In particular, the authors demonstrated the switching of a laser beam deflection angle from zero to 12° with an efficiency of 50%, as shown in Fig. 7.10B, C. Importantly, during the switching process, the transmitted power through the metasurface remains relatively constant (Fig. 7.10D), which reveals the practicality of the concept. Another LC-based electrically tunable beam deflector was demonstrated by Li et al. at the visible red wavelength [93]. Importantly, they demonstrated tunable beam deflections at ±11° and 0° with three segmented electrodes. These designs open important future opportunities for tunable ultra-thin beam-steering metadevices. However, note that, for such applications, a continuous tuning of the deflection angle would be desirable, which has not been demonstrated yet based on this approach. Another recent demonstration of dynamic diffraction grating based on absorption loss tuning due to induced carrier density modulation using a combination of dielectric resonators with an epsilon-near-
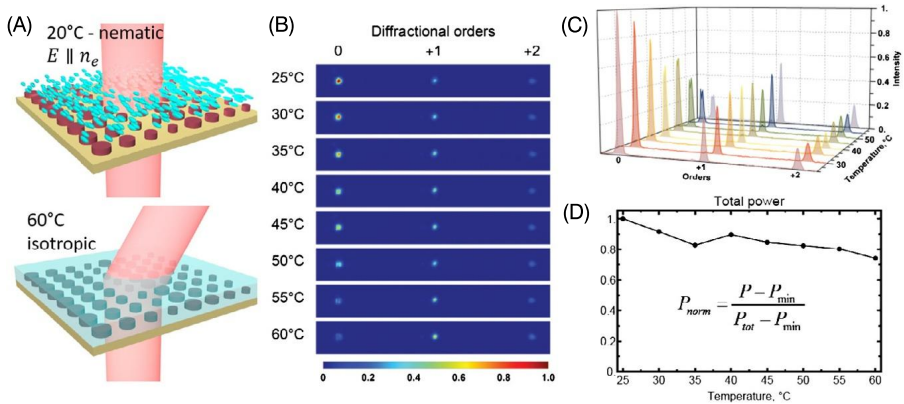
Figure 7.10 (A) Experimentally measured of the light passing through the tunable beam deflector, at different temperatures of the LC cell. (B) The intensity profiles of 0, +1 and +2 diffraction orders extracted from (A). (C) Experimentally measured change of the total power of transmitted light with temperature, showing high overall transmission for all temperature of the operation [92]. Figures reproduced with copyright permission from ACS Publications.

zero thin films used spatially segmented electrodes for turning on an off diffraction gratings [43]. To achieve this, several unit cells were grouped into each active region.

7.4   Outlook

The progress made in tunable optical metasurfaces in the last few years is truly outstanding. This is a fast developing field and many new and exciting opportunities remain ahead. The biggest challenge in the field remains the design and implementation a tunable metasurface that can perform pure phase modulation of an input beam in the full 2π phase range, while maintaining a consistently high transmission or reflection intensity of the beam. Increasing the spectral range of operation of the metasurfaces is also an enormous challenge, however, tuning the properties of broadband metadevices is more difficult than tuning resonant metasurfaces. Achieving these key functionalities will truly open the field of tunable metasurfaces to a plethora of practical applications, including tunable lenses, beam steering, and even dynamic holograms, to mention a few.

References

[1] A.I. Kuznetsov, A.E. Miroshnichenko, M.L. Brongersma, Y.S. Kivshar, B. Luk'yanchuk, Optically resonant dielectric nanostructures, Science 354 (6314) (2016 November) aag2472.

[2] A.Y. Zhu, A.I. Kuznetsov, B. Luk'yanchuk, N. Engheta, P. Genevet, Traditional and emerging materials for optical metasurfaces, Nanophotonics 6 (2) (2017) 452–471.

[3] P. Lalanne, P. Chavel, Metalenses at visible wavelengths: past, present, perspectives, Laser Photonics Rev. 11 (3) (2017) 1600295.

[4] Y. Kivshar, A. Miroshnichenko, Meta-optics with Mie resonances, Opt. Photonics News 28 (1) (2017) 24–31.

[5] I. Staude, J. Schilling, Metamaterial-inspired silicon nanophotonics, Nat. Photonics 11 (5) (2017) 274–284.

[6] A. Arbabi, Y. Horie, A.J. Ball, M. Bagheri, A. Faraon, Subwavelength-thick lenses with high numerical apertures and large efficiency based on high-contrast transmitarrays, Nat. Commun. 6 (2015 May) 7069.

[7] M. Khorasaninejad, W.T. Chen, R.C. Devlin, J. Oh, A.Y. Zhu, F. Capasso, Metalenses at visible wavelengths: diffraction-limited focusing and subwavelength resolution imaging, Science 352 (6290) (2016 Jun.) 1190–1194.

[8] R. Paniagua-Domínguez, Y.F. Yu, E. Khaidarov, S. Choi, V. Leong, R.M. Bakker, et al., A metalens with a near-unity numerical aperture, Nano Lett. 18 (3) (2018) 2124–2132.

[9] B.H. Chen, P.C. Wu, V.C. Su, Y.C. Lai, C.H. Chu, I.C. Lee, et al., GaN metalens for pixel-level full-color routing at visible light, Nano Lett. 17 (10) (2017 Oct.) 6345–6352.

[10] D. Lin, P. Fan, E. Hasman, M.L. Brongersma, Dielectric gradient metasurface optical elements, Science 345 (6194) (2014 Jul.) 298–302.

[11] Y.F. Yu, A.Y. Zhu, R. Paniagua-Domínguez, Y.H. Fu, B. Luk'yanchuk, A.I. Kuznetsov, High-transmission dielectric metasurface with 2π phase control at visible wavelengths, Laser Photonics Rev. 9 (4) (2015 Jul.) 412–418.

[12] K.E. Chong, I. Staude, A. James, J. Dominguez, S. Liu, S. Campione, et al., Polarization-independent silicon metadevices for efficient optical wavefront control, Nano Lett. 15 (8) (2015 Aug.) 5369–5374.

[13] D. Lin, M. Melli, E. Poliakov, P.S. Hilaire, S. Dhuey, C. Peroz, et al., Optical metasurfaces for high angle steering at visible wavelengths, Sci. Rep. 7 (1) (2017) 2286.

[14] E. Khaidarov, H. Hao, R. Paniagua-Dominguez, Y. Yu, Y.H. Fu, V. Valuckas, et al., Asymmetric nanoantennas for ultra-high angle broadband visible light bending, Nano Lett. 17 (10) (2017) 6267–6272.

[15] H. Chalabi, Y. Ra'di, D. Sounas, A. Alù, Efficient anomalous reflection through near-field interactions in metasurfaces, Phys. Rev. B 96 (7) (2017) 075432.

[16] D. Sell, J. Yang, S. Doshay, R. Yang, Fan JA. Large-Angle, Multifunctional metagratings based on freeform multimode geometries, Nano Lett. 17 (6) (2017) 3752–3757.

[17] A. Arbabi, Y. Horie, M. Bagheri, A. Faraon, Dielectric metasurfaces for complete control of phase and polarization with subwavelength spatial resolution and high transmission, Nat. Nanotechnol. 10 (11) (2015 Nov.) 937–943.

[18] L. Wang, S. Kruk, H. Tang, T. Li, I. Kravchenko, D.N. Neshev, et al., Grayscale transparent metasurface holograms, Optica 3 (12) (2016) 1504–1505.

[19] K.E. Chong, L. Wang, I. Staude, A.R. James, J. Dominguez, S. Liu, et al., Efficient polarization-insensitive complex wavefront control using Huygens' metasurfaces based on dielectric resonant meta-atoms, ACS Photonics 3 (4) (2016 Apr.) 514–519.

[20] M. Decker, I. Staude, M. Falkner, J. Dominguez, D.N. Neshev, I. Brener, et al., High-efficiency dielectric Huygens' surfaces, Adv. Opt. Mater. 3 (6) (2015 Jun.) 813–820.

[21] M.R. Shcherbakov, D.N. Neshev, B. Hopkins, A.S. Shorokhov, I. Staude, E.V. Melik-Gaykazyan, et al., Enhanced third-harmonic generation in silicon nanoparticles driven by magnetic response, Nano Lett. 14 (11) (2014) 6488–6492.

[22] V.F. Gili, L. Carletti, A. Locatelli, D. Rocco, M. Finazzi, L. Ghirardini, et al., Mono-lithic AlGaAs second-harmonic nanoantennas, Opt. Express 24 (14) (2016 Jul. 11) 15965–15971.

[23] S. Liu, M.B. Sinclair, S. Saravi, G.A. Keeler, Y.M. Yang, J. Reno, et al., Resonantly enhanced second-harmonic generation using III–V semiconductor all-dielectric metasur-faces, Nano Lett. 16 (9) (2016 Sep.) 5426–5432.

[24] R. Camacho-Morales, M. Rahmani, S. Kruk, L. Wang, L. Xu, D.A. Smirnova, et al., Non-linear generation of vector beams from AlGaAs nanoantennas, Nano Lett. 16 (11) (2016 Nov.) 7191–7197.

[25] I. Staude, V.V. Khardikov, N.T. Fofang, S. Liu, M. Decker, D.N. Neshev, et al., Shaping photoluminescence spectra with magnetoelectric resonances in all-dielectric nanoparticles, ACS Photonics 2 (2) (2015) 172–177.

[26] S. Liu, A. Vaskin, S. Addamane, B. Leung, M.C. Tsai, Y. Yang, et al., Light-emitting metasurfaces: simultaneous control of spontaneous emission and far-field radiation, Nano Lett. 18 (11) (2018) 6906–6914.

[27] C. Wu, N. Arju, G. Kelpp, J. Fan, J. Dominguez, E. Gonzales, et al., Spectrally selective chiral silicon metasurfaces based on infrared Fano resonances, Nat. Commun. 5 (2014) 3892.

[28] Y. Yang, I.I. Kravchenko, D.P. Briggs, J. Valentine, All-dielectric metasurface analogue of electromagnetically induced transparency, Nat. Commun. 5 (2014) 5753.

[29] Y.H. Fu, A.I. Kuznetsov, A.E. Miroshnichenko, Y.F. Yu, B. Luk'yanchuk, Directional vis-ible light scattering by silicon nanoparticles, Nat. Commun. 4 (2013 Feb.) 1527.

[30] S. Person, M. Jain, Z. Lapin, J.J. Sáenz, G. Wicks, L. Novotny, Demonstration of zero optical backscattering from single nanoparticles, Nano Lett. 13 (4) (2013) 1806–1809.

[31] I. Staude, A.E. Miroshnichenko, M. Decker, N.T. Fofang, S. Liu, E. Gonzales, et al., Tai-loring directional scattering through magnetic and electric resonances in subwavelength silicon nanodisks, ACS Nano 7 (9) (2013 Sep.) 7824–7832.

[32] R. Paniagua-Domínguez, Y.F. Yu, A.E. Miroshnichenko, L.A. Krivitsky, Y.H. Fu, V. Val-uckas, et al., Generalized Brewster effect in dielectric metasurfaces, Nat. Commun. 7 (2016) 10362.

[33] S. Campione, L.I. Basilio, L.K. Warne, M.B. Sinclair, Tailoring dielectric resonator ge-ometries for directional scattering and Huygens' metasurfaces, Opt. Express 23 (3) (2015) 2293–2307.

[34] J. Sautter, I. Staude, M. Decker, E. Rusak, D.N. Neshev, I. Brener, et al., Active tuning of all-dielectric metasurfaces, ACS Nano 9 (4) (2015 Apr.) 4308–4315.

[35] M.R. Shcherbakov, P.P. Vabishchevich, A.S. Shorokhov, K.E. Chong, D.Y. Choi, I. Staude, et al., Ultrafast all-optical switching with magnetic resonances in nonlinear dielectric nanostructures, Nano Lett. 15 (10) (2015) 6985–6990.

[36] P. Gutruf, C. Zou, W. Withayachumnankul, M. Bhaskaran, S. Sriram, C. Fumeaux, Me-chanically tunable dielectric resonator metasurfaces at visible frequencies, ACS Nano 10 (1) (2016) 133–141.

[37] Y. Yang, W. Wang, A. Boulesbaa, I.I. Kravchenko, D.P. Briggs, A. Puretzky, et al., Non-linear Fano-resonant dielectric metasurfaces, Nano Lett. 15 (11) (2015) 7388–7393.

[38] A. Karvounis, J.Y. Ou, W. Wu, K.F. MacDonald, N.I. Zheludev, Nano-optomechanical nonlinear dielectric metamaterials, Appl. Phys. Lett. 107 (19) (2015) 191110.

[39] A. Karvounis, B. Gholipour, K.F. MacDonald, N.I. Zheludev, All-dielectric phase-change reconfigurable metasurface, Appl. Phys. Lett. 109 (5) (2016) 051103.

[40] A. Komar, Z. Fang, J. Bohn, J. Sautter, M. Decker, A. Miroshnichenko, et al., Electrically tunable all-dielectric optical metasurfaces based on liquid crystals, Appl. Phys. Lett. 110 (7) (2017 Feb.) 071109.

[41] A.L. Holsteen, S. Raza, P. Fan, P.G. Kik, M.L. Brongersma, Purcell effect for active tuning of light scattering from semiconductor optical antennas, Science 358 (6369) (2017) 1407–1410.

[42] M.R. Shcherbakov, S. Liu, V.V. Zubyuk, A. Vaskin, P.P. Vabishchevich, G. Keeler, et al., Ultrafast all-optical tuning of direct-gap semiconductor metasurfaces, Nat. Commun. (2017) 8.

[43] A. Howes, W. Wang, I. Kravchenko, J. Valentine, Dynamic transmission control based on all-dielectric Huygens metasurfaces, Optica 5 (7) (2018) 787–792.

[44] D.A. Powell, K. Hannam, I.V. Shadrivov, Y.S. Kivshar, Near-field interaction of twisted split-ring resonators, Phys. Rev. B 83 (23) (2011) 235420.

[45] N. Liu, H. Giessen, Coupling effects in optical metamaterials, Angew. Chem. Int. Ed. 49 (51) (2010) 9838–9852.

[46] N. Liu, H. Liu, S. Zhu, H. Giessen, Stereometamaterials, Nat. Photonics 3 (3) (2009) 157–162.

[47] E. Prodan, C. Radloff, N.J. Halas, P. Nordlander, A hybridization model for the plasmon response of complex nanostructures, Science 302 (5644) (2003) 419–422.

[48] A. Bitzer, J. Wallauer, H. Helm, H. Merbold, T. Feurer, M. Walther, Lattice modes mediate radiative coupling in metamaterial arrays, Opt. Express 17 (24) (2009) 22108–22113.

[49] J. Li, C.M. Shah, W. Withayachumnankul, B.S.Y. Ung, A. Mitchell, S. Sriram, et al., Mechanically tunable terahertz metamaterials, Appl. Phys. Lett. 102 (12) (2013) 121101.

[50] I.M. Pryce, K. Aydin, Y.A. Kelaita, R.M. Briggs, H.A. Atwater, Highly strained compliant optical metamaterials with large frequency tunability, Nano Lett. 10 (10) (2010) 4222–4227.

[51] S. Aksu, M. Huang, A. Artar, A.A. Yanik, S. Selvarasah, M.R. Dokmeci, et al., Flexible plasmonics on unconventional and nonplanar substrates, Adv. Mater. 23 (38) (2011) 4422–4430.

[52] J.Y. Ou, E. Plum, L. Jiang, N.I. Zheludev, Reconfigurable photonic metamaterials, Nano Lett. 11 (5) (2011) 2142–2144.

[53] H. Tao, A. Strikwerda, K. Fan, W. Padilla, X. Zhang, R. Averitt, Reconfigurable terahertz metamaterials, Phys. Rev. Lett. 103 (14) (2009) 147401.

[54] W.M. Zhu, A.Q. Liu, X.M. Zhang, D.P. Tsai, T. Bourouina, J.H. Teng, et al., Switchable magnetic metamaterials using micromachining processes, Adv. Mater. 23 (15) (2011) 1792–1796.

[55] W. Zhang, A. Liu, W. Zhu, E. Li, H. Tanoto, Q. Wu, et al., Micromachined switchable metamaterial with dual resonance, Appl. Phys. Lett. 101 (15) (2012) 151902.

[56] P. Kapitanova, M. Odit, D. Dobrykh, A. Andryieuski, A.V. Lavrinenko, P. Belov, Tunable water-based microwave metasurface, in: 2017 11th European Conference on Antennas and Propagation (EUCAP), IEEE, 2017, pp. 2599–2602.

[57] S.G. O'Keefe, S.P. Kingsley, Tunability of liquid dielectric resonator antennas, IEEE Antennas Wirel. Propag. Lett. 6 (2007) 533–536.

[58] A. Petosa, A. Ittipiboon, Dielectric resonator antennas: a historical review and the current state of the art, IEEE Antennas Propag. Mag. 52 (5) (2010) 91–116.

[59] D. Morin, Introduction to Classical Mechanics: With Problems and Solutions, Cambridge University Press, 2008.

[60] J. Zhang, K.F. MacDonald, N.I. Zheludev, Giant optical forces in planar dielectric photonic metamaterials, Opt. Lett. 39 (16) (2014) 4883–4886.

[61] J.D. Jackson, Classical Electrodynamics, John Wiley & Sons, 2007.

[62] J. Zhang, K.F. MacDonald, N.I. Zheludev, Nonlinear dielectric optomechanical metamaterials, Light: Sci. Appl. 2 (8) (2013) e96.

[63] J. Gérard, B. Sermage, B. Gayral, B. Legrand, E. Costard, V. Thierry-Mieg, Enhanced spontaneous emission by quantum boxes in a monolithic optical microcavity, Phys. Rev. Lett. 81 (5) (1998) 1110.

[64] J. van de Groep, M.L. Brongersma, Metasurface mirrors for external control of Mie resonances, Nano Lett. (2018).

[65] K.A. Willets, R.P. Van Duyne, Localized surface plasmon resonance spectroscopy and sensing, Annu. Rev. Phys. Chem. 58 (2007) 267–297.

[66] C. Wu, N. Arju, J. Fan, I. Brener, G. Shvets, Spectrally selective chiral silicon metasurfaces based on infrared Fano resonances, in: 2014 Conference on Lasers and Electro-Optics (CLEO), IEEE, 2014, pp. 1–2.

[67] K.E. Chong, H.W. Orton, I. Staude, M. Decker, A.E. Miroshnichenko, I. Brener, et al., Refractive index sensing with Fano resonances in silicon oligomers, Philos. Trans. R. Soc. A 375 (2090) (2017) 20160070.

[68] N. Bontempi, K.E. Chong, H.W. Orton, I. Staude, D.Y. Choi, I. Alessandri, et al., Highly sensitive biosensors based on all-dielectric nanoresonators, Nanoscale 9 (15) (2017) 4972–4980.

[69] O. Yavas, M. Svedendahl, P. Dobosz, V. Sanz, R. Quidant, On-a-chip biosensing based on all-dielectric nanoresonators, Nano Lett. 17 (7) (2017) 4421, PMID: 28616986.

[70] I.C. Khoo, Liquid Crystals, vol. 64, John Wiley & Sons, 2007.

[71] A. Minovich, J. Farnell, D.N. Neshev, I. McKerracher, F. Karouta, J. Tian, et al., Liquid crystal based nonlinear fishnet metamaterials, Appl. Phys. Lett. 100 (12) (2012) 121113.

[72] M. Decker, C. Kremers, A. Minovich, I. Staude, A.E. Miroshnichenko, D. Chigrin, et al., Electro-optical switching by liquid-crystal controlled metasurfaces, Opt. Express 21 (7) (2013) 8879–8885.

[73] M. Parry, A. Komar, B. Hopkins, S. Campione, S. Liu, A.E. Miroshnichenko, et al., Active tuning of high-Q dielectric metasurfaces, Appl. Phys. Lett. 111 (5) (2017) 053102.

[74] S. Campione, S. Liu, L.I. Basilio, L.K. Warne, W.L. Langston, T.S. Luk, et al., Broken symmetry dielectric resonators for high quality factor Fano metasurfaces, ACS Photonics 3 (12) (2016) 2362–2367.

[75] J. Bohn, T. Bucher, K.E. Chong, A. Komar, D.Y. Choi, D.N. Neshev, et al., Active tuning of spontaneous emission by Mie-resonant dielectric metasurfaces, Nano Lett. 18 (6) (2018) 3461–3465.

[76] M. Decker, I. Staude, Resonant dielectric nanostructures: a low-loss platform for functional nanophotonics, J. Opt. 18 (10) (2016) 103001.

[77] Q. Zhang, Y. Zhang, J. Li, R. Soref, T. Gu, J. Hu, Broadband nonvolatile photonic switching based on optical phase change materials: beyond the classical figure-of-merit, Opt. Lett. 43 (1) (2018) 94–97.

[78] C.H. Chu, M.L. Tseng, J. Chen, P.C. Wu, Y.H. Chen, H.C. Wang, et al., Active dielectric metasurface based on phase-change medium, Laser Photonics Rev. 10 (6) (2016) 986–994.

[79] M. Rahmani, L. Xu, A.E. Miroshnichenko, A. Komar, R. Camacho-Morales, H. Chen, et al., Reversible thermal tuning of all-dielectric metasurfaces, Adv. Funct. Mater. (2017 Jul.) 1700580.

[80] G. Cocorullo, I. Rendina, Thermo-optical modulation at 1.5 μm in silicon etalon, Electron. Lett. 28 (1992 January 2) 83–85.

[81] T. Lewi, H.A. Evans, N.A. Butakov, Schuller JA. Ultrawide, Thermo-optic tuning of PbTe meta-atoms, Nano Lett. 17 (6) (2017 Jun.) 3940–3945.

[82] P.P. Iyer, M. Pendharkar, J.A. Schuller, Electrically reconfigurable metasurfaces using heterojunction resonators, Adv. Opt. Mater. 4 (10) (2016 Oct.) 1582–1588.

[83] A. Forouzmand, M. Salary Mohammad, G. Kafaie Shirmanesh, R. Sokhoyan, H.A. Atwater, H. Mosallaei, Tunable all-dielectric metasurface for phase modulation of the reflected and transmitted light via permittivity tuning of indium tin oxide, Nanophotonics 8 (3) (2019).

[84] G. Della Valle, B. Hopkins, L. Ganzer, T. Stoll, M. Rahmani, S. Longhi, et al., Nonlinear anisotropic dielectric metasurfaces for ultrafast nanophotonics, ACS Photonics 4 (9) (2017) 2129–2136.

[85] S. Makarov, S. Kudryashov, I. Mukhin, A. Mozharov, V. Milichko, A. Krasnok, et al., Tuning of magnetic optical response in a dielectric nanoparticle by ultrafast photoexcitation of dense electron–hole plasma, Nano Lett. 15 (9) (2015) 6187–6192.

[86] K. Fan, J. Zhang, X. Liu, G.F. Zhang, R.D. Averitt, W.J. Padilla, Phototunable dielectric Huygens' metasurfaces, Adv. Mater. 30 (22) (2018) 1800278.

[87] P.P. Iyer, N.A. Butakov, J.A. Schuller, Reconfigurable semiconductor phased-array metasurfaces, ACS Photonics 2 (8) (2015) 1077–1084.

[88] A. She, S. Zhang, S. Shian, D.R. Clarke, F. Capasso, Adaptive metalenses with simultaneous electrical control of focal length, astigmatism, and shift, Sci. Adv. 4 (2) (2018) eaap9957.

[89] S.M. Kamali, A. Arbabi, E. Arbabi, Y. Horie, A. Faraon, Decoupling optical function and geometrical form using conformal flexible dielectric metasurfaces, Nat. Commun. 7 (2016).

[90] S.M. Kamali, E. Arbabi, A. Arbabi, Y. Horie, A. Faraon, Highly tunable elastic dielectric metasurface lenses, Laser Photonics Rev. 10 (6) (2016) 1002–1008.

[91] E. Arbabi, A. Arbabi, S.M. Kamali, Y. Horie, M. Faraji-Dana, A. Faraon, MEMS-tunable dielectric metasurface lens, Nat. Commun. 9 (1) (2018) 812.

[92] A. Komar, R. Paniagua-Dominguez, A.E. Miroshnichenko, Y. Yu, Y.S. Kivshar, A.I. Kuznetsov, et al., Dynamic beam switching by liquid crystal tunable dielectric metasurfaces, ACS Photonics 5 (5) (2018) 1742–1748.

[93] S.Q. Li, X. Xu, R.M. Veetil, V. Valuckas, R. Paniagua-Domínguez, A.I. Kuznetsov, Phase-only transmissive spatial light modulator based on tunable dielectric metasurface, Science 364 (6445) (2019) 1087–1090.

Nonlinear and ultrafast effects

8

Maxim Shcherbakov[a,b], Sheng Liu[c], Igal Brener[c,d], Andrey Fedyanin[b]
[a]School of Applied and Engineering Physics, Cornell University, Ithaca, NY, United States, [b]Faculty of Physics, Lomonosov Moscow State University, Moscow, Russia, [c]Sandia National Laboratories, Albuquerque, NM, United Sates, [d]Center for Integrated Nanotechnologies, Sandia National Laboratories, Albuquerque, NM, United States

8.1 Introduction

In 1961, a mere year after the first laser was invented, the world witnessed the birth of nonlinear optics (NLO), when the second harmonic was observed in a nonlinear crystal [1]. Fast forward more than 50 years, and NLO phenomena are abundant and found anywhere from research laboratories to data centers and manufacturing. Examples of commercially available systems that operate via NLO processes are ultrashort-pulse lasers used in surgery and other biomedical applications, multiphoton microscopes, fiber amplifiers and repeaters for optical telecommunications, tunable parametric oscillators and other light sources such as the green laser pointer. Despite the success of NLO, a well-acknowledged limitation of its processes is their inherently low efficiency requiring macroscopic volumes of materials for light-light interaction. This limitation prohibits scalability of NLO to the nanoscale. Finding routes to enhanced optical nonlinearities has been a subject of intense research for the past several decades.

The main approach to enhanced nonlinearities at the nanoscale consists on finding paths to increased light confinement. Nanostructures with surface plasmons, like metal films, nanoantennas, gratings and metamaterials, do an excellent job of localizing light to subwavelength volumes, yielding enhanced generation of optical harmonics [2], all-optical switching [3], and other nonlinearities [4]. Light confinement in plasmonic nanostructures suffers from the drawback of increased optical losses, which hinders conversion efficiencies and thus limits the application scope of these materials for NLO. A different approach to light confinement has recently been developed using all-dielectric nanostructures [5,6], a paradigm in nanophotonics that is the main topic of this book. Nanostructured materials with high refractive indices ($n > 2$) can provide ultrastrong light confinement through Mie resonant modes [7], as well as provide venues for light wavefront and polarization control (and other exciting properties), as explored in other chapters of this book. One of the obvious advantages of using dielectrics as the constituent materials is their resilience to high-power laser radiation; this property serves as one of the main motivations for the work reviewed in this chapter. In this chapter, we survey experimental studies of how strong laser pulses interact with all-dielectric Mie resonators and metasurfaces. The chapter is organized as follows. In Section 8.2, we briefly recall the basics of nonlinear light–matter interaction, providing a classical, phenomenological description of optical nonlinearities reviewed in this chapter. Section 8.3 discusses nonlinear all-dielectric metaatoms and

metasurfaces: methods of fabrication, typical measurement techniques, and results in generation of optical harmonics and other frequency-mixing phenomena, nonlinear refraction and effects under ultrastrong excitation. Section 8.4 showcases ultrafast phenomena in semiconductor-based metasurfaces, including instantaneous and free-carrier-related responses. Section 8.5 concludes the chapter, outlining future research directions within the young and exciting field of nonlinear all-dielectric metamaterials.

8.2 Basics of nonlinear optics

Nonlinear optics describes the interaction of intense laser light with matter, e.g., dielectrics or semiconductors. In this section, we provide just the basic expressions that highlight the rich nature of the NLO effects; we refer the reader to the excellent textbook material should they find themselves interested in further details [8,9].

In linear optics, the polarization $\mathbf{P}^{\mathrm{L}}$ induced by the external electromagnetic field with the electric-field vector $\mathbf{E}$:

$$\mathbf{P}^{\mathrm{L}} = \epsilon_0 \chi^{(1)} \cdot \mathbf{E}, \tag{8.1}$$

where $\chi^{(1)}$ is the linear susceptibility tensor of the material and the dot symbols denotes the inner tensor product. Under strong illumination, a nonlinear electric polarization $\mathbf{P}^{\mathrm{NL}}$ is induced in materials: $\mathbf{P}^{\mathrm{tot}} = \mathbf{P}^{\mathrm{L}} + \mathbf{P}^{\mathrm{NL}}$. This polarization is a nonlinear function of the fundamental beam electric-field strength $\mathbf{E}$, and can be represented as a series:

$$\mathbf{P}^{\mathrm{NL}} = \mathbf{P}^{(2)} + \mathbf{P}^{(3)} + ... \quad . \tag{8.2}$$

This series is a Taylor expansion over the small parameter $\mathbf{P}^{(i)} \approx (E/E_{\mathrm{at}})^i$, where $E_{\mathrm{at}} \approx 5 \cdot 10^{11}$ V/m is the atomic scale of the electric-field strength:

$$\mathbf{P}^{\mathrm{NL}} = \epsilon_0 [\chi^{(2)} : \mathbf{EE} + \chi^{(3)} \vdots \mathbf{EEE} + ...]. \tag{8.3}$$

Here, $\chi^{(i)}$ are the ith-order susceptibilities of the material, which are $(i+1)$st-rank tensors. The leading terms in this series are the second- and the third-order terms:

$$\mathbf{P}^{(2)}(\omega_1) = \epsilon_0 \chi^{(2)}(\omega_1; \omega_2, \omega_3) : \mathbf{E}_{\omega_2} \mathbf{E}_{\omega_3}, \tag{8.4}$$

$$\mathbf{P}^{(3)}(\omega_1) = \epsilon_0 \chi^{(3)}(\omega_1; \omega_2, \omega_3, \omega_4) \vdots \mathbf{E}_{\omega_2} \mathbf{E}_{\omega_3} \mathbf{E}_{\omega_4}. \tag{8.5}$$

Here, ω_i are the frequencies of the pump fields and the polarization induced in the material. Importantly and as seen from these expressions, the nonlinear polarization can mix external fields at different frequencies. The key observation here is that the polarization of materials under strong illumination contains terms oscillating at frequencies that are different from the frequencies of the incident fields $\mathbf{E}_{\omega_i}$. Such frequency conversion is a staple of NLO that is widely used in photonics.

Various NLO phenomena can be observed, depending on the frequencies of the interacting pump and nonlinear response fields. The simplest NLO effect based on the quadratic susceptibility $\chi^{(2)}$ is second-harmonic generation (SHG) that manifests itself as radiation at the doubled pump laser frequency: $\mathbf{P}^{(2)}(2\omega) = \epsilon_0 \chi^{(2)}(2\omega; \omega, \omega) : \mathbf{E}_\omega \mathbf{E}_\omega$. Other $\chi^{(2)}$ effects include optical rectification as a static electric field is induced in the nonlinear media, difference frequency generation, which is now very popular for generation of electromagnetic fields in the mid-infrared and THz frequency ranges, and sum frequency generation. Note that the quadratic susceptibility is a third-rank tensor. Due to symmetry considerations in centrosymmetric media, its components are equal to zero; furthermore, all the NLO effects governed by quadratic susceptibilities are small. Four-wave processes, whereby four electromagnetic waves exchange energy within the nonlinear material through Eq. (8.5), are based on the third-order nonlinear susceptibility, $\chi^{(3)}$. Typically, these processes can be observed in all materials, regardless of the material symmetry. Most notably, the frequency-degenerate case when three photons of the same frequency merge to create a photon of a tripled frequency corresponds to third-harmonic generation (THG): $\mathbf{P}^{(3)}(3\omega) = \epsilon_0 \chi^{(3)}(3\omega; \omega, \omega, \omega) \vdots \mathbf{E}_\omega \mathbf{E}_\omega \mathbf{E}_\omega$. Other nonlinear processes covered in this chapter are four-wave mixing, nonlinear refraction and nonlinear absorption, as well as higher-order frequency-mixing processes that utilize $\chi^{(i)}$, where $i > 3$.

On a final note, it is important to point out the importance of the electromagnetic field strength in the magnitude of $\mathbf{P}^{(i)}$, as locally enhanced electromagnetic fields can significantly boost the efficiencies of the nonlinear processes. Creating resonant response and enhanced localized fields is key to efficient nonlinearities in nanostructures, as shown throughout this chapter.

8.3 Nonlinear optics in Mie-resonant nanostructures

Enhancement of optical nonlinearities by nanostructures dates back to the 1970s when it was realized that the local fields that give rise to the nonlinear polarization in Eq. (8.3) can be enhanced by propagating surface plasmons [10] or localized surface plasmons [11] in noble metal films. In spite of the vast body of research on nonlinear plasmonic nanostructures [4], their applicability has been limited by low efficiencies, high Ohmic losses and low damage thresholds. Semiconductor-based nanostructures for nonlinear optics were introduced later [12,13]. They, in contrast with the main topic of the current Chapter, did not utilize enhancement of nonlinearities by electromagnetic modes but rather by resonant transitions occurring in quantum-confined systems. While the latter provide very strong NLO response through large nonlinear susceptibilities, they suffer from saturation effects and are limited to the mid-infrared spectrum range. Photonic crystals were one of the first patterned materials to have been suggested for strong NLO response via engineered electromagnetic wave propagation [14–17].

An approach for enhanced NLO effects utilizing strongly localized Mie-type resonances of nanoparticles emerged later, when it was realized that subwavelength
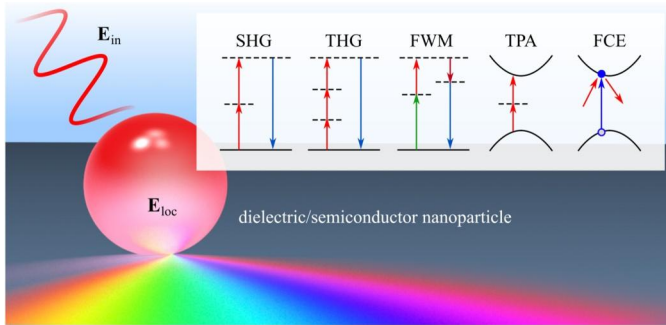
Figure 8.1 Illustration of resonantly enhanced nonlinear-optical processes in all-dielectric/semiconductor nanoparticles. Some of the processes covered in this chapter are second-harmonic generation (SHG), third-harmonic generation (THG), four-wave mixing (FWM), two-photon absorption (TPA), and free-carrier effects (FCE).

particles of high-index materials, e.g., silicon, can resonantly scatter light in the visible and IR [18–20]. For a simple geometry, such as a nanosphere, its localized fields are described by electromagnetic eigenmodes that can be expressed analytically:

$$\mathbf{E}_{\text{loc}} = E_{\text{in}} \sum_{n=1}^{\infty} i^n \frac{2n+1}{n(n+1)} \left(c_n \mathbf{M}_{o1n}^{(1)} - i d_n \mathbf{N}_{e1n}^{(1)} \right), \tag{8.6}$$

where E_{in} is the amplitude of the incident field, $\mathbf{M}_{o1n}^{(1)}$, and $\mathbf{N}_{e1n}^{(1)}$ are vector spherical harmonics (see [21], p. 95 for detailed expressions), and c_n and d_n are coefficients defined by [21], p. 100 (see also Chapter 3 of this book):

$$c_n = \frac{j_n(x)[x h_n^{(1)}(x)]' - h_n^{(1)}(x)[x j_n(x)]'}{j_n(mx)[x h_n^{(1)}(x)]' - h_n^{(1)}(x)[m x j_n(mx)]'}, \tag{8.7}$$

$$d_n = \frac{m j_n(x)[x h_n^{(1)}(x)]' - m h_n^{(1)}(x)[x j_n(x)]'}{m^2 j_n(mx)[x h_n^{(1)}(x)]' - h_n^{(1)}(x)[m x j_n(mx)]'}. \tag{8.8}$$

Here, $j_n(x)$ is the first-kind spherical Bessel function, $h_n^{(1)}(x)$ is the first-kind spherical Hankel function, $x = kr$ is the size parameter, k is the wavevector inside the sphere, r is the radius of the sphere, and m is the relative refractive index of the sphere. The magnetic permeability of the sphere is 1. Note that these are expressions for *internal* fields, as opposed to those used in problems involving scattering from a sphere.

An example of volume integrated local fields of a sphere is given in Fig. 8.2 for a set of refractive indices n_0 from 1.5 to 3.5. For all the spectra, the condition of the particle having a subwavelength dimension (compared to the free-space wavelength), $\lambda > 2r$, is met. Here, the role of the magnetic eigenmodes is apparent: for the wavelengths corresponding to the magnetic dipole mode (near $\lambda/n_0 = 0.85$) and the magnetic quadrupole mode (near $\lambda/n_0 = 0.6$), a considerable overall enhancement of the local electric field is obtained. In contrast, in the wavelength region of
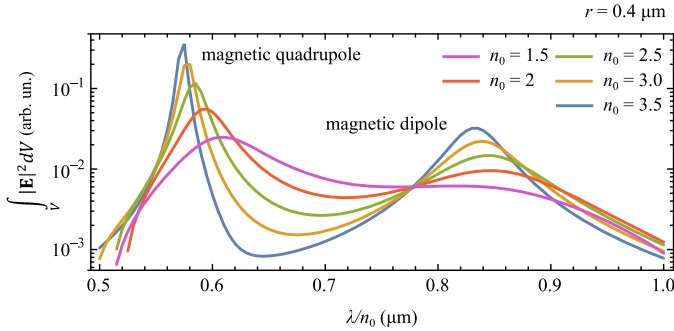
Figure 8.2 Integrated local fields inside a dielectric sphere with a refractive index of n and a radius of $r = 400$ nm, calculated using Eq. (8.6). The spectral region was chosen so that it captures the magnetic dipolar, magnetic quadrupolar resonances (indicated) and the electric-dipolar resonance (not apparent on the plots). For all spectra, the condition $\lambda > 2r$ is met.

the electric-dipole resonance, around $\lambda/n_0 = 0.65 - 0.8$, the enhancement is much less pronounced. These simplistic calculations give a clear indication of the role of the magnetic-type modes in the NLO response of Mie-resonant nanoparticles. The local fields within the nanoparticles $\mathbf{E}_{loc}$ that are supported by Mie-type modes can significantly enhance the nonlinear polarizability given by Eq. (8.3), giving rise to various frequency conversion processes and all-optical modulation schemes, as illustrated in Fig. 8.1.

8.3.1 Fabrication techniques

Here, we briefly outline the main methods to fabricate the nonlinear all-dielectric Mie-resonant nanostructures and metasurfaces. As shown in Fig. 8.3, the fabrication of the dielectric resonators shares common processing steps despite the variety of materials employed for studying NLO phenomena. The fabrication starts from a thin layer of a high refractive index material with a thickness of the order of λ/n_0; the exact thickness is determined by full-wave simulations of the particular design that is being implemented. Thin films of crystalline silicon are widely available as silicon-on-insulator (SOI) wafers with a SiO_2 under layers of a few microns followed by a Si substrate. However, the high refractive index contrast between the SiO_2 and the Si substrate inevitably produces undesired spectral interference [36]. Alternatively, to eliminate the interference, Si thin films can be directly deposited on low refractive index substrates [37,25,38–40]. Utilizing different deposition techniques, such as low pressure chemical vapor deposition or plasma enhanced chemical vapor deposition, either polycrystalline or amorphous Si thin films with desired thicknesses can be achieved. As an alternative, amorphous germanium can be used. Note that different Si crystal structures correspond to various refractive indices, bandgap and nonlinear coefficients. Different from group IV semiconductors, III–V semiconductors (such as GaAs) thin films are typically grown by metal-organic chemical vapor deposition (MOCVD) or molecular beam epitaxy (MBE) on lattice matched III–V substrates.
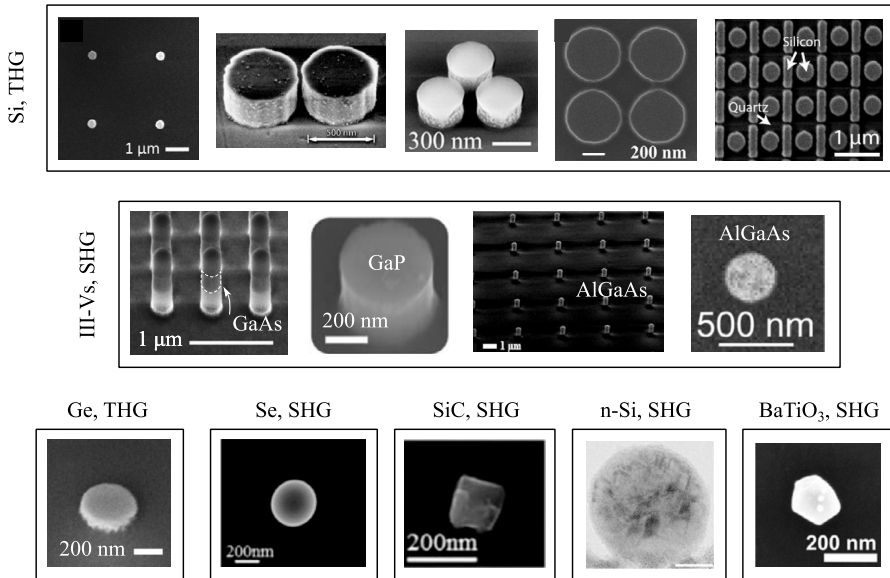
Figure 8.3 Designs of all-dielectric nanostructures for frequency conversion. Top row (Si-based), left to right: individual nanoparticles [22], dimers [23], trimers [24], quadrumers [25] and metasurfaces [26] for third-harmonic generation enhancement. Middle row (III–V-based), left to right: GaAs metasurfaces [27], GaP nanoparticles [28] and AlGaAs nanoparticles [29,30]. Bottom row, left to right (miscellaneous): Ge nanoparticles [31], Se nanoparticles [32], SiC nanoparticles [33], nanocrystalline Si nanoparticles [34], and perovskite nanoparticles [35]. Reprinted with permission from the corresponding sources. Third figure in the middle row reprinted with permission from V.F. Gili, L. Carletti, A. Locatelli, D. Rocco, M. Finazzi, L. Ghirardini, I. Favero, C. Gomez, A. Lemaître, M. Celebrano, C. De Angelis, G. Leo, Monolithic AlGaAs second-harmonic nanoantennas, Opt. Express 24 (2016) 15965, Optical Society of America.

Following the thin film growth, electron-beam lithography is often used to define etch masks. Electron-beam resists are chosen for high etching selectivity between the resists and the resonator materials. For example, negative-tone resist NEB-31A is often used for Si-based dielectric resonators, and HSQ (hydrogen silsesquioxane) can be used for III–V semiconductors. Next, inductively coupled plasma etch is typically used to transfer the shape of etch mask onto the semiconductor thin film for dielectric resonator formation. Variations of the ideal recipe are typically required because the plasma etch determines the resonator sidewall slope angle and roughness. Next, removing the etch mask can be optional depending on the purpose of the experiment and the refractive index of the mask. Finally, if the resonators are placed on top of a high-index substrate, either transferring them to a low-index substrate or oxidizing the high-index materials to their low index oxide is required [41].

8.3.2   Measurement apparatuses

Below, we briefly summarize the main principles of measurements that characterize the NLO response of the nanostructures described in this chapter.
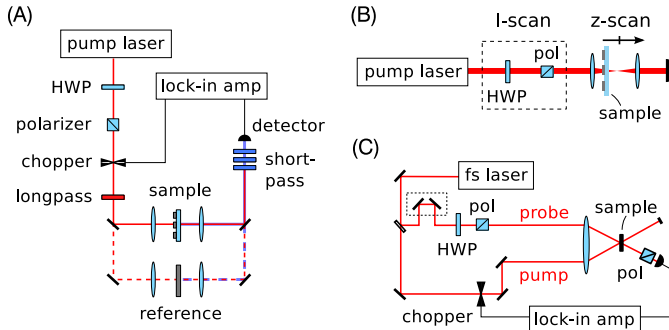
Figure 8.4 Typical experimental setups to study optical nonlinearities of nanostructures. (A) Harmonics generation spectroscopy setup. (B) Z-scan and I-scan setup. (C) Frequency-degenerate pump–probe setup.

8.3.2.1 Harmonic generation

A typical setup for harmonics generation spectroscopy is provided in Fig. 8.4, as adapted from earlier work [42,43]. A pulsed laser source is used as the pump beam. It is desirable to employ a wavelength-tunable pump so as to cover both resonant and non-resonant regimes of harmonics generation. Here, the pump beam is modulated by an optical chopper at a frequency of several kHz and focused by an aspheric lens to a beam waist of about 10 μm in diameter, leading to a maximum peak intensity spanning from $I = 1$ GW/cm^2 to 100 GW/cm^2. The generated harmonic radiation is collected and filtered out from the pump by a set of optical filters. The collimated harmonic radiation is directed to the cathode of a photomultiplier tube assembly or avalanche photodiode, in the case of a weak signal, or to a regular semiconductor photodetector if the signal is strong enough. The output of the detector is analyzed with a lock-in amplifier. Typically, the power dependence of the signal on the pump power is used as an indication that the signal arises from harmonic generation: $I_{n\omega} \propto I_{pump}^n$. If the harmonic generation process is efficient enough, its spectra can be measured directly with a spectrometer. Polarization of the pump beam can be controlled by a polarizer. Analyzing the harmonic radiation with an analyzer placed after the sample can reveal the structure of the nonlinear susceptibility tensor. Transmittance, reflectance and scattered-signal schemes have been successfully used for more detailed studies [44, 45,23,46].

8.3.2.2 Z-scan, I-scan

Techniques of z-scan and intensity scan (I-scan) are routinely used to determine the third-order nonlinear susceptibilities of materials, both their real and the imaginary parts [47]. While studying the real part of $\chi^{(3)}$ requires thick samples and cannot be readily applicable to ultrathin materials like metasurfaces, Im$\chi^{(3)}$ has been reported in a number of references; we will discuss those in Section 8.3.4. A typical setup for z-scan and I-scan measurements is shown in Fig. 8.4B.

8.3.2.3   Pump–probe spectroscopy

When a strong ultrashort laser pulse impinges on a solid-state medium, the state of the material can get strongly modified. If these modifications are reversible and consistent from pulse to pulse, then a technique called pump–probe spectroscopy can be used to study the transient optical properties caused by the pulses. A typical implementation of pump–probe spectroscopy is given in Fig. 8.4C. A train of femtosecond laser pulses is split into two: a stronger pump and a weaker probe. In order to remove unwanted pump scattering towards the detector, the polarization states of the beams are chosen to be orthogonal. The beams are focused onto the sample surface, and the intensity of the probe beam is then measured as a function of the delay between the pump and the probe. Pump–probe measurements are a powerful tool to characterize the strength of how light interacts with light through matter, and the lifetimes of the processes involved.

8.3.3   Harmonics generation and frequency mixing

In this section, we review recent experimental efforts to tailor harmonic generation from all-dielectric nanostructures. The subsections will address frequency conversion processes of different nonlinear orders, their conversion efficiencies and enhancement by Mie-type resonances, polarization properties and the roles of the nonlinear susceptibility tensor structure.

8.3.3.1   Second-harmonic generation

The most common materials for all-dielectric nanophotonics, such as silicon, germanium, titanium dioxide and many others, are centrosymmetric. This property makes detection of second-order nonlinear effects, such as second-harmonic generation (SHG), challenging. It was not until metasurfaces made from noncentrosymmetric materials (such as III–V-semiconductors) were developed [41,30,48] that SHG was observed in all-dielectric Mie-resonant structures. Earlier manifestations of size-dependent SHG from nanostructured semiconductors was observed in arrays of GaP nanowires [49], although the role of the nanowire eigenmodes was not emphasized. The first demonstration of SHG by magnetic Mie-type resonances in GaAs nanoparticles was reported later [44,27] and revealed four orders of magnitude enhancement with respect to an unstructured GaAs substrate and a conversion efficiency of $\eta_{2\omega} \approx 2 \times 10^{-5}$, see Fig. 8.5A. Conversion efficiency is defined as the intensity of the incoming pump beam divided by the intensity of the generated harmonic beam: $\eta_{2\omega} = I_{2\omega}/I_\omega$. This figure was further improved [27,30,50,51,28,52], resulting in $\eta_{2\omega} \approx 10^{-4}$ in AlGaAs nanostructures [53].

The zinc blende crystal structure of most III–V semiconductors defines a particular $\chi^{(2)}$ tensor where $\chi^{(2)}_{ijk} \neq 0$ only for $i \neq j \neq k$. As a consequence, SHG emitted from nanostructures based on III–V semiconductors has certain polarization and scattering properties. For a bulk GaAs wafer with two out of three crystallographic axes lying within the wafer's surface (x and y), no SHG will be observed at normal incidence.
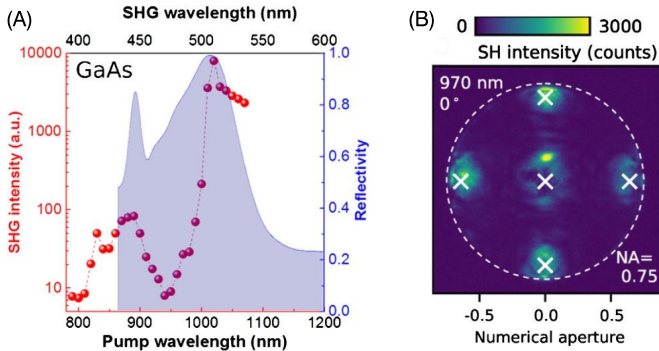
Figure 8.5 Second-harmonic generation in GaAs metasurfaces. (A) Enhancement of the second-harmonic output at the magnetic Mie-type resonance excited by pump pulses at $\lambda \approx 1000$ nm. Reproduced with permission from [27]. (B) Second-harmonic diffraction from a metasurface excited at a dark mode. Diffraction at an angle of close to 0°, which is forbidden in bulk GaAs, is observed. Reproduced with permission from [46].

The only nonlinear polarization will be generated along z: $P_z = 2\chi^{(2)}_{zyx} E_x E_y$, and it will not create a radiating field along z. However, fabricating an array of Mie-resonant nanopartices (nanodisks) out of such a wafer, will allow efficient far-field SHG for two reasons [46]. First, if the period of the array is larger than the SHG wavelength, the diffraction pattern will utilize the P_z polarization, giving rise to detectable diffraction orders. Second, the certain Mie-type resonances will support local fields along the z direction, creating SH polarizability along x or y, thus enabling the previously-forbidden normally-emitting SHG, see Fig. 8.5B. Other implications of the nontrivial III–V tensor structure are the polarization properties of the SHG radiation itself [50], which can be utilized to unambiguously verify that the main contribution to the SHG signal comes from the bulk material rather than being a surface effect. On the practical side, the structure of the tensor allows nonlinear generation of a specific type of optical beams – vector beams – such as azimuthally or radially polarized light [53].

Periodic arrangements of nanoparticles, typically with a subwavelength period, are referred to as metasurfaces. Coupling between resonances of individual nanoparticles yields a more complicated spectral response beyond Mie theory. One of the advantageous consequences of such coupling is the emergence of dark modes of the metasurfaces; these modes do not couple to free-space, unless a defect is introduced that breaks the symmetry of the nanoparticle. The defect can couple dark mode to bright modes (i.e., modes that couple to free-space), causing a Fano-type interference [54] that shows up as a prominent narrow-band dip or peak in the transmittance or reflectance spectra [55,56]. Dark resonances support local fields that are larger by orders of magnitude compared to the fields of the incoming beam. A recent study of a GaAs-based Fano-resonant metasurface showed nontrivial spectral shaping of second-harmonic generation and multifold efficiency enhancement induced by high field localization and enhancement inside the broken-symmetry resonators [52].

The success of III–V-based nanostructures in achieving high SHG conversion efficiencies stems in part, from their high nonlinear susceptibility values, one of the

highest available (and typically non-phase matchable in bulk form). A downside is the relatively small values of the band gap energies, which translates into higher absorption coefficients for the harmonic generation radiation, impairing the conversion efficiency in certain spectral ranges [27]. Other material platforms have been utilized for efficient SHG at shorter wavelengths, with notable examples being perovskites (such as $BaTiO_3$ [57,35,33]), silicon carbide [32], and selenium [58]. Finally, a route to surpass the limitations of centrosymmetric materials is to create a nanocrystalline structure introducing interfaces where the symmetry is broken. For instance, in [34], SHG from a nanocrystalline silicon Mie nanoparticle was enhanced by two orders of magnitude with respect to an unstructured silicon film.

8.3.3.2   Third-harmonic generation

One of the most widespread and well-understood materials, silicon, has historically been the most popular source for all-dielectric nanophotonics structures, due to its abundance in nanotechnology and microelectronics. Being a centrosymmetric material, silicon exhibits little efficiency for second-order NLO effects. However, third-order nonlinearities are routinely measured through third-harmonic generation, two-photon absorption and other effects. Unsurprisingly, the first manifestations of nonlinearities enhanced by magnetic Mie-types resonances were found in silicon nanoparticles [22], where third-harmonic generation was found to be enhanced by two orders of magnitude with respect to a thick silicon wafer (Fig. 8.6A). The conversion efficiency was on the order of $\eta_{3\omega} \approx 10^{-7}$, on par with the best-performance plasmonic nanostructures. Over time, conversion efficiencies from the IR to visible and UV have been successfully optimized by choices of geometry, materials, polarization, spectral range and other parameters [59,22,26,25,60,31,61]. We give an account of THG conversion efficiency reports in Fig. 8.7.

Studies of THG from single nanoparticles can shed light on the role of different Mie resonances in their nonlinear response. As seen in Fig. 8.2, magnetic resonances are more likely to produce efficient THG than electric modes. This was experimentally and numerically verified in ref. [62], where single silicon nanodisks were excited by a tunable femtosecond laser source at either the electric or magnetic dipole resonances. Having a certain spatial distribution, these modes can be selectively excited by structured light beams, as revealed by enhanced THG [63]. Higher-order modes, such as anapole modes [64], have shown to further aid in efficient frequency conversion, as proved in refs. [31,61] (Fig. 8.6B). Here, amorphous germanium was used instead of silicon, as it has a larger refractive index of $n \approx 4$, and higher nonlinear susceptibility in the chosen spectral range. As a result, an enhancement of about 4 orders of magnitude was found with respect to an unstructured film (in addition to another three orders with respect to a silicon wafer) [31].

Optical resonators that are placed close to each other can provide additional degrees of freedom through optical coupling between the Mie modes of the individual resonators. If several nanoparticles are combined so that the distance between them is less or on the order of a wavelength, they are commonly referred to as oligomers [65]. Pairs of nanoparticles, or dimers, were shown to create hot spots of enhanced local fields [66] which were then used to tailor the THG in the far-field [23]. Changing
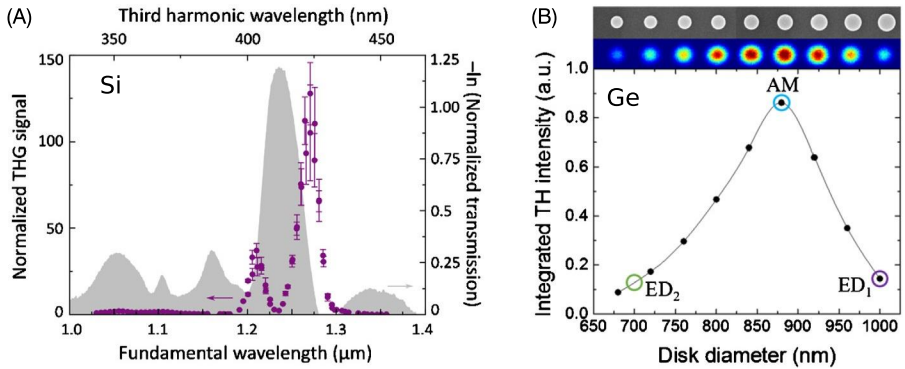
Figure 8.6 Third-harmonic generation from group IV semiconductor Mie-resonant nanostructures. (A) Third-harmonic output from a silicon metasurface normalized by THG intensity from an unstructured silicon wafer. Reproduced with permission from [22]. (B) Size-dependent third-harmonic generation from germanium nanodisks at a fixed wavelength reveals the maximum enhancement at the anapole mode (AM). Reproduced with permission from [31].
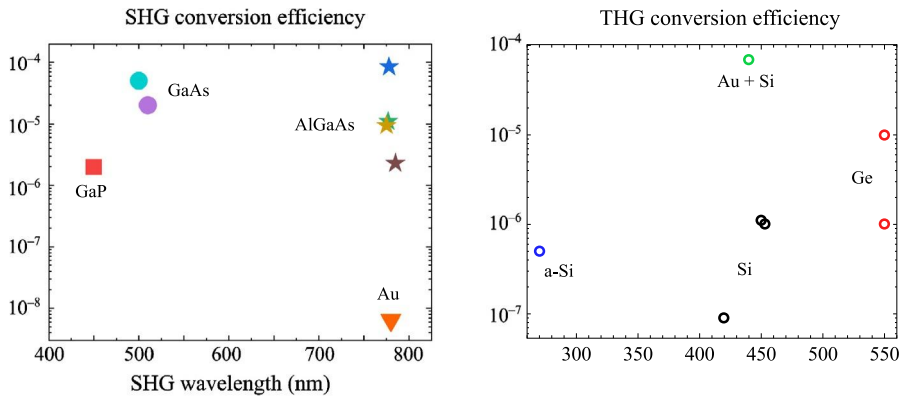
Figure 8.7 Experimentally measured conversion efficiencies of second- and third-harmonic generation processes in Mie-resonant nanostructures based on different materials. Left: GaP [28], GaAs [27,52], AlGaAs [53,30,50,51], and Au [71]. Right: a-Si [59,26,25], c-Si [22], a hybrid approach (Au + Si) [60], Ge [31,61].

the distance between the nanoparticles within oligomers modifies coupling between the individual nanoparticles' modes, which tunes their nonlinear response. In [37], oligomers consisting of three nanoparticles (trimers) excited at their magnetic dipole mode showed prominently different THG spectra for different sets of nanoparticle diameters and inter-particle spacing. Magnetic Fano resonances excited in subwavelength quadrumers provided additional enhancement of THG [25].

Quasi-infinite arrays of nanoparticles that have periods of less than a free-space wavelength – metasurfaces – can be used to further increase the nonlinear response when using high-quality factor (high-Q) collective modes. In [26], a metasurface with a Q-factor of up to 500 was used to enhance the THG by five orders of magnitude with

respect to a silicon film of the same thickness. A similar approach was used in [67] with a different structure that possesses dark modes with a small net dipole moment to enhance THG by a factor of 300 with respect to a bulk silicon substrate. Although high-Q metasurfaces represent a promising route to enhanced optical nonlinearities, both papers expressed concerns regarding wasting most of the bandwidth of the femtosecond pulse that is typically much wider than the bandwidth of the resonance. The time-bandwidth limit is a major obstacle to efficient interactions of femtosecond laser pulses with high-Q cavities, and the full advantage of the field enhancement within a high-Q cavity remains an open question.

Other functionalities of THG from Mie-resonant nanostructures are generation of UV light [59], manipulation of the nonlinear wavefront and directional nonlinear diffraction [68], enhanced nonlinearities by complementary structures [69], and possibilities in probing optical coupling of all-dielectric nanostructures to optical waveguides [70].

8.3.3.3   Other cases of frequency mixing

Second- and third-harmonic generation processes are enabled by the merging of two or three fundamental photons to a higher-energy photon, so that the overall energy is conserved: $\hbar\omega_n = n\hbar\omega$, where n is the process order. For a general frequency-mixing process, a nonlinear susceptibility can mix any number of photons having an arbitrary set of frequencies: $\sum_{i=1}^{N} \hbar\omega_i = \sum_{j=1}^{M} \hbar\omega_j$. First manifestations of four-wave mixing were provided in germanium nanodisks [72], where effective third-order susceptibilities as high as 2.8×10^{-16} m^2/V^2 were found. A more sophisticated technique utilized bi-color pump experiment, where 11 new frequencies were generated in III–V-based semiconductor metasurfaces [51]. It is important to note that the simultaneous mixing of such a vast amount of frequencies at comparable efficiencies is hard to observe in bulk materials, as the phase-matching conditions usually benefit one or few frequency conversion pathways while sacrificing the efficiency for others.

8.3.4   Self-action effects

In nonlinear materials, light beams can modify themselves without causing considerable conversion from one frequency to another. These effects, often referred to as self-action effects, give rise to a series of applications like power limiting, passive mode-locking, filament formation, solitons and others. Phenomenologically, these effects can be expressed by an intensity-dependent complex refractive index:

$$\tilde{n}(I) = \tilde{n}_0 + \tilde{n}_2 I, \tag{8.9}$$

where $\tilde{n}_0 = n_0 + i\kappa_0$ is the unperturbed complex refractive index, and $\tilde{n}_2 I = (n_2 + i\kappa_2)I$ is the part of the refractive index that is proportional to intensity. Since the refractive index depends on I, Mie resonances, which lead to field localization and enhancement, can substantially boost self-action in materials.

Self-action effects can be classified by the dominating term in $\tilde{n}_2 = n_2 + i\kappa_2$, either real or imaginary, and by its sign. Additionally, these effects can be categorized by the

physical nature behind $\tilde{n}_2$. Here, we will classify those effects that have been studied in Mie-resonant nanostructures.

8.3.4.1 Nonlinear absorption

If $n_2 = 0$ and $\kappa_2 > 0$, the effect is referred to as nonlinear absorption. More traditionally, it is expressed in terms of a nonlinear absorption coefficient $\alpha = \alpha_0 + \beta I$, which is interrelated with $\kappa = \alpha\lambda/4\pi$. The most common cause of nonzero nonlinear absorption is the two-photon absorption (TPA) process, which routinely occurs when a powerful IR laser pulse propagates through a semiconductor with the bandgap energy lying in the range of $2\hbar\omega > E_g > \hbar\omega$, where $\hbar\omega$ is the photon energy. Therefore, the simultaneous absorption of two photons can generate an electron–hole pair. Two-photon absorption has been extensively studied in all the commonly used semiconductors leading to applications in optical power limiters, mode-locking, etc.

In all-dielectric nanoantennas and metasurfaces, local fields can boost the nonlinear absorption cross-section, lowering the intensity requirements for optical limiting. For instance, a typical value for the TPA coefficient in silicon is on the order of $\beta = 1$ cm/GW [73]; for hydrogenated amorphous silicon it strongly depends on the lattice structure and hydrogen content, and was found to be on the order of $\beta = 10 - 100$ cm/GW [74]. Metasurfaces fabricated out of a thin amorphous silicon film enhance TPA by a factor of 80 with respect to an unpatterned film, resulting in a value of $\beta = 5600$ cm/GW [37]. Subsequent generation of free carriers can induce significant changes in the linear response of the nanoparticles, such as reflectance or scattering directionality [75].

8.3.4.2 Nonlinear refraction

When $n_2 \neq 0$ and $\kappa_2 = 0$, the situation is referred to as nonlinear refraction. There are numerous microscopic mechanisms that lead to an intensity-dependent refractive index; these can be separated into two major categories: parametric and non-parametric. The former, the optical Kerr effect, is defined by an instantaneous value of the electric field in the material and relies on the nonlinear coherent response of electrons in the material; this effect is usually fairly weak: $n_2 \approx 10^{-16} - 10^{-13}$ cm^2/W in common dielectrics and semiconductors. In most cases, this contribution to n is present only when light is within the material, as electron decoherence times are on the femtosecond scale, which is shorter than the vast majority of the pulsed light sources. Since the Kerr effect magnitude is weak, parametric nonlinear refraction in nanostructures has been usually considered elusive; however, novel materials such chalcogenide glasses look promising in this context [76].

In contrast, the non-parametric additions to n are not connected to the nonlinearity of the electron response, and are not due to the presence of light *per se* but rather due to the changes in the material parameters such as temperature or the concentration of free charge carriers. Light can heat materials causing thermally induced changes in $n = n_0 + T dn/dT = n_0 + I(dT/dI)(dn/dT)$. The large values of refractive index modulation come at the expense of speed: recovery takes microseconds or even seconds (although faster relaxation times can occur at the nanoscale).

A much faster process of index modulation is photogeneration of free carriers, created through either single- or multi-photon absorption processes in semiconductors. Here, $n = n_0 + \Delta n_{FC}$, where Δn_{FC} is the refractive index addition, usually negative, caused by the photogenerated electron–hole pairs. We will discuss this type of nonlinearity further in section 8.4.2.

8.3.5 High-order effects

Eq. (8.3) is a Taylor series with E/E_{at} as the expansion parameter, where E is the incident field strength and $E_{at} \approx 5 \cdot 10^{11}$ V/m. Under the condition of $E \ll E_{at}$, nonlinear polarization is much smaller than the linear one and the regime is called perturbative. The closer the E is to E_{at}, the more inaccurately the series describes the real polarization of materials, as the high-order terms become comparable to each other. In GaAs, for instance, one can estimate the critical intensity at which $P^{(2)} \approx P^{(3)}$, or, conversely, $E_{crit} \approx \chi^{(2)}/\chi^{(3)} \approx 10^9$ V/m, which corresponds to intensities of approximately 1 TW/cm^2. This so-called non-perturbative regime has become accessible through both the advent of femtosecond laser sources, which can easily reach such intensities, and resonant nanostructures [77], which can funnel light to hot spots of much higher field intensity than the incident light.

The most straightforward manifestation of non-perturbative nonlinearities is the process of high-harmonic generation (HHG). In solids, photogenerated free electrons move in highly non-parabolic potentials due to large spatial displacements, generating optical harmonics in the extreme UV [78]. The intensity requirements for this process are high, and one of the approaches to significantly reducing them is to use localized resonances. Semiconductor metasurfaces with Mie-type resonances have been successfully used to observe even harmonics up to the fourth in noncentrosymmetric materials [51] and odd harmonics up to the 11th in silicon-based metasurfaces [79]. The ninth harmonic from the metasurface can be detected at intensities as low as 50 GW/cm^2 with the signal two orders of magnitude above the noise level, whereas any detectable ninth harmonic from an unpatterned film of the same thickness shows up only at 200 GW/cm^2 [79].

One of the most straightforward results of Eq. (8.3) is that, if pumped by a narrowband laser centered at frequency ω, the resulting harmonics will have spectra centered at $n\omega$, where n is the order of the nonlinear process. On the other hand, this rule may fail in dynamically evolving systems, such as rapidly generated plasmas in gases and semiconductors [80]. In these systems, generation of free carriers leads to blue shifting of the emitted fundamental and harmonic generation, a process sometimes dubbed "photon acceleration" [81]. However, typical intensities of 10^{15} W/cm^2 are needed to observe considerable blue-shifts of the emitted photons. At much lower intensities of up to 30 GW/cm^2, photon acceleration has been recently revealed in semiconductor metasurfaces by observing the spectrum of the THG radiation blue-shift as the pump intensity is increased [82]. In this experiment, the generated photons had a variable carrier frequency from 3ω to 3.1ω, tuned by the intensity of the mid-infrared pump, thus expanding the scope of frequency conversion beyond integer harmonics.
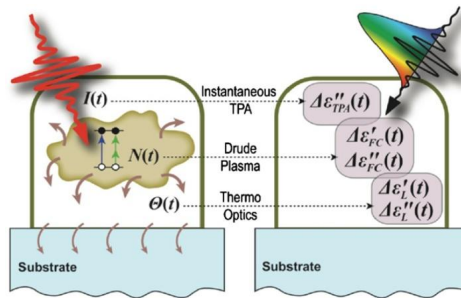
Figure 8.8 Ultrafast processes in semiconductor nanostructures. Reproduced with permission after [38].

8.4 Ultrafast phenomena in Mie-resonant nanostructures

By convention, ultrafast phenomena are those with relaxation time of approximately 1 ps and shorter [83], allowing characteristic modulation frequencies of more than 1 THz. Since few electric-current-based devices can provide bandwidths above several hundreds of GHz, many people consider the all-optical approach to be a major candidate for ultrafast signal processing.

Ultrafast processes in materials are routinely investigated using pump–probe spectroscopy, or time-resolved spectroscopy. A powerful ultrashort laser pulse ("pump") causes modifications to the materials under study that are then probed by a weaker pulse ("probe") in the form of transmittance, reflectance, scattering, polarization or frequency conversion. The response of the probe is monitored as a function of the time delay between the pulses, reconstructing the relaxation process of the material. The probe and the pump can have different polarizations, frequencies, and temporal profiles, so as to reveal different aspects of the underlying processes (Fig. 8.8).

Semiconductors are the most popular materials for all-dielectric Mie-resonant nanostructures. The most common semiconductors – silicon, germanium, gallium arsenide and others – have been extensively studied using pump–probe spectroscopy. A simplified timeline of the microscopic processes following a femtosecond pulse impinging on a surface of a bulk semiconductor is as follows [84]:

- $\tau < 200$ fs: Free carriers (FCs) are generated through single- or multi-photon absorption. At this point in time, the electromagnetic field is typically still within the material, thus opened to coherent frequency-mixing processes. FCs lose coherence via carrier-carrier scattering events. The energy distribution is non-Boltzmann, i.e., the electron gas has not yet thermalized.
- $\tau < 2$ ps: Electrons and holes have thermalized to Boltzmann-type energy distributions. The electron-lattice energy exchange is under way through electron–phonon scattering. Light is no longer present in the material.
- $\tau < 100$ ps: Electrons and holes have lost their energy to phonons and recombined. Lattice is sinking its excess energy to the environment. The end time of this process is highly dependent on many parameters, including substrate material.

In every step of this process, the transient value of the complex dielectric permittivity of the material $\tilde{\varepsilon}(t)$ differs from its equilibrium value $\tilde{\varepsilon}_0$: $\tilde{\varepsilon}(t) = \tilde{\varepsilon}_0 + \Delta\tilde{\varepsilon}(t)$. There are three main contributions to $\Delta\tilde{\varepsilon}$: the instantaneous one (as discussed in Section 8.3.4.2), the one induced by the presence of the free carriers $\Delta\tilde{\varepsilon}_{FC}$ and the one induced by lattice heating, or the presence of phonons $\Delta\tilde{\varepsilon}_L$. The free-carrier contribution is the one that is often utilized in all-optical switches [85]. However, in bulk semiconductors, recombination of free carriers is a slow process that does not allow for ultrafast relaxation times.

Fortunately, in nanostructures and under high intensity laser illumination, the recombination processes can happen much faster, enabling novel devices that could operate at ultrafast modulation frequencies. The general (simplified) recombination rate equation for FC density $N(t)$ is [86]:

$$\frac{dN}{dt} = -AN - BN^2 - CN^3, \tag{8.10}$$

where A, B, and C are the monomolecular, bimolecular and Auger recombination rates. These coefficients are specific to a given semiconductor. For a typical example, in bulk GaAs, $A < 5 \times 10^7$ s^{-1}, $B = (1.7 \pm 0.2) \times 10^{-10}$ cm^3/s, and $C = (7 \pm 14) \times 10^{30}$ cm^6/s [86]. At low pump intensities, Eq. (8.10) leads to N being less than 10^{18} cm^{-3}; the first term in Eq. (8.10) dominates over the second and the third ones, giving a relaxation time of 200 ns. This figure can be improved by either increasing the pump intensity leading to a higher FC density, or decreasing the value of A. The latter can be achieved by introducing impurities (a good example being low-temperature-grown GaAs) or by increasing the surface area by nanostructuring [87]. Both approaches have been utilized in semiconductor metasurfaces, as shown below.

8.4.1   *Instantaneous all-optical modulation*

The only instantaneous mechanisms of all-optical modulation implemented so far in semiconductor metasurfaces are two-photon absorption (TPA) and frequency mixing. TPA manifests itself as a sharp dip at near-zero delay on time-resolved transmittance or reflectance traces [37,26,38], with a duration of the dip limited to the duration of the optical pulses used in the experiment. For typical TPA dips in pump–probe traces for metasurfaces, see Fig. 8.9C. Frequency mixing, as discussed in previous sections, can be cross-modulated by two separate beams, allowing all-optical modulation of the resulting signal [51]; see Fig. 8.9D. Instantaneous phenomena, in sharp contrast with the free-carrier-related contributions, allow for potential switching rates at frequencies of more than 10 THz, paving the way to ultrafast logic gates using photonics.

8.4.2   *Free-carrier effects*

Optical response of a semiconductor that contains free carriers, such as electrons and/or holes, is frequently dominated by the Drude dispersion of the dielectric per-

mittivity:

$$\varepsilon(\omega) = \varepsilon_{\infty} - \frac{\omega_p^2}{\omega^2 + i\gamma\omega}, \tag{8.11}$$

where $\omega_p = \sqrt{Ne^2/\varepsilon_0 m^*}$ is the plasma frequency, N is the free-carrier concentration, e is the elementary charge, m^* is the effective free-carrier mass, and γ is the damping constant. This approximation holds for most experimental cases, especially when the probe beam's photon energy is below the band gap, and if the free-carrier concentration is sufficiently low. Free carriers have experimentally changed the refractive index by up to $\Delta n/n \approx -0.04$ in metasurfaces [88], which, with an appropriate Q-factor of the resonance, can shift its central frequency by about its full width at half maximum (causing considerable changes in reflectance of up to 0.35). The presence of free carriers in Mie-resonant semiconductor nanoparticles not only changes the back- or forward-scattering of light but tailors the scattering pattern in general, as shown by several theoretical efforts [89–91].

The rate of relaxation to the initial state strongly depends on the material used as the constituent material for a metasurface. Crystalline materials with an indirect band gap, such as silicon, are poor candidates for ultrafast metasurfaces, as relaxation times in these materials can be as long as hundreds of picoseconds [92]. This can be mitigated by introducing higher-order terms of the rate Eq. (8.10) through hard pumping of the metasurfaces. In Ref. [90], silicon nanoparticles were pumped at high fluences of around 40 mJ/cm^2 so as to achieve large estimated FC density of about 5×10^{20} cm^{-3}. This led to dominance of the Auger recombination process, making it as fast as 2.5 ps; see Fig. 8.9A for a typical pump–probe trace.

Another approach to shortening the lifetime of FCs in a semiconductor is to increase the probability of monomolecular recombination through inhomogeneities of the crystal structure or non-radiative centers. Fortunately, metasurfaces naturally possess an increased relative surface area due to nanostructuring, which increases the likelihood of surface recombination. This effect was shown to dominate the relaxation in GaAs-based metasurfaces, leading to relaxation of the magnetic dipolar Mie-mode back to its initial state in only 6 ps and $1/e$ relaxation time of 2.5 ps [88]; see Fig. 8.9B.

In general and beyond the Drude approximation, the refractive index change relies on three main components [93]: the Drude term, the band filling effect and the band shrinkage effect. The resulting index modulation is given by

$$\Delta n = \Delta n_{\mathrm{D}} + \Delta n_{\mathrm{BF}} + \Delta n_{\mathrm{BS}}. \tag{8.12}$$

The extra terms may become important in some experimental cases [88]. As an example, the band filling effect on the refractive index is defined by the decline of the interband transitions due to occupation of the electron and hole states in the conduction and valence bands, respectively. In the parabolic band approximation, the interband absorption is given by the following expression:
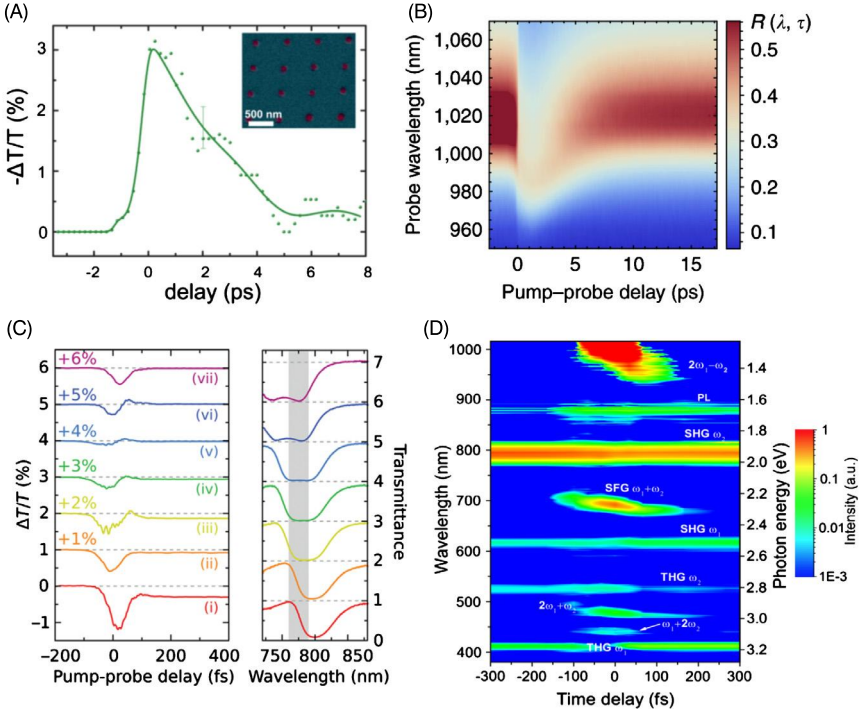
Figure 8.9 Routes to ultrafast all-optical modulation in semiconductor metasurfaces. (A) At high FC concentrations, bimolecular and Auger terms lead to faster recombination, enabling relaxation times of 2.5 ps in a-Si. Reprinted with permission from [90]. (B) Surface recombination in direct-gap semiconductors (GaAs) can provide rapid all-optical tuning of the resonance and relaxation times of 2.5 ps. Reprinted with permission from [88]. (C) Overcoming FC contributions by judicious choice of the pump wavelength versus the resonance wavelength for coherent all-optical modulation. Reprinted with permission from [37]. (D) Utilizing parametric frequency-mixing processes facilitates ultrafast, subpicosecond all-optical response. Reprinted with permission from [51].

$$
\alpha(E) = \begin{cases} 0, & \text{if } E \le E_\mathrm{g}, \\ \frac{C_\mathrm{hh}}{E}\sqrt{E - E_\mathrm{g}} + \frac{C_\mathrm{lh}}{E}\sqrt{E - E_\mathrm{g}}, & \text{if } E > E_\mathrm{g}. \end{cases} \tag{8.13}
$$

For instance, in GaAs, $C_\mathrm{hh} = 3.1 \cdot 10^6 \ \mathrm{cm}^{-1}\mathrm{eV}^{1/2}$ and $C_\mathrm{lh} = 1.6 \cdot 10^6 \ \mathrm{cm}^{-1}\mathrm{eV}^{1/2}$, and $E_\mathrm{g} = 1.42$ eV is the band gap width of GaAs at room temperature. Absorption of GaAs saturates as the bands get filled, as given by

$$
\Delta\alpha = \frac{C_\mathrm{hh}}{E}\sqrt{E - E_\mathrm{g}}[f_\mathrm{v}(E_\mathrm{ah}) - f_\mathrm{c}(E_\mathrm{bh}) - 1]
$$
$$
+ \frac{C_\mathrm{lh}}{E}\sqrt{E - E_\mathrm{g}}[f_\mathrm{v}(E_\mathrm{al}) - f_\mathrm{c}(E_\mathrm{bl}) - 1], \tag{8.14}
$$

where $f_\mathrm{c}(E_\mathrm{bh,bl})$ and $f_\mathrm{v}(E_\mathrm{ah,al})$ are the Fermi–Dirac distributions in for electrons and holes, respectively. The band shrinkage effect is phenomenologically introduced as E_g being directly dependent on the carrier concentration: $\Delta E_\mathrm{g} \propto -N^{1/3}$, which in

turn, affects Eq. (8.13). The refractive index addition by both band filling and band shrinkage are then calculated through Kramers–Kronig relations from Eq. (8.13). The full derivation of these contributions in some of III–Vs is given in [93]. In metasurfaces operating at photon energies close to the band gap of GaAs, ≈ 1.24 eV, the band filling contribution was shown to be equally important in all-optical tuning of the Mie-resonance as the Drude term [88].

8.5 Conclusions and outlook

Although nonlinear and ultrafast properties of Mie-resonant nanostructures have been extensively studied for more than 5 years, it is still a developing field with many unknowns. Below, we attempt to outline a roadmap of this exciting area of nanophotonics.

8.5.1 Beyond the visible and near-IR

Studies of nonlinear all-dielectric metamaterials have been traditionally limited to the near-IR and visible spectral regions. On the other hand, many applications, such as molecular fingerprinting, night vision, and others, require efficient nonlinear materials in other spectral ranges. Mid-infrared radiation, or radiation with wavelengths of $\lambda = 3-12$ μm, is an important spectral range, for it carries information about chemical composition of materials and contains most of the thermal radiation emitted at room temperature and higher. Relevant to nonlinear materials, the following features of the mid-IR are of particular interest:

- The most common semiconductor materials, such as Si, GaAs, Ge and many others, are transparent in the mid-IR, granted by the low energies of optical phonons in these materials.
- Nonlinear absorption is lower than that seen in the near-IR, since it requires more photons to induce an interband transition of an electron to the conduction band.
- Generation of free carriers has a larger effect on the dielectric permittivity of semiconductors. The Drude term, which dominates the permittivity of semiconductors in the mid-IR, scales as $\propto \lambda^2$, lowering the power requirements to all-optical switching.
- Optical properties of semiconductors, such as their band gap and resonant polarizabilities, can be manipulated by growth of heterostructures with inter-subband transitions, which has already been implemented for plasmonic nanostructures [94,95].

For these and other reasons, the mid-IR spectral range has been hailed as one of the possible directions for integrated photonics [96,97]. We predict an elevated interest of the community to this region in the coming years. For similar reasons, the THz band has also been attractive for ultrafast and nonlinear response of semiconductor-based metamaterials.

8.5.2 Emerging materials

The current roster of materials for nonlinear Mie-resonant nanoparticles and metasurfaces has mainly contained silicon, germanium, and $Al_xGa_{1-x}As$, with few exceptions. On the other hand, a variety of high-index materials for Mie-resonant photonics has been used to date, many of which are promising nonlinear materials too. We expect more exciting results in the nearest future from the following platforms: traditional nonlinear crystals such as $LiNbO_3$ [23], large bandgap materials such as GaN, GaP and others [28], diamond [98], and nanostructures with tailored intersubband transitions [94,95], as well as various phase-change materials. From the ultrafast perspective, of interest are materials with defects – such as low-temperature-grown GaAs and amorphous Ge – and materials with low effective FC masses, such as narrow-gap semiconductors like InSb, engineered superlattices [99], as well as graphene and other 2D materials.

8.5.3 Exotic nonlinearities

The richness of NLO lies beyond generation of harmonics, nonlinear absorption and all-optical modulation. Many rarer, yet no less intriguing NLO effects are yet to be observed in Mie-resonant systems. These effects include, to name a few: electric-field-induced second-harmonic generation in centrosymmetric materials, tunneling ionization and ponderomotive effects, Franz–Keldysh effect, ultrafast magnetism [100], optical rectification and generation of THz radiation, as well as effects emerging through time-varying refractive index. With the expansion of material platforms and spectral range, we envision exciting opportunities in nonlinear all-dielectric and semiconductor metamaterials.

References

[1] P.A. Franken, A.E. Hill, C.W. Peters, G. Weinreich, Generation of optical harmonics, Phys. Rev. Lett. 7 (1961) 118.

[2] M.W. Klein, C. Enkrich, M. Wegener, S. Linden, Second-harmonic generation from magnetic metamaterials, Science 313 (2006) 502.

[3] M. Ren, B. Jia, J.Y. Ou, E. Plum, J. Zhang, K.F. MacDonald, A.E. Nikolaenko, J. Xu, M. Gu, N.I. Zheludev, Nanostructured plasmonic medium for terahertz bandwidth all-optical switching, Adv. Mater. 23 (2011) 5540.

[4] M. Kauranen, A.V. Zayats, Nonlinear plasmonics, Nat. Photonics 6 (2012) 737.

[5] S. Jahani, Z. Jacob, All-dielectric metamaterials, Nat. Nanotechnol. 11 (2016) 23.

[6] A.I. Kuznetsov, A.E. Miroshnichenko, M.L. Brongersma, Y.S. Kivshar, B. Lukyanchuk, Optically resonant dielectric nanostructures, Science 354 (2016) aag2472.

[7] P. Kapitanova, V. Ternovski, A. Miroshnichenko, N. Pavlov, P. Belov, Y. Kivshar, M. Tribelsky, Giant field enhancement in high-index dielectric subwavelength particles, Sci. Rep. 7 (2017) 731.

[8] R.W. Boyd, Nonlinear Optics, 3rd ed., Academic Press, 2008.

[9] Y.R. Shen, The Principles of Nonlinear Optics, Wiley–Interscience, New York, 1984.

[10] H.J. Simon, D.E. Mitchell, J.G. Watson, Optical second-harmonic generation with surface plasmons in silver films, Phys. Rev. Lett. 33 (1974) 1531.

[11] C.K. Chen, A.R.B. De Castro, Y.R. Shen, Surface-enhanced second-harmonic generation, Phys. Rev. Lett. 46 (1981) 145.

[12] L. Tsang, D. Ahn, S.L. Chuang, Electric field control of optical second-harmonic generation in a quantum well, Appl. Phys. Lett. 52 (1988) 697.

[13] P. Boucaud, F.H. Julien, D.D. Yang, J. Lourtioz, E. Rosencher, P. Bois, J. Nagle, Detailed analysis of second-harmonic generation near 10.6 μm in GaAs/AlGaAs asymmetric quantum wells, Appl. Phys. Lett. 57 (1990) 215.

[14] V. Berger, Nonlinear photonic crystals, Phys. Rev. Lett. 81 (1998) 4136.

[15] M. Soljac, J.D. Joannopoulos, Enhancement of nonlinear effects using photonic crystals, Nat. Mater. 3 (2004) 211.

[16] B. Corcoran, C. Monat, C. Grillet, D.J. Moss, B.J. Eggleton, T.P. White, L. O'Faolain, T.F. Krauss, Green light emission in silicon through slow-light enhanced third-harmonic generation in photonic-crystal waveguides, Nat. Photonics 3 (2009) 206.

[17] J. Leuthold, C. Koos, W. Freude, Nonlinear silicon photonics, Nat. Photonics 4 (2010) 535.

[18] A.I. Kuznetsov, A.E. Miroshnichenko, Y.H. Fu, J. Zhang, B. Luk'yanchuk, Magnetic light, Sci. Rep. 2 (2012) 492.

[19] A.B. Evlyukhin, S.M. Novikov, U. Zywietz, R.L. Eriksen, C. Reinhardt, S.I. Bozhevolnyi, B.N. Chichkov, Demonstration of magnetic dipole resonances of dielectric nanospheres in the visible region, Nano Lett. 12 (2012) 3749.

[20] J.C. Ginn, I. Brener, D.W. Peters, J.R. Wendt, J.O. Stevens, P.F. Hines, L.I. Basilio, L.K. Warne, J.F. Ihlefeld, P.G. Clem, M.B. Sinclair, Realizing optical magnetism from dielectric metamaterials, Phys. Rev. Lett. 108 (2012) 097402.

[21] C.F. Bohren, D.R. Huffman, Absorption and Scattering of Light by Small Particles, Wiley, New York, 2004.

[22] M.R. Shcherbakov, D.N. Neshev, B. Hopkins, A.S. Shorokhov, I. Staude, E.V. Melik-gaykazyan, M. Decker, A.A. Ezhov, A.E. Miroshnichenko, I. Brener, A.A. Fedyanin, Y.S. Kivshar, Enhanced third-harmonic generation in silicon nanoparticles driven by magnetic response, Nano Lett. 14 (2014) 6488.

[23] L. Wang, S. Kruk, L. Xu, M. Rahmani, D. Smirnova, A. Solntsev, I. Kravchenko, D. Neshev, Y. Kivshar, Shaping the third-harmonic radiation from silicon nanodimers, Nanoscale 9 (2017) 2201.

[24] M.R. Shcherbakov, A.S. Shorokhov, D.N. Neshev, B. Hopkins, I. Staude, E.V. Melik-Gaykazyan, A.A. Ezhov, A.E. Miroshnichenko, I. Brener, A.A. Fedyanin, Y.S. Kivshar, Nonlinear interference and tailorable third-harmonic generation from dielectric oligomers, ACS Photonics 2 (2015) 578.

[25] A.S. Shorokhov, E.V. Melik-Gaykazyan, D.A. Smirnova, B. Hopkins, K.E. Chong, D.Y. Choi, M.R. Shcherbakov, A.E. Miroshnichenko, D.N. Neshev, A.A. Fedyanin, Y.S. Kivshar, Multifold enhancement of third-harmonic generation in dielectric nanoparticles driven by magnetic Fano resonances, Nano Lett. 16 (2016) 4857.

[26] Y. Yang, W. Wang, A. Boulesbaa, I.I. Kravchenko, D.P. Briggs, A. Puretzky, D. Geohegan, J. Valentine, Nonlinear Fano-resonant dielectric metasurfaces, Nano Lett. 15 (2015) 7388.

[27] S. Liu, M.B. Sinclair, S. Saravi, G.A. Keeler, Y. Yang, J. Reno, G.M. Peake, F. Setzpfandt, I. Staude, T. Pertsch, I. Brener, Resonantly enhanced second-harmonic generation using III–V semiconductor all-dielectric metasurfaces, Nano Lett. 16 (2016) 5426.

[28] J. Cambiasso, G. Grinblat, Y. Li, A. Rakovich, E. Cortés, S.A. Maier, Bridging the gap between dielectric nanophotonics and the visible regime with effectively lossless gallium phosphide antennas, Nano Lett. 17 (2017) 1219.

[29] L. Carletti, A. Locatelli, O. Stepanenko, G. Leo, C. De Angelis, Enhanced second-harmonic generation from magnetic resonance in AlGaAs nanoantennas, Opt. Express 23 (2015) 26544.

[30] V.F. Gili, L. Carletti, A. Locatelli, D. Rocco, M. Finazzi, L. Ghirardini, I. Favero, C. Gomez, A. Lemaître, M. Celebrano, C. De Angelis, G. Leo, Monolithic AlGaAs second-harmonic nanoantennas, Opt. Express 24 (2016) 15965.

[31] G. Grinblat, Y. Li, M.P. Nielsen, R.F. Oulton, S.A. Maier, Enhanced third harmonic generation in single germanium nanodisks excited at the anapole mode, Nano Lett. 16 (2016) 4635.

[32] C.R. Ma, J.H. Yan, Y.M. Wei, G.W. Yang, Second harmonic generation from an individual amorphous selenium nanosphere, Nanotechnology 27 (2016) 425206.

[33] C. Ma, J. Yan, Y. Wei, P. Liu, G. Yang, Enhanced second harmonic generation in individual barium titanate nanoparticles driven by Mie resonances, J. Mater. Chem. C 5 (2017) 4810.

[34] S.V. Makarov, M.I. Petrov, U. Zywietz, V. Milichko, D. Zuev, N. Lopanitsyna, A. Kuksin, I. Mukhin, G. Zograf, E. Ubyivovk, D.A. Smirnova, S. Starikov, B.N. Chichkov, Y.S. Kivshar, Efficient second-harmonic generation in nanocrystalline silicon nanoparticles, Nano Lett. 17 (2017) 3047.

[35] F. Timpu, A. Sergeyev, N.R. Hendricks, R. Grange, Second-harmonic enhancement with Mie resonances in perovskite nanoparticles, ACS Photonics 4 (2017) 76.

[36] I. Staude, A.E. Miroshnichenko, M. Decker, N.T. Fofang, S. Liu, E. Gonzales, J. Dominguez, T.S. Luk, D.N. Neshev, I. Brener, Y. Kivshar, Tailoring directional scattering through magnetic and electric resonances in subwavelength silicon nanodisks, ACS Nano 7 (2013) 7824.

[37] M.R. Shcherbakov, P.P. Vabishchevich, A.S. Shorokhov, K.E. Chong, D.Y. Choi, I. Staude, A.E. Miroshnichenko, D.N. Neshev, A.A. Fedyanin, Y.S. Kivshar, Ultrafast all-optical switching with magnetic resonances in nonlinear dielectric nanostructures, Nano Lett. 15 (2015) 6985.

[38] G. Della Valle, B. Hopkins, L. Ganzer, T. Stoll, M. Rahmani, S. Longhi, Y.S. Kivshar, C. De Angelis, D.N. Neshev, G. Cerullo, Nonlinear anisotropic dielectric metasurfaces for ultrafast nanophotonics, ACS Photonics 4 (2017) 2129.

[39] L. Xu, M. Rahmani, K. Zangeneh Kamali, A. Lamprianidis, L. Ghirardini, J. Sautter, R. Camacho-Morales, H. Chen, M. Parry, I. Staude, G. Zhang, D. Neshev, A.E. Miroshnichenko, Boosting third-harmonic generation by a mirror-enhanced anapole resonator, Light: Sci. Appl. 7 (2018).

[40] G. Grinblat, R. Berte, M.P.P. Nielsen, Y. Li, R.F. Oulton, S.A. Maier, Sub-20 fs all-optical switching in a single Au-Clad Si nanodisk, Nano Lett. 18 (2018) 7896.

[41] S. Liu, G.A. Keeler, J.L. Reno, M.B. Sinclair, I. Brener, III–V semiconductor nanoresonators – a new strategy for passive, active, and nonlinear all-dielectric metamaterials, Adv. Opt. Mater. 4 (2016) 1457.

[42] T.V. Dolgova, A.I. Maidykovski, M.G. Martemyanov, A.A. Fedyanin, O.A. Aktsipetrov, G. Marowsky, V.A. Yakovlev, G. Mattei, Giant microcavity enhancement of second-harmonic generation in all-silicon photonic crystals, Appl. Phys. Lett. 81 (2002) 2725.

[43] M.G. Martemyanov, E.M. Kim, T.V. Dolgova, A.A. Fedyanin, O.A. Aktsipetrov, G. Marowsky, Third-harmonic generation in silicon photonic crystals and microcavities, Phys. Rev. B 70 (2004) 073311.

[44] S. Liu, G.A. Keeler, J. Reno, Y. Yang, M.B. Sinclair, I. Brener, Efficient second harmonic generation from GaAs all-dielectric metasurfaces, CLEO:QELS_Fundam. Sci. 1 (2016) 2.

[45] S.S. Kruk, R. Camacho-Morales, L. Xu, M. Rahmani, D.A. Smirnova, L. Wang, H.H. Tan, C. Jagadish, D.N. Neshev, Y.S. Kivshar, Nonlinear optical magnetism revealed by second-harmonic generation in nanoantennas, Nano Lett. 17 (2017) 3914.

[46] F.J. Löchner, A.N. Fedotova, S. Liu, G.A. Keeler, G.M. Peake, S. Saravi, M.R. Shcherbakov, S. Burger, A.A. Fedyanin, I. Brener, T. Pertsch, F. Setzpfandt, I. Staude, Polarization-dependent second harmonic diffraction from resonant GaAs metasurfaces, ACS Photonics 5 (2018) 1786.

[47] M. Sheik-Bahae, A.A. Said, T.H. Wei, D.J. Hagan, E.W.V. Stryland, Sensitive measurements of optical nonlinearities using a single beam, IEEE J. Quantum Electron. 26 (1990) 760.

[48] L. Carletti, D. Rocco, A. Locatelli, C. De Angelis, V.F. Gili, M. Ravaro, I. Favero, G. Leo, M. Finazzi, L. Ghirardini, M. Celebrano, G. Marino, A.V. Zayats, Controlling second-harmonic generation at the nanoscale with monolithic AlGaAs-on-AlOx antennas, Nanotechnology 28 (2017) 114005.

[49] R. Sanatinia, M. Swillo, S. Anand, Surface second-harmonic generation from vertical GaP nanopillars, Nano Lett. 12 (2012) 820.

[50] L. Ghirardini, L. Carletti, V. Gili, G. Pellegrini, L. Duò, M. Finazzi, D. Rocco, A. Locatelli, C. De Angelis, I. Favero, M. Ravaro, G. Leo, A. Lemaître, M. Celebrano, Polarization properties of second-harmonic generation in AlGaAs optical nanoantennas, Opt. Lett. 42 (2017) 559.

[51] S. Liu, P.P. Vabishchevich, A. Vaskin, J.L. Reno, G.A. Keeler, M.B. Sinclair, I. Staude, I. Brener, An all-dielectric metasurface as a broadband optical frequency mixer, Nat. Commun. 9 (2018) 2507.

[52] P.P. Vabishchevich, S. Liu, M.B. Sinclair, G.A. Keeler, G.M. Peake, I. Brener, Enhanced second-harmonic generation using broken symmetry III–V semiconductor Fano metasurfaces, ACS Photonics 5 (2018) 1685.

[53] R. Camacho-Morales, M. Rahmani, S. Kruk, L. Wang, L. Xu, D.A. Smirnova, A. Solntsev, A.E. Miroshnichenko, H.H. Tan, F. Karouta, S. Naureen, K. Vora, L. Carletti, C. de Angelis, C. Jagadish, Y.S. Kivshar, D.N. Neshev, Nonlinear generation of vector beams from AlGaAs nanoantennas, Nano Lett. 16 (2016) 7191.

[54] M.F. Limonov, M.V. Rybin, A.N. Poddubny, Y.S. Kivshar, Fano resonances in photonics, Nat. Photonics 11 (2017) 543.

[55] Y. Yang, I.I. Kravchenko, D.P. Briggs, J. Valentine, All-dielectric metasurface analogue of electromagnetically induced transparency, Nat. Commun. 5 (2014) 5753.

[56] S. Campione, S. Liu, L.I. Basilio, L.K. Warne, W.L. Langston, T.S. Luk, J.R. Wendt, J.L. Reno, G.A. Keeler, I. Brener, M.B. Sinclair, Broken symmetry dielectric resonators for high quality factor Fano metasurfaces, ACS Photonics 3 (2016) 2362.

[57] F. Timpu, N.R. Hendricks, M. Petrov, S. Ni, C. Renaut, H. Wolf, L. Isa, Y. Kivshar, R. Grange, Enhanced second-harmonic generation from sequential capillarity-assisted particle assembly of hybrid nanodimers, Nano Lett. 17 (2017) 5381.

[58] C.R. Ma, J.H. Yan, P. Liu, Y.M. Wei, G.W. Yang, Second harmonic generation from an individual all-dielectric nanoparticle: resonance enhancement versus particle geometry, J. Mater. Chem. C 4 (2016) 6063.

[59] S.V. Makarov, A.N. Tsypkin, T.A. Voytova, V.A. Milichko, I.S. Mukhin, A.V. Yulin, S.E. Putilin, M.A. Baranov, A.E. Krasnok, I.A. Morozov, P.A. Belov, Self-adjusted all-

dielectric metasurfaces for deep ultraviolet femtosecond pulse generation, Nanoscale 8 (2016) 17809.

[60] T. Shibanuma, G. Grinblat, P. Albella, S.A. Maier, Efficient third harmonic generation from metal-dielectric hybrid nanoantennas, Nano Lett. 17 (2017) 2647.

[61] G. Grinblat, Y. Li, M.P. Nielsen, R.F. Oulton, S.A. Maier, Efficient third harmonic generation and nonlinear subwavelength imaging at a higher-order anapole mode in a single germanium nanodisk, ACS Nano 11 (2017) 953.

[62] E.V. Melik-Gaykazyan, M.R. Shcherbakov, A.S. Shorokhov, I. Staude, I. Brener, D.N. Neshev, Y.S. Kivshar, A.A. Fedyanin, Third-harmonic generation from Mie-type resonances of isolated all-dielectric nanoparticles, Philos. Trans. R. Soc. A 375 (2017) 20160281.

[63] E.V. Melik-Gaykazyan, S.S. Kruk, R. Camacho-Morales, L. Xu, M. Rahmani, K. Zangeneh Kamali, A. Lamprianidis, A.E. Miroshnichenko, A.A. Fedyanin, D.N. Neshev, Y.S. Kivshar, Selective third-harmonic generation by structured light in Mie-resonant nanoparticles, ACS Photonics 5 (2018) 728.

[64] A.E. Miroshnichenko, A.B. Evlyukhin, Y.F. Yu, R.M. Bakker, A. Chipouline, A.I. Kuznetsov, B. Luk'yanchuk, B.N. Chichkov, Y.S. Kivshar, Nonradiating anapole modes in dielectric nanoparticles, Nat. Commun. 6 (2015) 8069.

[65] B. Hopkins, A.N. Poddubny, A.E. Miroshnichenko, Y.S. Kivshar, Revisiting the physics of Fano resonances for nanoparticle oligomers, Phys. Rev. A 88 (2013) 053819.

[66] R.M. Bakker, D. Permyakov, Y.F. Yu, D. Markovich, R. Paniagua-Domínguez, L. Gonzaga, A. Samusev, Y. Kivshar, B. Lukyanchuk, A.I. Kuznetsov, Magnetic and electric hotspots with silicon nanodimers, Nano Lett. 15 (2015) 2137.

[67] W. Tong, C. Gong, X. Liu, S. Yuan, Q. Huang, J. Xia, Y. Wang, Enhanced third harmonic generation in a silicon metasurface using trapped mode, Opt. Express 24 (2016) 19661.

[68] L. Wang, S.S. Kruk, K.L. Koshelev, I.I. Kravchenko, B. Luther-Davies, Y.S. Kivshar, Nonlinear wavefront control with all-dielectric metasurfaces, Nano Lett. 18 (2018) 3978.

[69] S. Chen, M. Rahmani, K.F. Li, A. Miroshnichenko, T. Zentgraf, G. Li, D. Neshev, S. Zhang, Third harmonic generation enhanced by multipolar interference in complementary silicon metasurfaces, ACS Photonics 5 (2018) 1671.

[70] K.I. Okhlopkov, A.A. Ezhov, P. Shafirin, N.A. Orlikovsky, M.R. Shcherbakov, A.A. Fedyanin, Optical coupling between resonant dielectric nanoparticles and dielectric waveguides probed by third harmonic generation microscopy, ACS Photonics 6 (2019) 189.

[71] M. Celebrano, X. Wu, M. Baselli, S. Großmann, P. Biagioni, A. Locatelli, C. De Angelis, G. Cerullo, R. Osellame, B. Hecht, L. Duò, F. Ciccacci, M. Finazzi, Mode matching in multiresonant plasmonic nanoantennas for enhanced second harmonic generation, Nat. Nanotechnol. 10 (2015) 412.

[72] G. Grinblat, Y. Li, M.P. Nielsen, R.F. Oulton, S.A. Maier, Degenerate four-wave mixing in a multiresonant germanium nanodisk, ACS Photonics 4 (2017) 2144.

[73] H.K. Tsang, C.S. Wong, T.K. Liang, I.E. Day, S.W. Roberts, A. Harpin, J. Drake, M. Asghari, Optical dispersion, two-photon absorption and self-phase modulation in silicon waveguides at 1.5 μm wavelength, Appl. Phys. Lett. 80 (2002) 416.

[74] K. Ikeda, Y. Shen, Y. Fainman, Enhanced optical nonlinearity in amorphous silicon and its application to waveguide devices, Opt. Express 15 (2007) 17761.

[75] S. Makarov, S. Kudryashov, I. Mukhin, A. Mozharov, V. Milichko, A. Krasnok, P. Belov, Tuning of magnetic optical response in a dielectric nanoparticle by ultrafast photoexcitation of dense electron-hole plasma, Nano Lett. 15 (2015) 6187.

[76] Y. Xu, J. Sun, J. Frantz, M.I. Shalaev, W. Walasik, A. Pandey, J.D. Myers, R.Y. Bekele, A. Tsukernik, J.S. Sanghera, N.M. Litchinitser, Reconfiguring structured light beams using nonlinear metasurfaces, Opt. Express 26 (2018) 30930.

[77] I.Y. Park, S. Kim, J. Choi, D.H. Lee, Y.J. Kim, M.F. Kling, M.I. Stockman, S.W. Kim, Plasmonic generation of ultrashort extreme-ultraviolet light pulses, Nat. Photonics 5 (2011) 677.

[78] S. Ghimire, A.D. Dichiara, E. Sistrunk, P. Agostini, L.F. Dimauro, D.A. Reis, Observation of high-order harmonic generation in a bulk crystal, Nat. Phys. 7 (2011) 138.

[79] H. Liu, C. Guo, G. Vampa, J.L. Zhang, T. Sarmiento, M. Xiao, P.H. Bucksbaum, J. Vučković, S. Fan, D.A. Reis, Enhanced high-harmonic generation from an all-dielectric metasurface, Nat. Phys. 14 (2018) 1006.

[80] C.W. Siders, N.C. Turner, M.C. Downer, A. Babine, A. Stepanov, A.M. Sergeev, Blue-shifted third-harmonic generation and correlated self-guiding during ultrafast barrier suppression ionization of subatmospheric density noble gases, J. Opt. Soc. Am. B 13 (1996) 330.

[81] S.C. Wilks, J.M. Dawson, W.B. Mori, T. Katsouleas, M.E. Jones, Photon accelerator, Phys. Rev. Lett. 62 (1989) 2600.

[82] M.R. Shcherbakov, K. Werner, Z. Fan, N. Talisa, E. Chowdhury, G. Shvets, Photon acceleration and tunable broadband harmonics generation in nonlinear time-dependent metasurfaces, Nat. Commun. 10 (2019) 1345.

[83] A. Weiner, Ultrafast Optics, John Wiley & Sons, 2011.

[84] J. Shah, Ultrafast Spectroscopy of Semiconductors and Semiconductor Nanostructures, 2nd ed., Springer, New York, 1999.

[85] V.R. Almeida, C.A. Barrios, R.R. Panepucci, M. Lipson, All-optical control of light on a silicon chip, Nature 431 (2004) 1081.

[86] U. Strauss, W.W. Rühle, K. Köhler, Auger recombination in intrinsic GaAs, Appl. Phys. Lett. 62 (1993) 55.

[87] A.D. Bristow, J.P.R. Wells, W.H. Fan, A.M. Fox, M.S. Skolnick, D.M. Whittaker, A. Tahraoui, T.F. Krauss, J.S. Roberts, Ultrafast nonlinear response of AlGaAs two-dimensional photonic crystal waveguides, Appl. Phys. Lett. 83 (2003) 851.

[88] M.R. Shcherbakov, S. Liu, V.V. Zubyuk, A. Vaskin, P.P. Vabishchevich, G. Keeler, T. Pertsch, T.V. Dolgova, I. Staude, I. Brener, A.A. Fedyanin, Ultrafast all-optical tuning of direct-gap semiconductor metasurfaces, Nat. Commun. 8 (2017) 17.

[89] P.P. Iyer, N.A. Butakov, J.A. Schuller, Reconfigurable semiconductor phased-array metasurfaces, ACS Photonics 2 (2015) 1077.

[90] D.G. Baranov, S.V. Makarov, V.A. Milichko, S.I. Kudryashov, A.E. Krasnok, P.A. Belov, Nonlinear transient dynamics of photoexcited resonant silicon nanostructures, ACS Photonics 3 (2016) 1546.

[91] A. Rudenko, K. Ladutenko, S. Makarov, T.E. Itina, Photogenerated free carrier-induced symmetry breaking in spherical silicon nanoparticle, Adv. Opt. Mater. 6 (2018) 1701153.

[92] A. Sabbah, D. Riffe, Femtosecond pump–probe reflectivity study of silicon carrier dynamics, Phys. Rev. B 66 (2002) 165217.

[93] B.R. Bennett, R.A. Soref, J.A. Del Alamo, Carrier-induced change in refractive index of InP, GaAs, and InGaAsP, IEEE J. Quantum Electron. 26 (1990) 113.

[94] J. Lee, M. Tymchenko, C. Argyropoulos, P.-Y. Chen, F. Lu, F. Demmerle, G. Boehm, M.-C. Amann, A. Alù, M.A. Belkin, Giant nonlinear response from plasmonic metasurfaces coupled to intersubband transitions, Nature 511 (2014) 65.

[95] O. Wolf, S. Campione, A. Benz, A.P. Ravikumar, S. Liu, T.S. Luk, E.A. Kadlec, E.A. Shaner, J.F. Klem, M.B. Sinclair, I. Brener, Phased-array sources based on nonlinear metamaterial nanocavities, Nat. Commun. 6 (2015) 7667.

[96] L. Zhang, A.M. Agarwal, L.C. Kimerling, J. Michel, Nonlinear Group IV photonics based on silicon and germanium: from near-infrared to mid-infrared, Nanophotonics 3 (2014) 247.

[97] R. Soref, Mid-infrared photonics in silicon and germanium, Nat. Photonics 4 (2010) 495.

[98] D.A. Shilkin, M.R. Shcherbakov, E.V. Lyubin, K.G. Katamadze, O.S. Kudryavtsev, V.S. Sedov, I.I. Vlasov, A.A. Fedyanin, Optical magnetism and fundamental modes of nanodiamonds, ACS Photonics 4 (2017) 1153.

[99] S. Suchalkin, G. Belenky, M. Ermolaev, S. Moon, Y. Jiang, D. Graf, D. Smirnov, B. Laikhtman, L. Shterengas, G. Kipshidze, S.P. Svensson, W.L. Sarney, Engineering Dirac materials: metamorphic $InAs_{1-x}Sb_x$/$InAs_{1-y}Sb_y$ superlattices with ultralow bandgap, Nano Lett. 18 (2018) 412.

[100] M.G. Barsukova, A.S. Shorokhov, A.I. Musorin, D.N. Neshev, Y.S. Kivshar, A.A. Fedyanin, Magneto-optical response enhanced by Mie resonances in nanoantennas, ACS Photonics 4 (2017) 2390.

Non-resonant dielectric metamaterials

9

Alexander Sprafke, Jörg Schilling
Institute of Physics, Martin-Luther-University Halle–Wittenberg, Halle, Germany

9.1 Definition of nonresonant spectral range

As described in the chapters before, the appearance of Mie resonances governs the scattering properties of dielectric elements in a spectral range when the wavelength is roughly of the size of the elements or shorter. Starting from the dipolar magnetic and electric Mie resonances many more higher-order resonances (quadrupole, octopole, etc.) follow at shorter wavelengths. When a metamaterial is constructed from these scattering elements or "meta-atoms" the non-resonant regime corresponds to the low frequency/long wavelength range which extends from the lowest-order Mie resonance down to static conditions ($\omega \rightarrow 0$). In a dielectric sphere the lowest Mie resonance is the magnetic dipole resonance which appears at

$$\lambda_{0,Mie} = 2r \frac{n_i}{n_h} \tag{9.1}$$

where r is the radius of the sphere and n_i and n_h are the refractive indices of the sphere and the surrounding host material, respectively. In random arrangements of dielectric spheres $\lambda_{0,Mie}$ therefore represents a hard limit for the non-resonant regime.

However, since a metamaterial consists of an arrangement of scattering elements the order of the ensembles of these elements has to be considered. Man-made metamaterials are mostly periodic structures where, in addition to the mentioned Mie resonances, lattice resonances also occur leading to the well-known Bragg diffraction. Therefore, most metamaterials also represent photonic crystals, where the first Bragg resonance occurs at

$$\lambda_{0,Bragg} = 2n_{eff}a \tag{9.2}$$

where a is the lattice period and n_{eff} describes the effective refractive index of the periodic structure in the long wavelength limit. Which one of the two resonance conditions, (9.1) or (9.2), results in the lower resonance is not necessarily straightforward and depends on the interplay between the r/a-ratio and the refractive indices n_i, n_h, and n_{eff}. To find a conservative estimate for the upper frequency bound of the non-resonant regime requires some approximations be introduced to the Mie and Bragg condition based on (9.1) and (9.2): For an overall arrangement of non-touching spheres we have $r < \frac{a}{2}$, so that from (9.1) follows $\lambda_{0,Mie} < a \frac{n_i}{n_h}$ and furthermore $\lambda_{0,Mie} < an_i$, since the refractive index of a natural host medium is $n_h \geq 1$. One has to also consider that

Bragg diffraction in photonic crystal structures occurs over a wavelength range (the photonic bandgap) and the single wavelength $\lambda_{0,Bragg}$ from (9.2) corresponds only roughly to the center wavelength of this Bragg diffraction/photonic bandgap range. To determine the lowest possible frequency for the onset of Bragg diffraction the lower band edge of this bandgap region is decisive. Since the standing waves at this band edge concentrate their field in the material with high refractive index /dielectric constant one can conservatively estimate $\lambda_{0,Bragg-onset} < 2an_i$. Following these approximations one can conservatively conclude that the non-resonant spectral range of metamaterials extends for wavelengths $\lambda_0 > 2an_i$. For most of the metamaterials the Bragg condition determines this wavelength limit. Only in cases where dense arrays of very high index spheres occur, the Mie resonance might drop below the actual Bragg resonance. In a related case lattices of dielectric rods were investigated and the spectral positions of the Mie resonances and photonic bandgaps exactly determined [1]. Also in this case the Bragg resonances appeared at frequencies below the Mie resonances for usual refractive-index values < 4. Only for ultra-high-refractive indices of the rods, as they appear in the far IR or microwave region, did the Mie resonances drop below the Bragg resonances.

9.2 Theoretical description – homogenization and effective-medium theories

9.2.1 Isotropic effective media

In the limit of long wavelengths all structure sizes, such as the size of the scattering elements and their separation, are small compared to the wavelength. In this case the electric field of an electromagnetic wave does not change much over these structure sizes and can therefore be approximated to be constant. This corresponds to the quasi-static limit and classic effective-medium theories are formulated assuming this condition. As this excludes ring-like patterns of the electric polarization, metamaterial induced magnetism does not occur in this case and the resulting permeability $\mu \approx 1$ can be assumed as long as non-magnetic materials are considered.

In the following we provide a short overview of the main two effective-medium theories, the Maxwell–Garnett and the Bruggeman effective-medium theories, since they are easy to use, widely accepted and it can be shown that they appear as extrapolated solutions of more rigorous models in the limit $\omega \to 0$.

9.2.1.1 Maxwell–Garnett effective-medium model

The determination of an effective dielectric constant in the quasi-static case is usually performed in two steps:

1. The electric field in and around the scattering element is determined for the case that a static (external) electric field is assumed.
2. The effective dielectric constant ε_{eff} is determined from the relation

$$\boldsymbol{D}_{eff} = \varepsilon_{eff}\boldsymbol{E}_{eff} \tag{9.3}$$

where $\boldsymbol{D}_{eff}$ describes the averaged dielectric displacement field $\boldsymbol{D}_{eff} = \frac{1}{V}\int \boldsymbol{D}(\boldsymbol{r})\,d\boldsymbol{r}^3$ and $\boldsymbol{E}_{eff}$ the averaged electric field $\boldsymbol{E}_{eff} = \frac{1}{V}\int \boldsymbol{E}(\boldsymbol{r})\,d\boldsymbol{r}^3$ in a volume V much larger than a single scattering element. In order to solve (9.3) for ε_{eff} and come to an analytical solution additional simplifying assumptions are made.

The case of a spherical particle with dielectric constant ε_i, which is placed in a matrix of dielectric constant ε_{ex}, forms the starting point for most effective-medium theories. When a static electric field $\boldsymbol{E}_{ex0}$ is applied along the z-direction, the sphere becomes polarized, which can be represented by a surface charge density at the surface of the sphere. The field inside the sphere forms then as a superposition of $\boldsymbol{E}_{ex0}$ and the depolarizing field exerted by the polarization (the polarization surface charges) of the sphere. In addition, the overall electric field in the immediate surrounding of the sphere is also affected by the field exerted by the polarization surface charges of the sphere. To determine the resulting inner and outer electric fields the Laplace equation $\varepsilon_{i,ex}\varepsilon_0\Delta\Phi = 0$ has to be solved under the boundary condition that the electric field far away ($r \to \infty$) corresponds to $\boldsymbol{E}_{ex0}$ [2]. Treating the problem in spherical coordinates, the electrostatic potential Φ inside and outside of the sphere can be expressed as a series of Legendre polynomials. Observing the boundary condition for $r \to \infty$ and the continuity of $\frac{\partial\Phi}{\partial r}$ and $\frac{\partial\Phi}{\partial\theta}$ at the surface of the sphere, the constants in the series can be determined, so that the electrostatic potential takes the following form [2]:

$$\Phi_i = -\frac{3\varepsilon_{ex}}{\varepsilon_i + 2\varepsilon_{ex}}E_{ex0}r\cos\theta = -\frac{3\varepsilon_{ex}}{\varepsilon_i + 2\varepsilon_{ex}}E_{ex0}z \quad \text{(inside the sphere)} \tag{9.4}$$

$$\Phi_{ex} = -E_{ex0}r\cos\theta + \frac{\varepsilon_i - \varepsilon_{ex}}{\varepsilon_i + 2\varepsilon_{ex}}E_{ex0}\frac{R^3}{r^2}\cos\theta \quad \text{(outside the sphere)} \tag{9.5}$$

Applying the general relation, $E = -\operatorname{grad}\Phi$, the electric fields inside and outside the sphere are obtained [3]:

$$\boldsymbol{E}_{in} = \frac{3\varepsilon_{ex}}{\varepsilon_i + 2\varepsilon_{ex}}E_{ex0}\boldsymbol{e}_z \quad \text{(inside the sphere)} \tag{9.6}$$

$$\boldsymbol{E}_{ex} = E_{ex0}\boldsymbol{e}_z + \frac{\varepsilon_i - \varepsilon_{ex}}{\varepsilon_i + 2\varepsilon_{ex}}E_{ex0}\frac{R^3}{r^3}(2\cos\theta\,\boldsymbol{e}_r + \sin\theta\,\boldsymbol{e}_\theta) \quad \text{(outside the sphere)} \tag{9.7}$$

The field inside the sphere is homogeneous and aligned with the external (inducing) field $\boldsymbol{E}_{ex0}$. When the dielectric constant of the sphere is higher than the surrounding matrix material, the internal field is decreased with respect to $\boldsymbol{E}_{ex0}$ and vice versa. This is the effect of the induced response field due to the polarization of the sphere. The external field is a superposition of the original field $\boldsymbol{E}_{ex0}$ (first term in (9.7)) and a dipole field generated by the polarization charges of the sphere (second term in (9.7)) [Fig. 9.1A]. Due to the $1/r^3$ dependence of the dipole field it decays quickly away from the surface of the sphere. For ac-fields this dipole field corresponds to the near field of a Hertz dipole.
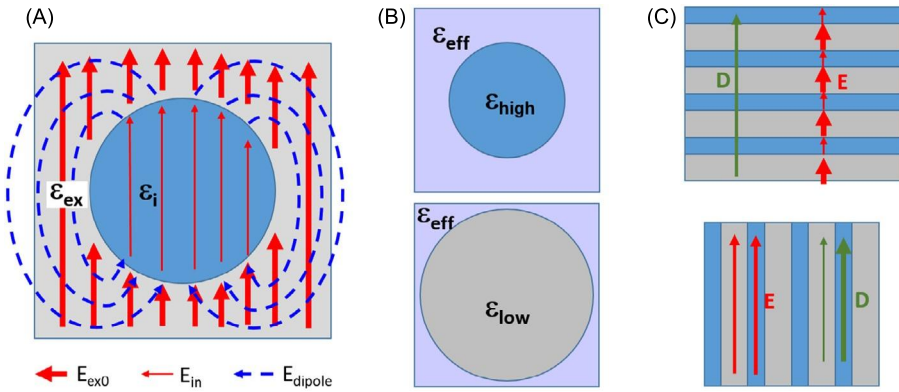
Figure 9.1 Effective-medium concepts (A) Maxwell–Garnett model: A sphere with dielectric constant ε_i is immersed in a host medium with dielectric constant ε_{ex}. (B) Bruggeman model: A sphere of either dielectric constant ε_i or ε_{ex} is immersed in the effective medium with ε_{eff}. (C) Wiener formulas: Exact formulas can be obtained for the simple case of layered metamaterials where the continuity conditions at plane interfaces for the D- and E-fields can be exploited.

To calculate the effective dielectric constant for an ensemble of spheres dispersed in a matrix using (9.3) expressions for D_{eff} and E_{eff} have to be found. When the spheres are well separated, the Maxwell–Garnett approximation can be applied. In this effective-medium theory the whole field outside the sphere is approximated by the homogeneous field E_{ex0}. The dipole field in (9.7) is neglected. This allows for the following simple forms for D_{eff} and E_{eff}:

$$D_{eff} = f\varepsilon_i E_{in} + (1 - f)\varepsilon_{ex} E_{ex0}$$
$$E_{eff} = f E_{in} + (1 - f) E_{ex0},$$

where f describes the volume fraction (filling factor or filling fraction) occupied by the spheres. Together with (9.6) and (9.3) the effective dielectric constant for the Maxwell–Garnett theory results in [3]

$$\varepsilon_{eff-MG} = \varepsilon_{ex} + \varepsilon_{ex} \frac{3f(\varepsilon_i - \varepsilon_{ex})}{\varepsilon_i + 2\varepsilon_{ex} - f(\varepsilon_i - \varepsilon_{ex})} \quad \text{or}$$

$$\frac{\varepsilon_{eff-MG} - \varepsilon_{ex}}{\varepsilon_{eff-MG} + 2\varepsilon_{ex}} = f\frac{(\varepsilon_i - \varepsilon_{ex})}{\varepsilon_i + 2\varepsilon_{ex}} \tag{9.8}$$

In randomly arranged effective media the Maxwell–Garnett formula is only valid for filling fractions of a few percent. Only then the approximation of independent spheres with dielectric constant ε_i in a surrounding matrix with ε_{ex} is realistic as particle agglomerations are rare and the mutual interaction of the dipolar near fields of neighboring spheres can be neglected. Interestingly, the range of validity is extended for strictly periodic arrangements of spheres, as it occurs e.g. in a 3D cubic lattice of spheres. This is shown in Fig. 9.2. A strictly periodic arrangement of spheres with a dielectric constant of 12 (e.g. silicon spheres) in an environment with dielectric constant of 1 (e.g. air) represents a photonic crystal and the dispersion relation of light
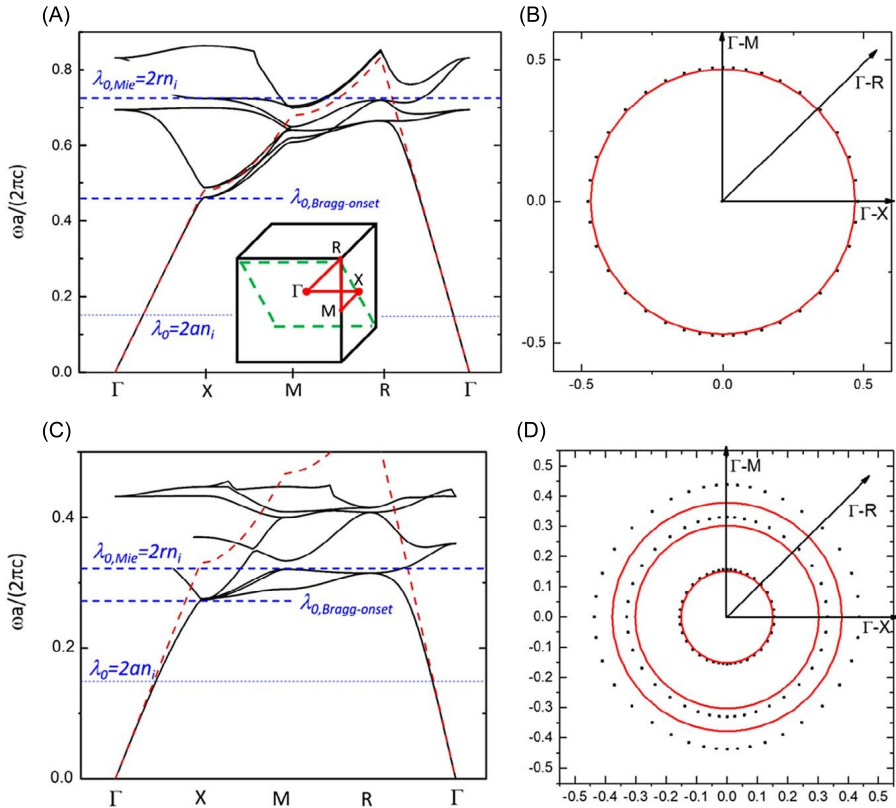
Figure 9.2 Photonic bandstructure calculations for a 3D cubic array of dielectric spheres with dielectric constant $\varepsilon_i = 12$ (e.g. Si) in a host with $\varepsilon_{ex} = 1$ (air). (A, B) for $r/a = 0.2$; (C, D) for $r/a = 0.45$. For the case of small spheres (A, B) the dispersion relation up to the onset of Bragg reflection (represented by the upper end of the first band at the X-point) is linear and can be well approximated by an effective refractive index calculated after the Maxwell–Garnett theory (red dashed line). This is also shown in (B), where the equi-frequency surface in the green rendered cross sectional plane is shown for $\omega a/(2\pi c) = 0.45$. The numerically exact calculated wavevectors (black dots) agree very well with the Maxwell–Garnett approximation (solid red). For larger spheres (C, D) the Maxwell–Garnett effective index is only a good approximation in the very long wavelength range for wavelengths above the very conservative limit of $\lambda_0 = 2an_i$.

in this structure can be represented by a photonic bandstructure. The spatially varying dielectric constant can be developed into a Fourier series and the electromagnetic waves are represented as series of plane waves. In this case, the frequencies of the electromagnetic waves at specified wavevectors are obtained as eigenvalues of the coefficient matrix [4]. The wavevectors are "scanned" across the first Brillouin zone choosing a path within the 3D cubic Brillouin zone, which covers the critical points Γ, X, M, R where the band edges appear. As pointed out above the non-resonant spectral range is represented by the first photonic band and extends from $\omega = 0$ towards the onset of Bragg reflection, which occurs first along the Γ-X direction. For small

spheres whose radius r is only 20% of the period a ($r/a = 0.2$) the nonresonant range reaches up to $\omega a/(2\pi c) = 0.46$ and the linear dispersion of the band can be well approximated up to the photonic bandgap by an effective refractive index obtained by the Maxwell–Garnett formula (red dashed line in Fig. 9.2A). "Cutting" the bandstructure at a fixed frequency of $\omega a/(2\pi c) = 0.45$ just below the onset of Bragg reflection reveals a spherical equi-frequency surface (a circle in the Γ-X-R plane) [Fig. 9.2], which agrees perfectly with the isotropic Maxwell-Garnet effective refractive index. For such small spheres the first Mie resonance after (9.1) is situated at a high frequency of $\omega a/(2\pi c) = 0.72$, so that indeed the lattice Bragg resonance limits the non-resonant range.

When a cubic array of large, almost touching spheres with $r/a = 0.45$ is considered, the bandstructure shifts to lower frequencies as the overall amount of high index material increases. The Mie resonance drops to $\omega a/(2\pi c) = 0.32$ and the onset of Bragg reflection drops to $\omega a/(2\pi c) = 0.27$, so that the Bragg resonance still limits the non-resonant range. However, the first band is now bending much earlier (at lower frequencies) due to the influence of Bragg diffraction, so that a linear dispersion is only observed for the long wavelength region. This is also represented by the equi-frequency contours in Fig. 9.2D, which were taken at $\omega a/(2\pi c) = 0.1, 0.2$, and 0.25. While the spherical shape of the equi-frequency surfaces still remains well preserved, the Maxwell–Garnett effective index can only describe the lowest frequency contour accurately. For the higher frequencies of $\omega a/(2\pi c) = 0.2$ and 0.25, which are approaching the photonic bandgap, the gradual impact of Bragg diffracted waves grows leading to a standing wave at the band edge with a predominant concentration of the light intensity in the high index spheres. Since the light at these frequencies "sees" more of the high index material the internal wavevector increases away from the fixed Maxwell–Garnett approximation. At these frequencies a clear gap between the exact equi-frequency contours (black dots) and the MG-effective Medium model (solid red) occurs. In summary, the Maxwell–Garnett effective-medium model provides a very accurate value for the effective dielectric constant in the long wavelength region of periodic metamaterials of high symmetry resulting in a linear dispersion relation in this spectral range (as long as material dispersion can be neglected). For low filling fractions (small scatterers) this approximation can also be safely applied up to the onset of Bragg diffraction. For higher filling fractions considerable band bending begins to occur for frequencies below the photonic bandgap and the Maxwell–Garnett model becomes inaccurate.

9.2.1.2 Bruggeman model

While the Maxwell–Garnett model is well suited for media where clearly separated, well defined, scattering elements are surrounded by the host medium, it becomes inaccurate when the elements agglomerate and the structure develops a more interconnected/interwoven character, where a clear distinction between "element" and "host material" can no longer be made. This becomes obvious when inclusion and host are exchanged in the Maxwell–Garnett theory, for instance, instead of having high index inclusions with filling factor f in a low index host, assume low index inclusion of filling factor (1-f) in a high index host [Fig. 9.3].
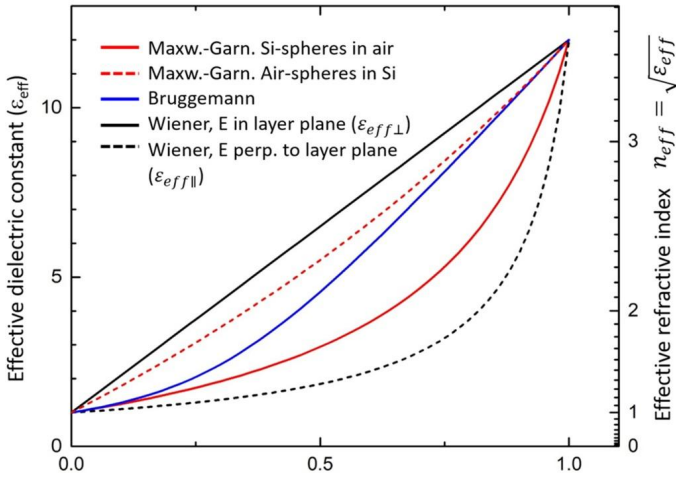
Figure 9.3 Comparison of effective dielectric constants and indices using different effective-media models and assuming silicon ($\varepsilon_{Si} = 12$) and air ($\varepsilon_{air} = 1$) as the underlying two materials.

For the same filling fraction two different effective dielectric constants and indices are obtained depending on the assignment of one material as inclusion or host. To overcome this asymmetry inherent to the MG-formula, Bruggeman suggested another model: It is based on the idea that in an effective medium the average dielectric displacement field D_{eff} is chosen in such a way that the positive deviation $\Delta D_{high\text{-}\varepsilon} = D_{high\text{-}\varepsilon} - D_{eff}$ from D_{eff} in regions with high dielectric constant is just compensated by the negative deviation $\Delta D_{low\text{-}\varepsilon} = D_{low\text{-}\varepsilon} - D_{eff}$ in regions with low dielectric constant. Furthermore it is assumed that the spherical inclusion is surrounded by an effective medium with the effective constant ε_{eff} [Fig. 9.1B]. Based on these assumptions the following relation is obtained:

$$f \Delta D_{high\text{-}\varepsilon} + (1 - f) \Delta D_{low-\varepsilon}$$
$$= f \left[\varepsilon_{high} E_i - \varepsilon_{eff} E_{eff} \right] + (1 - f) \left[\varepsilon_{low} E_i - \varepsilon_{eff} E_{eff} \right] = 0$$
$$f \left[\varepsilon_{high} \frac{3\varepsilon_{eff}}{\varepsilon_{high} + 2\varepsilon_{eff}} E_{eff} - \varepsilon_{eff} E_{eff} \right]$$
$$+ (1 - f) \left[\varepsilon_{low} \frac{3\varepsilon_{eff}}{\varepsilon_{low} + 2\varepsilon_{eff}} E_{eff} - \varepsilon_{eff} E_{eff} \right] = 0$$

which is cast in the more familiar form

$$f \frac{\varepsilon_1 - \varepsilon_{eff}}{\varepsilon_1 + 2\varepsilon_{eff}} + (1 - f) \frac{\varepsilon_2 - \varepsilon_{eff}}{\varepsilon_2 + 2\varepsilon_{eff}} = 0 \tag{9.9}$$

The resulting effective dielectric constant has values between the two MG-cases. For low filling fractions it approaches the MG-case of isolated high index inclusions surrounded by a low index host material while for high filling fractions it approaches the MG values for isolated low index inclusions in a high index host.

As both the Maxwell–Garnett and the Bruggeman formulas are based on highly symmetric inclusions (spheres) and no assumptions on the ordering of the scatterers are made, both formulas can only describe isotropic effective media in their original form. For most material systems where the inclusions are arranged randomly this is sufficiently fulfilled. However, since metamaterials are usually intentionally designed, reduced symmetries and an intentional ordering of the scattering elements introduce anisotropic effective dielectric constants. This is discussed in the following section.

9.2.2 Anisotropic effective media

Anisotropies can enter due to the reduction of symmetry in metamaterials. This leads to different densities of the scattering material along different directions in the metamaterial which can be realized in two different ways:

(a) Regular positioning of highly symmetric scattering elements (e.g. spheres) in a low symmetry arrangement (e.g. tetragonal or orthorhombic lattice).
(b) Reduction of symmetry of the individual scattering elements and (on average) uniform orientation of the scattering elements.

Both strategies will be discussed in the following using some examples.

(a) Highly symmetric scattering elements in low symmetry arrangements

The arrangement of the scattering elements in a low symmetry lattice results in a variation of density of the scatterers along different directions in the "metacrystal". This is comparable to the case of atomic crystals where atoms are periodically positioned in the same lattices and the scatterers in the metacrystal can be viewed as "artificial atoms". In analogy to the field of crystal optics the overall anisotropic effective dielectric constant is then described by a second order dielectric tensor (3×3 matrix) leading to birefringence. Based on this the conventional approach taken with crystal optics can be applied. As an example for this a photonic bandstructure of a tetragonal lattice with the lattice vectors $\begin{pmatrix} a \\ 0 \\ 0 \end{pmatrix}$, $\begin{pmatrix} 0 \\ a \\ 0 \end{pmatrix}$, and $\begin{pmatrix} 0 \\ 0 \\ 1.5a \end{pmatrix}$ formed from dielectric spheres ($\varepsilon_i = 12$) is shown in Fig. 9.4A. In this tetragonal lattice the lower two bands are now generally split and stay only degenerate along the Γ-Z direction which corresponds to the distinguished z-direction of the tetragonal lattice. The lower two bands also exhibit a clear polarization difference in the field profiles (see insets in Fig. 9.4A). While along the Γ-X section of the Brillouin zone (corresponding to x-direction of the real lattice) the modes of band 1 are strongly y-polarized and the modes of band 2 show a dominating polarization in the z-direction. These observations from the bandstructure agree well with the birefringent properties of tetragonal crystals in crystal optics and one can conclude that for wavelengths below the onset of Bragg diffraction the structure exhibits uniaxial anisotropic properties. The z-direction corresponds to the optical axis, which agrees with the observation that bands 1 and 2 are degenerate along this direction leading to the same refractive indices for modes of both bands. Along the Γ-X-direction (corresponds to x- and y-direction in real lattice) the two different effective refractive indices $n_{band1-x} = n_{band1-y} \approx 1.41$ and $n_{band2-x} = n_{band2-y} \approx 1.27$ can be derived
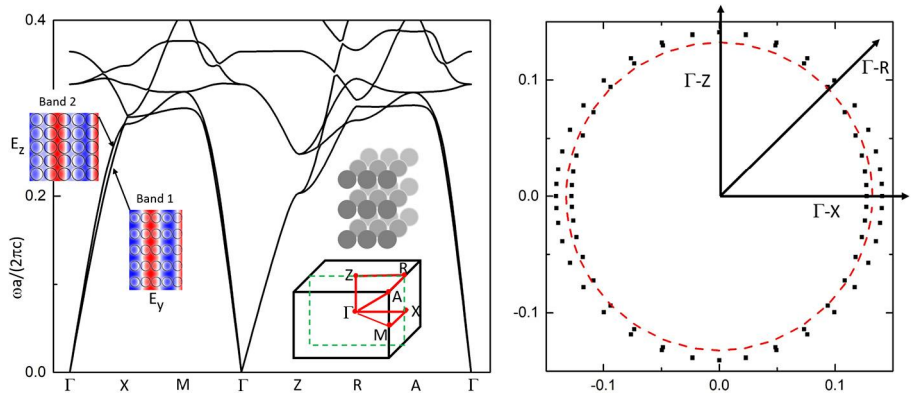
Figure 9.4 Dispersion relation in a tetragonal lattice of spheres with $\varepsilon_i = 12$ in air with $r/a = 0.45$. (A) Photonic bandstructure showing the splitting of band 1 and 2 in the long wavelength range. The inset represents the different polarizations of the modes belonging to band 1 and 2 representing ordinary and extraordinary waves. (B) Equi-frequency contours in the Γ-A-Z-plane for $\frac{\omega a}{2\pi c} \approx 0.1$ exhibiting two shells (represented by black symbols): outer shell for ordinary waves of band 1, inner shell for extraordinary waves of band 2. For comparison a contour based on the MG theory is added (red dashed line).

from the gradient of both bands. This corresponds to the refractive indices of ordinary and extraordinary waves along these crystal directions. Along the Γ-Z direction a common effective refractive index of $n_{band1-z} = n_{band2-z} \approx 1.41$ is derived as expected from the degeneracy of the bands in this direction and in agreement with the occurrence of the optical axis along this direction. Based on these numbers the following dielectric tensor can be constructed describing the wave propagation in the long wavelength regime below $\frac{\omega a}{2\pi c} \approx 0.2$:

$$\begin{pmatrix} \varepsilon_{xx} & 0 & 0 \\ 0 & \varepsilon_{yy} & 0 \\ 0 & 0 & \varepsilon_{zz} \end{pmatrix} = \begin{pmatrix} 1.99 & 0 & 0 \\ 0 & 1.99 & 0 \\ 0 & 0 & 1.61 \end{pmatrix}$$

where $\varepsilon_{xx} = \varepsilon_{yy} = n_{band1-z}^2 = n_{band2-z}^2 = 1.41^2$ and $\varepsilon_{zz} = n_{band2-x}^2 = n_{band2-y}^2 = 1.27^2$. The equi-frequency contour in the Γ-A-Z-plane (Fig. 9.4B) taken at $\frac{\omega a}{2\pi c} \approx 0.1$ also shows the corresponding split into two shells: an outer circular contour corresponding to the wave vector surface of the ordinary wave and an inner elliptical contour belonging to the extraordinary wave. For comparison, a wavevector contour based on the Maxwell–Garnett model is included (red dashed line), which forms a single circle corresponding to an effective index of $n_{MG} = 1.32$. Since the MG theory is based on a single scatterer and the arrangement of the scattering elements is not considered in this theory, the birefringent phenomena due to the tetragonal lattice can understandably not be captured by this model.

(b) Uniformly aligned low symmetry scattering elements

To obtain low symmetry scattering elements the highly symmetric spheres can e.g. be deformed into ellipsoids leading, in the extreme cases, to rods or plates. A po-

sitional order is not necessary. As long as the deformed elements have on average the same alignment the resulting dielectric tensor will contain unequal elements. This situation can be compared to the nematic phase in liquid crystals where the rod-like molecules are all parallel aligned leading to a uniaxial dielectric tensor. Since this resulting birefringence is caused by the shape, or "form", of the scattering elements, the resulting birefringent effect is called form birefringence. Moving away from the highly symmetric spherical shape complicates the mathematical derivation of the relationship between the inner electric field and the outer electric field of the dielectric scattering element as it was done to arrive at (9.6) and (9.7). Nevertheless, for ellipsoidal particles it is analytically still possible [5] and the effects of the shape of the ellipsoidal scattering element can be represented by the depolarization factors L_x, L_y, and L_z, which apply when the electric field is aligned with the x-, y-, and z-semiaxes of the ellipsoid [3]:

$$E_{ix,y,z} = \frac{\varepsilon_{ex}}{\varepsilon_{ex} + L_{x,y,z}(\varepsilon_i - \varepsilon_{ex})} E_{ex0} \qquad (9.10)$$

For the derivation of the depolarization factors, in general, elliptical integrals have to be calculated [5,3] but for the simpler (but relevant) case of rotational ellipsoids, where two semiaxes have the same length and the ellipsoid exhibits an axis of rotation, two analytical expressions can be found [6]:

$$L_\parallel = \frac{1}{1-\xi^2} \left(1 - \xi \frac{\arcsin\left(\sqrt{1-\xi^2}\right)}{\sqrt{1-\xi^2}} \right) \quad \text{and}$$

$$L_\perp = \frac{1}{\xi^2-1} \left(\frac{1}{2} \frac{\xi}{\sqrt{\xi^2-1}} \ln\left(\frac{\xi + \sqrt{\xi^2-1}}{\xi - \sqrt{\xi^2-1}} \right) \right),$$

where ξ corresponds to the ratio of the semiaxes $\xi = a/b$ and the semiaxis a is aligned with the rotational axis of the ellipsoid. The depolarization factors vary between 0 and 1 (Fig. 9.5). For spheres the excentricity ξ is 1 ($a = b$) and the resulting depolarization factors are equal $L_\perp = L_\parallel = 1/3$. In this case (9.10) reproduces (9.6). In the case where the rotational semiaxis a is shorter than b, an oblate ellipsoid occurs, which leads in the extreme case of $a/b = 0$ ($b \to \infty$) to $L_\perp = 0$ and $L_\parallel = 1$ for a laterally infinitely extended disc or layer. For $a > b$ a polar ellipsoid (cigar-shape) is formed which leads, in the extreme case, to an infinitely elongated circular rod when $a/b = \infty$ ($a \to \infty$) resulting in $L_\perp = 0.5$ and $L_\parallel = 0$.

With the help of the now direction dependent Eq. (9.10) the Maxwell–Garnett and Bruggeman formulas can also be modified leading to direction dependent effective dielectric constants, where we restrict ourselves again to the most relevant case of rotational ellipsoidal scattering elements [6]:

$$\text{MG:} \quad \frac{\varepsilon_{eff\perp} - \varepsilon_{ex}}{L_\perp \left(\varepsilon_{eff\perp} - \varepsilon_{ex} \right) + \varepsilon_{ex}} = f \frac{\varepsilon_i - \varepsilon_{ex}}{\varepsilon_{ex} + L_\perp \left(\varepsilon_i - \varepsilon_{ex} \right)} \quad \text{and}$$

$$\frac{\varepsilon_{eff\parallel} - \varepsilon_{ex}}{L_\parallel \left(\varepsilon_{eff\parallel} - \varepsilon_{ex} \right)} = f \frac{\varepsilon_i - \varepsilon_{ex}}{\varepsilon_{ex} + L_\parallel \left(\varepsilon_i - \varepsilon_{ex} \right)} \qquad (9.11)$$
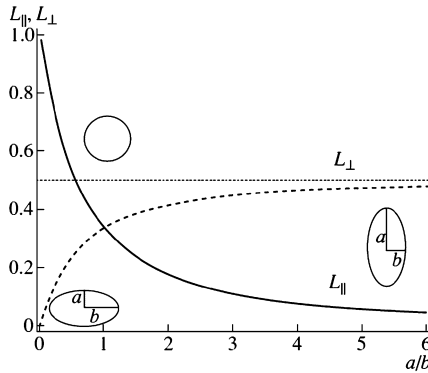
Figure 9.5 Values of the depolarization factors in rotational ellipsoids. For a sphere ($a/b = 1$) both depolarization factors are equal and have a value of $1/3$. Reprinted with permission from [6] [Springer Nature].

Bruggeman:

$$f_1 \frac{\varepsilon_1 - \varepsilon_{eff\perp}}{\varepsilon_{eff\perp} + L_\perp (\varepsilon_1 - \varepsilon_{eff\perp})} + (1 - f_1) \frac{\varepsilon_2 - \varepsilon_{eff\perp}}{\varepsilon_{eff\perp} + L_\perp (\varepsilon_2 - \varepsilon_{eff\perp})} = 0 \quad \text{and}$$

$$f_1 \frac{\varepsilon_1 - \varepsilon_{eff\|}}{\varepsilon_{eff\|} + L_\| (\varepsilon_1 - \varepsilon_{eff\|})} + (1 - f_1) \frac{\varepsilon_2 - \varepsilon_{eff\|}}{\varepsilon_{eff\|} + L_\| (\varepsilon_2 - \varepsilon_{eff\|})} = 0 \quad (9.12)$$

Based on these constitutive relations for the effective dielectric constant parallel and perpendicular to the rotational axis of the ellipsoids, and assuming that the rotational axis of all ellipsoidal scattering elements is aligned parallel to z, the dielectric tensor takes the form

$$\begin{pmatrix} \varepsilon_{eff\perp} & 0 & 0 \\ 0 & \varepsilon_{eff\perp} & 0 \\ 0 & 0 & \varepsilon_{eff\|} \end{pmatrix} \quad (9.13)$$

Interestingly, the principal effective dielectric constant derived from the Bruggeman Eq. (9.12) under the assumption of a layered medium ($L_\perp = 0$ and $L_\| = 1$) takes the form of the well-known Wiener formulas:

$$\frac{1}{\varepsilon_{eff\|}} = \frac{f}{\varepsilon_1} + \frac{1 - f}{\varepsilon_2} \quad \text{and} \quad (9.14)$$

$$\varepsilon_{eff\perp} = f \varepsilon_1 + (1 - f) \varepsilon_2$$

These are analytically exact solutions in the quasi-static case for a multilayer structure and can be directly obtained from the continuity conditions of the E- and D-field across plane interfaces or considering a serial or parallel capacitor model. The Wiener formulas also represent the most extreme values the effective dielectric constants can reach for a given set of constituting materials with ε_1 and ε_2 and fill factor f and are therefore also referred to as "Wiener bounds". This is already shown in Fig. 9.2, where Maxwell–Garnett and Bruggeman effective constants have values between the two

Wiener bounds (black curves). The construction of a layered metamaterial consisting of two constituent materials with a strong dielectric contrast is therefore a simple strategy to achieve a strong form birefringence with large absolute values of $\Delta n = n_e - n_0 = \sqrt{\varepsilon_{eff\parallel}} - \sqrt{\varepsilon_{eff\perp}}$, where n_o is the refractive index of the ordinary wave and n_e the minimum refractive index of the extraordinary wave. Since for a layered arrangement $n_e < n_0$ $\left(\varepsilon_{eff\parallel} < \varepsilon_{eff\perp}\right)$, the layered metamaterial exhibits the birefringent properties of a negative uniaxial material.

The opposite case of extreme positive form birefringence can be obtained when an ensemble of parallel aligned infinitely long rods is considered. In this case the optical axis is aligned with the axis of the cylindrical rods (z-axis) and with $L_\parallel = 0$ it follows:

$$\varepsilon_{eff\parallel} = f\varepsilon_1 + (1 - f)\varepsilon_2 \tag{9.15}$$

This can also be derived from the continuity conditions for the E- and D- field when they are aligned along z and therefore parallel to the surface of the cylindrical rods. $\varepsilon_{eff\perp}$ in the long wavelength range can be obtained from the Maxwell–Garnett equation (9.11) assuming $L_\perp = 0.5$:

$$\varepsilon_{eff\perp} = \varepsilon_{ex} + \varepsilon_{ex} 2f \frac{\varepsilon_i - \varepsilon_{ex}}{\varepsilon_i + \varepsilon_{ex} - f(\varepsilon_i - \varepsilon_{ex})} \tag{9.16}$$

An example of a square arrangement of circular rods is shown in Fig. 9.6. The photonic bandstructure shows a clear splitting of bands 1 and 2, corresponding to the extraordinary and ordinary waves, respectively. Due to the homogeneity of the structure along z (infinitely extended rods) the polarization of the waves propagating within the Γ-X-M-Γ-plane (xy-plane) is split into TE and TM polarized waves represented by the red and blue photonic bands in the left section of the bandstructure in Fig. 9.6A. For propagation within the xy-plane this also shows, that the extraordinary waves belonging to band 1 (blue) are purely TM-polarized and the ordinary waves belonging to band 2 (red) are TE-polarized. Since the optical axis of the structure corresponds to the z-axis, the extreme values of the refractive index, $n_e = 1.57$ and $n_o = 1.12$, are obtained for waves traveling in the xy-plane. This correspondence of photonic bandstructures with concepts of crystal optics is supported by the equi-frequency contours taken for $\omega a/(2\pi c) = 0.1$ in Fig. 9.6B. The two shells represent the k-values of bands 1 (blue symbols) and bands 2 (red symbols) in the Γ-A-Z-plane. They show a very good agreement with the calculated values using the dispersion relation of ordinary $(k_x^2 + k_y^2 + k_z^2 = \varepsilon_{eff\perp} \frac{\omega}{c})$ and extraordinary waves $(\frac{k_x^2 + k_y^2}{\varepsilon_{eff\parallel}} + \frac{k_z^2}{\varepsilon_{eff\perp}} = \frac{\omega}{c})$ with $\varepsilon_{eff\perp}$ and $\varepsilon_{eff\parallel}$ coming from (9.16) and (9.15).

This demonstrates that in the long wavelength regime the effect of form birefringence can be well modeled by effective-medium concepts which take into account the specific shape of the scattering elements. This leads to a dielectric permittivity tensor, and using the concepts of crystal optics, allows the dispersion relation for extraordinary and ordinary waves to be extracted. Overall, this opens the possibility of determining the refractive index for polarized waves traveling along different directions.
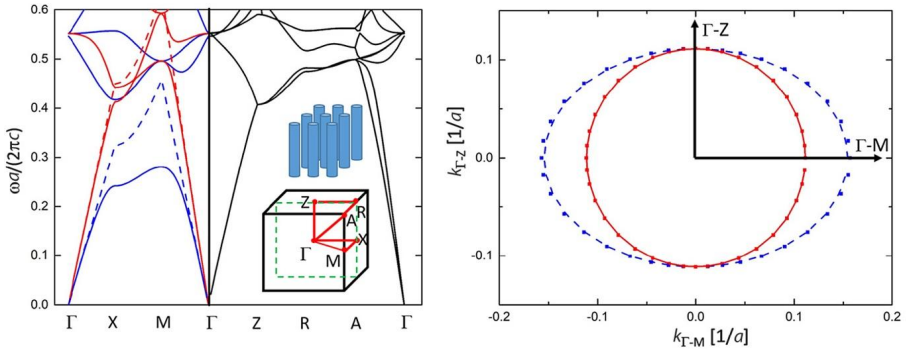
Figure 9.6 Dispersion relation for a square array of cylinders with $\varepsilon_i = 12$ in air with $r/a = 0.2$. (A) Photonic bandstructure. The left section Γ-X-M-Γ corresponds to the wave propagation perpendicular to the cylinder axis and agrees with the well-known photonic bandstructure of 2D photonic crystals which separates in TE-polarized modes (solid red) and TM-polarized modes (solid blue). For comparison the effective-medium approximations for both polarizations (TE, dashed red; TM dashed blue) according to (9.16) and (9.15) are shown. (B) Equi-frequency contours in the Γ-A-Z-plane for $\frac{\omega a}{2\pi c} \approx 0.1$ exhibiting two shells (represented by red and blue symbols): outer (blue) shell for extraordinary waves of band 1, inner shell of ordinary waves of band 2. For comparison the equi-frequency contours resulting from the dielectric tensor with the components $\varepsilon_{eff\perp}$ and $\varepsilon_{eff\parallel}$ from (9.16) and (9.15) are shown (red and blue lines).

9.2.3 Effective media beyond the quasi-static approximation

The assumption of a homogeneous external field surrounding the inclusions in the MG and Bruggeman formulas neglects the external dipole field from the inclusions. Furthermore, the restriction on spherical particles in the original MG and Bruggeman formulas often does not match the geometries used in experimental systems. Researchers have tried to find effective-medium formulas which better match specific cases and several of them can be considered as power law models described by Lichtenecker's mixture formula [7], where

$$\varepsilon_{eff}^{\beta} = f\varepsilon_1^{\beta} + (1 - f) f\varepsilon_2^{\beta}$$

Several different values have been considered for the exponent β. For $\beta = 1/3$ the well-known Looyenga formula follows and $\beta = 1/2$ results in a simple averaging of the refractive indices [3]. The exponent β can in principal vary between -1 and $+1$ where for the extreme cases of $\beta = -1$ or $\beta = +1$ the Wiener bounds from (9.14) are reproduced. The ambiguity of the exponent β is the result of shape variations of the inclusions. For a mixture of cigar-shaped and oblate-shaped inclusions a mix of different depolarization factors occurs, so that a certain β-exponent between -1 and $+1$ can be found to fit the experimental data. This was applied in the investigation of various soils containing differently shaped inclusions [7].

However, all these effective-medium formulas still assume quasi-static fields, where the wavelength is considered infinite compared to the size of the structure. However, in most metamaterials the scattering elements (inclusions) are not much smaller than the wavelength and for wavelengths approaching the onset of Bragg

diffraction the electric field varies markedly within a cell containing the scattering element and the surrounding media (see e.g. the field plot in Fig. 9.4). An approach by Alu [8] incorporates the phase factor $e^{i\mathbf{k}\cdot\mathbf{r}}$ in the averaging integral leading to $\mathbf{E}_{eff} = \frac{1}{V} \int \mathbf{E}(\mathbf{r}) e^{i\mathbf{k}\cdot\mathbf{r}} d\mathbf{r}^3$ and $\mathbf{P}_{eff} = \frac{1}{V} \int \mathbf{P}(\mathbf{r}) e^{i\mathbf{k}\cdot\mathbf{r}} d\mathbf{r}^3$. This approach takes into account that in an effective medium the wave will travel with a single dominating wavevector $\mathbf{k}$, which is included in the phase factor $e^{i\mathbf{k}\cdot\mathbf{r}}$ in the integral. In the last integral $e^{i\mathbf{k}\cdot\mathbf{r}}$ is developed into a Taylor series resulting in a multipole development of $\mathbf{P}_{eff}$. A similar treatment is also applied to $\mathbf{H}_{eff}$ and $\mathbf{M}_{eff}$. Applying Maxwell's equations for $\nabla \times \mathbf{E}$ and $\nabla \times \mathbf{H}$ and rearranging the multipole terms results in new forms of averaged $\mathbf{E_{av}}$, $\mathbf{H_{av}}$, $\mathbf{D_{av}}$, and $\mathbf{B_{av}}$ fields, which include contributions of several multipole terms from P and M. Even when keeping only the low-order dipolar terms of the **P** and **M** expansion the resulting newly defined averaged fields contain a magnetoelectric coupling where, for example, $\mathbf{B_{av}}$ contains a contribution from a magnetic dipole moment $\mathbf{M}_E$ which is created by a circular electric polarization ($\mathbf{M}_E \sim \int \frac{\mathbf{r} \times \mathbf{P}(\mathbf{r})}{2} d\mathbf{r}$). From such terms the artificially created magnetic response in high index dielectric Mie-resonant elements is derived. This treatment leads to newly defined versions of $\varepsilon_{eff}(k)$ and $\mu_{eff}(k)$ which depend on the wavenumber k and therefore contain a weak spatial dispersion. Due to their wavenumber dependence they are non-local constants. Using these new versions for $\varepsilon_{eff}(k)$ and $\mu_{eff}(k)$ the appearance of unphysical values for the effective parameters retrieved from experiments (see section 9.3) can be avoided [8]. To take higher-order forms of spatial dispersion into account Mnasri et al. considered up to four orders in an expansion of the **D**-field with respect to the E-field [9]. In addition, new interface conditions for the coupling of external plane waves to the metamaterial exhibiting non-local effective parameters had to be derived leading to alternative versions of Fresnel's equations. For the very long wavelength regime, where the wavelength is several times larger than the period or size of the scattering elements, the aforementioned advanced homogenization schemes lead to the local parameters attained, for example, from the Maxwell–Garnett effective-medium theory. For wavelengths shorter than the Bragg condition they also become inaccurate, so they are mainly useful in describing the effective parameters close to the resonances especially when high index Mie-resonant particles play a role. In the non-resonant case considered here, the simple effective-medium formulas are usually sufficient to gain a reasonable approximation. For exact simulations of underlying modes and wave propagation, plane-wave expansion methods (for periodic metamaterials) or finite element calculations have to be employed.

9.3 Experimental observation – retrieval methods of effective parameters

While in theory the effective dielectric constants can be derived from the shape of the scattering elements and their arrangement applying the aforementioned homogenization techniques for the local electric and magnetic fields inside the metamaterial, in experiments this is usually not possible. In addition, for experiments and applica-

tions the interaction of metamaterials with incident and transmitted waves is of much greater importance. The question of what dielectric constants a metamaterial exhibits is therefore only used as a simple way of describing the interaction of light with it and aims to allow simple predictions of amplitude and phase of transmitted and reflected waves. In this picture the metamaterial is just replaced by an effective material of the same outer geometric dimensions exhibiting a (possibly anisotropic) effective permeability and permittivity. The expected reflected and transmitted waves can then be obtained from the Fresnel formulas using the effective permeability and permittivity. On the other hand, the measurements of reflection and transmission coefficients can be applied to derive or retrieve the effective constants of the metamaterial [10]. In the literature this experimental retrieval of the effective parameters is almost exclusively used and known as the scattering parameter technique. While this concept usually works well in the extreme long wavelength regime, at shorter wavelengths – where a/λ approaches the Bragg condition – special care has to be taken.

It is obvious, that in cases where spatial dispersion appears and ε and/or μ depend on the wavevector (and with this also on the direction of propagation of the light through the metamaterial), a single dielectric constant cannot be defined. For the coupling of external light to the light propagating inside a spatially dispersive metamaterial more complicated interface conditions as e.g. discussed in [9] have to be applied or numerical solutions have to be found. However, several other effects also become important for larger a/λ ratios which are connected with the "granularity" of the metamaterial [Fig. 9.7]. Since the metamaterial ends at its surface or interface with another region, the local density of the elements at the surface/interface is different from inside the metamaterial. This influences the local field distribution so that the condition inside the metamaterial cannot be simply applied to the surface. This becomes clear when the two different surface regions marked by gray bars in Fig. 9.7 are considered. While in the bottom high symmetry surface layer the same density of elements appears as in the bulk of the metamaterial, the obliquely cut upper interface (S2) exhibits a step-like shape and the corresponding interface layer contains considerably less scattering elements. This has an impact on the surface impedance which can be connected to these two different surface layers and which is different from the bulk impedance, which is connected with the inside region of the metamaterial. In the retrieval procedure therefore the surface impedances from the surface layers would have to be taken into account [11]. Furthermore due to the inherent granularity of the metamaterial at obliquely cut surfaces (S2 in Fig. 9.7) a step grating can occur. Since the apparent surface period a_{S2} can be considerably larger than the inherent lattice period a in a metamaterial and the step height produces for an incidence wave a nonnegligible phase difference between the steps, diffraction can occur from the surface which is normally frustrated inside the metamaterial. The energy which is channeled into diffracted orders is then missing from the transmitted or reflected beams, so that a retrieval procedure, which is only based on the absolute values of zero-order reflection and transmission coefficients will necessarily derive incorrect values for ε and μ. In addition scattering losses due to roughness of fabricated elements complicate the accurate determination of absolute values of reflection and transmission coefficients.
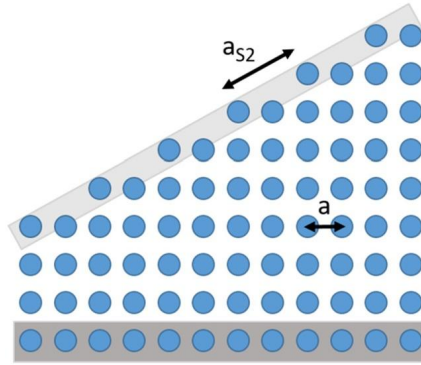
Figure 9.7 Sketch of a metamaterial highlighting the different applicable element densities and lattice constants near differently cut surfaces.

Therefore, in the following section a method is presented which can be used to experimentally derive the group velocity or group index. Assuming negligible dispersion in the long wavelength regime the refractive (phase) index can also be determined. The technique is based on the spectroscopic measurement of normal incidence transmission or reflection from a metamaterial slab. When the light is incident on the slab the multiple reflections from the top and bottom interface of the metamaterial lead to Fabry–Pérot oscillations in the transmission spectrum. The condition for the appearance of a maximum in transmission is $\pi m = k_m d$, where the number m is the order of the Fabry–Pérot resonance and d is the geometric thickness of the metamaterial. The wavenumber k_m describes the wavenumber inside the metamaterial and thus incorporates the effective refractive index into the model. From the difference in the conditions for resonances m and $m + 1$ one obtains the equi-distant spacing of the resonances in k-space of the material $\Delta k = \frac{d}{\pi}$. As the spectral difference of the transmission maxima $\Delta \omega$ can be measured, the group velocity can be determined via

$$v_g = \frac{d\omega}{dk} \approx \frac{\Delta\omega}{\Delta k} = \frac{\pi}{d}\Delta\omega \tag{9.17}$$

When a constant effective refractive index n_{eff} can be assumed (e.g. in the long wavelength regime) n_{eff} can also be obtained from (9.17): $n_{eff} = \frac{c}{v_p} \approx \frac{c}{v_g}$.

This analysis was carried out for a macroporous silicon photonic crystal in the long wavelength range [Fig. 9.8]. In the transmission spectrum for light propagating along the pores, whose diameter is modulated periodically with pore depth (see the inset SEM image), two spectral ranges (500–1150 cm^{-1} and 1400–2250 cm^{-1}) with Fabry–Pérot oscillations occur and are separated by a region of zero transmission which corresponds to the stop band caused by the periodic diameter modulations of the pores. From the bandstructure along the pores (Γ-A-direction) it can be seen that below and above the stop band only a single band exists which can transmit light. Determining the maxima of the Fabry–Pérot oscillations from the spectra (indicated by horizontal blue dashed lines) and using (9.17) the absolute value of the group ve-
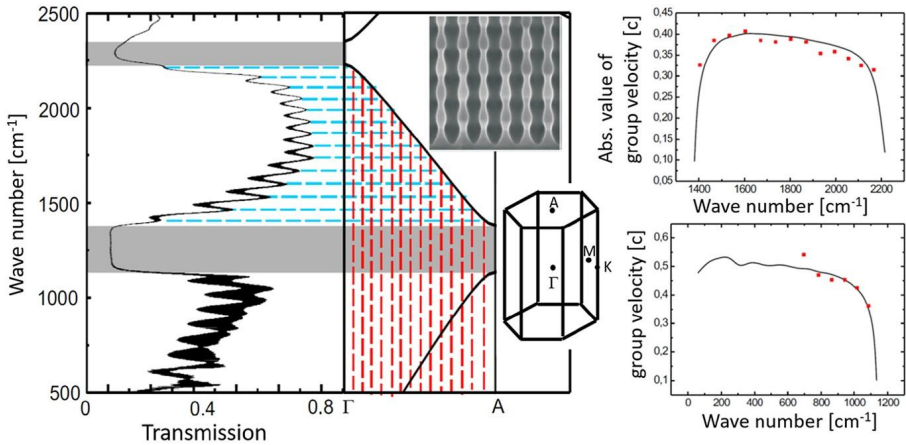
Figure 9.8 Determination of group velocity based on Fabry–Pérot oscillations in transmission applied to a macroporous Si photonic crystal in the long wavelength range. The small insets show an SEM cross section of the macroporous Si structure revealing the periodic modulation of pore diameter with pore depth and a sketch of the corresponding hexagonal Brillouin zone indicating the Γ-A-direction. On the right the modeled group velocity (solid black) and the experimentally determined group velocity (red markers) in frequency ranges above and below the stop band are compared.

locity for the band below, and even above, the stop gap is determined [Fig. 9.8 (right)]. Comparing the experimentally determined values (red dots) with values obtained from bandstructure calculations (solid lines) a good correspondence is obtained. Even the drop of group velocity close to the band gap due to the increased band bending can be observed. The vertical red dashed lines in Fig. 9.8 represent the projection of the Fabry–Pérot resonances onto k-space and, as expected, a constant spacing Δk exists. In the long wavelength regime below about 900 cm^{-1} a nearly constant effective refractive index of about 2.2 is found.

The method is much less affected by losses as the determination of the group velocity, and possibly the effective refractive index at long wavelengths, is only dependent on the accurate extraction of the spectral position of the Fabry–Pérot maxima from the transmission spectra. As the technique is an interference technique it measures the transmission phase which is directly dependent on the bulk effective refractive index. The impact of possible surface layers is reduced, especially for thick metamaterial samples. This method can be extended by measuring the transmission at different angles of incidence resulting in spectral shifts of the Fabry–Pérot oscillations with increasing angles of incidence. An evaluation of these shifts was also used to experimentally map the equi-frequency surfaces of hyperbolic metamaterials [12,13].

A related method, which is also based on the propagation phase, which the light picks up when passing through the metamaterial, can be used to determine the birefringence, $\Delta n = n_e - n_0$, of an anisotropic metamaterial. For this purpose, the light has to propagate in a uniaxial metamaterial perpendicular to the optical axis so that the extraordinary beam and the ordinary beam propagate along the same direction through the metamaterial. Depending on the thickness, d, of the metamaterial both waves ob-
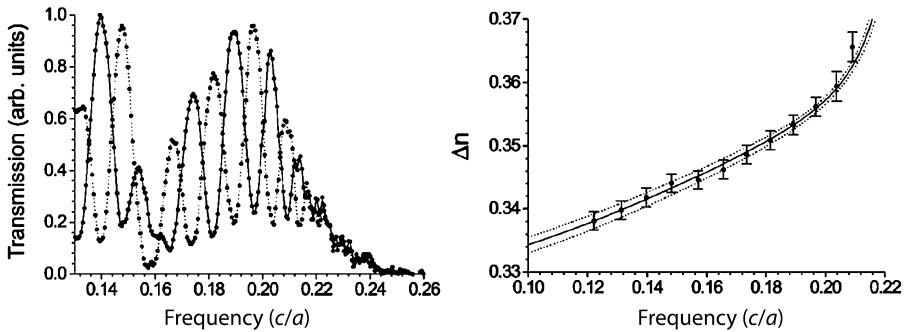
Figure 9.9 Experimental determination of the birefringence in the long wavelength regime of a 2D macro-porous silicon photonic crystal. Left: Transmission perpendicular to the pore axis with parallel (solid curve) and crossed polarizers (dotted curve). Right: variation of the birefringence in the long wavelength regime reaching a maximum of $\Delta n = 0.36$ close to the Bragg band gap. Reproduced with permission from [14], © IOP Publishing, All rights reserved.

tain then a relative phase difference, $\Delta\varphi = \Delta n k_0 d = \Delta n \frac{\omega}{c} d$, after penetrating the metamaterial. To excite both ordinary and extraordinary waves, the incident light is usually polarized 45° with respect to the optical axis. Another polarizer is placed behind the sample which can be aligned parallel or crossed to the one on the incident side. When $\Delta\varphi = 2\pi m$ ordinary and extraordinary beam are in phase and for parallel polarizers a maximum in transmission is realized while for crossed polarizers a minimum in transmission is realized. On the other hand when $\Delta\varphi = (2m+1)\pi$ both beams have opposite phase resulting in a 90° polarization flip of the superimposed light wave and an intensity minimum for parallel polarizers, and a maximum for crossed ones, is achieved. Determining the light frequencies of neighboring maxima and minima (ω_m and ω_{m+1}) then allows one to derive Δn via $\delta(\Delta\varphi) = \pi = \Delta n \frac{d}{c}(\omega_{m+1} - \omega_m)$ assuming a piece-wise constant Δn.

The method was applied to determine the birefringence in a 2D macroporous silicon photonic crystal [14]. The light was transmitted perpendicular to the straight pores and the polarizer on the incident side was aligned 45° with respect to the pore axis (optical axis) as outlined above. The measured anticyclical oscillating behavior of transmission for parallel and crossed polarizers is shown in Fig. 9.9 (left). From the spectral positions of the minima and maxima the birefringence was determined as described in Fig. 9.9 (right). The observed birefringence lies above 0.3, reaching a maximum of 0.36 close to the Bragg gap. Thus, it is a factor 43 higher than for usual quartz crystals. This impressively shows the strong anisotropy which can be obtained in structures exhibiting form birefringence. Form birefringent metamaterials consisting of high index contrast materials can therefore be employed in polarization-sensitive phase shifting devices and wave plates.

9.4 Spatial variation of effective dielectric constant – graded index (GRIN) photonics

The ability to control the refractive index locally over a larger range became especially important with the advent of transformation optics, which provides a mathematical technique to derive a suitable GRIN-profile to achieve a desired arbitrary light path based on a coordinate transformation (mapping) of light propagation in a virtual space. In this approach controlling the refractive-index landscape using a GRIN-material allows molding the flow of light. Although this method provides a quite universal tool to arrive at a permeability μ and permittivity ε landscape, which would warrant the desired ray propagation, some of these theoretically derived ε and μ distributions are difficult or impossible to realize – especially when they involve extreme, complex or extremely anisotropic values of ε or μ. These complications are partially alleviated when only the propagation within a plane (2D) is investigated and several devices have been realized employing GRIN-structures e.g. in a silicon-on-insulator (SOI) waveguide layer geometry [15–24]. In addition, the designed 2D nanostructures can be fabricated in a relatively straightforward fashion by applying established lithography and plasma etching techniques. In the following, several examples of devices are described which are based on GRIN-structures. They are grouped together according to their number of structured spatial dimensions and light propagation direction.

(a) Metasurfaces – 2D structures, light propagation perpendicular to plane

Metasurfaces are 2D planar structures exhibiting tailored reflection and transmission properties for light which is normally incident on them. They are often used to imprint a specific locally varying phase landscape onto the incident beam. A straightforward approach to achieve this position dependent phase control is based on the acquisition of *propagation phase* upon transmittance through a dielectric layer with a space-variant refractive index. This can be achieved by nanostructuring a silicon film on a deep-subwavelength scale, yielding effective refractive-index values, depending on the local silicon filling fraction. In contrast to conventional diffractive optical elements, which require control of the local film thickness, this concept allows for the realization of a range of phase values with a single lithographic step. A simple example for this approach is the fabrication of effective-index phase gratings where the fill factor varies gradually within each period of the grating resulting in a gradual effective-index change within each period [Fig. 9.10A] [25]. This imprints a periodic variation of the phase on the transmitted wave and leads to an efficient first-order diffraction similar to a blazed grating. However, contrary to a blazed grating which involves the accurate generation of a sloped subwavelength profile the effective-index grating involves only a single lithography and etch step. Various functional optical devices were realized along these lines, including focusing lenses for visible, near-infrared and THz radiation based on silicon posts or subwavelength hole arrays in silicon slabs with spatially varying density or radii [26,27]. These structures were already covered extensively in Chapter 6 with a brief summary provided here.

However, the anisotropy of the effective refractive index of designed elements can also be employed to achieve locally varying phase changes and as a result also com-
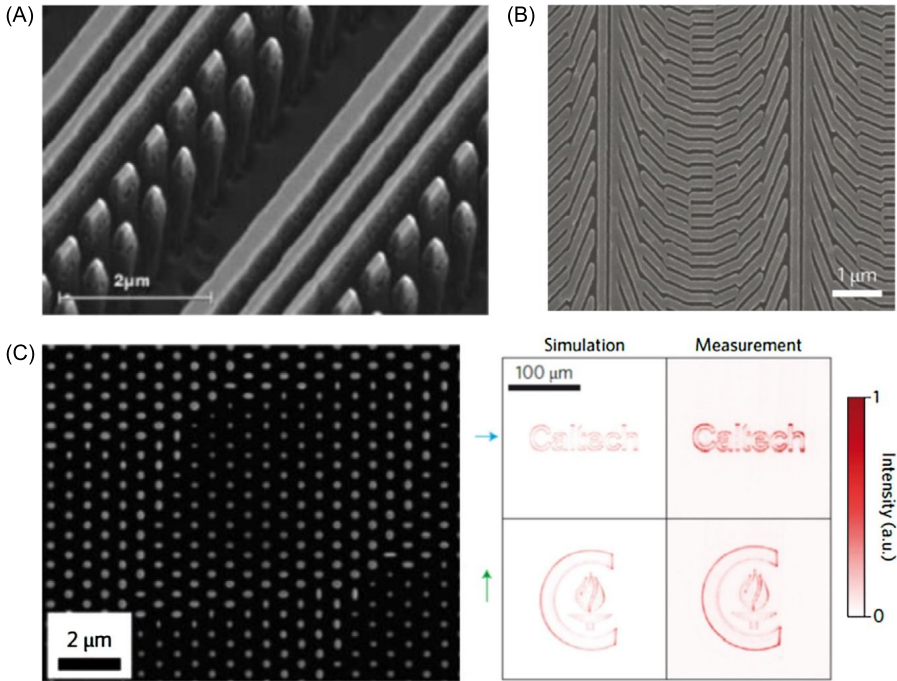
Figure 9.10 Non-resonant metasurfaces (A) Scanning-electron micrograph (SEM) of a highly efficient grating for satellite applications utilizing the effective-medium concept. Reprinted with permission from [25]. (B) SEM image of a blazed grating realized by silicon metasurfaces imprinting a space-variant geometric phase. From [29], reprinted with permission from AAAS. (C) SEM (left) as well as the simulated and measured generated images for horizontal and vertical linear polarization of a polarization-sensitive silicon metasurface hologram consisting of silicon posts with spatially varying elliptical cross section. Reprinted with permission from [33].

plete changes of polarization. An interesting example of how this can be used to create quite complex phase landscapes with a photonic metasurface relies on the acquisition of Pancharatnam–Berry phase, a geometric phase originating from space-variant polarization manipulations [28–30]. This can be accomplished by tiling a surface with wave plate elements for which the orientation of the fast axes depends on the in-plane position [Fig. 9.10B]. Such elements can be realized by silicon nanobeams [29] or nanofins [30] with space-variant orientations (see Fig. 9.10B). For example, an arrangement of half-wave plates with their fast axes orientations following a function $\theta(x, y)$, will transform an incident circularly polarized light beam to a beam of opposite helicity and imprinted with a geometric phase equal to $\phi_g(x, y) = \pm 2\theta(x, y)$. A sizable geometric phase can be achieved when the elements, which are used to create the local half-wave plates (e.g. aligned rods), exhibit a Mie resonance for one polarization leading to an enhanced phase shift for this polarization [29].

A method related to the effective-index approach is transmission through planar arrangements of high-aspect-ratio silicon posts, as it also depends on the acquisition of a spatially varying propagation phase [31]. This concept was demonstrated

in nanostructured TiO$_2$ films in the 1990s [32]. For appropriately chosen feature sizes, such posts function as upright-standing waveguides, with the lateral dimensions of the waveguides determining the propagation constant and its finite vertical dimensions introducing low-quality-factor Fabry–Pérot resonator behavior and allowing for high transmittance efficiency. Elliptically shaped cross sections allow for simultaneous control of both phase and polarization, thereby enabling the realization of polarization-sensitive devices and the generation of arbitrary vector beams [Fig. 9.10C] [33].

Besides the prospect of replacing bulky optical components by ultra-flat optical devices, one of the main driving factors for metasurfaces is the capability of combining several functionalities in a single structure. For instance, wavefront shaping devices can at the same time control the polarization, or be polarization-selective, owing to the capability of generating any desired spatially varying polarization and phase profiles by a silicon metasurface [33,30].

(b) 2D structures, light propagation within the plane

The graded index concept can also be employed to control the propagation of light within the structured plane. When the structured layer exhibits an effective index which is higher than the surroundings above and below, the light is confined by total internal reflection to it, forming a horizontal waveguiding layer. Several gradient index metamaterials have been realized by employing SOI-substrates as the material platform. There are two basic strategies to design an effective refractive-index variation by varying the local filling fraction within the plane:

(1) Varying the distances between the structural building blocks (e.g. high index rods/ low index pores) but leaving the size of the scattering elements constant,

(2) varying the size of the scattering elements (e.g. their diameter) but enforcing a locally regular/periodic placement of elements.

The first strategy was realized using a dithering technique (Fig. 9.11A, B) [22]. For this purpose the continuously varying ("gray-scale") index map has to be digitized in a density map of individual scatterers varying the distance between the scatterers. This leads to arrangements which are locally reminiscent of QR-codes. However, the dithered structures also exhibit scattering losses due to the irregular placement of the scatterers. To minimize these scattering losses, the second strategy – using the periodic placement of scatterers – is advantageous. Due to the local subwavelength periodic (crystalline) grid of scatterers diffraction is frustrated [35] and scattering losses are lowered. To achieve a variation in effective index the strength of each scatterer is controlled (e.g. by adapting the width of individual rods/pores). Using a hexagonal arrangement of rods/pores the maximum range of effective refractive indices can be realized [18]. Periodic 2D arrangements of silicon rods or pores were e.g. used to realize carpet cloaks [Fig. 9.11C] [23] or an optical "Janus" device, which allows different functionalities in two directions perpendicular to each other [20]. Furthermore, a planar Lüneburg lens, which focuses an horizontally propagating extended wave onto a spot at the opposite rim of the circular planar lens area, was developed [18].

Although the characteristic structure sizes are small enough so that Mie or Bragg resonances do not play a role, dispersion is still observable in these planar SOI-based
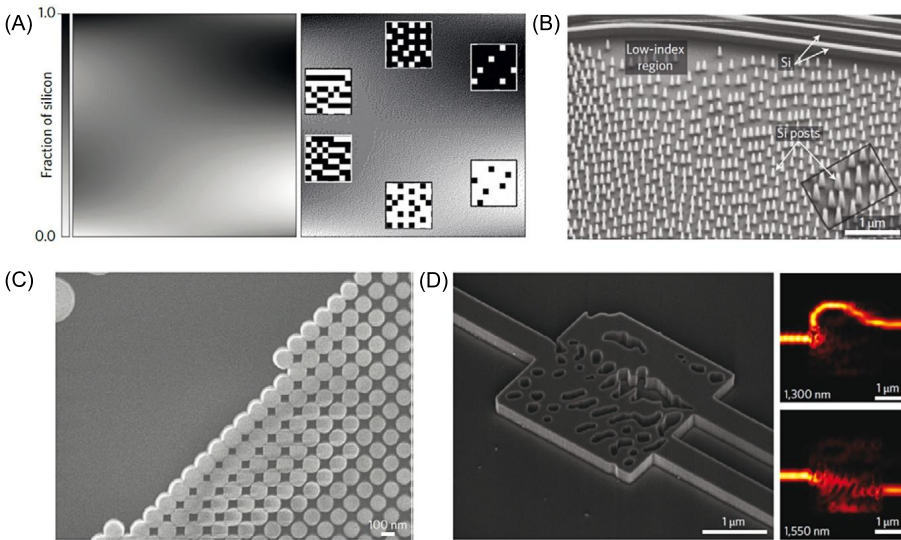
Figure 9.11 2D planar GRIN-structures for in-plane propagation. (A) Digitization of a continuous index map (left) to irregular arrangements of individual Si-posts using a dithering technique. Reproduced with permission from [22], © IOP Publishing, All rights reserved. The local effective index depends on the local density of the scatterers. (B) SEM-Detail of a carpet cloak based on the dithering technique. Reprinted with permission from [21]. (C) SEM-detail of a similar carpet cloak based on periodically arranged rods, where the effective index is controlled by locally adjusting the diameter of the rods leading to lower Raleigh scattering losses. Reprinted with permission from [23]. (D) Left: SEM image of a compact and broadband on-chip waveguide demultiplexer as an example of a free-form metamaterial device, whose structure was determined by an inverse-design computer algorithm. Reprinted with permission from [34]. Right: the operation of the splitter was observed for the wavelengths 1300 nm and 1550 nm.

structures, as the finite height of the building blocks introduces horizontal waveguide dispersion to the structures. This becomes crucial when longer wavelengths (e.g. $\lambda > 1550$ nm) are considered, which lie beyond the cut-off of the horizontal waveguide mode and therefore lead to substantial radiation losses [23]. On the other hand this waveguide dispersion can be used intentionally to create a smoothly varying effective refractive index within the plane by locally controlling the thickness (height) of the waveguide layer. Using a gray scale mask for etching, a Lüneburg lens was implemented by a continuously varying index profile [17].

(c) Subwavelength structured waveguides – 1D structured, light propagation along waveguide

Besides the use of 2D metamaterial slabs for full scale planar transformation optic devices, periodic subwavelength sized structures were also used in simpler geometries. A chain of 300 nm wide and 150 nm thick Si-posts with a period of 300 nm was prepared from SOI-substrates and represents a subwavelength grating waveguide (SWG) [Fig. 9.12A]. Since the period is below the onset of Bragg diffraction, the waveguide exhibits an effective mode index in the NIR which depends on the duty cycle of the posts. This provides a convenient way to adjust the effective index of the
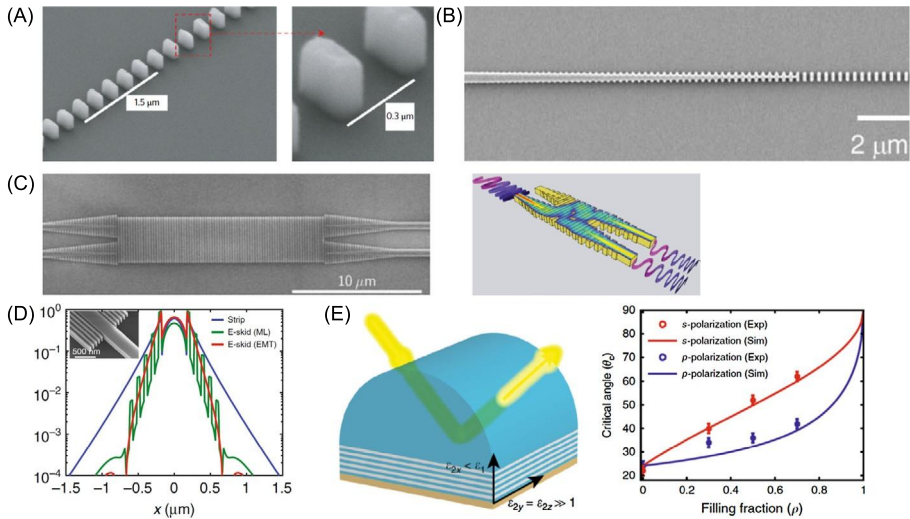
Figure 9.12 Subwavelength structured waveguides (A) Subwavelength grating waveguide consisting of a 1D periodic array of silicon blocks with periods below the onset of Bragg diffraction. Reprinted with permission from [36]. (B) Subwavelength grating waveguide taper with a gradual variation of effective waveguide core index. Reprinted with permission from [37]. (C) Broadband beamsplitter based on multimode subwavelength grating waveguide. Reprinted with permission from [38]. (D) Field confinement in an E-skid waveguide with anisotropic cladding showing enhanced electric field confinement compared with a classic strip waveguide. Reprinted with permission from [39]. (E) Investigation of total internal reflection from layered anisotropic metamaterial. Dependence of critical angle of total reflection on polarization (right). Reprinted with permission from [39].

waveguide core by controlling the duty cycle (filling factor) and forms the key characteristic of these waveguides which can be exploited for several applications. Low duty cycles (large air gaps) lead to smaller mode indices resulting in extended mode profiles which can be matched better to the large mode profiles of fibers allowing a more efficient but coupling. Increasing the duty cycle (smaller air gaps and gradual introduction of solid core) increases the effective mode index resulting in a gradually stronger mode confinement [Fig. 9.12B] [37]. Waveguide tapers for improved fiber – chip coupling can be designed in this way [38,40,41]. Since the waveguide corresponds to a layered (stratified) effective medium along the propagation direction the Wiener equations (9.14) can be applied as a first approximation to calculate an effective dielectric constant along the z-direction (propagation direction) and perpendicular to it [38]. For the waveguide propagation along z one would therefore be tempted to conclude an effective index of $n_{zz} = \sqrt{\varepsilon_{eff\parallel}}$. However, due to the confinement of the light to the waveguide by total internal reflection the wave also has a field component along the propagation direction (E_z), so that the mode index is actually a mixture of $n_{zz} = \sqrt{\varepsilon_{eff\parallel}}$ and $n_{xx} = \sqrt{\varepsilon_{eff\perp}}$. To obtain the exact mode indices a full 3D simulation has to be performed. This was used to obtain broadband beamsplitter operation employing a multimode SWG section [Fig. 9.12C]. Here the incoming wave in one port excites two or more modes of the central broad multimode SWG section which

propagate with different individual propagation constants β_1 and β_2. The beat length between the modes L_π (which is important for the transfer of "images" of the incoming mode to the exit port) depends on the ratio of $\frac{n_{zz}^2}{n_{xx}}$: $L_\pi \approx \frac{4W^2}{3\lambda} \frac{n_{zz}^2}{n_{xx}}$, where W is the waveguide width. Due to $n_{zz} < n_{xx}$ a short beating length results. Furthermore the normal dispersion n_{zz} and n_{xx} compensate the influence of λ on L_π partially leading to a weak overall dispersion of L_π [38]. In addition a low 2,1 dB/cm loss of the waveguides was observed, which is comparable to usual silicon-strip waveguides [36] and mode converters [35]. Furthermore, waveguide crossings with low cross-talk and only minimal loss were created [42].

Another subwavelength structured waveguide geometry consists of a solid core and has a layered subwavelength cladding [Fig. 9.12D] [39]. The cladding acts as an anisotropic layered metamaterial whose effective dielectric properties can again be approximated by the Wiener formulas (9.14). However, now the optical axis of uniaxial metamaterial is oriented perpendicular to the propagation direction. For the geometry shown in the inset of [Fig. 9.12D] and TE-like waveguide modes a faster evanescent decay of the electric mode field than in air can be obtained resulting in a considerably better mode confinement. This unusual property is connected with the TE-like modes, which couple to the extraordinary waves of the anisotropic cladding which has a ratio $\frac{\varepsilon_{eff\perp}}{\varepsilon_{eff\parallel}} > 1$. This can be understood by considering the geometry of [Fig. 9.12E, left]. When a p-polarized wave (corresponds to TE-like wave in waveguide) from the isotropic material with refractive index n_1 (represented by the top hemisphere) is incident on the subwavelength multilayer metamaterial with effective dielectric tensor $\begin{pmatrix} \varepsilon_{2x} & 0 & 0 \\ 0 & \varepsilon_{2y} & 0 \\ 0 & 0 & \varepsilon_{2z} \end{pmatrix}$, where $\varepsilon_{2z} = \varepsilon_{2y} = \varepsilon_{eff\perp}$ and $\varepsilon_{2x} = \varepsilon_{eff\parallel}$, it couples to the extraordinary waves with the dispersion relation,

$$k_x = \sqrt{\varepsilon_{eff\perp} k_0^2 - \frac{\varepsilon_{eff\perp}}{\varepsilon_{eff\parallel}} \left(k_y^2 + k_z^2 \right)} \qquad (9.18)$$

The critical angle of total reflection θ_c then occurs for $k_x = 0$ and with $k_y^2 + k_z^2 = (\sin\theta_c \, n_1 k_0)^2$ the critical angle becomes $\theta_c = \arcsin\left(\frac{\sqrt{\varepsilon_{eff\parallel}}}{n_1} \right)$. Therefore, as long as $\varepsilon_{eff\parallel} < n_1^2$ total internal reflection can occur. Interestingly this condition does not include $\varepsilon_{eff\perp}$ and thus $\varepsilon_{eff\perp}$ can be much larger than n_1^2 and the condition of total internal reflection can still be fulfilled. This offers considerable design freedom and leads to the observed faster evanescent decay. With (9.18) k_x takes the imaginary values $k_x = i \sqrt{\frac{\varepsilon_{eff\perp}}{\varepsilon_{eff\parallel}} (\sin\theta n_1 k_0)^2 - \varepsilon_{eff\perp} k_0^2}$ for angles of incidence θ, which are larger than θ_c. This has to be compared to the case of a classic isotropic cladding material with $\varepsilon_2 = n_2^2 < n_1^2$, where $k_x = i \sqrt{(\sin\theta \, n_1 k_0)^2 - \varepsilon_2 k_0^2}$. For layered metamaterials the Wiener formulas result in $\varepsilon_{eff\perp} > \varepsilon_{eff\parallel}$ (see also Fig. 9.3), so that $\frac{\varepsilon_{eff\perp}}{\varepsilon_{eff\parallel}} > 1$ results in a faster rise of the imaginary values of k_x for the anisotropic cladding than for an isotropic one. For anisotropic metamaterials consisting of layers with vastly different dielectric constants the ratio $\frac{\varepsilon_{eff\perp}}{\varepsilon_{eff\parallel}}$ can become quite prominent leading to a strongly

reduced skin depth of the evanescent field, reduced cross-talk between neighboring waveguides and three times reduced bending losses [39].

Further reviews of subwavelength structured waveguides for refractive index engineering in silicon photonics including fully etched, broadband grating couplers as well as directive and multimode interference couplers can be found in [43] and [44].

Apart from these analytical design strategies, different numerical algorithms have been developed, which allow a computer to design and optimize free-form metamaterial structures to fulfill specific purposes. These algorithms are based on an inverse-design strategy, where the desired functionality enters the algorithm as an input. In this way compact, on-chip integrated mode converters [45], waveguide splitters [46], broadband wavelength demultiplexers [34] and polarization beam-splitters [47] have been demonstrated.

(d) 3D dielectric metamaterial

Due to the aforementioned fabrication difficulties, the creation of deliberately designed highly controlled metamaterials is mostly limited to 2D planar structures. An exception are the three-dimensional invisibility cloaks created by direct laser writing by Wegener et al. [48,49]. Here, a woodpile structure based on a polymer is created using two-photon polymerization by a highly focused laser. Applying a stimulated-emission-depletion (STED)-inspired technique the rod spacing in the woodpile structure can be reduced from $a = 800$ nm down to $a = 350$ nm [49]. The wavelength ranges for which cloaking is observed are in the mid-IR for the larger, and in the visible, for the smaller rod spacing. In both cases the woodpile structure operates at frequencies below the photonic bandgap, so that an effective refractive index can be assigned. Adjusting the volume filling fraction of the woodpile structure around a bump in a gold surface allows one to tune the effective refractive index from about $n = 1.5$ close to the bump to about $n = 1.1$ about 5 µm away. Due to this effective index profile the bump is hidden in bright and dark field microscopic images even when unpolarized, relatively broadband, light is incident under a wide range of angles.

Apart from these highly controlled structures the concept of 3D-GRIN-structures can also be applied to thick self- or disordered 3D structured layers, which can naturally form during specific deposition or etching processes. Avoiding reflection losses are an important topic in many optical applications, such as photovoltaics, lighting, and imaging. In solar cells reflection has to be reduced to a minimum to couple as much sun light as possible into the absorber material for a maximal photo current [50]. A conventional approach to reduce reflection between two materials, for example air (or an encapsulation material) and silicon, in silicon solar cell, is the deposition of a dielectric planar thin film at the interface. This coating should have a thickness of $\lambda/4$ so that the light wave reflected from the top interface of the coating and the wave reflected from the bottom interface interfere destructively, ideally resulting in $R = 0$ for a particular design wavelength λ_{des}. Fig. 9.13A shows the reflectance of such an AR coating applied to an air/silicon interface (violet line). Compared to the bare interface (gray dashed line), the average reflection is reduced considerably from 35.6% down to 11.0% for the wavelength range of 350 to 1100 nm.
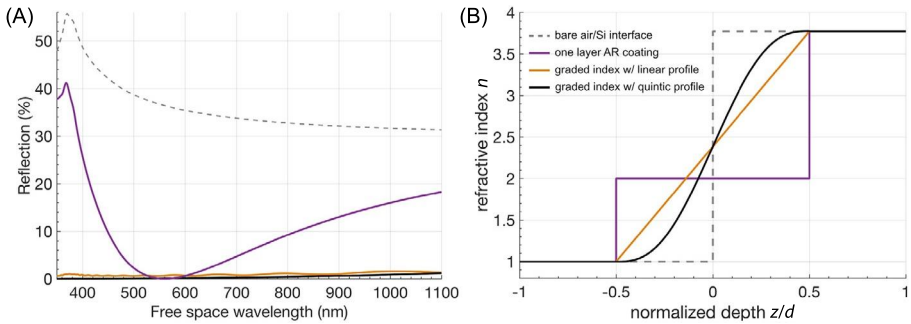
Figure 9.13 (A) Reflection of a planar air/silicon interface with different refractive index profiles at the interface under normal light incidence. The considered profiles (for free space wavelength $\lambda = 700$ nm) are depicted in (B): The bare air/silicon interface, a 70 nm thick coating with constant refractive index of $n = 2$, a linear, and a quintic profile (both 750 nm thick). For silicon, the refractive index has been taken from Green.

A drawback of these types of AR coatings is that they only minimize reflection for a particular wavelength. Additionally, their performance is strongly dependent on the angle of incidence. This is particularly a drawback for solar cells since the solar irradiation is spectrally broadband and its angle of incidence changes during the course of the day.

Much better AR performance is possible by a coating with a refractive index that gradually changes from the refractive index of the one medium to the refractive index of the other medium. Due to avoidance of abrupt changes of the refractive index, Fresnel reflections are strongly reduced. As Fresnel reflection depends on the difference of the refractive indices of two adjacent media, $R = (n_2 - n_1)^2/(n_2 + n_1)^2$, a layer with a gradient refractive index can be considered as a sequence of many sublayers with very little reflection. Vanishing light reflection, $R = 0$, can only be achieved by an infinite graded index layer. However, gradient layers with thicknesses in the range of the wavelength of the incoming light already perform much better than the conventional AR coatings with regard to the value of reflection, spectral bandwidth, and angular sensitivity [51].

The reflectance of a gradient index layer with a linear profile is plotted in Fig. 9.13A (orange line). Compared to a conventional AR coating the reflectance is significantly lowered over the whole spectrum to values between 0.5% and 1.6% – the averaged reflectance over the shown spectral range is 1.0%. This can even be further lowered by using other profiles, such as a quintic profile that has a continuous first and second derivative and is considered to perform best regarding AR [51]. For the quintic profile, the averaged reflectance is as low as 0.4% (black line in Fig. 9.13A). For comparison, in Fig. 9.13B the refractive-index profiles of the bare air/silicon interface, the one layer AR coating, and the linear and the quantic graded index layers are shown.

Realizing such a gradient refractive-index profile with a homogeneous material is impossible due to the lack of materials that provide the whole range of different refractive indices needed. However, structures exist that allow for such gradient refractive-index profiles. These structures are essentially porous on length scales smaller than the
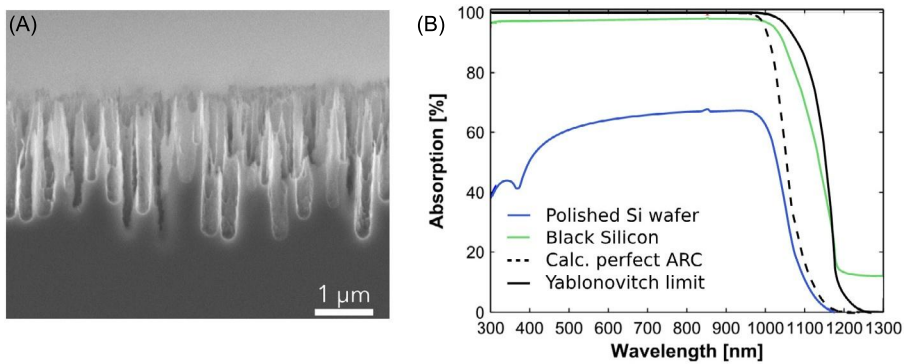
Figure 9.14 (A) Scanning electron micrograph of a typical black silicon interface fabricated by reactive ion etching. (B) Measured absorption of a bare silicon wafer (blue line) and a black silicon wafer (green line). Thickness of the wafers is 250 μm.
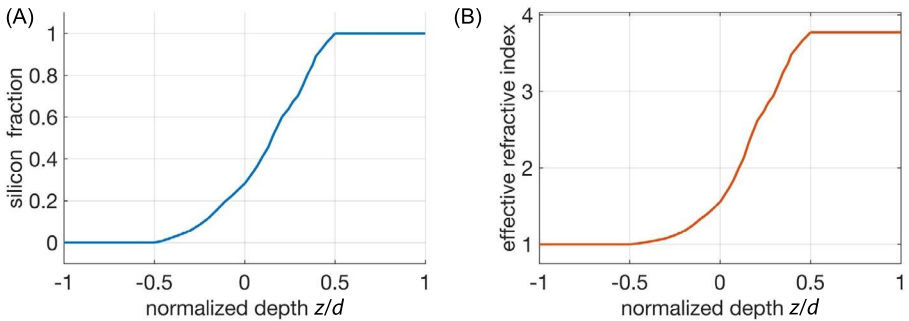
Figure 9.15 (A) Experimentally determined filling fraction of a typical black silicon interface fabricated by reactive ion etching plotted versus the normalized depth, i.e. from the air side to silicon. (B) Effective refractive index according to the Bruggeman theory (for $\lambda = 700$ nm).

wavelength of light, with a varying degree of porosity, which translates into a gradient refractive index.

One famous example of a porous material for AR is black silicon [52]. Black silicon is a strongly nano- or microtextured silicon surface which consists of stochastically arranged tapered silicon needles with feature sizes in the nanometer to the micron range; see Fig. 9.14A. Such textured silicon surfaces offer a broadband and quasi-omnidirectional strong antireflection such that it appears black to the naked eye (green line in Fig. 9.14B).

The strong antireflection properties of black silicon surfaces can be understood when considering the volume fraction of silicon at its interface.

Fig. 9.15A shows the silicon material fraction of a typical black silicon interface deduced by FIB slicing. Trivially, the filling fraction gradually increases from the small silicon tips pointing to the air side towards the thicker parts of the silicon needles until the bulk is reached. From this filling fraction one can deduce an effective refractive index according to the Bruggeman model by finding the zeros of Eq. (9.9). The results

are plotted in Fig. 9.15B and reveal a gradient refractive-index profile similar to that of the smooth quintic gradient profile shown in Fig. 9.13B, thus explaining the superior AR properties of black silicon textures.

Unfortunately, effective-medium theories as the Bruggeman model can only be applied to black silicon to a limited extent and give only a qualitative explanation. This is due to the fact that the condition for applying effective-medium theories, i.e. that all feature sizes of the structure are much smaller than the wavelength, is not always fulfilled. For example, the correlation length L_C, which is the statistically averaged distance between the scatterers is typically just smaller than, or in the range of, the incoming free space wavelength (here: 400–1000 nm) [53]. Inside silicon, the wavelength becomes even smaller than L_C due to the high refractive index of silicon ($n = 3.5$) given that the wavelength in the material is $\lambda = \lambda_0/n$. Thus, black silicon structures might appear subwavelength on the air side but not from the silicon side. As a consequence, wave propagation within the black silicon interface usually cannot be assumed to be plane-wave-like as effective-medium theory demands. As the correlation length increases, the spatial frequency distribution becomes more narrow which results in an increase in reflection losses. However, black silicon interfaces with a broadband reflectance of around 1%, and even less, have been experimentally demonstrated and integrated into solar cells [54–56]. Even commercial crystalline silicon solar cells exploiting black silicon for AR have recently been introduced into the market by Wuxi Suntech Power Co., Ltd [57].

9.5   Disordered metamaterials

Even if perfectly periodic metamaterial structures are intended, real-world structures will always possess at least a small amount of disorder such as slightly varying geometries within each unit cell due to unavoidable fabrications inaccuracies. In some cases, this kind of disorder is intentionally introduced as it can lead to a spectrally more broadband performance, a property that is especially helpful for applications that need to operate in a broadband manner, such as solar cells or lighting systems. Instead of starting from a periodic pattern and introducing disorder one can also start from the other end and take a random distribution of elements and introduce positional correlations, for example by forcing a mean average distance between neighboring elements. How different degrees of disorder influence the light propagation in metamaterials is an interesting but also complex question.

An intuitive and common tool to characterize the degree of order of a structure is to look at its spatial Fourier transform. If the elements of the structure are identical, one can even only look at the Fourier transform of the corresponding point pattern, where each point corresponds to one element of the metamaterial structure. By doing so one can, at least in a first approximation in which the near-field interactions between the elements are neglected, separate the optical response of the single element from the influence of the specific arrangement of the elements. The Fourier transform of a point pattern is called structure factor $S(q)$, with q being the spatial frequency. $S(q)$ can be
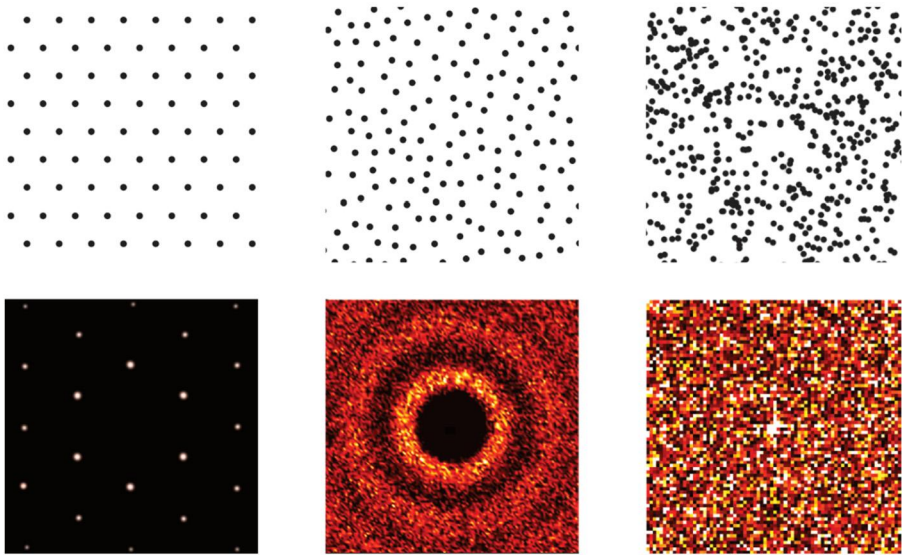
Figure 9.16 Classes of differently ordered metamaterials. Each point in the upper row represents a metamaterial element in real space, whereas the Fourier transform of the point pattern, the structure factor, is plotted in the bottom row. When a strict periodic order of metamaterial elements is maintained (left column), the structure is crystalline and the metamaterial corresponds to a photonic crystal exhibiting sharp peaks in the spectrum of the structure factor. For completely random structures (right column) allowing also agglomeration of scatterers the structure factor corresponds to "white noise" without any certain features. Structures of correlated disorder (center column) are comparable to amorphous structures where the distance between neighboring elements is quite well defined. The case shown here is disordered point pattern with strong correlations resulting in a structure factor with a hole in the center and a surrounding pronounced ring of higher amplitude. When a structure factor becomes zero at the origin, the structure is also called hyperuniform.

deduced directly from real-space representations such as SEM images from N particle positions r:

$$S(q) = \frac{1}{N} \sum_{i,j}^{N} e^{-iq \cdot (r_i - r_j)}$$

Using the structure factor provides a first approach to distinguishing different degrees of order. One possible categorization is shown in Fig. 9.16. A perfectly periodical arrangement of scattering elements corresponds to a photonic crystal exhibiting a sharply peaked structure factor which can be entirely described by the reciprocal lattice. The other extreme is represented by a completely random structure with a Poisson distribution of elements. Neighboring elements can have any separation distance and agglomeration of several elements is also allowed. Since they do not contain any element of order the structure factor is a random noisy pattern. Good examples of such ensembles of scatterers are dust or water droplets (fog) in air. In between these two extreme cases, a regime exists in which the distances between neighboring elements is
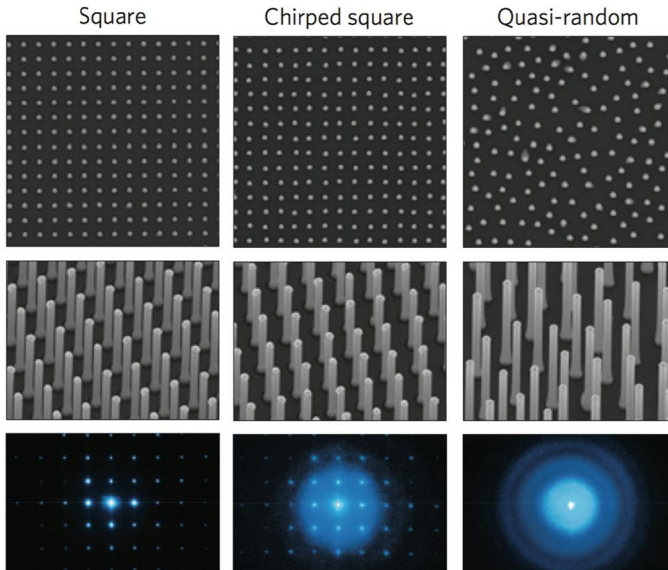
Figure 9.17 Top and middle row: Scanning electron micrographs of different arrangements of Si nanowire arrays: Periodic square (left), periodic square with slight variation of position (middle), and quasi-random (right). Bottom row: Corresponding transmitted diffraction patterns. Figure reprinted with permission from [61].

more or less well defined. The point pattern is neither completely random nor periodic, but a correlation still exists. Correlated disorder can be compared to the amorphous structure of atoms in glasses where the length of the chemical bonds determines the distance between atoms but the angles between the bonds can vary. A special case occurs when the structure factor becomes zero at the origin. Then long-range correlations are completely suppressed and the pattern is called hyperuniform [58–60]. Some interesting properties of the hyperuniform case will be described later in this chapter.

Fig. 9.17 shows real-space images together with the corresponding diffraction patterns of different two-dimensional arrangements of Si nanowires. In the case of an almost perfect square lattice (left column), light that is impinging perpendicularly to the plane of the sample is scattered only into the diffraction orders as prescribed by Bragg's law. As slight variations of the positions of the scatterers are introduced (center panel), the diffractions peaks are broadened, which is particularly visible for the zeroth diffraction order that is showing a large circle of diffusely scattered light. This phenomenon originates from the deviation of the nanowire positions from the ideal lattice positions. The disorder adds a whole range of additional lateral k-vectors to the ones of the strictly periodic case. Thus, coupling of slab modes to more modes of the free space continuum than it is possible for the (almost) ideal arrangement is enabled. As a consequence, each diffraction mode propagating into free space becomes blurred, i.e. broadened, due to Bragg's condition transitioning from a set of only a few strictly defined k-values into sets of ranges of k-values. When the disorder

increases towards randomness, any long-range order is eventually lost and no translational symmetry exists. Then collective interference effects of scattered light such as the appearance of diffraction orders vanish and only diffusely scattered light is emitted. This case is shown in Fig. 9.17 (right panel). The scatterers are randomly arranged and the diffraction peaks have been replaced by a broad, polar angle independent, scattering pattern.

9.5.1 Exploiting disorder

Disorder is mostly considered detrimental for applications which require working in narrow spectral ranges, such as transmissive or reflective filters. However, in the past decade there has been interest in disorder to the extent it can be beneficial for applications that deal with a broad spectral range [62–64]. A high efficiency solar cell intrinsically calls for a broadband approach. Besides antireflection, an important optical property that a thin film solar cell should have is light trapping. Light trapping is the ability to keep light that is only weakly absorbed inside the absorber material to prolong its effective light path and thus increase the probability of absorbing the light.

Historically, means to achieve light trapping in crystalline silicon solar cells were either based on structures operating solely in the ray-optics regime, such as several micron sized pyramids in monocrystalline silicon solar cells, or random surface structures fabricated by wet-etching to achieve strong scattering. The rise of nanotechnology has enabled the investigation of photonic nanostructures to enhance light trapping in solar cells. Although research was extensive, strictly periodic structures could seldom outperform conventional state-of-the-art light trapping structures. The recurring issue was the conflict between the limited bandwidth of strictly periodic structures and the large spectral width of sunlight to be converted.

Only in recent years have researchers started to look into intentionally introduced disorder in periodic structures to tackle this conflict by aiming for a more broadband diffraction response while still retaining distinct diffraction orders. In one example, Bittkau et al. numerically evaluated and compared the potential light trapping performance of a strictly periodic 2D structure to the light trapping performance of structures with either position disorder or scatterer size disorder [65]. Their platform was a thin film amorphous silicon solar cell (see Fig. 9.18A) in which the absorber material itself was structured. The Fourier transform of the pattern in real space (Fig. 9.18B) reveals that disorder significantly diffusively broadens the range of k-vectors made available by the structure. Since the absorber layer is rather thin and light propagates in this layer as distinct waveguide modes, this leads to a broadening of the spectral width of these waveguide modes as well. Both effects lead to a much better coupling of incoming light into the absorber layer and thus increased absorption. In their work, disorder is characterized by the standard deviation σ of the position (deviation from strict periodic case) or radius (of the scatterer) that is varied according to a Gaussian distribution. In Fig. 9.18C the short-circuit current density J_{SC}, which is essentially the absorption weighted and integrated over the sun spectrum, in dependence of σ is plotted. It is obvious that disorder indeed increases J_{SC} and the effect is stronger
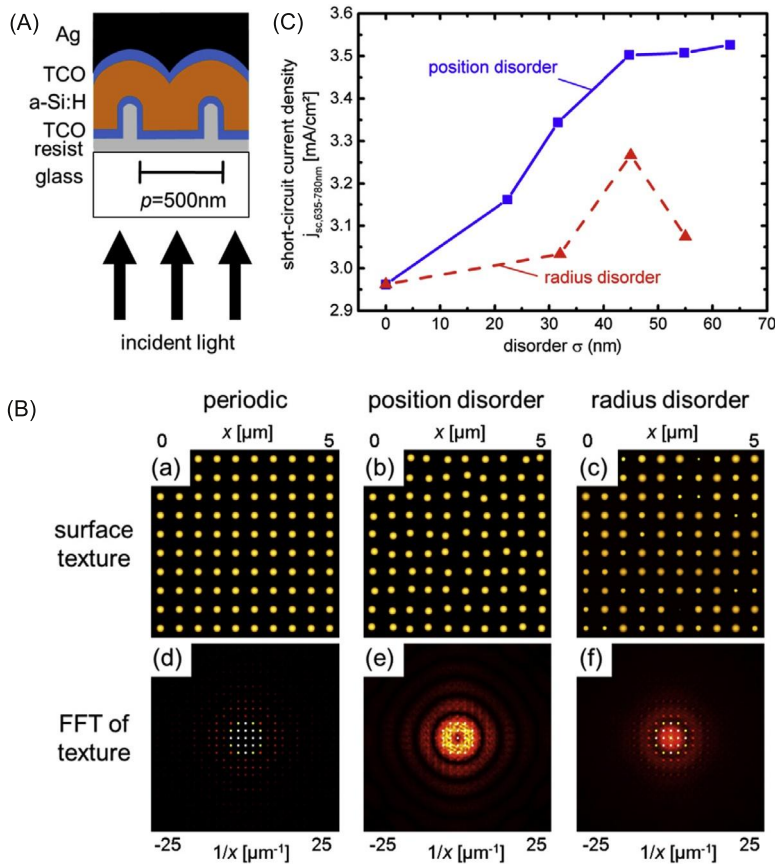
Figure 9.18 (A) Sketch of a thin film amorphous silicon solar cell. (B) Patterning of the solar cell in real space (top) and Fourier space (bottom). (C) Short-circuit current density of the patterned cell in dependence of the disorder. Sigma = 0 is the strictly periodic case. Figure reprinted with permission from Ref. [65].

for position disorder than for radius disorder. In the case of the position disorder, the improvement of J_{SC} can be explained by significant diffuse wave vector transfer. The Fourier transforms of the topographies show the strongest diffuse part in the case of the position disorder. The increase of J_{SC} in the case of the radius disorder is due to a broadening of the waveguide mode. Here, the Fourier transforms of the textures have only a weak diffuse part. Furthermore, since the local layer thickness depends on the scatterer radius (assuming isotropic growth of the amorphous silicon layer), the layer thickness varies strongly from unit cell to unit cell. Thus, the individual resonances of the scatterers of each unit cell are modified as well. If the increase of radius disorder is too large, the waveguide modes are strongly disturbed because the differences between the individual resonances become too large to form an extended optical mode within the layer. As a result, J_{SC} decreases for larger radius disorder.

9.5.2 Correlated disorder

Photonic structures with point patterns of correlated disorder, i.e. without any translational symmetry as a periodic pattern nor entirely random as a Poisson distribution, are currently an active research field as they bear the potential of a whole new class of optical materials. Since correlations lead to certain features in the spectrum of the structure factor, novel ways to manipulate k-space are enabled. In terms of optics, to mention one simple example, one could bring together the advantages of periodic and entirely disordered structures, i.e., enable a strong, grating-like but spectrally broadband and azimuth-angle independent diffraction.

On small scales, e.g. for proof-of-principle structures, fabrication of correlated disorder patterns can easily be accomplished by lithographic means [66,67]. Only in very few works the large-scale fabrication of correlated disorder samples has been investigated [68]. An attractive technique to obtain 2D patterns of correlated disorder on large-scale samples is the colloidal deposition as demonstrated by Piechulla et al. [68]. In their work, they exploit the fact that suspended colloids made of PMMA or PS are usually charged for stabilization purposes. When these colloids adsorb onto a substrate repulsive electrostatic forces lead to more or less well defined mean distances between the colloidal particles which can be finely tuned though the amount of ions present in the suspension. This process is self-organized and thus homogeneous and large-scale areas can be fabricated; see Fig. 9.19 for a macroscopic (A) and microscopic (B) view and (C) for the evaluation of the next neighbor interparticle distances histograms for different ionic strengths of the colloidal suspension.

Interestingly, light scattered off such an arrangement of colloids clearly shows a chromatic dispersion (Fig. 9.19A) which one would not expect from a truly random pattern. This is due to the correlations, i.e. the near-range order, which is in contrast to a truly random pattern that would scatter light isotropically and appear white to the eye. Therefore, constructive and destructive interference of light scattered by close-by particles takes place and enhanced and suppressed scattering occurs in analogy to diffraction orders of a strictly periodic pattern. However, there are two distinct differences. One is that diffraction now is rotational symmetric due to the isotropic arrangement of scatterers. The other one being the fact that there is not one discrete next neighbor distance but a distribution of next neighbor distances leading to a strong broadening of the diffraction peak. This can also be observed in the diffraction pattern using only a single wavelength in Fig. 9.19F.

In Fig. 9.19D, the 2D representation ($q = q_x e_x + q_y e_y$) of the structure factor $S(q)$ of a typical sample is plotted. Due to the isotropic nature of the pattern in real space, the structure factor is invariant to rotation. Therefore, the structure can be angularly averaged over all q of the same length as shown in Fig. 9.19E. With the help of the structure factor one can easily recognize the correlations present in the pattern. E.g., the oscillating behavior of $S(q)$ visualizes that each element has a similar distance to its next neighbor. Low values of $S(q)$ for low q's indicate that there are no to little long-range correlations, such as translational symmetry. Furthermore, since the structure factor essentially describes the additional momentum $\mathbf{q}$ a certain pattern can add to a light wave with incident wave vector $\mathbf{k}$, it resembles the scattering/diffraction
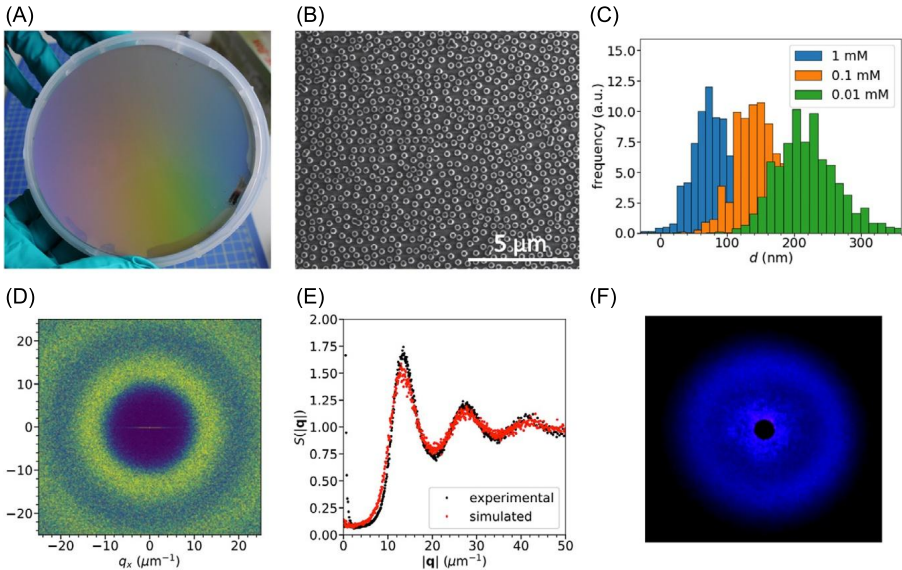
Figure 9.19 (A) Large-scale homogeneous deposition of colloids into an arrangement of correlated disorder onto a 4-inch silicon wafer. (B) SEM image of the colloids. (C) Nearest neighbor distance histogram of samples prepared with different ionic strengths of the suspension. (D) Structure factor and (E) radially averaged structure factor. The black circular area in the center is due to a beam block for nonscattered light. (F) Reprinted with permission from Ref. [68].

pattern. This can be seen when comparing the structure factor shown in Fig. 9.19E with the photographed scattering pattern shown in Fig. 9.19F. In the simplified case that near-field interaction between neighboring particles and multiple scattering can be neglected, the scattering pattern $I(k_\parallel)$ of a sample of correlated disorder can easily be calculated by multiplying the structure factor $S(q = k_\parallel)$ with the scattering pattern of the individual element of the pattern $I_0(k_\parallel)$.

A mathematical framework to describe and categorize correlated disorder is the concept of hyperuniformity as introduced by Torquato [58,59,69,70]. Hyperuniform point patterns in d-dimensional space are characterized such that the number variance $\sigma_N^2(R) \equiv \langle N(R)^2 \rangle - \langle N(R) \rangle^2$ of points within a spherical sampling window of growing radius R increases less than R^d (the volume of the window) for large R. In other words, density fluctuations are suppressed on larger scales. This statement is equivalent to the structure factor approaching zero for $q \to 0$, i.e. $S(q \to 0) = 0$. Furthermore, disordered hyperuniform structures are called 'stealthy' hyperuniform when $S = 0$ not only for $q \to 0$ but for a range q's $[q \to 0, q_0]$. Truly random patterns are not hyperuniform as they possess no correlations and their window volume scaling is $\sigma_N^2(R) \sim R^d$ and the structure factor stays essentially constant for all q. On the other hand, all periodic and quasiperiodic patterns and thus photonic crystals are trivially hyperuniform as then $\sigma_N^2(R) \sim R^{d-1}$ and their structure factor only reveals delta peaks. Interestingly, there exist a class of disordered systems which meet the requirement of hyperuniformity.
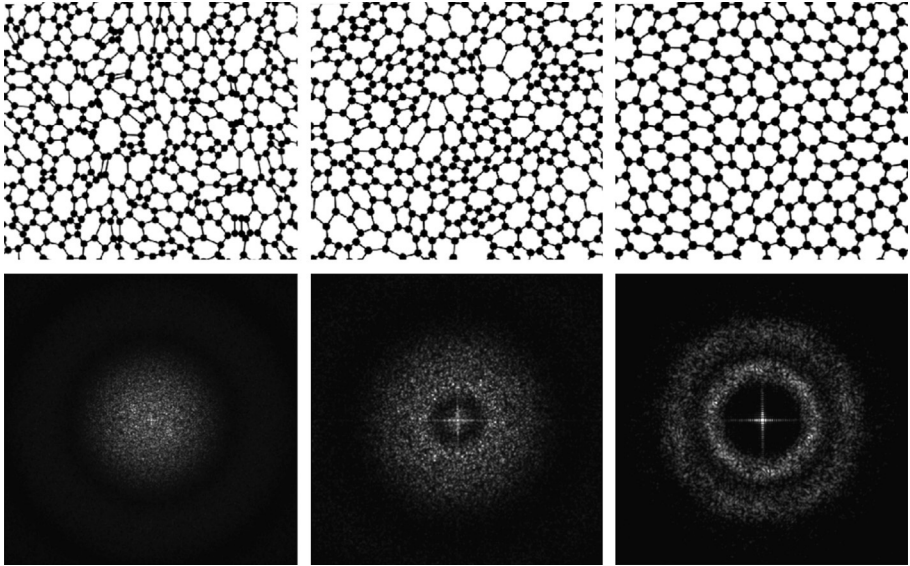
Figure 9.20 Point patterns (top) and their corresponding structure factor S (bottom). Left: Poisson random pattern. Middle: Disordered pattern with some geometric order but still $S > 0$ for $q \rightarrow 0$. Right: Disordered hyperuniform point pattern. Reprinted with permission from [71].

Several algorithms have been introduced to generate disordered hyperuniform point patterns based on conjugate gradient methods or Delaunay triangulation [71]. Examples to visualize different disordered point patterns are shown in Fig. 9.20. On the left, a random point pattern based on a Poisson distribution is plotted; the structure factor does not reveal any correlations. Shifting the point positions such that the distance between the points becomes more homogeneous, the structure factor decreases around the origin, as number density fluctuations are lowered, though not completely suppressed as still $S > 0$ holds (center). On the right hand side, the point positions have been shifted in such a way that long-range density fluctuations are completely suppressed and thus the structure factor is zero around the origin; this point pattern is stealthy hyperuniform. Comparing these three structures, it is clearly visible by eye that for the hyperuniform structure the point distribution is much more homogeneous than for the other patterns. Nevertheless, the pattern is still disordered and isotropic, i.e. it has no translational symmetry.

Stealthy hyperuniform disordered media operating in the stealthy regime (where $S(q) = 0$) will behave like a periodic medium operating in the frequency range below the first Bragg resonance. Since no additional k-values are provided in these regimes, no scattering of light waves will occur, i.e. the disordered hyperuniform medium acts like a periodic medium with sub-wavelength grating constant, which is in stark contrast to a non-hyperuniform disordered medium. So the light could be still confined to a hyperuniformly structured waveguide layer avoiding out-of plane scattering losses. The loss-less propagation of light within the planar structure would basically be pro-
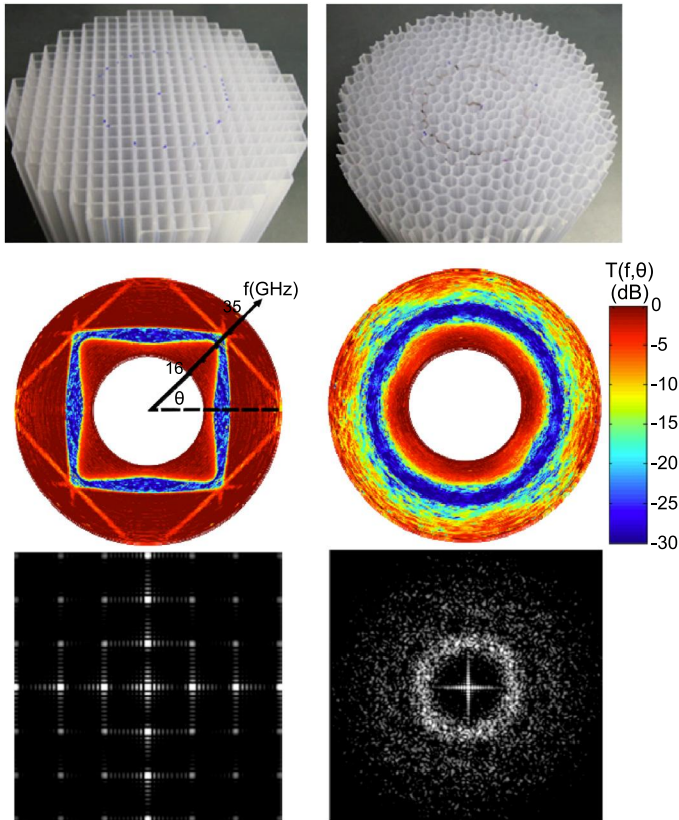
Figure 9.21 Top panel: Photograph of samples made of plastic fabricated by stereo lithography (height 100 mm). Middle panel: Contour plots (top) in polar coordinates of the measured transmission as a function of frequency (15–35 MHz). Bottom panel: Corresponding structure factors. Left hand side: Square lattice. Right hand side: disordered hyperuniform structure. Reprinted with permission from [72].

tected by the central "hole" in the Fourier-space/structure factor which is characteristic for hyperuniform structures.

At higher frequencies hyperuniform materials also offer interesting properties. It can be shown theoretically, as well as experimentally, that even disordered media (i.e. Bragg reflection does not occur) can reveal photonic band gaps when they meet the condition of hyperuniformity [71–73]. Florescu et al. impressively demonstrated the existence of photonic band gaps in disordered media in the microwave regime as shown in Fig. 9.21. Angularly resolved transmission spectra clearly reveal the existence of a stop band (blue region) for which no incoming waves are allowed to propagate through the structure. Furthermore, since the disordered structure is isotropic, the stop band is isotropic as well and thus is always equivalent to the band gap enabling e.g. the implementation of arbitrarily bent waveguides [73].

The precise mechanisms of band gap formation in disordered hyperuniform media is still a matter of investigation [74]. Nevertheless, research on this new class

of disordered photonic material is currently very active. For example, Scheffold et al. demonstrated a three-dimensional hyperuniform photonic structure [67]. A disordered medium being transparent for a certain frequency band but opaque for other frequency was also realized [75]. Finally, findings on hyperuniform structures are not restricted to photonics but apply to any type of wave propagating in a structured medium, such as phononics [76].

Overall the research on correlated disorder for photonics and the ability to fabricate such structures is still in its infancy. Correlated disorder and actively tailored disorder represent a new tool for tailored photonics. Furthermore, the patterns fabricated using methods such as colloidal particles allow for relatively easy fabrication of extended disordered metamaterials and could also serve as a template, for example, for subsequent etching or deposition processes, to imprint the disordered pattern into other materials. Preparing scatterers based on plasmonic metals or high-refractive-index materials with more pronounced resonances would lead to stronger scattering intensities and could open the door to realizing angular scattering patterns which have not been explored to date.

9.6   Conclusion

Although in the non-resonant, long wavelength regime, the dramatic effects on phase shifts, transmission and reflection attributed to Mie resonances are absent, it offers another powerful advantage: the flexibility for a robust and broadband index engineering. Using constituent materials with high refractive indices like silicon allow for a wide range of effective dielectric constants and index values to be obtained by controlling the filling fraction of the subwavelength structures. Furthermore a strong form birefringence can be created by shaping the subwavelength elements into anisotropic structures such as layers or rods. These can then be arranged to create artificial birefringence values not seen in nature – and not only for a single frequency but in the whole long wavelength range. The ability to control the effective index in a plane offers the possibility to create a planar GRIN-photonic platforms for realizing lenses, phase plates, and cloaking devices. The use of effective indices in subwavelength grating waveguides allows a much larger flexibility for mode matching and dispersion engineering. New waveguide concepts employing metamaterial claddings have been realized for enhancing mode confinement and minimizing bending losses and cross-talk. In general, the concept of metamaterials is not bound to periodic structures, although most of the investigated designs have employed a periodic lattice. In the future systems with a controlled disorder, such as hyperuniform disorder, ensembles of scattering elements may become interesting. These structures relax the requirements for nanofabrication opening the door to large-scale 3D dielectric metamaterials employing bottom up self-ordering techniques. Although ohmic losses might be avoided in such metamaterials, when loss-free components are used, the level of scattering losses due to disorder needs to be further investigated. This can still lead to a large extinction of a propagating wave especially for wavelengths close to the Mie resonances [77].

References

[1] M.V. Rybin, D.S. Filonov, K.B. Samusev, P.A. Belov, Y.S. Kivshar, M.F. Limonov, Nat. Commun. 6 (2015) 1.

[2] J.D. Jackson, Classical Electrodynamics, 3rd ed., John Wiley & Sons, Inc., 1999.

[3] A. Sihvola, Electromagnetic Mixing Formulas and Applications, The Institution of Electrical Engineers, London, 1999.

[4] S. Johnson, J. Joannopoulos, Opt. Express 8 (2001) 173.

[5] C.F. Bohren, D.R. Huffman, Absorption and Scattering of Light by Small Particles, John Wiley & Sons, Inc., 2008.

[6] L.A. Golovan', P.K. Kashkarov, V.Y. Timoshenko, Crystallogr. Rep. 52 (2007) 672.

[7] T. Zakri, J. Laurent, M. Vauclin, 2014.

[8] A. Alù, Phys. Rev. B, Condens. Matter Mater. Phys. 84 (2011) 1.

[9] K. Mnasri, A. Khrabustovskyi, C. Stohrer, M. Plum, C. Rockstuhl, Phys. Rev. B 97 (2018) 1.

[10] D.R. Smith, S. Schultz, P. Markoš, C.M. Soukoulis, Phys. Rev. B, Condens. Matter Mater. Phys. 65 (2002) 1.

[11] C.R. Simovski, J. Opt. 13 (2011).

[12] J. Kanungo, J. Schilling, Appl. Phys. Lett. 97 (2010) 2008.

[13] J. Schilling, J. Kanungo, in: Proc. SPIE 7711, Metamaterials V, 2010, 77111T, 7 pp.

[14] J. Schilling, R.B. Wehrspohn, a Birner, F. Muller, R. Hillebrand, U. Gosele, S.W. Leonard, J.P. Mondia, F. Genereux, H.M. van Driel, P. Kramper, V. Sandoghdar, K.C.N.-B. Busch, J. Opt. A, Pure Appl. Opt. 3 (2001) S121.

[15] J. Valentine, J. Li, T. Zentgraf, G. Bartal, X. Zhang, Nat. Mater. 8 (2009) 568.

[16] M. Gharghi, C. Gladden, T. Zentgraf, Y. Liu, X. Yin, J. Valentine, X. Zhang 2825 (2011).

[17] A. Di Falco, S.C. Kehr, U. Leonhardt, Opt. Express 19 (2011) 5156.

[18] J. Hunt, T. Tyler, S. Dhar, Y. Tsai, P. Bowen, S. Larouche, N.M. Jokerst, D.R. Smith, Opt. Express 20 (2012) 1706.

[19] L.H. Gabrielli, D. Liu, S.G. Johnson, M. Lipson, Nat. Commun. 3 (2012) 1217.

[20] B.T. Zentgraf, J. Valentine, N. Tapia, J. Li, Adv. Mater. 22 (2010) 2561.

[21] L.H. Gabrielli, J. Cardenas, C.B. Poitras, M. Lipson, Nat. Photonics 3 (2009) 461.

[22] L.H. Gabrielli, M. Lipson, J. Opt. 13 (2011) 024010.

[23] V.A. Tamma, J. Blair, C.J. Summers, W. Park, Opt. Express 18 (2010) 25746.

[24] D.H. Spadoti, L.H. Gabrielli, C.B. Poitras, M. Lipson, Opt. Express 18 (2010) 3181.

[25] U.D. Zeitner, E.-B. Kley, A. Tünnermann, Opt. Photonik 46 (2010).

[26] P.R. West, J.L. Stewart, A.V. Kildishev, V.M. Shalaev, V.V. Shkunov, F. Strohkendl, Y.A. Zakharenkov, K. Robert, R. Byren, Opt. Express 22 (2014) 26212.

[27] S. Park, K. Lee, D. Han, J. Ahn, K. Jeong, S. Park, K. Lee, D. Han, J. Ahn, K. Jeong, Appl. Phys. Lett. 105 (2016) 091101.

[28] A. Niv, G. Biener, V. Kleiner, E. Hasman, Opt. Express 14 (2006) 4208.

[29] D. Lin, P. Fan, E. Hasman, M.L. Brongersma, Science (80–.) 345 (2014) 298.

[30] M. Khorasaninejad, A. Ambrosio, P. Kanhaiya, F. Capasso, Sci. Adv. 2 (2016) e1501258.

[31] E. Arbabi, A. Arbabi, S.M. Kamali, Y. Horie, A. Faraon, Optica 3 (2016) 628.

[32] P. Lalanne 16 (1999) 2517.

[33] A. Arbabi, Y. Horie, M. Bagheri, A. Faraon, Nat. Nanotechnol. 10 (2015) 937.

[34] A.Y. Piggott, J. Lu, K.G. Lagoudakis, J. Petykiewicz, T.M. Babinec, J. Vučković, Nat. Photonics 9 (2015) 374.

[35] P. Cheben, D.-X. Xu, S. Janz, A. Densmore, Opt. Express 14 (2006) 4695.

[36] P.J. Bock, P. Cheben, J.H. Schmid, J. Lapointe, A. Delâge, S. Janz, G.C. Aers, D.X. Xu, A. Densmore, T.J. Hall, Opt. Express 18 (2010) 20251.

[37] P. Cheben, P.J. Bock, J.H. Schmid, J. Lapointe, S. Janz, D.-X. Xu, A. Densmore, A. Delâge, B. Lamontagne, T.J. Hall, Opt. Lett. 35 (2010) 2526.

[38] R. Halir, P. Cheben, J.M. Luque-González, J.D. Sarmiento-Merenguel, J.H. Schmid, G. Wangüemert-Pérez, D.X. Xu, S. Wang, A. Ortega-Moñux, Í. Molina-Fernández, Laser Photonics Rev. 10 (2016) 1039.

[39] S. Jahani, S. Kim, J. Atkinson, J.C. Wirth, F. Kalhor, A. Al Noman, W.D. Newman, P. Shekhar, K. Han, V. Van, R.G. Decorby, L. Chrostowski, M. Qi, Z. Jacob, Nat. Commun. 9 (2018).

[40] P. Markov, J.G. Valentine, S.M. Weiss 20 (2012) 14705.

[41] P. Cheben, J.H. Schmid, S. Wang, D.-X. Xu, M. Vachon, S. Janz, J. Lapointe, Y. Painchaud, M.-J. Picard, Opt. Express 23 (2015) 22553.

[42] P.J. Bock, P. Cheben, J.H. Schmid, J. Lapointe, A. Delâge, D. Xu, S. Janz, A. Densmore, T.J. Hall, Opt. Express 18 (2010) 16146.

[43] R. Halir, A. Ortega-mo, J.H. Schmid, C. Alonso-ramos, J. Lapointe, D. Xu, J.G. Wanguemert-Perez, I. Molina-Fernandez, S. Janz, IEEE J. Sel. Top. Quantum Electron. 20 (2014) 8201313.

[44] P. Cheben, R. Halir, J.H. Schmid, H.A. Atwater, D.R. Smith, Nature 560 (2018) 565.

[45] L.H. Frandsen, Y. Elesin, L.F. Frellsen, M. Mitrovic, Y. Ding, O. Sigmund, K. Yvind, Opt. Express 22 (2014) 8525.

[46] P.I. Borel, B. Bilenberg, L.H. Frandsen, T. Nielsen, J. Fage-Pedersen, A.V. Lavrinenko, J.S. Jensen, O. Sigmund, A. Kristensen, Opt. Express 15 (2007) 1261.

[47] B. Shen, P. Wang, R. Polson, R. Menon, Nat. Photonics 9 (2015) 378.

[48] T. Ergin, N. Stenger, P. Brenner, J.B. Pendry, M. Wegener 328 (2010) 337.

[49] J. Fischer, T. Ergin, M. Wegener, Opt. Lett. 36 (2011) 2059.

[50] A. Luque, S. Hegedus (Eds.), Handbook of Photovoltaic Science and Engineering, 2nd ed., Wiley, 2011.

[51] W.H. Southwell, Opt. Lett. 8 (1983) 584.

[52] M. Otto, M. Algasinger, H. Branz, B. Gesemann, T. Gimpel, K. Füchsel, T. Käsebier, S. Kontermann, S. Koynov, X. Li, V. Naumann, J. Oh, A.N. Sprafke, J. Ziegler, M. Zilk, R.B. Wehrspohn, Adv. Opt. Mater. 3 (2015) 147.

[53] K. Füchsel, M. Kroll, T. Käsebier, M. Otto, T. Pertsch, E.-B. Kley, R.B. Wehrspohn, N. Kaiser, A. Tünnermann, Proc. SPIE 8438 (2012) 84390M.

[54] A. Ingenito, O. Isabella, M. Zeman, ACS Photonics 1 (2014) 270.

[55] J. Oh, H. Yuan, H. Branz, Nat. Nanotechnol. 7 (2012) 743.

[56] H. Savin, P. Repo, G. von Gastrow, P. Ortega, E. Calle, M. Garín, R. Alcubilla, Nat. Nanotechnol. 10 (2015) 624.

[57] B. Beetz, PV Mag. (2017).

[58] S. Torquato, Phys. Rep. 745 (2018) 1.

[59] S. Torquato, Phys. Rev. E 94 (2016) 022122.

[60] G. Zhang, F.H. Stillinger, S. Torquato, Sci. Rep. 6 (2016) 1.

[61] M.D. Kelzenberg, S.W. Boettcher, J.A. Petykiewicz, D.B. Turner-Evans, M.C. Putnam, E.L. Warren, J.M. Spurgeon, R.M. Briggs, N.S. Lewis, H.A. Atwater, Nat. Mater. 9 (2010) 239.

[62] P.D. García, R. Sapienza, C. Toninelli, C. López, D.S. Wiersma, Phys. Rev. A – At. Mol. Opt. Phys. 84 (2011) 1.

[63] U.W. Paetzold, M. Smeets, M. Meier, K. Bittkau, T. Merdzhanova, V. Smirnov, D. Michaelis, C. Waechter, R. Carius, U. Rau, Appl. Phys. Lett. 104 (2014).

[64] M.F. Schumann, S. Wiesendanger, J.C. Goldschmidt, B. Bläsi, K. Bittkau, U.W. Paetzold, A. Sprafke, R.B. Wehrspohn, C. Rockstuhl, M. Wegener, Optica 2 (2015) 850.

[65] K. Bittkau, A. Hoffmann, U. Paetzold, R. Carius, Appl. Sci. 7 (2017) 725.

[66] M. Castro-Lopez, M. Gaio, S. Sellers, G. Gkantzounis, M. Florescu, R. Sapienza, APL Photonics 2 (2017) 061302.

[67] J. Haberko, N. Muller, F. Scheffold, Phys. Rev. A – At. Mol. Opt. Phys. 88 (2013) 1.

[68] P.M. Piechulla, L. Mühlenbein, R.B. Wehrspohn, S. Nanz, A. Abass, C. Rockstuhl, A. Sprafke, Adv. Opt. Mater. 1701272 (2018).

[69] S. Torquato, J. Chem. Phys. 149 (2018).

[70] S. Torquato, F.H. Stillinger, Phys. Rev. E 68 (2003) 041113.

[71] M. Florescu, S. Torquato, P.J. Steinhardt, Proc. Natl. Acad. Sci. 106 (2009) 20658.

[72] W. Man, M. Florescu, K. Matsuyama, P. Yadak, G. Nahal, S. Hashemizad, E. Williamson, P. Steinhardt, S. Torquato, P. Chaikin, Opt. Express 21 (2013) 19972.

[73] W. Man, M. Florescu, E.P. Williamson, Y. He, S.R. Hashemizad, B.Y.C. Leung, D.R. Liner, S. Torquato, P.M. Chaikin, P.J. Steinhardt, Proc. Natl. Acad. Sci. USA 110 (2013) 15886.

[74] L.S. Froufe-Pérez, M. Engel, J.J. Sáenz, F. Scheffold, Proc. Natl. Acad. Sci. 114 (2017) 9570.

[75] O. Leseur, R. Pierrat, R. Carminati, Optica 3 (2015) 763.

[76] G. Gkantzounis, T. Amoah, M. Florescu, Phys. Rev. B 95 (2017) 1.

[77] F.J. Valdivia-Valero, M. Nieto-Vesperinas, Photonics Nanostruct. Fundam. Appl. 10 (2012) 423.

Index

Dielectric Metamaterials: Fundamentals, Designs, and Applications links fundamental Mie scattering theory with the latest dielectric metamaterial research, providing a valuable reference for new and experienced researchers in the field.

The book begins with a historical, evolving overview of Mie scattering theory. Next, the authors describe how to apply Mie theory to analytically solve the scattering of electromagnetic waves by subwavelength particles. Later chapters focus on Mie resonator-based metamaterials, starting with microwaves where particles are much smaller than the free space wavelengths. In addition, several chapters focus on wave-front engineering using dielectric metasurfaces, nonlinear optical effects, spontaneous emission manipulation, active devices, and 3D effective media using dielectric metamaterials.

Dielectric Metamaterials: Fundamentals, Designs, and Applications is a valuable volume for academics ranging from graduate students to established academic in Materials Science, Electrical Engineering and Physics departments who are researching metamaterials, as well as for professionals in the industry sector such as scientists and engineers in the semiconductor and photonics industry.

Key features

- Highlights a crucial link in between fundamental Mie scattering theory and with the latest dielectric metamaterial research spanning materials, design and applications
- Includes coverage of wave-front engineering and 3D metamaterials
- Provides computational codes for calculating and simulating Mie resonances

Editor bios

Dr. Igal Brener is a Senior Scientist at Sandia National Laboratories in Albuquerque, New Mexico. He has made pioneering contributions to semiconductor physics, terahertz science and technology, fiber telecommunications, metamaterials and nanophotonics.

Dr. Sheng Liu is currently an Optical Engineer at Apple Inc. and was previously a Senior Member of Technical Staff at Sandia National Laboratories. Dr. Liu has years of technical expertise in the design and simulation of optical and photonic devices and systems.

Dr. Isabelle Staude is a Junior Professor at the Institute of Applied Physics and the Abbe Center of Photonics at Friedrich-Schiller-University Jena, where she leads a research group on functional photonic nanostructures.

Dr. Jason Valentine is an Associate Professor in at the Mechanical Engineering Department at Vanderbilt University, where his research focuses on nanoscale optics and materials, including dielectric metamaterials.

Dr. Christopher Holloway is a Research Engineer at the National Institute of Standards and Technology in Boulder, Colorado where he works on electromagnetic theory.